量子化学計算における
Linear-Scaling 法の開発とその応用

（研究課題番号：１４７０３００５）

平成１４年度～平成１６年度科学研究費補助金

（若手研究（A））研究成果報告書

平成１７年３月

代表研究者　　中井　浩巳

（早稲田大学 理工学術院 教授）

研　究　組　織、　研　究　経　費

研究組織

研究代表者：　中井　浩巳　（早稲田大学 理工学術院 教授）

研究経費

平成１４年度	１１，４００千円
設備備品	７，６００千円
消耗品	５００千円
国内旅費	１，５００千円
外国旅費	５００千円
謝金	５００千円
その他	８００千円
平成１５年度	７，１００千円
設備備品	４，７００千円
消耗品	５００千円
国内旅費	５００千円
外国旅費	５００千円
謝金	３００千円
その他	６００千円
平成１６年度	３，６００千円
設備備品	１，５００千円
消耗品	５００千円
国内旅費	７２０千円
外国旅費	２８０千円
謝金	４００千円
その他	２００千円
計	２２，１００千円

研　究　発　表

（1）学会誌等

1) H. Nakai, "Energy density analysis with Kohn-Sham orbitals", *Chem. Phys. Lett.*, **363** (1-2), 73-79 (2002).

2) H. Nakai, Y. Yamauchi, A. Matsuda, Y. Okada, and K. Takeuchi, "*Ab initio* MD simulation of collision reaction between ammonia cluster ion and ammonia monomer", *J. Mol. Struct. (THEOCHEM)*, **592** (1-3), 61-67 (2002).

3) H. Nakai and K. Sodeyama, "Energy density analysis (EDA) of *cis*, *trans*-enol isomerization in malonaldehyde, tropolone, and 9-hydroxyphenalenone", *Chem. Phys. Lett.*, **365** (3-4), 203-210 (2002).

4) K. Itoh, T. Kiyohara, H. Shinohara, C. Ohe, Y. Kawamura, and H. Nakai, "DFT calculation analysis of the infrared spectra of ethylene adsorbed on Cu(110), Pd(110) and Ag(110)", *J. Phys. Chem. B*, **106** (41), 10714-10721 (2002).

5) H. Nakai and K. Sodeyama, "Many-body effects in nonadiabatic molecular theory for simultaneous determination of nuclear and electronic wave functions: *Ab initio* NOMO/ MBPT and CC methods", *J. Chem. Phys.*, **118** (3), 1119-1127 (2003).

6) Y. Kawamura and H. Nakai, "Energy density analysis of internal methyl rotations in halogenated toluenes", *Chem. Phys. Lett.*, **368** (5-6), 673-679 (2003).

7) Y. Kawai, S. Yamaguchi, Y. Okada, K. Takeuchi, Y. Yamauchi, S. Ozawa, and H. Nakai, "Reactions of protonated water clusters $H^+(H_2O)_n$ (n = 1-6) with dimethylsulfoxide in a guided ion beam apparatus", *Chem. Phys. Lett.*, **377** (1-2), 69-73 (2003).

8) H. Nakai, Y. Yamauchi, A. Nakata, T. Baba, and H. Takahashi, "*Ab initio* molecular dynamics study on the excitation dynamics of psoralen compounds", *J. Chem. Phys.*, **119** (8), 4223-4228 (2003).

9) H. Nakai and K. Sodeyama, "Energy density analysis (EDA) of proton transfer reactions in malonaldehyde, tropolone, and 9-hydroxyphenalenone", *J. Mol. Struct. (THEOCHEM)*, **637** (1-3), 27-35 (2003).

10) T. Homma, A. Tamaki, H. Nakai, and T. Osaka, "Molecular orbital study on the reaction process of dimethylamine borane as a reductant for electroless deposition", *J. Electroanalytical Chem.*, **559**, 131-136 (2003).

11) S. Yamaguchi, S. Kudoh, Y. Okada, T. Orii, K. Takeuchi, T. Ichikawa, and H. Nakai, "Size-dependent reaction cross section of protonated water clusters $H^+(H_2O)_n$ (n = 2-11) with D_2O", *J. Phys. Chem. A*, **107** (50), 10904-10910 (2003).

12) A. Nakata, T. Baba, H. Takahashi, and H. Nakai, "Theoretical study on the excited

states of psoralen compounds bonded to a thymine residue", *J. Comp. Chem.*, **25** (2), 179-188 (2004).

13) H. Nakai and M. Kobayashi, "New algorithm for the rapid evaluation of electron repulsion integrals: elementary basis algorithm", *Chem. Phys. Lett.*, **388** (1-3), 50-54 (2004).

14) T. Shimada, I. Komatsu, T. Homma, H. Nakai, and T. Osaka, "*Ab initio* molecular orbital study of the electron emission mechanism of $TiCl_3$ as a reductant for an electroless deposition process", *Electrochemistry*, **72** (6), 462-465 (2004).

15) M. Kobayashi and H. Nakai, "New recurrence relations for the rapid evaluation of electron repulsion integral based on accompanying coordinate expansion formula", *J. Chem. Phys.*, **121** (9), 4050-4058 (2004).

16) H. Nakai, M. Katouda, and Y. Kawamura, "Energy density analysis of cluster size dependence of surface-molecule interactions: H_2, C_2H_2, C_2H_4, and CO adsorption onto Si(100)-(2×1) surface", *J. Chem. Phys.*, **121** (10), 4893-4900 (2004).

17) Y. Kawamura and H. Nakai, "A hybrid approach combining energy density analysis with the interaction energy decomposition method", *J. Comput. Chem.*, **25** (15), 1882-1887 (2004).

18) Y. Yamauchi, H. Nakai, and Y. Okada, "Short-time Fourier transform analysis of *ab initio* molecular dynamics simulation: collision reaction between $NH_4^+(NH_3)_2$ and NH_3", *J. Chem. Phys.*, **121** (22), 11098-11103 (2004).

19) H. Nakai and T. Baba, "Theoretical study on excitation dynamics of 5-Dibenzosuberene and its derivatives", *J. Mol. Struct.*, **735-736**, 211-216 (2004).

20) M. Katouda, M. Kobayashi, H. Nakai, and S. Nagase, "Practical performance assessment of accompanying coordinate expansion recurrence relation algorithm for computation of electron repulsion integrals", *J. Theor. Comp. Chem.*, **4** (1), 139-150 (2005).

21) H. Nakai and Y. Kikuchi, "Extention of energy density analysis to treating chemical bonds in molecules", *J. Theor. Comp. Chem.*, **4** (1), 317-332 (2005).

22) M. Tamaoki, Y. Yamauchi, and H. Nakai, "Short-time Fourier transform analysis of *ab initio* molecular dynamics simulation: Collision reaction between CN and C_4H_6", *J. Comp. Chem.*, **26** (5), 436-442 (2005).

23) H. Nakai, M. Hoshino, K. Miyamoto, and S. Hyodo, "Elimination of translational and rotational motions in nuclear orbital plus molecular orbital theory", *J. Chem. Phys.*, **122** (22), 164101 1-10 (2005).

24) Y. Kawamura and H. Nakai, "Energy density analysis of embedded cluster models for an MgO crystal", *Chem. Phys. Lett.*, **410** (1-3), 64-69 (2005).

25) Y. Yamauchi and H. Nakai, "Hybrid approach for *ab initio* molecular dynamics simulation combining energy density analysis and short-time Fourier transform: Energy transfer spectrogram", *J. Chem. Phys.*, **123** (3), 034101 1-9 (2005).

（2）学会発表等

A．招待講演

1) 中井浩巳、"*ab initio* molecular dynamics (AIMD) 法による衝突反応および励起状態ダイナミクスの研究"，先端化学技術部コンピュータケミストリー分科会，新化学発展協会（東京），2003 年 12 月.
2) H. Nakai, "Ab initio NOMO theory for simultaneous determination of nuclear and electronic wave functions", Singapore International Chemical Conference 3 (SICC3): Frontiers in Physical and Analytical Chemistry, Shangri-La Hotel (Singapore), December 2003.
3) 中井浩巳、"エネルギー密度解析(EDA)の開発とその応用"，シンポジウム：量子的化学原理の深化と実現，京都リサーチパーク（京都），2003 年 12 月.
4) 中井浩巳、"大規模・高精度電子状態計算から何がわかるか－EDA によるアプローチ"，第 4 回スーパーコンピュータワークショップ，岡崎コンファレンスセンター（岡崎），2004 年 3 月.
5) H. Nakai, "Energy density analysis for surface-molecule interacting system", 1st Asian Pacific Conference on Theoretical & Computational Chemistry, Okazaki Conference Center (Okazaki), May 2004.
6) H. Nakai, "Development of Accurate Non-Born-Oppenheimer Theory", 11th Japan-Korea Joint Symposium on Frontiers in Molecular Science, Okazaki Conference Center (Okazaki), March 2005.

B．国際会議

1) H. Nakai, "Ab initio molecular dynamics simulation of collision reaction and excitation dynamics", The 6th Japan-China Symposium on Theoretical Chemistry (CSTC), Institute for Fundamental Chemistry (Kyoto), April 2002.
2) H. Nakai, "Development of Energy Density Analysis and Its Applications", Southwest Theoretical Chemistry Conference (SWTCC), University of Houston (Texas), November 2002.
3) H. Nakai, "Theoretical study of the band structure of rutile and anatase titanium dioxide", 2003 Excited State Processes in Electronic and Bio Nano-Materials (ESP2003), Los Alamos National Laboratory (New Mexico), August 2003.

4) H. Nakai, "Development of nonadiabatic molecular theory for simultaneous determination of nuclear and electronic wave function: ab initio NOMO theory", 226th ACS National Meeting, Javits Convention Center (New York), September 2003.
5) T. Baba, Y. Kawamura, and H. Nakai, "Development of energy density analysis and its applications", 226th ACS National Meeting, Javits Convention Center (New York), September 2003.
6) K. Sodeyama and H. Nakai, "Numerical assessment of ab initio NOMO theory", 226th ACS National Meeting, Javits Convention Center (New York), September 2003.
7) Y. Kawamura and H. Nakai, "Surface system modeling by the energy density analysis", 226th ACS National Meeting, Javits Convention Center (New York), September 2003.
8) M. Kobayashi and H. Nakai, "New algorithm for the rapid computation of molecular integrals: elementary basis algorithm", 226th ACS National Meeting, Javits Convention Center (New York), September 2003.
9) T. Otsuka and H. Nakai, "Nuclear Dynamics Analysis of Core-excited BF_3 by Wavelet Transform Technique", 1st Asian Pacific Conference on Theoretical & Computational Chemistry, Okazaki Conference Center (Okazaki), May 2004.
10) Y. Kawamura and H. Nakai, "Combination of Energy Density Analysis and Energy Decomposition Methods", 1st Asian Pacific Conference on Theoretical & Computational Chemistry, Okazaki Conference Center (Okazaki), May 2004.
11) K. Sodeyama, H. Kiryu, K. Miyamoto, and H. Nakai, "Many-body effects in nonadiabatic molecular theory for simultaneous determination of nuclear and electronic wave functions", 1st Asian Pacific Conference on Theoretical & Computational Chemistry, Okazaki Conference Center (Okazaki), May 2004.
12) Y. Yamauchi, Y. Okada, and H. Nakai, "Spectrogram analysis of collision reaction using ab initio molecular dynamics simulation", 1st Asian Pacific Conference on Theoretical & Computational Chemistry, Okazaki Conference Center (Okazaki), May 2004.
13) M. Kobayashi, H. Nakai, M. Katouda, and S. Nagase, "New algorithm for the rapid evaluation of electron repulsion integrals", 1st Asian Pacific Conference on Theoretical & Computational Chemistry, Okazaki Conference Center (Okazaki), May 2004.
14) Y. Kikuchi, M. Ishii, T. Baba, and H. Nakai, "Energy density analysis for chemical bonds in molecules", 1st Asian Pacific Conference on Theoretical & Computational Chemistry, Okazaki Conference Center (Okazaki), May 2004.
15) T. Shimada, K. Sakata, S. Odagiri, H. Nakai, T. Homma, and T. Osaka, "Density functional theory study of the oxidation mechanisms of reductants at the metal surface for electroless deposition processes", the 5th International Symposium on Electrochemical Micro & Nano System Technologies (EMT2004), (Tokyo), September 2004.

16) K. Sakata, N. Kubo, H. Nakai, T. Homma, and T. Osaka, "Characterization of strained silicon wafer surface by density functional theory analysis", the 5th International Symposium on Electrochemical Micro & Nano System Technologies (EMT2004), (Tokyo), September 2004.

17) T. Shimada, H. Nakai, T. Homma, and T. Osaka, "Density functional theory study on the reaction mechanism of reductants for electroless silver deposition processes", 2004 Joint International Meeting (206th Meeting of The Electrochemical Society (ECS) and 2004 Fall Meeting of The Electrochemical Society of Japan (ECSJ)), (Hawaii), October 2004.

18) K. Sakata, T. Shimada, H. Nakai, T. Homma, and T. Osaka, "Density functional theory study on the oxidation mechanisms of aldehydes as reductants for electroless deposition process", 2004 Joint International Meeting (206th Meeting of The Electrochemical Society (ECS) and 2004 Fall Meeting of The Electrochemical Society of Japan (ECSJ)), (Hawaii), October 2004.

19) H. Nakai, "Development of energy density analysis", The World Association of Theoretically Oriented Chemists, New International Convention Centre (Cape Town), January 2005.

C．その他の研究集会

1) 中井浩巳，"Energy Density Analysis (EDA)"，第 6 回理論化学討論会，大阪大学（大阪），2002 年 5 月.

2) 馬場健，中井浩巳，"Energy Density Analysis (EDA)による 3 中心結合の解析"，第 6 回理論化学討論会，大阪大学（大阪），2002 年 5 月.

3) 袖山慶太郎，星野稔，中井浩巳，"Energy Density Analysis (EDA)によるプロトン移動過程の解析"，第 6 回理論化学討論会，大阪大学（大阪），2002 年 5 月.

4) 河村芳海，中井浩巳，"Energy Density Analysis (EDA)によるメチル基内部回転運動の解析"，第 6 回理論化学討論会，大阪大学（大阪），2002 年 5 月.

5) 山内佑介，中井浩巳，"Ab initio MD シミュレーションによる励起状態ダイナミクスの研究"，第 6 回理論化学討論会，大阪大学（大阪），2002 年 5 月.

6) 千葉真人，中井浩巳，"TDDFT 計算の効率化とその応用"，第 6 回理論化学討論会，大阪大学（大阪），2002 年 5 月.

7) 菊池那明，河村芳海，中井浩巳，"Energy Density Analysis (EDA)による固体表面モデルの検討"，第 6 回理論化学討論会，大阪大学（大阪），2002 年 5 月.

8) 中井浩巳，"エネルギー密度解析の提案とその応用"，日本コンピュータ化学会 2002 春季年会，北とぴあ（東京），2002 年 7 月.

9) 中田彩子，馬場健，高橋博彰，中井浩巳，"ソラレン化合物の DNA 光付加反応の電子的メカニズムに関する理論的研究"，日本コンピュータ化学会 2002 春季年会，

北とぴあ（東京），2002 年 7 月．

10) 中田彩子，馬場健，高橋博彰，中井浩巳，“ソラレン化合物の DNA 光付加反応における励起状態ダイナミクスの理論的研究”，第 29 回生体分子科学討論会，岡崎コンファレンスセンター（愛知），2002 年 7 月．

11) 島田拓哉，阪田薫穂，中井浩巳，本間敬之，逢坂哲彌，“無電解析出反応における析出金属の触媒活性に関する理論計算とエネルギー密度解析(EDA)”，電気化学会 2002 年秋季大会，東京工芸大学（厚木），2002 年 9 月．

12) 馬場健，副田隆介，中井浩巳，“アンチモン(V)ポルフィリン錯体の励起状態と光化学反応に関する理論的研究”, 分子構造総合討論会 2002, 神戸国際会議場(神戸)，2002 年 10 月．

13) 河村芳海，中井浩巳，“Energy Density Analysis(EDA)の QM/MM 法への拡張とその応用”，分子構造総合討論会 2002，神戸国際会議場（神戸），2002 年 10 月．

14) 河東田道夫, 中井浩巳, “Energy Density Analysis(EDA)による固体表面反応の解析”，分子構造総合討論会 2002，神戸国際会議場（神戸），2002 年 10 月．

15) 星野稔，兵頭志明，中井浩巳，“FEM（有限要素法）基底による原子核波動関数の数値的解法の開発”，分子構造総合討論会 2002，神戸国際会議場（神戸），2002 年 10 月．

16) 渥美照夫，河村芳海，山内佑介，中井浩巳，“Ab intio MD シミュレーションによる銅クラスターイオンの衝突反応の研究”，分子構造総合討論会 2002，神戸国際会議場（神戸），2002 年 10 月．

17) 阪田薫穂，島田拓哉，中井浩巳，本間敬之，逢坂哲彌，“無電解めっきにおける還元剤としてのアルデヒド類の反応機構に関する理論計算解析”，表面技術協会第 107 回講演大会，工学院大学（東京），2003 年 3 月．

18) 副田隆介，馬場健，中井浩巳、“アンチモン(V)ポルフィリン錯体の光解離に関する理論的研究”，日本化学会第 83 春季年会，早稲田大学（東京），2003 年 3 月．

19) 島田拓哉，阪田薫穂，中井浩巳，本間敬之，逢坂哲彌，“無電解析出における還元剤酸化反応に対する金属触媒活性の理論的及び実験的検討”，日本化学会第 83 春季年会，早稲田大学（東京），2003 年 3 月．

20) 中井浩巳，“ガウス基底周期境界条件計算による酸化チタン光触媒活性の理論的解析”，第 7 回理論化学討論会，岡崎コンファレンスセンター（岡崎），2003 年 5 月．

21) 河村芳海，中井浩巳，“Energy Density Analysis による酸化チタン光触媒活性の理論的解析”，第 7 回理論化学討論会，岡崎コンファレンスセンター（岡崎），2003 年 5 月．

22) 小林正人，中井浩巳，“分子積分計算の高速化：Element Basis 法の開発”，第 7 回理論化学討論会，岡崎コンファレンスセンター（岡崎），2003 年 5 月．

23) 竹内真理，中田彩子，中井浩巳，“Energy Density Analysis (EDA)を用いた主成分分

析による機能性材料の設計”， 第 7 回理論化学討論会，岡崎コンファレンスセンター（岡崎），2003 年 5 月．

24) 中井浩巳，“酸化チタンバルクおよび表面に対するガウス基底周期境界条件計算”，日本コンピュータ化学会 2003 春季年会，北とぴあ（東京），2003 年 5 月．

25) 河村芳海，中井浩巳，“Energy Density Analysis の酸化チタン系への適用”，日本コンピュータ化学会 2003 春季年会，北とぴあ（東京），2003 年 5 月．

26) 小林正人，中井浩巳，“Element Basis 法を用いた分子積分計算の高速化：大規模系計算に向けて”，日本コンピュータ化学会 2003 春季年会，北とぴあ（東京），2003 年 5 月．

27) 竹内真理，中田彩子，中井浩巳，“エネルギー密度解析（EDA）を用いた主成分分析—機能性材料の設計に向けて—”，日本コンピュータ化学会 2003 春季年会，北とぴあ（東京），2003 年 5 月．

28) 山内佑介，中井浩巳，“AIMD/EDA によるエネルギー移動過程の理論的研究”， 分子構造総合討論会 2003，京都テルサ（京都），2003 年 9 月．

29) 大塚教雄，山内佑介，中井浩巳，“Ab initio MD 計算による分子の内殻励起ダイナミクスに関する理論的研究”，分子構造総合討論会 2003，京都テルサ（京都），2003 年 9 月．

30) 小澤志保，山内佑介，河井葉子，山口悟，岡田芳樹，中井浩巳，“ab initio 法による水クラスターイオン[$H^+(H_2O)_n$ (n=2-6)]の核生成過程に関する理論的研究”，分子構造総合討論会 2003，京都テルサ（京都），2003 年 9 月．

31) 河村芳海，馬場健，中井浩巳，“Energy Density Analysis (EDA)の GAMESS への組み込みといくつかの応用”，分子構造総合討論会 2003，京都テルサ（京都），2003 年 9 月．

32) 阪田薫穂，島田拓哉，中井浩巳，本間敬之，逢坂哲彌，“無電解析出における還元剤酸化反応の置換基効果に関する DFT 計算による検討”，分子構造総合討論会 2003，京都テルサ（京都），2003 年 9 月．

33) 袖山慶太郎，中井浩巳，“原子核と電子の運動を量子的に取り扱う ab initio NOMO 法の開発”，21COE International Symposium on 'Practical Nano-Chemistry'，早稲田大学（東京），2003 年 12 月．

34) 山内佑介，中井浩巳，“AIMD と EDA を使ったエネルギー移動過程の解析”，21COE International Symposium on 'Practical Nano-Chemistry'，早稲田大学（東京），2003 年 12 月．

35) 中田彩子，中井浩巳，“TDDFT 法によるソラレン化合物の DNA 光付加反応に関する理論的研究”，21COE International Symposium on 'Practical Nano-Chemistry'，早稲田大学（東京），2003 年 12 月．

36) 島田拓哉，中井浩巳，本間敬之，逢坂哲彌，“無電解析出における還元剤酸化反応

機構の理論的解析”，21COE International Symposium on 'Practical Nano-Chemistry'，早稲田大学（東京），2003 年 12 月.

37) 島田拓哉，中井浩巳，本間敬之，逢坂哲彌，“無電解銀めっきにおける還元剤酸化反応機構の理論計算解析”，表面技術協会第 109 回講演大会，東京都立大学（八王子），2004 年 3 月.

38) 河村芳海，河東田道夫，菊池那明，中井浩巳，“表面－分子相互作用系に対するエネルギー密度解析”，NAREGI ナノサイエンス実証研究第 2 回公開シンポジウム，岡崎コンファレンスセンター（岡崎），2004 年 2 月.

39) 山内佑介，渥美照夫，小澤志保，中井浩巳，“Ab Initio Molecular Dynamics (AIMD) シミュレーションによる衝突反応の解析”，NAREGI ナノサイエンス実証研究第 2 回公開シンポジウム，岡崎コンファレンスセンター（岡崎），2004 年 2 月.

40) 河東田道夫，永瀬茂，小林正人，中井浩巳，“分子積分計算高速化のための ACE 表式の改良”，NAREGI ナノサイエンス実証研究第 2 回公開シンポジウム，岡崎コンファレンスセンター（岡崎），2004 年 2 月.

41) 馬場健，中井浩巳，“機能性新素材の開発に向けた量子化学的手法の展開とその応用”，ハイテクリサーチセンター報告会，早稲田大学（東京），2004 年 3 月.

42) 菊池那明，中井浩巳，“結合領域へのエネルギー密度の分割法”，日本化学会第 84 春季年会，関西学院大学（西宮），2004 年 3 月.

43) 宮本開任，袖山慶太郎，中井浩巳，“Ab initio NOMO 法における並進・回転運動の分離に関する一考察”，日本化学会第 84 春季年会，関西学院大学（西宮），2004 年 3 月.

44) 河村芳海，菊池那明，馬場健，河東田道夫，石井基樹，中井浩巳，“量子化学計算における新しい解析法の開発と応用：Energy Density Analysis”，ナノ学会第 2 回大会，学士会館（東京），2004 年 5 月.

45) 渥美照夫，小澤志保，山内佑介，中井浩巳，“AIMD シミュレーションを用いたクラスターの反応ダイナミクスに関する理論的研究”，ナノ学会第 2 回大会，学士会館（東京），2004 年 5 月.

46) 大塚教雄，中井浩巳，“内殻励起ダイナミクスに対する Wavelet 変換を用いた解析”，日本コンピュータ化学会 2004 春季年会，東京工業大学（東京），2004 年 5 月.

47) 菊池那明，中井浩巳，“結合エネルギー密度解析(Bond-EDA)の開発とその応用”，日本コンピュータ化学会 2004 春季年会，東京工業大学（東京），2004 年 5 月.

48) 小林正人，中井浩巳，“新しい漸化式を用いた電子反撥積分の高速計算アルゴリズムの開発：ACE-RR 法”，日本コンピュータ化学会 2004 春季年会，東京工業大学（東京），2004 年 5 月.

49) 石川佳奈，河村芳海，中井浩巳，“二酸化チタンの光触媒反応に関する理論的研究”，日本コンピュータ化学会 2004 春季年会，東京工業大学（東京），2004 年 5 月.

50) 石井基樹，菊池那明，中井浩巳，“結合エネルギー密度解析(Bond-EDA)を用いた化学反応メカニズムの検討”， 日本コンピュータ化学会 2004 春季年会，東京工業大学（東京），2004 年 5 月.

51) 玉置麻理，山内佑介，渥美照夫，中井浩巳，“短時間フーリエ変換を用いた AIMD シミュレーションの解析”， 日本コンピュータ化学会 2004 春季年会，東京工業大学（東京），2004 年 5 月.

52) 倉林佑二，菊池那明，中井浩巳，“カーボンナノチューブのサイズ依存性に関する理論的研究”， 日本コンピュータ化学会 2004 春季年会，東京工業大学（東京），2004 年 5 月.

53) 小林正人，中井浩巳，“電子反撥積分の高速計算法：随伴座標展開(ACE)表式に対する漸化関係式の導出”，第 8 回理論化学討論会，広島大学（東広島），2004 年 6 月.

54) 山内佑介，中井浩巳，“エネルギー移動スペクトログラムの提案”，第 8 回理論化学討論会，広島大学（東広島），2004 年 6 月.

55) 渥美照夫，中井浩巳，“AIMD シミュレーションにおける SCF 収束性の向上”，第 8 回理論化学討論会，広島大学（東広島），2004 年 6 月.

56) 小澤志保，山内佑介，岡田芳樹，中井浩巳，“水クラスターイオンの冷却過程に関する ab initio MD シミュレーション”，第 8 回理論化学討論会，広島大学（東広島），2004 年 6 月.

57) 玉置麻理，山内佑介，中井浩巳，“Analysis of AIMD simulation for the collision reaction between cyano radical and 2-butyne”，星間物質ワークショップ 2004，野辺山宇宙電波観測所（長野），2004 年 8 月.

58) 今村穣，大塚教雄，中井浩巳，“時間依存密度汎関数法(TDDFT)を用いた内殻励起に関する理論的研究”，分子構造総合討論会 2004，広島国際会議場（広島），2004 年 9 月.

59) 袖山慶太郎，宮本開任，星野稔，中井浩巳，“電子状態理論における重心運動の取り扱いに対する一考察”，分子構造総合討論会 2004，広島国際会議場（広島），2004 年 9 月.

60) 菊池那明，中井浩巳，“DFT 計算に対する結合エネルギー密度解析(Bond-EDA)”，分子構造総合討論会 2004，広島国際会議場（広島），2004 年 9 月.

61) 山内佑介，中井浩巳，“エネルギー移動スペクトログラム(ETS)による化学反応の解析”，分子構造総合討論会 2004，広島国際会議場（広島），2004 年 9 月.

62) 星野稔，宮本開任，中井浩巳，“Ab initio NOMO 法における回転運動の取り扱い”，分子構造総合討論会 2004，広島国際会議場（広島），2004 年 9 月.

63) 渥美照夫，中井浩巳，“AIMD シミュレーションにおける SCF 収束性の向上(2)”，分子構造総合討論会 2004，広島国際会議場（広島），2004 年 9 月.

64) 石川佳奈，河村芳海，中井浩巳，“アナターゼ型酸化チタン表面での水吸着及び光励起過程に関する理論的研究”，第 11 回光触媒シンポジウム，安田講堂（東京），2004 年 12 月.

65) 佐倉大輔，玉置麻理，山内佑介，中井浩巳，“シアノラジカルと不飽和炭化水素の衝突反応に対する AIMD シミュレーション”，第 18 回分子シミュレーション討論会，京都大学（京都），2004 年 12 月.

66) 鈴木潤，菊池那明，石井基樹，中井浩巳，“結合エネルギー密度解析を用いた S_N2 反応の反応性に関する理論的研究”，第 18 回分子シミュレーション討論会，京都大学（京都），2004 年 12 月.

67) 山内佑介，中井浩巳，“水クラスターイオン衝突過程の理論的研究：エネルギー移動スペクトログラム”， The 2nd 21COE International Symposium on 'Practical Nano-Chemistry'，早稲田大学（東京），2004 年 12 月.

68) 小林正人，中井浩巳，“高速な電子状態計算手法の開発”，The 2nd 21COE International Symposium on 'Practical Nano-Chemistry'，早稲田大学（東京），2004 年 12 月.

69) 菊池那明，中井浩巳，“エネルギー密度解析(EDA)の結合領域への拡張とその応用”，The 2nd 21COE International Symposium on 'Practical Nano-Chemistry'，早稲田大学（東京），2004 年 12 月.

70) 星野稔，中井浩巳，“電子・核波動関数同時決定法の高精度化に向けた試み：回転運動の分離”，The 2nd 21COE International Symposium on 'Practical Nano-Chemistry'，早稲田大学（東京），2004 年 12 月.

71) 島田拓哉，本間敬之，中井浩巳，逢坂哲彌，“無電解銅析出における還元剤酸化反応機構の密度汎関数法による解析”，The 2nd 21COE International Symposium on 'Practical Nano-Chemistry'，早稲田大学（東京），2004 年 12 月.

72) 阪田薫穂，本間敬之，中井浩巳，逢坂哲彌，“ストレインドシリコン表面の化学的特性に対する DFT 計算による検討”，The 2nd 21COE International Symposium on 'Practical Nano-Chemistry'，早稲田大学（東京），2004 年 12 月.

73) 小田切秀一，島田拓哉，中井浩巳，本間敬之，逢坂哲彌，“無電解析出における次亜リン酸酸化反応律速段階の DFT による解析”， 第 15 回日本 MRS 学術シンポジウム，日本大学（東京），2004 年 12 月.

74) 渥美照夫，中井浩巳，“AIMD シミュレーションにおける SCF 計算の高速化”，NAREGI ナノサイエンス実証研究第 3 回公開シンポジウム，岡崎コンファレンスセンター（岡崎），2005 年 2 月.

75) 倉林佑二，菊池那明，中井浩巳，“Energy Density Analysis によるカーボンナノチューブの特性に関する理論的研究”， NAREGI ナノサイエンス実証研究第 3 回公開シンポジウム，岡崎コンファレンスセンター（岡崎），2005 年 2 月.

76) 小田切秀一，島田拓哉，中井浩巳，本間敬之，逢坂哲彌，“無電解析出における次亜リン酸酸化反応機構の DFT による解析”，第 111 回表面技術協会講演大会，千葉工業大学（千葉），2004 年 3 月.

77) 山内佑介，中井浩巳，“エネルギー移動スペクトログラム：ab initio 分子動力学シミュレーションの新規な解析手法”，日本化学会第 85 春季年会，神奈川大学（横浜），2005 年 3 月.

78) 一色俊宏，河村芳海，中井浩巳，“直鎖アルケンのメチル基内部回転運動における π^*-σ^*超共役効果”，日本化学会第 85 春季年会，神奈川大学（横浜），2005 年 3 月.

79) 中田彩子，今村穣，中井浩巳，“内殻励起に適した hybrid 汎関数の開発”，日本化学会第 85 春季年会，神奈川大学（横浜），2005 年 3 月.

80) 竹内真理，馬場健，中井浩巳，“Natural Atomic Orbital に基づく Energy Density Analysis の改良”，日本化学会第 85 春季年会，神奈川大学（横浜），2005 年 3 月.

81) 宮本開任，星野稔，中井浩巳，“ab initio NOMO 法における回転運動の取り扱い：振動と回転のカップリング”，日本化学会第 85 春季年会，神奈川大学（横浜），2005 年 3 月.

82) 桐生大義，袖山慶太郎，中井浩巳，“Knowles-Handy アルゴリズムに基づく ab initio NOMO/FCI 法の開発とその応用”，日本化学会第 85 春季年会，神奈川大学（横浜），2005 年 3 月.

83) 赤間知子，小林正人，中井浩巳，“大規模電子状態計算のための divide-and-conquer 法の検証と改良”，日本化学会第 85 春季年会，神奈川大学（横浜），2005 年 3 月.

84) 飯田涼子，河村芳海，中井浩巳，“Interaction-EDA を用いた Cu/Zn 触媒による Methanol 合成反応の理論的研究”，日本化学会第 85 春季年会，神奈川大学（横浜），2005 年 3 月.

85) 島田拓哉，小田切秀一，中井浩巳，本間敬之，“無電解析出における還元剤酸化反応に対する銅表面触媒活性の DFT 計算による定量的解析”，日本化学会第 85 春季年会，神奈川大学（横浜），2005 年 3 月.

研　究　成　果

量子化学計算における Linear-Scaling 法の開発とその応用

早稲田大学 理工学術院 教授　　中井　浩巳

分子軌道(MO)法や密度汎関数理論(DFT)などに基づく量子化学計算は、分子の構造や振動状態、化学反応や光吸収に伴うエネルギー変化、電磁場に対する応答などを高い精度で求める方法として、広く普及している。その使用目的も、以前のように現象の解釈や理解にとどまらず、新しい機能や反応の設計にまで拡大している。一方、量子化学計算の欠点は、対象が大きくなると極端に計算コストが増大することである。これは、量子化学計算がすべての電子を同時に扱うため、対象が大きくなると電子数あるいはそれを扱うための基底関数の数(N)が増大することに由来している。さらにその計算コストは、HF 法で N^4、MP2 法で N^5、CCSD 法で N^6、CCSD(T)法で N^7 に比例して増加することが知られている。たとえば、現在 $N = 300$ の HF 計算は CPU 時間が 5 分程度であるが、それが $N = 3000$ の計算になると約 35 日かかるわけである。CCSD 計算は HF 計算より厳密な計算をしているので、$N = 300$ の分子でさえ 3 時間程度かかる。それが $N = 3000$ になると理論上は 340 年と莫大な計算時間が必要となる。そこで、この N 依存性を 1 次（線形）にまで落とせないかという試みが、Linear-Scaling (LS)法である。

本研究では、種々の量子化学計算に対する LS 法あるいは効果的な計算アルゴリズムの提案とそのプログラム開発を目指した。

（1）分子積分の高速計算プログラム開発：分子積分、とりわけ電子間反発積分(ERI)の計算は、いまなお量子化学計算のボトルネックの一つである。本研究では、2 種類の高速化を提案した。1 つは、元素基底の概念に基づく高速化(EBA)である。もう 1 つは、ACE 表式に対する新しい漸化式を導出することによる高速化(ACE-RR)である。ACE-RR に関しては、GAMESS プログラムに組み込むことにより汎用性の向上を目指した。実際、ACE-RR 法は従来のアルゴリズムより 20 %程度高速化していることが確かめられた。

（2）Divide-and-Conquer (DC)法の発展：Yang によって提案された LS 法の一つである DC 法は、主に DFT に適用されてきた。しかし、原理的には HF 交換項を含むハイブリッド法にも応用できる。本研究では、DC-HF プログラムを作成し、HF 交換項に対する DC 法の是非を検討した。その結果、HF 交換項の非局所性のため、十分な相互作用領域を用いる必要があること、打ち切りによる SCF 収束性が悪化することが明らかとなった。さらに、SCF 収束性を改善するために DC 法に適した DIIS の開発を行った。

（3）AIMD 法における SCF 収束性の向上：AIMD 法は時間ステップごとに MO/DFT 計算を行うため、膨大な計算時間を必要とする。本研究では、MO の時間発展を考慮することにより、効果的な初期 MO を推定し、SCF 収束性の向上を目指した。具体的には、過去の数ステップの収束した MO から Lagrange 補間により予測するというアルゴリズム(LI-MO)であ

る。このLI-MO法を用いると、多くの系で2～4倍程度の高速化が実現された。

また、LS法の発展により大規模計算が可能となった場合、次に結果の解析が問題となる。本研究では、解析手法の開発も同時に検討した。

（4）活性部位のエネルギー変化を見積るための解析法の開発：全系のエネルギーを構成原子に分割するための新しい解析法(EDA)を提案した。さらに、EDA法を発展させ、結合エネルギーを評価する方法(Bond-EDA)や相互作用エネルギーを解析する方法(Interaction-EDA)を提案した。同時に、これらの方法を用いてその有効性を確認するとともに、新しい知見を得ることに成功した。

（5）AIMD法における非平衡状態の解析法の開発：AIMD法は非平衡状態を記述する有用な方法であるが、その情報を効果的に引き出す手法が存在しなかった。そこで、本研究では短時間フーリエ変換(ST-FT)を用いた方法を提案し、分子振動のダイナミックスを解析することに成功した。さらに、先のEDAと組み合わせることにより、エネルギー移動に関連する振動状態のダイナミックスを検討することに成功した(ETS)。

（6）NOMO法の高精度化：電子と核の波動関数を同時に決定するNOMO法は、我々が提案してきた独自の方法で、世界的にも注目されている。NOMO法は、原子核の波動関数を与えるので、新たな解析手法としても用いることができる。しかし、その精度は従来のMO法に比べ劣る。その原因は、電子－核および核－核相関といった特殊な多体効果に加えて、並進・回転運動の混入が挙げられる。本研究では、並進・回転運動の寄与を取り除く効果的なスキームを提案し、それによる高精度化を図った。

LS法の開発は、量子化学計算の発展には不可欠である。にもかかわらず、これまでわが国ではLS法はほとんど研究されてこなかった。これは、アルゴリズムやプログラムの開発に対するわが国における評価の低さに由来しているのかもしれない。実際、LS法が開発されたとしても、それを用いて得られる結果は従来の方法と異なる値、言い換えると、より高精度な計算結果を与えるものではない。むしろ、全く同じ値が得られて完成なのである。そのため、理論化学者の中にも低い評価をする者も少なくない。一方、欧米では90年代に入って活発に研究され、HF, DFT計算に対するLS法として多重極展開によるFMM法、MP2計算に対してはラプラス変換を用いるLT-MP2法、CCSD計算に対しては局在軌道あるいは原子軌道を用いるLMO-CCSD法およびAO-CCSD法などが提案されてきた。本研究の成果が、わが国におけるこの分野の遅れを取り戻すのに少しでも役に立てば幸いである。

論　文　別　刷

ELSEVIER

2 September 2002

Chemical Physics Letters 363 (2002) 73–79

CHEMICAL PHYSICS LETTERS

www.elsevier.com/locate/cplett

Energy density analysis with Kohn–Sham orbitals

Hiromi Nakai

Department of Chemistry, School of Science and Engineering, Waseda University, Tokyo 169-8555, Japan

Received 22 May 2002; in final form 24 June 2002

Abstract

We have proposed a new technique analyzing the results of the density functional theory calculations in the Kohn–Sham (KS) approach. It is named the energy density analysis (EDA), which partitions the total energy of the molecular system into atomic energies. The EDA involves two partition schemes. One is for the exchange-correlation energy computed by the numerical quadrature method with the grid points. The other is for the kinetic, nuclear attraction, Coulomb, and exact exchange energies computed by the analytical integration with the KS orbitals. Numerical applications of the EDA to H_2O molecule confirm its reliability and usefulness. © 2002 Elsevier Science B.V. All rights reserved.

Quantum chemical calculation based on the molecular orbital (MO) theory or the density functional theory (DFT) is not usually called simulation, but theoretical calculation. It is because the quantum chemical calculation has been used not only to derive observable quantities, but also to rationalize chemical and physical phenomena by analyzing the results such as wave functions and energies. However, its recent development seems only to be focused on computing the observables in higher accuracy, further, for larger systems. As a result, the analyzing step often becomes a bottleneck of the theoretical research. It seems that the success of analysis depends on intuition of individual researchers.

The present study predicts a simple but new analyzing technique, named energy density analysis (EDA), which divides the ground state energy of molecule computed by the Kohn–Sham approach [1] into atomic contributions. The basic idea of the EDA is as follows. The modern DFT is based on the Hohenberg–Kohn (HK) theorem [2], which allows us to construct a rigorous many-body theory using the electron density as the fundamental quantity. The exchange-correlation functionals widely used in the KS approach are defined as the functions of the local electron density and its gradient. Noted that the gradient is also local quantity, although it is introduced in order to describe the non-local effect. Therefore, the total energy of molecule can be divided into atomic energies by partitioning the local electron density and the local density gradient.

The electronic energy in the KS formulation is expressed by

$$E_{\mathrm{ELC}}[\rho] = T_{\mathrm{S}}[\rho] + E_{\mathrm{Ne}}[\rho] + E_{\mathrm{CLB}}[\rho] + E_{\mathrm{XC}}[\rho], \quad (1)$$

where $T_{\mathrm{S}}[\rho]$ is the non-interacting kinetic energy, $E_{\mathrm{Ne}}[\rho]$ is the nucleus–electron attraction energy,

E-mail address: nakai@waseda.jp

0009-2614/02/$ - see front matter
PII: S0009-2614(02)01151-X

$E_{\mathrm{CLB}}[\rho]$ is the classical Coulomb interaction, and $E_{\mathrm{XC}}[\rho]$ is the exchange-correlation energy including the self-interaction correction and the difference between the true kinetic energy of the interacting system and $T_{\mathrm{S}}[\rho]$. The EDA decomposes each term into atomic contributions.

The exchange-correlation energy is usually evaluated by using numerical quadrature technique (see, however, Refs. [3–5]). The integral I is approximated by a weighted sum of the values of the integrand $F(\mathbf{r})$ at a set of finite grid

$$I = \int F(\mathbf{r})\mathrm{d}\mathbf{r} \cong \sum_{A}^{\mathrm{atom}} \sum_{g}^{\mathrm{grid}} \omega_g p_A(\mathbf{r}_g) F(\mathbf{r}_g), \tag{2}$$

where $\omega_g(\mathbf{r})$ is the weight. The partition functions $p_A(\mathbf{r})$, which are required to be positive definite and to be normalized at each grid point, decompose $F(\mathbf{r})$ into a sum of terms $p_A(\mathbf{r})F(\mathbf{r})$ related to atoms (see, for example, [6]). Although the partition functions are originally introduced in order to define the grid points at ease, we use them to divide the exchange-correlation energy into atomic contributions followingly

$$E_{\mathrm{XC}}^{A} = \sum_{g}^{\mathrm{grid}} \omega_g p_A(\mathbf{r}_g) F_{\mathrm{XC}}(\mathbf{r}_g), \tag{3}$$

where the exchange-correlation functionals, F_{XC}, practically consists of the exchange and correlation functionals, F_{X} and F_{C}, respectively. Thus, E_{XC}^{A} can be divided into E_{X}^{A} and E_{C}^{A}.

Next, we propose a partitioning scheme of $T_{\mathrm{S}}[\rho]$, $E_{\mathrm{Ne}}[\rho]$, and $E_{\mathrm{CLB}}[\rho]$, which are evaluated by the analytical integration with the KS orbitals, $\{\phi_i\}$. For example, the kinetic energy is written by

$$T_{\mathrm{S}}[\rho] = \sum_{i}^{N} \left\langle \varphi_i \middle| -\frac{1}{2}\nabla^2 \middle| \varphi_i \right\rangle = \sum_{i}^{N} \langle \varphi_i | \hat{t} | \varphi_i \rangle. \tag{4}$$

Since the KS orbitals are normally expanded by a set of atomic orbitals (AOs), $\{\chi_\mu\}$, $T_{\mathrm{S}}[\rho]$ is computed by the following matrix operation:

$$T_{\mathrm{S}}[\rho] = \sum_{\mu}\sum_{\nu} P_{\mu\nu}\langle \chi_\nu | \hat{t} | \chi_\mu \rangle = \sum_{\mu}\sum_{\nu} P_{\mu\nu} T_{\nu\mu} = \sum_{\mu} (\mathbf{PT})_{\mu\mu}. \tag{5}$$

We here use the analogy of Mulliken population analysis [7], in which the total number of electrons, N, is divided into the electron density, $(\mathbf{PS})_{\mu\mu}$, for the AO, χ_μ

$$N = \int \rho(\mathbf{r})\mathrm{d}\mathbf{r} = \sum_{\mu}\sum_{\nu} P_{\mu\nu} S_{\nu\mu} = \sum_{\mu} (\mathbf{PS})_{\mu\mu}, \tag{6}$$

where $S_{\nu\mu}$ is an overlap integral between χ_ν and χ_μ. Summing of the electron densities associated with each atom gives atomic electron density, N_{MUL}^{A}

$$N_{\mathrm{MUL}}^{A} = \sum_{\mu\in A} (\mathbf{PS})_{\mu\mu}. \tag{7}$$

We define $(\mathbf{PT})_{\mu\mu}$ in Eq. (5) as the kinetic energy density for χ_μ, and further, the atomic kinetic energy density by

$$T_{\mathrm{S}}^{A} = \sum_{\mu\in A} (\mathbf{PT})_{\mu\mu} \tag{8}$$

E_{Ne} and E_{CLB} can be partitioned in a similar manner. Here, one should notice

$$E_{\mathrm{CLB}}[\rho] = \frac{1}{2}\sum_{\mu}\sum_{\nu}\sum_{\rho}\sum_{\sigma} P_{\mu\nu}P_{\rho\sigma}(\chi_\nu\chi_\mu|\chi_\sigma\chi_\rho) = \frac{1}{2}\sum_{\mu}\sum_{\nu} P_{\mu\nu}G_{\nu\mu} = \frac{1}{2}\sum_{\mu}(\mathbf{PG})_{\mu\mu}. \tag{9}$$

If one uses $(\chi_\sigma\chi_\mu|\chi_\nu\chi_\rho)$ as $G_{\nu\mu}$ in Eq. (9), the exact exchange energy, which is used not only in the hybrid functionals but also in the Hartree–Fock (HF) method, can be partitioned into atomic contributions. It indicates that the EDA can be formally applied to the HF method.

The total energy, E_{TOT}, of molecule is the sum of the electronic energy, E_{ELC}, given by Eq. (1) and the nuclear repulsion energy, E_{NN}

$$E_{\mathrm{NN}} = \frac{1}{2}\sum_{A}^{\mathrm{atom}}\sum_{B\neq A}^{\mathrm{atom}} \frac{Z_A Z_B}{r_{AB}} \tag{10}$$

The nuclear repulsion energy for atom, A, is evaluated by the partial sum

$$E_{\mathrm{NN}}^{A} = \frac{1}{2}\sum_{B\neq A}^{\mathrm{atom}} \frac{Z_A Z_B}{r_{AB}}. \tag{11}$$

From the above procedure, all the components of the ground state energy of the molecular system computed by the Kohn–Sham method can be divided into atomic contributions.

In this Letter, the reliability and usefulness of the EDA proposed here are tested by numerical applications to H_2O. At first, we examine how the EDA technique can divide the energy components for the stable water molecule in a numerical sense. The geometry of H_2O used here is the experimental one; that is, the O–H distance of 0.9575 Å (R_e) and the H–O–H angle of 104.51° [8]. Basis sets adopted for O and H are the correlation-consistent polarization plus valence double zeta (cc-pVDZ) sets of Dunning [9]. The DFT calculations are performed by using the B3LYP hybrid functional [10], which consists of the HF (exact) exchange, the Slater exchange [11], the Becke (B88) exchange [12], the Vosco–Wilk–Nusair (VWN) correlation [13], and the Lee–Yang–Parr (LYP) correlation [14] functionals

$$E_{XC}^{B3LYP} = aE_X^{EXC} + (1-a)E_X^{SLT} + bE_X^{B88} + (1-c)E_C^{VWN} + cE_C^{LYP}. \quad (12)$$

Here, the values of the three parameters are directly taken from Becke's original paper; that is, $(a,b,c) = (0.20, 0.72, 0.81)$ [15]. As mentioned above, the EDA technique can divide each term in Eq. (12) into atomic contributions. The computations of the electron density and the total energy are carried out by using the program HONDO99 [16], and the EDA calculations by linking the original code for the EDA [17] with HONDO99.

Table 1 shows the nuclear repulsion (E_{NN}), one-electron (E_{1EL}), Coulomb (E_{CLB}), exchange (E_X), and correlation (E_C) energy densities of H and O atoms in the stable H_2O molecule, which are evaluated by the present EDA technique. As is the case for the total values of the H_2O molecule, E_{NN}, T_S, and E_{CLB} of both H and O atoms are positive values, whereas E_{Ne}, E_X, and E_C are negative values. The orderings of $|E_{1EL}| > E_{CLB} > E_{NN} > |E_X| > |E_C|$ of H and O atoms are the same for the molecular case. It indicates that the partition of each component is reasonable.

Differences from the energy densities of the isolated atoms are also shown in parentheses in Table 1. Great instability due to the nucleus–nucleus and electron–electron repulsion in the mo-

Table 1
Nuclear repulsion (E_{NN}), one-electron (E_{1EL}), Coulomb (E_{CLB}), exchange (E_X), and correlation (E_C) energy densities of H and O in the stable H_2O molecule

Component	H	O	H_2O
E_{NN}	2.38539 (+2.38539)	4.42132 (+4.42132)	9.19211 (+9.19211)
T_S	0.71150	74.50994	75.93293
E_{Ne}	−5.80840	−187.52466	−199.14147
E_{1EL}[a]	−5.09691 (−4.59763)	−113.01472 (−9.71533)	−123.20853 (−18.91058)
E_{CLB}	2.55793 (+2.24529)	41.84508 (+5.12665)	46.96094 (+9.61724)
E_X^{EXC}	−0.36919	−8.22906	−8.96744
E_X^{SLT}	−0.30032	−7.53400	−8.13464
E_X^{B88}	−0.04239	−0.78332	−0.86810
E_X[b]	−0.34462 (−0.03199)	−8.23700 (−0.08881)	−8.92624 (−0.15278)
E_C^{VWN}	−0.06338	−0.73469	−0.86145
E_C^{LYP}	−0.01952	−0.30188	−0.34093
E_C[c]	−0.02786 (−0.02786)	−0.38412 (−0.04367)	−0.43983 (−0.09938)
E_{ELC}[d]	−2.91145 (−2.41217)	−79.79075 (−4.72115)	−85.61366 (−9.54550)
E_{TOT}[e]	−0.52606 (−0.02678)	−75.36943 (−0.29982)	−76.42155 (−0.35339)

Difference from the energy component of the isolated atom is shown in parentheses.
[a] $E_{1EL} = T_S + E_{Ne}$.
[b] $E_X = 0.20 \times E_X^{EXC} + 0.80 \times E_X^{SLT} + 0.72 \times E_X^{B88}$.
[c] $E_C = 0.19 \times E_C^{VWN} + 0.81 \times E_C^{LYP}$.
[d] $E_{ELC} = E_{1EL} + E_{CLB} + E_X + E_C$.
[e] $E_{TOT} = E_{NN} + E_{ELC}$.

lecular system is canceled mainly by the stability of the nucleus–electron attraction. It corresponds to the well-known shielding effect. The EDA results lead to the conclusion that the binding energy, or atomization energy of 9.6 eV (0.35 hartree) in H_2O at the B3LYP/cc-pVDZ level is the sum of the stabilization energies of 0.7 eV (0.027 hartree) in two H atoms and that of 8.2 eV (0.30 hartree) in O.

Next, we investigate the effect of the geometrical change on the partitioned atomic energies. Two types of bond-breaking processes are examined. The first one is a homogeneous process, in which the O–H_a and O–H_b distances are changed together from $1.0R_e$ to $1.5R_e$, and further to $2.0R_e$. The second one is a heterogeneous process, in which only the O–H_b distance is changed from $1.0R_e$ to $1.5R_e$, and further to $2.0R_e$, in keeping the O–H_a distance at $1.0R_e$.

Table 2 shows the nuclear repulsion (E_{NN}), electronic (E_{ELC}), and total (E_{TOT}) energy densities of H_a, H_b, and O in the H_2O molecule in the homogeneous and heterogeneous bond-breaking processes. Both E_{NN} and $|E_{ELC}|$ decrease in absolute numbers as the O–H distances are elongated. Since the decrease of $|E_{ELC}|$ is a little bit larger than that of E_{NN}, the atoms directly related to the bond breaking become unstable. On the other hand, the total energy density of the bond-keeping hydrogen atom, i.e., H_a in the heterogeneous process, does not change much, while both E_{NN} and $|E_{ELC}|$ of H_a decrease.

Fig. 1a,b shows the total energy density changes (ΔE_{TOT}) from the stable H_2O molecule in the homogeneous and heterogeneous processes, respectively. In the homogeneous process, where both O–H_a and O–H_b bonds are weaken, the energy density change in H_a is equal to that in H_b. In the heterogeneous process, following only the O–H_b bond breaking, the energy density change in H_a is almost zero; that is, $\Delta E_{TOT}^{H_a} = -0.001$ and $+0.000$ hartree at $R(O\text{–}H) = 1.5R_e$ and $2.0R_e$, respectively. The energy density change in H_b is close to that in the homogeneous process; namely, $(\Delta E_{TOT}^{H_b}(\text{hetero}), \Delta E_{TOT}^{H_b}(\text{homo})) = (+0.039, +0.038)$ and $(+0.075, +0.075)$ hartree at $R(O\text{–}H) = 1.5R_e$ and $2.0R_e$, respectively. The energy change in O in the homogeneous process is about twice as large as that in the heterogeneous one, i.e., $(\Delta E_{TOT}^{O}$

Table 2
Nuclear repulsion (E_{NN}), electronic (E_{ELC}), and total (E_{TOT}) energy densities of H and O in the H_2O molecule in the homogeneous and heterogeneous bond-breaking processes

	$R(O\text{–}H_a)$	$R(O\text{–}H_b)$	H_a			H_b			O			H_2O
	E_{NN}	E_{ELC}	E_{TOT}	E_{NN}	E_{ELC}	E_{TOT}	E_{NN}	E_{ELC}	E_{TOT}	E_{NN}	E_{ELC}	E_{TOT}
$1.0R_e$	2.38539	−2.91145	−0.52606	2.38539	−2.91145	−0.52606	4.42132	−79.79075	−75.36943	9.19211	−85.61366	−76.42155
$1.5R_e$	1.59026	−2.07797	−0.48771	1.59026	−2.07797	−0.48771	2.94755	−78.23483	−75.28728	6.12807	−82.39076	−76.26269
$2.0R_e$	1.19270	−1.64424	−0.45154	1.19270	−1.64424	−0.45154	2.21066	−77.40096	−75.19030	4.59605	−80.68943	−76.09338
$1.0R_e$	2.34880	−2.87587	−0.52707	1.61191	−2.09853	−0.48662	3.68444	−79.00988	−75.32544	7.64515	−83.98428	−76.33913
$1.0R_e$	2.32345	−2.84917	−0.52572	1.21812	−1.66897	−0.45085	3.31599	−78.59144	−75.27545	6.85757	−83.10959	−76.25202

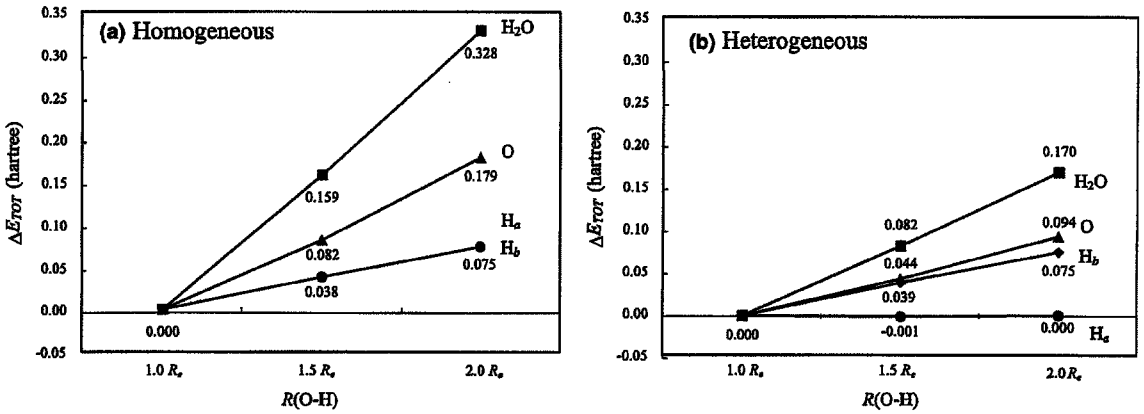

Fig. 1. Total energy density changes (ΔE_{TOT}) of H_a, H_b, and O in H_2O in the homogeneous (a) and heterogeneous (b) bond-breaking processes, with respect to the values in the stable H_2O molecule.

(hetero), ΔE^{O}_{TOT}(homo)) = (+0.082, +0.159) and (+0.170, +0.328) hartree, respectively. The O atom concerns with two bonds breaking in the homogeneous process, whereas it is related to one bond breaking in the heterogeneous one. These results indicate that the energy change in the H_2O molecule in the heterogeneous process is mainly due to the local energy changes in the O and H_b atoms or on the O–H_b bond. Furthermore, these results qualitatively demonstrate the additive property of the bond energy.

As is well known, Mulliken population analysis depends strongly on the basis sets and sometimes gives unreliable results. Since the EDA partially adopts the Mulliken-type partitioning, we examine the basis-set dependence of the EDA results. The basis sets used here are STO-3G [18], D95 [19], cc-pVDZ [9], AUG-cc-pVDZ [9,20], and cc-pVTZ [9] ones. For these sets, Mulliken populations of (O, H) in the stable H_2O molecule are (8.368, 0.816), (8.694, 0.653), (8.254, 0.873), (7.886, 1.057), and (8.366, 0.817), respectively. The result with the AUG-cc-pVDZ set seems to be unreliable in a chemical sense. Namely, O and H atoms are positively and negatively charged, respectively. It is due to large overlap between diffuse functions.

Fig. 2 shows the total energy density changes (ΔE_{TOT}) of (a) (H_a and H_b) and (b) O from the stable H_2O molecule in the homogeneous process, respectively, by using the basis sets. Although ΔE_{TOT} of O and H changes by using several basis sets, the basis-set dependence of ΔE_{TOT} is different from that of the Mulliken population. The energy densities of O with the use of STO-3G and D95 sets have minima at R(O–H) = $1.5R_e$. It gives an unreliable interpretation that the O–H dissociation stabilizes the oxygen atom. On the other hand, the EDA gives reasonable interpretation for the better sets (cc-pVDZ, AUG-cc-pVDZ, and cc-pVTZ). Namely, ΔE_{TOT} of H and O increase monotonically as the elongation of the O–H bond. Note that the EDA with the diffuse functions does not lead to an unreliable behavior as seen in the population analysis.

Thus, the present EDA technique gives atomic energies in molecules, which depend on basis sets but are reliable for better basis sets. The concept of the energy density leads to the essential information to realize the chemical phenomena such as the bond-breaking and bond-keeping processes. It is claimed that the analyzing technique generalizes the essence from the results, without lowering the accuracy as much as possible. The EDA has a good feature that the atomic energies are given at the same accuracy of the molecular energy.

We are now performing applications of EDA to various systems and various phenomena. In particular, the idea of atomic energy presented by the EDA should become more important for larger systems such as surface–molecule interacting systems, biomolecules, and nanoclusters. For example, without the EDA, one can only get a single

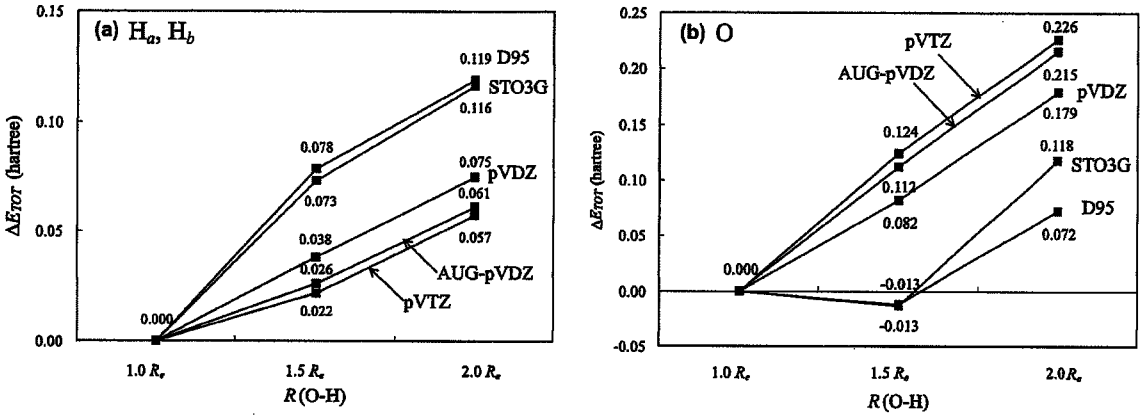

Fig. 2. Basis-set dependence of total energy changes (ΔE_{TOT}) of (a) (H_a, H_b) and (b) O in the homogeneous bond-breaking process, with respect to the values in the stable H_2O molecule.

value, namely, the total energy of the total system. With the EDA, one can get 'energy densities' of individual atoms in the total system. The results would clarify which atoms contribute the energy transfer. This is one possibility led by the EDA. We expect, however, that what insight the EDA yields will be expanded in the future work. Furthermore, we are also undertaking the theoretical extension of EDA.

Finally, we should mention that the EDA is different from the established energy decomposition method, which was first proposed by Morokuma [21], and developed to the constrained space orbital variation (CSOV) method by Bagus et al. [22] or to the reduced variational space self-consistent-field (RVS SCF) method by Stevens and Fink [23]. These methods give the sophisticated decomposition of the molecular interaction; that is, electrostatic, exchange, polarization, and charge transfer energies. The combination between the energy decomposition methods and the present EDA will become a promising technique to analyze complicated interacting systems.

Acknowledgements

This study was supported by a Grant-in-Aid for Scientific Research from the Japanese Ministry of Education, Culture, Sports, Science, and Technology (MEXT), and by a Waseda University Grant for Special Research Projects. Part of the calculations was performed at the Research Center for Computational Science (RCCS) of the Okazaki National Research Institutes.

References

[1] W. Kohn, L.J. Sham, Phys. Rev. 140 (1965) A1133.
[2] P. Hohenberg, W. Kohn, Phys. Rev. 136 (1964) B864.
[3] Y.C. Zheng, J. Almlöf, Chem. Phys. Lett. 214 (1993) 397.
[4] K.R. Glaesemann, M.S. Gordon, J. Chem. Phys. 108 (1998) 9959.
[5] K.R. Glaesemann, M.S. Gordon, J. Chem. Phys. 110 (1999) 6580.
[6] A.D. Becke, J. Chem. Phys. 88 (1988) 2547.
[7] R.S. Mulliken, J. Chem. Phys. 23 (1955) 1833.
[8] R.D. Levine, R.B. Bernstein, Molecular Reaction Dynamics and Chemical Reactivity, Oxford University Press, New York, 1987.
[9] T.H. Dunning Jr., J. Chem. Phys. 90 (1989) 1007.
[10] P.J. Stevens, J.F. Devlin, C.F. Chabalowski, M.J. Frish, J. Phys. Chem. 98 (1994) 11623.
[11] J.C. Slater, Phys. Rev. 81 (1951) 385.
[12] A.D. Becke, Phys. Rev. A 38 (1988) 3098.
[13] S.H. Vosco, L. Wilk, M. Nusair, Can. J. Phys. 58 (1980) 1200.
[14] C. Lee, W. Yang, R.G. Parr, Phys. Rev. B 37 (1988) 785.
[15] A.D. Becke, J. Chem. Phys. 98 (1993) 5648.
[16] M. Dupuis, A. Marquez, E.R. Davidson, "HONDO99.6", 1999, based on HONDO 95.3;
M. Dupuis, A. Marquez, E.R. Davidson, Quantum Chemistry Program Exchange (QCPE), Indiana University, Bloomington, in 47405.
[17] H. Nakai, in: "EDA2002", Waseda University, Tokyo, 2002.

[18] W.J. Hehre, R.F. Stewart, J.A. Pople, J. Chem. Phys. 51 (1969) 2657.
[19] T.H. Dunning Jr., J. Chem. Phys. 53 (1970) 2823.
[20] R.A. Kendall, T.H. Dunning Jr., R.J. Harrison, J. Chem. Phys. 96 (1992) 6769.
[21] K. Morokuma, J. Chem. Phys. 55 (1971) 1236.
[22] P.S. Bagus, K. Hermann, C.W. Bauschlicher Jr., J. Chem. Phys. 80 (1984) 4378.
[23] W.J. Stevens, W.H. Fink, Chem. Phys. Lett. 139 (1987) 15.

ELSEVIER

Journal of Molecular Structure (Theochem) 592 (2002) 61–67

THEO CHEM

www.elsevier.com/locate/theochem

Ab initio MD simulation of collision reaction between ammonia cluster ion and ammonia monomer

Hiromi Nakai[a,*], Yusuke Yamauchi[a], Aiko Matsuda[a], Yoshiki Okada[b], Kazuo Takeuchi[b]

[a]*Department of Chemistry, School of Science and Engineering, Waseda University, Tokyo 169-8555, Japan*
[b]*RIKEN (The Institute of Physical and Chemical Research), 2-1 Hirosawa, Wako, Saitama 351-0198, Japan*

Received 3 November 2001; revised 31 January 2002; accepted 31 January 2002

Abstract

Ab initio molecular dynamic (MD) simulations were performed for investigating collision reaction between $NH_4^+(NH_3)_2$ trimer and ND_3 monomer. Collision cross-section with the use of three criteria was obtained for the collision energy of 0.1–1.0 eV. The MD simulation showed that the reaction followed by the collision is closely connected with the degree of contact in the first collision. © 2002 Elsevier Science B.V. All rights reserved.

Keywords: Ab initio molecular dynamic simulation; Ammonia cluster ion; Collision reaction; Collision cross-section; Ionic nucleation process

1. Introduction

Dynamics of ion-induced nucleation process has been important in many scientific and technological fields [1–5]. Some groups suggested that an initial step of the ionic nucleation involves a metastable state [6,7]. Orii et al. measured reaction cross-sections between ammonia cluster ions $NH_4^+(NH_3)_{n-1}$ ($n = 3$–9) and deuterated ammonia monomer ND_3 [8]. They reported that reaction between $NH_4^+(NH_3)_{n-1}$ and ND_3 includes fusion and evaporation processes:

$$\text{Fusion}: NH_4^+(NH_3)_{n-1} + ND_3 \rightarrow NH_4^+(NH_3)_{n-m}ND_3 + (m-1)NH_3 \quad (1)$$

$$\text{Evaporation}: NH_4^+(NH_3)_{n-1} + ND_3 \rightarrow NH_4^+(NH_3)_{n-m-1} + ND_3 + mNH_3 \quad (2)$$

Furthermore, it was reported that fusion and evaporation cross-sections have different dependencies on collision energy, E_C.

We have recently examined collision cross-section analytically with the use of ab initio attractive potential [9]. Dependencies of the calculated collision cross-sections on collision energy and cluster size are comparable to those of measured fusion cross-section. However, there was some limitation in the previous method. For example, analytical solution was given only for $0.0 < E_C < 0.1$ eV. Reaction followed by the collision could not be investigated.

In the present study, we applied an ab initio molecular dynamics (MD) simulation to the collision reaction. Our original MD program, which is based on

* Corresponding author.
E-mail address: nakai@waseda.jp (H. Nakai).

PII: S0166-1280(02)00227-0

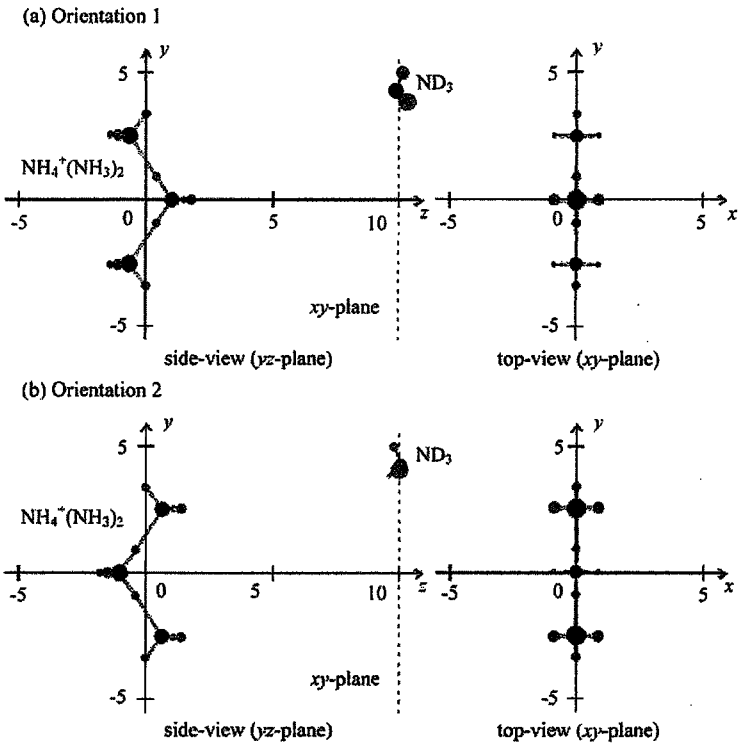

Fig. 1. Two initial orientations 1 and 2 for the ab initio MD simulations of $NH_4^+(NH_3)_2$ and ND_3.

the Gear's predictor–corrector algorithm, is combined with ab initio molecular orbital (MO) calculations. The collision cross-section was obtained by the ab initio MD simulation. It was clarified that the degree of contact is related with the reaction followed by the collision.

2. Computational methods

We examine collision reaction between ammonia cluster ions and ammonia monomer by using an ab initio MD simulation. In the classical MD simulations, statistical averages of physical properties are usually obtained from the results of more than 10,000 trajectories. However, it is very difficult to calculate the statistical average in the ab initio MD simulations, since it involves the time-consuming ab initio MO or density functional theory (DFT) calculations. For example, computation of atomic forces in $NH_4^+(NH_3)_3$ by the HF/D95V and B3LYP/cc-pVTZ methods requires central processing unit (CPU) times of 9.7 and 1748.3 s on Alpha 21264/700 MHz workstation, respectively. It is well known that in the HF- and DFT-type calculations, the requirement of computer resources, including the CPU time and memory, scales as N^2 to N^3, where N is a size of the system.

As the first trial of the ab initio MD simulation on the collision reaction, we deal with $NH_4^+(NH_3)_2 + ND_3$, which is the smallest system observed experimentally [8], and adopt the HF/D95V method for the ab initio calculations. The accuracy of the HF/D95V method for the present system has been already checked in our previous studies [7,9]. Binding enthalpy between $NH_4^+(NH_3)_2$ and ND_3 was calculated to be 14.84 kcal/mol in comparison with the B3LYP/cc-pVTZ calculation of 14.87 kcal/mol and the experimental value of 13.5–14.2 kcal/mol [10–12].

The time step, Δt, to numerically solve Newton equation is directly related to the CPU time of the MD simulation. However, there exists some limitation for

Table 1
Three collision criteria by using the distances between H in $NH_4^+(NH_3)_2$ and N or D in ND_3 (in Å)

	Collision criteria		
	I	II	III
R(N–H)	2.75	2.35	1.95
R(D–H)	2.40	2.00	1.60

the longer Δt in order to satisfy the energy conservation law. It depends on the nuclear motion included in the simulation. Thus, we classified the simulation into two steps.

The first step is to examine only collision process, where the geometries of $NH_4^+(NH_3)_2$ and ND_3 are fixed at the optimized ones and Δt is set to 1.0 fs. In this step, we calculated both collisional and non-collisional trajectories in order to determine the collision region. The second step is to examine the reaction process followed by the collision, where the intermolecular geometries between NH_4^+ and NH_3 are relaxed and Δt is set to 0.1 fs. The geometries of NH_4^+, NH_3, and ND_3 are fixed in the simulations.

As a result, the equation-of-motion for the rigid body should be solved numerically. We have developed the original MD program, which is based on the Gear's predictor–corrector algorithm [13]. In this study, the fifth- and fourth-order treatments are used for the translational and rotational motions, respectively. Ab initio MO calculations were performed by GAUSSIAN 98 program [14], which was combined with our MD program.

3. Results and discussion

At first, we performed an ab initio MD simulation for the collision process between $NH_4^+(NH_3)_2$ trimer and ND_3 monomer. Geometries of the trimer and monomer are fixed at the optimized ones during the simulation. Fig. 1 shows a schematic illustration of the initial configuration of $NH_4^+(NH_3)_2 + ND_3$. Center-of-mass (COM) in $NH_4^+(NH_3)_2$ is situated at the original point. In orientation 1 shown in Fig. 1(a), two N atoms of NH_3 are set on the yz-plane at the opposite side of ND_3, and two terminal H atoms in NH_4^+ are on the xz-plane at the same side of ND_3. On the other hand, in orientation 2 shown in Fig. 1(b), the two N atoms and the two H atoms are set to the same and the opposite side of ND_3, respectively. Initial velocities of the trimer, which correspond to the collision energies of 0.1, 0.3, 0.6, and 1.0 eV, are given in the direction of the z-axis. Initial z-coordinate of COM in ND_3 is set to 10 Å, while its x- and y-coordinates are changed at the lattice points of $\Delta x = \Delta y = 1$ Å. The time step used in the MD simulation is $\Delta t = 1.0$ fs.

Three kinds of collision criteria are used for the simulation, which are shown in Table 1. In the criterion I, it is judged that the collision occurs if the interatomic distances between $NH_4^+(NH_3)_2$ and ND_3 become less than Van der Waals radii; that is, the N–H and D–H distances of 2.75 and 2.40 Å, respectively [15]. The criteria II and III correspond to Van der Waals radii -0.40 and -0.80 Å, respectively. Note that the N–H distances of 2.00 and 1.60 Å are near the intermolecular hydrogen bonds for the first- and second-shell structures in $NH_4^+(NH_3)_{16}$ [7].

We first examine the orientation 1 in Fig. 1(a). When $(x, y, z) = (5, 15, 10)$ in Å is used as an initial coordinate of COM in ND_3, the three criteria I–III are not satisfied throughout the ab initio MD simulation, which corresponds to a non-collisional trajectory. A trajectory with an initial coordinate of $(x, y, z) = (5, 10, 10)$ satisfies the criterion I, whereas it does not satisfy the criteria II and III. It is judged that the trajectory corresponds to a collisional one, while the degree of contact is the lowest one. A trajectory with an initial coordinate of $(x, y, z) = (5, 5, 10)$ satisfies the criteria I and II, which corresponds to the middle degree of contact. Furthermore, a trajectory with an initial coordinate of $(x, y, z) = (5, 0, 10)$ satisfies the three criteria, which corresponds to the highest degree of contact.

We have performed the ab initio MD simulations, of which initial coordinates of COM in ND_3 are changed at the lattice points of $(x, y) = (-15, -15)$–$(15, 15)$ with $\Delta x = \Delta y = 1$ Å, by fixing z-coordinate of 10 Å. Fig. 2 shows the degree of contact in the ab initio MD simulations. A white spot corresponds to a non-collisional trajectory. Gray, dark gray, and black spots correspond to the lowest (I), middle (I + II), and highest (I + II + III) degrees of contact, respectively. As a result, Fig. 2 expresses collision regions and/or collision cross-sections judged by three different criteria.

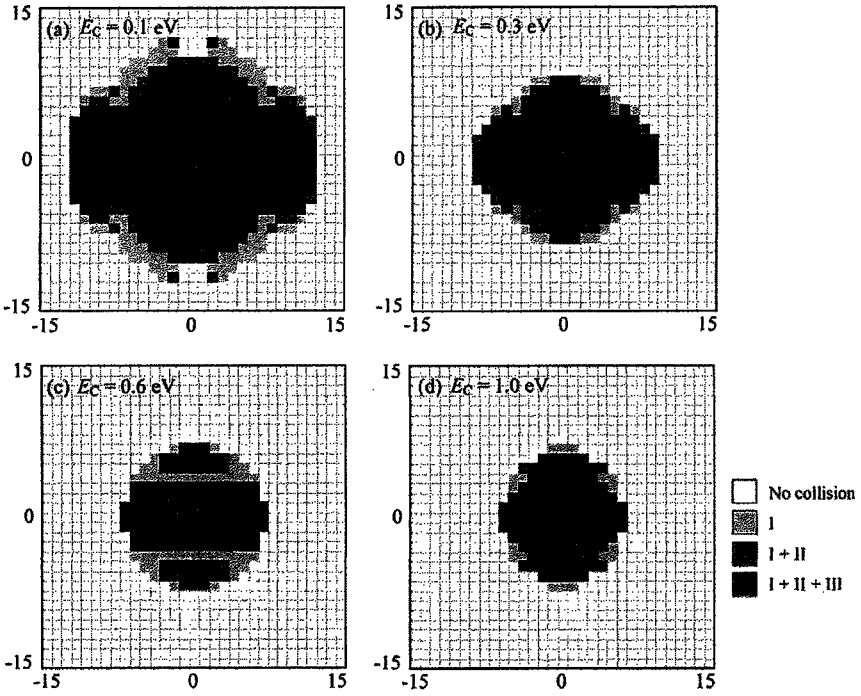

Fig. 2. Collision cross-sections obtained for the initial orientation 1 with collision energies E_C of (a) 0.1, (b) 0.3, (c) 0.6, and (d) 1.0 eV.

In Fig. 2, we have also investigated the collision energy dependence of the collision cross-sections. As larger collision energy, the collision cross-section becomes smaller. It is consistent with the phenomena that the centrifugal barrier increases for larger collision energy.

While the shape of the region I is almost a circle at $E_C = 0.6$ eV, that at $E_C = 1.0$ eV is an ellipse having major axis in the direction of y-axis, which corresponds to the initial configuration of the trimer. On the other hand, the region III in the direction of x-axis increases at $E_C = 0.3$ and 0.1 eV. It means that the attractive force due to the two terminal H atoms in NH_4^+ reaches this region.

For the opposite initial orientation of $NH_4^+(NH_3)_2$ and ND_3 as shown in Fig. 1(b), the collision cross-section has been investigated at $E_C = 0.1$ and 1.0 eV. The opposite orientation is negative for the intermolecular hydrogen bond. The regions I in Fig. 3(a) and (b) become smaller than those in Fig. 2(a) and (d),

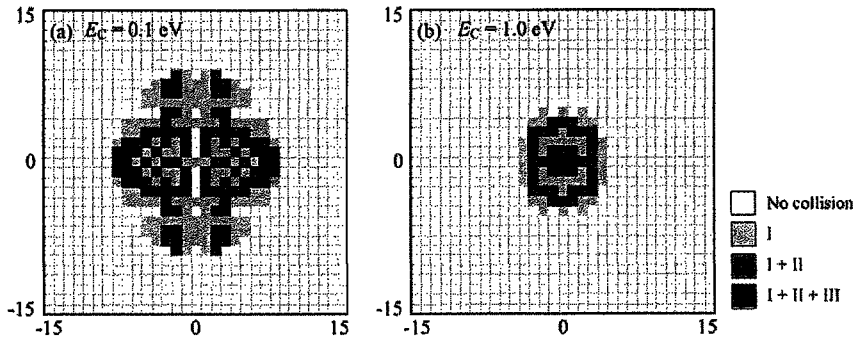

Fig. 3. Collision cross-sections obtained for the initial orientation 2 with collision energies E_C of (a) 0.1 and (b) 1.0 eV.

Table 2
Numerical values of three collision cross-sections σ_C^I, σ_C^{II}, and σ_C^{III} obtained by the ab initio MD simulation in comparison with the experimental fusion σ_F, evaporation σ_E, and total reaction σ_R (in Å^2)

E_C (eV)	Orientation 1			Orientation 2			Average			Exptl. [8]		
	σ_C^I	σ_C^{II}	σ_C^{III}	σ_C^I	σ_C^{II}	σ_C^{III}	σ_C^I	σ_C^{II}	σ_C^{III}	σ_F	σ_E	σ_R
0.1	517	417	265	221	104	15	292	179	75	80.3	1.4	81.7
0.3	243	213	141	–	–	–	–	–	–	–	–	–
0.6	177	135	83	–	–	–	–	–	–	–	–	–
1.0	143	125	63	79	39	0	94	60	15	14.1	38.5	52.6

respectively. It is noted that Fig. 3(b) does not involve the region III.

Summation of the regions I–III gives numerical data for the collision cross-sections, σ_C^i (i = I–III), which are shown in Table 2. Table 2 also shows the experimental fusion, evaporation, and total reaction cross-sections; namely, σ_F, σ_E, and σ_R, respectively. In the real system, two extreme situations examined in Figs. 2 and 3 appear in different probability due to rotation of the trimer and monomer and, furthermore, due to the interaction between them. Based on the average dipole orientation (ADO) theory [16–18], the dipole locking constant of ND_3 is estimated to be 0.24 [9]. Table 2 also shows the average values of σ_C^i using the locking constant; namely, the weight of 24 and 76% for the attractive and repulsive orientations, respectively. The average values of σ_C^{III} at $E_C = 0.1$ and 1.0 eV are 75 and 15 Å^2, respectively, which are comparable to the respective σ_F of 80.3 and 14.1 Å^2.

Next, we carried out the ab initio MD simulation for the reaction process between $NH_4^+(NH_3)_2$ and ND_3. As mentioned earlier, the intermolecular N–H distances are relaxed in the simulation, whereas the intramolecular N–H ones are fixed. Fig. 4 shows the time dependence of the intermolecular distances between NH_4^+ and NH_3 (or ND_3); that is, R_1 for the NH_4^+–ND_3 distance and R_2 and R_3 for two NH_4^+–NH_3 distances in the trimer. The ab initio MD simulation has been performed for the collision energies of 0.1 and 1.0 eV. Fig. 4(a) and (c) correspond to the initial ND_3 configuration of (4, 1, 10) in Å, which belongs to the region III in Fig. 2(b) and (c). On the other hand, Fig. 4(b) and (d) correspond to that of (1, 4, 10), which only belongs to the region II.

In Fig. 4(a), R_1 decreases monotonically until $t \approx$ 690 fs, which indicates that ND_3 approaches NH_4^+. At $t \approx$ 690 fs, R_1 becomes as long as R_2 and R_3, which indicates that collision occurs there. The ND_3 molecule approaches NH_4^+ again and again; that is, $t \approx$ 920 and 1060 fs. As a result, the collision in Fig. 4(a) leads to a fusion reaction. It is noted that the vibration between the first and second collisions has 1.6 times longer period and 2.1 times larger amplitude than those of the usual NH_4^+–NH_3 vibration. Similar large molecular vibration is seen in Fig. 4(c). The collision in Fig. 4(c) also leads to fusion. On the other hand, there are no large molecule vibrations after the first collision in Fig. 4(b) and (d). They correspond to non-reactive collisions.

Therefore, it seems that the existence of the large molecule vibration in the initial step determines, which process, such as fusion, evaporation, and non-reactive collision will be brought about. The degree of contact in the first collision, distinguished in Figs. 2 and 3, is related with the large molecule vibration and further, with the collision reaction.

4. Conclusion

In this study, we have developed an ab initio MD simulation program, in which a classical MD part based on the Gear's predictor–corrector algorithm is combined with an ab initio MO part of GAUSSIAN 98 program [14]. Collision reaction between ammonia cluster ion and ammonia monomer has been investigated with the use of the ab initio MD simulation. The collision cross-section between $NH_4^+(NH_3)_2$ and ND_3 has been obtained for the collision energy of 0.1–1.0 eV, which could not be treated by the analytical method in our previous study [9]. The degree of contact in the first collision, distinguished by using

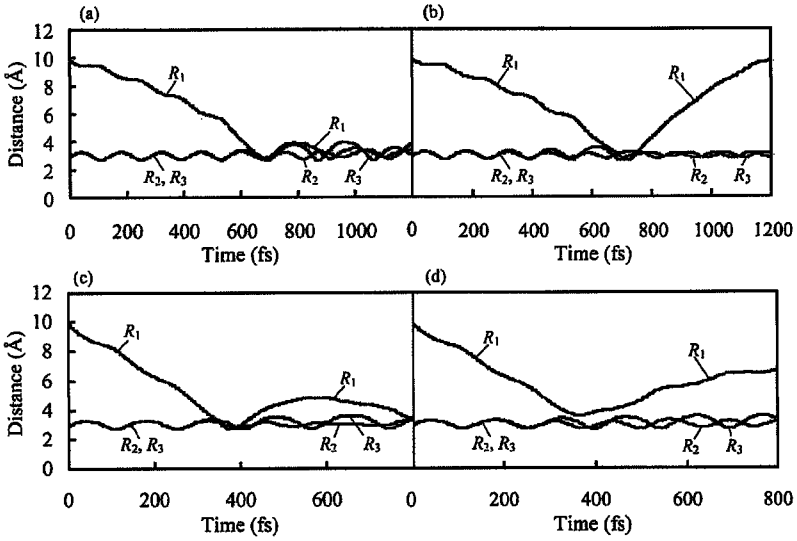

Fig. 4. Time dependence of the intermolecular distance R_1, R_2, and R_3 between NH_4^+ and NH_3 (or ND_3). Collision energies of $NH_4^+(NH_3)_2$ are 0.1 eV for (a) and (b), and 1.0 eV for (c) and (d). Initial configuration of ND_3 are (4, 1, 10) for (a) and (c) and (1, 4, 10) for (b) and (d).

three criteria, is found to be related with the reaction followed by the collision. Thus, the combination of the ab initio MO method and MD simulation is shown to be a powerful method for the investigation of the collision reaction. Cluster-size dependence of the collision cross-section is now investigated by using the present MD program combined with the semi-empirical MO method, which will be published elsewhere [19].

Acknowledgments

Part of the calculations was performed at the Research Center for Computational Science (RCCS) of the Okazaki National Research Institutes and the Media Network Center (MNC) of Waseda University. Part of this study was supported by a Grant-in-Aid for Scientific Research on Priority Areas 'Molecular Physical Chemistry' from the Japanese Ministry of Education, Culture, Sports, Science, and Technology, and by a Waseda University Grant for Special Research Projects.

References

[1] R.J. Beuhler, L. Friedman, J. Chem. Phys. 77 (1982) 2549.
[2] A.W. Castleman Jr., R.B. Keesee, Chem. Rev. 86 (1986) 589.
[3] M.L. Mandich, W.D. Reents Jr., M.F. Jarrold, J. Chem. Phys. 88 (1988) 1703.
[4] M. Ichihashi, S. Nonose, T. Nagata, T. Kondow, J. Chem. Phys. 100 (1994) 6458.
[5] R. Caldwell, D. Wright, M.S. El-Shall, Z. Phys. D 26 (1993) S189.
[6] A.W. Castleman Jr., W.B. Tzeng, S. Wei, S. Morgan, J. Chem. Soc. Faraday Trans. 86 (1990) 2417.
[7] H. Nakai, T. Goto, T. Ichikawa, Y. Okada, T. Orii, K. Takeuchi, Chem. Phys. 262 (2000) 201.
[8] T. Orii, Y. Okada, K. Takeuchi, J. Chem. Phys. 113 (2000) 8026.
[9] H. Nakai, T. Goto, Y. Okada, T. Orii, K. Takeushi, M. Ichihasi, T. Kondow, J. Chem. Phys. 112 (2000) 7409.
[10] I.N. Tang, A.W. Castleman Jr., J. Chem. Phys. 62 (1975) 4576.
[11] M.R. Arshadi, J.H. Futrell, J. Phys. Chem. 78 (1974) 1482.
[12] J.D. Payzant, A.J. Cunningham, P. Kebarle, Can. J. Chem. 51 (1973) 3242.
[13] M.P. Allen, D.J. Tildesley, Computer Simulation of Liquids, Clarendon, Oxford, 1987.
[14] M.J. Frisch, G.W. Trucks, H.B. Schlegel, G.E. Scuseria, M.A. Robb, J.R. Cheeseman, V.G. Zakrzewski, J.A. Montgomery Jr., R.E. Stratmann, J.C. Burant, S. Dapprich, J.M. Millam, A.D. Daniels, K.N. Kudin, M.C. Strain, O. Farkas, J. Tomasi, V. Barone, M. Cossi, R. Cammi, B. Mennucci, C. Pomelli, C. Adamo, S. Clifford, J. Ochterski, G.A. Petersson, P.Y. Ayala, Q. Cui, K. Morokuma, D.K. Malick, A.D. Rabuck, K. Raghavachari, J.B. Foresman, J. Cioslowski, J.V. Ortiz, A.G. Baboul, B.B. Stefanov, G. Liu, A. Liashenko, P. Piskorz, I. Komaromi, R. Gomperts, R.L. Martin, D.J. Fox, T. Keith, M.A. Al-Laham, C.Y. Peng, A. Nanayakkara, M. Challacombe, P.M.W. Gill, B. Johnson, W. Chen, M.W. Wong,

J.L. Andres, C. Gonzalez, M. Head-Gordon, E.S. Replogle, J.A. Pople, GAUSSIAN 98, Revision A.9, Gaussian, Inc., Pittsburgh, PA, 1998.
[15] A. Bondi, J. Phys. Chem. 68 (1964) 441.
[16] T. Su, M.T. Bowers, J. Chem. Phys. 58 (1972) 3027.
[17] T. Su, M.T. Bowers, Int. J. Mass Spectr. Ion Phys. 17 (1975) 211.
[18] L. Bass, T. Su, W.J. Chesnavich, M.T. Bowers, Chem. Phys. Lett. 34 (1975) 119.
[19] Y. Yamauchi, A. Matsuda, Y. Okada, H. Nakai, unpublished.

Available online at www.sciencedirect.com
SCIENCE DIRECT®
Chemical Physics Letters 365 (2002) 203–210
CHEMICAL PHYSICS LETTERS
www.elsevier.com/locate/cplett

Energy density analysis (EDA) of *cis*, *trans*-enol isomerization in malonaldehyde, tropolone and 9-hydroxyphenalenone

Hiromi Nakai *, Keitaro Sodeyama

Department of Chemistry, School of Science and Engineering, Waseda University, Tokyo 169-8555, Japan

Received 25 July 2002; in final form 4 September 2002

Abstract

We have recently proposed an energy density analysis (EDA) that partitions the total energy of a molecular system into atomic energy densities. In this study, the EDA is applied to *cis*, *trans*-enol isomerization reactions of malonaldehyde, tropolone and 9-hydroxyphenalenone. Energy density changes in the reactions are shown to be closely related to the formation and breaking of the chemical bonds. By analyzing the energy density changes, we can find the reason why the hydrogen atom moves through the *out-of-plane* pathway instead of the *in-plane* pathway.

1. Introduction

Cis, *trans*-enol isomerization reactions have been widely investigated by both experimental and theoretical studies [1]. The *cis*-enol form of malonaldehyde (MA) has an internal hydrogen bond connecting two oxygen atoms, while the *trans*-enol form does not. Stabilization energy due to the hydrogen bond is reported to be in the range of 11.5–22.5 kcal/mol [1]. It has been shown that there are two equivalent (asymmetric) configurations of the *cis*-enol form of MA between which the proton tunneling reactions occur [2–15]. The transition state (TS) of the proton tunneling, whose energy barrier is reported to be about 3 kcal/mol, has a planar structure.

Recently, Yagi et al. [16] have reported the isomerization dynamics in MA with the use of a full-dimensional potential energy surface, which was evaluated by a modified Shepard interpolation scheme [17–19]. They found two kinds of saddle points on the reaction. One is the real TS having one imaginary mode, and the other is the second-order saddle point (SOSP) with two imaginary modes. While the SOSP has a planar structure, the moving H atom is out-of-plane in the TS. Why does the hydrogen atom go through the *out-of-plane* pathway in the *cis*, *trans*-enol isomerization reaction, whereas it goes through the *in-plane* pathway in the tunneling reaction?

In order to rationalize the chemical and physical phenomena theoretically, it is essential to

* Corresponding author. Fax: +81-3-3205-2504.
E-mail address: nakai@waseda.ac.jp (H. Nakai).

0009-2614/02/$ - see front matter © 2002 Elsevier Science B.V. All rights reserved.
PII: S0009-2614(02)01433-1

analyze the wave functions and energies obtained by the quantum chemical calculations. We have recently proposed a simple analyzing technique, named energy density analysis (EDA) [20], which partitions the total energy of the molecule computed using the Kohn–Sham type density functional theory (DFT) [21] into atomic energy densities without extra computing costs. In the present study, the EDA is applied to the *cis*, *trans*-enol isomerization reactions in MA, tropolone (TRN) and 9-hydroxyphenalenone (9HPO). Both the *out-of-plane* TS and the *in-plane* SOSP are obtained for the three systems. We evaluate atomic energy densities at the TS and SOSP, from which the energy difference between the two states are shown to be due to the oxygen atom bonded to H.

2. Computational details

The present study deals with the *cis*, *trans*-enol isomerization reactions in MA, TRN and 9HPO. Fig. 1 shows the structural formula of the *cis*-enol species of the three molecules. The electronic structures of these systems are obtained by the DFT calculations with the B3LYP hybrid functional [22–24]. Correlation-consistent polarization plus valence double zeta (cc-pVDZ) basis sets of Dunning [25] are adopted for H, C and O atoms. Geometry optimizations are carried out at the B3LYP/cc-pVDZ level. The electronic state calculations are performed by using the program system HONDO 99 [26].

The EDA [20] has been performed to evaluate the changes of the atomic energy densities in the isomerization reaction. In the EDA, the atomic energy density for the exchange–correlation term is evaluated by the partial sum for the numerical quadrature technique

$$E_{\mathrm{XC}}^{\mathrm{A}} = \sum_{g}^{\mathrm{grid}} \omega_g p_{\mathrm{A}}(\mathbf{r}_g) F_{\mathrm{XC}}(\mathbf{r}_g), \tag{1}$$

where $\omega_g(\mathbf{r})$ is the weight, $p_{\mathrm{A}}(\mathbf{r})$ is the partition function (for example, see [27]), and $F_{\mathrm{XC}}(\mathbf{r})$ is the exchange–correlation functional. The other terms, which are evaluated by the analytical integration with the KS orbitals, are partitioned into their energy densities by using the analogy of Mulliken population analysis [28]. For example, the Coulomb energy density for atom A, $E_{\mathrm{CLB}}^{\mathrm{A}}$, is evaluated by

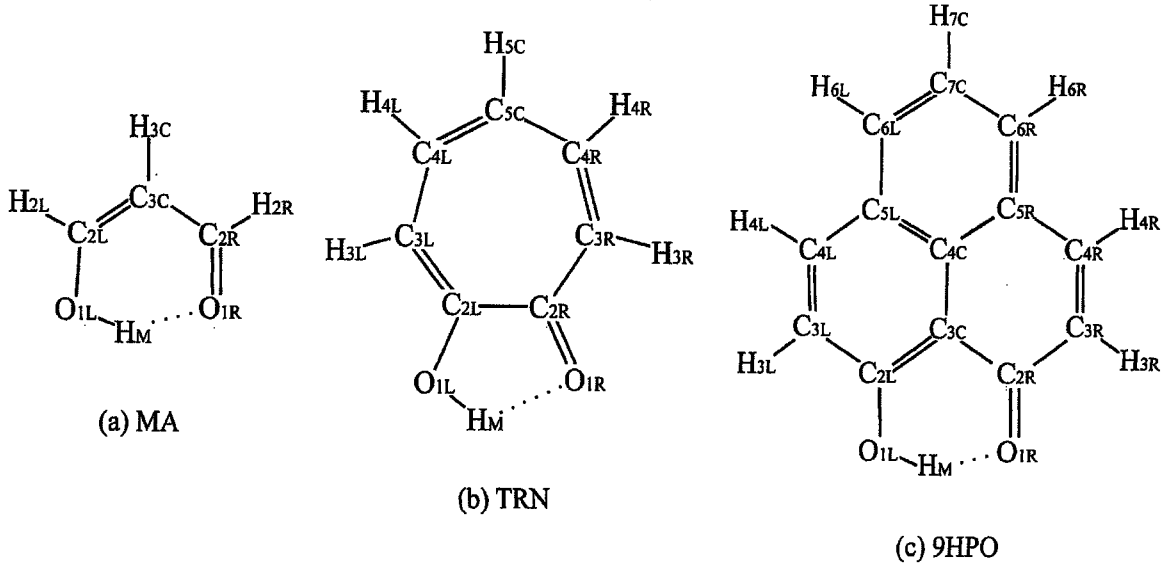

Fig. 1. Structural formula of (a) MA, (b) TRN and (c) 9HPO.

$$E^{A}_{CLB} = \frac{1}{2}\sum_{\mu\in A}(\mathbf{PG})_{\mu\mu}, \quad (2)$$

where **P** is the AO-basis density matrix and the element of **G** is given by

$$G_{\nu\mu} = \sum_{\rho}\sum_{\sigma} P_{\rho\sigma}(\chi_\nu\chi_\mu|\chi_\sigma\chi_\rho). \quad (3)$$

By adding the atomic contributions for the nuclear repulsion, kinetic, nuclear attraction, Coulomb and exchange–correlation terms, the total atomic energy density is evaluated by

$$E^{A} = E^{A}_{NN} + T^{A}_{S} + E^{A}_{Ne} + E^{A}_{CLB} + E^{A}_{XC}. \quad (4)$$

The EDA calculations are carried out by linking the original code for the EDA [29] with HONDO 99.

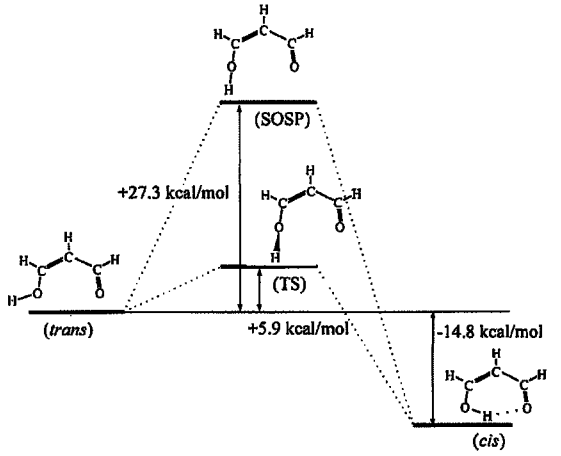

Fig. 2. Energy diagram for *cis*, *trans*-enol isomerization of MA along the two reaction pathways.

Table 1
Energetics of the *cis*, *trans*-enol isomerization reaction in MA, TRN and 9HPO

	ΔE_{TS}	ΔE_{SOSP}	ΔE_{cis}
MA	+5.93	+27.27	−14.82
TRN	+5.81	+28.22	−13.43
9HPO	+4.65	+27.02	−17.51

3. Results and discussion

Fig. 2 shows the energy diagram for the *cis*, *trans*-enol isomerization along two pathways. Schematic illustrations for *trans*, TS, SOSP and *cis* species are also shown in Fig. 2. The energy barrier of 27.3 kcal/mol along the *in-plane* pathway corresponds to SOSP, and that of 5.9 kcal/mol along the *out-of-plane* pathway corresponds to TS. This result supports the previous theoretical study [16]. Stabilization by the transformation from *trans* to *cis* species amounts to 14.8 kcal/mol, which is due to the formation of the hydrogen bond.

Table 1 shows the energetics of the *cis*, *trans*-enol isomerization reactions in TRN and 9HPO in addition to MA. As is the case for MA, the energy barriers along the *in-plane* and *out-of-plane* pathways correspond to the SOSP and TS in TRN and 9HPO, respectively. The barrier heights of the

Table 2
Atomic energy densities at *trans*, *cis*, TS, SOSP species (E_{trans}, E_{cis}, E_{TS} and E_{SOSP}) in MA are given in hartree

Atom[a]	E_{trans}	E_{TS}		E_{SOSP}		E_{cis}	
H_M	−0.4913	−0.4958	(−2.79)	−0.4877	(+2.28)	−0.5094	(−11.32)
O_{1L}	−75.3040	−75.3033	(+0.44)	−75.2725	(+19.74)	−75.2960	(+4.99)
O_{1R}	−75.2441	−75.2438	(+0.18)	−75.2455	(−0.90)	−75.2584	(−8.97)
C_{2L}	−38.1635	−38.1597	(+2.34)	−38.1544	(+5.67)	−38.1622	(+0.82)
C_{2R}	−38.1836	−38.1772	(+4.01)	−38.1852	(−1.04)	−38.1684	(+9.51)
C_{3C}	−38.1622	−38.1576	(+2.94)	−38.1566	(+3.52)	−38.1740	(−7.36)
H_{2L}	−0.5336	−0.5359	(−1.49)	−0.5354	(−1.15)	−0.5353	(−1.11)
H_{2R}	−0.5333	−0.5334	(−0.04)	−0.5336	(−0.18)	−0.5350	(−1.08)
H_{3C}	−0.5371	−0.5366	(+0.33)	−0.5382	(−0.68)	−0.5376	(−0.30)
Total	−267.1526	−267.1432	(+5.93)	−267.1091	(+27.27)	−267.1762	(−14.82)

Energy density differences with respect to the *trans* are shown in parentheses in kcal/mol.
[a] Numbering of atoms is defined in Fig. 1a.

Table 3
Atomic energy densities at *trans*, *cis*, TS, SOSP species (E_{trans}, E_{cis}, E_{TS} and E_{SOSP}) in TRN are given in hartree

Atom[a]	E_{trans}	E_{TS}		E_{SOSP}		E_{cis}	
H_M	−0.4939	−0.4957	(−1.17)	−0.4882	(+3.55)	−0.5007	(−4.28)
O_{1L}	−75.2927	−75.2933	(−0.42)	−75.2565	(+22.67)	−75.2863	(+3.98)
O_{1R}	−75.2382	−75.2385	(−0.17)	−75.2384	(−0.13)	−75.2494	(−7.04)
C_{2L}	−38.1341	−38.1150	(+11.99)	−38.1125	(+13.56)	−38.1502	(−10.08)
C_{2R}	−38.1691	−38.1747	(−3.51)	−38.1735	(−2.77)	−38.1521	(+10.66)
C_{3L}	−38.1478	−38.1688	(−13.20)	−38.1671	(−12.11)	−38.1633	(−9.75)
C_{3R}	−38.1511	−38.1453	(+3.66)	−38.1498	(+0.86)	−38.1555	(−2.76)
C_{4L}	−38.1782	−38.1676	(+6.64)	−38.1736	(+2.92)	−38.1717	(+4.10)
C_{4R}	−38.1659	−38.1663	(−0.25)	−38.1671	(−0.79)	−38.1677	(−1.16)
C_{5C}	−38.1724	−38.1705	(+1.19)	−38.1720	(+0.30)	−38.1703	(+1.32)
H_{3L}	−0.5313	−0.5295	(+1.15)	−0.5305	(+0.50)	−0.5297	(+1.01)
H_{3R}	−0.5303	−0.5303	(+0.02)	−0.5306	(−0.18)	−0.5302	(+0.10)
H_{4L}	−0.5292	−0.5294	(−0.14)	−0.5291	(+0.02)	−0.5289	(+0.16)
H_{4R}	−0.5289	−0.5290	(−0.10)	−0.5290	(−0.10)	−0.5286	(+0.16)
H_{5C}	−0.5305	−0.5303	(+0.12)	−0.5307	(−0.10)	−0.5303	(+0.14)
Total	−420.7937	−420.7844	(+5.81)	−420.7487	(+28.22)	−420.8151	(−13.43)

Energy density differences with respect to the *trans* are shown in parentheses in kcal/mol.
[a] Numbering of atoms is defined in Fig. 1b.

Table 4
Atomic energy densities at *trans*, *cis*, TS, SOSP species (E_{trans}, E_{cis}, E_{TS} and E_{SOSP}) in 9HPO are given in hartree

Atom[a]	E_{trans}	E_{TS}		E_{SOSP}		E_{cis}	
H_M	−0.4926	−0.4944	(−1.15)	−0.4861	(+4.08)	−0.5145	(−13.70)
O_{1L}	−75.2978	−75.3005	(−1.70)	−75.2640	(+21.22)	−75.2893	(+5.36)
O_{1R}	−75.2389	−75.2398	(−0.54)	−75.2401	(−0.74)	−75.2509	(−7.53)
C_{2L}	−38.1438	−38.1280	(+9.91)	−38.1213	(+14.10)	−38.1390	(+3.03)
C_{2R}	−38.1493	−38.1447	(+2.89)	−38.1538	(−2.82)	−38.1338	(+9.73)
C_{3L}	−38.1362	−38.1632	(−16.93)	−38.1589	(−14.22)	−38.1583	(−13.87)
C_{3C}	−38.0882	−38.0884	(−0.10)	−38.0827	(+3.46)	−38.0955	(−4.58)
C_{3R}	−38.1476	−38.1483	(−0.46)	−38.1483	(−0.47)	−38.1558	(−5.14)
C_{4L}	−38.1536	−38.1423	(+7.12)	−38.1473	(+3.95)	−38.1453	(+5.23)
C_{4C}	−38.2153	−38.2093	(+3.77)	−38.2168	(−0.97)	−38.2190	(−2.32)
C_{4R}	−38.1452	−38.1443	(+0.57)	−38.1449	(+0.18)	−38.1435	(+1.08)
C_{5L}	−38.1619	−38.1620	(−0.05)	−38.1625	(−0.38)	−38.1600	(+1.21)
C_{5R}	−38.1642	−38.1643	(−0.07)	−38.1646	(−0.26)	−38.1617	(+1.58)
C_{6L}	−38.1461	−38.1467	(−0.35)	−38.1464	(−0.14)	−38.1451	(+0.67)
C_{6R}	−38.1450	−38.1445	(+0.33)	−38.1450	(−0.02)	−38.1440	(+0.64)
C_{7C}	−38.1636	−38.1630	(+0.32)	−38.1638	(−0.13)	−38.1635	(+0.06)
H_{3L}	−0.5325	−0.5308	(+1.07)	−0.5321	(+0.29)	−0.5310	(+0.94)
H_{3R}	−0.5318	−0.5318	(−0.01)	−0.5319	(−0.09)	−0.5316	(+0.15)
H_{4L}	−0.5308	−0.5309	(−0.06)	−0.5307	(+0.07)	−0.5306	(+0.09)
H_{4R}	−0.5304	−0.5304	(+0.02)	−0.5305	(−0.02)	−0.5304	(+0.02)
H_{6L}	−0.5315	−0.5314	(+0.05)	−0.5315	(+0.01)	−0.5316	(−0.05)
H_{6R}	−0.5315	−0.5316	(−0.04)	−0.5316	(−0.04)	−0.5317	(−0.11)
H_{7L}	−0.5319	−0.5318	(+0.07)	−0.5320	(−0.04)	−0.5319	(+0.01)
Total	−650.7098	−650.7024	(+4.65)	−650.6668	(+27.02)	−650.7377	(−17.51)

Energy density differences with respect to the *trans* are shown in parentheses in kcal/mol.
[a] Numbering of atoms is defined in Fig. 1c.

in-plane SOSP and the *out-of-plane* TS lie in the range of 4.7–5.9 and 27.0–28.2 kcal/mol, respectively. The stabilization energy of 13.4 kcal/mol in the *cis*-enol structure of TRN is similar but a little bit smaller than that of 14.8 kcal/mol in MA, while the stabilization energy of 17.5 kcal/mol in 9HPO is also similar but a little bit larger. Thus, the energetics of the *cis*, *trans*-enol isomerization reactions are similar to each other in the three systems. It may indicate that the energetics are mainly determined by the local interaction.

Tables 2–4 show the atomic energy densities in the *trans*, TS, SOSP and *cis* species of MA, TRN and 9HPO molecules, respectively. All the data are evaluated by the EDA technique. In Tables 2–4, the energy density differences with respect to the *trans* species are also shown in parentheses in kcal/mol. From the viewpoint of the atomic energy density, the hydrogen atoms in the three molecules fall into two categories: the hydrogen atoms bonding to oxygen which are denoted by H_M in Fig. 1; and the hydrogen atoms bonding to carbon such as H_{2L}, H_{2R} and H_{3C} in MA. The hydrogen atoms in the first category have atomic energy densities in the range of −0.49 to −0.51 hartree, whereas those in the second category have atomic energy densities in the range of −0.53 to −0.54 hartree. Generally, in the same element, the absolute value of the atomic energy density may increase as the atomic population increases. In fact, the populations of the former category of hydrogen atoms are between 0.81 and 0.86, while those of the latter category of hydrogen atoms are between 0.97 and 1.01.

The energy densities of carbon atoms in MA and TRN are in the range of −38.15 to −38.19 and −38.11 to −38.18 hartree, respectively. Those in 9HPO are in the range of −38.12 to −38.16 hartree, except for C_{3C} and C_{4C}. The energy densities of C_{3C} are a little bit smaller than the above range, and those of C_{4C} are a little bit larger. Note that the atomic energy densities of C_{3C} and C_{4C} do not change much throughout the *cis*, *trans*-enol isomerization. Both absolute values and changes of the atomic energy densities of O_{1L} and O_{1R} are comparatively similar amongst the three molecules.

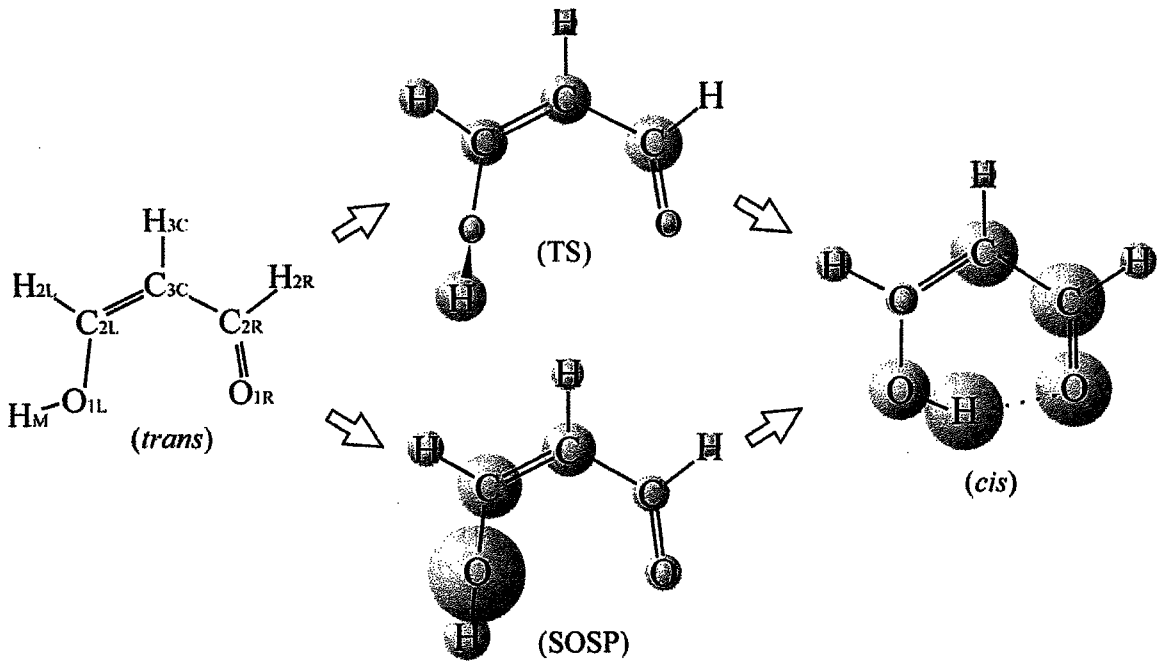

Fig. 3. Energy density changes from the *trans* species in MA along the two reaction pathways. Stabilized and destabilized atoms are represented by blue and red balls, respectively, whose volume is proportional to the degree of the stabilization and destabilization.

Figs. 3–5 show the energy density changes with respect to the *trans* species in MA, TRN and 9HPO, respectively, along the two pathways of the *cis*, *trans*-enol isomerization. Blue and red balls stand for stabilized and destabilized atoms, respectively. The volume of the ball is proportional to the degree of the stabilization or destabilization estimated by the EDA results in Tables 2–4, respectively.

On comparing the TS and SOSP illustrations, characteristic behaviors are seen in O_{1L} at the SOSP in the three systems. The destabilization energies in O_{1L} are 19.7, 22.7 and 21.2 kcal/mol in MA, TRN and 9HPO, which are of the same magnitude and comprise most of the total barrier height at the SOSP. On the other hand, the destabilization energy in O_{1L} is only 0.4 kcal/mol at the TS in MA. In TRN and 9HPO, O_{1L} becomes rather stabilized. These differences in O_{1L} are the reasons why the energy levels at the SOSP are about 22 kcal/mol higher than those at the TS in the three systems.

At the TS, H_M–O_{1L}–C_{2L} angles in MA, TRN and 9HPO are 110.2°, 109.7° and 109.6°, respectively, which are very close to the tetrahedral angle of 109.5°. On the other hand, those at the SOSP are 176.4°, 177.5° and 175.3°, respectively, which are almost linear. This means that in the case of the *out-of-plane* pathway, the oxygen atom can maintain the sp^3 bonding with the hydrogen atom, whereas in the case of the *in-plane* pathway it cannot do so.

Finally, we discuss the energy density changes in forming the *cis*-enol structure. Both H_M and O_{1R} atoms become stable in the case of the *cis* species in MA, TRN and 9HPO due to the formation of the hydrogen bond. The energy density changes in H_M and O_{1R} are (−11.32, −8.97),

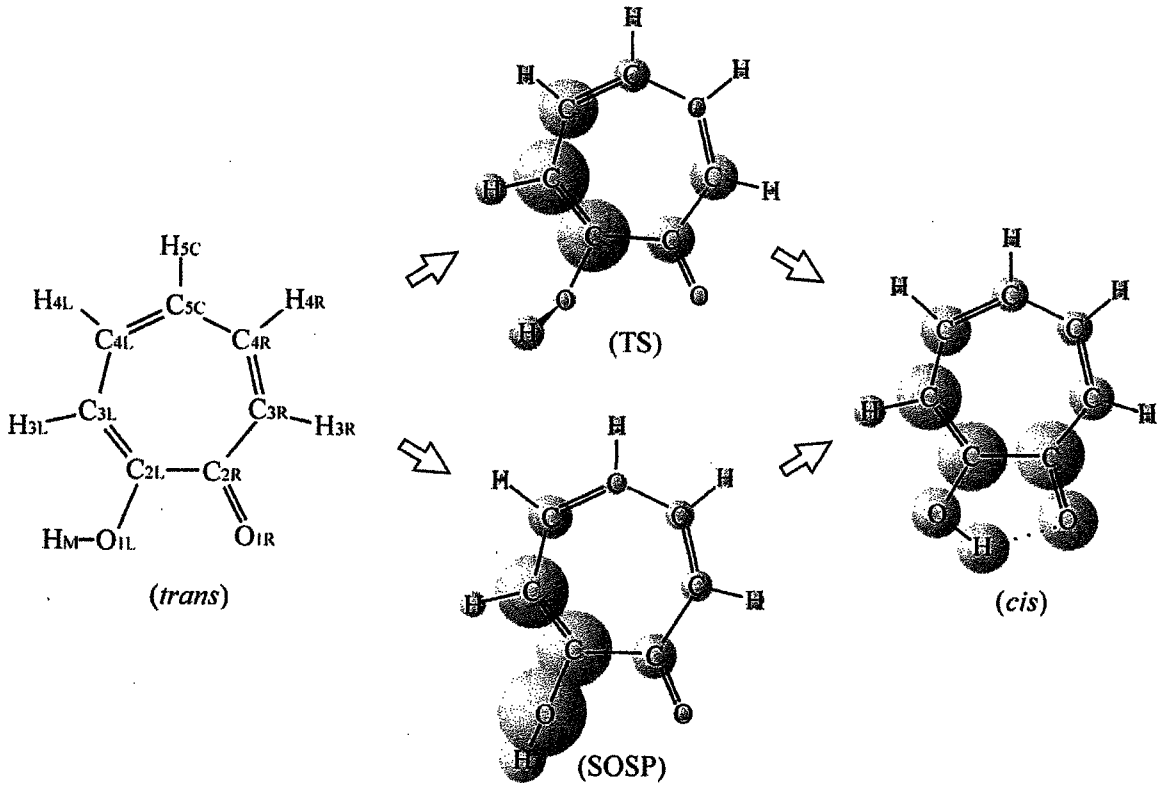

Fig. 4. Energy density changes from the *trans* species in TRN along the two reaction pathways. Stabilized and destabilized atoms are represented by blue and red balls, respectively, whose volume is proportional to the degree of the stabilization and destabilization.

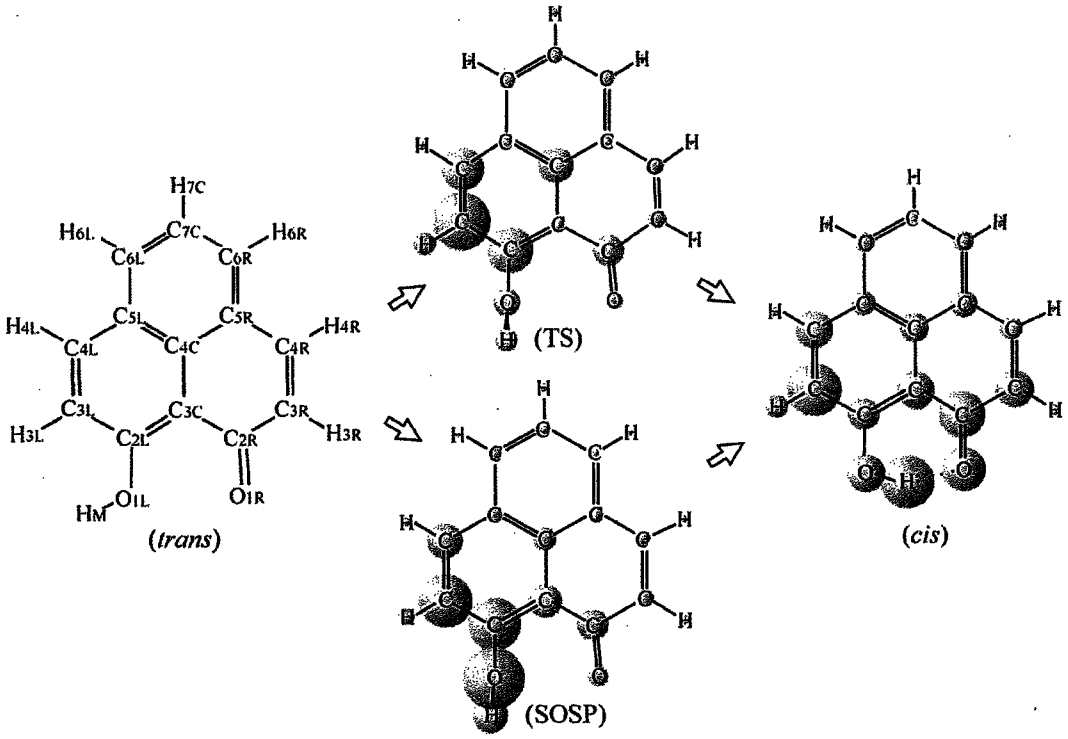

Fig. 5. Energy density changes from the *trans* species in 9HPO along the two reaction pathways. Stabilized and destabilized atoms are represented by blue and red balls, respectively, whose volume is proportional to the degree of the stabilization and destabilization.

(−4.28, −7.04) and (−13.70, −7.53) in kcal/mol, respectively. The sum of the stabilization energies in H_M and O_{1R} in TRN is less than those in MA and 9HPO. Similarly, the total stabilization energy in TRN is also less. In MA and 9HPO, the *cis*-enol species has a six-membered ring, whereas it has a five-membered ring in TRN. As a result, the H_M–O_{1R} length of 1.732 Å in TRN is longer than the 1.616 Å in MA and the 1.558 Å in 9HPO. Because of the long H_M–O_{1R} distance in TRN, the hydrogen bond in TRN is expected to be weaker. Thus, the EDA technique can give an appealing picture for understanding the chemical and physical phenomena.

4. Conclusion

Recently we have proposed the EDA method [20] to partition the total energy of molecules into atomic energy densities. The present study is an application of the EDA method to the *cis*, *trans*-enol isomerization reactions in MA, TRN and 9HPO. The changes of the atomic energy densities along the reaction pathways are shown to be consistent with the formation and breaking of the chemical bonds. In particular, the difference between the *out-of-plane* TS and the *in-plane* SOSP is found to be due to the chemical bonding of the O–H bond. The former case can keep the sp^3 bonding, but the latter cannot. Thus, it is shown that the EDA technique is a very useful and powerful tool for investigating chemical and physical processes.

Acknowledgements

Part of the calculations was performed at the Research Center for Computational Science

(RCCS) of the Okazaki National Research Institutes and the Media Network Center (MNC) of Waseda University. Part of this study was supported by a Grant-in-Aid for Young Scientists (A) 'KAKENHI 14703005' from Japanese Society for the Promotion of Science (JSPS) and by a Waseda University Grant for Special Research Projects.

References

[1] W. Koch, M.C. Holthausen, A Chemist's Guide to Density Functional Theory, Wiley, New York, 2000.
[2] W.F. Rowe, R.W. Duerst, E.B. Wilson, J. Am. Chem. Soc. 98 (1976) 4021.
[3] S.L. Baughcum, R.W. Duerst, W.F. Rowe, Z. Smith, E.B. Wilson, J. Am. Chem. Soc. 103 (1981) 6296.
[4] S.L. Baughcum, Z. Smith, E.B. Wilson, R.W. Duerst, J. Am. Chem. Soc. 106 (1984) 2260.
[5] P. Turner, S.L. Baughcum, S.L. Coy, Z. Smith, J. Am. Chem. Soc. 106 (1984) 2265.
[6] D.W. Firth, K. Beyer, M.A. Dvorak, S.W. Reeve, A. Grushow, K.R. Loepold, J. Chem. Phys. 94 (1991) 1812.
[7] T. Baba, T. Tanaka, I. Morino, K.M.T. Yamada, K. Tanaka, J. Chem. Phys. 110 (1999) 4131.
[8] T. Carrington Jr., W.H. Miller, J. Chem. Phys. 81 (1984) 3942.
[9] T. Carrington Jr., W.H. Miller, J. Chem. Phys. 84 (1986) 4364.
[10] N. Sato, S. Iwata, J. Chem. Phys. 89 (1988) 2932.
[11] N. Shida, P.F. Barbara, J. Almlöf, J. Chem. Phys. 91 (1989) 4061.
[12] N. Shida, J. Almlöf, P.F. Barbara, J. Phys. Chem. 95 (1991) 10457.
[13] D. Babić, S.D. Bosanac, N. Došlić, Chem. Phys. Lett. 358 (2002) 337.
[14] S. Sadhukhan, D. Muñoz, C. Adamo, G.E. Scuseria, Chem. Phys. Lett. 306 (1999) 83.
[15] H. Nakai, K. Sodeyama, J. Mol. Struct. (THEOCHEM), in press.
[16] K. Yagi, T. Taketsugu, K. Hirao, J. Chem. Phys. 115 (2001) 10647.
[17] J. Ischtman, M.A. Collins, J. Chem. Phys. 100 (1994) 8080.
[18] M.A. Collins, in: I. Prigogine, S.A. Rice (Eds.), New Method in Computational Quantum Mechanics, Wiley, New York, 1996, p. 389.
[19] T. Takata, T. Taketsugu, K. Hirao, M.S. Gordon, J. Chem. Phys. 109 (1998) 4281.
[20] H. Nakai, Chem. Phys. Lett. 363 (2002) 73.
[21] W. Kohn, L.J. Sham, Phys. Rev. 140 (1965) A1133.
[22] P.J. Stevens, J.F. Devlin, C.F. Chabalowski, M.J. Frish, J. Chem. Phys. 98 (1998) 11623.
[23] A.D. Becke, Phys. Rev. A 38 (1988) 3098.
[24] C. Lee, W. Yang, R.G. Parr, Phys. Rev. B 37 (1988) 785.
[25] T.H. Dunning Jr., J. Chem. Phys. 90 (1989) 1007.
[26] M. Dupuis, A. Marquez, E.R. Davidson, 'HONDO 99.6', 1999, based on HONDO 95.3, M. Dupuis, A. Marquez, E.R. Davidson, Quantum Chemistry Program Exchange (QCPE), Indiana University, Bloomington, IN 47405.
[27] A.D. Becke, J. Chem. Phys. 88 (1988) 2547.
[28] R.S. Mulliken, J. Chem. Phys. 23 (1955) 1833.
[29] H. Nakai, 'EDA2002', 2002, Waseda University, Tokyo 169-8555.

DFT Calculation Analysis of the Infrared Spectra of Ethylene Adsorbed on Cu(110), Pd(110), and Ag(110)

Koichi Itoh,* Tairiku Kiyohara, Hironao Shinohara, Chikaomi Ohe, Yoshiumi Kawamura, and Hiromi Nakai

Department of Chemistry, School of Science and Engineering, Waseda University, Shinjuku-ku, Tokyo 169-8555, Japan

Received: June 6, 2002; In Final Form: July 23, 2002

A density functional theory (DFT) calculation was performed on the cluster models of ethylene on Cu(110), Ag(110), and Pd(110) to clarify the correlation between the IR spectra of the adsorbate and the modes of ethylene−surface interaction. The metal surfaces were modeled by two- or three-layered clusters consisting of 13−34 metal atoms. Four kinds of adsorption sites were considered: atop bonding sites with the CC bond parallel and perpendicular to the $\langle 1\bar{1}0\rangle$ direction (ST and LT sites), a short bridge site with the CC bond parallel to the $\langle 1\bar{1}0\rangle$ direction (SB site), and a long bridge site with the CC bond perpendicular to the $\langle 1\bar{1}0\rangle$ direction (LB site). The results of calculations for three-layered models consisting of more than 20 metals could be compared reasonably with the experimental data. The comparison indicated that (i) upon increasing surface coverage, ethylene on Cu(110) converts its adsorption site from an SB to an ST site, (ii) ethylene adsorbs at an LT site of Ag(110), and (iii) ethylene on Pd(110) takes on an ST site. These conclusions are consistent with those derived from STM and other spectroscopic measurements including UPS and NEXAFS, indicating that the DFT calculation on the cluster models is efficient for the analysis of the IR spectra of ethylene adsorbed on metal surfaces, which delineates the adsorption modes. The contribution of donation and back-donation of electrons to the ethylene−metal bonding was estimated by calculating the projections to the π-bonding and π^*-antibonding orbitals of the isolated ethylene in the adsorbed geometries. The results proved that both the π donation and π^* back-donation make appreciable contributions to the ethylene−surface interaction on Cu(110), whereas the π^* back-donation is negligible in the ethylene−Ag(110) interaction. It was suggested that the frequency increase of the CH_2 out-of-plane wagging vibration from that of the free ethylene observed for ethylene on Ag(110) is a measure of the contribution of the π donation to the ethylene−surface interaction.

1. Introduction

The adsorption mode of ethylene on well-defined transition-metal surfaces has been the subject of considerable interest as a prototype for the interaction of olefinic hydrocarbons with catalysts. Many experimental studies have been conducted to gain insight into the geometric and electronic aspects of the adsorption. Vibrational spectra of ethylene adsorbed on transition metals have provided ample information about bonding modes, adsorption sites, and structures of the adsorbate. In 1988, Shepard[1] wrote an extensive review paper on the vibrational spectra, which had been mainly observed by using high-resolution electron energy loss spectroscopy (HREELS) of ethylene adsorbed nondissociatively at a variety of single-crystal metal surfaces at low temperatures. He concluded that the spectra can be classified in terms of the bonding modes of the adsorbate (i.e., di-σ-bonded (type I) and π-bonded states (type II)). Since then, additional vibrational spectra of ethylene adsorbed on metal surfaces[2,3] has been acquired because of the advent of Fourier transform infrared reflection absorption spectroscopy (FT-IRAS), which can give spectra with a higher energy resolution than HREELS.

In the π-bonded state, the sp^2 hybridization of the free ethylene molecule has been assumed to remain nearly unchanged upon adsorption, whereas the di-σ-bonded state is associated with significant rehybridization toward the sp^3 configuration. These processes have been interpreted in terms of the well-known Dewer−Chatt−Duncanson mechanism,[4,5] which states that attractive interaction between ethylene and metal surfaces could be ascribed to donation and back-donation processes. The donation (hereafter denoted as π donation.) involves a transfer of electrons from a π orbital of the adsorbate to unoccupied metal orbitals, whereas the back-donation (denoted as π^* back-donation) populates a π^* orbital of the adsorbate with electrons from the occupied metal orbitals. These two processes lead to a loss of bond order and thus to an increased C−C bond distance accompanied by partial hybridization toward the sp^3 configuration. The hybridization causes a frequency lowering of the C=C stretching (ν(C=C)) and CH_2 symmetric scissoring (δ_s-(CH_2)) modes of the adsorbed ethylene compared to the frequencies of the free molecule.

To estimate the hybridization as well as the strength of the surface−ethylene interaction on the basis of the frequency lowering, Stuve and Madix[6] introduced the so-called "$\sigma\pi$ parameter". The parameter is obtained from the degree to which the ν(C=C) and $\delta_s(CH_2)$ vibrations are red-shifted below the values for the free ethylene, with an appropriate normalization so that the parameter ranges from zero for the free ethylene to 0.38 for Zeise's salt, which is Pt−C_2H_4 and is commonly taken

* Corresponding author. E-mail: itohk@waseda.jp.

10.1021/jp021377p CCC: $22.00
Published on Web 09/25/2002

as a model for a π-bonded state, to unity for $C_2H_4Br_2$, which is taken as a model for a di-σ-bonded state. Although the parameter is instructive and efficient to the discussion of differences in the coordination mode of ethylene on different metals, quantum chemical calculations should be performed to correlate the vibrational frequencies (or their shifts from those for the free ethylene) to the site of bonding, the structures of the adsorbate, and the relative contribution of the π donation and π^* back-donation to the surface−ethylene interaction.

One of the theoretical approachs along this line has been performed by Wong and Hoffmann,[7] who employed a tight-binding extended Hückel method to trace the adsorption mode of ethylene on transition-metal surfaces, including Ni(111), Pd(111), and Pt(111). They determined the preferred adsorption sites (a di-σ-bonded or a 2-fold bridge site and a π-bonded or atop-bonded site) and the relative importance of the π donation and π^* back-donation to the ethylene−surface interaction. Although these results were supported by the vibrational data obtained by HREELS, the correlation between the mode of adsorption and the vibrational frequencies was discussed only at a qualitative level. In recent years, nonlocal density functional theory (DFT) calculations have been applied to ethylene−metal cluster models to delineate the adsorption mode of ethylene on transition-metal surfaces, including Ni(110),[8] Cu(110),[9,11,12] Cu(111),[10] Ni(111),[11] Ag(110),[12] Pt(110),[12] and Pt(111).[13,14] It has been recognized that the DFT method can reproduce the vibrational spectra of free molecules quite well.[15] The calculated vibrational frequencies of ethylene adsorbed on Ag(110), Cu(110), and Pt(110)[12] by using the DFT calculation method, however, are in a poor agreement with the observed frequencies. This is mainly because the cluster size employed in the calculation is so small that the local potential of ethylene and neighboring metal atoms including the adsorption site is not correctly described because the truncation of the bond on the periphery of the cluster seriously affects the local potential.

The main purpose of the present paper is to simulate quantitatively the vibrational spectra of ethylene adsorbed on Cu(110), Ag(110), and Pd(110) at ca. 80 K by using the DFT calculation method and to clarify differences in the adsorption modes (i.e., the adsorption energy, the adsorption site and structures, and the vibrational frequencies of the adsorbate) among the ethylene/metal surface systems. The vibrational frequencies of ethylene have been accurately determined for the adsorbate on Cu(110),[16−18] on Pd(110),[19] and on Ag(110).[20−22] The adsorption structure of ethylene on Cu(110) has been studied by using UV photoelectron spectroscopy (UPS),[23] photoelectron diffraction,[24] and scanning tunneling microscopy (STM).[25,26] All these studies have shown that ethylene adsorbs on Cu(110) with its CC bond almost parallel to the surface and oriented in the $\langle 1\bar{1}0\rangle$ direction, although ambiguity still exists as to whether the adsorbate takes an atop bonding site or a bridge site. The adsorption structure of ethylene on Ag(110) has been studied by UPS, low-energy electron diffraction (LEED) and thermal desorption spectroscopy (TDS),[27] and near-edge X-ray absorption fine-structure (NEXAFS) measurements,[28] all of which suggested that at 80−110 K ethylene adsorbs on Ag(110) with its CC bond parallel to the surface, taking the π-bonding mode. LEED and TDS have been applied to the study of the adsorption structure of ethylene on Pd(110),[19,29] suggesting that the adsorbate is π bonded to Pd(110) below 280 K. A recent study by STM[30] indicated that the π bonding takes place on top of a Pd atom. Thus, all the studies on the adsorption structures of ethylene on Cu(110), Ag(110), and Pd(110) indicated that ethylene adsorbs molecularly on these surfaces at low temperatures, with the CC bond parallel to the surfaces, taking either a bridge or an atop bonding (or π bonding) site. Although the vibrational spectra of ethylene on Cu(110), Ag(110), and Pd(110)[16−22] can be classified as type II (the π-bonded state) in Shepard's classification,[1] the spectra exhibit appreciable difference depending on the kind of substrate metals used, which can be partly ascribed to the difference in the adsorption site. Therefore, simulating these spectra by using the DFT calculation method can help us to decide how this method can be applied to the determination of the adsorption modes and structures on single-crystal metal surfaces.

The paper is arranged as follows. In section 2, the computational method is described. Employed cluster models are explained in section 3. Section 4 gives the results of calculations, which are compared with the observed data to determine the adsorption site and structures. The contribution of π donation and π^* back-donation to the ethylene−surface interaction is also discussed on the basis of the calculated projection to the π-bonding (HOMO) and π^*-antibonding (LUMO) orbitals of the isolated ethylene in the adsorbed geometry from the orbitals of the ethylene/metal cluster models.[31] Conclusions are given in section 5.

2. Method of Calculations

The DFT calculation was carried out by using the Gaussian 98 program[32] and the BLYP functional, which consists of the Slater exchange,[33] the Becke (B88) exhange,[34] the Vosco−Wilk−Nusair (VWN) correlation,[35] and the Lee−Yang−Parr (LYP) correlation[36] functionals. The basis sets of all the metal atoms (Cu, Ag, and Pd) were those developed by Hay and Wadt.[37] The electrons treated explicitly on Cu, Ag, and Pd are the outermost core and valence electrons ($3s^23p^63d^{10}4s^1$ for Cu, $4s^24p^64d^95s^1$ for Pd, and $4s^24p^64d^{10}5s^1$ for Cu), with the remaining core electrons treated with relativistic effective core potentials. The basis sets of the metals were contracted as (5s, 5p,5d)/[2s,2p,1d] (Cu) and (5s,6p,4d)/[2s,2p,1d] (Pd and Ag). The C and H atoms were treated with the 6-31G** basis sets. The adsorption energy E(ads) was calculated as a change in electronic energy for the adsorption of ethylene on a metal cluster, which is defined as follows:

$$E(\text{ads}) = E(\text{cluster}) + E(\text{ethylene}) - E(\text{ethylene/cluster}) \quad (1)$$

A positive E(ads) means that the adsorbate is stabilized on adsorption to a metal cluster. E(cluster) is the total energy of a bare metal cluster, E(ethylene) is the energy of the free ethylene molecule, and E(ethylene/cluster) is the energy of an ethylene/metal cluster model.

The density of states projected on an orbital, μ, of the isolated ethylene in an adsorbed geometry (PDOS$_\mu(E)$) as a function of energy is plotted by assuming a Lorentzian function with a width of $\sigma = 0.1$ eV:

$$\text{PDOS}_\mu(E) = \sum_k P_\mu^k \frac{\sigma/\pi}{(E-\epsilon_k)^2 + \sigma^2} \quad (2)$$

where ϵ_k is the energy of the kth orbital of an ethylene/metal model and the weight factor P_μ^k is the orbital population of the orbital μ in the kth orbital. P_μ^k was calculated in the following manner. First, the DFT calculation was performed on isolated ethylene in an adsorbed geometry as well as on a metal cluster to obtain the orbitals of ethylene $\{\varphi^e\}$ and the metal cluster $\{\varphi^m\}$. Because orbitals within the orbital set $\{\varphi^e \oplus \varphi^m\}$ are

not always orthogonal with each other, symmetric orthonormalization was performed to obtain an orthonormal set $\{\phi^e \oplus \phi^m\}$ by using the following equation:

$$\phi_i = \sum_j S_{ji}^{-1/2} \varphi_j \tag{3}$$

where S_{ji} is an overlap integral between φ_j and φ_i. Second, the DFT calculation was carried out to obtain the orbitals $\{\psi\}$ of the ethylene/metal cluster model by using the orthonormal set $\{\phi^e \oplus \phi^m\}$ as a basis. As a result, an orbital of the ethylene/metal cluster model ψ_k was represented by a linear combination of the orthonormal sets:

$$\psi_k = \sum_\mu c_{\mu k} \phi_\mu \tag{4}$$

Finally, the orbital population was given by

$$P_\mu^k = |c_{\mu k}|^2 \tag{5}$$

3. Ethylene/Metal Cluster Models and the Method of Structural Optimization

The Cu, Ag, and Pd substrates have a face-centered cubic (fcc) structure. The metal surfaces are modeled by two- or three-layered clusters consisting of 13−34 metal atoms. Because the calculated frequencies depend strongly on the number of metal atoms, it is crucial to employ cluster models that are large enough so that the calculated frequencies are only slightly affected by enlarging the size of the clusters if we are to obtain results that are reliable enough to be compared with the observed frequencies. Four kinds of adsorption modes are considered: (i) ethylene adsorbed on an atop bonding site with the CC bond parallel to the $\langle 1\bar{1}0 \rangle$ direction (abbreviated ST), (ii) the adsorbate on an atop bonding site with the CC bond parallel to the $\langle 100 \rangle$ direction (abbreviated LT), (iii) ethylene adsorbed on a bridge site with the CC bond parallel to the $\langle 1\bar{1}0 \rangle$ direction (abbreviated SB), and (iv) ethylene adsorbed on a bridge site with the CC bond parallel to the $\langle 100 \rangle$ direction (abbreviated LB). As illustrated in Figure 1, each of the cluster models is denoted by ETCu(SB/ST/LB/LT), followed by a series of numbers indicating the number of Cu atoms in the cluster. For example, for ETCuSB12-10-8, ethylene adsorbs on the SB site of the copper cluster with 12 metals in the first layer, 10 in the second layer, and 8 in the third layer. The geometry optimization of each ethylene/cluster model is carried out by taking all the internal degree of freedom of the adsorbate and the height of the CC bond above the first cluster plane while the metal clusters are always kept fixed at the bulk structure. (The unit cell lengths of the fcc cells are fixed at 3.615 (Cu), 4.086 (Ag), and 3.890 Å (Pd).) In all optimazation processes, the adsorbate and metal clusters are forced to have C_{2v} symmetry as a whole, which means that the CC bond is kept parallel to the surface and the adsorbate is also forced to have a mirror plane containing the CC bond and the surface normal.

4. Results and Discussion

4.1. Free Ethylene Molecule. The structural parameters optimized at the BLYP/6-31G** level and the calculated vibrational frequencies of the free ethylene molecule are compared with the corresponding experimental values in Table 1. The calculated parameters reproduce the experimental parameters well. The theoretical frequencies, which have not been scaled by any factor, are again in good agreement with the experimental frequencies. Although the theoretical frequencies are listed only for the vibrational modes observed for ethylene adsorbed on Cu(110), Ag(110), and Pd(110) (vide infra), the agreement between the theoretical and experimental frequencies for the other modes is appreciably good. These results validate the calculation at the BLYP/6-31G** level, at least for the adsorbed ethylene molecule.

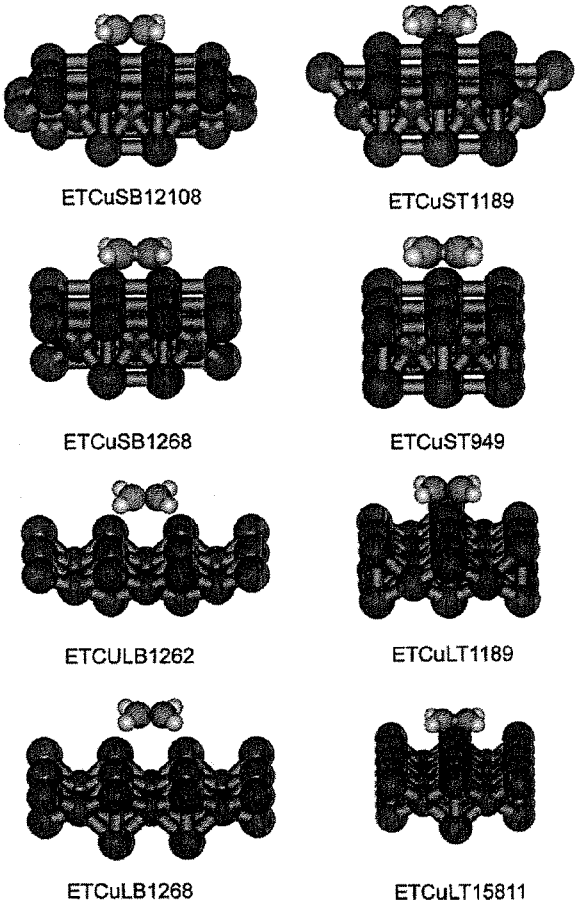

Figure 1. Cluster models for ethylene on Cu(110).

TABLE 1: Comparison between the Experimental and Calculated Values for Structural Parameters and Vibrational Frequencies

	structural parameters[a]	
	experimental values[b]	theoretical values
R(CC) (Å)	1.337 ± 0.003	1.340
R(CH) (Å)	1.086 ± 0.003	1.094
A(HCH) (deg)	121.35 ± 1	121.87
T(CCH) (deg)	0.0	0.0
	vibrational frequencies (cm^{-1})	
	experimental values[c]	theoretical values
ν(C=C, Ag))	1623	1659
γ_s(CH_2, Ag)	1342	1352
ω(CH_2, B_{1u})	949	941

[a] R(CC) and R(CH) are the optimized values of the CC and CH distances of ethylene. A(HCH) and T(CCH) are the optimized values of the HCH angle and the dihedral angle, respectively, between the CCH planes of ethylene. [b] Taken from ref 38. [c] Taken from ref 39.

4.2. Ethylene/Cu(110). The structural parameters (R(M−C), R(CC), and T(CCH)) optimized for a series of ethylene/metal cluster models and the adsorption energies are summarized in

TABLE 2: Optimized Structural Parameters[a] and Adsorption Energies

	R(M−C) (Å)	R(CC) (Å)	T(CCH) (deg)	E(ads) (kJ/mol)
ETCuSB12-10-8	2.521	1.364	4.295	22.556
ETCuSB12-6-8	2.419	1.376	6.500	26.598
ETCuSB12-6	2.358	1.372	6.070	59.049
ETCuST11-8-9	2.363	1.377	5.678	45.106
ETCuST9-4-9	2.477	1.359	1.787	30.011
ETCuST9-4-5	3.441	1.343	0.445	10.164
ETCuST9-4	2.555	1.360	2.441	−32.370
ETCuLB12-6-8	3.666	1.343	0.439	11.142
ETCuLB12-6-2	3.417	1.345	0.643	0.387
ETCuLB12-6	2.880	1.352	2.591	73.324
ETCuLT15-8-11	2.428	1.363	2.416	41.188
ETCuLT11-8-9	2.476	1.360	1.943	32.331
ETCuLT9-4-9	2.477	1.359	1.787	25.030
ETCuLT9-4-5	3.558	1.343	0.287	10.164
ETAgLT15-8-11	2.846	1.353	1.377	20.964
ETAgLT9-4-9	2.907	1.351	1.008	216.512
ETAgST9-4-9	2.937	1.353	1.549	14.517
ETAgSB12-6	2.945	1.353	2.810	55.647
ETPdST9-4-9	2.319	1.396	9.508	287.906
ETPdLT9-4-9	2.295	1.395	0.449	64.178

[a] R(M−C) is the shortest distance between the carbon atom of ethlylene and a metal atom in the cluster, and R(CC) is the CC bond distance of the adsorbate. T(CCH) is the dihedral angle between the CCH plane of the adsorbate and the plane parallel to the top surface of the metal cluster.

Table 2. The results indicate the following: (i) The calculated adsorption energies depend on the number of metals in the clusters. The two-layered models ETCuSB12-6 and ETCuLB12-6 give abnormally large values compared to those calculated for the three-layered models in the same series. In addition, the two-layered model ETCuST9-4 gives a negative value, indicating that the adsorbate does not form a stable state, in contradiction to the experimental finding (vide infra). Thus, the two-layered models are not appropriate to the estimation of the adsorption energy. (ii) As the number of metals in the cluster models increases, the energy increases continuously for the ST and LT models, whereas the energy decreases for the SB and LB models. Although the calculated energies show a converging trend for each model, the result for the largest cluster should be considered as either a lower limit (ETCuST and ETCuLT) or an upper limit (ETCuSB and ETCuLB) to the adsorption energy. The adsorption energy is calculated for ETCuST11-8-9 to be 45.106 kJ/mol, which is in agreement with the experimental value[24] of 35−47 kJ/mol. Thus, the ST site is favored over the other sites considered, which partly conforms to the experimental results. As already explained, the photoelectron spectroscopic and diffraction studies[23,24] showed that ethylene adsorbs at either an ST or an SB site of Cu(110), whereas the STM measurements[25,26] indicated that the adsorbate occupies an SB site. (iii) As the calculated adsorption energy increases, the deviation of structural parameters R(CC) and T(CCH) from those of the free ethylene increases, which suggests that the energy increase parallels the degree of the hybridization toward the sp^3 configuration. The optimized value of R(CC) and the perpendicular height of the substrate above the surface (abbreviated R(MT), not listed in Table 2) for the SB and ST bonding states are 1.364 and 2.449 Å (ETCuSB12-10-8) and 1.377 and 2.260 Å (ETCuST11-8-9), respectively. The experimental R(CC) and R(MT) values reported by Schaff et al.[24] are 1.53 ± 0.13 and 2.09 ± 0.02 Å (SB) and 1.32 ± 0.09 and 2.08 ± 0.02 Å (ST), which are appreciably different from the optimized parameters. As explained below, the ν(CC) band for the SB bonding state of ethylene on Cu(110) is observed at 1532 cm^{-1}, and that for the ST state, at 1525 cm^{-1}. The former frequency indicates that the CC bond of the adsorbate retains appreciable double-bond nature, contradicting the experimental CC bond length, which is similar to that of a CC single bond (ca. 1.54 Å). The experimental CC bond length reported for the ST bonding state is shorter than that of the free ethylene (1.337 ± 0.003 Å, see Table 1),[38] which is also inconsistent with the observed frequency lowering from the free ethylene[39] (1623 → 1525 cm^{-1}). These results strongly suggest that the experimental parameters should be reexamined.

TABLE 3: Comparison between the Observed and Calculated Frequencies (cm^{-1}) for Cluster Models

	observed and calculated frequencies[a]		
	ν(C=C)	$\delta_s(CH_2)$	$\omega(CH_2)$
obsd frequencies[b] for ethylene/Cu(110)	1532[c]	1275[c]	909[c]
	(1525)	(1264)	
ETCuSB12-10-8	1574	1301	891
ETCuSB12-6-8	1543	1269	842
ETCuSB12-6	1556	1285	910
ETCuST11-8-9	1544	1279	865
ETCuST9-4-9	1564	1301	880
ETCuST9-4-5	1645	1347	940
ETCuST9-4	1586	1318	912
ETCuLB12-6-8	1645	1346	933
ETCuLB12-6-2	1635	1341	922
ETCuLB12-6	1610	1328	910
ETCuLT15-8-11	1584	1314	924
ETCuLT11-8-9	1594	1320	922
ETCuLT9-4-9	1596	1321	919
ETCuLT9-4-5	1645	1346	933
obsd frequencies[d] for ethylene/Ag(110)			955
ETAgLT15-8-11	1614	1334	956
ETAgLT9-4-9	1621	1337	952
ETAgSB12-6	1610	1330	941
ETAgST9-4-9	1611	1332	936
obsd frequencies[e] for ethylene/Pd(110)	1525	1235	900
ETPdST9-4-9	1519	1243	885
ETPdLT9-4-9	1533	1252	905

[a] ν(CC) and $\delta_s(CH_2)$ are CC stretching and CH_2 symmetric scissoring vibrations, which correspond to the Ag vibrational modes observed at 1623 and 1342 cm^{-1}, respectively, for free ethylene.[39] $\omega(CH_2)$ denotes a CH_2 out-of-plane wagging mode corresponding to the B_{1u} mode at 949 cm^{-1} for free ethylene.[39] [b] See ref 40. [c] Numbers indicate frequencies observed at lower coverages, and numbers in the parentheses indicate frequencies observed at higher coverages. [d] Taken from ref 22. [e] Taken from ref 29.

Table 3 lists the calculated vibrational frequencies of the optimized structures for a series of cluster models together with the experimental frequencies. The adsorbate on Cu(110) at low coverage gives the ν(CC), $\delta_s(CH_2)$, and $\omega(CH_2)$ vibrational bands at 1532, 1275, and 909 cm^{-1}, respectively, and upon increasing the coverage, the former two bands shift to 1525 and 1264 cm^{-1}, whereas the third band decreases in intensity and becomes almost unobservable.[40] The ν(CC) and $\delta_s(CH_2)$ bands correspond to the 1623 and 1342 cm^{-1} bands, respectively, of the A_g species observed for free ethylene, and the $\omega(CH_2)$ band, to the 949 cm^{-1} band of the B_{1u} species for free ethylene.[39] The frequency lowering and the appearance of the

IR-inactive modes have been ascribed to an appreciable surface−ethylene interaction.

From Table 3, it is clear that the calculated frequencies appreciably depend on the type of adsorption site, whereas the dependence of the frequencies calculated for the same site on the number of metals is not so large if the number is taken to be larger than 20. For example, the calculated frequencies for the ν(CC), $\delta_s(CH_2)$, and $\omega(CH_2)$ modes are located at 1558.5 ± 15.5, 1285 ± 16, and 866.5 ± 24.5 cm^{-1} for the SB models, 1554 ± 10 cm^{-1}, 1290 ± 11 cm^{-1}, and 872.5 ± 7.5 cm^{-1} for the ST models, 1640 ± 5 cm^{-1}, 1343.5 ± 2.5 cm^{-1}, and 927.5 ± 5.5 cm^{-1} for the LB models, and 1590 ± 6, 1317.5 ± 3.5, and 921.5 ± 2.5 cm^{-1} for the LT models. Although the dependence on the number of metals is a little larger for the SB and ST models, the results suggest that the comparison between the calculated frequencies for each adsorption site and the observed frequencies could be used to predict the adsorption site for ethylene on Cu(110). Actually, the calculated frequencies for the LB and LT models do not reproduce the observed frequencies, and there exists much better agreement between the observed frequencies and the calculated frequencies for the SB and ST models. ETCuSB12-10-8 gives the frequencies for the ν(CC), $\delta_s(CH_2)$, and $\omega(CH_2)$ modes at 1574, 1301, and 891 cm^{-1}, which compare well with the observed frequencies at 1532, 1275, and 909 cm^{-1}, respectively, for the absorbate at relatively low surface coverage.[40] This is consistent with the STM observation, which indicated that the adsorbate takes on a short bridge site with the CC bond parallel to the ⟨110⟩ direction.[25,26] However, ETCuST11-8-9 gives the ν(CC), $\delta_s(CH_2)$, and $\omega(CH_2)$ frequencies at 1544, 1279, and 865 cm^{-1}, each of which is appreciably lower than the corresponding frequency calculated for ETCuSB12-10-8. The result corresponds to the experimental fact that ethylene on Cu(110) shifts the ν(CC) and $\delta_s(CH_2)$ bands to 1525 and 1264 cm^{-1}, respectively, on increasing the surface coverage (see Table 3). Thus, the results of the calculations suggests that the frequency lowering observed for the ν(CC) and $\delta_s(CH_2)$ bands upon increasing the surface coverage can be ascribed to the conversion of the adsorption site from SB to ST. As Table 2 shows, upon conversion, the optimized CC distance (R(CC)) and twisting angle (T(CCH)) exhibit increases of 1.364 → 1.377 Å and 4.295 → 5.678°, respectively. The increase suggests a slight rehybridization toward the sp^3 configuration, which conforms to the frequency lowering of the ν(CC) and $\delta_s(CH_2)$ bands.

4.3. Ethylene/Ag(110). The results of structural optimization on a series of cluster models for ethylene on Ag(110) are listed in Table 2. Although the optimization was performed on a limited number of cluster models, the results gave some insight into the relationship between the adsorption sites and the vibrational frequencies. The calculated adsorption energies for ETAgLT15-8-11 and ETAgST9-4-9 are the same order of magnitude as the experimental value of ca. 40 kJ/mol reported by Backx et al.[41] and are appreciably smaller than the energies calculated for ETCuLT15-8-11 and ETCuST11-8-9. (The energy calculated for ETAgLT9-4-9 is abnormally large, indicating that the cluster size is too small to give a reasonable adsorption energy for the LT model.) The optimized values of the nearest Ag−C distance (R(M−C)) for the LT, ST, and SB models of ethylene on Ag(110) are appreciably larger than those for the LT, ST, and SB models of ethylene on Cu(110). The optimized structural parameters R(CC) and T(CCH) for the former models are smaller than those for the latter models. All these results indicate that ethylene molecularly adsorbs on Ag(110) and that the geometric structures of ethylene on Ag(110) are perturbed by adsorption to a lesser extent than those of the adsorbate on Cu(110). All of the studies on the adsorption structure of ethylene on Ag(110)[20,27,28] have reported that at low temperature (80−110 K) ethylene adsorbs molecularly on Ag(110) with the CC bond parallel to the surface, although the precise adsorption site has not been determined yet.

The IR spectrum of ethylene on Ag(110) exhibits the $\omega(CH_2)$ band at 955 cm^{-1}, which is appreciably higher than the $\omega(CH_2)$ frequency of the free ethylene (949 cm^{-1}). Thus, the frequency shift due to the adsorption shows an opposite trend to the case of ethylene on Cu(110), where the $\omega(CH_2)$ band shifts to the lower-frequency side (949 → 909 cm^{-1}). Table 3 lists the frequencies of the $\omega(CH_2)$ mode calculated for the cluster models of ethylene on Ag(110). From the Table, it is clear that only the LT models (ETAgLT15-8-11 and ETAgLT9-4-9) give calculated frequencies for this mode that are higher than that for free ethylene (941 cm^{-1}, see Table 1). Although the ν(CC) and $\delta(CH_2)$ frequencies have not been experimentally determined, thus hampering more reliable comparison between the experimental and theoretical frequencies, the result strongly suggests that ethylene on Ag(110) takes on the LT adsorption site.

As already explained, the ethylene−metal surface interactions have been interpreted in terms of the balance between π donation and π^* back-donation. The opposite trend in $\omega(CH_2)$ frequency shifts may reflect the difference in the balance between ethylene on Cu(110) and on Ag(110). To clarify this point and gain better insight into the difference in the ethylene−surface interaction between ethylene on Cu(110) and on Ag(110), the projections to the π-bonding and π^*-antibonding orbitals of the isolated ethylene in the asdsorbed geometries from the molecular orbitals of the ethylene/cluster modes were calculated, as explained in section 4.5.

4.4. Ethylene/Pd(110). The optimized structures and adsorption energies calculated for ETPdST9-4-9 and ETPdLT9-4-9 are listed in Table 2. The optimized R(CC) values for ethylene taking both the ST and LT sites are appreciably larger than those for the adsorbate on Cu(110) and Ag(110). The optimized T(CCH) for the ST model gives the largest value (9.508°) in Table 2. These results suggest a larger extent of sp^3 rehybridization of ethylene on Pd(110) compared to that of the adsorbate on Cu(110) and Pd(110). The energy for the ST model is much larger than that for the LT model, indicating that the adsorbate taking the ST site is more stable than that taking the LT site.

As Table 3 shows, the frequencies of the ν(CC), $\delta_s(CH_2)$, and $\omega(CH_2)$ modes calculated for ETPdST9-4-9 and ETPdLT9-4-9 are similar to each other, and the frequencies for both adsorption models reproduce the observed frequencies well. As mentioned above, however, the adsorption energy for the ST model is much larger than that for the LT model. Thus, the DFT calculation suggests that ethylene adsorbs on Pd(110), taking the ST site. This is consistent with the STM observation reported by Ichihara et al.[30]

4.5. Contribution of π Donation and π^* Back Donation to the Ethylene−Surface Interaction on Cu(110) and Ag(110). Figure 2 exhibits the density of states (PDOS) projected onto the π orbital (HOMO) and π^* orbital (LUMO) of isolated ethylene in the adsorbed geometries for ETCuSB12-10-8, ETCuST11-8-9, and ETAgLT15-8-11. The HOMO energy of each ethylene/metal cluster model, which is equivalent to the Fermi level of ethylene adsorbed on the corresponding single crystal, is indicated by a vertical line as E_F, and the energies of the π and π^* orbitals of ethylene in the adsorption geometries are given by vertical dashed lines. The comparison of the

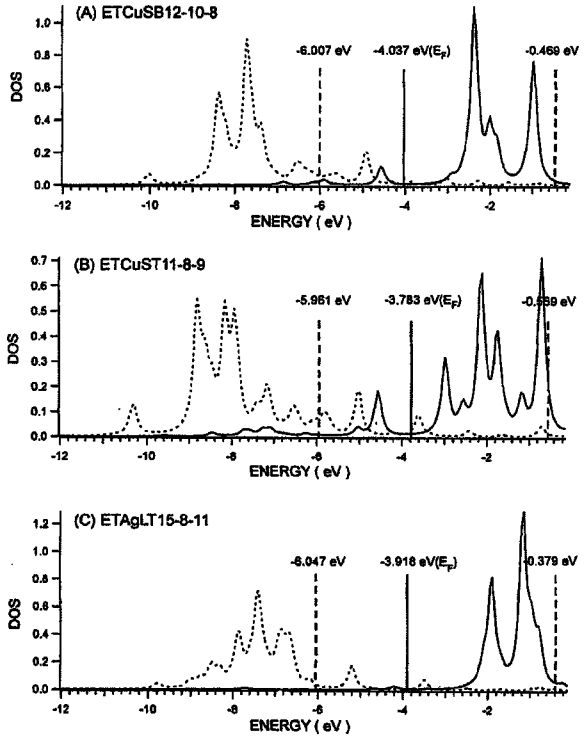

Figure 2. Projections of the π HOMO (- - -) and π^* LUMO orbitals (—) of isolated ethylene in the adsorbed geometries calculated for ethylene/Cu(110) (A, B) and ethylene/Ag(110) (C) cluster models. The solid vertical lines indicate the energy of the HOMO of the corresponding ethylene/metal cluster model (see text.) The dashed vertical lines on the left and right sides of A, B, and C indicate the energies of the π (HOMO) and π^* (LUMO) orbitals, respectively, of isolated ethylene in the adsorption geometry (see text.)

TABLE 4: Charge Transfer between Ethylene Frontier Orbitals and the Cu and Ag Clusters and the Frequency Shifts of the $\omega(CH_2)$ Band

	ETCuSB12-10-8	ETCuST11-8-9	ETAgLT15-8-11
π (HOMO)[a]	1.92	1.88	1.90
π^* (LUMO)[b]	0.15	0.28	0.03
$\Delta\nu$[c](cm^{-1})	−50 (−40)	−76	11 (7)

[a] Transferred electrons from the π orbital. [b] Back-donated electrons to the π^* orbital. [c] Calculated frequency shift of the $\omega(CH_2)$ band relative to that of the free ethylene molecule. The numbers in parentheses indicate the observed frequency shifts.[40]

projection curves of the π and π^* orbitals with the positions of the orbital energies indicates how the states are shifted in energy by adsorption. Both PDOSs are broadened over a large energy range because of overlap with metal-cluster orbitals. Bonding contributions appear below the Fermi level (E_F); the area of the π-orbital projection below E_F corresponds to the number of electrons transferred from the π orbital of the isolated ethylene to ethylene/metal-cluster orbitals, and the area of the π^*-orbital projection corresponds to the number of electrons transferred from ethylene/metal-cluster orbitals to the π^* orbital. As summarized in Table 4, the number of electrons transfer from the π orbital is 1.92 for ETCuSB12-10-8, 1.88 for ETCuST11-8-9, and 1.90 for ETAgLT15-8-11, which means that the donation of electrons from the π orbital to unoccupied metal-cluster orbitals (π donation) amounts to 0.08 for ETCuSB12-10-8, 0.12 for ETCuST11-8-9, and 0.10 for ETAgLT15-8-11. (Two electrons originally occupy the π orbital of the isolated ethylene molecule. Then, the difference between the two electrons and the amount of electron transfer from the π orbital of the ethylene/metal cluster can be considered to be the donation of electrons from the π orbital to unoccupied metal-cluster orbitals.) However, the amount of electron transfer to the π^* orbital (π^* back-donation) is 0.15 for ETCuSB12-10-8, 0.28 for ETCuST11-8-9, and 0.03 for ETAgLT15-8-11. From these results, it is clear that both of π donation and π^* back-donation play important roles in the ethylene−Cu(110) interaction, whereas π donation is the main contributor to the ethylene−Ag(110) interaction.

The calculated frequency shifts of the $\omega(CH_2)$ band relative to that of the free ethylene are also listed in Table 4. The observed shifts for ethylene on Cu(110) and Ag(110) (−40 and 7 cm^{-1}, respectively) are in good agreement with the calculated shifts for ETCuSB12-10-8 and ETAgLT15-8-11. Thus, the DFT calculation reproduces well the opposite trend of the $\omega(CH_2)$ frequency shifts for ethylene on Cu(110) and Ag(110). The IR spectra of ethylene adsorbed on Ag(110) and its atomic oxygen-reconstructed surfaces, p($n \times 1$)O−Ag(110) ($n = 6, 4, 3$), were measured by Akita et al.[21,22] They observed that the $\omega(CH_2)$ band at 955 cm^{-1} for ethylene on Ag(110) shifts to 972 cm^{-1} on the p(6 × 1) and p(4 × 1) surfaces and to 976 cm^{-1} on the p(3 × 1) surface, indicating that the $\omega(CH_2)$ frequency increases with the surface coverage of atomic oxygen. The desorption temperature of ethylene adsorbed on the reconstructed surfaces increases in the following order: 130 K (p(6 × 1)) < 145 K (p(4 × 1)) < 160 K (p(3 × 1)).[22] Thus, the stability of the adsorbate increases with the surface coverage of atomic oxygen. The electron-withdrawing nature of atomic oxygen induces positive charges on neighboring Ag atoms, resulting in an increase in the contribution of π donation as well as in the stability of the adsorbate on the surfaces. As already explained, the DFT calculation has indicated that the ethylene−Ag(110) interaction is mainly due to π donation. Thus, the results of observations and the DFT calculation suggest that in the case of ethylene on Ag(110) the frequency increase of the $\omega(CH_2)$ band relative to the corresponding frequency observed for the free ethylene molecule can be considered to be a measure of both π donation and the stability of the ethylene−surface interaction.

5. Conclusions

The DFT calculations,[8−14] which have been performed so far on ethylene/metal cluster models to clarify the adsorption modes including the adsorption energies, the optimized adsorption structures, and vibrational frequencies of ethylene, employed cluster models consisting of only a limited number of metal atoms. As explained above, the results of calculations obtained from the ethylene/metal cluster models depend strong on cluster size. Therefore, it is clear that the previous studies do not always present reliable theoretical predictions of the adsorption modes. To obtain predictions that are reliable enough to be compared with experimental results, it is crucial to employ metal clusters that are large enough so that the calculated results are only slightly affected by enlarging the cluster sizes further.

In the case of ethylene on Cu(110), which was the most extensively studied species in the present paper, the adsorption energies calculated for the ST and LT models increase with cluster size, whereas the energies for the SB and LB models decrease with cluster size (see Table 2.) Although the changes show a converging trend, the calculated energies for the largest cluster models should still be considered to be either an upper limit (for ETCuSB12-10-8 and ETCuLB12-6-8) or a lower limit

(for ETCuST11-8-9 and ETCuLT15-8-11). These limits suggest that the stability of ethylene taking on the four kinds of adsorption sites follows the order ST ≈ LT > SB > LB. As already explained, ethylene does not take the LT site, thus contradicting the predicted order of stability, which indicates the limitation of determining the stable adsorption site on the basis of adsorption energies calculated for the adsorbate/metal-cluster models. Presumably, this is partly due to the fact that the structural relaxation of the metal clusters was prohibited during the optimization processes.

However, if the number of metals is taken to be larger than approximately 20, the dependence of the frequencies calculated for the ethylene/Cu(110) cluster models on cluster size is not so large compared with that of the adsorption energies, and the calculated ν(CC), $\delta_s(CH_2)$, and $\omega(CH_2)$ frequencies for the SB, ST, LB and LT models clearly reflect each adsorption mode. Therefore, comparison of the calculated and observed frequencies allows us to conclude that ethylene on Cu(110) takes on an SB site at lower surface coverage, and upon increasing the coverage, the adsorbate changes from the SB site to ST site. These conclusions are consistent with the experimental results.[25,26]

Comparison of the optimized structural parameters of ethylene on Ag(110) with those of ethylene on Cu(110) indicated that the geometric structure of ethylene is less perturbed by the adsorption on Ag(110) than by that on Cu(110). Corresponding to this fact, the calculated ν(CC) and $\delta_s(CH_2)$ frequencies for the LT, SB, and ST models of ethylene/Ag(110) are similar to each other, and the shifts of these frequencies from those of free ethylene are smaller than those calculated for the corresponding models of ethylene/Cu(110). The characteristic feature of the IR spectrum of ethylene on Ag(110) is that the adsorbate exhibits the $\omega(CH_2)$ band at 955 cm^{-1}, which is 6 cm^{-1} higher than the band for free ethylene; this is contrasted with the cases of ethylene/Cu(110) and ethylene/Pd(110), where the bands are observed at appreciably lower frequency sites compared with that of free ethylene. The frequency increase observed for ethylene adsorbed on Ag(110) was reproduced only by the results of calculations for the LT model, which strongly suggested that ethylene takes the LT site on Ag(110).

The frequency decreases of the ν(CC), $\delta_s(CH_2)$, and $\omega(CH_2)$ bands relative to those of free ethylene due to the adsorption of ethylene on Pd(110) are larger than those on Cu(110), indicating that the perturbation proceeds further on Pd(110). Both the ST and LT models well reproduce the frequencies and the frequency shifts. The calculated adsorption energy for the former model, however, is much larger than that for the latter. On the basis of these results, it was concluded that ethylene takes the ST site on Pd(110), which is consistent with the STM observation.[30]

Thus, the analysis of the frequencies of the IR bands of ethylene on Cu(110), Ag(110), and Pd(110) by means of the DFT calculation performed on reasonably large cluster models predicts the correct adsorption site on each surface, indicating that the analysis is one of the most reliable and efficient methods to determine the adsorption site.

The calculated intensities of the IR bands by means of the DFT calculation, however, largely deviate from the experimental results. For example, the IR spectra of ethylene on Cu(110) at lower surface coverage gives rise to the ν(CC) and $\delta_s(CH_2)$ bands, the intensities of which are comparable to that of the $\omega(CH_2)$ band.[40] However, the DFT calculation for ETCuSB12-10-8 predicts the intensities of the ν(CC), $\delta_s(CH_2)$, and $\omega(CH_2)$ bands to be 0.3 (1574 cm^{-1}), 1.9 (1301 cm^{-1}) and 66.9 km/mol (891 cm^{-1}), respectively. (The numbers in parentheses indicate the calculated frequencies. See Table 3.) The appearance of the ν(CC) and $\delta_s(CH_2)$ bands, which are infrared-inactive for free ethylene with D_{2h} symmetry, are ascribable not only to the symmetry lowering due to adsorption but also to other factors such as charge-transfer interaction, which has been proposed to explain the enhancement of totally symmetric vibrations of molecular complexes such as benzene−halogen complexes[42] and the appearance of the IR bands due to ν(CC) and $\delta_s(CH_2)$ of ethylene adsorbed on mordenites.[43] Presumably, the charge-transfer effect, which cannot be treated by the DFT calculation based on the Born−Oppenheimer approximation, plays an important role in the appearance of the ν(CC) and $\delta_s(CH_2)$ bands, with the intensities comparable to that of the $\omega(CH_2)$ band.

The calculation of the PDOS of the π and π^* orbitals of isolated ethylene in the adsorbed geometries indicated that the amounts of π donation and π^* back-donation are 0.08 and 0.15 for ETCuSB12-10-8 and 0.12 and 0.28 for ETCuST11-8-9, respectively. Thus, both π donation and π^* back-donation play important roles in the ethylene−surface interaction on Cu(110). The total amount of electron transfer of 0.40 for ETCuST11-8-9 is much larger than that of 0.23 for ETCuSB12-10-8, corresponding to the larger adsorption energy (45.1 kJ/mol) of the former model compared to that (22.6 kJ/mol) of the latter. However, the amounts of π donation and π^* back-donation are 0.10 and 0.03, respectively, for ETAgLT15-8-11. Thus, only π donation plays a major role in the interaction on Ag(110).

The opposite trend in frequency shifts of the $\omega(CH_2)$ band of adsorbed ethylene compared to that of free ethylene could be ascribed to the difference in the contribution of π donation and π^* back-donation between ethylene on Cu(110) and ethylene on Ag(110). That is, the larger the frequency lowering of the $\omega(CH_2)$ band, the stronger the ethylene−surface interaction on Cu(110), and the larger the frequency increase of the band, the stronger the ethylene−surface interaction on Ag(110). It was suggested that the frequency increase is a good measure of the contribution of π donation to the interaction, where only π donation plays an important role in the interaction.

References and Notes

(1) Sheppard, N. *Annu. Rev. Phys. Chem.* **1988**, *39*, 589.
(2) Sheppard, N.; De La Cruz, C. *Adv. Catal.* **1996**, *41*, 1.
(3) Trenary, M. *Annu. Rev. Phys. Chem.* **2000**, *51*, 381.
(4) Dewer, M. S. J. *Bull. Soc. Chim. Fr.* **1951**, *18*, C79.
(5) Chatt, J.; Duncanson, L. A. *J. Chem. Soc.* **1953**, 2939.
(6) Stuve, E. M.; Madix, R. J. *J. Phys. Chem.* **1985**, *89*, 3183.
(7) Wong, Y.-T.; Hoffmann, R. *J. Chem. Soc., Faraday Trans.* **1990**, *86*, 4083.
(8) Weinelt, M.; Huber, W.; Zebisch, P.; Steinrück; Pabst, M.; Rösch *Surf. Sci.* **1992**, *271*, 539.
(9) Triguero, L.; Pettersson, G. M.; Minaev, B.; Ågren, H. *J. Chem. Phys.* **1998**, *108*, 1193.
(10) Michalak, A.; Witko, M.; Hermann, K. *J. Mol. Catal.* **1997**, *119*, 213.
(11) Fahmi, A.; van Santen, R. A. *Surf. Sci.* **1997**, *371*, 53.
(12) Bernardo, C. G. P. M.; Gomes, J. A. N. F. *J. Mol. Struct.: THEOCHEM* **2002**, *582*, 159.
(13) Kua, J.; Goddard, W. A., III. *J. Phys. Chem. B* **1998**, *102*, 9492.
(14) Watwe, R. M.; Spiewak, B. E.; Cortright, D. R.; Dumesic, J. A. *J. Catal.* **1998**, *180*, 184.
(15) Matsuura, H.; Yoshida, H. In *Handbook of Vibrational Spectroscopy*; Chalmers, J. M., Griffiths, P. R., Eds.; Wiley & Sons: New York, 2002; Vol. 3, pp 4203.
(16) Jenks, C. J.; Bent, B. E.; Bernstein, N.; Zaera, F. *Surf. Sci. Lett.* **1992**, *277*, L89.
(17) Kubota, J.; Kondo, J. N.; Domen, K.; Hirose, C. *J. Phys. Chem.* **1994**, *98*, 7653..
(18) Raval, R. *Surf. Sci.* **1995**, *331−333*, 1.
(19) Nishijima, M.; Yoshinobu, J.; Sekitani, T.; Onchi, M. *J. Chem. Phys.* **1989**, *90*, 5114.

(20) Backx, C.; de Groot, C. P. M.; Biloen, P. *Appl. Surf. Sci.* **1980**, *6*, 256.
(21) Akita, M.; Osaka, N.; Itoh, K. *Surf. Sci.* **1999**, *427−428*, 381.
(22) Akita, M.; Hiramoto, S.; Osaka, N.; Itoh, K. *J. Phys. Chem. B* **1999**, *103*, 10189.
(23) Ritz, A.; Spitzer, A.; Lüth, H. *Appl. Phys. A* **1984**, *34*, 31.
(24) Schaff, O.; Stampfl, A. P. J.; Hofmann, Ph.; Bao, S.; Schindler, K.-M.; Bradshaw, A. M.; Davis, R.; Woodruff, D. P.; Fritzsche, V. *Surf. Sci.* **1995**, *343*, 201.
(25) Doering, M.; Buisset, J.; Rust, H. P.; Briner, B. G.; Bradshaw, A. M. *Faraday Discuss.* **1996**, *105*, 163.
(26) Buisset, J.; Rust, H.-P.; Schweizer, E. K.; Cramer, L.; Bradshaw, A. M. *Phys. Rev. B* **1996**, *54*, 10373.
(27) Krüger, B.; Benndorf, C. *Surf. Sci.* **1986**, *178*, 704.
(28) Solomon, J. L.; Madix, R. J.; Stöhr, J. *J. Chem. Phys.* **1990**, *93*, 8379.
(29) Chester, M. A.; McDougall, G. S.; Pemble, M. E.; Sheppard, N. *Surf. Sci.* **1985**, *22−23*, 369.
(30) Ichihara, S.; Yoshinobu, J.; Ogasawara, H.; Nantoh, M.; Kawai, M.; Domen, K. *J. Electron Spectrosc. Relat. Phenom.* **1998**, *88−91*, 1003.
(31) Strictly speaking, the molecular orbitals in the DFT calculation should be called Kohn−Sham orbitals (KSOs). However, we use orbitals (MO) in place of KSOs hereafter to simplify the expression.
(32) Frisch, M. J.; Trucks, G. W.; Schlegel, H. B.; Scuseria, G. E.; Robb, M. A.; Cheeseman, J. R.; Zakrzewski, V. G.; Montgomery, J. A., Jr.; Stratmann, R. E.; Burant, J. C.; Dapprich, S.; Millam, J. M.; Daniels, A. D.; Kudin, K. N.; Strain, M. C.; Farkas, O.; Tomasi, J.; Barone, V.; Cossi, M.; Cammi, R.; Mennucci, B.; Pomelli, C.; Adamo, C.; Clifford, S.; Ochterski, J.; Petersson, G. A.; Ayala, P. Y.; Cui, Q.; Morokuma, K.; Malick, D. K.; Rabuck, A. D.; Raghavachari, K.; Foresman, J. B.; Cioslowski, J.; Ortiz, J. V.; Stefanov, B. B.; Liu, G.; Liashenko, A.; Piskorz, P.; Komaromi, I.; Gomperts, R.; Martin, R. L.; Fox, D. J.; Keith, T.; Al-Laham, M. A.; Peng, C. Y.; Nanayakkara, A.; Gonzalez, C.; Challacombe, M.; Gill, P. M. W.; Johnson, B. G.; Chen, W.; Wong, M. W.; Andres, J. L.; Head-Gordon, M.; Replogle, E. S.; Pople, J. A. *Gaussian 98*; Gaussian, Inc.: Pittsburgh, PA, 1998.
(33) Slater, J. C. *Phys. Rev.* **1951**, *81*, 385.
(34) Becke, A. D. *Phys. Rev. A* **1988**, *38*, 3098.
(35) Vosco, S. H.; Wilk, L.; Nusair, M. *Can. J. Phys.* **1980**, *58*, 1200.
(36) Lee, C.; Yang, W.; Parr, R. G. *Phys. Rev. B* **1988**, *37*, 785.
(37) Hay, P. J.; Wadt, W. R. *J. Chem. Phys.* **1985**, *82*, 299.
(38) Allen, H. C.; Plyer, E. K. *J. Am. Chem. Soc.* **1985**, *80*, 2673.
(39) Scott, A. P.; Radom, L. *J. Phys. Chem.* **1996**, *100*, 16502.
(40) The ν(CC), δ(CH_2), and ω(CH_2) frequencies are those we recorded at 80 K (unpublished work). They are almost identical to those that have been reported.[16−18]
(41) Backx, C.; de Groot, C. P. M.; Biloen, P. *Appl. Surf. Sci.* **1980**, *6*, 256.
(42) Friedrich, H. B.; Person, W. B. *J. Chem. Phys.* **1966**, *44*, 2161.
(43) Matsuzawa, H.; Yamashita, H.; Ito, M.; Iwata, S. *Chem. Phys.* **1990**, *147*, 77.

Many-body effects in nonadiabatic molecular theory for simultaneous determination of nuclear and electronic wave functions: *Ab initio* NOMO/MBPT and CC methods

Hiromi Nakai[a] and Keitaro Sodeyama
Department of Chemistry, School of Science and Engineering, Waseda University, Tokyo 169-8555, Japan

(Received 5 August 2002; accepted 22 October 2002)

We have investigated the many-body effects in a molecular theory to determine simultaneously nuclear and electronic wave functions without the Born–Oppenheimer (BO) approximation. We first apply the many-body perturbation theory using the electron–nucleus and nucleus–nucleus interactions to the non-BO theory and show the importance of the electron–nucleus correlation rather than the nucleus–nucleus one. We next combine the non-BO theory with the coupled cluster double and Brueckner double methods using the one-electron plus one-nucleus excitation operators.
 [DOI: 10.1063/1.1528951]

I. INTRODUCTION

In order to treat the nuclear motion, we[1–3] have proposed the molecular theory without the Born–Oppenheimer (BO) approximation.[4] In Ref. 3, we have derived the Hartree–Fock (HF) equations for the nuclear orbital (NO), which is one-nucleus wave function, and the electronic molecular orbital (MO). We call this method the *ab initio* NOMO/HF theory. It has been clarified that basis set expansion with Gaussian functions is suitable for the description of the NO.[3] The application of the configuration interaction method with singles (CIS) to the NOMO theory, referred as the *ab initio* NOMO/CIS theory, gives not only the electronic excited states but also the vibrational excited states such as $v=1$ and 2.[2] Furthermore, the analysis with the nuclear density difference map obtained by the nuclear wave function provides us more real image for the nuclear motion than the usual normal mode analysis.[2]

Several groups have explored a similar kind of approach. Shigeta *et al.*[5] proposed coupled mean-field theory for electronic and nuclear fields which is equivalent to the NOMO/HF theory.[3] They have further developed the density functional theory (DFT) and the Green's function method.[6,7] An equivalent theory was proposed by Kreibich and Gross.[8] Recently, Tachikawa applied the CI technique to the non-BO theory.[9] Numerical calculations in the previous studies have been limited to hydrogen molecules.[2,3,5–9]

In the present study we examine the many-body effects such as nucleus–nucleus and electron–nucleus correlations in the non-BO molecular theory. By applying the many-body perturbation theory (MBPT)[10–12] to the NOMO method, we first clarify the importance of the electron–nucleus correlation rather than the nucleus–nucleus one. Next, we combine the NOMO theory with the coupled cluster (CC) method[13] using the one-electron plus one-nucleus excitation operators. The orbital optimization in the NOMO/CC wave function is carried out to obtain Brueckner orbitals.[14–17] The NOMO/CC method is shown to treat the electron–nucleus correlation efficiently.

II. *AB INITIO* NOMO/HF METHOD

In this section, we briefly review the NOMO/HF method proposed previously.[3] The NOMO/HF method uses the total Hamiltonian without the BO approximation expressed by

$$H=T+V=T_e+T_n+V_{ee}+V_{nn}+V_{en}, \tag{1}$$

where

$$T_e=\sum_{\alpha}^{\text{elec}} t_e(\alpha)=-\sum_{\alpha}\frac{1}{2}\nabla^2(\alpha), \tag{2}$$

$$T_n=\sum_{A}^{\text{nuc}} t_n(A)=-\sum_{A}\frac{1}{2m_A}\nabla^2(A), \tag{3}$$

$$V_{ee}=\sum_{\alpha>\beta}^{\text{elec}} v_{ee}(\alpha,\beta)=\sum_{\alpha>\beta}\frac{1}{r_{\alpha\beta}}, \tag{4}$$

$$V_{nn}=\sum_{A>B}^{\text{nuc}} v_{nn}(A,B)=\sum_{A>B}\frac{q_A\cdot q_B}{r_{AB}}, \tag{5}$$

$$V_{en}=\sum_{\alpha}^{\text{elec}}\sum_{A}^{\text{nuc}} v_{en}(\alpha,A)=-\sum_{\alpha}\sum_{A}\frac{q_A}{r_{\alpha A}}. \tag{6}$$

Here, one-particle operators are only kinetic operators, T_e and T_n. Two-particle operators consist of electron–electron V_{ee}, nucleus–nucleus V_{nn}, and electron–nucleus V_{en} interactions.

The Hartree–Fock wave function Φ_0 is represented by a simple product of the electronic wave function and nuclear

[a]Corresponding author. Telephone: +81-3-5286-3452; fax: +81-3-3205-2504; electronic mail: nakai@waseda.jp

wave functions. Of course, the exact or correlated wave function Ψ, however, is not a simple product.

To express the nuclear wave function, we have introduced the one-particle wave function of the nucleus, NO, in addition to MO, that is, the one-particle wave function of the electron. The HF wave function of electrons and nuclei is given by antisymmetric (or symmetric) product of MOs and NOs:

$$\Phi_0^e = \|\varphi_i \varphi_j \cdots \varphi_k\|, \tag{7}$$

$$\Phi_0^n = \|\varphi_I \varphi_J \cdots \varphi_K\|. \tag{8}$$

One can easily derive the HF equations to determine both NO and MO as follows.

$$f_e \varphi_i = \varepsilon_i \varphi_i, \tag{9}$$

$$f_n \varphi_I = \varepsilon_I \varphi_I, \tag{10}$$

where

$$f_e = t_e + \sum_i^{\text{elec}} (J_i - K_i) + \sum_I^{\text{nuc}} J_I = t_e + u_e, \tag{11}$$

$$f_n = t_n + \sum_I^{\text{nuc}} (J_I \mp K_I) + \sum_i^{\text{elec}} J_i = t_n + u_n. \tag{12}$$

The Fock operator includes a mean-field type of coupling between NO and MO. By solving these HF equations, one can get the NOs and MOs, and the nuclear and electronic wave functions simultaneously.

In Eq. (12), the minus and plus signs are for fermionic and bosonic nuclei, respectively. The exchange integral K_{IJ} between the NOs often becomes zero in the numerical treatment, because the NOs treated by the valence-bond type expansion are more rigid than the usual electronic MOs.[3] Thus, the effect of the signs in Eq. (12) is not important in many cases except for the phenomena contributed by fermionic and bosonic characters such as the superfluidity of ^{4}He. As a result, the individual nuclei can be assumed to be like independent particles, which do not exchange one another. We call this treatment the independent particle model (IPM).

III. *AB INITIO* NOMO/MBPT METHOD

A. Theory

In this section, we analyze the many-body effects in the NOMO theory by using the MBPT,[10–12] which is named to the *ab initio* NOMO/MBPT method. In the formalism of perturbation theory, one assumes that the exact Hamiltonian H may be separated into unperturbed Hamiltonian H_0 and perturbation W.

$$H = H_0 + W. \tag{13}$$

The Schrödinger equations for the unperturbed and the exact problem are then

$$H_0 |\Phi_m\rangle = E_m^0 |\Phi_m\rangle, \tag{14}$$

$$H|\Psi\rangle = E|\Psi\rangle. \tag{15}$$

Here, the index m indicates the state number. When one defines a resolvent or Green's function,

$$R = \frac{Q}{E_0 - H_0}, \tag{16}$$

where

$$Q = \sum_{n \neq 0} |\Phi_n\rangle\langle\Phi_n| = 1 - |\Phi_0\rangle\langle\Phi_0| = 1 - P, \tag{17}$$

we may obtain the explicit formulas for the energy in the Rayleigh–Schrödinger perturbation theory (RSPT):

$$\begin{aligned}\Delta E(RSPT) = E - E_0 &= \sum_{n=1}^{\infty} \langle\Phi_0| W[R(W - \Delta E)]^{n-1} |\Phi_0\rangle \\ &= \sum_{n=1}^{\infty} \langle\Phi_0| W[RW]^{n-1} |\Phi_0\rangle \\ &\quad + (\text{renormalization terms}).\end{aligned} \tag{18}$$

The easiest procedure for generating the renormalization terms may be the "bracketing technique".[10]

Another expression for the energy is the linked-diagram expansion, i.e., MBPT:

$$\Delta E(\text{MBPT}) = E - E_0 = \sum_{n=1}^{\infty} \langle\Phi_0| W[RW]^{n-1} |\Phi_0\rangle_L, \tag{19}$$

where L indicates the limitation to "linked" diagrams. Equations (18) and (19) are equal order-by-order as long as the space identified by Q in Eq. (17) is not restricted.

In the NOMO theory, one can write H_0 in the form

$$\begin{aligned}H_0 = T + U &= T_e + T_n + U_e + U_n \\ &= \sum_{\alpha}^{\text{elec}} \{t_e(\alpha) + u_e(\alpha)\} + \sum_{A}^{\text{nuc}} \{t_n(A) + u_n(A)\},\end{aligned} \tag{20}$$

where U represents one-particle approximation of V as, for example, the HF potential. The perturbation operator W for the non-BO Hamiltonian H given by Eq. (1) then becomes

$$W = H - H_0 = V - U = V_{ee} + V_{nn} + V_{en} - U_e - U_n. \tag{21}$$

In order to develop a diagrammatic MBPT approach in the NOMO theory, it is convenient to work within a second-quantized formalism. Then, the operators H_0 and W become

$$H_0 = \sum_p^{\text{elec}} \varepsilon_p a_p^+ a_p + \sum_P^{\text{nuc}} \varepsilon_P a_P^+ a_P. \tag{22}$$

$$W = W_1 + W_2, \tag{23}$$

$$W_1=-\sum_{p,q}^{\text{elec}}\langle p|u_e|q\rangle a_p^+ a_q-\sum_{P,Q}^{\text{nuc}}\langle P|u_n|Q\rangle a_P^+ a_Q, \quad (24)$$

$$W_2=\frac{1}{4}\sum_{p,q,r,s}^{\text{elec}}\langle pq\|rs\rangle a_p^+ a_q^+ a_s a_r + \frac{1}{4}\sum_{P,Q,R,S}^{\text{nuc}}\langle PQ\|RS\rangle a_P^+ a_Q^+ a_S a_R + \sum_{p,q}^{\text{elec}}\sum_{P,Q}^{\text{nuc}}\langle pP|qQ\rangle a_p^+ a_P^+ a_Q a_q. \quad (25)$$

If we use the NOMO/HF Hamiltonian as H_0, ε_p, and ε_P become the orbital energies for the electron and nucleus determined by Eqs. (9) and (10), respectively. $\langle pq||rs\rangle$ is the antisymmetrized integral for electrons and $\langle PQ||RS\rangle$ is the antisymmetrized (or symmetrized) integral for fermionic (or bosonic) nuclei, respectively. In the IPM, $\langle PQ||RS\rangle$ can be replaced by simple $\langle PQ|RS\rangle$. The operators $\{a_p^+, a_q^+, \ldots\}$ and $\{a_p, a_q, \ldots\}$ are creation and annihilation operators for electrons, respectively. These operators establish the following anticommutation relations:

$$[a_p^+, a_q]_+ \equiv a_p^+ a_q + a_q a_p^+ = \delta_{pq}, \quad (26)$$

$$[a_p^+, a_q^+]_+ = [a_p, a_q]_+ = 0. \quad (27)$$

On the other hand, creation and annihilation operators for nuclei expressed by $\{a_P^+, a_Q^+, \ldots\}$ and $\{a_P, a_Q, \ldots\}$ satisfy the following relations:

$$[a_P^+, a_Q]_\pm \equiv a_P^+ a_Q \pm a_Q a_P^+ = \delta_{PQ}, \quad (28)$$

$$[a_P^+, a_Q^+]_\pm = [a_P, a_Q]_\pm = 0, \quad (29)$$

where plus and minus signs correspond to fermionic and bosonic nuclei, respectively. Note that the creation and/or annihilation operators between different particles $\{\mu, \nu\}$ such as $\{e^-, H^+\}$ or $\{H^+, D^+\}$ satisfy the commutation relation:

$$[a_\mu^+, a_\nu]_- = [a_\mu^+, a_\nu^+]_- = [a_\mu, a_\nu]_- = 0. \quad (30)$$

When dealing with the ground and lower excited states, it is much more convenient to adopt the particle–hole formalism. We define the normal-product (N-product) of the second-quantized operators, which is indicated by the symbol $N[\cdots]$, by moving all "particle" annihilation $\{a_a, a_b, \ldots; a_A, a_B, \ldots\}$ and "hole" annihilation $\{a_i^+, a_j^+, \ldots; a_I^+, a_J^+, \ldots\}$ operators to the right by using the above anticommutation (or commutation) relations Eqs. (26)–(29). In this paper, we use the indices $\{i, j, k, l, \ldots; I, J, K, L, \ldots\}$ corresponding to occupied orbitals, $\{a, b, c, d, \ldots; A, B, C, D, \ldots\}$ to unoccupied ones, and $\{p, q, r, s, \ldots; P, Q, R, S, \ldots\}$ to arbitrary ones in a certain reference function, respectively. Then, we reach the exact and unperturbed Hamiltonian and perturbation in the N-product forms:

$$H^N \equiv H - \langle\Phi_0|H|\Phi_0\rangle, \quad (31)$$

$$H_0^N \equiv H_0 - \langle\Phi_0|H_0|\Phi_0\rangle = \sum_p^{\text{elec}}\varepsilon_p N[a_p^+ a_p] + \sum_P^{\text{nuc}}\varepsilon_P N[a_P^+ a_P], \quad (32)$$

$$H^N - H_0^N \equiv W^N = W_1^N + W_2^N, \quad (33)$$

$$W_1^N \equiv Q^N = Q_e^N + Q_n^N = G^N - U^N = G_e^N - U_e^N + G_n^N - U_n^N = \sum_{p,q}^{\text{elec}}\langle p|g_e - u_e|q\rangle N[a_p^+ a_q] + \sum_{P,Q}^{\text{nuc}}\langle P|g_n - u_n|Q\rangle N[a_P^+ a_Q], \quad (34)$$

$$W_2^N \equiv V^N = V_{ee}^N + V_{nn}^N + V_{en}^N = \sum_{p,q,r,s}^{\text{elec}}\langle pq\|rs\rangle N[a_p^+ a_q^+ a_s a_r] + \sum_{P,Q,R,S}^{\text{nuc}}\langle PQ\|RS\rangle N[a_P^+ a_Q^+ a_S a_R] + \sum_{p,q}^{\text{elec}}\sum_{P,Q}^{\text{nuc}}\langle pP|qQ\rangle N[a_p^+ a_P^+ a_Q a_q], \quad (35)$$

where the g_e and g_n operators are components of the W_2 operators containing one contraction,

$$\langle p|g_e|q\rangle = \sum_i^{\text{elec}}\langle pi||qi\rangle, \quad (36)$$

$$\langle P|g_n|Q\rangle = \sum_I^{\text{nuc}}\langle PI||QI\rangle. \quad (37)$$

If one uses the NOMO/HF potential as the one-particle potentials u_e and u_n, the one-particle perturbation W_1^N vanishes.

With the preceding N-product Hamiltonians, the Schrödinger equations (14) and (15) take the form

$$H_0^N|\Phi_m\rangle = \Delta E_m^0|\Phi_m\rangle, \quad (38)$$

$$H^N|\Psi\rangle = \Delta E|\Psi\rangle, \quad (39)$$

where

$$\Delta E_m^0 = E_m^0 - E_0, \quad (40)$$

$$\Delta E = E - E_0 = E^{(1)} + E_{\text{corr}}. \quad (41)$$

B. Diagrammatics

Here we extend the diagrammatic method for the usual electronic system to the electronic plus nuclear system. At first, we define the electron and nucleus vertices, which are

represented by ● (black dot) and ○ (white circle), respectively. The Q_e and Q_n diagrams, i.e., ●·····× and ○·····×, correspond to the one-electron and one-nucleus potentials, respectively. The V_{ee}, V_{nn}, and V_{en} diagrams, i.e., ●·····●, ○·····○, and ●·····○, represent electron–electron, nucleus–nucleus, and electron–nucleus interactions, respectively. The electron and nucleus creation operators $\{a_p^+, a_q^+, \ldots; a_P^+, a_Q^+, \ldots\}$ are represented by arrows leaving the electron and nucleus vertices, ←● and ←○, respectively. Similarly, those annihilation operators $\{a_p, a_q, \ldots; a_P, a_Q, \ldots\}$ are drawn by arrows entering the corresponding vertices, →● and →○, respectively. In the particle–hole formalism, upward and downward arrows represent "particle" and "hole" lines, respectively.

Note that the arrows cannot connect between the electron and nucleus vertices such as ●→○. Also, the arrows cannot connect between different nuclei such as different elements and different mass numbers. This rule naturally leads to the fact that only a Coulomb interaction is involved as the electron–nucleus interaction in the Fock operators whereas both Coulomb and exchange interactions are involved as the electron–electron and nucleus–nucleus interactions.

We examine the electron–nucleus pair correlation by the diagrammatic MBPT technique. When one uses the NOMO/HF wave function as the zeroth order function, the one-particle perturbation, W_1^N, vanishes. Thus, one has only to take into account the two-particle perturbation, W_2^N. The explicit forms of the second- and third-order perturbation are represented by

$\Delta E_{en}^{(2)} =$ 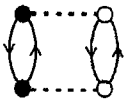

(42)

and

$\Delta E_{en}^{(3)} =$ 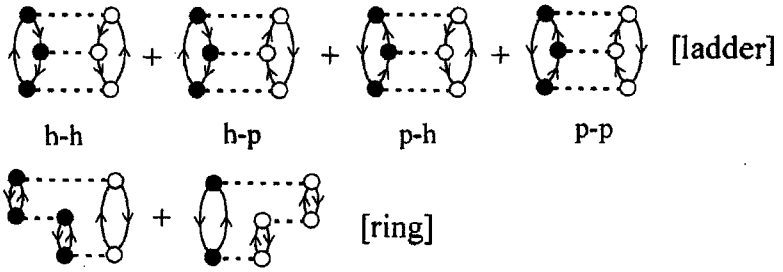

(43)

When one limits the ladder and ring diagrams, the fourth-order perturbation becomes

$\Delta E_{en}^{(4)} \cong$ 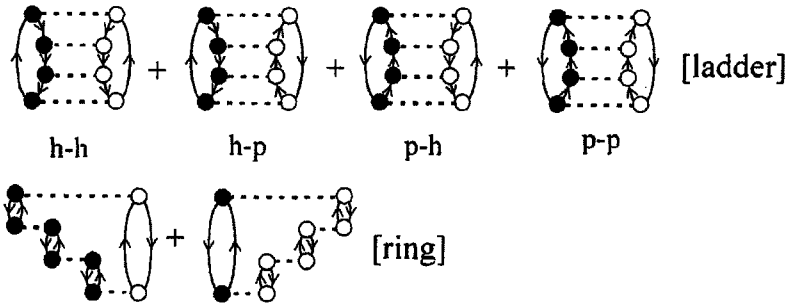

(44)

C. Numerical applications

Next, we apply the NOMO/MBPT method presented here to H_2, D_2, T_2, N_2, and F_2 molecules. The $(5s2p)$ primitive functions, of which exponents correspond to correlation-consistent polarization plus valence triple-ζ (cc-pVTZ) bases of Dunning,[18] are adopted as the electronic basis functions (EBFs) of H, D, and T. The $(10s5p2d)$ primitive functions with the same exponents of cc-pVTZ bases are used as the EBFs of N and F. The $(5s5p)$ primitive functions are used for nuclear basis functions (NBFs) of H, D, T, N, and F, where the same exponents are used for s- and p-functions and correspond to the vibrational frequencies from 1,000 to 100,000 cm^{-1}.[3] The orbital centers of both electronic and nuclear functions are settled at the experimental geometries.[19]

Table I shows the electron–nucleus and nucleus–nucleus correlation energies of H_2, D_2, and T_2; that is, ΔE_{en} and

TABLE I. Electron–nucleus and nucleus–nucleus correlation energies of H_2, D_2, and T_2 (in mHartree).

	H_2				D_2				T_2			
	ΔE_{en}		ΔE_{nn}		ΔE_{en}		ΔE_{nn}		ΔE_{en}		ΔE_{nn}	
MBPT2	−24.7118	(−24.7118)	−2.8690	(−2.8690)	−17.7272	(−17.7272)	−1.9886	(−1.9886)	−14.1457	(−14.1457)	−1.5245	(−1.5245)
MBPT3	−28.9371	(−4.2253)	−2.8101	(+0.0589)	−20.7331	(−3.0059)	−1.9453	(+0.0433)	−16.5328	(−2.3871)	−1.4978	(+0.0267)
MBPT4[a]	−29.8118	(−0.8746)	−2.8116	(−0.0015)	−21.3507	(−0.6179)	−1.9465	(−0.0012)	−17.0216	(−0.4887)	−1.4984	(−0.0006)

[a]The fourth-order perturbation is limited to the ladder and ring diagrams.

ΔE_{nn}, respectively. In any cases, the electron–nucleus correlation energies are larger than the nucleus–nucleus ones. Both ΔE_{en} and ΔE_{nn} become smaller as the heavier mass number; namely, $H_2 \rightarrow D_2 \rightarrow T_2$. At the limit of infinity mass number, these correlation energies should become zero, because it corresponds to the conventional BO treatment at the limit.

In Table I, the correlation energies at each order of the perturbation, i.e., $\Delta E_{en}^{(i)}$ and $\Delta E_{nn}^{(i)}$, are also shown in parentheses. There are oscillations for the nucleus–nucleus correlation energies. For example, $\Delta E_{nn}^{(i)}$ of H_2 are −2.8690, +0.0589, and −0.0015 mHartree at the second-, third-, and fourth-order perturbations, respectively. This kind of oscillation has often been reported for the ordinary electron correlation, namely, the electron–electron correlation. On the other hand, the electron–nucleus correlation energies are always negative values. It may be based on the difference that the electron–nucleus interaction is attractive, while the nucleus–nucleus and electron–electron interactions are repulsive. In fact, the Coulomb type integrals for the electron–nucleus interaction have negative values, whereas those for the nucleus–nucleus and electron–electron interactions have positive values.

Table II shows the electron–nucleus and nucleus–nucleus correlation energies of N_2 and F_2. In these molecules, the electron–nucleus correlation energies are much greater than the nucleus–nucleus ones. For example, $(\Delta E_{en}^{(2)}, \Delta E_{nn}^{(2)}) = (-304.3705, -0.0008)$ and $(-530.3601, -0.0001)$ in mHartree for N_2 and F_2, respectively. The small values of ΔE_{nn} of N_2 and F_2 are due to the NOs shrinking. The electron–nucleus correlation energies of N_2 and F_2 become fairly larger than those of H_2, D_2, and T_2. It is because the attraction force is expected to be stronger as the nuclear charge becomes larger.

Table III shows the core-electron and valence-electron contributions to the second order electron–nucleus correlation energies of N_2 and F_2. In both molecules, the correlation energies decrease exponentially in the order of $1s$, $2s$, and $2p$ electrons. Therefore, the correlation between the core–electron and nucleus is more important than that between the valence–electron and nucleus. It is because the spatial distribution of the core–electron is close to that of the nucleus, in comparison with the valence–electron.

This is the first study to examine the many-body effects in N_2 and F_2 as well as H_2. From the present results, it is found that the correlation between core–electron and nucleus is important energetically. We suppose that this correlation is also essential to evaluate other physical properties.

IV. *AB INITIO* NOMO/CCD METHOD

A. Theory

In this section, we apply the CC method[13] to the NOMO theory. The CC wave function for the ground state is expressed in terms of cluster operators T as

$$|\Psi_0^{CC}\rangle = \exp(T)|\Phi_0\rangle, \tag{45}$$

where

$$T = T_1 + T_2 + T_3 + \cdots = \sum_l T_l. \tag{46}$$

The T operators are in N-product form,

$$T_l = \sum_{\substack{a>b>c\cdots \\ i>j>k\cdots}} t_{ijk\cdots}^{abc\cdots} N[a_a^+ a_i a_b^+ a_j a_c^+ a_k \cdots]. \tag{47}$$

When premultiplying the Schrödinger equation for H^N by $\exp(-T)$, we have

$$\exp(-T)H^N \exp(T)|\Phi_0\rangle = \Delta E_0 |\Phi_0\rangle. \tag{48}$$

The Campbell–Baker–Hausdorff commutator formula leads to

TABLE II. Electron–nucleus and nucleus–nucleus correlation energies of N_2 and F_2 (in mHartree).

	N_2				F_2			
	ΔE_{en}		ΔE_{nn}		ΔE_{en}		ΔE_{nn}	
MBPT2	−304.3705	(−304.3705)	−0.0008	(−0.0008)	−530.3601	(−530.3601)	−0.0001	(−0.0001)
MBPT3	−312.2959	(−7.9254)	−0.0008	(−0.0000)	−540.9782	(−10.6181)	−0.0001	(−0.0000)
MBPT4[a]	−312.5806	(−0.2846)	−0.0008	(−0.0000)	−541.2777	(−0.2995)	−0.0001	(−0.0000)

[a]The fourth-order perturbation is limited to the ladder and ring diagrams.

TABLE III. Core– and valence–electron contributions to the second-order electron–nucleus correlation energies of N_2 and F_2 (in mHartree).

	N_2	F_2
$1s\sigma$	−143.6552	−246.9022
$1s\sigma^*$	−143.8460	−247.4932
$2s\sigma$	−7.0794	−12.0454
$2s\sigma^*$	−6.1646	−13.9864
$2p\pi$	−1.7400	−3.5168
$2p\sigma$	−1.8852	−2.3582
$2p\pi^*$		−4.0576
Total	−304.3705	−530.3601

$$\exp(-T)H^N\exp(T)|\Phi_0\rangle=H^N\exp(T)|\Phi_0\rangle_C. \tag{49}$$

Where C indicates the limitation to the "connected" diagram.

Correlation energy ΔE_0 is given by projecting (48) and (49) on the left by $\langle\Phi_0|$:

$$\Delta E_0=\langle\Phi_0|H^N\exp(T)|\Phi_0\rangle_C, \tag{50}$$

which is referred as the ΔE–equation. Projection onto excitation configuration $\langle\Phi_{ij\cdots}^{ab\cdots}|$ provides equations for the T amplitudes, which are called the T_J–equation.

$$0=\langle\Phi_{ij\cdots}^{ab\cdots}|H^N\exp(T)|\Phi_0\rangle_C. \tag{51}$$

In order to examine the electron–nucleus correlation effect, we here limit ourselves to double excitation cluster with single-electron plus single-nucleus excitations $T_2(en)$,

$$T_2(en)=\sum_{i,a}^{\text{elec}}\sum_{I,A}^{\text{nuc}} t_{iI}^{aA}N[a_a^+a_ia_A^+a_I]. \tag{52}$$

The ΔE– and T_2–equations are given by

$$\Delta E_0=\langle\Phi_0|H^N+[\dot{H}^N\dot{T}_2]|\Phi_0\rangle_C \tag{53}$$

and

$$0=\langle\Phi_{iI}^{aA}|H^N+[\dot{H}^N\dot{T}_2]+[\dot{H}^N\dot{T}_2^2]/2|\Phi_0\rangle_C. \tag{54}$$

The symbol $[\dot{A}\dot{B}\dot{C}\cdots]$ means all possible contractions among N-product operators.

For the optimization of the MO and NO in the CCD wave function, the following T_1–equations, coupled to Eq. (54), suffice to determine the separation of the orbital space into occupied and virtual parts, which provides the Brueckner orbitals:

$$0=\langle\Phi_i^a|H^N+[\dot{H}^N\dot{T}_2]|\Phi_0\rangle_C, \tag{55}$$

$$0=\langle\Phi_I^A|H^N+[\dot{H}^N\dot{T}_2]|\Phi_0\rangle_C. \tag{56}$$

The solution of Eq. (54) gives the amplitudes of the $T_2(en)$ operators, while the iterative solution between Eqs. (54) and (55)–(56) determines not only the $T_2(en)$ amplitudes but also the optimized NOs and MOs; that is, the Brueckner orbitals. We call the former the *ab initio* NOMO/CCD method, and the latter the *ab initio* NOMO/BD method.

B. Diagrammatics

The diagrammatic equations for the NOMO/CC theory are presented here. Since the operator $T_2(en)$ has external lines, its diagrammatic expression is defined by the following open diagram:

$T_2(en)=$ 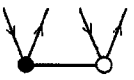 (57)

The vertices $\vee$ and $\vee$ correspond to electronic and nuclear excitations, respectively. Upward arrows represent "particle" lines and downward "hole" lines. To construct the quantity $H^N\exp(T_2(en))|\Phi_0\rangle_C$, we first expand $\exp(T_2(en))$. For example, $T_2(en)^2$ is described by

$T_2(en)^2=$  (58)

Then we add the components of H^N to each $T_2(en)$ vertex or combination of $T_2(en)$ vertices. Here, one- and two-particle interactions of H^N are symbolized as

$H_0^N+W_1^N=$ 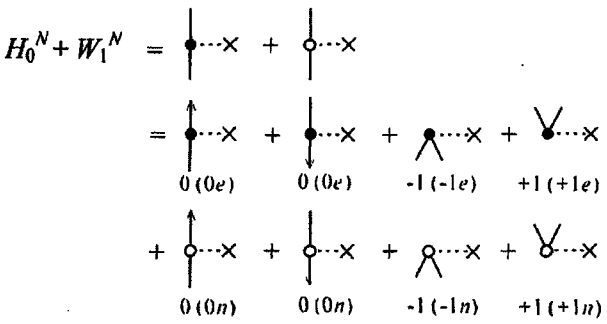

(59)

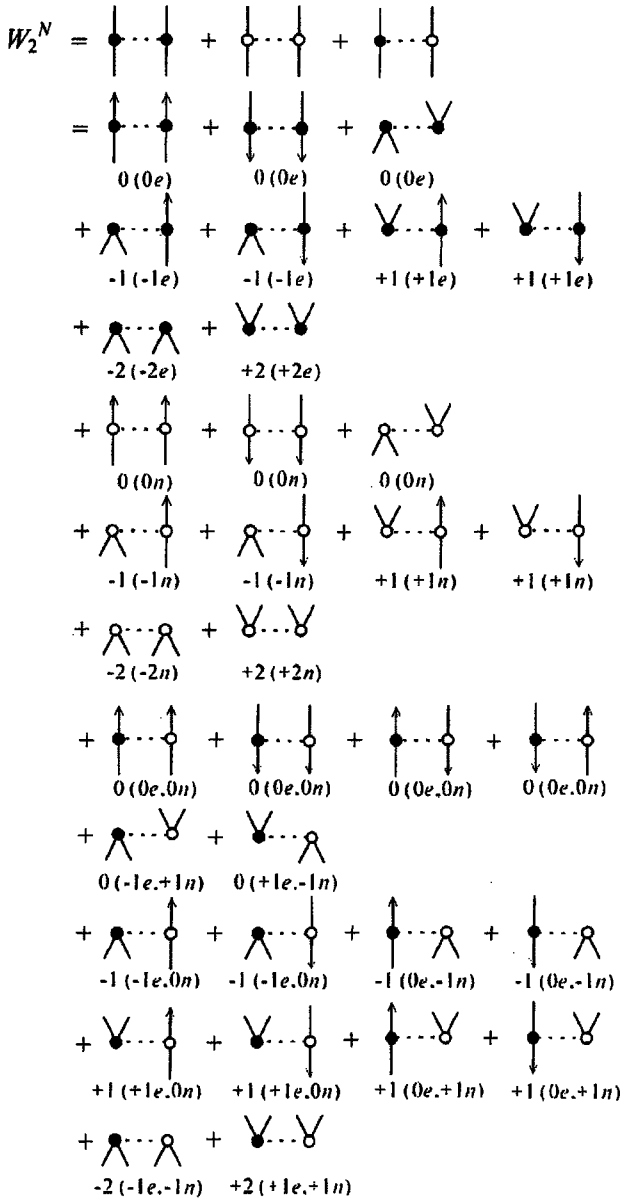

(60)

where the interaction ⟊···× and ⟊···× stand for the operators $\varepsilon_p N[a_p^+ a_p] - \langle p|g_e - u_e|q\rangle N[a_p^+ a_q]$ and $\varepsilon_P N[a_P^+ a_P] - \langle P|g_n - u_n|Q\rangle N[a_P^+ a_Q]$, respectively. On the other hand, ⟊···⟊ and ⟊···⟊ stand for antisymmetrized (or symmetrized) operators $\langle pq||rs\rangle N[a_p^+ a_q^+ a_s a_r]$ and $\langle PQ||RS\rangle N[a_P^+ a_Q^+ a_S a_R]$, respectively, while ⟊···⟊ stands for the simple operator $\langle pP||qQ\rangle N[a_p^+ a_P^+ a_Q a_q]$. The labels at the bottom of the $H_0^N + W_1^N$ and W_2^N operators refer to the change in excitation level caused by that form of the operators. Furthermore, changes in electron and nucleus excitation levels are also shown in parentheses.

In adding the H^N diagrams to the $T_2(en)$ vertices, we should retain the correct excitation level and the connected requirement of the diagram. The simplest example is the ΔE −equation in Eq. (53). Here, since the $T_2(en)$ vertex creates two-particle excitation and the excitation level of the ΔE −equation is zero, we require the (-2) de-excitation operators from H^N, and this can only come from W_2^N. As a result, we get

$$\Delta E_0 = \langle \Phi_0 | H^N + [\dot{H}^N \dot{T}_2] | \Phi_0 \rangle_c = \quad \text{(61)}$$

In a similar manner, we can get the T_2–equation in Eq. (54) as follows:

$$0=\left\langle \Phi_{II}^{aA}\left|H^N+\left[\dot{H}^N\dot{T}_2\right]+\left[\dot{H}^N\dot{T}_2^2\right]/2\right|\Phi_0\right\rangle_C$$

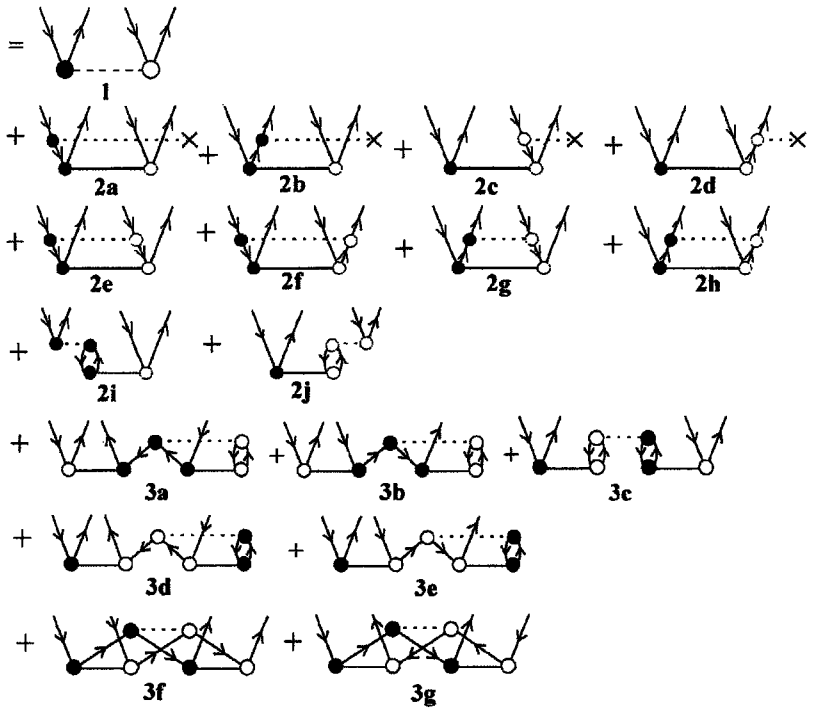

(62)

In Eq. (62), the term **1** comes from expansion of the first term in Eq. (54), whereas the terms **2a–2j** and **3a–3g** are originated from the second and third terms, respectively. In the IPM, the terms **3d–3g** are not taken into account. When one uses the NOMO/HF orbitals, the terms **2a–2d** vanish.

The T_1–equations in Eqs. (55) and (56), for the optimization of the NOs and MOs in the CCD wave function, are represented by

$$0=\left\langle \Phi_I^a\left|H^N+\left[\dot{H}^N\dot{T}_2\right]\right|\Phi_0\right\rangle_C$$

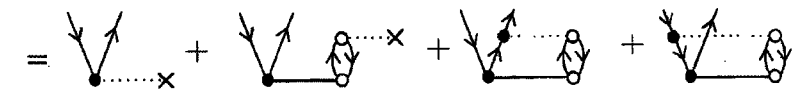

(63)

and

$$0=\left\langle \Phi_I^A\left|H^N+\left[\dot{H}^N\dot{T}_2\right]\right|\Phi_0\right\rangle_C$$

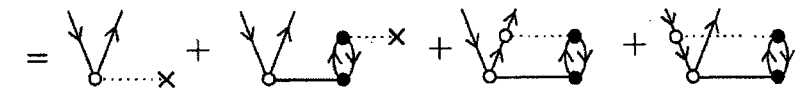

(64)

Here, since the NOs and MOs are no longer the HF orbitals, the second terms in Eqs. (63) and (64) never vanish. Similarly, the terms **2a–2d** in Eq. (62) do not vanish in the iterative solution between Eqs. (62) and (63)–(64), which is needed to determine the amplitudes of the $T_2(en)$ operators and the Brueckner orbitals.

C. Numerical applications

Finally, we apply the NOMO/CCD and BD methods to H_2, D_2, and T_2 molecules. The same basis sets as the NOMO/MBPTn calculations presented in Sec. III are used for the EBFs and the NBFs. Table IV shows the electron–nucleus correlation energies of H_2, D_2, and T_2 calculated by the NOMO/CCD and BD methods in comparison with the NOMO/MBPTn results. Energy differences between the sequential two calculations are also shown in parentheses. For example, the differences in H_2 are −4.23, −0.87, −0.46, and −4.93 mHartree for the MBPT2→MBPT3→MBPT4→CCD→BD results, respectively. The electron–nucleus correlation energies apparently converge up to the CCD cal-

TABLE IV. Electron–nucleus correlation energies of H_2, D_2, and T_2 calculated by the NOMO/CCD and BD methods in comparison with the NOMO/MBPT results (in mHartree). Differences with respect to the MBPT2 results are shown in parentheses.

	H_2		D_2		T_2	
MBPT2	−24.7118	(0.0000)	−17.7272	(0.0000)	−14.1457	(0.0000)
MBPT3	−28.9371	(−4.2253)	−20.7331	(−3.0059)	−16.5328	(−2.3871)
MBPT4[a]	−29.8118	(−5.0999)	−21.3507	(−3.6235)	−17.0216	(−2.8758)
CCD	−30.2805	(−5.5687)	−21.6933	(−3.9662)	−17.2939	(−3.1481)
BD	−35.2142	(−10.5023)	−24.5144	(−6.7872)	−19.4075	(−5.2617)

[a]The fourth-order perturbation is limited to the ladder and ring diagrams.

culations. However, the NOMO/BD calculations give greater electron–nucleus correlation energies even compared with the NOMO/CCD results.

In the ordinary MO theory, the effect of the orbital optimization in the correlated wave function is usually so small that the electron correlation energy calculated by the MO/BD method is very close to that by the MO/CCD or CCSD method.[16,17] The greater effect of the orbital optimization may be specific to the non-BO molecular theory. In the NOMO/HF method, the NOs and MOs are determined by using the mean-field type of the interaction between the electron and nucleus; namely,  and  . On the other hand, the effective interactions shown in Eqs. (63) and (64) are used for the NOMO/BD calculation. One of the most characteristic behaviors of the electron–nucleus interaction is that it is based on the attractive force, not the repulsive one. Therefore, the optimizations of nuclear and electronic orbitals are essential in order to evaluate the electron–nucleus correlation energies.

V. CONCLUSION

In the present study we have developed the *ab initio* NOMO/MBPT*n*, CCD, and BD methods to treat many-body effects in the non-BO molecular theory. Both algebraic and diagrammatic formulations have been proposed. From the analysis of the numerical results by the NOMO/MBPT calculations, the electron–nucleus correlation is found to be more important than the nucleus–nucleus one. Furthermore, correlations between core–electrons and nuclei are greater than those between valence-electrons and nuclei. The *ab initio* NOMO/CCD and BD methods adopt the one-electron plus one-nucleus excitation operator as the double excitation operator. The numerical results have shown that the NOMO/BD method can efficiently take into account the electron–nucleus correlation.

ACKNOWLEDGMENTS

Part of the calculations was performed at the Research Center for Computational Science (RCCS) of the Okazaki National Research Institutes and the Media Network Center (MNC) of Waseda University. Part of this study was supported by a Grant-in-Aid for Young Scientists (A) "KAKENHI 14703005" from Japanese Society for the Promotion of Science (JSPS) and by a Waseda University Grant for Special Research Projects.

[1] M. Tachikawa, K. Mori, H. Nakai, and K. Iguchi, Chem. Phys. Lett. **290**, 437 (1998).
[2] H. Nakai, K. Sodeyama, and M. Hoshino, Chem. Phys. Lett. **345**, 118 (2001).
[3] H. Nakai, Int. J. Quantum Chem. **86**, 511 (2002).
[4] M. Born and R. Oppenheimer, Ann. Phys. (Paris) **84**, 457 (1927).
[5] Y. Shigeta, Y. Ozaki, K. Kodama, H. Nagao, H. Kawabe, and K. Nishikawa, Int. J. Quantum Chem. **69**, 629 (1998).
[6] Y. Shigeta, H. Takahashi, S. Yamanaka, M. Mitani, H. Nagao, and K. Yamaguchi, Int. J. Quantum Chem. **70**, 659 (1998).
[7] Y. Shigeta, H. Nagao, K. Nishikawa, and K. Yamaguchi, J. Chem. Phys. **111**, 6171 (1999).
[8] T. Kreibich and E. K. U. Gross, Phys. Rev. Lett. **86**, 2984 (2001).
[9] M. Tachikawa, Chem. Phys. Lett. **360**, 494 (2002).
[10] J. Paldus and J. Čížek, Adv. Quantum Chem. **9**, 106 (1975).
[11] B. H. Brandow, Adv. Quantum Chem. **10**, 187 (1977).
[12] S. A. Kucharski and R. J. Bartlett, Adv. Quantum Chem. **18**, 281 (1986).
[13] R. J. Bartlett, *Recent Advances in Coupled-Cluster Methods* (World Scientific, Singapore, 1997).
[14] K. A. Brueckner, C. A. Levinson, and H. M. Mahmoud, Phys. Rev. **95**, 217 (1954).
[15] K. A. Brueckner, Phys. Rev. **96**, 508 (1954).
[16] G. E. Scuseria, Chem. Phys. Lett. **226**, 251 (1994).
[17] N. C. Handy, J. A. Pople, M. Head-Gordon, K. Raghavachari, and G. W. Trucks, Chem. Phys. Lett. **164**, 185 (1989).
[18] T. H. Dunning, Jr., J. Chem. Phys. **90**, 1007 (1989).
[19] K. P. Huber and G. Herzberg, *Constants of Diatomic Molecules* (Van Nostrand Reinhold, New York, 1979).

Available online at www.sciencedirect.com
SCIENCE DIRECT®
Chemical Physics Letters 368 (2003) 673–679
CHEMICAL PHYSICS LETTERS
www.elsevier.com/locate/cplett

Energy density analysis of internal methyl rotations in halogenated toluenes

Yoshiumi Kawamura, Hiromi Nakai *

Department of Chemistry, School of Science and Engineering, Waseda University, 3-4-1 Okubo, Shinjuku-ku, Tokyo 169-8555, Japan

Received 13 September 2002; in final form 21 November 2002

Abstract

We have recently proposed an energy density analysis (EDA) that partitions the total energy of a molecular system into atomic energy densities. In this study, the EDA was applied to internal methyl rotations of *o*- and *m*-halogenated toluenes. For toluene and *m*-halogenated toluenes, the energy density changes of the *ortho*-carbons are significant for the rotational barrier height. For *o*-fluorotoluene, the in-plane hydrogen of the methyl group and fluorine forms a hydrogen bond, decreasing the barrier height. It is shown that the EDA technique is a very useful and powerful tool for investigating chemical and physical phenomena.

1. Introduction

Internal rotation of methyl groups presents us with a fundamental and profound problem concerning the nature of non-covalent interaction. The methyl rotational barriers of various molecules in the ground (S_0), excited (S_1) and cationic states (C_0) have been measured using infrared, Raman, microwave and supersonic jet techniques [1–10]. It has been revealed that the rotational barriers of substituted toluenes are very sensitive to their electronic states. In order to clarify the mechanism of barrier change by excitation and ionization, several groups have taken theoretical approaches to investigate the barrier change [11–17]. Our group has found a new type of interaction that leads to chemical bonding between the methyl group and *ortho*-carbons in substituted toluenes. We have named this interaction π^*–σ^* hyperconjugation (HC). By taking the π^*–σ^* HC into account, a reasonable interpretation has been given for the barrier change by $S_0 \rightarrow S_1$ excitation in the substituted toluenes [13,14], methylnaphthalenes [15] and methyl azabenzenes [16]. We have also described a π–σ^* HC, which dominates the barrier change by $S_0 \rightarrow C_0$ ionization [17]. Although the π^*–σ^* and π–σ^* HC mechanisms clarify the barrier changes by excitation and ionization, the absolute values of barriers in the S_0 state remain unexplained because these barriers are effected by various factors, such as steric and electrostatic effects.

Sonoda and Iwata have shown that the rotational barrier changes by $S_0 \rightarrow C_0$ ionization correlate with the differences of the net charges on two

* Corresponding author. Fax: +81-3-3205-2504.
E-mail address: nakai@waseda.jp (H. Nakai).

0009-2614/02/$ - see front matter © 2002 Elsevier Science B.V. All rights reserved.
doi:10.1016/S0009-2614(02)01883-3

ortho-carbons. Lu et al. [12] have shown that methyl rotational barriers are proportional to the bond order difference between *ortho*-carbons. Both groups have shown that the nature of *ortho*-carbons correlates with the methyl rotational barriers. However, the contribution of the *ortho*-carbons to the rotational barrier heights has not been evaluated numerically.

Recently, we have proposed a new analyzing technique, named energy density analysis (EDA) [18,19], which partitions the total energy of a molecule computed using the Kohn–Sham (KS) type density functional theory (DFT) [20] into atomic energy densities without extra computing costs. In the present study, the EDA method is applied to the internal methyl rotations of *o*- and *m*-halogenated toluenes in the S_0 state. We evaluate the changes of atomic energy densities by the internal methyl rotation. We show that the change of the energy density of the *ortho*-carbon is significant for the rotational barrier.

2. Computational method

The present study deals with the internal methyl rotations in *o*- and *m*-halogenated toluenes ($C_6H_4(CH_3)X$, X = F, Cl, Br, I) theoretically. The methyl rotational barriers were obtained by the DFT calculations. The DFT calculations were performed with the B3LYP hybrid functional [21], which consists of the HF (exact) exchange, the Slater exchange [22], the Becke (B88) exchange [23], the Vosco–Wilk–Nusair (VWN) correlation [24] and the Lee–Yang–Parr (LYP) correlation [25] functionals. Correlation-consistent polarized valence double zeta (cc-pVDZ) basis sets of Dunning [26–28] were adopted for H, C, F, Cl and Br. The valence double zeta basis set of Huzinaga [29] was adopted for I. Geometry optimizations were carried out using the B3LYP method. The electronic state calculations were performed by using the program system HONDO99 [30].

The EDA was performed to evaluate the change of the atomic energy densities by the methyl rotation. In the EDA, the atomic energy density for the exchange-correlation term (E^A_{XC}) is evaluated by the partial sum in the numerical quadrature technique.

$$E^A_{XC} = \sum_g^{grid} \omega_g p_A(\mathbf{r}_g) F_{XC}(\mathbf{r}_g), \tag{1}$$

where $\omega_g(\mathbf{r})$ is the weight, $p_A(\mathbf{r})$ is the partition function (for example, see [31]) and $F_{XC}(\mathbf{r})$ is the exchange-correlation functional. The other terms, which are evaluated by analytical integration with the KS orbitals, are partitioned into their energy densities by using the analogy of Mulliken population analysis [32]. For example, the Coulomb energy density for atom A, E^A_{CLB}, is evaluated by

$$E^A_{CLB} = \frac{1}{2}\sum_{\mu\in A}(\mathbf{PG})_{\mu\mu}, \tag{2}$$

where **P** is the AO-basis density matrix and the element of **G** is given by

$$G_{\nu\mu} = \sum_\rho \sum_\sigma P_{\rho\sigma}(\chi_\nu\chi_\mu|\chi_\sigma\chi_\rho). \tag{3}$$

By adding the atomic contributions for the nuclear repulsion, kinetic energy, nuclear attraction, Coulomb and exchange-correlation terms, the total atomic energy density is evaluated by

$$E^A = E^A_{NN} + T^A_S + E^A_{Ne} + E^A_{CLB} + E^A_{XC}. \tag{4}$$

The EDA calculations were carried out by linking the original code for the EDA [33] with HONDO99.

3. Results and discussion

Table 1 shows the calculated and experimental rotational barriers of *o*- and *m*-halogenated toluenes. The difference between the total energy of pseudo-*trans* and pseudo-*cis* conformers,

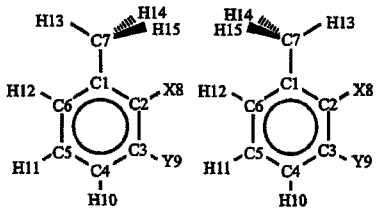

pseudo -*trans* pseudo -*cis*

X=F, Cl, Br, I, Y=H for *ortho* system

X=H, Y=F, Cl, Br, I for *meta* system

Table 1
Calculated and experimental rotational barriers (mHartree) of *m*- and *o*-halogenated toluenes

	Calc.	Exptl.
m-Halogenated toluenes		
–F	0.05	0.07
–Cl	0.02	–
–Br	0.01	–
–I	–0.02	–
o-Halogenated toluenes		
–F	0.92	1.04
–Cl	1.87	1.82
–Br	1.85	–
–I	2.00	–

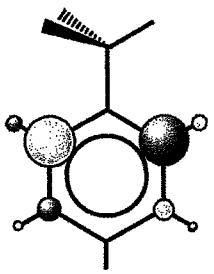

Fig. 1. Energy density changes (ΔE^A) by the methyl rotation of toluene. Blue and red balls represent stabilized and destabilized atoms, respectively. Their volume is proportional to the degree of stabilization and destabilization.

is taken as the rotational barrier. The maximum discrepancy between experimental and computational barriers is 0.13 mHartree. In previous studies [11–17], the experimental rotational barriers were reproduced well even by the HF method, which does not include the electron correlation effect. The present DFT calculations with B3LYP functionals also reproduce well the experimental rotational barriers.

The absolute values of rotational barriers of *m*-halogenated toluenes are less than 0.05 mHartree. For *o*-halogenated toluenes, large rotational barriers are obtained. The barriers of *o*-chlorotoluene (*o*-CT), *o*-bromotoluene (*o*-BT) and *o*-iodotoluene (*o*-IT) are in the range of 1.8–2.0 mHartree. The rotational barrier of *o*-FT is 0.92 mHartree, which is about half that of the other halogenated toluenes.

Table 2
Changes of atomic energy densities (ΔE^A) by methyl rotation in toluene and *m*-halogenated toluenes in mHartree

	Toluene	*m*-Halogenated toluenes							
		–F		–Cl		–Br		–I	
		ΔE^A	$(\Delta\Delta E^A)$	ΔE^A	$(\Delta\Delta E^A)$	ΔE^A	$(\Delta\Delta E^A)$	ΔE^A	$(\Delta\Delta E^A)$
C_1	0.00	–0.24	(–0.24)	–0.22	(–0.22)	–0.25	(–0.25)	0.34	(+0.34)
C_2	5.13	5.33	(+0.21)	5.58	(+0.45)	5.68	(+0.55)	5.35	(+0.23)
C_3	–0.49	–0.45	(+0.03)	–0.59	(–0.11)	–0.62	(–0.14)	–0.34	(+0.15)
C_4	0.00	0.28	(+0.28)	0.21	(+0.21)	0.28	(+0.28)	–0.18	(–0.18)
C_5	0.49	0.23	(–0.26)	0.24	(–0.24)	0.24	(–0.25)	0.27	(–0.21)
C_6	–5.13	–5.14	(–0.01)	–5.08	(+0.05)	–5.04	(+0.09)	–5.12	(+0.01)
C_7	0.00	0.02	(+0.02)	0.10	(+0.10)	0.13	(+0.13)	0.14	(+0.14)
H_8	–0.13	–0.11	(+0.02)	–0.18	(–0.05)	–0.20	(–0.07)	–0.32	(–0.19)
X_9	0.02	0.08	(+0.05)	–0.03	(–0.05)	–0.14	(–0.16)	–0.08	(–0.10)
H_{10}	0.00	–0.01	(–0.01)	–0.01	(–0.01)	–0.01	(–0.01)	0.01	(+0.01)
H_{11}	–0.02	–0.01	(+0.02)	–0.02	(+0.01)	–0.02	(+0.00)	–0.02	(+0.00)
H_{12}	0.13	0.08	(–0.04)	0.08	(–0.04)	0.08	(–0.05)	0.08	(–0.04)
H_{13}	0.00	0.03	(+0.03)	–0.01	(–0.01)	–0.09	(–0.09)	–0.30	(–0.30)
H_{14}	0.00	–0.03	(–0.03)	–0.03	(–0.03)	–0.01	(–0.01)	0.07	(+0.07)
H_{15}	0.00	–0.03	(–0.03)	–0.03	(–0.03)	–0.01	(–0.01)	0.07	(+0.07)
Total	0.00	0.04	(+0.04)	0.02	(+0.02)	0.01	(+0.01)	–0.01	(–0.01)

Differences between ΔE^A of toluene and *m*-halogenated toluenes ($\Delta\Delta E^A$) are shown in parentheses.

Next, we evaluated the changes of the atomic energy density by the methyl rotation of toluene and of *o*- and *m*-halogenated toluenes. The changes are denoted by

$$\Delta E^{A} = E^{A}_{\text{pseudo-}cis} - E^{A}_{\text{pseudo-}trans}. \quad (5)$$

Fig. 1 shows the energy density changes by a 180° methyl rotation in toluene, obtained by the EDA technique. The blue and red balls represent stabilized and destabilized atoms, respectively. The volume of the balls is proportional to the degree of the stabilization or destabilization evaluated by the EDA. Numerical data of the EDA results are shown in Table 2.

As shown in Fig. 1, the maximum ΔE^{A} appears in the C_2 and C_6 atoms due to the steric repulsion with the in-plane hydrogen atoms of the methyl group in toluene. ΔE^{A} of the H_8 and H_{12} atoms, located near the in-plane hydrogen atoms of the methyl, are rather small at ± 0.13 mHartree. Only ΔE^{A} of the *ortho*-carbons is large.

Fig. 2a shows the ΔE^{A} of *m*-halogenated toluenes obtained using the same procedure as for Fig. 1. Numerical data of ΔE^{A} are shown in Table 2. The largest changes in ΔE^{A} in *m*-FT by the methyl rotation appear in C_2 and C_6, at 5.33 and −5.14 mHartree, respectively. The *m*-CT, *m*-BT and *m*-IT also have the largest ΔE^{A} values in the C_2 and C_6 atoms. The ΔE^{A} of *ortho*-carbons are as large in the *m*-halogenated toluenes as they are in toluene. The differences between ΔE^{A} of toluene and that of halogenated toluenes are denoted as follows,

$$\Delta\Delta E^{A} = \Delta E^{A}(\text{halogenatedtoluene}) - \Delta E^{A}(\text{toluene}). \quad (6)$$

$\Delta\Delta E^{A}$ of *m*-halogenated toluenes are shown in Fig. 2b. The absolute values of $\Delta\Delta E^{A}$ of *m*-halogenated toluenes are less than 0.60 mHartree, which means that the ΔE^{A} of *m*-halogenated toluenes are similar to that of toluene. Thus, *meta*-halogenation does not affect the rotational barrier height much.

Figs. 3a and b show ΔE^{A} and $\Delta\Delta E^{A}$ of *o*-halogenated toluenes, respectively. Numerical data are shown in Table 3. Unlike the cases of toluene and *m*-halogenated toluenes, stabilization and destabilization of energy density do not appear only in *ortho*-carbons. As shown in Fig. 3b, the largest destabilization appears in the C_1 atom in *o*-CT, *o*-BT and *o*-IT. The destabilization of the *ortho*-carbons is smaller than that of

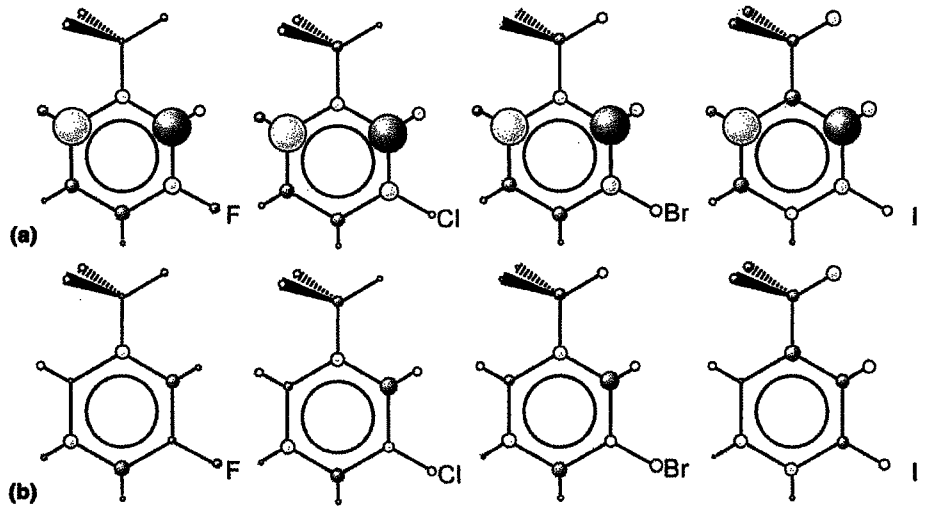

Fig. 2. Energy density changes (ΔE^{A}) by the methyl rotation of *m*-halogenated toluenes (a). Blue and red balls represent stabilized and destabilized atoms, respectively. Their volume is proportional to the degree of stabilization and destabilization. Differences of energy density changes ($\Delta\Delta E^{A}$) between *m*-halogenated toluenes and toluene are shown in (b).

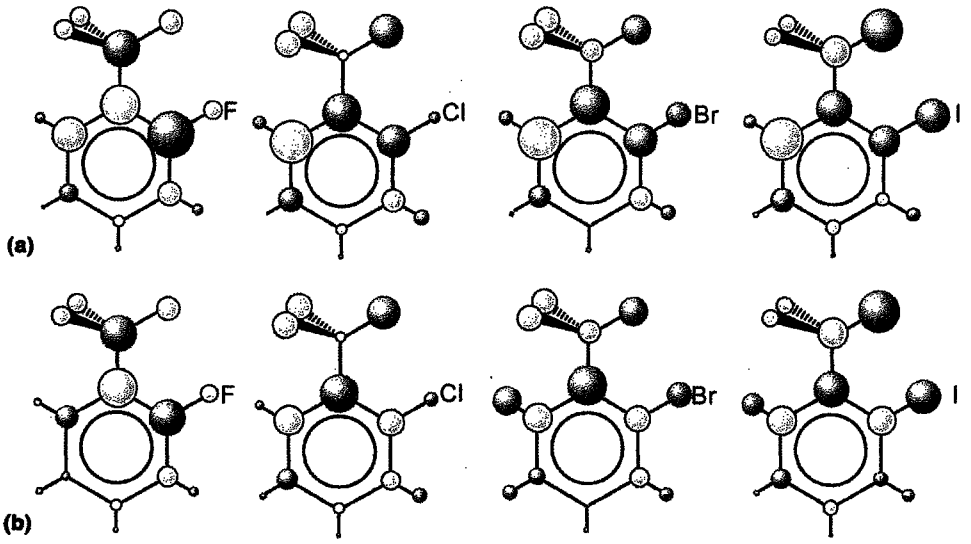

Fig. 3. Energy density changes (ΔE^A) by the methyl rotation of *o*-halogenated toluenes (a). Blue and red balls represent stabilized and destabilized atoms, respectively. Their volume is proportional to the degree of stabilization and destabilization. Differences of energy density changes ($\Delta\Delta E^A$) between *o*-halogenated toluenes and toluene are shown in (b).

toluene. Large destabilizations also appear in the halogens (X_8) and the in-plane hydrogen (H_{13}) of the methyl group. In contrast, ΔE^A of fluorine (F_8) and H_{13} are stabilized in *o*-FT. The stabilization of F_8 and H_{13} indicate that F_8 and H_{13} form a hydrogen bond.

Table 3
Changes of atomic energy densities (ΔE^A) by methyl rotation in *o*-halogenated toluenes in mHartree

	o-Halogenated toluenes							
	–F		–Cl		–Br		–I	
	ΔE^A	$(\Delta\Delta E^A)$	ΔE^A	$(\Delta\Delta E^A)$	ΔE^A	$(\Delta\Delta E^A)$	ΔE^A	$(\Delta\Delta E^A)$
C_1	−5.91	(−5.91)	5.51	(+5.51)	6.06	(+6.06)	4.53	(+4.53)
C_2	9.99	(+4.86)	3.33	(−1.80)	3.52	(−1.61)	2.87	(−2.26)
C_3	−1.30	(−0.81)	−1.14	(−0.65)	−1.18	(−0.69)	−0.21	(+0.28)
C_4	−0.13	(−0.13)	−0.11	(−0.11)	0.00	(−0.00)	−0.31	(−0.31)
C_5	0.55	(+0.06)	1.31	(+0.82)	0.92	(+0.43)	1.19	(+0.71)
C_6	−3.99	(+1.14)	−7.58	(−2.46)	−7.53	(−2.40)	−7.48	(−2.35)
C_7	4.78	(+4.78)	−0.09	(−0.09)	−1.09	(−1.09)	−2.77	(−2.77)
X_8	−0.60	(−0.48)	0.12	(+0.24)	1.37	(+1.50)	3.74	(+3.87)
H_9	0.10	(+0.07)	0.30	(+0.27)	0.26	(+0.23)	0.19	(+0.17)
H_{10}	0.01	(+0.01)	0.01	(+0.01)	0.01	(+0.01)	0.00	(+0.00)
H_{11}	0.00	(+0.03)	0.00	(+0.02)	0.01	(+0.03)	−0.01	(+0.01)
H_{12}	0.09	(−0.03)	0.19	(+0.06)	0.23	(+0.11)	0.19	(+0.06)
H_{13}	−1.26	(−1.26)	3.53	(+3.53)	2.34	(+2.34)	0.99	(+0.99)
H_{14}	−0.71	(−0.71)	−1.75	(−1.75)	−1.54	(−1.54)	−0.45	(−0.45)
H_{15}	−0.71	(−0.71)	−1.75	(−1.75)	−1.54	(−1.54)	−0.45	(−0.45)
Total	0.92	(+0.92)	1.87	(+1.87)	1.85	(+1.85)	2.04	(+2.04)

Differences between ΔE^A of toluene and *o*-halogenated toluenes ($\Delta\Delta E^A$) are shown in parentheses.

From the EDA results, it is concluded that the atomic energy density change of the *ortho*-carbons are significant for the internal methyl rotation of the toluene and *m*-halogenated toluenes. In previous studies, Sonoda and Iwata [11] and Weisshaar and co-workers [12] found a correlation between the rotational barriers and the nature of *ortho*-carbons; that is, the net charge differences and the bond order differences. In this sense, the EDA results support the previous theoretical analyses.

m-Halogenation of toluene does not affect the rotational barriers much. *o*-Halogenation of toluene leads to high rotational barriers. The EDA shows the steric repulsion between in-plane hydrogen of the methyl group and halogens by destabilization of atomic energy density. Furthermore, the formation of a hydrogen bond in *o*-FT is evidenced by the stabilization of the hydrogen of the methyl group and of the fluorine.

4. Conclusion

Recently, we have proposed the EDA method to partition the total energy of molecules into atomic energy densities. The present study is an application of the EDA method to internal methyl rotations in *o*- and *m*-halogenated toluenes. From the EDA results, it is shown that the changes of the energy density of *ortho*-carbons are significant for the methyl rotational barriers. In *o*-FT, the EDA reveals the formation of a hydrogen bond in the unstable *pseudo-cis* conformation. The hydrogen bond in the *o*-FT lowers the rotational barriers of *o*-FT. The EDA technique gives a plausible interpretation of chemical bonding and is a powerful tool for investigating chemical and physical phenomena.

Acknowledgements

Part of the calculations was performed at the Research Center for Computational Science (RCCS) of the Okazaki National Research Institutes and the Media Network Center (MNC) of Waseda University. Part of this study was supported by a Grant-in-Aid for Young Scientists (A) 'KAKENHI 14703005' from the Japanese Society for the Promotion of Science (JSPS) and by a Waseda University Grant for Special Research Projects.

References

[1] J.D. Kemp, K.S. Pitzer, J. Chem. Phys. 4 (1936) 749.
[2] S. Kamei, K. Okuyama, H. Abe, N. Mikami, M. Ito, J. Chem. Phys. 90 (1986) 93.
[3] D.B. Moss, C.S. Parmenter, G.E. Ewing, J. Chem. Phys. 86 (1987) 51.
[4] K. Okuyama, N. Mikami, M. Ito, J. Phys. Chem. 89 (1985) 5617.
[5] Z. Zhao, C.S. Parmenter, D.B. Moss, A.J. Bradley, E.W. Knight, K.G. Owens, J. Chem. Phys. 96 (1992) 6362.
[6] H. Mizuno, K. Okuyama, T. Ebata, M. Ito, J. Phys. Chem. 91 (1987) 5589.
[7] M. Fujii, M. Yamaguchi, K. Takazawa, M. Ito, Spectrochim. Acta 50A (1994) 1421.
[8] M. Fujii, K. Takazawa, M. Ito, J. Chin. Chem. Soc. 42 (1995) 335.
[9] H. Ikoma, K. Takazawa, Y. Emura, S. Ikeda, H. Abe, H. Hayashi, M. Fujii, J. Chem. Phys. 105 (1996) 10201.
[10] K. Suzuki, S. Ishiuchi, M. Fujii, Faraday Discuss. 115 (2000) 229.
[11] Y. Sonoda, S. Iwata, Chem. Phys. Lett. 243 (1995) 176.
[12] K. Lu, F. Weinhold, J. Weisshaar, J. Chem. Phys. 102 (1995) 6787.
[13] H. Nakai, M. Kawai, Chem. Phys. Lett. 307 (1999) 272.
[14] H. Nakai, M. Kawai, J. Chem. Phys. 113 (2000) 2168.
[15] H. Nakai, Y. Kawamura, Chem. Phys. Lett. 318 (2000) 198.
[16] Y. Kawamura, T. Nagasawa, H. Nakai, J. Chem. Phys. 114 (2001) 8357.
[17] H. Nakai, M. Kawai, Chem. Phys. 273 (2001) 191.
[18] H. Nakai, Chem. Phys. Lett. 363 (2002) 73.
[19] H. Nakai, K. Sodeyama, Chem. Phys. Lett. 365 (2002) 203.
[20] P.J. Stephens, J.F. Devlin, C.F. Chabalowski, M.J. Frisch, J. Phys. Chem. 98 (1998) 11623.
[21] P.J. Stevens, J.F. Devlin, C.F. Chabalowski, M.J. Frish, J. Chem. Phys. 98 (1998) 11623.
[22] J.C. Slater, Phys. Rev. 81 (1951) 385.
[23] A.D. Becke, Phys. Rev. A 38 (1988) 3098.
[24] S.H. Vosco, L. Wilk, M. Nusair, Can. J. Phys. 58 (1980) 1200.
[25] C. Lee, W. Yang, R.G. Parr, Phys. Rev. B 37 (1988) 785.
[26] T.H. Dunning Jr., J. Chem. Phys. 90 (1989) 1007.
[27] D.E. Woon, T.H. Dunning Jr., J. Chem. Phys. 98 (1993) 1358.
[28] A.K. Wilson, D.E. Woon, K.A. Peterson, T.H. Dunning Jr., J. Chem. Phys. 110 (1999) 7667.
[29] S. Huzinaga, J. Andzelm, M. Klobukowski, E. Radzio-andzelm, Y. Sakai, H. Tatewaki, Gaussian Basis Sets for Molecular Calculations, Elsevier, New York, 1984.

[30] M. Dupuis et al., 'HONDO 99.6', 1999, based on HONDO 95.3, M. Dupuis et al., Quantum Chemistry Program Exchange (QCPE), Indiana University, Bloomington, In 47405.
[31] A.D. Becke, J. Chem. Phys. 88 (1988) 2547.
[32] R.S. Mulliken, J. Chem. Phys. 23 (1955) 1833.
[33] H. Nakai, 'EDA2002', Waseda University, Tokyo, 2002, 169–8555.

Available online at www.sciencedirect.com
SCIENCE DIRECT®
Chemical Physics Letters 377 (2003) 69–73
CHEMICAL PHYSICS LETTERS
www.elsevier.com/locate/cplett

Reactions of protonated water clusters $H^+(H_2O)_n$ ($n = 1$–6) with dimethylsulfoxide in a guided ion beam apparatus

Yoko Kawai [a,*], Satoru Yamaguchi [a,b], Yoshiki Okada [a], Kazuo Takeuchi [a,b], Yusuke Yamauchi [c], Shiho Ozawa [c], Hiromi Nakai [c]

[a] *RIKEN (The Institute of Physical and Chemical Research) Hirosawa, Nanomaterial Processing Laboratory, Wako-shi, Saitama 351-0198, Japan*
[b] *Graduate School of Science and Engineering, Saitama University, 255, Shimoohkubo, Saitama-shi, Saitama 338-8570, Japan*
[c] *Department of Chemistry, School of Science and Engineering, Waseda University, Tokyo 169-8555, Japan*

Received 18 March 2003; in final form 29 May 2003
Published online: 22 July 2003

Abstract

Reaction cross sections for the reactions of protonated water clusters, $H^+(H_2O)_n$ ($n = 1$–6) with dimethylsulfoxide (DMSO) were measured at the collision energy of 0.1 eV. The cross section at $n = 2$, which was found to be twice as large as that at $n = 4$, showed a possibility of direct proton transfer process. The proton is likely to transfer directly from $H^+(H_2O)_2$ to DMSO without forming an intermediate complex because of the larger proton affinity of DMSO than that of water dimer.

1. Introduction

Dimethylsulfoxide (DMSO), which is primarily generated by the addition reaction of OH and dimethylsulfide (DMS), is one of the major precursors of H_2SO_4, and DMSO has been detected in the atmosphere in the aerosol phase, gas phase, and in rainwater [1,2]. The atmospheric chemistry involving DMSO has been investigated in relation to the biogeochemical cycle of sulfur and air pollution [3,4]. Chemical ionization mass spectrometry (CIMS) is one of the most powerful methods of detecting trace compounds in the atmosphere. For CIMS, NH_4^+ has been used to detect DMSO [2,3], while Thomas and Viggiano [5] have shown the possibility of using $H^+(H_2O)_n$ by studying the reactions of $H^+(H_2O)_n$ ($n = 1$–5) with DMSO in a selected ion flow tube (SIFT). They found that the sensitivity of CIMS was improved by using $H^+(H_2O)_n$ instead of NH_4^+.

Studies of the reactions of protonated water clusters and chemical compounds such as DMSO may also aid our understanding of atmospheric chemistry itself. In the lower atmosphere, protonated water clusters, $H^+(H_2O)_n$, are primary ions in positive ion chemistry, and water clusters react

* Corresponding author. Fax: +81-48-467-9308.
E-mail address: ykawai@postman.riken.go.jp (Y. Kawai).

0009-2614/$ - see front matter © 2003 Elsevier B.V. All rights reserved.
doi:10.1016/S0009-2614(03)01095-9

with various trace compounds that have higher proton affinity than water [6]. Despite the low concentrations of these compounds, they are known to play significant roles in atmospheric chemistry; for instance, trace compounds contribute to ozone depletion and acid rain and may accelerate nucleation in the atmosphere [7]. DMSO may be one of the compounds that contribute to the acceleration of the nucleation and generation of acid rain. Studies of elementary reaction processes are important for understanding atmospheric chemistry. The guided ion beam (GIB) method enables accurate measurement of reaction cross sections of a particular elementary process at various collision energies under the condition of a single collision [8,9].

We report here the collision-induced reactions of protonated water cluster ions $H^+(H_2O)_n$ ($n = 1$–6) with DMSO. The cluster size effects on the reaction cross sections is discussed in comparison with those of $H^+(H_2O)_n$ with acetone. DMSO, $(CH_3)_2SO$, and acetone, $(CH_3)_2CO$, have an equal number of atoms and have similar geometrical structures.

2. Experimental setup

A GIB apparatus [10,11] was used. It is composed of a corona discharge cluster-ion source, two octopole ion beam guides, a quadrupole mass filter, a Bessel box energy analyzer, a collision cell, and a quadrupole mass spectrometer. Water vapor was supplied from a glass chamber in a bath kept at 15 °C. Nitrogen was used as a carrier gas with a rate of 12–12.5 sccm. The kinetic energy spread of the cluster ion beam was set in the range of 0.01–0.04 eV at $n = 2$–6, and 0.1–0.14 eV at $n = 1$. The pressure of the target gas was measured by a spinning rotor gauge (MKS SRG-2) with accuracy better than 5%.

3. Data analysis

We observed reaction product ions having DMSO molecules at the collision energy of 0.1 eV. The total reaction cross section is given by

$$\sigma_r = \frac{k_B T}{Pl} \ln \frac{I(0)}{I(l)}, \tag{1}$$

where $I(0)$ and $I(l)$ are the intensities of the parent cluster ion at the entrance to and exit from the collision cell, respectively, l is the effective path length of the collision cell, T and P are the temperature and pressure of the target gas, and k_B is the Boltzmann constant. We used the intensity of the mass spectra taken in the absence of DMSO to obtain $I(0)$. The mass spectra taken without DMSO were also used to estimate the internal energy of the parent clusters, which were 1.2, 1.1, 1.1, 0.89, and 0.96 eV at $n = 2$, 3, 4, 5, and 6, respectively, according to the RRK theory [12].

The pressure dependences of the reaction cross sections were studied in the range of 0.7–4×10^{-4} Pa. The total ion intensity was confirmed to be independent of the pressure. It was also confirmed that the total reaction cross sections were independent of the pressure within the fluctuation of ±10–20% at $n = 2$–6. At $n = 1$, the fluctuation exceeded ±50% because the intensity of the parent cluster ion was less abundant and the kinetic energy spread was wider. We measured the total reaction cross sections 7–13 times at the collision energy of 0.1 eV and averaged.

4. Results and discussion

The total reaction cross sections of $H^+(H_2O)_n$ with DMSO, σ_{DMSO}, are plotted as a function of water cluster size in Fig. 1 together with that of $H^+(H_2O)_n$ with acetone, σ_{ace} [11]. The reaction cross sections σ_{DMSO} and σ_{ace} showed a similar trend at $n = 4$–6. The σ_{DMSO} value at $n = 6$ seemed to be slightly smaller than that expected from the increase from $n = 4$ to 5. This is probably because the hexamer has a closed shell structure with $(H_5O_2)^+$ core surrounded by four H_2O molecules. In contrast, they had opposite trends from $n = 2$ to 4. The σ_{DMSO} value at $n = 2$ was found to be approximately twice that at $n = 4$. Such an enhancement of the cross section at $n = 2$ was not observed for acetone, nor was it observed for σ_{DMSO} at $n = 1$. The geometrical cross sections taken as πr^2 are also plotted in Fig. 1. Here, r was

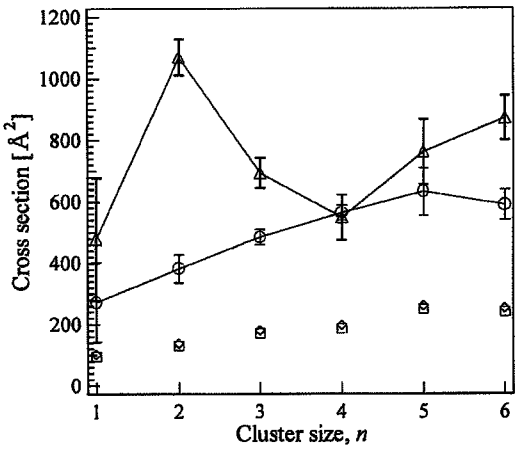

Fig. 1. Total cross sections of the reaction of $H^+(H_2O)_n$ ($n = 1$–6) with X at collision energy of 0.1 eV in the center-of-mass frame. Triangles and circles represent X = DMSO and acetone, respectively. Error bars show probable errors. Open lozenges and squares represent geometrical cross sections for DMSO and acetone, respectively.

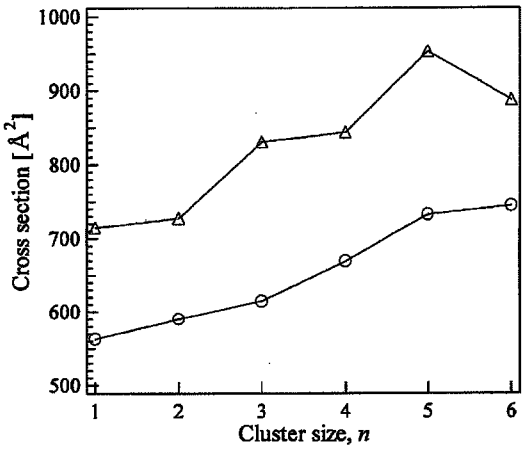

Fig. 2. Classical cross sections in the collision of $H^+(H_2O)_n$ ($n = 1$–6) with X at collision energy of 0.1 eV in the center-of-mass frame. Triangles and circles represent X = DMSO and acetone, respectively.

estimated as the distance between the center of mass of the reactant water cluster ion and the most distant H atom under the most probable cluster structure [13] plus the distance between the center of mass of DMSO or acetone molecule and the hydrogen atom plus the van der Waals radii of hydrogen atoms. It is clear that the enhancement of the σ_{DMSO} at $n = 2$ is not due to the geometric size.

We calculated the classical collision cross sections, σ_{col}, shown in Fig. 2 from the effective potential between the cluster ion and the molecule. The detail will be reported elsewhere [14]. The effective potential, V_{eff}, is given as a sum of the potential energy at an ion–molecule separation R and the centrifugal potential energy [15–17]

$$V_{eff}(R) = V(R) + \frac{E_{coll}b^2}{R^2}, \quad (2)$$

where E_{coll} is the collision energy and b the impact parameter. The calculations to obtain the collision cross sections were performed by using the program system GAUSSIAN 98 [18]. Geometry optimizations and frequency calculations of neutral and protonated states of DMSO and water clusters were carried out by the DFT calculations with the B3LYP hybrid functional [19,20], where the geometrical structures of the water cluster ions were discussed elsewhere [13]. Correlation-consistent polarization plus valence double zeta (cc-pVDZ) basis sets of Dunning and co-workers [21] were adopted for H, C, O, and S atoms. The optimized structures of the cluster and molecule were fixed, and the distance between their centers of mass was varied with optimized orientation to obtain $V(R)$ by an ab initio calculation. The calculation gives the upper limit of the collision cross section. The maximum of the effective potential at R_{max}, defined as

$$\left[\frac{dV_{eff}(R)}{dR}\right]_{R_{max}} = \left[\frac{dV(R)}{dR}\right]_{R_{max}} - \frac{2E_{coll}b^2}{R_{max}^3} = 0, \quad (3)$$

is required to obtain the collision cross section. The first term of the right-hand side in Eq. (3) was also obtained by an ab initio calculation. The following procedure for calculating the collision cross section was described in [16]. It was found that σ_{coll} increased with the water cluster size n for both DMSO and acetone. The enhancement at $n = 2$ for X = DMSO was not seen in the collision cross section. Furthermore, the observed σ_{DMSO} at $n = 2$, ~1070 Å^2, was found to be much larger than that of σ_{coll}, ~730 Å^2.

We calculated the values of proton affinity (PA) of the clusters and reactants with B3LYP/cc-pVTZ (correlation-consistent polarization plus valence triple zeta). The proton affinities, defined as $PA = E(H^+Y) - E(Y)$ and corrected with zero-point vibrational energies, are shown in Table 1, where E is the total energy and $Y = (H_2O)_n$, DMSO, and acetone. It is noted that the PA of DMSO is higher than that of water dimer, while the PA of acetone is lower than that of water dimer. This may be the clue to understand why σ_{DMSO} was enhanced at $n = 2$ whereas σ_{ace} was not.

The averaged numbers of the evaporated water molecules m from the reaction product, $H^+(H_2O)_{n-m}X$ ($n \geqslant m$), were found to be 2.7 ± 0.1 and 2.0 ± 0.1 with X = DMSO and acetone, respectively, where m was almost independent of n. More water molecules were lost in the DMSO case probably because of the larger bond energy of DMSO to $H^+(H_2O)_{n-m}$. The internal energy of the intermediate, which can be given as a sum of the internal energy of $H^+(H_2O)_n$, bond energy of X to $H^+(H_2O)_n$, and collision energy, is larger with larger bond energy. Thus, more molecules can evaporate from the intermediate. No water molecule remains in the reaction products at $n = 1$ and 2; this seems to be reasonable from the energy balance.

The products in the form of H^+X, observed at $n = 1$ and 2, can be generated via both of the following processes:

$$\begin{aligned} H^+(H_2O)_n + X &\rightarrow [H^+(H_2O)_nX]^* \\ &\rightarrow [H^+(H_2O)_{n-1}X]^* + H_2O \\ &\rightarrow \cdots \rightarrow H^+X + nH_2O \end{aligned} \quad \text{(i)}$$

Table 1
Proton affinities of water clusters, DMSO, and acetone

	Size (n)	Proton affinity (eV)	
		Calc.	Exp. [22]
Water	1	7.21	7.16
	2	8.63	–
	3	9.21	–
	4	9.53	–
	5	9.60	–
	6	9.85	–
DMSO		9.34	9.17
Acetone		8.51	8.42

and

$$H^+(H_2O)_n + X \rightarrow H^+X + (H_2O)_n \quad \text{(ii)}$$

In path (i), the cluster ion $H^+(H_2O)_n$ and reactant X form an intermediate $[H^+(H_2O)_nX]^*$ as they collide each other. Water molecules evaporate from the intermediate one by one, and finally the protonated state of the product H^+X is formed. A water molecule preferably evaporates from the intermediate because the PA of water is lower than that of X; that is, the bond energy of water to the rest part of intermediate is smaller. In path (i), proton transfer occurs within the intermediate cluster. Therefore, the property of water dimer is inessential in the proton transfer process. This appears inconsistent with the observation that the reaction cross section was enhanced only for X = DMSO at $n = 2$. Moreover, the cross section cannot exceed the classical collision cross section when the proton transfer occurs only within the intermediate in the reaction path (i).

In the direct proton transfer reaction (ii), however, the reactant X may extract the proton from the cluster ion when the PA of X is higher than that of the water cluster. Reaction (ii) may occur in $n = 2$ for DMSO because the parent cluster is hot and the PA of DMSO is higher than that of water dimer. In the case of acetone, reaction (i) is probably dominant because the PA of acetone is lower than that of water dimer. The fact that the enhancement of σ_r was not observed at $n = 1$ suggests that the structure of $H^+(H_2O)_2$ is also important; X is accessible to an H atom in $H^+(H_2O)_2$ from almost all directions, while X is not accessible to H from the side of O atom in the case of $H^+(H_2O)$. The reaction cross section σ_{DMSO} at $n = 2$ may be enhanced because $H^+(CH_3)_2SO$ is generated by the direct proton transfer process (ii) in addition to process (i).

Acknowledgements

Y.K. is grateful to the Special Postdoctoral Researchers Program of RIKEN.

References

[1] H. Berresheim, J.W. Huey, R.P. Thorn, F.L. Eisele, D.J. Tanner, A. Jefferson, J. Geophys. Res. 103 (D1) (1998) 1629.
[2] J. Sciare, N. Mihalopoulos, Atmos. Environ. 34 (2000) 151.
[3] V. Librando, G. Tringali, J. Hjorth, N. Jensen, Ann. Chim. 91 (2001) 415.
[4] D. Davis, G. Chen, P. Kasibhatla, A. Jefferson, D. Tanner, F. Eisele, D. Lenshow, W. Neff, H. Berresheim, J. Geophys. Res. 103 (D1) (1998) 1657.
[5] J.M. Thomas, A.A. Viggiano, J. Phys. Chem. A 103 (1999) 2720.
[6] A.A. Viggiano, Mass Spectrom. Rev. 12 (1993) 115.
[7] R.J. Weber, P.H. McMurry, R.L. Mauldin III, D.J. Tanner, F.L. Eisele, A.D. Clarke, V.N. Kapustin, Geophys. Res. Lett. 26 (1999) 307.
[8] K. Honma, L.S. Sunderlin, P.B. Armentrout, Int. J. Mass Spectrom. Ion Process. 117 (1992) 237.
[9] K. Honma, L.S. Sunderlin, P.B. Armentrout, J. Chem. Phys. 99 (1993) 1623.
[10] T. Orii, Y. Okada, K. Takeuchi, M. Ichihashi, T. Kondow, J. Chem. Phys. 113 (2000) 8026.
[11] Y. Kawai, S. Yamaguchi, Y. Okada, K. Takeuchi, Int. J. Mass Spectrom. 220 (2002) 375.
[12] S. Yamaguchi, S. Kudoh, Y. Okada, T. Orii, K. Takeuchi, Chem. Phys. Lett. 359 (2002) 480.
[13] S. Yamaguchi, S. Kudoh, Y. Okada, T. Orii, K. Takeuchi, T. Ichikawa, H. Nakai, J. Phys. Chem. A., submitted.
[14] H. Nakai, T. Ichikawa, Y. Okada, S. Yamaguchi, Y. Kawai, unpublished data.
[15] T. Su, M. Bowers, J. Chem. Phys. 58 (1973) 3027.
[16] T. Su, M.T. Bowers, in: M.T. Bowers (Ed.), Gas Phase Ion Chemistry, vol. 1, Academic, New York, 1979 (Chapter 3).
[17] T. Su, J. Chem. Phys. 100 (1994) 4703.
[18] M.J. Frisch et al., GAUSSIAN 98, Revision A.7, Gaussian, Inc., Pittsburgh, PA, 1998.
[19] P.J. Stephens, F.J. Devlin, M.J. Frisch, C.F. Chabalowski, J. Phys. Chem. 98 (1994) 11623.
[20] A.D. Becke, Phys. Rev. A 38 (1988) 3098.
[21] R.A. Kendall, T.H. Dunning Jr., R.J. Harrison, J. Chem. Phys. 96 (1992) 6796.
[22] D.R. Lide (Ed.), CRC Handbook of Chemistry and Physics, 81st ed., 2000–2001.

Ab initio molecular dynamics study on the excitation dynamics of psoralen compounds

H. Nakai,[a] Y. Yamauchi, A. Nakata, T. Baba, and H. Takahashi
Department of Chemistry, School of Science and Engineering, Waseda University, Tokyo 169-8555, Japan

(Received 1 August 2002; accepted 29 May 2003)

Ab initio molecular dynamics (AIMD) simulations are performed for studying the $S_0 \rightarrow T_1$ excitation dynamics of psoralen compounds; namely, nonsubstituted psoralen, 5-methoxypsoralen (5-MOP), and 8-methoxypsoralen (8-MOP). The density functional theory calculations at the B3LYP/D95V level are used for evaluating the atomic forces in every AIMD step. The specific behavior of 8-MOP in the T_1 state, which has been reported by the experimental study, is found to be due to a unique open-ring structure, which leads to a different spin distribution in comparison with the cases of psoralen and 5-MOP and further to a crossing between the S_0 and T_1 states. © *2003 American Institute of Physics.* [DOI: 10.1063/1.1592792]

I. INTRODUCTION

Psoralens exhibit strong photobiological and phototherapeutic activities.[1–4] The structural formula of psoralens is described as follows:

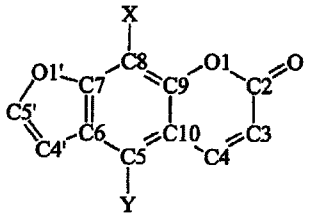

Psoralen; X=H, Y=H
5-MOP; X=H, Y=OCH_3
8-MOP; X=OCH_3, Y=H

Psoralens have three rings; namely, furan-, benzene-, and pyron-rings. In addition to the nonsubstituted psoralen, 5-methoxypsoralen (5-MOP) and 8-methoxypsoralen (8-MOP) are used for photochemotherapy. Among them, 8-MOP is the most used drug.

In order to clarify the excitation dynamics of psoralens experimentally, Uesugi and Takahashi[5] have observed the transient absorption spectra of psoralen, 5-MOP, and 8-MOP. The remarkable difference is seen in the intensity of the peak assigned to the lowest triplet (T_1) transient species, which is much related with the existence probability. It has been shown that three psoralen compounds have similar chemical bondings both in the anion radical (AR) and T_1 transient species as well as in the singlet ground (S_0) state, except for the T_1 transient species of 8-MOP. Then, why does only the T_1 transient species of 8-MOP show specific behavior?

One of the most powerful methodologies to study the excitation dynamics theoretically could be *ab initio* molecular dynamics (AIMD) simulation. The AIMD is the combination of standard MD, that is, numerical integration of the classical equations of motion (EOM) of a system, and accurate electronic structure calculations to obtain the internuclear forces. Due to the explicit treatment of the electronic structure and the resulting forces acting on the atoms, formation and breaking of chemical bonds can be treated in contrast to the conventional MD calculations. For example, we have studied the collision reaction between ammonia cluster ion and ammonia monomer and have dealt successfully with an incorporative collision.[6]

In the present study, the AIMD simulations of psoralen, 5-MOP, and 8-MOP in the T_1 state have been carried out. A remarkable difference has been found in the AIMD simulation of 8-MOP. By comparing with the results of psoralen and 5-MOP, the geometrical relaxation of 8-MOP in the T_1 state leads to a crossing between the S_0 and T_1 states. The reactivity of 8-MOP in the T_1 state is also shown to be different from other species.

II. COMPUTATIONAL METHOD

We have coded a MD program based on the Verlet algorithm.[7] In the Verlet method, the EOM

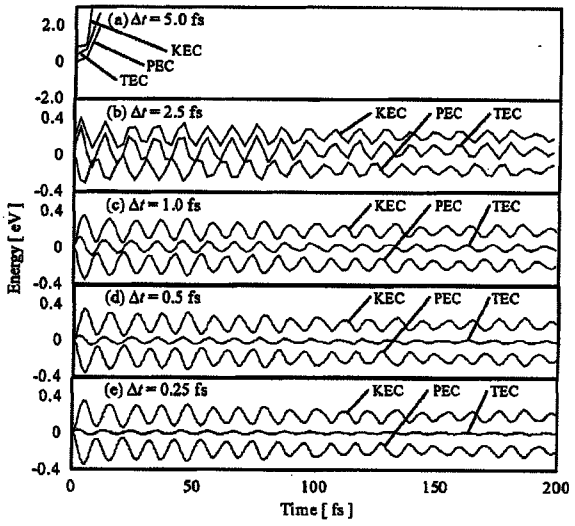

FIG. 1. KEC, PEC, and TEC for the AIMD simulations of psoralen in the T_1 state with the use of Δt = (a) 5.0, (b) 2.5, (c) 1.0, (d) 0.5, and (e) 0.25 fs.

[a]Author to whom all correspondence should be addressed. Electronic mail: nakai@waseda.jp

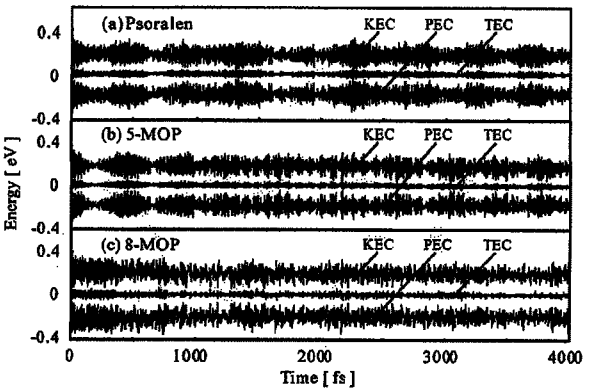

FIG. 2. KEC, PEC, and TEC for the AIMD simulations of (a) psoralen, (b) 5-MOP, and (c) 8-MOP in the T_1 state with the use of $\Delta t = 1.0$ fs.

$$\frac{d^2\mathbf{r}_i}{dt^2} = \frac{\mathbf{F}_i}{m_i} \tag{1}$$

is solved by numerical integration. As a result, the time evolutions of coordinates and velocities of atoms are expressed by

$$\mathbf{r}_i(t+\Delta t) = 2\mathbf{r}_i(t) - \mathbf{r}_i(t-\Delta t) + (\Delta t)^2 \frac{\mathbf{F}_i(t)}{m_i}, \tag{2}$$

$$\mathbf{v}_i(t) = \frac{1}{2\Delta t}\{\mathbf{r}_i(t+\Delta t) - \mathbf{r}_i(t-\Delta t)\}. \tag{3}$$

Here, it is noted that the timings to evaluate the velocities and the coordinates are different by Δt between them.

To determine atomic forces by electronic structure calculations, the present MD program is connected with the GAUSSIAN 98 program.[8] In the present study, we have performed the force calculations at the B3LYP level.[9–13] The basis sets used in the density functional theory (DFT) calculations are the valence double zeta sets of Dunning (D95V).[14]

Two kinds of AIMD simulations have been performed for psoralen, 5-MOP, and 8-MOP in the T_1 state. One is that the most stable geometry in the S_0 state and zero velocities are used as an initial guess. The other is that the vibrating molecules in the S_0 state are used as an initial guess. In order to get the initial guess, the AIMD simulation in the S_0 state is carried out after adding the energy corresponding to the amount of the zero point vibrational energies. We adopted the time of 1000 fs to achieve the equilibrium condition in the S_0 vibration.

III. RESULTS AND DISCUSSION

First of all, we examine the reliability of the present AIMD simulation. Generally speaking, one should use short time step (Δt) to avoid numerical error in the MD simulation. However, the AIMD simulation involves the time-consuming force calculation in every iteration. The central processing unit time for the force calculations of psoralen and 8-MOP at the B3LYP/D95V level are about 20 and 30 min on Pentium 4/1.7 GHz, respectively. Thus, 16- and 25-day computations are needed for the 1.0 ps simulation even in the case of $\Delta t = 1.0$ fs. Thus, it is necessary to use as long a Δt as possible.

We have checked the performance of various time steps; that is, $\Delta t =$ (a) 5.0, (b) 2.5, (c) 1.0, (d) 0.50, and (e) 0.25 fs. Figure 1 shows the kinetic energy curve (KEC), the potential energy curve (PEC), and the total energy curve (TEC) for the AIMD simulations of psoralen in the T_1 state. The initial geometry is the optimized one in the S_0 state. The initial velocities of the atoms are all zero.

With the use of $\Delta t = 5.0$ fs, both KEC and PEC increase rapidly, resulting in the increase of the TEC. It is because the molecule decomposes by the initial force ($\Delta t = 0$ fs). Although the oscillations in the KEC and PEC have physical meanings, that in the TEC does not. As Δt is gradually changed from 2.5 to 0.25, the amplitude of the oscillation in the TEC becomes smaller. One of the reasons for the oscillation is thought to be due to the numerical error in the numerical integration of the EOM. Another reason is based

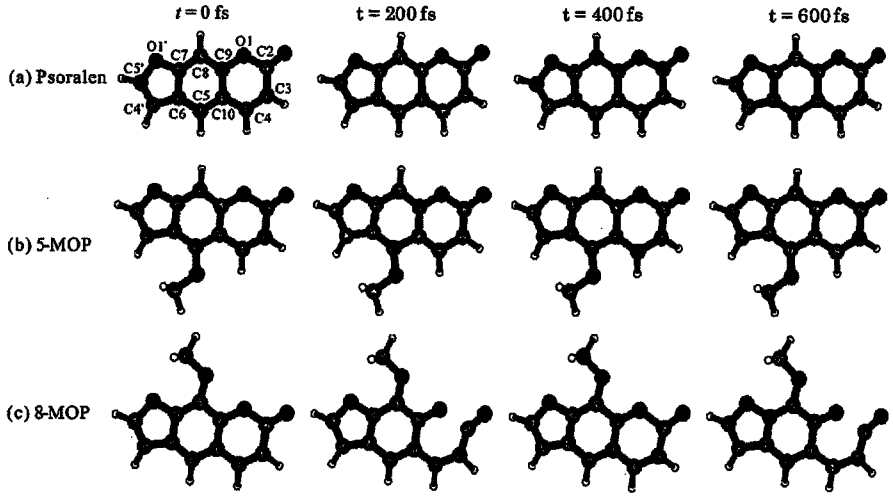

FIG. 3. Snapshots of the geometrical changes for (a) psoralen, (b) 5-MOP, and (c) 8-MOP at $t = 0$, 200, 400, and 600 fs.

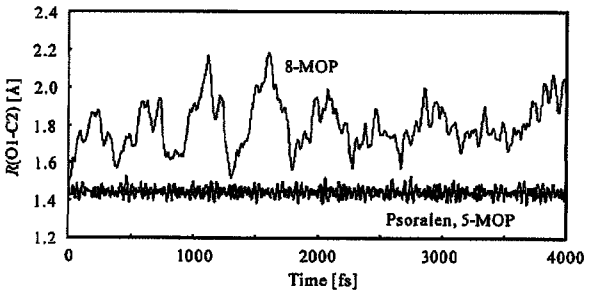

FIG. 4. Time evolution of O1–C2 distance in psoralen, 5-MOP, and 8-MOP in the T_1 state.

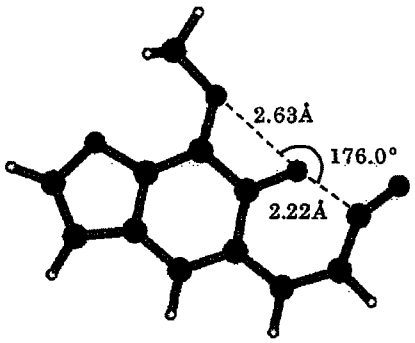

FIG. 6. Geometrical parameters for the open-ring structure of 8-MOP.

on the Verlet method, which involves the time gap to evaluate the coordinates and velocities.

However, the average seems to be kept in the range of $\Delta t = 0.25-1.0$ fs. Moreover, the periods of the oscillations in the KEC and PEC are close to each other for $\Delta t = 0.25-1.0$ fs. By using $\Delta t = 2.5$ fs, the periods slightly becomes shorter than those for $\Delta t = 0.25-1.0$ fs. Therefore, the results using Δt shorter than 1.0 fs are thought to be reliable. The reliable range of the time step, namely, $\Delta t \leq 1.0$ fs, in the present AIMD simulation may be longer than that in the conventional MD one, e.g., $\Delta t \leq 0.1$ fs. It comes from a reason that the cutoff for the long-range interaction is not carried out in the AIMD simulation, whereas it has been done in the conventional MD one.

Figure 2 shows the KEC, PEC, and TEC for the AIMD simulations of (a) psoralen, (b) 5-MOP, and (c) 8-MOP in the T_1 state. The initial condition is the same as Fig. 1. The time step of $\Delta t = 1.0$ fs is used. Although there is the oscillation in the TEC, the average of the total energy seems to be conserved in the long time simulation. For more detail on the oscillation of the total energy in Verlet integrators, Mazur[15] has reported general and interesting results.

To clarify the specific behavior of 8-MOP in the T_1 state in comparison with those of psoralen and 5-MOP, we analyze the results of the AIMD simulations in Fig. 2. We first focus on the geometrical relaxation in the T_1 excited state. Figure 3 shows snapshots of the geometrical changes for (a) psoralen, (b) 5-MOP, and (c) 8-MOP at $t = 0$, 200, 400 and 600 fs. Although the vibrations are seen in psoralen and 5-MOP, there are not great changes from the ground-state geometry, which corresponds to the geometry at $t = 0$ fs. On the other hand, a drastic change is seen in 8-MOP. The remarkable difference is in the pyron-ring. In particular, the geometries of 8-MOP at $t = 200$ and 600 fs correspond to open-ring structures, in which the O1–C2 bond is cleaved.

Figure 4 shows the time changes of the O1–C2 distance in psoralen, 5-MOP and 8-MOP in the T_1 excited state. The O1–C2 distance in psoralen and 5-MOP vibrates around the S_0 geometry ($t = 0$ fs). On the other hand, the O1–C2 distance in 8-MOP is elongated from 1.4 to 2.2 Å, following a large molecular vibration. While $t = 0-3200$ fs, there are seven large molecular vibrations. After 3200 fs, the large molecular vibration disappears and the O1–C2 distance is gradually elongated, following small vibrations. From these results, the specificity of 8-MOP in the T_1 state observed by the transient spectroscopy[5] is thought to be due to the open-ring structure.

Figure 5 shows the energy diagram of (a) psoralen, (b) 5-MOP, and (c) 8-MOP in the S_0 and T_1 states. The geometry optimizations were carried out at the B3LYP/cc-pVDZ[16] level. The energy levels at the left-hand side in Figs. 5(a)–5(c) correspond to the S_0 and T_1 energies at the optimized geometry in the S_0 state. For psoralen and 5-MOP, both closed-ring and open-ring structures were obtained as stable systems in the T_1 state, which are represented by T_1- close and T_1- open, respectively. The closed-ring structures are more stable than the open-ring ones for both molecules. Furthermore, the transition state between them was obtained. On the other hand, only the open-ring structure was obtained for 8-MOP. Furthermore we calculated the geometry of psoralens in the S_0 and T_1 states by using several computational levels such as Hartree–Fock, BLYP and B3LYP with D95V, cc-pVDZ, and cc-pVTZ.[9–14,16] These results also show that only the open-ring structure was obtained for 8-MOP in the T_1 state. The present AIMD results calculating at the B3LYP/D95V level are consistent with this fact. The disappearance of the closed-ring structure in 8-MOP is thought to be a larger stabilization of the open-ring structure. Actually, the stabilization energy at the open-ring structure with respect to the S_0 optimized geometry in 8-MOP amounts to 0.48 eV, in

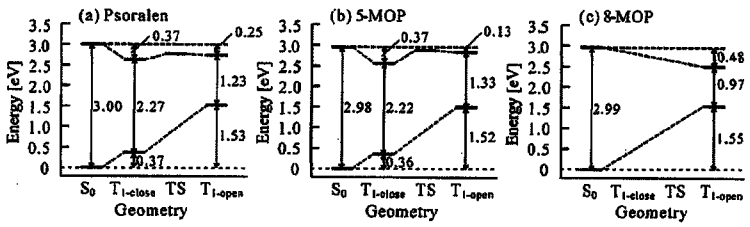

FIG. 5. Energy diagrams in the S_0 ground state and T_1 excited state for (a) psoralen, (b) 5-MOP, and (c) 8-MOP, respectively.

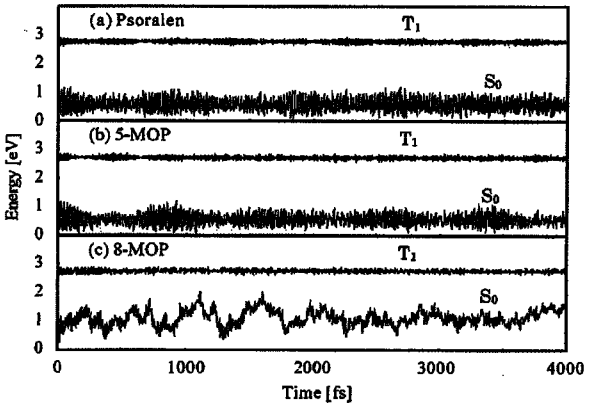

FIG. 7. PECs in the *imaginary* S_0 state and the *real* T_1 state for (a) psoralen, (b) 5-MOP, and (c) 8-MOP. The potential energies in the S_0 state are evaluated by using the geometries in the T_1 state.

comparison with 0.25 and 0.13 eV in psoralen and 5-MOP, respectively.

Figure 6 shows the geometry of the open-ring structure in 8-MOP. The angle O*–O1–C2 is almost linear, where O* means the oxygen atom in the methoxy group. The distances O*–O1 and O1–C2 are 2.63 and 2.22 Å, respectively. It suggests that there exists a three-center bond among the O*–O1–C2 atoms in the excited state. However, we could not confirm its evidence from the analysis of the electron density and Kohn–Sham orbitals.

The DFT calculations for the S_0 state at the B3LYP/D95V level are performed using the geometrical change in the AIMD simulation of the T_1 state. Figure 7 shows the PECs in the S_0 state for (a) psoralen, (b) 5-MOP, and (c) 8-MOP in comparison with those in the T_1 state. The molecule does not move on the S_0-state potential energy surface, but on the T_1-state surface. Therefore, Fig. 7 indicates how the *imaginary* S_0 level changes, when the molecule moves on the T_1-state potential energy surface. Note that this type of analysis is difficult or impossible for the conventional MD simulation.

Since the geometrical relaxations of psoralen and 5-MOP in the T_1 state are small, the PECs do not change much. It is interesting that the PEC of 8-MOP in the T_1 state, which gives the large geometrical relaxation, has a similar behavior. The amplitude in energy is less than 0.3 eV in the three curves. On the other hand, the maximum change of the S_0 energy of 2.04 eV ($t=1112$ fs) for 8-MOP is about twice as large as those of 1.17 eV ($t=10$ fs) and 1.15 eV ($t=52$ fs) for psoralen and 5-MOP, respectively. As a result, the energy gap between the S_0 and T_1 states in 8-MOP becomes much smaller than those in psoralen and 5-MOP. However, the crossing between them does not appear in this simulation.

Figure 8 shows the comparison between the time evolution of O1–C2 distance and the S_0-state PEC in 8-MOP. These data are taken from Figs. 4 and 7, respectively. The two curves are close to each other. For example, the period of large molecular vibration for the O1–C2 bond is almost equal to that of the energetic change in the S_0 state. Therefore, the geometrical relaxation in the T_1 state affects the potential energy in the S_0 state rather than that in the T_1 state.

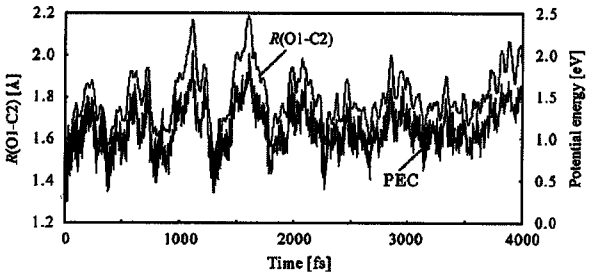

FIG. 8. Comparison between the time evolution of O1–C2 distance and the S_0-state PEC in 8-MOP.

Furthermore, we examine the changes of the electronic structure in the T_1-state relaxation. Figure 9 shows snapshots of the time changes of the spin densities in (a) psoralen, (b) 5-MOP, and (c) 8-MOP in the T_1 state at $t=0$, 200, 400, and 600 fs, respectively. The spin densities of psoralen and 5-MOP do not change much. On the other hand, the spin density at C3 moves to O1 in 8-MOP at the early stage of the O1–C2 elongation. The difference leads to the different photoreactivity of 8-MOP from those of psoralen and 5-MOP.

It has been reported that the psoralen compounds yield monoadduct or diadduct to thymine residues of DNA at C3=C4 and/or C4′=C5′ double bonds. The addition reactions correspond to Woodward–Hoffman forbidden reactions in the thermal condition. It is known that the monoadduct has a therapeutic activity. The formation of the diadduct, leading to the cross-linking of the DNA chain, is responsible for the mutagenic and carcinogenic effects of psoralens.[1–3] Figures 7(a) and 7(b) indicate that the C3 and C4 sites of psoralen and 5-MOP are active in the T_1 state. Figure 7(c) means that the C3 site of 8-MOP is not active in the T_1 state. Therefore, it is expected that 8-MOP does not lead to undesirable cross-linking DNA. We have separately examined the photoaddition reactions of psoralen, 5-MOP, and 8-MOP to the thymine residue by the DFT calculations.[17] The DFT results have shown that all three compounds can lead to the therapeutic monoadducts. Although the monoadducts of psoralen and 5-MOP have closed-ring structures as stable systems in the T_1 state, that of 8-MOP does not. The results have also shown that the monoadduct of 8-MOP leads to a stable open-ring structure.

Finally, we show the results of the AIMD simulations using the vibrating molecules as an initial condition. Figure 10 shows the time development of the potential energy of the T_1 excited state for (a) psoralen, (b) 5-MOP, and (c) 8-MOP. The PECs in the S_0 state using the same geometry as the T_1 state are also given. The amplitudes of the three PECs in the T_1 state become slightly larger than those in Fig. 7, where the molecules do not vibrate at the beginning. The amplitudes in the T_1 state are still smaller than those in the S_0 state. A great difference between Figs. 7 and 10 is that there exists a crossing between the T_1 and S_0 PECs in Fig. 10(c); that is, at $t=605$ fs. The geometry of 8-MOP at $t=605$ fs corresponds to the open-ring structure. It indicates that there

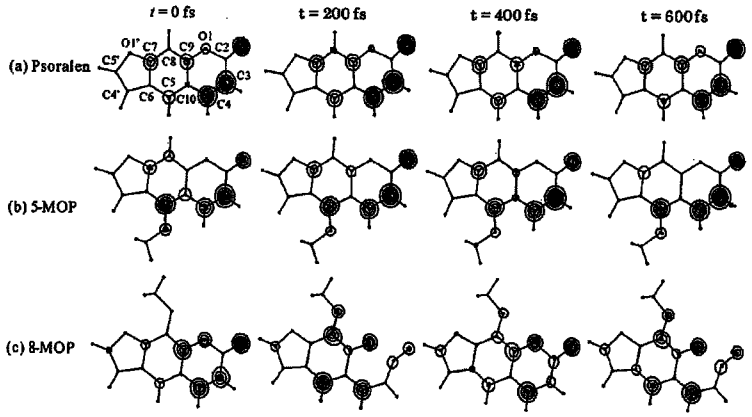

FIG. 9. Snapshots of the time changes of spin densities in (a) psoralen, (b) 5-MOP, and (c) 8-MOP at $t=0$, 200, 400, and 600 fs.

is a channel for the transition from the T_1 state to the S_0 state without radiation. This intersystem crossing is supposed to be related to the short lifetime of the T_1 transient species of 8-MOP.[5]

The effect of the zero-point vibration is not only to lead to the large amplitude but also to create a new mode toward the out-of-plane. In case of Fig. 7, the dihedral angles (ϕ) between O1–C2–C3 and C2–C3–O′ are conserved to be zero because the initial geometries of the molecules are in-plane and the initial velocities are zero. Here, O′ means the oxygen atom in carbonyl group. However, in the AIMD simulation of Fig. 10, the dihedral angles are changing. Figure 11 shows the time evolution of the dihedral angle in (a) psoralen, (b) 5-MOP, and (c) 8-MOP. The maximum and average dihedral angles in the absolute values are 59.0° and 23.7° in 8-MOP, respectively. They are almost twice larger than psoralen and 5-MOP; namely, (26.1°, 9.1°) in psoralen and (39.5°, 12.3°) in 5-MOP, respectively. As a result, the large out-of-plane vibration in the open-ring structure brings about the intersystem crossing between the T_1 excited state and the S_0 ground state.

IV. CONCLUSION

In the present study, AIMD simulations are carried out for treating the excitation dynamics of psoralen compounds; namely, nonsubstituted psoralen, 5-MOP, and 8-MOP. The DFT calculations with the B3LYP hybrid functional and the D95V basis sets are adopted to evaluate the atomic forces in every AIMD step. At first, we examine the reliability of the AIMD simulations with the use of several time steps Δt. It is found that the comparatively long time step of $\Delta t=1.0$ fs gives reasonable results. The great differences in the changes of the kinetic and potential energies among the three molecules do not appear in the T_1 state. However, the geometrical change of 8-MOP is quite difference from psoralen and 5-MOP. The closed pyron-ring in the S_0 state becomes open in the T_1 state in 8-MOP. It is clarified that the open-ring structure leads to the great instability of the *imaginary* S_0 level, resulting in the intersystem crossing between the T_1 excited state and the S_0 ground state. The specific open-ring structure in 8-MOP brings about the different spin distribution from others. As a result, the reactivity of 8-MOP in the

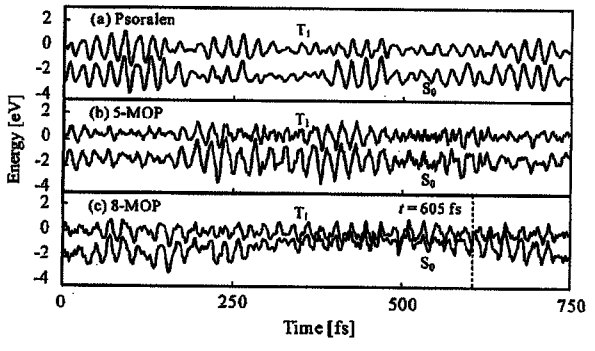

FIG. 10. PECs in the *imaginary* S_0 and the *real* T_1 state for (a) psoralen, (b) 5-MOP, and (c) 8-MOP, which have zero-point energies as the initial condition. The potential energies in the S_0 state are evaluated by using the geometries in the T_1 state. Dashed line corresponds to the timing for the intersystem crossing.

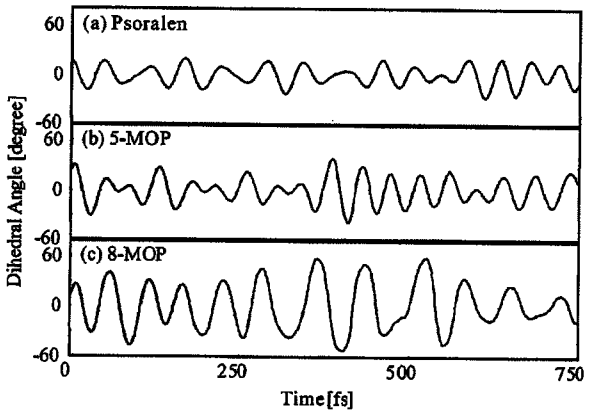

FIG. 11. Time evolution of dihedral angle between O1–C2–C3 and C2–C3–O′ in psoralen, 5-MOP, and 8-MOP in the T_1 state. O′ means the oxygen atom in carbonyl group.

T_1 state is expected to be much different from those of psoralen and 5-MOP. The present conclusion is consistent with the previous experimental studies.[1–5]

ACKNOWLEDGMENTS

Part of the calculations was performed at the Research Center for Computational Science (RCCS) of the Okazaki National Research Institutes and the Media Network Center (MNC) of Waseda University. This study was supported by a Grant-in-Aid for Young Scientists (A) "KAKENHI 14703005" from Japanese Society for the Promotion of Science (JSPS), by the Joint Studies Program of the Institute for Molecular Science, and by a Waseda University Grant for Special Research Projects.

[1] R. V. Bensasson, E. J. Land, and T. G. Truscott, *Excited States and Free Radicals in Biology and Medicine* (Oxford University Press, New York, 1993).
[2] T. Otsuki, J. Synthetic Org. Chem., Japan **49**, 809 (1991).
[3] P. S. Song and K. J. Tapley, Jr., Photochem. Photobiol. **29**, 1177 (1979).
[4] H. P. Spielmann, T. J. Dwyer, J. E. Hearst, and D. E. Wemmer, Biochemistry **34**, 12937 (1995).
[5] Y. Uesugi and H. Takahashi, Symposium on Structure Dynamics and Control of Excited States, Hawaii, 1995.
[6] H. Nakai, Y. Yamauchi, A. Matsuda, Y. Okada, and K. Takeuchi, J. Mol. Struct.: THEOCHEM **592**, 61 (2002).
[7] M. P. Allen and D. J. Tildesley, *Computer Simulation of Liquids* (Clarendon, Oxford, 1987).
[8] M. J. Frisch, G. W. Trucks, H. B. Schlegel *et al.*, GAUSSIAN 98, Revision A.7, Gaussian, Inc., Pittsburgh, PA, 1998.
[9] P. J. Stevens, J. F. Devlin, C. F. Chabalowski, and M. J. Frish, J. Phys. Chem. **98**, 11623 (1994).
[10] J. C. Slater, Phys. Rev. **81**, 385 (1951).
[11] A. D. Becke, Phys. Rev. A **38**, 3098 (1988).
[12] S. H. Vosco, L. Wilk, and M. Nusair, Can. J. Phys. **58**, 1200 (1980).
[13] C. Lee, W. Yang, and R. G. Parr, Phys. Rev. B **37**, 785 (1988).
[14] T. H. Dunning, Jr. and P. J. Hay, in *Methods of Electronic Structure Theory*, edited by H. F. Schaefer III (Plenum, New York, 1976), Vol. 3, p. 1.
[15] A. K. Mazur, J. Comput. Phys. **136**, 354 (1997).
[16] T. H. Dunning, Jr., J. Chem. Phys. **90**, 1007 (1989).
[17] A. Nakata, T. Baba, H. Takahashi, and H. Nakai (unpublished).

ELSEVIER

Journal of Molecular Structure (Theochem) 637 (2003) 27–35

THEO CHEM

www.elsevier.com/locate/theochem

Energy density analysis (EDA) of proton transfer reactions in malonaldehyde, tropolone, and 9-hydroxyphenalenone

Hiromi Nakai*, Keitaro Sodeyama

Department of Chemistry, School of Science and Engineering, Waseda University, Tokyo 169-8555, Japan

Received 17 July 2002; accepted 4 September 2002

Abstract

We have recently proposed the energy density analysis (EDA) that partitions the total energy of molecular system into atomic energy densities [Chem. Phys. Lett. 363 (2002) 73]. In this study, the EDA is applied to symmetric proton tunneling reactions in malonaldehyde, tropolone, and 9-hydroxyphenalenone. Energy density changes in the reactions are shown to be much related to the formation and breaking of the chemical bonds. It is clarified that the energy density change followed by the proton transfer is allowed to decay rapidly as the distance from the proton increases.

Keywords: Energy density analysis; Proton transfer reaction; Malonaldehyde; Tropolone; 9-Hydroxyphenalenone

1. Introduction

Proton transfer reactions are significantly important in understanding many physical, chemical, and biological processes. Malonaldehyde (MA), tropolone (TRN), and 9-hydroxyphenalenone (9HPO) have intramolecular hydrogen bonds of O–H···O, which lead to proton (or hydrogen atom) tunneling reactions.

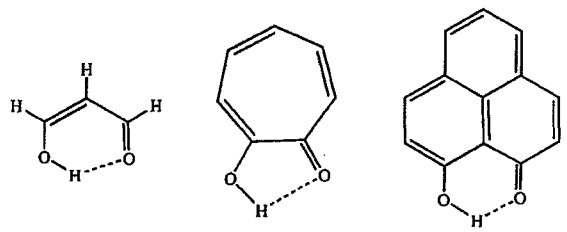

Extensive spectroscopic studies have determined tunneling splittings of the vibrational levels for MA [1–6], TRN [7–17], and 9HPO [18,19]. The proton tunneling, however, is not a simple process involving only the motion of a proton. Simultaneous rearrangements of both electronic and nuclear structures are necessary for the proton tunneling to occur.

In spite of the importance of the multi-dimensional character of the proton tunneling, most of theoretical studies [20–25] have adopted the low-dimensional potential energy surface (PES), of which reaction coordinates are selected by chemical intuition. A sophisticated method, which evaluates the effect of the proton tunneling is necessary to select the reaction coordinates. Recently, we have proposed a new analyzing technique, named energy density analysis (EDA) [26], which partitions the total energy of molecule computed by the Kohn–Sham type density

* Corresponding author. Tel.: +81-3-5286-3452; fax: +81-3-3205-2504.

E-mail address: nakai@waseda.jp (H. Nakai).

0166-1280/03/$ - see front matter © 2003 Published by Elsevier B.V.
doi:10.1016/S0166-1280(03)00417-2

functional theory (DFT) [27] into atomic energy densities without extra computing costs.

In the present study, the EDA method is applied to the proton transfer reactions in MA, TRN, and 9HPO. We evaluate atomic energy densities in proton transfer reactions with the full consideration of the electronic and nuclear rearrangements. The degrees of the couplings between the proton transfer and the rearrangements are compared among the three molecules in a numerical sense.

2. Theoretical aspect

The EDA has been proposed to analyze the local energy in the total system [26]. In this section, we briefly review the EDA method. The electronic energy in the Kohn–Sham formulation [27] is given by

$$E_{\mathrm{ELC}}[\rho] = T_{\mathrm{S}}[\rho] + E_{\mathrm{Ne}}[\rho] + E_{\mathrm{CLB}}[\rho] + E_{\mathrm{XC}}[\rho] \quad (1)$$

where $T_{\mathrm{S}}[\rho]$ is the non-interacting kinetic energy, $E_{\mathrm{Ne}}[\rho]$ is the nucleus–electron attraction energy, $E_{\mathrm{CLB}}[\rho]$ is the classical Coulomb interaction, and $E_{\mathrm{XC}}[\rho]$ is the exchange-correlation energy. The EDA decomposes these terms into atomic contributions.

The exchange-correlation energy E_{xc} is usually evaluated by using numerical quadrature technique

$$E_{\mathrm{XC}} = \int F_{\mathrm{XC}}(\mathbf{r})\mathrm{d}\mathbf{r} \cong \sum_{\mathrm{A}}^{\mathrm{atom}} \sum_{g}^{\mathrm{grid}} \omega_g p_{\mathrm{A}}(\mathbf{r}_g) F_{\mathrm{XC}}(\mathbf{r}_g) \quad (2)$$

where $\omega_g(\mathbf{r})$ is the weight, $p_{\mathrm{A}}(\mathbf{r})$ is the partition function (see Ref. [28]), and $F_{\mathrm{XC}}(\mathbf{r})$ is the exchange-correlation functional. In Eq. (2), the partial sum gives an exchange-correlation energy density for atom A, $E^{\mathrm{A}}_{\mathrm{XC}}$

$$E^{\mathrm{A}}_{\mathrm{XC}} = \sum_{g}^{\mathrm{grid}} \omega_g p_{\mathrm{A}}(\mathbf{r}_g) F_{\mathrm{XC}}(\mathbf{r}_g) \quad (3)$$

The other terms in Eq. (1), i.e. T_{S}, E_{Ne}, and E_{CLB}, are partitioned into their energy densities by using the analogy of Mulliken population analysis [29]. For example, the kinetic energy density for atom A, $T^{\mathrm{A}}_{\mathrm{S}}$, is evaluated by

$$T^{\mathrm{A}}_{\mathrm{S}} = \sum_{\mu \in \mathrm{A}} (\mathbf{PT})_{\mu\mu} \quad (4)$$

where $\mathbf{P}$ is the AO-basis density matrix and $\mathbf{T}$ has an element of the AO integral for the kinetic operator. $E^{\mathrm{A}}_{\mathrm{Ne}}$ and $E^{\mathrm{A}}_{\mathrm{CLB}}$ are evaluated in a similar manner.

The total energy is the sum of the electronic energy E_{ELC} given by Eq. (1) and the nuclear repulsion energy E_{NN} given by

$$E_{\mathrm{NN}} = \frac{1}{2} \sum_{\mathrm{A}}^{\mathrm{atom}} \sum_{\mathrm{B}\neq\mathrm{A}}^{\mathrm{atom}} \frac{Z_{\mathrm{A}} Z_{\mathrm{B}}}{r_{\mathrm{AB}}} \quad (5)$$

The nuclear repulsion energy density for atom A, $E^{\mathrm{A}}_{\mathrm{NN}}$ is evaluated by the following partial sum

$$E^{\mathrm{A}}_{\mathrm{NN}} = \frac{1}{2} \sum_{\mathrm{B}\neq\mathrm{A}}^{\mathrm{atom}} \frac{Z_{\mathrm{A}} Z_{\mathrm{B}}}{r_{\mathrm{AB}}} \quad (6)$$

As a result, the total energy of molecular system can be partitioned into atomic energy densities.

3. Computational details

The present study deals with the symmetric proton tunneling in MA, TRN, and 9HPO. The electronic structures of these systems are obtained by the DFT calculations with the B3LYP hybrid functional [30], which consists of the HF (exact) exchange, the Slater exchange [31], the Becke (B88) exchange [32], the Vosco–Wilk–Nusair (VWN) correlation [33], and the Lee–Yang–Parr (LYP) correlation [34] functionals. Correlation-consistent polarization plus valence double zeta (cc-pVDZ) basis sets of Dunning [35] are adopted for H, C, and O atoms. Geometry optimizations are carried out at the B3LYP/cc-pVDZ level. The electronic state calculations are performed by using the program system HONDO 99 [36]. The EDA calculations are carried out by linking the original code for the EDA [37] with HONDO 99.

4. Results and discussion

We first examine the symmetric proton tunneling reaction in MA. In this process, a hydrogen atom denoted by $\mathrm{H_C}$ moves from the left-hand side to the right-hand side. Thus, the initial and final species are expressed by the L and R species, respectively. Fig. 1 shows the optimized geometries of the transition state

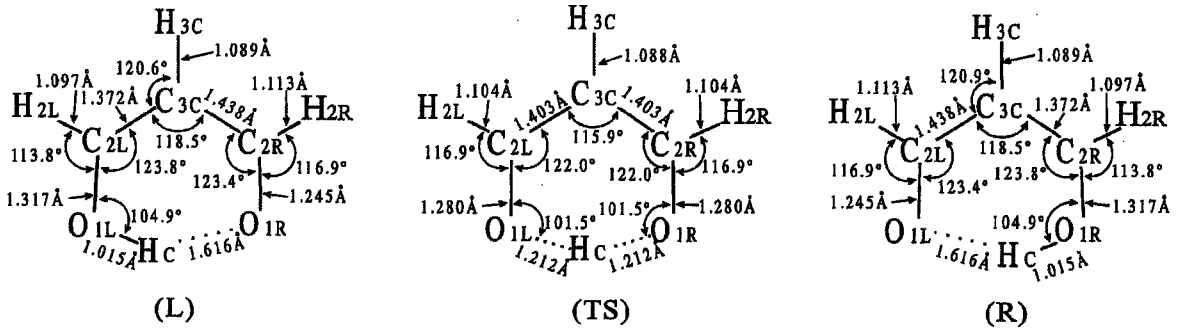

Fig. 1. Optimized geometries of the L, TS, and R species in MA.

(TS) in addition to the L and R species. In the L species, the O_{1L}–H_C and O_{1R}–H_C bond distances are 1.02 and 1.62 Å, respectively. They correspond to the covalent and hydrogen bonds, respectively. The reverse is true in the R species. The bond alternation is seen in the C–C skeleton including the C–O bonds by the L → R process.

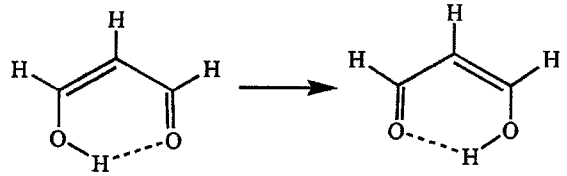

In the TS, the O_{1L}–H_C distance is equal to the O_{1R}–H_C one; namely, 1.21 Å. The C_{2L}–C_{3C} and C_{2R}–C_{3C} distances of 1.40 Å in the TS are longer than the C=C double bond of 1.37 Å and shorter than the C–C single bond of 1.44 Å in the L and R species. Similarly, the O_{1L}–C_{2L} and O_{1R}–C_{2R} distances of 1.28 Å in the TS are between the single and double bonds in the L and R species; that is, 1.32 and 1.25 Å, respectively. The changes of the C–H bond distances are very small in the L → TS → R process. These behaviors in the geometrical changes of the proton tunneling process are well investigated in the previous studies (for example, Refs. [38–40]).

Table 1 shows the energy densities in the L, TS, and R species, which are evaluated by the EDA technique. All the energy densities of H, C, and O in the three species are lower than the respective atomic energies, which are −0.4993, −37.8529, and −75.0696 hartree, respectively. It indicates that the chemical bondings lead to the stabilization of the individual atoms.

The energy density differences with respect to the TS are also shown in Table 1. A maximum change of

Table 1
Atomic energy densities at the L, TS, and R species (E_L, E_{TS}, and E_R) in MA are given in hartree

	E_L	E_{TS}	E_R
H_C	−0.5094 (+7.34)	−0.5211 (0.00)	−0.5094 (+7.34)
O_{1L}	−75.2960 (−15.68)	−75.2710 (0.00)	−75.2584 (+7.95)
O_{1R}	−75.2584 (+7.95)	−75.2710 (0.00)	−75.2960 (−15.68)
C_{2L}	−38.1622 (−0.92)	−38.1607 (0.00)	−38.1684 (−4.82)
C_{2R}	−38.1684 (−4.82)	−38.1607 (0.00)	−38.1622 (−0.92)
C_{3C}	−38.1740 (+3.86)	−38.1801 (0.00)	−38.1740 (+3.86)
H_{2L}	−0.5353 (−0.23)	−0.5350 (0.00)	−0.5350 (−0.05)
H_{2R}	−0.5350 (−0.05)	−0.5350 (0.00)	−0.5353 (−0.23)
H_{3C}	−0.5376 (+0.31)	−0.5381 (0.00)	−0.5376 (+0.31)
Total	−267.1762 (−2.25)	−267.1726 (0.00)	−267.1762 (−2.25)

Energy density differences with respect to the TS are shown in parentheses in kcal/mol.

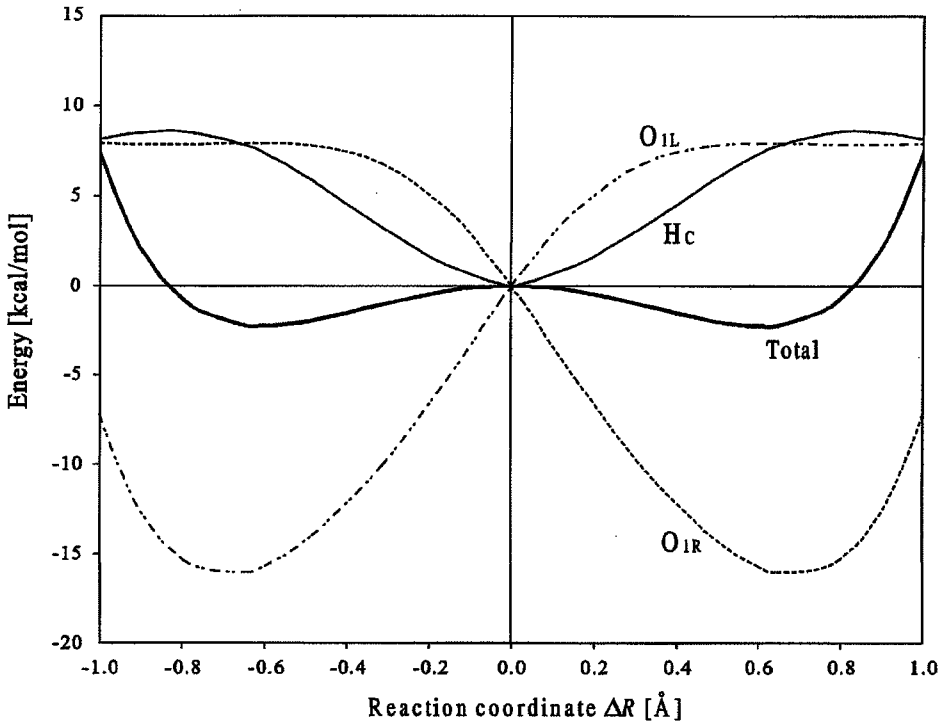

Fig. 2. Energy density curves of H_C, O_{1L}, and O_{1R} in the proton transfer reaction in MA.

the energy density appears in O_{1L} and O_{1R}. The energy density change of H_C is the about half of those of O_{1L} and O_{1R}. Thus, O_{1L}, O_{1R} and H_C atoms are the active site in the proton tunneling process. The energy density changes of C_{2L}, C_{2R}, and C_{3C}, which are related with the bond alternation, are smaller than those in the active site. In accordance with the small geometrical changes, the energy density changes of H_{2L}, H_{2R}, and H_{3C} are much smaller.

Fig. 2 shows the energy density curves (EDCs) of H_C, O_{1L}, and O_{1R} in comparison with the potential energy curve (PEC) of the total system in the symmetric proton tunneling process in MA. The difference ΔR between the H_C–O_{1L} and H_C–O_{1R} distances is adopted as an effective reaction coordinate. All the other geometrical parameters are optimized. Namely, the electronic and nuclear rearrangements are fully considered. In Fig. 2, the EDCs of H_C, O_{1L}, and O_{1R} are drawn by the relative values with respect to the energy densities in the TS, which corresponds to $\Delta R = 0$ Å. The positions at $\Delta R = -0.60$ and $+0.60$ Å correspond to the L and R species, respectively. The PEC of the total system, which is in the bold line, has a narrow minimum; namely, about 2 kcal/mol. On the other hand, the EDCs of O_{1L} and O_{1R} have deeper minima. The energy density difference of O_{1L} (or O_{1R}) between the L and R species is about 23 kcal/mol. As ΔR changes from -0.60 to $+0.60$ Å, the energy density of O_{1L} increases monotonically. The energy density change of O_{1R} is opposite to that of O_{1L}. The behavior of the EDC of H_C is different. The EDC of H_C has a minimum at the TS ($\Delta R = 0$ Å), not a maximum. The destabilization of O_{1L} from $\Delta R = -0.60$ to 0 Å is greater than the stabilization of O_{1R}. In this region, the H_C–O_{1L} bond corresponds to a covalent bond, whereas the H_C–O_{1R} bond corresponds to a hydrogen bond.

Next, we examine the symmetric proton tunneling processes in TRN and 9HPO. The optimized geometries of the L and R species in TRN and 9HPO are illustrated in Figs. 3 and 4, respectively. As the H_C

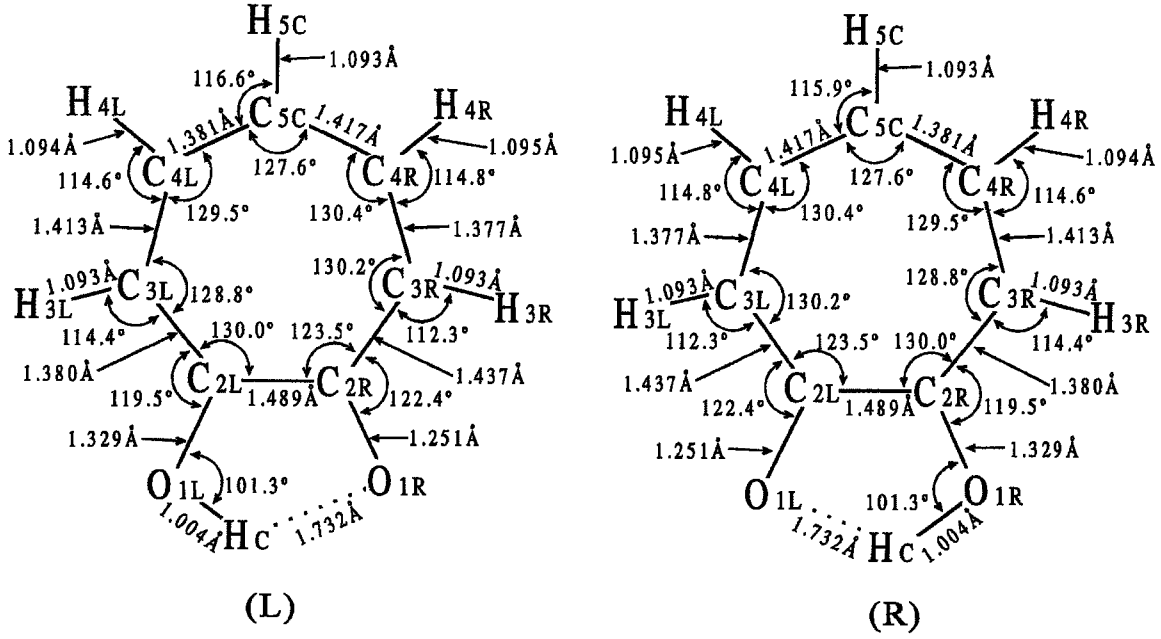

Fig. 3. Optimized geometries of the L, and R species in TRN.

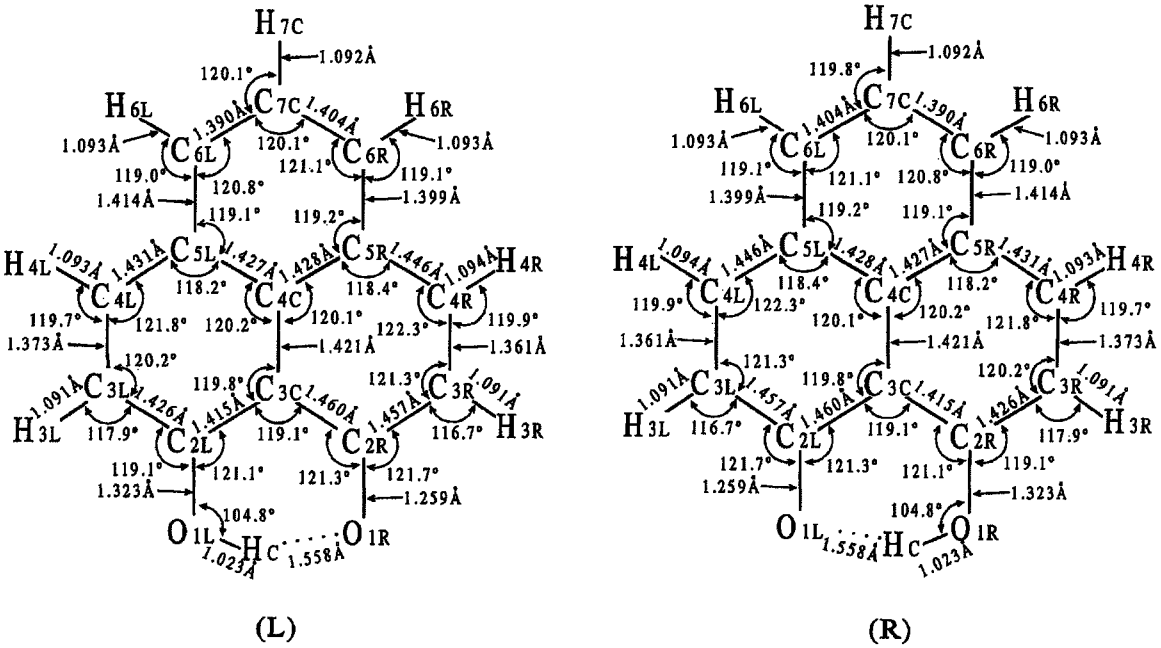

Fig. 4. Optimized geometries of the L, and R species in 9HPO.

Table 2
Atomic energy densities (E_L and E_R) at the L and R species in TRN are given in hartree

	E_L	E_R	$\Delta E_{L\to R}$
H_C	−0.5007	−0.5007	0.00
O_{1L}	−75.2863	−75.2494	+23.15
O_{1R}	−75.2494	−75.2863	−23.15
C_{2L}	−38.1502	−38.1521	−1.21
C_{2R}	−38.1521	−38.1502	+1.21
C_{3L}	−38.1633	−38.1555	+4.90
C_{3R}	−38.1555	−38.1633	−4.90
C_{4L}	−38.1717	−38.1677	+2.47
C_{4R}	−38.1677	−38.1717	−2.47
C_{5C}	−38.1703	−38.1703	0.00
H_{3L}	−0.5297	−0.5302	−0.27
H_{3R}	−0.5302	−0.5297	+0.27
H_{4L}	−0.5289	−0.5286	+0.18
H_{4R}	−0.5286	−0.5289	−0.18
H_{5C}	−0.5303	−0.5303	0.00
Total	−420.8151	−420.8151	0.00

Energy density differences ($\Delta E_{L\to R}$) with respect to the L species are shown in kcal/mol.

atom transfers from the left-hand side to the right-hand side, the O_{1L}–C_{2L} distance becomes shorter; that is, 1.33 → 1.25 Å in TRN and 1.32 → 1.26 Å in 9HPO. As seen in MA, the bond alternation in the C–C skeleton appears in TRN.

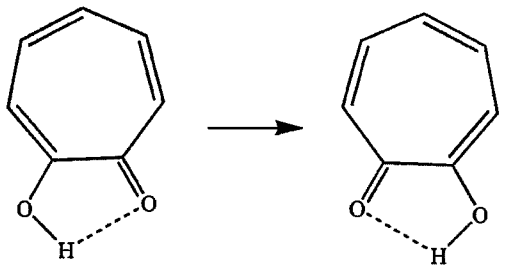

(L) (R)

For example, the C_{2L}–C_{3L} distance changes from 1.38 to 1.44 Å by the proton transfer. On the other hand, the changes of the C–C distances in 9HPO are smaller than those in MA and TRN. The C_{2L}–C_{3L} and C_{3L}–C_{4L} distances change 1.43 → 1.46 and 1.37 → 1.36, respectively. In the L and R species, the C_{2L}–C_{3L} (or C_{2R}–C_{3R}) distances are close to that of the C–C single bond, whereas the C_{3L}–C_{4L} (or C_{3R}–C_{4R}) distances are close to that of the C = C double bond. This behavior is due to a resonance hybrid among the following three extremes in the L (or R) species.

Table 3
Atomic energy densities (E_L and E_R) at the L and R species in 9HPO are given in hartree

	E_L	E_R	$\Delta E_{L\to R}$
H_C	−0.5145	−0.5145	0.00
O_{1L}	−75.2893	−75.2509	+24.05
O_{1R}	−75.2509	−75.2893	−24.05
C_{2L}	−38.1390	−38.1338	+3.24
C_{2R}	−38.1338	−38.1390	−3.24
C_{3L}	−38.1583	−38.1558	+1.59
C_{3C}	−38.0955	−38.0955	0.00
C_{3R}	−38.1558	−38.1583	−1.59
C_{4L}	−38.1453	−38.1435	+1.11
C_{4C}	−38.2190	−38.2190	0.00
C_{4R}	−38.1435	−38.1453	−1.11
C_{5L}	−38.1600	−38.1617	−1.08
C_{5R}	−38.1617	−38.1600	+1.08
H_{6L}	−38.1451	−38.1440	+0.68
H_{6R}	−38.1440	−38.1451	−0.68
H_{7C}	−38.1635	−38.1635	0.00
H_{3L}	−0.5310	−0.5316	−0.32
H_{3R}	−0.5316	−0.5310	+0.32
H_{4L}	−0.5306	−0.5304	+0.14
H_{4R}	−0.5304	−0.5306	−0.14
H_{6L}	−0.5316	−0.5317	−0.07
H_{6R}	−0.5317	−0.5316	+0.07
H_{7C}	−0.5319	−0.5319	0.00
Total	−650.7377	−650.7377	0.00

Energy density differences ($\Delta E_{L\to R}$) with respect to the L species are shown in kcal/mol.

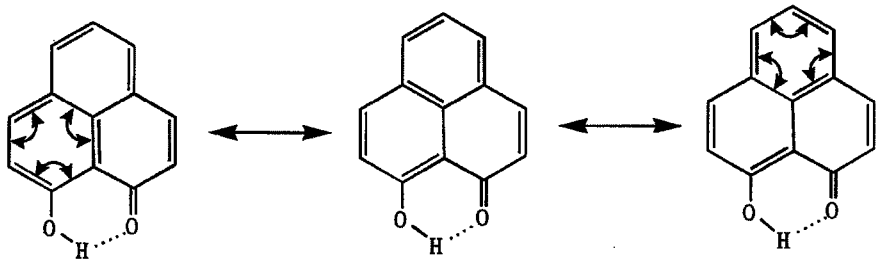

Tables 2 and 3 show the energy densities of H, C, and O atoms at the L and R species in TRN and 9HPO, respectively. In comparison with the total energies of isolated H, C, and O atoms, the atomic energy densities in TRN and 9HPO become lower due to the formation of the chemical bonds. The energy densities of O_{1L} and O_{1R} in MA, TRN, and 9HPO in the L species are (−75.296, −75.258), (−75.286, −75.249), and (−75.289, −75.251) in hartree, respectively. These results mean that the energy density is affected by the local bond structure rather than the molecular species. The energy densities of carbon atoms in TRN are in the range from −38.150 to −38.172 hartree. Similarly, those in MA are in the range from −38.162 to −38.174 hartree. On the other hand, the highest and lowest values in 9HPO are −38.096 and −38.219 hartree of C_{3C} and C_{4C}, respectively. The energy range of about 0.12 hartree in 9HPO is much larger than those of 0.01 and 0.02 hartree in MA and TRN, respectively. These results are correlated with the rearrangements of the C–C bonds, which in 9HPO are much smaller than those in MA and TRN.

The energy density differences between the L and R species, denoted by

$$\Delta E^{A}_{L\to R} = E^{A}_{R} - E^{A}_{L} \tag{7}$$

are also shown in Tables 2 and 3. The largest changes in both systems are seen in O_{1L} and O_{1R}. The energy density difference $\Delta E^{A}_{L\to R}$ corresponds to the energy transfer followed by the proton transfer. A neighboring index, i, is introduced to express the distance from the active site; that is, H_C. For example, the O_{1L}, C_{2L}, and C_{3C} atoms correspond to the indices $i = 1, 2$, and 3, respectively. In Fig. 5, $\Delta E^{i}_{L\to R}$ is plotted against the index, i, in order to investigate the region of the energy transfer. The energy density difference of H bonded to C is added to that of the C atom; for example, in MA

$$\Delta E^{2}_{L\to R} = \Delta E^{C_{L2}}_{L\to R} + \Delta E^{H_{L2}}_{L\to R}. \tag{8}$$

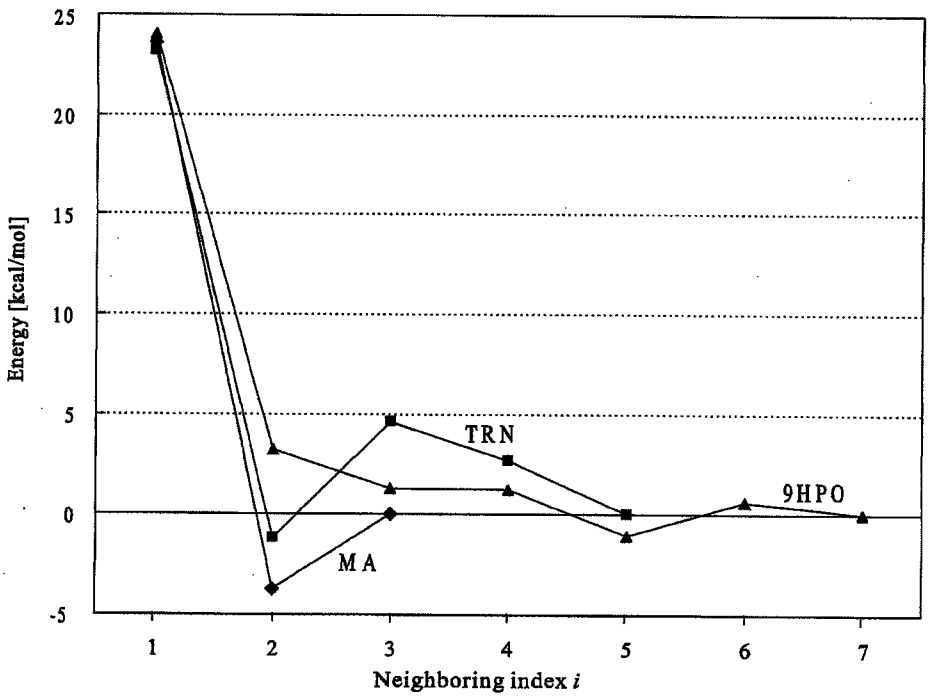

Fig. 5. Comparison of the energy density changes in MA, TRN, and 9HPO against the neighboring index i.

In the three systems, the energy density differences of O_{1L} are close to each other; namely, $\Delta E^1_{L\to R} = +23.60, +23.20$, and $+24.05$ kcal/mol in MA, TRN, and 9HPO, respectively. As the index i increases, the $\Delta E^i_{L\to R}$ curves in the three systems are allowed to decay to zero rapidly. Furthermore, there exists small oscillation. At $i = 3$, the energy density difference in TRN is larger than that in 9HPO; namely, $\Delta E^3_{L\to R} = +4.60$ and $+1.27$ kcal/mol in TRN and 9HPO, respectively. These results correspond to the geometrical changes in the two molecules. Namely, the bond alternation of the C–C skeleton occurs in TRN, while the geometrical rearrangements in 9HPO are small due to the resonance hybrid.

5. Conclusion

Recently we have proposed the EDA method [26] to partition the total energy of molecules into atomic energy densities. The present study is an application of the EDA method to the proton transfer reactions in MA, TRN, and 9HPO. The changes of the atomic energy densities along the reactions are shown to be consistent with the formation and breaking of the chemical bonds. The effect of the proton transfer is allowed to decay rapidly as the distance from the active site increases. By comparing the results for MA, TRN, and 9HPO, it is clarified that the decay in 9HPO is faster than those in MA and TRN, while the energy density changes in the active site are close to each other.

Acknowledgements

Part of the calculations was performed at the Research Center for Computational Science (RCCS) of the Okazaki National Research Institutes and the Media Network Center (MNC) of Waseda University. Part of this study was supported by a Grant-in-Aid for Young Scientists (A) 'KAKENHI 14703005' from Japanese Society for the Promotion of Science (JSPS) and by a Waseda University Grant for Special Research Projects.

References

[1] W.F. Rowe, R.W. Duerst, E.B. Wilson, J. Am. Chem. Soc. 98 (1976) 4021.
[2] S.L. Baughcum, R.W. Duerst, W.F. Rowe, Z. Smith, E.B. Wilson, J. Am. Chem. Soc. 103 (1981) 6296.
[3] S.L. Baughcum, Z. Smith, E.B. Wilson, R.W. Duerst, J. Am. Chem. Soc. 106 (1984) 2260.
[4] P. Turner, S.L. Baughcum, S.L. Coy, Z. Smith, J. Am. Chem. Soc. 106 (1984) 2265.
[5] D.W. Firth, K. Beyer, M.A. Dvorak, S.W. Reeve, A. Grushow, K.R. Loepold, J. Chem. Phys. 94 (1991) 1812.
[6] T. Baba, T. Tanaka, I. Morino, K.M.T. Yamada, K. Tanaka, J. Chem. Phys. 110 (1999) 4131.
[7] R. Rosseti, L.E. Brus, J. Chem. Phys. 73 (1980) 1546.
[8] Y. Tomioka, M. Ito, N. Mikami, J. Phys. Chem. 87 (1983) 4401.
[9] A.C.P. Alves, J.M. Hollas, H. Musa, T. Ridley, J. Mol. Spectrosc. 109 (1985) 99.
[10] R.L. Redington, Y. Chen, G.J. Scherer, R.W. Field, J. Chem. Phys. 88 (1988) 627.
[11] R.L. Redington, T.E. Redington, M. Hunter, R.W. Field, J. Chem. Phys. 92 (1990) 6456.
[12] R.L. Redington, C.W. Bock, J. Phys. Chem. 95 (1991) 10284.
[13] H. Sekiya, Y. Nagashima, Y. Nishimura, Bull. Chem. Soc. Jpn 62 (1989) 3229.
[14] H. Sekiya, Y. Nagashima, Y. Nishimura, J. Chem. Phys. 92 (1990) 5761.
[15] H. Sekiya, Y. Nagashima, Y. Nishimura, Chem. Phys. Lett. 160 (1989) 581.
[16] H. Sekiya, K. Sasaki, Y. Nishimura, Z.-H. Li, A. Mori, H. Takeshita, Chem. Phys. Lett. 173 (1990) 285.
[17] H. Sekiya, Y. Nagashima, T. Tsuji, Y. Nishimura, A. Mori, H. Takeshita, J. Phys. Chem. 95 (1991) 10311.
[18] R. Rossetti, R.C. Haddon, L.E. Brus, J. Am. Chem. Soc. 102 (1980) 6913.
[19] V.E. Bondybey, R.C. Haddon, J.H. English, J. Chem. Phys. 80 (1984) 5432.
[20] T. Carrington Jr., W.H. Miller, J. Chem. Phys. 81 (1984) 3942.
[21] T. Carrington Jr., W.H. Miller, J. Chem. Phys. 84 (1986) 4364.
[22] N. Sato, S. Iwata, J. Chem. Phys. 89 (1988) 2932.
[23] N. Shida, P.F. Barbara, J. Almlöf, J. Chem. Phys. 91 (1989) 4061.
[24] N. Shida, J. Almlöf, P.F. Barbara, J. Phys. Chem. 95 (1991) 10457.
[25] D. Babić, S.D. Bosanac, N. Došlić, Chem. Phys. Lett. 358 (2002) 337.
[26] H. Nakai, Chem. Phys. Lett. 363 (2002) 73.
[27] W. Kohn, L.J. Sham, Phys. Rev. 140 (1965) A1133.
[28] A.D. Becke, J. Chem. Phys. 88 (1988) 2547.
[29] R.S. Mulliken, J. Chem. Phys. 23 (1955) 1833.
[30] P.J. Stevens, J.F. Devlin, C.F. Chabalowski, M.J. Frish, J. Chem. Phys. 98 (1998) 11623.
[31] J.C. Slater, Phys. Rev. 81 (1951) 385.
[32] A.D. Becke, Phys. Rev. A 38 (1988) 3098.

[33] S.H. Vosco, L. Wilk, M. Nusair, Can. J. Phys. 58 (1980) 1200.
[34] C. Lee, W. Yang, R.G. Parr, Phys. Rev. B 37 (1988) 785.
[35] T.H. Dunning Jr., J. Chem. Phys. 90 (1989) 1007.
[36] M. Dupuis, A. Marquez, E.R. Davidson, 'HONDO 99.6', 1999, based on HONDO 95.3, M. Dupuis, A. Marquez, E.R. Davidson, Quantum Chemistry Program Exchange (QCPE), Indiana University, Bloomington, IN 47405.
[37] H. Nakai, 'EDA 2002', Waseda University, Tokyo 169-8555, 2002.
[38] S. Sadhukhan, D. Muñoz, C. Adamo, G.E. Scuseria, Chem. Phys. Lett. 306 (1999) 83.
[39] K. Yagi, T. Taketsugu, K. Hirao, J. Chem. Phys. 115 (2001) 10647.
[40] H. Nakai, K. Sodeyama, Chem. Phys. Lett. 365 (2002) 203.

Available online at www.sciencedirect.com
SCIENCE DIRECT®
Journal of Electroanalytical Chemistry 559 (2003) 131–136
Journal of Electroanalytical Chemistry
www.elsevier.com/locate/jelechem

Molecular orbital study on the reaction process of dimethylamine borane as a reductant for electroless deposition

Takayuki Homma [a,*], Amiko Tamaki [a], Hiromi Nakai [b,*], Tetsuya Osaka [a]

[a] Department of Applied Chemistry, Waseda University, 3-4-1 Okubo, Shinjuku, Tokyo 169-8555, Japan
[b] Department of Chemistry, Waseda University, 3-4-1 Okubo, Shinjuku, Tokyo 169-8555, Japan

Received 25 July 2002; received in revised form 7 December 2002; accepted 14 December 2002

Abstract

The oxidation mechanism of dimethylamine borane (DMAB), which acts as a reductant in the electroless deposition process, was studied using ab initio molecular orbital approaches such as Hartree–Fock (HF) and second order Møller–Plesset (MP2) calculations. The overall oxidation process of the DMAB was divided into each elementary reaction in which OH^- substitutes H one by one and eventually forms $B(OH)_4^-$. The oxidation mechanism of DMAB in the isolated state, which was previously proposed by us, was refined using more accurate basis sets, and the effects of solvation and interaction with metal surface sites on the oxidation mechanism were also studied. Taking the solvation effect into consideration using the self-consistent reaction field method with an isodensity polarized continuum model (SCRF-IPCM), the heat of oxidation was transferred to an exothermic reaction with decreasing dielectric constant. This indicated that the reaction preferably proceeds at the solid | liquid interface. Combined with Cu(111) and Pd(111) neutral cluster models as metal surface sites, it was found that the oxidation reaction proceeds preferentially at the metal surface sites. It was also suggested that the catalytic activity of the deposited metal is caused by its electron acceptivity.

Keywords: Electroless deposition; Metal nanostructure formation; Ab initio molecular orbital calculation; Dimethylamine borane; Copper; Palladium; Reductant

1. Introduction

Electroless deposition processes have been extensively applied to the area of advanced microfabrication, such as electronic device processes, featuring their capability to form metal thin films onto non-flat and non-conductive surfaces [1]. Because of its industrial importance, a great deal of research has been carried out to understand the mechanism using electrochemical and kinetic approaches [2,3]. In the electroless deposition process, the metal ion is reduced not by the external current but by the electron, which is released by the oxidation reaction of reductant molecules. Furthermore, the deposited metal acts as a catalyst for the oxidation reaction. The reaction mechanism is so complex that an adequate model to describe the reaction mechanism has not yet been established. On the other hand, using the ab initio molecular orbital method, we have been trying to explore the mechanism of electroless deposition reactions at the molecular level. It is believed that the oxidation reaction of a reductant is one of the key issues in the electroless deposition process, thus we have focused upon the oxidation mechanism of dimethylamine borane (DMAB) [4,6], hypophosphite ion ($H_2PO_2^-$) [5,6], and titanium trichloride ($TiCl_3$) [6], which are known as reductants for the electroless deposition. In our previous study on the oxidation mechanism of dimethylamine borane [4,6], the reaction mechanism of the isolated system, in which the effect of solvation or metal surface was not considered, was studied in a preliminary survey. However, the effect of catalytic activity of the metal surfaces is the most significant feature to characterize the mechanism of the electroless deposition reaction [1]. In addition, the dianion state, which was suggested to be an important

* Corresponding authors. Tel.: +81-3-5286-3209; fax: +81-3-3205-2074.
E-mail addresses: homma@mse.waseda.ac.jp (T. Homma), nakai@mn.waseda.ac.jp (H. Nakai).

0022-0728/03/$ - see front matter
doi:10.1016/S0022-0728(03)00042-1

factor in the oxidation mechanism [5], was not taken into account. In this study, we investigated the oxidation mechanism of DMAB in further detail, by considering the dianion state with further accurate basis sets. Furthermore, in order to investigate the reaction mechanism more realistically, the effects of solvation and metal surface activity on the oxidation reactions are also studied.

2. Computational details

Fig. 1 shows reaction pathways for the oxidation process of DMAB. The oxidation of a reductant is generally produced by the substitution of H^* of the reductant by OH^- in the solvent. A reaction pathway via a three-coordinate complex was proposed by van den Meerakker [3] to describe the oxidation mechanism of DMAB in the electroless deposition process. On the other hand, results of our recent studies using molecular orbital approaches indicated quantitatively that the alternative pathway via a five-coordinate complex was expected to be more stable than that via the three-coordinate complex, not only in the case of the DMAB but also in the case of other reductant species such as hypophosphite ion [4–6]. Furthermore, it was found that the dianion intermediate state is significant in the oxidation reaction of reductant. Thus, in the present work, we propose the modified pathway which includes the dianion states, shown as **4b**, **5a**, **7b**, **8a**, **10b** and **11a** in Fig. 1.

Since the electroless deposition reaction takes place at a solid/liquid interface, the reaction is influenced by a number of factors such as the solvation effect and catalytic activity of the surface sites of the deposited metal. In this study, the solvation effect and metal surface as a catalyst are considered for the oxidation reaction. The solvation effect is taken into account by the self-consistent reaction field method with an iso-density surface polarized continuum model (SCRF-IPCM [7]), which uses the dielectric constant as a parameter [8]. In the SCRF-IPCM calculations, the dielectric constant is changed from 1.0 (in the non-polar solvent or gas phase) to 78.5 [9] (in the pure water of the normal phase).

For the calculation of the Cu(111) and Pd(111) surfaces, Cu_4 and Pd_4 neutral clusters consisting of four atoms were used as model surfaces. The geometry optimization is performed at the Hartree–Fock (HF) level for all intermediates shown in Fig. 1, not only in the isolated state but also in the solvation and on the metal surface. The electron correlation effects are taken into account by the second-order Møller–Plesset perturbation (MP2) method [10]. For the basis sets, which describe the molecular orbital of the ground state, cc-pVDZ [11] was used for hydrogen, boron, nitrogen and carbon. For oxygen, AUG-cc-pVDZ [11] was used, which took the effect of the diffuse function into consideration. Taking into account the diffuse function for oxygen atoms, we obtained the effective electron affinity of OH^-. For copper and palladium, the Hay and Wadt effective core pseudopotential [12] was used.

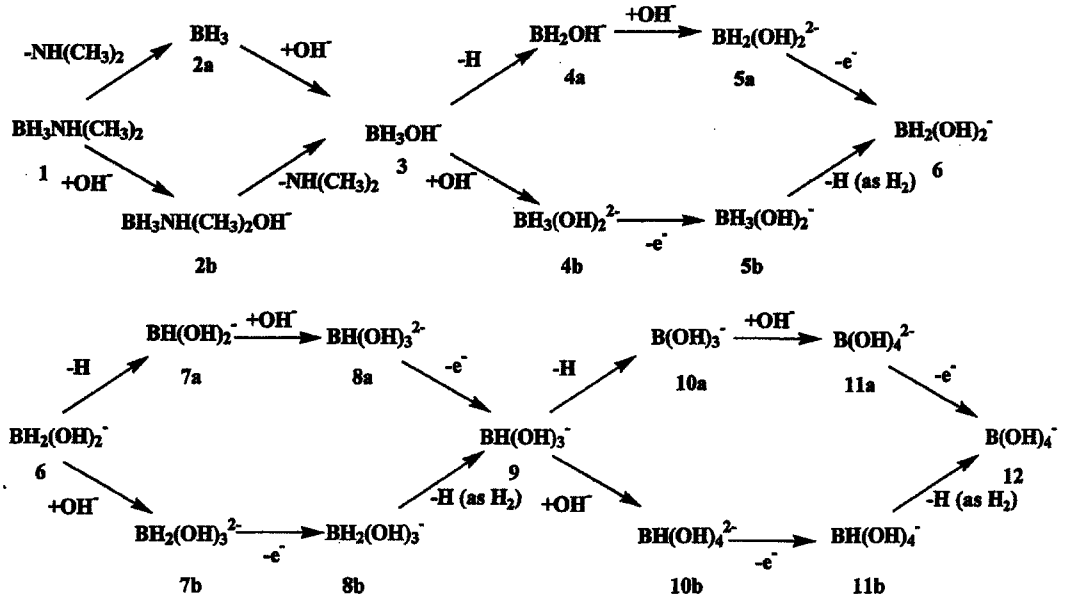

Fig. 1. Reaction pathways for the oxidation process of dimethylamine borane (DMAB) via three-coordinate intermediates (**2a**, **4a**, **5a**, **7a**, **8a**, **10a** and **11a**) and five-coordinate intermediates (**2b**, **4b**, **5b**, **7b**, **8b**, **10b** and **11b**).

All molecular orbital calculations were performed using the Gaussian 98 software package [13].

3. Results and discussion

3.1. Isolated systems

At first, the oxidation reaction of DMAB in the isolated state was examined, using the basis set with the diffuse function for oxygen in the pathway. Since the H_2 generation, which is a recombination of emitted hydrogen radicals, is considered to induce the stabilization of the overall reaction, its reaction heat ($H+H \rightarrow H_2+Q$/kcal mol^{-1}) was calculated ($Q=49$ kcal mol^{-1}; 1 kcal = 4.184 kJ) and taken into account.

Fig. 2 shows energy profiles for the oxidation process in which the energy is shown in kcal mol^{-1} with respect to that of DMAB (step 1). The graduations at the transverse correspond to the two reaction pathways via either the three- or five-coordinate intermediates, which are shown in Fig. 1. In this diagram, it is indicated that the total reaction is stabilized and the energy pathway becomes exothermic. As is observed experimentally, it is considered that H_2 generation plays a key role in the oxidation of DMAB. It is also suggested in this reaction pathway that the dianion states formed via the five-coordinate intermediates (**4b**, **7b** and **10b**) are more stable than those formed via the three-coordinate intermediates (**5a**, **8a** and **11a**). As was expected from the result of our previous study [4], the reaction pathway via the five-coordinate intermediate is more favorable than that via the three-coordinate intermediate, due to the stabilization effect caused by the three-center three- or four-electron bondings of boron. Such a five-coordinate pathway was also expected to be stable for the reaction of hypophosphite ion [5].

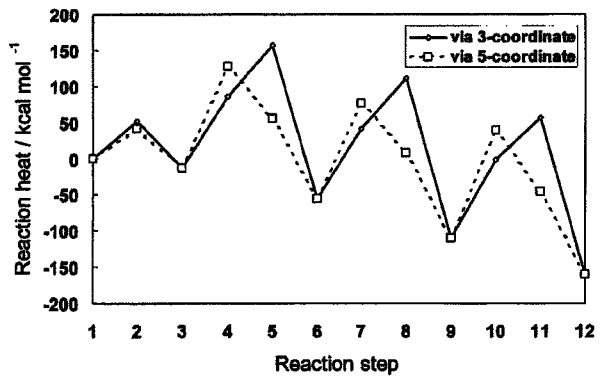

Fig. 2. Energy diagram for the oxidation process of DMAB via three-coordinate intermediates and five-coordinate intermediates.

3.2. Solvation effect

Next the solvation effect for this reaction was examined using the self-consistent reaction field method with an isodensity surface polarized continuum model (SCRF-IPCM). IPCM expresses the effect of solvation using the dielectric constant, ε, namely, IPCM at $\varepsilon = 1.0$ corresponds to the gas phase and the value for bulk pure water is $\varepsilon = 78.3$. The reaction heat is defined as follows:

$$DMAB + 4OH^- \rightarrow B(OH)_4^- + 3/2H_2 + 3e^- + Q/\text{kcal mol}^{-1}$$

Fig. 3 shows the change of Q with a change in dielectric constant, ε. In Fig. 3, two regions, corresponding to the dielectric constants of the inner and outer Helmholtz layers, are indicated, which are estimated by the Bockris–Devanathan–Muller model [14]. The Q value increases exponentially with a decrease in the dielectric constant, which corresponds to the calculated result for hypophosphite ion [5]. Such an increase in the Q value is considered to be caused by the stabilization of OH^- accompanied by an increase in the dielectric constant. Thus, the oxidation reaction of the reductant is expected to take place at the nearest-neighbor surface region of the deposited metals. In other words, it is expected that the overall reaction is enhanced at the surface region of the metals.

3.3. Effect of metal surface sites

It is confirmed experimentally that the oxidation reaction of DMAB is activated on the surfaces of nickel, cobalt, copper, palladium, silver, gold, etc. Of these, copper and palladium are focused upon in the present work, since copper is applied extensively to electronic devices and devices such as ULSI interconnections, and palladium is the most typical catalyst for the electroless

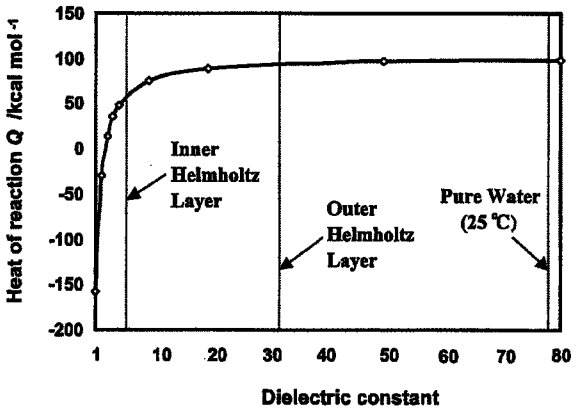

Fig. 3. Reaction heat of the oxidation reaction of the dimethylamine borane under solvation.

deposition process. As models to express the metal surface, neutral clusters of Cu_4 and Pd_4 are used. The cluster geometry is fixed in the Cu(111) and Pd(111) crystal lattice positions, for which the atom distances are 0.2556 and 0.2751 nm [9], respectively. The oxidation mechanism of DMAB on the metal was examined with respect to the pathway shown in Fig. 1. Since the stable geometries of the three-coordinate intermediate on the metal was not obtained, it is expected that, on the Cu_4 and Pd_4 clusters, the reaction via the five-coordinate intermediate is favorable, as was expected from the result in the context of isolated systems.

Fig. 4 shows the adsorbed geometries and charge distributions at each atom of the intermediates on the oxidation of DMAB on Cu_4 and Pd_4 surfaces. The same adsorbed structures were acquired except **3** and **4b** on the Cu_4 and Pd_4 cluster models. At the electron emitting steps (4, 7, and 10), it is observed that the metal atoms possess negative charge, indicating that the metal surface accepts the emitted electron from the reductant.

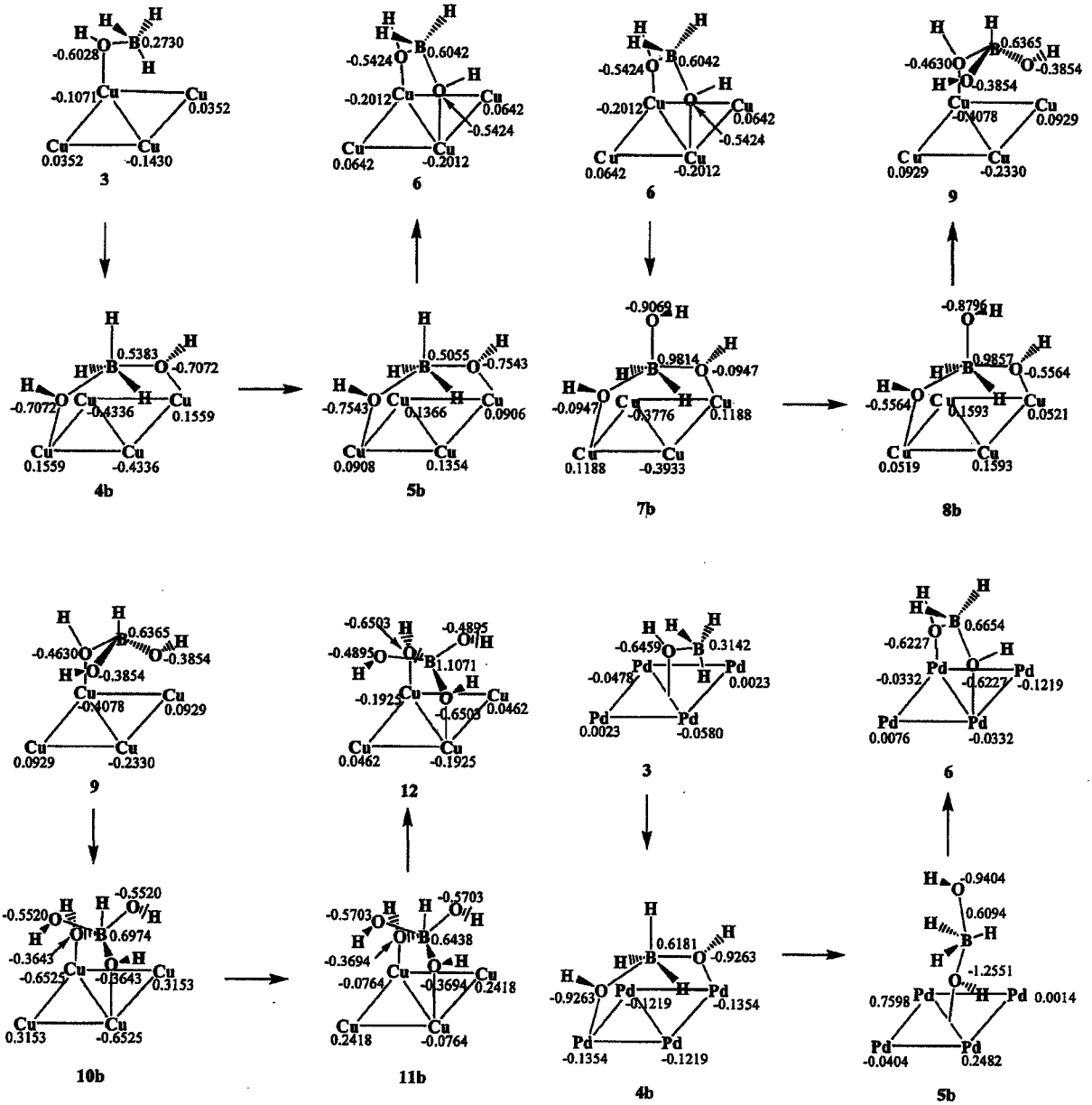

Fig. 4. Adsorbed geometries of intermediates on the oxidation of dimethylamine borane on Cu_4 and Pd_4 clusters.

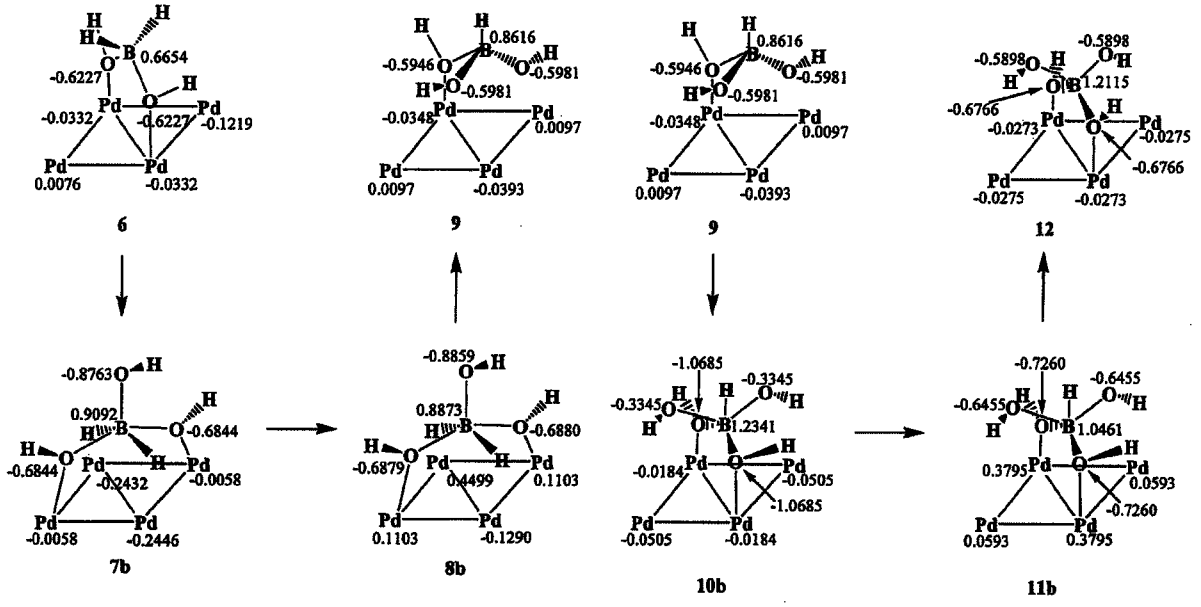

Fig. 4 (*Continued*)

Such an electron transfer is expected to take place, since the metal atoms possess electron acceptivity, and is considered to be the significant step of the reaction of the reductant molecule.

Fig. 5 shows the energy profile for the oxidation reaction on Cu_4 and Pd_4 cluster. It is clarified that all of the intermediate species are stabilized on the metal cluster, and the energy barrier of electron emission steps (4 to 5, 7 to 8, and 10 to 11) is decreased on the metal surfaces. This indicates that the oxidation reaction of DMAB is accelerated on the surface of Cu and Pd.

Table 1 shows the net charges of the Cu_4 and Pd_4 clusters at each step. From this result, it is expected that the electron transfer from dianion intermediates to metal cluster is much enhanced on the Cu_4 cluster compared with the case on the Pd_4 cluster. Such a difference is considered to be caused by the electronic affinity, which the metal originally possesses. It is shown in Fig. 5 that the adsorption heat on the Pd_4 cluster is smaller than that on the Cu_4 cluster, whereas the electron transfer barrier of the Pd_4 cluster is smaller than that of the Cu_4 cluster. Thus, the more electron transfer occurs, the higher is the adsorption heat. This indicates that the amount of electron transfer from the adsorbate to the metal cluster is related to the energy of adsorption.

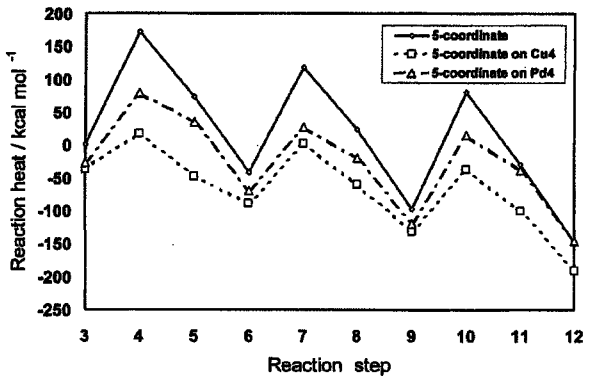

Fig. 5. Energy diagram for the oxidation process of DMAB via five-coordinate intermediates on Cu_4 and Pd_4 clusters.

Fig. 6 shows the change in the local charge density of boron in the five-coordinate intermediate species. In the case of the isolated system, the local charge increases at the electron emitting steps (4, 7 and 10), showing peak-like features. On the other hand, such increases in the local charge density of boron are not clearly observed when the reactions take place on the meal cluster surfaces, indicating that the charge generated does not remain on the boron atom. Since no significant change in the local charge density of oxygen in the OH is observed in the results shown in Fig. 4, it is expected that the emitted electron be transferred to the metal side, which corresponds to the change in the charges of the metals as described above. These results indicate that the metal surface enhances the oxidation reaction of DMAB, not only by lowering the barrier height of the reaction energy but also by accepting the emitted electron from the reductant species.

4. Conclusion

We have studied the oxidation mechanism of a dimethylamine borane, which is a representative reduc-

Table 1
Net charge of the Cu_4 and Pd_4 clusters at each step

	3	4b	5b	6	7b	8b	9	10b	11b	12
Cu_4	−0.180	−0.555	−0.438	−0.274	−0.518	0.423	−0.455	−0.677	0.331	−0.293
Pd_4	−0.101	−0.515	0.969	−0.171	−0.499	0.542	−0.050	−0.138	0.878	−0.109

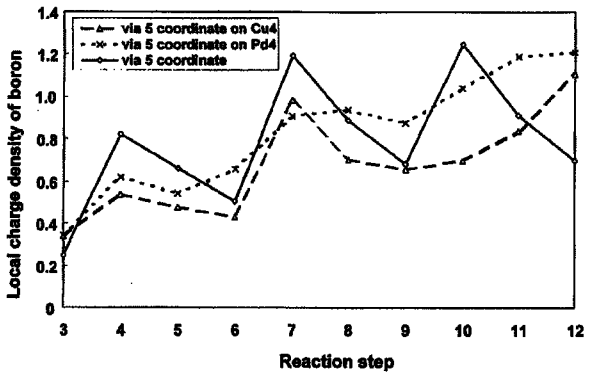

Fig. 6. Change in the local density of boron in five-coordinate intermediates at each reaction step.

tant for the electroless deposition process, using the ab initio molecular orbital method. The pathway of this oxidation process was investigated from the elementary reaction level, and it was indicated quantitatively that the reaction proceeds via five-coordinate intermediates, in which OH^- coordinates to B before the elimination of H radical and that the total oxidation reaction is stabilized by the generation of H_2. It is also suggested that the reaction preferably proceeds in the electric double layer that is formed at the surface region of the deposited metals, rather than in the bulk solution. Furthermore, it is expected that the metal surface stabilizes this reaction due to its electron receptivity, which enhances the electron emitting reaction of the reductant.

Acknowledgements

This work was supported financially in part by the Industrial Technology Research Grant Program in 00 from the New Energy and Industrial Technology Development Organization (NEDO) of Japan and also by a grant-in-aid for Scientific Research for Priority Areas 'Highly Functionized Global Interface Integration', by the Ministry of Education, Science and Culture.

References

[1] For example: M. Schlesinger, M. Paunovic (Eds.), Modern Electroplating, 4th ed., Wiley, New York, 2000.
[2] I. Ohno, O. Wakabayashi, S. Haruyama, J. Electrochem. Soc. 132 (1985) 2323.
[3] J.E.A.M. van den Meerakker, J. Appl. Electrochem. 11 (1981) 397.
[4] T. Homma, H. Nakai, M. Onishi, T. Osaka, J. Phys. Chem. B 103 (1999) 1774.
[5] H. Nakai, T. Homma, I. Komatsu, T. Osaka, J. Phys. Chem. B 105 (2001) 1701.
[6] T. Homma, I. Komatsu, A. Tamaki, H. Nakai, T. Osaka, Electrochim. Acta 47 (2001) 47.
[7] J.B. Foresman, T.A. Keith, K.B. Winberg, J.M. Sniinian, J. Frisch, J. Phys. Chem. 100 (1996) 16098.
[8] J. Tomasi, M. Persico, Chem. Rev. 94 (1994) 2927.
[9] The Chemical Society of Japan, Kagaku-binran, Maruzen, Tokyo, 1984.
[10] C. Møller, M.S. Plesset, Phys. Rev. 46 (1934) 618.
[11] W.J. Hehre, L. Random, P.v.R. Schleyer, J.A. Pople, Ab Initio Molecular Orbital Theory, Wiley, New York, 1986.
[12] P.J. Hay, W.R. Wadt, J. Chem. Phys. 82 (1985) 299.
[13] M.J. Frisch, G.W. Trucks, H.B. Schlegel, G.E. Scuseria, M.A. Robb, J.R. Cheeseman, V.G. Zakrzewski, J.A. Montgomery, R.E. Stratmann, J.C. Burant, S. Dapprich, J.M. Millam, A.D. Daniels, K.N. Kudin, K.N. Strain, O. Farkas, J. Tomasi, V. Barone; M. Cossi, R. Cammi, B. Mennucci, C. Pomelli, C. Adamo, S. Clifford, J. Ochterski, G.A. Petersson, P.Y. Ayala, Q. Cui, K. Morokuma, D.K. Malick, A.D. Rabuck, K. Raghavachari, J.B. Foresman, J. Cioslowski, J.V. Ortiz, B.B. Stefanov, G. Liu, A. Liashenko, P. Piskorz, I. Komaromi, R. Gomperts, R.L. Martin, D.J. Fox, T. Keith, M.A. Al-Laham, C.Y. Peng, A. Nanayakkara, C. Gonzalez, M. Challacombe, P.M.W. Gill, B.G. Johnson, W. Chen, M.W. Wong, J.L. Andres, M. Head-Gordon, E.S. Replogle, J.A. Pople, Gaussian 98, Gaussian Inc., Pittsburgh, PA, 1998.
[14] J.O'M. Bockris, M.A.V. Devanathan, K. Muller, Proc. Roy. Soc. A274 (1963) 55.

Size-Dependent Reaction Cross Section of Protonated Water Clusters $H^+(H_2O)_n$ ($n = 2-11$) with D_2O

Satoru Yamaguchi,[†,‡,#] Satoshi Kudoh,[‡,⊥] Yoshiki Okada,*[‡] Takaaki Orii,[‡,∥] Kazuo Takeuchi,[†,‡] Takashi Ichikawa,[§] and Hiromi Nakai[§]

Graduate School of Science and Engineering, Saitama University, 255, Shimoohkubo, Saitama-shi, Saitama 338-8570, Japan, RIKEN (The Institute of Physical and Chemical Research), 2-1 Hirosawa, Wako-shi, Saitama 351-0198, Japan, and Department of Chemistry, School of Science and Engineering, Waseda University, Tokyo 169-8555, Japan

Received: January 17, 2003; In Final Form: October 17, 2003

Collisional dynamics of size- and translational-energy-selected protonated water clusters $H^+(H_2O)_n$ ($n = 2-11$) in single collisions with D_2O were investigated using guided-ion beam tandem mass spectrometry. The dominant reaction channel for the collision involves the incorporation of D_2O into $H^+(H_2O)_n$ at low collision energy, whereas at high collision energy, the dissociation of $H^+(H_2O)_n$ is predominant. The measured total reaction cross section of $H^+(H_2O)_n$ with D_2O is found to depend strongly on the cluster size; the cross section drastically increases as the cluster size increases from $n = 4$ to 5, 6 to 7, and 8 to 9 and has local minima at $n = 6$ and 8 at collision energies of 0.05 and 0.10 eV, respectively. The size dependence of the total cross section is discussed herein in terms of a comparison with the collision cross section obtained from ab initio calculations.

Introduction

Protonated water clusters $H^+(H_2O)_n$ are abundant in the earth's atmosphere. $H^+(H_2O)_n$ is important in ion chemistry in the lower ionosphere and stratosphere.[1] In addition, $H^+(H_2O)_n$ in the troposphere plays an important role as a generation source of aerosol particles.[2] Studies of the properties of $H^+(H_2O)_n$ clusters, including their structures and chemical dynamics, are essential to a further understanding of cluster science, with particular attention being paid to their size-specific properties.[3] For instance, the structures of $H^+(H_2O)_n$ have been studied theoretically, and it is known that two candidates for the ion core of $H^+(H_2O)_n$ are the H_3O^+ and $H_5O_2^+$ cations, called the Eigen cation[4] and the Zundel cation,[5] respectively. The nature of the exact form of $H^+(H_2O)_n$ has been discussed extensively.[6−11] Recently, measurements of vibrational predissociation spectroscopy and ab initio calculations have indicated that $H^+(H_2O)_3$ and $H^+(H_2O)_4$ possess the Eigen cation, whereas $H^+(H_2O)_6$ is a mixture of isomers with the Eigen and Zundel cations, respectively, and that the energy difference between these two isomers is insignificant.[12]

The reactions of $H^+(H_2O)_n$ with a variety of atmospheric molecules have been studied. The reaction mechanism (e.g., proton and ligand transfer from the cluster to reactants, ligand switching between the cluster and reactants, and the association of the reactant with the cluster) and its rate have been investigated experimentally.[13,14] For instance, the reactions of $H^+(H_2O)_n$ with chlorine nitrate $ClONO_2$, an important "reservoir compound" involved in the stratospheric ozone chemistry, were investigated in order to study the role of heterogeneously catalyzed reactions in ozone depletion.[15] It was found in that study that hypochlorous acid HOCl, a molecule related to ozone destruction, is produced by hydrolysis on the $H^+(H_2O)_n$ cluster surface and evaporates almost immediately from the cluster.

The bimolecular reactions of $H^+(H_2O)_n$ ($n = 2-4$) with D_2O were studied using a selected ion-flow tube apparatus.[16] It was revealed that thorough randomization of the H and D atoms occurs prior to unimolecular dissociation in the ion−molecule transient complex. However, this kind of study has typically been undertaken under multiple-collision conditions, which introduce undesired complexity to our understanding of the reaction mechanism. In addition, the collisional dynamics of $H^+(H_2O)_n$, which are related to the size and structure of the cluster, have not yet been satisfactorily elucidated, despite the size dependence of chemical and physical properties being one of the important issues of atmospheric chemistry and cluster science.

In the present study, we investigated the collisions of size- and translational-energy-selected $H^+(H_2O)_n$ ($n = 2-11$) under single-collision conditions with D_2O using guided-ion beam tandem mass spectrometry to clarify the size-specific collisional dynamics of $H^+(H_2O)_n$.

Experimental Section

Figure 1 shows a schematic drawing of the apparatus employed in this experiment. A detailed description of the

* To whom correspondence should be addressed. Fax: +81-462-4702. E-mail: yokada@riken.jp.
† Saitama University.
‡ RIKEN.
§ Waseda University.
⊥ Present address: Graduate School of Bio-Applications and Systems Engineering (BASE), Tokyo University of Agriculture and Technology, 3-5-8 Saiwai-cho, Koganei-shi, Tokyo 183-8509, Japan.
∥ Present address:Research Center for Advanced Manufacturing on Nanoscale Science and Engineering, National Institute of Advanced Industrial Science and Technology (AIST), 1-2-1 Namiki, Tsukuba, Ibaraki 305-8564, Japan.
Present address: Power and Industrial Systems R&D Laboratory, Hitachi, Ltd., 832-2, Horiguchi, Hitachinaka-shi, Ibaraki 312-0034, Japan.

10.1021/jp034129h CCC: $25.00
Published on Web 11/22/2003

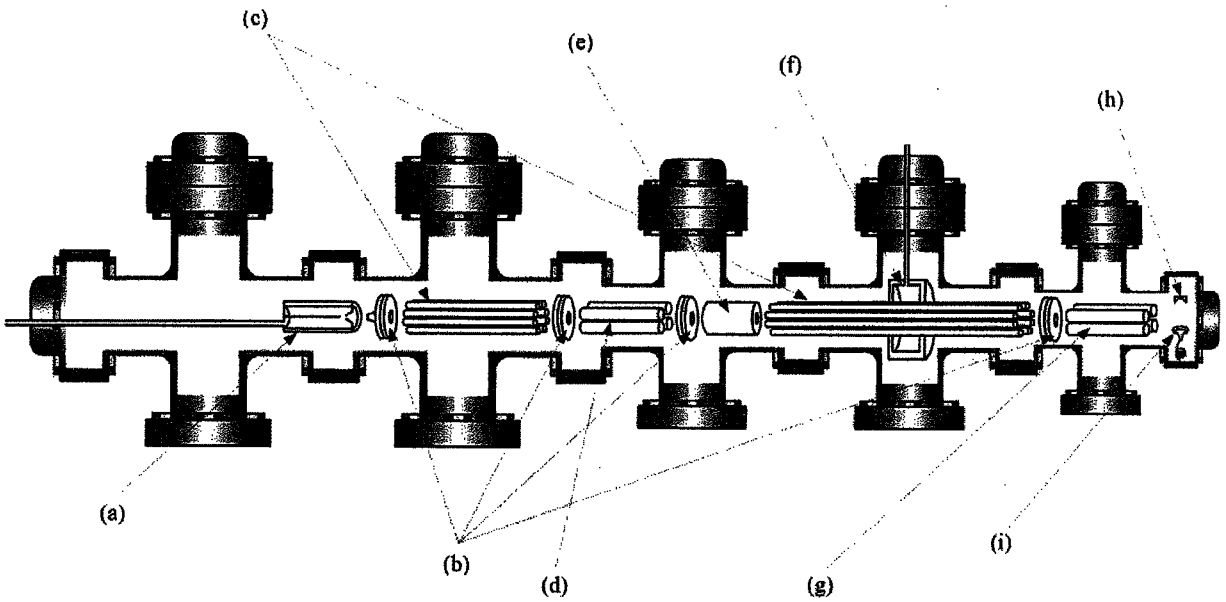

Figure 1. Schematic diagram of the apparatus: (a) corona discharge cluster ion source; (b) ion optics; (c) octopole ion beam guide; (d) quadrupole mass filter; (e) Bessel box energy analyzer; (f) collision cell; (g) quadropole mass analyzer; (h) ion-conversion dynode; (i) secondary electron multiplier.

apparatus and experimental procedures are given elsewhere.[17] Thus, only the details pertinent to this experiment are given here. Nitrogen gas bubbled through a water reservoir at 25 °C was introduced to the corona discharge cluster ion source, and protonated water clusters $H^+(H_2O)_n$ ($n = 2-11$) were produced in a free jet through a nozzle 100 μm in diameter. The cluster ions were focused by a series of ion optics and transferred by the first octopole ion beam guide (OPIG) into a quadrupole mass filter. The size-selected cluster ions passing through the mass filter were focused by a series of ion optics into a Bessel box translational energy analyzer. The translational energy distributions of the size-selected cluster ions were narrowed to approximately 0.03 eV in the center-of-mass frame by the Bessel box translational energy analyzer. The size-selected and translational-energy-selected cluster ions were focused by a series of ion optics into a collision cell equipped with the second OPIG. The collision cell was filled with D_2O gas at pressures of $5-6 \times 10^{-6}$ Torr, where $H^+(H_2O)_n$ was allowed to collide with a D_2O molecule. It was confirmed that the single-collision conditions were fulfilled in the given pressure range because no fragments of multiple-collision product ions were observed. After the collision cell, the cluster ions were focused by ion optics into a quadropole mass spectrometer to be mass-analyzed. The mass-selected ions were detected by a secondary electron multiplier equipped with an ion-conversion dynode. The pressure of the collision cell was monitored with a spinning rotor gauge. The background pressure in the collision cell was less than 2×10^{-7} Torr. The temperature of D_2O gas in the collision cell was 25 °C. The collision energies were controlled by changing the DC potential of the second OPIG. We measured the translational energy distribution of the parent cluster ions and determined the collision energy at the center of the distribution.

Results

Figure 2a–c shows typical mass spectra of the cluster ions produced from $H^+(H_2O)_3$ with and without the target gas D_2O in the collision cell, respectively. The cluster ions observed were the parent ion $H^+(H_2O)_3$ at 55 *m/z* and the daughter ion $H^+(H_2O)_2$ at 37 *m/z* without the target gas, as shown in Figure 2c. With the target gas D_2O in the collision cell, the ions observed were $H^+(H_2O)_2(D_2O)$ at 57 *m/z*, $H^+(H_2O)_2(HDO)$ at 56 *m/z*, $H^+(H_2O)_3$ at 55 *m/z*, $H^+(H_2O)(D_2O)$ at 39 *m/z*, $H^+(H_2O)(HDO)$ at 38 *m/z*, and $H^+(H_2O)_2$ at 37 *m/z*, as shown in Figure 2, parts a and b. We observed the ions containing D_2O at 57 and 39 *m/z* and ions produced by the H/D exchange reaction at 56 and 38 *m/z* in the collision of $H^+(H_2O)_3$ with D_2O. When the collision energy was 1.00 eV, as shown in Figure 2a, these ions drastically decreased compared with those in Figure 2b at the collision energy of 0.10 eV. The products that contained D_2O and HDO molecules and those that did not contain D atoms were also observed for other sizes of protonated water clusters $H^+(H_2O)_n$ ($n = 2-11$). The overlapping mass spectra peaks in Figure 2 were deconvoluted by fitting them

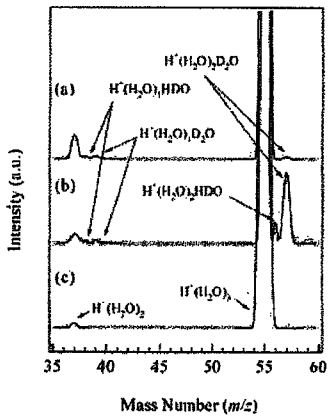

Figure 2. Typical mass spectra of the cluster ions produced from $H^+(H_2O)_3$ with the target gas D_2O in the collision cell: (a) at a collision energy of 1.00 eV in the center-of-mass frame and (b) at a collision energy of 0.10 eV. (c) The mass spectra of the cluster ions produced from $H^+(H_2O)_3$ without the target gas D_2O in the collision cell.

SCHEME 1

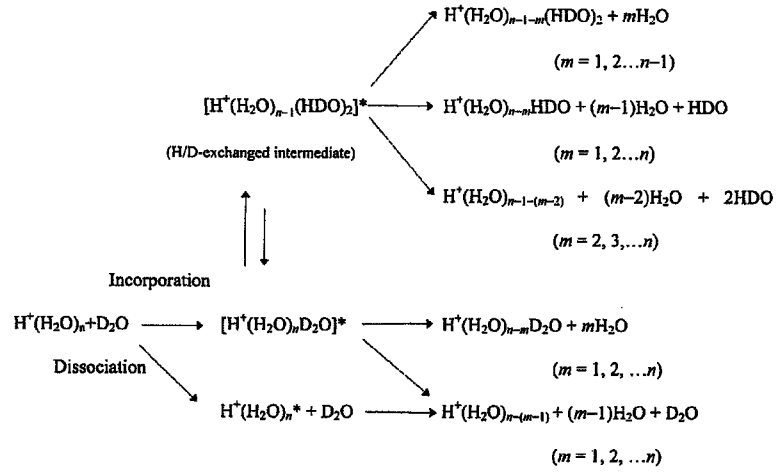

with modified Gaussian functions. The intensities of these peaks were calculated from the integrated area of the modified Gaussians curves.

Discussion

1. Reaction Scheme. In addition to the parent cluster ion, three types of product cluster ions, including the H/D-unexchanged incorporation product containing a D_2O molecule, the H/D-exchanged incorporation product containing HDO molecules, and the dissociation product containing no D atoms, were observed in the collision of $H^+(H_2O)_n$ ($n = 2-11$) with a D_2O molecule, as shown in Figure 2, parts a and b. The reaction mechanism is considered to be as follows.[18] In the incorporation process, the D_2O molecule is first captured by the parent cluster ion to form a hot cluster ion, $H^+(H_2O)_nD_2O^*$. The H/D-exchanged intermediate, $H^+(H_2O)_{n-1}(HDO)_2^*$, is then generated by a randomization of H and D atoms. Subsequently, several H_2O and HDO molecules and one D_2O molecule are released from either of the hot ions. In the dissociation process, the parent cluster ion is heated by collision energy transfer from the D_2O molecule and subsequently releases some H_2O molecules. All of the reaction pathways are described in Scheme 1.

A similar reaction scheme has been proposed in the cases of collision-induced reactions of $H^+(NH_3)_n$ with ND_3 and Ar_n^+ with ^{36}Ar,[17,19] though no proof of a H/D exchange reaction was seen in the former case.

2. Reaction Cross Section. The total cross section σ_n^r was calculated as

$$\sigma_n^r = \frac{k_B T}{Pl} \ln \frac{I_n^0}{I_n^l} \tag{1}$$

where I_n^0 and I_n^l are the intensities of the parent cluster ions at the entrance and exit of the collision cell, respectively, l is the effective path length of the collision cell, P and T are the pressure and temperature of the target gas, respectively, and k_B is the Boltzmann constant. The daughter ions $H^+(H_2O)_n$ ($n < 3$) were observed even without the target gas, as shown in Figure 2c. These ions were produced by unimolecular dissociation of the parent cluster ion. The daughter cluster ions produced by unimolecular dissociation were included in the mass spectra obtained with the target gas. Therefore, the values of I_n^0 and I_n^l can be evaluated by the following equations, in the same manner as that reported in ref 17:

$$I_n^0 = (i_n^P + \sum_{m=1}^{n} i_{n-m}^{Uex} + \sum_{m=1}^{n} i_{n-m}^{Ex} + \sum_{m=1}^{n} i_{n-m}^{D}) S_n^m \tag{2}$$

$$I_n^l = i_n^P \tag{3}$$

and

$$S_n^{n-m} = \frac{i_{n-m}^U}{\sum_{m=0}^{n-1} i_{n-m}^U} \tag{4}$$

where i_n^P, i_{n-m}^{Uex}, i_{n-m}^{Ex}, i_{n-m}^D, and i_{n-m}^U represent the intensities of the parent cluster ions, the cluster ions produced by the loss of m ($m = 1, 2, 3, ..., n$) molecules of H_2O from $H^+(H_2O)_n(D_2O)^*$, those produced by the loss of $m - 1$ ($m = 1, 2, 3, ..., n$) molecules of H_2O and one molecule of HDO from $H^+(H_2O)_{n-1}(HDO)_2^*$, those produced by the loss of $m - 1$ ($m = 1, 2, 3, ..., n$) molecules of H_2O from $H^+(H_2O)_n^*$ observed with the target gas, and those produced by unimolecular dissociation observed without the target gas, respectively. S_n^{n-m} indicates the ratio of clusters of a specific size that were produced by the unimolecular dissociation of $H^+(H_2O)_n$.

For the neutral mixed $(H_2O)_m(D_2O)_n$ cluster, the isotope effect has been experimentally observed and theoretically described using RRKM theory to have a large value of 30%,[20] whereas when the ion product distributions have been analyzed for the collision-induced dissociation of H_2O, HOD, or D_2O from $L^+(L_2O)_n$ (L = H, D; $n = 2-4$), the measured isotope effect has been found to be primarily disregarded (about 3%) in the protonated water cluster.[21] In addition, an ab initio calculation has suggested that $H^+(H_2O)_n$ can overcome negligibly small energy barriers among possible geometric isomers.[12] We therefore assumed that the vibrationally excited water cluster ions were freely interconverted to all of the geometric isomers and that H_2O, D_2O, and HDO molecules were released from the isomers with equal probability. Based on this assumption, the intensity I_n^{In} of the incorporation product was estimated[17] using the following equation from the intensities i_{n-m}^{Uex} and i_{n-m}^{Ex} of the observed daughter ions of $H^+(H_2O)_n(D_2O)^*$ and

$H^+(H_2O)_{n-1}(HDO)_2^*$, respectively:

$$I_n^{In} = \sum_{m=1}^{n} \frac{{}_{n+1}C_m}{{}_nC_m}(i_{n-m}^{Uex} + i_{n-m}^{Ex}) \quad (5)$$

where ${}_nC_m$ represents the combination of numbers given as $n!/(n-m)!m!$. The intensity I_n^D of the dissociation product is given by

$$I_n^D = \sum_{m=1}^{n}\left(i_{n-m}^D - \frac{S_n^{n-m}}{S_n^n} i_n^P - \frac{{}_nC_{m-1}}{{}_nC_m}(i_{n-m}^{Uex} + i_{n-m}^{Ex})\right) \quad (6)$$

Branching fractions R_n^{In} for incorporation and R_n^D for dissociation are given by

$$R_n^{In} = \frac{I_n^{In}}{I_n^{In} + I_n^D} \quad (7)$$

and

$$R_n^D = \frac{I_n^D}{I_n^{In} + I_n^D} \quad (8)$$

respectively. The incorporation cross section, σ_n^{In}, and the dissociation cross section, σ_n^D, are given by

$$\sigma_n^{In} = R_n^{In}\sigma_n^r \quad (9)$$

and

$$\sigma_n^D = R_n^D\sigma_n^r \quad (10)$$

respectively.

3. Collision Energy Dependence of the Reaction Cross Section. Figure 3 shows the collision energy dependence of the reaction cross section in the collision of $H^+(H_2O)_n$ ($n = 4$ and 10) with D_2O. It can be seen from the figure that the total cross sections are strongly dependent on the collision energy. The total cross sections have the largest value of 202 ($n = 4$) and 734 Å^2 ($n = 10$) at 0.05 eV, which is the lowest collision energy used in this study, and decrease rapidly with an increase in the collision energy. In the region of the collision energy higher than approximately 0.40 ($n = 4$) and 0.80 eV ($n = 10$), the total cross sections decrease gradually with an increase in the collision energy and approach the geometrical cross sections of $H^+(H_2O)_n$ with D_2O.

The incorporation and dissociation cross sections in the collision of $H^+(H_2O)_n$ ($n = 4$ and 10) with D_2O are plotted as a function of the collision energy in Figure 3. We find that the incorporation and dissociation cross sections are strongly dependent on the collision energy. At high collision energy, the dissociation cross section is dominant, whereas at low collision energy, the incorporation cross section is dominant. As the collision energy decreases, the incorporation cross section dramatically increases. Similar collision-energy dependences of the reaction cross sections are observed for other sizes of protonated water clusters, $H^+(H_2O)_n$ ($n = 2-11$).

It has been reported[17] that the collision-energy dependence of the reaction probability for the incorporation of ND_3 into $H^+(NH_3)_n$ can be interpreted in terms of the transfer efficiency of the collision energy from the target gas to the internal energy of the parent cluster ion. This previous interpretation suggests

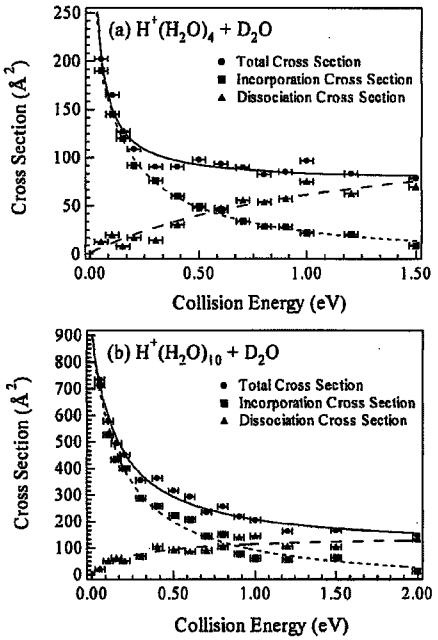

Figure 3. Collision energy dependence of total, incorporation, and dissociation cross sections of (a) $H^+(H_2O)_4 + D_2O$ and (b) $H^+(H_2O)_{10} + D_2O$.

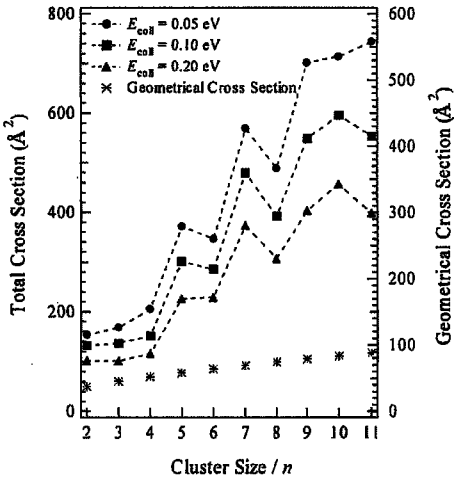

Figure 4. Cluster size dependence of the total cross section for $H^+(H_2O)_n$ ($n = 2-11$) at collision energies of 0.05, 0.10, and 0.20 eV, respectively. The asterisk (*) represents the geometrical cross section estimated from the density of liquid water.

that the D_2O molecule having a large impact parameter in the collision of $H^+(H_2O)_n$ ($n = 2-11$) with D_2O can be captured at low collision energy because the recoil energy decreases due to the small incident angle produced by the orbiting, and consequently, the reaction probability for incorporation increases in such a low-collision energy region. This interpretation suggests that incorporation is the dominant reaction at low collision energy.

4. Size Effect on the Total, Incorporation, and Dissociation Cross Sections. Figure 4 shows the total cross sections as a function of the size of the parent cluster ion. The cross sections increase drastically as the cluster size increases from $n = 4$ to 5, 6 to 7, and 8 to 9. For collision energies of 0.05 and 0.10 eV, the total cross sections have local minima at $n = 6$ and 8. At 0.20 eV, the total cross section at $n = 6$ slightly increases

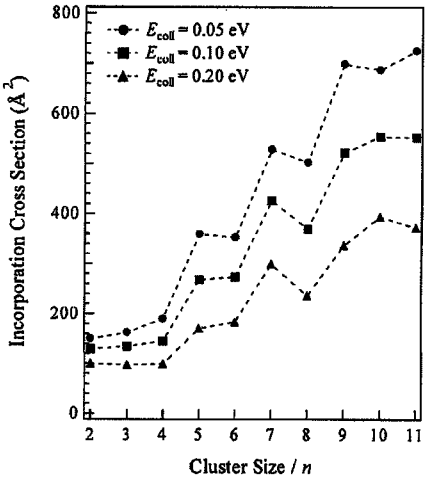

Figure 5. Cluster size dependence of the incorporation cross section for $H^+(H_2O)_n$ ($n = 2-11$) at collision energies of 0.05, 0.10, and 0.20 eV, respectively.

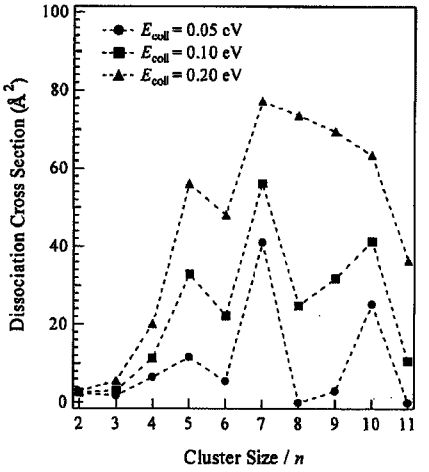

Figure 6. Cluster size dependence of the dissociation cross section for $H^+(H_2O)_n$ ($n = 2-11$) at collision energies of 0.05, 0.10, and 0.20 eV, respectively.

and at $n = 8$ has a local minimum. The geometrical cross sections of the water cluster ions, which are estimated from the density of liquid water, are plotted by the asterisk (*) in Figure 4. The geometrical cross section monotonically increases as the cluster size increases.

Figures 5 and 6 show the incorporation and dissociation cross sections, respectively, as a function of the size of the parent cluster ion. The incorporation cross section indicates a cluster-size dependence similar to that of the total cross section. The incorporation cross section increases drastically as the cluster size increases from $n = 4$ to 5, 6 to 7, and 8 to 9. For the collision energy of 0.05 eV, the incorporation cross section has local minima at $n = 6$ and 8. In addition, the dissociation cross section decreases as the cluster size increases from $n = 5$ to 6 and 7 to 8, as shown in Figure 6.

A cluster is stable when it has a particular "magic number" of constituent molecules. The magic number of the hydrogen-bonded ionic water cluster is associated with the thermodynamical stability due to its specific geometric structure.[22] The water molecule has an extremely high proton affinity and forms a very stable C_{3v} symmetric H_3O^+ hydronium ion with three equivalent protons, known as the Eigen cation.[4] In addition, the water

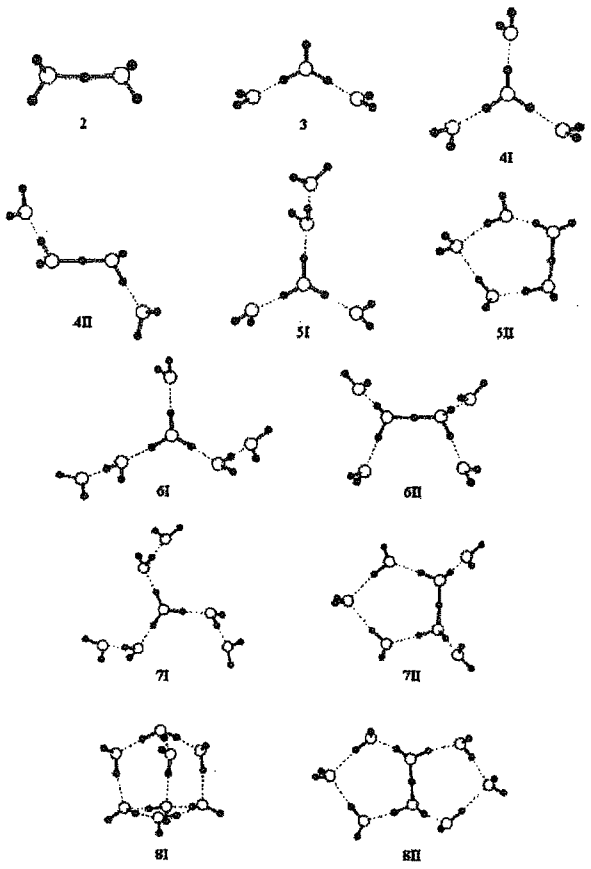

Figure 7. Ab initio optimized geometries of $H^+(H_2O)_n$ for $n = 2-8$. The O and H atoms are denoted by O and ●, respectively.

molecules form a C_2 symmetric $H_5O_2^+$ ion, sometimes called the Zundel cation, in which the proton is equally shared between two water molecules.[5] It has been reported that the respective cores of the Eigen and Zundel cations are completely surrounded by the first water shell at $n = 4$ and 6 and form symmetric $H_3O^+(H_2O)_3$ and $H_5O_2^+(H_2O)_4$, respectively.[22] First-principles Born–Oppenheimer molecular dynamics simulations suggest that the following new features are present for protonated water clusters of a size larger than $n = 7$, in which molecules tend to form two- and three-dimensional networks.[23] Basin-hopping Monte Carlo simulations indicate that water clusters $H^+(H_2O)_8$ have many low-energy structures, and that the most stable isomer has a symmetric cubic structure in which an H_3O^+ core ion and seven water molecules combine in three dimensions.[24] Therefore, the local minima of the cross sections at $n = 6$ and 8 shown in Figures 4–6 suggest that the water clusters $H^+(H_2O)_n$ have stable closed structures such as the symmetric $H_5O_2^+$-centered and cubic structures.

5. Collision Cross Section Calculated from the DFT-Based ab Initio Potential Curve. To obtain the collision cross section for the protonated water cluster $H^+(H_2O)_n$ ($n = 2-8$) with D_2O, density function theory (DFT) calculations were performed using the Gaussian 98 program package[25] with the cc-pVDZ basis set, where the hybrid density functional[26] was used in combination with the Lee, Yang, and Parr correlation functional (B3LYP)[27] to calculate the potential energy curves (PECs) for an attractive collision between $H^+(H_2O)_n$ and D_2O. For $H^+(H_2O)_n$ ($n = 2-8$), we selected the lowest-energy structures for each type of H_3O^+ or $H_5O_2^+$ ion core isomer in the total electronic

TABLE 1: Total Electronic Energy Change (ΔE) of the Clustering $H^+(H_2O) + (n-1)H_2O \rightarrow H^+(H_2O)_n$ ($n = 4-8$)

isomers $H^+(H_2O)_n$	ΔE (kcal/mol)
4 I	−88.9
4 II	−87.2
5 I	−105.0
5 II	−103.5
6 I	−119.7
6 II	−120.1
7 I	−133.0
7 II	−136.3
8 I	−156.4
8 II	−149.7

energy changes of the clustering $H^+(H_2O) + (n-1)H_2O \rightarrow H^+(H_2O)_n$, as shown in Figure 7. The optimized respective structures of $H^+(H_2O)_n$ and D_2O were fixed, and the distance between their centers of mass, R, was varied. The PECs between $H^+(H_2O)_n$ and D_2O, the orientation of which was optimized, were calculated for various Rs.

To calculate the collision cross sections, we used a classical molecular collision theory with the DFT-based ab initio PECs. When an impact parameter b is defined, the effective potential $V_{eff}(R)$ is given by

$$V_{eff}(R) = V(R) + \frac{E_{coll}b^2}{R^2} \tag{11}$$

where $V(R)$ is the potential for collision between $H^+(H_2O)_n$ and D_2O and E_{coll} is the collision energy. At a certain collision energy E_{coll}, the second term on the right-hand side of eq 11 behaves as a potential barrier with an increase in the impact parameter b. The maximum value of the impact parameter, b_{max}, at which the incident molecule having the collision energy E_{coll} can overcome the potential barrier gives the collision cross section. Therefore, the collision cross section, σ_n^{coll}, is given by

$$\sigma_n^{coll} = \pi b_{max}^2 \tag{12}$$

6. Comparison between the Total Cross Section and Collision Cross Section. Table 1 shows the total electronic energy changes (ΔE) of clustering for the H_3O^+ and $H_5O_2^+$ ion core structures shown in Figure 7 at $n = 4-8$. The structures of 6 II and 8 I are more stable than those of 6 I and 8 II by 0.4 and 6.7 kcal/mol, respectively. This result suggests that the $H^+(H_2O)_n$ at $n = 6$ and 8 are favored energetically to take the symmetric $H_5O_2^+$-centered structure 6 II and the cubic structure 8 I, respectively. We selected the most stable $H^+(H_2O)_n$ structures with the lowest ΔE among the clusters illustrated in Figure 7 and calculated the collision cross sections for their most stable structures. Figure 8 shows the collision cross section of $H^+(H_2O)_n$ calculated as a function of the cluster size $n = 2-8$. At the collision energy of 0.05 eV, our calculations show that the collision cross section has local minima at $n = 6$ and 8, at which the structures of 6 II and 8 I are selected as the most stable structures, respectively. At collision energies of 0.10 and 0.20 eV, the collision cross section slightly increases at $n = 6$ and has a local minimum at $n = 8$. These results are consistent with the tendency of the total cross section obtained from the experiment for $n = 6$ and 8. Only the selected structures of 4I, 5I, 6II, 7II, and 8I can reproduce the experimental curve showing local minima at $n = 6$ and 8. This finding therefore suggests that these selected structures are most probable for the $H^+(H_2O)_n$ clusters generated in our experiments. In addition, we conclude that the local minima of the total cross section at $n = 6$ and 8, shown in Figure 4, are related to the small values

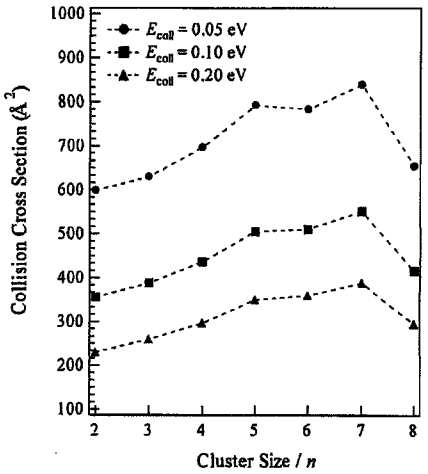

Figure 8. Cluster size dependence of the collision cross section for $H^+(H_2O)_n$ ($n = 2-8$) at collision energies of 0.05, 0.10, and 0.20 eV, respectively.

of the collision cross section for $H^+(H_2O)_6$ and for $H^+(H_2O)_8$ with the closed structures of symmetric $H_5O_2^+$-centered structure 6 II and cubic structure 8 I, respectively. Such closed structures with the small geometrical cross sections cause a decrease in the attractive force between the solvent molecule in the cluster ion and a D_2O molecule and thereby result in small collision cross sections and small total cross sections. In contrast, at $n = 5$ and 7, water cluster ions have the structures 5 I and 7 II, respectively, in which the water molecule present on the outermost shell causes a large geometrical cross section and a large collision cross section.

Conclusions

We investigated the collisions of size- and translational-energy-selected protonated water clusters $H^+(H_2O)_n$ ($n = 2-11$) under a single-collision condition with D_2O using guided-ion beam tandem mass spectrometry. Two types of reactions, incorporation and dissociation, were observed in the collisions, and these reaction cross sections were determined as a function of the collision energy. Our results demonstrated that the incorporation cross section is dominant at low collision energy and that the dissociation cross section is increased as the collision energy increases. The total cross section was found to depend strongly on the cluster size; the cross section drastically increased as the cluster size increased from $n = 4$ to 5, 6 to 7, and 8 to 9 and had local minima at $n = 6$ and 8 at respective collision energies of 0.05 and 0.10 eV. The collision cross section calculated from the DFT-based ab initio potential curve had a tendency similar to the cluster size dependence of the total cross section. From a comparison of the collision cross section with the total cross section, we found that the local minima of the total cross section at $n = 6$ and 8, respectively, originated from the symmetric $H_5O_2^+$-centered structure for $H^+(H_2O)_6$ and the cubic structure for $H^+(H_2O)_8$, which are the most stable energetically.

References and Notes

(1) Viggiano, A. A. *Mass Spectrom. Rev.* **1993**, *12*, 115.
(2) Turco, R. P.; Zhao, J.-X.; Yu, F. *Geophys. Res. Lett.* **1998**, *25*, 635.
(3) Mactaylor, R. S.; Castleman, A. W., Jr. *J. Atmos. Chem.* **2000**, *36*, 23.
(4) Eigen, M. *Ang. Chem., Int. Ed. Eng.* **1964**, *3*, 1.

(5) Zundel, G. In *The Hydrogen Bond-Recent Developments in Theory and Experiment*: Schuster, P., Zundel, G., Sandorfy, C., Eds.; North-Holland: Amsterdam, 1976; Vol. 2, Chapter 15.
(6) Downing, H. D.; Williams, D. *J. Phys. Chem.* **1976**, *80*, 1640.
(7) Giguère, P. A. *J. Chem. Educ.* **1979**, *56*, 571.
(8) Giguère, P. A. *Chem. Phys.* **1981**, *60*, 421.
(9) Librovich, N. B.; Sakun, V. P.; Sokolov, N. D. *Chem. Phys.* **1981**, *60*, 425.
(10) Agmon, N. *J. Phys. Chem.* **1998**, *102*, 192.
(11) Kameda, Y.; Usuki, T.; Uemura, O. *Bull. Chem. Soc. Jpn.* **1998**, *71*, 1305.
(12) Jiang, J.-C.; Wang, Y.-S.; Chang, H.-C.; Lin, S. H.; Lee, Y. T.; Niedner-Schatteburg, G.; Chang, H.-C. *J. Am. Chem. Soc.* **2000**, *122*, 1398.
(13) Honma, K.; Sunderlin, L. S.; Armentrout, P. B. *Int. J. Mass Spectrom. Ion Processes* **1992**, *117*, 237.
(14) Honma, K.; Sunderlin, L. S.; Armentrout, P. B. *J. Chem. Phys.* **1993**, *99*, 1623.
(15) Schindler, T.; Berg, C.; Niedner-Schatteburg, G.; Bondybey, V. E. *J. Chem. Phys.* **1996**, *104*, 3998.
(16) Smith, D.; Adams, N. G.; Henchman, M. J. *J. Chem. Phys.* **1980**, *72*, 4951.
(17) Orii, T.; Okada, Y.; Takeuchi, K.; Ichihashi, M.; Kondow, T. *J. Chem. Phys.* **2000**, *113*, 8026.
(18) Yamaguchi, S.; Kudoh, S.; Okada, Y.; Orii, T.; Takeuchi, K. *Chem. Phys. Lett.* **2002**, *359*, 480.
(19) Ichihashi, M.; Nonose, S.; Nagata, T.; Kondow, T. *J. Chem. Phys.* **1994**, *100*, 6458.
(20) Kay, B. D.; Castleman, A. W., Jr. *J. Chem. Phys.* **1983**, *78*, 4297.
(21) Graul, S. T.; Brickhouse, M. D.; Squires, R. R. *J. Am. Chem. Soc.* **1990**, *112*, 631.
(22) Niedner-Schatteburg, G.; Bondybey, V. E. *Chem. Rev.* **2000**, *100*, 4059.
(23) Cheng, H.-P. *J. Phys. Chem.* **1998**, *102*, 6201.
(24) Singer, S. J.; McDonald, S.; Ojamäe, L. *J. Chem. Phys.* **2000**, *112*, 710.
(25) Frisch, M. J.; Trucks, G. W.; Schlegel, H. B.; Scuseria, G. E.; Robb, M. A.; Cheeseman, J. R.; Zakrzewski, V. G.; Montgomery, J. A., Jr.; Stratmann, R. E.; Burant, J. C.; Dapprich, S.; Millam, J. M.; Daniels, A. D.; Kudin, K. N.; Strain, M. C.; Farkas, O.; Tomasi, J.; Barone, V.; Cossi, M.; Cammi, R.; Mennucci, B.; Pomelli, C.; Adamo, C.; Clifford, S.; Ochterski, J.; Petersson, G. A.; Ayala, P. Y.; Cui, Q.; Morokuma, K.; Malick, D. K.; Rabuck, A. D.; Raghavachari, K.; Foresman, J. B.; Cioslowski, J.; Ortiz, J. V.; Stefanov, B. B.; Liu, G.; Liashenko, A.; Piskorz, P.; Komaromi, I.; Gomperts, R.; Martin, R. L.; Fox, D. J.; Keith, T.; Al-Laham, M. A.; Peng, C. Y.; Nanayakkara, A.; Gonzalez, C.; Challacombe, M.; Gill, P. M. W.; Johnson, B. G.; Chen, W.; Wong, M. W.; Andres, J. L.; Head-Gordon, M.; Replogle, E. S.; Pople, J. A. *Gaussian 98*, revision A.7; Gaussian, Inc.: Pittsburgh, PA, 1998.
(26) Beck, A. D. *J. Chem. Phys.* **1993**, *98*, 5648.
(27) Lee, C.; Yang, W.; Parr, R. G. *Phys. Rev.* **1988**, *37B*, 785.

Theoretical Study on the Excited States of Psoralen Compounds Bonded to a Thymine Residue

A. NAKATA, T. BABA, H. TAKAHASHI, H. NAKAI
Department of Chemistry, School of Science and Engineering, Waseda University, Tokyo 169-8555, Japan

Received 30 April 2003; Accepted 17 August 2003
Published online 18 November 2003 in Wiley InterScience (www.interscience.wiley.com). DOI 10.1002/jcc.10380

Abstract: Time-dependent density functional theory calculations have been performed for the excited states of psoralen, 5-methoxypsoralen, and 8-methoxypsoralen in systems and furan and pyrone monoadducts bonded to a thymine residue. The theoretical assignments to ultraviolet (UV) absorption spectra of isolated systems have been performed. The present calculations have clarified that the excitation energies of the first singlet excited (S_1) state of monoadducts are blue-shifted compared with the isolated systems. It is shown that, in particular, the S_1 excitation energy of the pyrone monoadduct is significantly blue-shifted and, therefore, the pyrone monoadduct is not excited by UV-A light (300–400 nm), which is used in the photochemotherapy.

 J Comput Chem 25: 179–188, 2004

Key words: psoralen compounds; thymine residue; density functional theory calculations

Introduction

Psoralen (7-H-furo[3,2-g][1]benzopyran-7-one) compounds are a class of drugs used to treat dermatologic diseases, such as psoriasis and vitiligo, by phototherapy.[1] In these diseases, there is loss of control of DNA synthesis, and consequently, cellular proliferation. Psoralens, the structure of which is given in Figure 1, are generally thought to inhibit the rogue hyperproliferation of DNA by bridging DNA strands via the pyrimidine bases. The therapy uses near-UV-A light (UV-A; 300–400 nm) and so is called PUVA (Psoralen-UV-A) therapy. In the PUVA therapy, the psoralens insert themselves between adjacent thymine base pairs in the DNA duplex and, upon the UV-A irradiation, photoreact with two pyrimidine bases to form a crosslink between the two strands of DNA.

The photoreactive process is thought to involve two steps, as illustrated in Figure 1.[1] In the first step, the psoralen compound absorbs a photon and forms a monoadduct. The psoralen compounds can form two types of monoadducts, the furan monoadduct and the pyrone monoadduct, by reacting with the C5–C6 double bond of the thymine via the C4′–C5′ double bond in the furan ring or the C3–C4 double bond in the pyrone ring. In the second step, the monoadduct also absorbs a photon, inducing the other photoreactive double bond of the monoadduct to react with a thymine on the opposite strand of DNA. Therefore, in the second stage a diadduct that crosslinks the DNA is formed.[1–3] However, the formation of the diadduct severely damages the DNA, requiring a long time for its restoration. The diadduct is thought to cause adverse effects and is considered to be a carcinogen or mutagen.[1–3]

Several studies have suggested that, whereas the furan monoadduct forms a diadduct, the pyrone monoadduct does not.[4,5] To understand their different mechanisms, it is important to know the electronic structures of the furan and pyrone monoadducts in the ground and excited states, in addition to knowing those of the isolated psoralen compounds. However, to our knowledge, experimental and theoretical studies on the excited states have only been done for the isolated psoralens.[6–10] Furthermore, the theoretical studies, although they have a historical importance, adopted semiempirical calculations.

In the present study, we performed time-dependent density functional theory (TDDFT) calculations of psoralen, 5-methoxypsoralen (5-MOP), and 8-methoxypsoralen (8-MOP) in isolated systems and in furan and pyrone monoadducts to the thymine residue. Based on the TDDFT calculations, new assignments of the UV absorption spectra have been proposed for the isolated systems. For the monoadducts, we investigated the effect of the bonding to the thymine residue on the electronic structures in the ground and excited states. The difference between furan and pyrone monoadducts is also discussed.

Correspondence to: H. Nakai; e-mail: nakai@waseda.jp

Contract/grant sponsor: Grant-in-Aid for Young Scientists (A) [from the Japanese Society for the Promotion of Science (JSPS)]; contract/grant number: KAKENHI 14703005

Contract/grant sponsor: Waseda University Grant for Special Research Projects

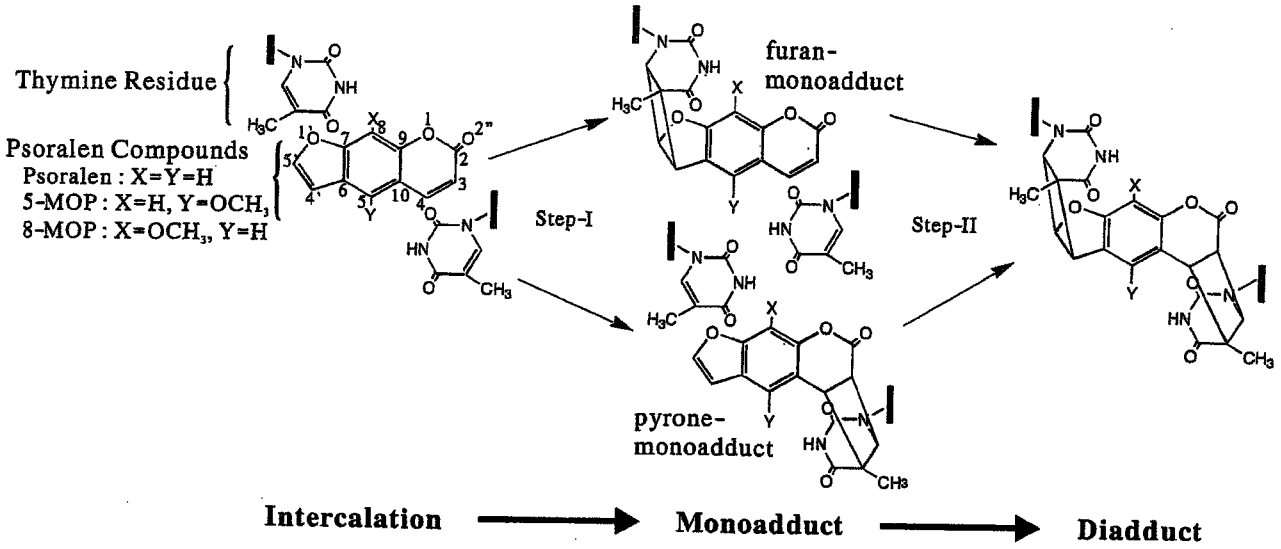

Figure 1. Photoaddition scheme of psoralen compound to DNA.

Computational Details

Electronic structures of psoralen compounds in the ground and excited states were examined by the DFT and TDDFT calculations. We investigated nonsubstituted psoralen, 5-MOP, and 8-MOP in isolated systems and their pyrone and furan monoadducts, which are bound to a thymine residue at the C3–C4 and C4′–C5′ sites, respectively. The B3LYP hybrid functional,[11] which comprises the HF (exact) exchange, the Slater exchange,[12] the Becke (B88) exchange,[13] the Vosco–Wilk–Nusair (VWN) correlation,[14] and the Lee–Yang–Parr (LYP) correlation[15] functionals, was adopted in the DFT and TDDFT calculations.

The basis sets used for H, C, and O were the correlation-consistent polarization plus valence double zeta (cc-pVDZ) sets of Dunning.[16]

The geometries of the psoralen compounds in the ground state were optimized at the B3LYP/cc-pVDZ level. To our knowledge, there are no experimental data concerning the geometries of combined systems, except for the interplanar angle between 8-MOP and thymine residue.[3] All the DFT and TDDFT calculations were performed using a Gaussian 98 program.[17]

Results and Discussion

Ground State of Isolated Psoralen Compounds

Table 1 compares the geometrical parameters of psoralen, 5-MOP, and 8-MOP in their ground state. Because the benzene ring is a resonance hybrid, all the carbon to carbon distances in the ring, that is C5–C6, C6–C7, C7–C8, C8–C9, C9–C10, and C10–C5, are in the range of 1.39–1.42 Å, which corresponds to the conjugated bond. On the other hand, as neither the pyrone ring nor the furan ring is a resonance hybrid, the C3–C4 and C4′–C5′ bond lengths are about 1.35 Å, which corresponds to the C=C double bond, while the other C—C bond lengths, C2–C3, C4–C10, and C6–C4′, are about 1.45 Å, which is only slightly shorter than the C—C single bond.

The methoxy group lengthens its neighboring bonds only slightly: in 5-MOP, the C5–C10 and C5–C6 bonds are elongated by 0.014 and 0.013 Å, respectively, and in 8-MOP, the C7–C8 and C8–C9 bonds are elongated by 0.013 and 0.014 Å, respectively. These geometrical changes are due to π electron donation from the methoxy group to the benzene ring.

Figure 2 shows the contour maps of the four highest occupied and three lowest unoccupied Kohn–Sham (KS) orbitals[18] of pso-

Table 1. Bond Distances in Isolated Psoralen, 5-MOP and 8-MOP Molecules (in Å).

	Psoralen	5-MOP[a]	8-MOP[a]
O1—C2	1.400	1.403 (+0.003)	1.396 (−0.004)
C2—C3	1.460	1.457 (−0.003)	1.461 (+0.001)
C3—C4	1.353	1.355 (+0.002)	1.353 (0.000)
C4—C10	1.443	1.440 (−0.003)	1.444 (+0.001)
C10—C9	1.422	1.418 (−0.004)	1.416 (−0.006)
C9—O1	1.366	1.363 (−0.003)	1.366 (0.000)
C2—O2″	1.204	1.205 (+0.001)	1.205 (+0.001)
C10—C5	1.405	1.419 (+0.014)	1.404 (−0.001)
C5—C6	1.395	1.408 (+0.013)	1.393 (−0.002)
C6—C7	1.416	1.421 (+0.005)	1.417 (+0.001)
C7—C8	1.388	1.387 (−0.001)	1.401 (+0.013)
C8—C9	1.395	1.393 (−0.002)	1.412 (+0.017)
C7—O1′	1.363	1.363 (0.000)	1.373 (+0.010)
C6—C4′	1.447	1.456 (+0.009)	1.447 (0.000)
C4′—C5′	1.356	1.354 (−0.002)	1.354 (−0.002)
C5′—O1′	1.379	1.375 (−0.004)	1.376 (−0.003)

[a]Differences from the bond distances in psoralen are shown in parentheses.

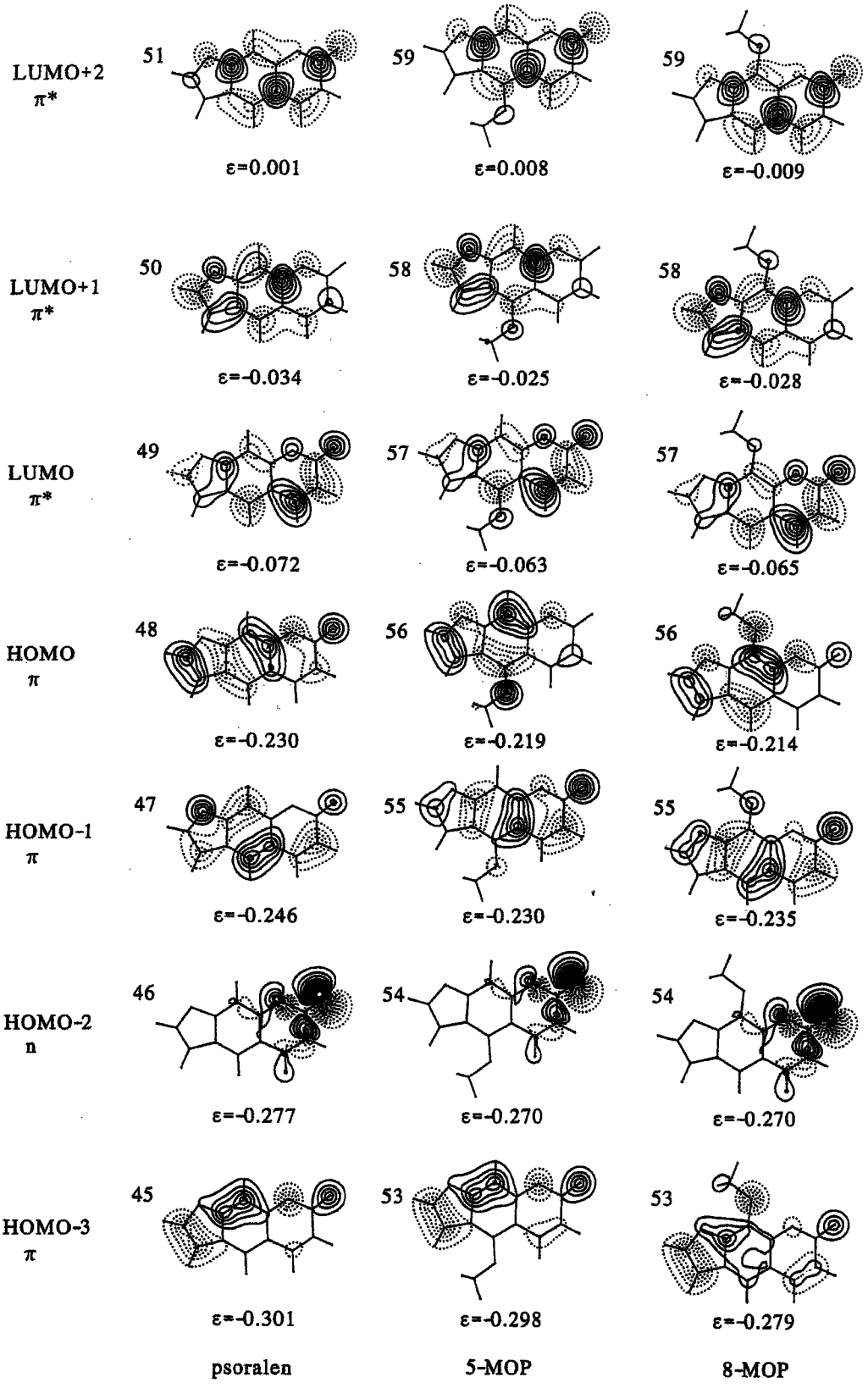

Figure 2. Contour maps of KS orbitals of psoralen, 5-MOP, and 8-MOP at contour intervals of 0.02. Orbital energies α are given in hartree.

ralen, 5-MOP, and 8-MOP. The numbers of the KS orbitals correspond to the order of the KS orbital energies. The low-energy excited states, which will be discussed in the next subsection, mainly have characteristics of the transitions between these occupied and unoccupied KS orbitals. The physical and chemical interpretation of the KS orbitals and their energies is a long-standing problem of the one-electron KS-type DFT approach. However, it has been argued extensively[19–21] that the KS orbitals are physically meaningful owing to the KS potential, which incorporates important terms such as the Coulomb hole potential and the kinetic correlation potential. The interpretation of the KS orbital energies in terms of approximate ionization potentials has been recently discussed.[22]

The 45th, 47th, and 48th occupied orbitals in psoralen have a π bonding nature, the 46th occupied orbital has a nonbonding nature, and the 49th, 50th, and 51st unoccupied orbitals have a π^* antibonding nature. The 48th orbital, which is the highest occupied molecular orbital (HOMO), has the largest amplitude at the C4′–C5′ bond, while the 49th orbital, which is the lowest unoccupied molecular orbital (LUMO), has the largest amplitude at the C3–C4 bond. The orderings of the KS orbitals of 5-MOP and 8-MOP are the same as that in psoralen, whereas the shape of the KS orbitals is slightly changed by the presence of the methoxy group. Because of the π electron donation from the methoxy group, the KS orbital energies in 5-MOP and 8-MOP are shifted, giving them higher energy than those in psoralen.

Excited States of Isolated Psoralen Compounds

Figure 3 shows the absorption spectra of (a) psoralen, (b) 5-MOP, and (c) 8-MOP. The upper spectra were obtained by experimental measurement in cyclohexane solution,[23] whereas the lower ones are theoretical spectra calculated by the TDDFT method. The theoretical spectra were obtained using a Lorenzian-type function for the line shape with the half-width at a half-maximum of 10 nm. The white circles in the theoretical spectra represent the positions of n–π^* excited states. Table 2 lists the excitation energy, oscillator strength, and main configuration of psoralen, 5-MOP, and 8-MOP.

The experimental absorption spectrum of psoralen has five bands near 330 nm (**A**), 290 nm (**B**), 260 nm (**C**), 250 nm (**D**), and 210 nm (**E**). The **A** band is weak and broad. From its peak position and intensity, this band can be assigned to the transition to the $2^1A'$ state, that is excitation from the π orbital of the C4′–C5′ bond in the furan ring to the π^* orbital of the C3–C4 bond in the pyrone ring. Because only the transition to the $2^1A'$ state occurs on UV-A irradiation, the electronic structure of the $2^1A'$ state is of particular interest for clarifying the mechanism of the PUVA therapy.

The **B** band has a strong intensity and it has fine structure. The **B** band was resolved into three peaks, at 296, 285, and 275 nm, in experimentation. In this region, the present TDDFT calculation gives only two states, the $3^1A'$ and $1^1A''$ states. Transition to the $3^1A'$ state gives a large oscillator strength because of its π–π^* excitation character. On the other hand, the oscillator strength of the transition to the $1^1A''$ state is almost zero because of the n–π^* excitation character. Therefore, the strong **B** band can be assigned to the transition to the $3^1A'$ state. The fine structure of this band is thought to be vibrational. Evidence for this is the absence of fine

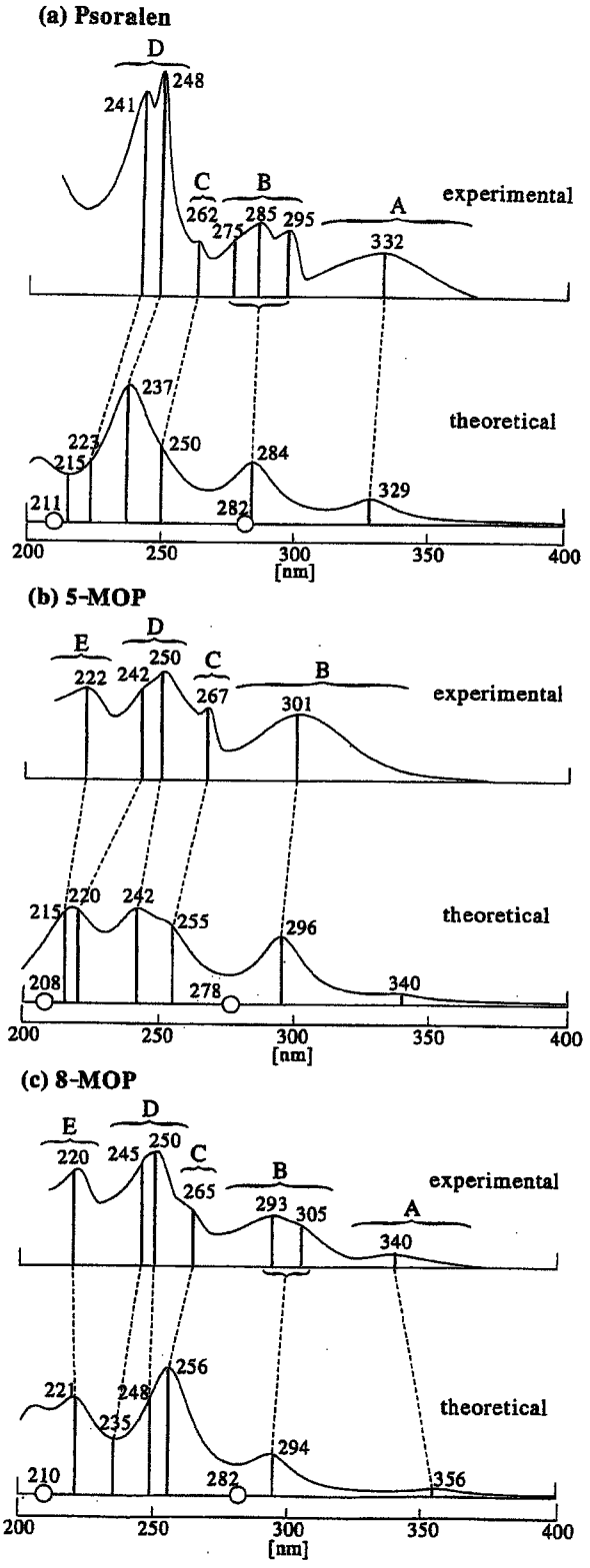

Figure 3. Experimental and theoretical spectra of psoralen, 5-MOP, and 8-MOP.

Table 2. Excitation Energy, Oscillator Strength, and Main Configuration of Psoralen, 5-MOP, and 8-MOP.

	Calc.				Exptl.[b]		
Compound	State	Main configuration	Excitation energy[a]	Oscillator strength	Excitation energy[a]	Band	Oscillator strength
Psoralen	X^1A'		0.000				
	$2^1A'$	48 → 49	3.770 (329)	0.0746	3.734 (332)	A	weak
					4.509 (275)	B	shoulder
	$3^1A'$	47 → 49	4.363 (284)	0.1958	4.350 (285)	B	middle
					4.189 (296)	B	middle
	$1^1A''$	46 → 49	4.400 (282)	0.0000			
	$4^1A'$	48 → 50	4.966 (250)	0.0824	4.732 (262)	C	weak
	$5^1A'$	47 → 50	5.237 (237)	0.4509	4.999 (248)	D	strong
	$6^1A'$	45 → 49	5.560 (223)	0.0216	5.145 (241)	D	
	$7^1A'$	48 → 51	5.760 (215)	0.1276	5.904 (210)	E	shoulder[c]
	$2^1A''$	46 → 50	5.888 (211)	0.0000			
5-MOP	X^1A'		0.000				
	$2^1A'$	56 → 57	3.650 (340)	0.0231			
	$3^1A'$	55 → 57	4.191 (296)	0.2551	4.119 (301)	B	strong
	$1^1A''$	54 → 57	4.460 (278)	0.0000			
	$4^1A'$	56 → 58	4.867 (255)	0.1964	4.644 (267)	C	weak
	$5^1A'$	55 → 58	5.131 (242)	0.2612	4.959 (250)	D	strong
	$6^1A'$	53 → 57	5.633 (220)	0.1923	5.123 (242)	D	shoulder
	$7^1A'$	55 → 59	5.761 (215)	0.1478	5.585 (222)	E	strong
	$2^1A''$	54 → 58	5.958 (208)	0.0000			
8-MOP	X^1A'		0.000				
	$2^1A'$	56 → 57	3.479 (356)	0.0230	3.647 (340)	A	very weak
					4.065 (305)	B	shoulder
	$3^1A'$	55 → 57	4.219 (294)	0.1390	4.232 (293)	B	middle
	$1^1A''$	54 → 57	4.401 (282)	0.0000			
	$4^1A'$	56 → 58	4.846 (256)	0.4709	4.679 (265)	C	shoulder
	$5^1A'$	55 → 58	5.005 (248)	0.0679	4.959 (250)	D	strong
	$6^1A'$	53 → 57	5.269 (235)	0.0021	5.061 (245)	D	shoulder
	$7^1A'$	56 → 59	5.621 (221)	0.3058	5.636 (220)	E	strong
	$2^1A''$	54 → 58	5.917 (210)	0.0000			

[a]Wavelength corresponding to the excitation energy is shown in parentheses in nm.
[b]Measurement in cyclohexane solution.[24]
[c]Measurement in HFP solution.[24]

structure in polar solvents such as dioxane, methanol, and acetonitrile.[23]

The **C** band appears as a shoulder on the longer wavelength side of the strong **D** band. The **D** band has two peaks, a strong one at 248 nm and a weak one at 241 nm. In the wavelength region of 220–270 nm, three excited states with π–π^* character, namely, $4^1A'$, $5^1A'$, and $6^1A'$, were obtained by the present TDDFT calculation. The 248-nm peak of the **D** band can be assigned to the transition to the $5^1A'$ state, because its oscillator strength was calculated to be the largest. The transitions to the $4^1A'$ and $6^1A'$ states, which are a factor smaller in absorption intensities than transitions to the $5^1A'$ state, can be assigned to the **C** band and the 241-nm peak of the **D** band, respectively.

The **E** band, which was obtained in 1,1,1,3,3,3-hexafluoro-2-propanol (HFP), not in cyclohexane solution, appears near 210 nm as a shoulder on the long wavelength side of a very strong band. In the wavelength region around 210 nm, two excited states, $7^1A'$ and $2^1A''$, are obtained. Because the $2^1A''$ state has an n–π^* character, the oscillator strength is zero, so the **E** band can be assigned to the transition to the $7^1A'$ state.

In the experimental spectrum of 5-MOP, the **A** band was not measured. However, the TDDFT calculation gave a very weak band at 340 nm, which corresponds to the transition to the $2^1A'$

Table 3. Reaction Heats of the Reaction between the Psoralens and the Thymine (in kcal/mol).

	Reaction heat	
	Furan-monoadduct	Pyrone-monoadduct
Psoralen	8.58	12.06
5-MOP	8.48	11.03
8-MOP	7.86	11.84

Table 4. Bond Distances in Furan- and Pyrone-Monoadduct of Psoralen, 5-MOP, and 8-MOP Molecules (in Å).

		Psoralen			5-MOP			8-MOP		
		Isolated	Furan[a]	Pyrone[b]	Isolated	Furan[a]	Pyrone[b]	Isolated	Furan[a]	Pyrone[b]
Psoralen part	O1—C2	1.400	1.408 (+0.008)	1.362 (−0.038)	1.403	1.411 (+0.008)	1.364 (−0.039)	1.396	1.408 (+0.012)	1.359 (−0.037)
	C2—C3	1.460	1.457 (−0.003)	1.508 (+0.048)	1.457	1.454 (−0.003)	1.507 (+0.050)	1.461	1.457 (−0.004)	1.507 (+0.046)
	C3—C4	1.353	1.356 (+0.003)	1.551 (+0.198)	1.355	1.357 (+0.002)	1.548 (+0.193)	1.353	1.356 (+0.003)	1.550 (+0.197)
	C4—C10	1.443	1.439 (−0.004)	1.508 (+0.065)	1.440	1.437 (−0.003)	1.500 (+0.060)	1.444	1.440 (−0.004)	1.508 (+0.064)
	C10—C9	1.422	1.415 (−0.007)	1.413 (−0.009)	1.418	1.409 (−0.009)	1.407 (−0.011)	1.416	1.415 (−0.001)	1.409 (−0.007)
	C9—O1	1.366	1.359 (−0.007)	1.393 (+0.027)	1.363	1.357 (−0.006)	1.393 (+0.030)	1.366	1.361 (−0.005)	1.392 (+0.026)
	C2—O2″	1.204	1.204 (0.000)	1.204 (0.000)	1.205	1.204 (−0.001)	1.204 (−0.001)	1.205	1.204 (−0.001)	1.205 (0.000)
	C10—C5	1.405	1.413 (+0.008)	1.401 (−0.004)	1.419	1.430 (+0.011)	1.408 (−0.011)	1.404	1.412 (+0.008)	1.399 (−0.005)
	C5—C6	1.395	1.383 (−0.012)	1.400 (+0.005)	1.408	1.399 (−0.009)	1.411 (+0.003)	1.393	1.383 (−0.010)	1.398 (+0.005)
	C6—C7	1.416	1.410 (−0.006)	1.410 (−0.006)	1.421	1.416 (−0.005)	1.413 (−0.008)	1.417	1.407 (−0.010)	1.410 (−0.007)
	C7—C8	1.388	1.389 (+0.001)	1.388 (0.000)	1.387	1.382 (−0.005)	1.388 (+0.001)	1.401	1.395 (−0.006)	1.401 (0.000)
	C8—C9	1.395	1.401 (+0.006)	1.395 (0.000)	1.393	1.399 (+0.006)	1.392 (−0.001)	1.412	1.411 (−0.001)	1.412 (0.000)
	C7—O1′	1.363	1.366 (+0.003)	1.364 (+0.001)	1.363	1.366 (+0.003)	1.364 (+0.001)	1.373	1.366 (−0.007)	1.374 (+0.001)
	C6—C4′	1.447	1.508 (+0.061)	1.446 (−0.001)	1.456	1.515 (+0.059)	1.452 (−0.004)	1.447	1.508 (+0.061)	1.446 (−0.001)
	C4′—C5′	1.356	1.557 (+0.201)	1.358 (+0.002)	1.354	1.555 (+0.201)	1.356 (+0.002)	1.354	1.557 (+0.203)	1.356 (+0.002)
	C5′—O1′	1.379	1.435 (+0.056)	1.378 (−0.001)	1.375	1.433 (+0.058)	1.374 (−0.001)	1.376	1.435 (+0.059)	1.376 (0.000)
Interacting part	C4′—C15		1.580			1.601			1.588	
	C5′—C16		1.571			1.560			1.569	
	C4—C15			1.570			1.597			1.591
	C3—C16			1.591			1.577			1.569
Thymine part	N1—C2	1.391	1.368 (−0.023)	1.371 (−0.020)	1.391	1.371 (−0.020)	1.372 (−0.019)	1.391	1.369 (−0.022)	1.370 (−0.021)
	C2—N3	1.387	1.409 (+0.022)	1.408 (+0.021)	1.387	1.410 (+0.023)	1.408 (+0.021)	1.387	1.406 (+0.019)	1.408 (+0.021)
	N3—C4	1.407	1.378 (−0.029)	1.378 (−0.029)	1.407	1.377 (−0.030)	1.380 (−0.027)	1.407	1.380 (−0.027)	1.378 (−0.029)
	C4—C5	1.470	1.522 (+0.052)	1.521 (+0.051)	1.470	1.523 (+0.053)	1.524 (+0.054)	1.470	1.523 (+0.053)	1.521 (+0.051)
	C5—C6	1.354	1.564 (+0.210)	1.558 (+0.204)	1.354	1.562 (+0.208)	1.562 (+0.208)	1.354	1.565 (+0.211)	1.558 (+0.204)
	C6—N1	1.380	1.442 (+0.062)	1.448 (+0.068)	1.380	1.439 (+0.059)	1.443 (+0.063)	1.380	1.444 (+0.064)	1.448 (+0.068)
	C2—O7	1.216	1.216 (0.000)	1.215 (−0.001)	1.216	1.214 (−0.002)	1.215 (−0.001)	1.216	1.218 (+0.002)	1.216 (0.000)
	C4—O8	1.220	1.218 (−0.002)	1.219 (−0.001)	1.220	1.220 (0.000)	1.219 (−0.001)	1.220	1.218 (−0.002)	1.219 (−0.001)
	C5—C9	1.500	1.529 (+0.029)	1.530 (+0.030)	1.500	1.528 (+0.028)	1.527 (+0.027)	1.500	1.527 (+0.027)	1.530 (+0.030)

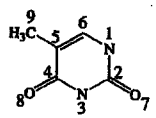

[a]Bond distances in furan-monoadduct. Differences with respect to the isolated compounds are shown in parentheses.
[b]Bond distances in pyrone-monoadduct. Differences with respect to the isolated compounds are shown in parentheses.

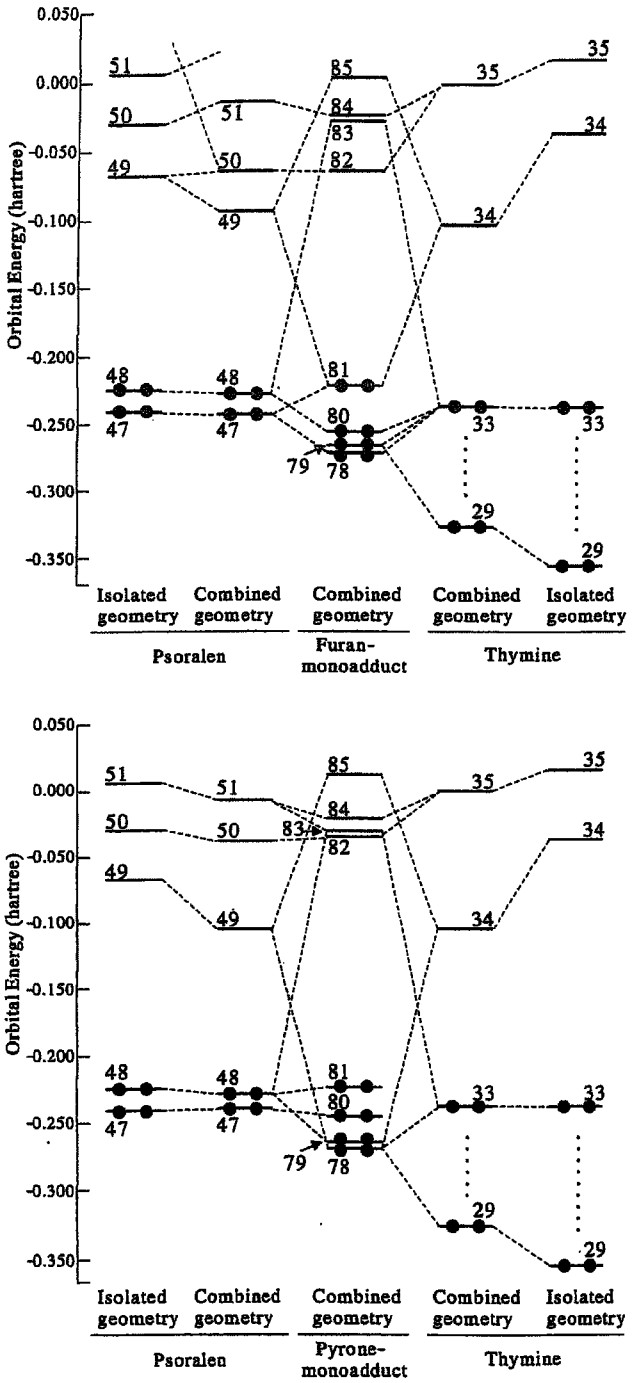

Figure 4. Orbital correlation diagrams for the interaction of psoralen and thymine in the furan and pyrone monoadducts.

state. As in the case of psoralen, the $2^1A'$ state has an excitation character, mainly from the π orbital of the C4′–C5′ bond in the furan ring to the π^* orbital of the C3–C4 bond in the pyrone ring. Thus, we believe that more sensitive measurements will give a weak and broad band due to the transition to the $2^1A'$ state.

Because the methoxy group donates π electrons, the other bands, **B**, **C**, **D**, and **E**, are red-shifted compared with those in psoralen. The **B** band no longer has a fine structure. All the peaks in the **B**, **C**, **D**, and **E** bands can be assigned to the π–π^* excited state.

For 8-MOP, five bands (**A**–**E**) are observed. Their peak positions are also red-shifted compared with those in psoralen. The weak and broad **A** band at 340 nm can be assigned to the transition to the $2^1A'$ state. The $2^1A'$ state has π–π^* excitation character from the C4′–C5′ and the C3–C4 bond.

In the **B** band, the peak at 305 nm appears as a shoulder on the peak at 293 nm. The peak at 293 nm can be assigned to the transition to the $3^1A'$ state. The peak at 305 nm can be assigned to vibrational structure or to the transition to the $1^1A''$ state, which has an oscillator strength of almost zero.

The **C**, **D**, and **E** bands can be assigned to the π–π^* excitation states from $4^1A'$ to $7^1A'$. As for the excitation energies, the peak at 265 nm in the **C** band and the peak at 250 nm in the **D** band should be assigned to the $4^1A'$ and $5^1A'$ states, respectively. However, the oscillator strength calculated for the $4^1A'$ state is a factor larger than that for the $5^1A'$ state. Thus, the opposite assignment should be made. The peak at 245 nm in the **D** band and the peak at 220 nm in the **E** band can be easily assigned to the $6^1A'$ and $7^1A'$ states, respectively.

Ground State of Psoralen Compounds Bonded to the Thymine Residue

We have optimized the geometries of furan and pyrone monoadducts. By using the total energies at the optimized geometries, we obtained the reaction heats of the additions between the psoralens and the thymine leading the furan and pyrone monoadducts, which are shown in Table 3. These reactions are all endothermic in the ground state. All the furan monoadducts have lower reaction heats than the pyrone monoadducts. Only one experimental data concerning the geometries of monoadducts is the interplanar angle between 8-MOP and thymine residue,[3] as far as we know. The calculated value of 53 degrees agrees well with the experimental data of 44–53 degrees.

Table 4 shows the bond lengths of furan and pyrone monoadducts of psoralen compounds in the ground state. In Table 4, the compounds are divided into three parts: psoralen, thymine, and their interacting regions. The changes in bond length from the isolated compounds are shown in parentheses. Because the furan monoadducts are formed by pericyclic reaction between the C4′–C5′ double bond of psoralens and the C5–C6 double bond of thymine, both bonds are elongated by more than 0.2 Å on reaction. This affects the adjacent bonds, i.e., C6–C4′ and C5′–O1′ in psoralens and C4–C5 and C6–N1 in thymine, which are elongated by about 0.06 Å. Similarly, in the pyrone monoadducts, the C3–C4 bond of psoralens, and the C5–C6 bond of thymine are elongated by about 0.2 Å. The adjacent bonds are also elongated by 0.046 to 0.068 Å. Note that in the pyrone monoadducts, the O1–C2 bond is decreased by about 0.04 Å and the C9–O1 bond is increased by about 0.03 Å.

Although the isolated psoralen compounds have 12 π electrons, both furan and pyrone monoadducts have 10 π electrons. Particularly in pyrone monoadducts, the 10 π electrons comprise eight π electrons in the furan and benzene rings and two π electrons in the

Table 5. Excited Energy, Oscillator Strength, and Main Configurations of Furan- and Pyrone-Monoadducts; Psoralen, 5-MOP, and 8-MOP.

			Calc.						Calc.		
	Compound	State	Main configuration	Excitation energy[a]	Oscillator strength		Compound	State	Main configuration	Excitation energy[a]	Oscillator strength
Furan-monoadduct	Psoralen	X^1A		0.000		Pyrone-monoadduct	Psoralen	X^1A		0.000	
		2^1A	81→82	3.996 (310)	0.3222			2^1A	81→83	4.491 (276)	0.0131
		3^1A	80→82	4.443 (279)	0.0163			3^1A	81→82	4.761 (260)	0.1710
		4^1A	77→82	4.466 (278)	0.0000			4^1A	81→84	4.854 (255)	0.0006
		5^1A	81→84	4.756 (261)	0.0071			5^1A	79→84	5.007 (248)	0.0092
		6^1A	80→82	4.925 (252)	0.0519			6^1A	80→82	5.189 (239)	0.0283
	5-MOP	X^1A		0.000			5-MOP	X^1A		0.000	
		2^1A	89→90	4.053 (306)	0.2669			2^1A	89→90	4.336 (286)	0.0655
		3^1A	88→90	4.130 (300)	0.0961			3^1A	89→92	4.651 (267)	0.0013
		4^1A	89→91	4.497 (276)	0.0020			4^1A	88→90	4.760 (260)	0.0591
		5^1A	86→90	4.526 (274)	0.0001			5^1A	89→91	4.956 (250)	0.0803
		6^1A	88→91	4.801 (258)	0.0088			6^1A	87→92	5.037 (246)	0.0399
	8-MOP	X^1A		0.000			8-MOP	X^1A		0.000	
		2^1A	89→90	3.987 (311)	0.2833			2^1A	89→90	4.248 (292)	0.0508
		3^1A	88→90	4.062 (305)	0.0364			3^1A	89→92	4.483 (277)	0.0408
		4^1A	86→90	4.470 (277)	0.0003			4^1A	89→92	4.704 (264)	0.1202
		5^1A	89→91	4.641 (267)	0.0129			5^1A	87→92	4.990 (248)	0.0343
		6^1A	89→92	4.826 (257)	0.0414			6^1A	88→90	5.030 (247)	0.0773

[a]Wavelength corresponding to the excitation energy is shown in parentheses in nm.

carbonyl group on the pyrone ring. The geometrical changes in the O1–C2 and C9–O1 bonds reflect this arrangement. As in psoralen, in both 5-MOP and 8-MOP, the furan monoadduct has 10 π electrons in the pyrone and benzene rings and the pyrone monoadduct has eight π electrons in the furan and benzene rings.

Figure 4 shows the orbital correlation diagrams[24] for the interaction of psoralen and thymine in the furan and pyrone monoadducts reactants. Two kinds of KS orbital energy levels are shown for psoralen and thymine; that is, energy levels in the optimized geometries for the isolated and combined systems. The differences between the two energy levels reflect the effects of the geometry relaxation by the addition reaction. In Figure 4a and b, the energy level of the HOMO of the thymine, which has a π-bonding character of the C5–C6 bond, does not change much. The LUMO of thymine, which is a π^* orbital of the C5–C6 bond, is largely shifted forward lower energy; namely, 0.067 and 0.069 hartree, respectively. The energy shifts of the HOMO of psoralen in Figure 4a and b are 0.003 and 0.005 hartree, respectively, which are also not large. On the other hand, the energies of the LUMO of psoralen shift a lot to the higher energy side, 0.026 and 0.039 hartree, respectively.

In Figure 4a, because the C4′–C5′ bond is combined with the thymine residue, the HOMO of psoralen, which has large amplitude at the C4′–C5′ bond, has no influence on the HOMO of the furan monoadduct. The LUMO is represented by a combination of the 50th orbital of psoralen in the combined system, which corresponds to the LUMO in the isolated system having a π^* antibonding character of the C3–C4 orbital, and the LUMO of thymine. Both the HOMO and the LUMO shift to the higher energy side by 0.002 and 0.003 hartree, respectively, compared with isolated psoralen. These energy shifts are quite small.

In Figure 4b, the HOMO of the pyrone monoadduct is represented mainly by the HOMO of psoralen. The LUMO is represented mainly by the HOMO of psoralen and the HOMO of thymine. Because the C3–C4 bond of psoralen is combined with the thymine residue in the pyrone monoadduct, the LUMO of psoralen, which has large amplitude on the C3–C4 bond, has no effect on the LUMO of the pyrone monoadduct. The LUMO shifts largely to the higher energy side by 0.032 hartree, while the HOMO shifts by only 0.006 hartree. Note that the energy shift of the LUMO of the pyrone monoadduct is quite large. The large energy shift in the LUMO of the pyrone monoadduct is also seen in both 5-MOP and 8-MOP.

Excited States of Psoralen Compounds Bonded to Thymine Residue

Table 5 lists the excitation energy, oscillator strength, and main configuration of monoadducts of psoralen compounds. Figure 5 is the theoretical spectra of monoadducts obtained using a Lorenzian-type function for the line shape with the half-width at a half-maximum of 10 nm. In Table 5, the lower excited states of furan monoadducts commonly have characteristics of the transitions to the LUMO, and the lower excited states of pyrone monoadducts result from transition from the HOMO.

The wavelengths of the first singlet excited (S_1) states of the isolated systems and the furan and pyrone monoadducts are 329, 310, and 276 nm, respectively. The excitation energies to the S_1

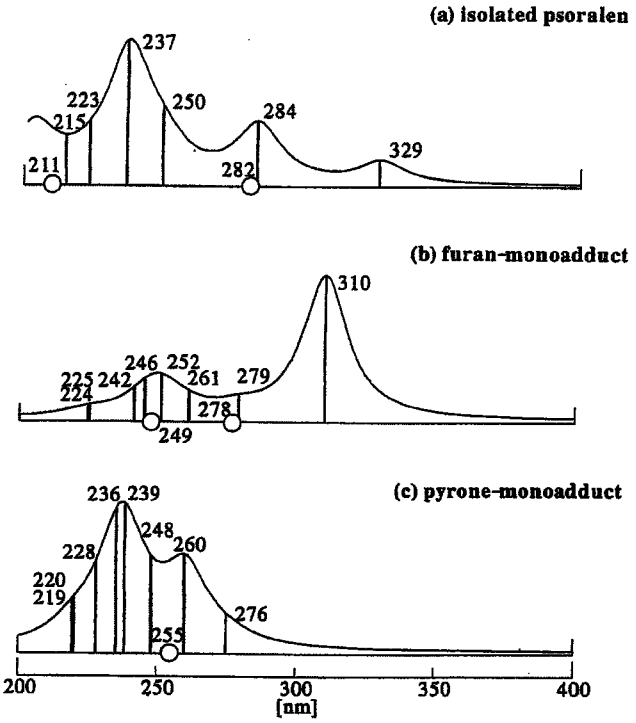

Figure 5. Theoretical spectra of psoralen monoadducts using Lorenzian functions with half-width at half-maximum of 10 nm.

states of the furan and the pyrone monoadduct are blue-shifted by 19 and 53 nm, respectively, from that of the isolated system. Therefore, the excitation energy to the S_1 state of the pyrone monoadduct lies outside the UV-A region, which extends from 300 to 400 nm, whereas those of isolated psoralen and of the furan monoadduct lie in the UV-A region. Consequently, the pyrone monoadduct is not excited by the UV-A light, and so the undesirable diadduct does not form.

The blue-shifts in the excitation energies of the S_1 states of the furan and pyrone monoadducts are due to the fewer number of electrons involved in the π-conjugation: Whereas isolated psoralen has 12 π-electron conjugation, the furan and pyrone monoadducts have 10 and 8 π-electron conjugations, respectively. The fewer number of electrons are involved in the π-conjugation, the larger the excitation energy becomes. Therefore, the excitation energies of the S_1 state in the pyrone monoadduct is blue-shifted greater than those in the furan monoadduct.

From the viewpoint of the orbital energies, the energy gaps between the HOMO and the LUMO in the isolated psoralen, furan monoadduct, and pyrone monoadduct, which correspond to the excitation energies of the main configuration of the S_1 states, are 0.158, 0.159, and 0.185 hartree, respectively. Note that the energy gap is the largest in the pyrone monoadduct. Because the energy shift of the LUMO is large, the energy gap is also large in the pyrone monoadduct.

In both 5-MOP and 8-MOP, the excitation energies to the S_1 states of the isolated and mono-additional compounds are close to that in psoralen, so although the excitation energy to the S_1 states

is within the UV-A region for their furan monoadduct, it is not for their pyrone monoadducts and does not form a diadduct. Therefore, using therapeutic UV light of a slightly longer wavelength such that its energy is less than the excitation energy of the S_1 state of the furan monoadduct may prevent generation of the undesirable diadduct.

Conclusions

In the present study, TDDFT calculations were carried out for the excited states of isolated systems, furan monoadducts, and pyrone monoadducts of psoralen compounds. For the isolated psoralen compounds, we assigned the peaks of experimental UV absorption spectra to the transitions and clarified the nature of the excited states. For the furan and pyrone monoadducts, the S_1 excitation energies are blue-shifted a lot compared with the isolated system. The S_1 excitation energy of the pyrone monoadduct is blue-shifted the greatest and is actually shifted to outside the UV-A wavelength region. It was found that pyrone monoadducts are not excited by UV-A light, and the diadducts that cause serious adverse effects are not generated from the pyrone monoadducts under UV-A light.

Acknowledgments

Part of the calculations was performed at the Research Center for Computational Science (RCCS) of the Okazaki National Research Institutes and the Media Network Center (MNC) of Waseda University.

References

1. Otsuki, T. J Synthet Org Chem Jpn 1991, 49, 809.
2. Bensasson, R. V.; Land E. J.; Truscott, T. G. Excited States and Free Radicals in Biology and Medicine; Oxford University Press: New York, 1993.
3. Song, P. S.; Tapley, K. J., Jr. Photochem Photobiol 1979, 29, 1177.
4. Spielmann, H. P.; Dwyer, T. J.; Hearst, J. E.; Wemmer, D. E. Biochemistry 1995, 34, 12937.
5. Kanne, D.; Straub, K.; Rapoport, H.; Hearst, J. E. Biochemistry 1982, 21, 861.
6. Bethea, D.; Fullmer, B.; Syed, S.; Seltzer, G.; Tiano, J.; Rischko, C.; Gillespie, L.; Brown, D.; Gasparro, F. P. J Dermatol Sci 1999, 19, 78 (and reference therein).
7. Estévetz, C. M.; Graña, A. M.; Ríos, M. A.; Rodríguez, J. J Mol Struct (Theochem) 1991, 231, 163.
8. Boggia, R.; Fanciullo, M.; Finzi, L.; Incani, O.; Mosti, L. Il Farmaco 1999, 54, 202.
9. Marques, A. D. S.; Takahata, Y.; Junior, J. R. L.; Souza, M. C.; Simoes, S. S.; Azevedo, W. M.; de Sa, G. F. J Lumin 2002, 97, 237.
10. Nakai, H.; Yamauchi, Y.; Nakata, A.; Baba, T.; Takahashi, H. J Chem Phys 2003, 119, 4223.
11. Stevens, P. J.; Devlin, J. F.; Chabalowski, C. F.; Frish, M. J. J Phys Chem 1994, 98, 11623.
12. Slater, J. C. Phys Rev 1951, 81, 385.
13. Becke, A. D. Phys Rev A 1988, 38, 3098.
14. Vosco, S. H.; Wilk, L.; Nusair, M. Can J Phys 1980, 58, 1200.
15. Lee, C.; Yang, W.; Parr, R. G. Phys Rev B 1988, 37, 785.
16. Dunning, T. H., Jr. J Chem Phys 1989, 90 1007.
17. Frisch, M. J.; Trucks, G. W.; Schlegel, H. B.; Scuseria, G. E.; Robb, M. A.; Cheeseman, J. R.; Zakrzewski, V. G.; Montgomery, J. A., Jr.; Stratmann, R. E.; Burant, J. C.; Dapprich, S.; Millam, J. M.; Daniels, A. D.; Kudin, K. N.; Strain, M. C.; Farkas, O.; Tomasi, J.; Barone, V.; Cossi, M.; Cammi, R.; Mennucci, B.; Pomelli, C.; Adamo, C.; Clifford, S.; Ochterski, J.; Petersson, G. A.; Ayala, P. Y.; Cui, Q.; Morokuma, K.; Malick, D. K.; Rabuck, A. D.; Raghavachari, K.; Foresman, J. B.; Cioslowski, J.; Ortiz, J. V.; Baboul, A. G.; Stefanov, B. B.; Liu, G.; Liashenko, A.; Piskorz, P.; Komaromi, I.; Gomperts, R.; Martin, R. L.; Fox, D. J.; Keith, T.; Al-Laham, M. A.; Peng, C. Y.; Nanayakkara, A.; Gonzalez, C.; Challacombe, M.; Gill, P. M. W.; Johnson, B.; Chen, W.; Wong, M. W.; Andres, J. L.; Gonzalez, C.; Head-Gordon, M.; Replogle, E. S.; Pople, J. A. Gaussian 98, Revision A.7; Gaussian, Inc.L Pittsburgh, PA, 1998.
18. Kohn, W.; Sham, L. J. Phys Rev 1965, 140, A1133.
19. Baerends, E. J.; Gritsenko, O. V.; van Leeuwen, R. Chemical Applications of Density Functional Theory; Ross, B. B.; Ziegler, T., Eds.; American Chemical Society: Washington, DC, 1996, p. 20, vol. 629.
20. Baerends, E. J.; Gritsenko, O. V. J Phys Chem A 1997, 101, 5383.
21. Baerends, E. J. Theor Chem Acc 2000, 103, 265.
22. Chong, D. P.; Gritsenko, O. V.; Baerends, E. J. J Chem Phys 2002, 116, 1760.
23. Matsumoto, H.; Ohkura, Y. Chem Pharm Bull 1978, 26, 3433.
24. Itoh, K.; Kiyohara, T.; Shinohara, H.; Ohe, C.; Kawamura, Y.; Nakai H. J Phys Chem B 2002, 106, 10714.

Available online at www.sciencedirect.com
SCIENCE DIRECT®
Chemical Physics Letters 388 (2004) 50–54
CHEMICAL PHYSICS LETTERS
www.elsevier.com/locate/cplett

New algorithm for the rapid evaluation of electron repulsion integrals: elementary basis algorithm

Hiromi Nakai *, Masato Kobayashi

Department of Chemistry, School of Science and Engineering, Waseda University, 3-4-1 Okubo, Shinjuku-ku, Tokyo 169-8555, Japan

Received 19 December 2003; in final form 20 February 2004
Published online: 18 March 2004

Abstract

We propose a new algorithm for the rapid evaluation of electron repulsion integrals over Gaussian type orbitals, termed elementary basis algorithm (EBA). In the EBA, the information of the atomic basis functions is divided into two parts: an elementary and an atomic basis part. In the conventional algorithm, all information is assigned to atoms, which requires that all computations must be performed in the atomic loops. In the EBA, computations can be partly carried out in the elementary loops. We apply the EBA to the accompanying coordinate expansion method of Ishida.

1. Introduction

The computation of molecular integrals, especially electron repulsion integrals (ERIs), is still one of the most time-consuming steps in ab initio calculations. Since Boys [1] proposed using Gaussian-type orbitals (GTOs) as basis functions for molecular systems, many efficient algorithms to compute ERIs have been developed [2–13]. The performance of an algorithm is often assessed using the floating-point operation (FLOP) count for a set of ERIs, which was introduced by Head-Gordon and Pople [2]. Assuming all contraction lengths (K) are equal, the FLOP count can be expressed as

$$xK^4 + yK^2 + z. \tag{1.1}$$

When a set of generally contracted GTOs (GCGTOs) is composed of J's GTOs, the FLOP count for generally contracted ERIs (GCERIs) can be written as follows:

$$J^4\left(xK^4 + yK^2 + z\right). \tag{1.2}$$

Yanai et al. [4] developed an alternative algorithm geared towards GCERIs and showed its efficiency by using the FLOP count,

$$\left(x_2J^2 + x_0\right)K^4 + \left(y_4J^4 + y_2J^2 + y_0\right)K^2 + z_4J^4. \tag{1.3}$$

Actually, the computational cost is reduced by a factor of $1/J^2$.

More recently, several techniques for reducing the total number of ERIs that require explicit calculation-have been proposed [14]. In the Kohn–Sham-type density functional theory (DFT), ERIs are used only for constructing Coulomb terms. The fast multipole method (FMM), originally developed for the Coulomb interaction between classical point charges [15], is adopted to evaluate the far-field potential approximately while keeping numerical accuracy [16,17]. Thus, in the FMM method, computation of ERIs is required only for the near-field potential.

In the Hartree–Fock (HF) and hybrid HF–DFT methods, ERIs are used not only for Coulomb terms, but also for exchange terms. Several research groups presented efficient screening techniques to compute the exchange terms. The exchange contributions to the Fock matrix can be written in terms of the real-space density matrix $\rho(\mathbf{r},\mathbf{r}')$ and GTOs $\{\phi_\mu(\mathbf{r})\}$

* Corresponding author. Fax: +81-3-3205-2504.
E-mail address: nakai@waseda.jp (H. Nakai).

0009-2614/$ - see front matter © 2004 Elsevier B.V. All rights reserved.
doi:10.1016/j.cplett.2004.02.070

$$K_{\mu\nu} = \int\int \mathrm{d}\mathbf{r}\,\mathrm{d}\mathbf{r}'\phi_\mu(\mathbf{r})\frac{\rho(\mathbf{r},\mathbf{r}')}{|\mathbf{r}-\mathbf{r}'|}\phi_\nu(\mathbf{r}'). \tag{1.4}$$

The density matrix in insulators has been shown to fall off exponentially [18],

$$\rho(\mathbf{r},\mathbf{r}') \sim \mathrm{e}^{-\kappa|\mathbf{r}-\mathbf{r}'|} \tag{1.5}$$

as $|\mathbf{r}-\mathbf{r}'| \to \infty$, where κ is a constant. Given the dependence of the exchange terms (1.4) on the density matrix (1.5), it follows that the exchange interaction should also fall off in the same manner. Schwegler and Challacombe [19] have developed an efficient screening technique based on the exponential decay of the density matrix and the exchange interaction.

Cutoff techniques, such as FMM and screening, would cause computational cost to become linearly dependent on system size. Decreasing the prefactor is essential in linear scaling techniques. We focus not only on the individual computational cost for a set of ERIs, but also on the total cost for ERIs computed explicitly.

In present-day quantum chemical calculations over Gaussian basis sets, the floating operations with the use of orbital exponents and contraction coefficients are performed in the atomic loops despite the fact that the same values are used for the same chemical element. We propose a refined algorithm by separating the information of the GTOs into atoms and chemical elements. In the present study, we employ the accompanying coordinate expansion (ACE) method developed by Ishida [3]. The type-3 formula in the ACE for bra- and ket-state (ACE-b3k3) is particularly applicable to our separation. In the following section, we will present the basic idea behind our algorithm, its theoretical derivation, a flow of its program code, and its numerical efficiency. We will present concluding remarks in Section 3.

2. Elementary basis algorithm

2.1. Basic idea

Target molecules, which are treated by ab initio calculations, are commonly made up of a maximum of 10 chemical elements. For example, a deoxyribonucleic acid (DNA) chain containing over 1000 atoms is composed of only six elements: C, H, O, N, P, and S. The Buckminster-fullerene and carbon nanotubes contain only one element, namely C.

For the atoms of a single chemical element, we commonly adopt the *same* basis set. Such GTOs consist of the same exponents $\{\alpha_k\}$ and coefficients $\{d_k\}$, while the atomic coordinates or the orbital centers $\{\mathbf{R}\}$ differ,

$$\phi^{\mathrm{A}}(\mathbf{r}) = \sum_{\lambda}^{K} d_\lambda^{\mathrm{A}} N_\lambda^{\mathrm{A}} \left(r_x - R_x^{\mathrm{A}}\right)^{l_{\mathrm{A}}} \left(r_y - R_y^{\mathrm{A}}\right)^{m_{\mathrm{A}}} \left(r_z - R_z^{\mathrm{A}}\right)^{n_{\mathrm{A}}} \times \exp\left(-\alpha_\lambda^{\mathrm{A}} r^2\right), \tag{2.1}$$

where N_λ^{A} is a normalization factor. The sum of the quantum numbers, $L_{\mathrm{A}} = l_{\mathrm{A}} + m_{\mathrm{A}} + n_{\mathrm{A}}$ gives the angular momentum quantum number. In the conventional computation of ERIs, however, all of these parameters are assigned to atoms and used in the atomic loops.

We divide these GTO parameters into two parts: an atomic basis and an elementary basis part. Computations are partly performed in the quadruple atomic loops in the conventional algorithm. By using the decomposition of the GTO parameters, some of these computations can be carried out in the quadruple elementary loops. Their computational cost will be reduced by a factor $(N_{\mathrm{E}}/N_{\mathrm{A}})^4$, where N_{A} and N_{E} denote numbers of atoms and elements, respectively. This factor approaches zero as the system size increases. For instance, it becomes $\sim 10^{-7}$ in the case of a DNA chain composed of 300 atoms and six elements. The present algorithm is termed elementary basis algorithm (EBA).

2.2. Theory and algorithm

The EBA can be applied to arbitrary formulae developed to compute a set of ERIs efficiently. However, in this initial study, we formulate the EBA in combination with the ACE method proposed by Ishida [3], one of the most efficient methods, at least as far as FLOP counts are concerned.

Using the ACE-b3k3 formula [3,4], contracted ERI (CERI) can be expressed as the summation of the products of an accompanying coordinate part, C_4^{ABCD}, and a core part, $\ddot{H}_4^{\mathrm{ABCD}}$,

$$\left(\phi^{\mathrm{A}}\phi^{\mathrm{B}}|\phi^{\mathrm{C}}\phi^{\mathrm{D}}\right) = \sum_{\mathbf{N}_3} C_4^{\mathrm{ABCD}}\{\mathbf{N}_3\}\ddot{H}_4^{\mathrm{ABCD}}\{\mathbf{N}_3\}, \tag{2.2}$$

where the term A_0 in [3], or $S_{\lambda\mu}^{\mathrm{AB}} S_{\nu\xi}^{\mathrm{CD}}$ in [4], is absorbed into the core part. The set $\{\mathbf{N}_3\}$ represents summation indices:

$$\{\mathbf{N}_3\} = \{M_{\mathrm{A}}M_{\mathrm{B}}M_{\mathrm{C}}M_{\mathrm{D}}i'j'k'h'i''j''k''h''\}. \tag{2.3}$$

While the accompanying coordinate part C_4^{ABCD} contains the atomic coordinates, it does not contain the orbital exponents or the contraction coefficients. Thus, it is computed only in the atomic basis loops.

The core part $\ddot{H}_4^{\mathrm{ABCD}}$ is expressed as:

$$\ddot{H}_4^{\mathrm{ABCD}}\{\mathbf{N}_3\} = \sum_{\lambda}^{K_{\mathrm{A}}}\sum_{\mu}^{K_{\mathrm{B}}} d_\lambda^{\mathrm{A}} d_\mu^{\mathrm{B}} N_\lambda^{\mathrm{A}} N_\mu^{\mathrm{B}} S_{\lambda\mu}^{\mathrm{AB}} \dot{H}_{4\lambda\mu}^{\mathrm{ABCD}}\{\mathbf{N}_3\}, \tag{2.4}$$

$$\dot{H}_{4\lambda\nu}^{\mathrm{ABCD}}\{\mathbf{N}_3\} = \sum_{\nu}^{K_{\mathrm{C}}}\sum_{\xi}^{K_{\mathrm{D}}} d_\nu^{\mathrm{C}} d_\xi^{\mathrm{D}} N_\nu^{\mathrm{C}} N_\xi^{\mathrm{D}} S_{\nu\xi}^{\mathrm{CD}} H_{4\lambda\mu\nu\xi}^{\mathrm{ABCD}}\{\mathbf{N}_3\}, \tag{2.5}$$

$$H^{\mathrm{ABCD}}_{4,\lambda\mu\nu\xi}\{\mathbf{N}_3\} = \sum_{i_1}^{\left[\frac{M_A+M_B}{2}\right]} \sum_{i_2}^{\left[\frac{M_C+M_D}{2}\right]} G_{i_1 i_2} \sigma_{\mathrm{A},\lambda\mu}^{b_A+d_A} \sigma_{\mathrm{B},\lambda\mu}^{a_B+c_B} \sigma_{\mathrm{C},\nu\xi}^{d_C+b_C} \sigma_{\mathrm{D},\nu\xi}^{c_D+a_D} \times \frac{\sigma_{1,\lambda\mu}^{M_A+M_B-i_1} \sigma_{2,\nu\xi}^{M_C+M_D-i_2}}{(\sigma_{1,\lambda\mu}+\sigma_{2,\nu\xi})^{M-i_1-i_2+1/2}} \times \sum_{s_1}^{a_B+b_A} \sum_{s_2}^{c_D+d_C} (-)^{s_1+s_2} \binom{a_B+b_A}{s_1} \times \binom{c_D+d_C}{s_2} \left(\frac{\sigma_{1,\lambda\mu}}{\sigma_{1,\lambda\mu}+\sigma_{2,\nu\xi}}\right)^{t'+f'+s_1} \times \left(\frac{\sigma_{2,\nu\xi}}{\sigma_{1,\lambda\mu}+\sigma_{2,\nu\xi}}\right)^{k'+h'+s_2} F_{\zeta+s_1+s_2}(z), \quad (2.6)$$

where only three terms, $S^{\mathrm{AB}}_{\lambda\mu}$, $S^{\mathrm{CD}}_{\nu\xi}$, and the molecular incomplete gamma function $F_{\zeta+s_1+s_2}(z)$, involve atomic coordinates. The remaining terms only contain information assigned to the chemical elements. This means that the remaining terms can be computed in the elementary basis loops and stored in the computer memory.

Let us define $U^{mn}_{\lambda\mu\nu\xi}$, $V_{\mathrm{AB},\lambda\mu}$, $W^{pqM}_{\mathrm{AB},\lambda\mu}$, $X_{\mathrm{AB},\lambda\mu}$, $Y_{\lambda\mu\nu\xi}$, and $Z_{\mathrm{AB},\lambda\mu}$ as

$$U^{mn}_{\lambda\mu\nu\xi} = \left(\frac{\sigma_{1,\lambda\mu}}{\sigma_{1,\lambda\mu}+\sigma_{2,\nu\xi}}\right)^m \left(\frac{\sigma_{2,\nu\xi}}{\sigma_{1,\lambda\mu}+\sigma_{2,\nu\xi}}\right)^n, \quad (2.7)$$

$$V_{\mathrm{AB},\lambda\mu} = d^{\mathrm{A}}_{\lambda} d^{\mathrm{B}}_{\mu} N^{\mathrm{A}}_{\lambda} N^{\mathrm{B}}_{\mu}, \quad (2.8)$$

$$W^{pqM}_{\mathrm{AB},\lambda\mu} = \sigma^{p}_{\mathrm{A},\lambda\mu} \sigma^{q}_{\mathrm{B},\lambda\mu} \sigma^{M}_{1,\lambda\mu}, \quad (2.9)$$

$$X_{\mathrm{AB},\lambda\mu} = \frac{\alpha^{\mathrm{A}}_{\lambda}\alpha^{\mathrm{B}}_{\mu}}{\gamma_{1,\lambda\mu}}, \quad (2.10)$$

$$Y_{\lambda\mu\nu\xi} = \sqrt{\sigma_{1,\lambda\mu}+\sigma_{2,\nu\xi}}, \quad (2.11)$$

$$Z_{\mathrm{AB},\lambda\mu} = (2\pi)^{-1/4} \left(\frac{\pi}{\gamma_{1,\lambda\mu}}\right)^{3/2}, \quad (2.12)$$

where

$$\gamma_{1,\lambda\mu} = \alpha^{\mathrm{A}}_{\lambda} + \alpha^{\mathrm{B}}_{\mu}, \quad \gamma_{2,\nu\xi} = \alpha^{\mathrm{C}}_{\nu} + \alpha^{\mathrm{D}}_{\xi}, \quad (2.13)$$

$$\sigma_{1,\lambda\mu} = \frac{1}{2\gamma_{1,\lambda\mu}}, \quad \sigma_{2,\nu\xi} = \frac{1}{2\gamma_{2,\nu\xi}}, \quad (2.14)$$

$$\sigma_{\mathrm{A},\lambda\mu} = \frac{\alpha^{\mathrm{A}}_{\lambda}}{\gamma_{1,\lambda\mu}}, \quad \sigma_{\mathrm{B},\lambda\mu} = \frac{\alpha^{\mathrm{B}}_{\mu}}{\gamma_{1,\lambda\mu}}. \quad (2.15)$$

The indices obey the following restrictions:

$$0 \leqslant m \leqslant L_{\mathrm{A}} + L_{\mathrm{B}}, \quad 0 \leqslant n \leqslant L_{\mathrm{C}} + L_{\mathrm{D}}, \quad (2.16)$$

$$0 \leqslant M \leqslant \min\left(\left[\frac{L_{\mathrm{A}}+L_{\mathrm{B}}}{2}\right], \left[\frac{L_{\mathrm{C}}+L_{\mathrm{D}}}{2}\right]\right), \quad (2.17)$$

$$0 \leqslant p, q \leqslant L_{\mathrm{A}} + L_{\mathrm{B}} + L_{\mathrm{C}} + L_{\mathrm{D}}. \quad (2.18)$$

By using the factors, $U^{mn}_{\lambda\mu\nu\xi}$, $V_{\mathrm{AB},\lambda\mu}$, $W^{pqM}_{\mathrm{AB},\lambda\mu}$, $X_{\mathrm{AB},\lambda\mu}$, $Y_{\lambda\mu\nu\xi}$, and $Z_{\mathrm{AB},\lambda\mu}$, all necessary $\ddot{H}^{pqrs}_{mn}$ and $\ddot{h}^{pqrs}_{mnM_2}$ corresponding to the core part $\ddot{H}^{\mathrm{ABCD}}_{4}$ can be expressed as follows:

$$S^{\mathrm{AB}}_{\lambda\mu} = Z_{\mathrm{AB},\lambda\mu} \exp\left(-X_{\mathrm{AB},\lambda\mu}\overline{\mathrm{AB}}^2\right), \quad S^{\mathrm{CD}}_{\nu\xi} = Z_{\mathrm{CD},\nu\xi} \exp\left(-X_{\mathrm{CD},\nu\xi}\overline{\mathrm{CD}}^2\right), \quad (2.19)$$

$$\tilde{F}_m(z) = \frac{F_m(z)}{Y_{\lambda\mu\nu\xi}}, \quad (2.20)$$

$$F_{mn} = U^{mn}_{\lambda\mu\nu\xi} \tilde{F}_{m+n}(z), \quad (2.21)$$

$$G^{pq}_{mn} = W^{pq0}_{\mathrm{AB},\lambda\mu} \sum_{t=0}^{\kappa_1} (-)^t \binom{\kappa_1}{t} F_{m+t,n}, \quad (2.22)$$

$$g^{pq}_{mM_1} = W^{pqM_1}_{\mathrm{AB},\lambda\mu} \sum_{t=0}^{\kappa_1} (-)^t \binom{\kappa_1}{t} F_{m+t-M_1,0}, \quad (2.23)$$

$$\dot{G}^{pq}_{mn} = \sum_{\lambda}^{K_{\mathrm{A}}} \sum_{\mu}^{K_{\mathrm{B}}} V_{\mathrm{AB},\lambda\mu} S^{\mathrm{AB}}_{\lambda\mu} G^{pq}_{mn}, \quad (2.24)$$

$$\dot{g}^{pq}_{mM_1} = \sum_{\lambda}^{K_{\mathrm{A}}} \sum_{\mu}^{K_{\mathrm{B}}} V_{\mathrm{AB},\lambda\mu} S^{\mathrm{AB}}_{\lambda\mu} g^{pq}_{mM_1}, \quad (2.25)$$

$$\dot{H}^{pqrs}_{mn} = W^{rs0}_{\mathrm{CD},\nu\xi} \sum_{u=0}^{\kappa_2} (-)^u \binom{\kappa_2}{u} \dot{G}^{pq}_{m,n+u}, \quad (2.26)$$

$$\dot{h}^{pqrs}_{mnM_2} = \begin{cases} W^{rsM_2}_{\mathrm{CD},\nu\xi} \sum_{u=0}^{\kappa_2} (-)^u \binom{\kappa_2}{u} \dot{G}^{pq}_{m,n+u-M_2} \\ \quad (n+u-M_2 \geqslant 0), \\ W^{rs0}_{\mathrm{CD},\nu\xi} \sum_{u=0}^{\kappa_2} (-)^u \binom{\kappa_2}{u} \dot{g}^{pq}_{m,-(n+u-M_2)} \\ \quad (n+u-M_2 < 0), \end{cases} \quad (2.27)$$

$$\ddot{H}^{pqrs}_{mn} = \sum_{\nu}^{K_{\mathrm{C}}} \sum_{\xi}^{K_{\mathrm{D}}} V_{\mathrm{CD},\nu\xi} S^{\mathrm{CD}}_{\nu\xi} \dot{H}^{pqrs}_{mn}, \quad (2.28)$$

$$\ddot{h}^{pqrs}_{mnM_2} = \sum_{\nu}^{K_{\mathrm{C}}} \sum_{\xi}^{K_{\mathrm{D}}} V_{\mathrm{CD},\nu\xi} S^{\mathrm{CD}}_{\nu\xi} \dot{h}^{pqrs}_{mnM_2}, \quad (2.29)$$

where $\kappa_1 = L_{\mathrm{A}} + L_{\mathrm{B}} - m$ and $\kappa_2 = L_{\mathrm{C}} + L_{\mathrm{D}} - n$.

The loop structures used in the conventional algorithm and our algorithm are illustrated in Figs. 1a and b. In Fig. 1a, all computations are carried out in the atomic loops since the elementary loops (E1) and (E2) correspond exactly to atomic loops (A1) and (A2), respectively. By contrast, computations are partly performed in the elementary loops in our algorithm (Fig. 1b). Namely, $V_{\mathrm{AB},\lambda\mu}$, $W^{pqM}_{\mathrm{AB},\lambda\mu}$, $X_{\mathrm{AB},\lambda\mu}$, and $Z_{\mathrm{AB},\lambda\mu}$, which include $V_{\mathrm{CD},\nu\xi}$, $W^{rsM}_{\mathrm{CD},\nu\xi}$, $X_{\mathrm{CD},\nu\xi}$, and $Z_{\mathrm{CD},\nu\xi}$, are calculated in the elementary loop (E1) outside the atomic loop (A1), and $U^{mn}_{\lambda\mu\nu\xi}$, $Y_{\lambda\mu\nu\xi}$ are calculated in the quadruple elementary

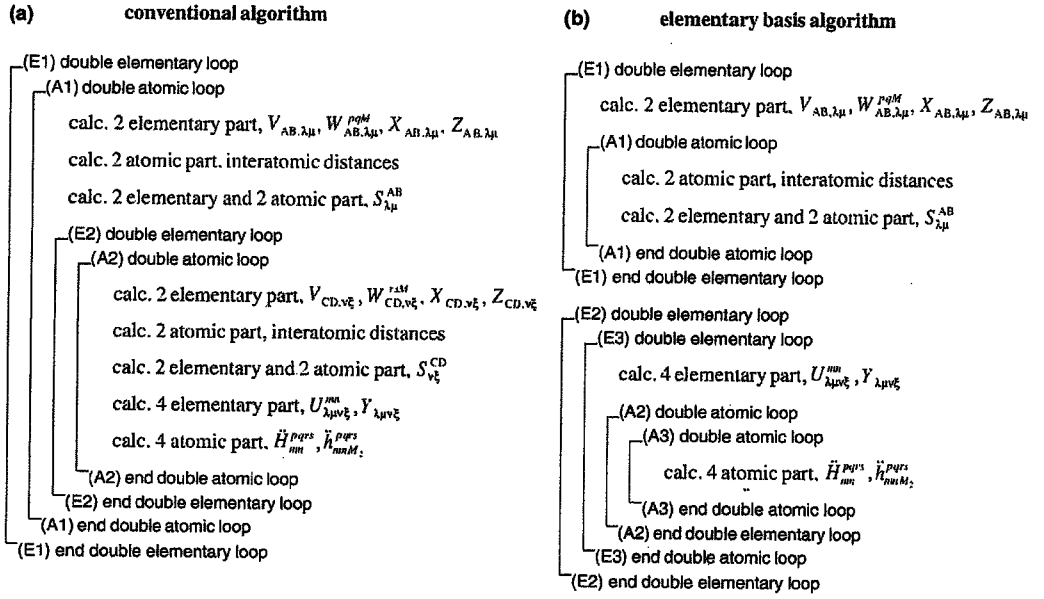

Fig. 1. Loop structures used in: (a) the conventional scheme and (b) the EBA scheme.

loops (E2) and (E3) outside the atomic loop (A3). Furthermore, $S^{AB}_{\lambda\mu}$ (and $S^{CD}_{\nu\xi}$) is computed in the atomic loops (A1), which can be stored in the computer memory.

Let us suppose that the total number of atomic and elementary quadratic loops for the benzene molecule, which has 12 atoms consisting of two elements, is 3081 and 6, respectively. The difference increases as the system becomes larger, e.g., in going from a benzene monomer to a dimer, and further to a trimer. Thus, the conventional algorithm shown in Fig. 1a clearly wastes time by performing the same computation in the atomic loops. By contrast, in our algorithm shown in Fig. 1b, the necessary factors are computed only once outside the atomic loops and stored in the computer memory. Furthermore, because the pre-computed factors have the elementary indices, they are relatively few in number. In the case of $U^{mn}_{\lambda\mu\nu\xi}$ and $Y_{\lambda\mu\nu\xi}$, necessary λ, μ, ν and ξ are restricted since these are computed after all corresponding elements are determined.

2.3. Computational performance

We developed the computational code based on the EBA and ACE-b3k3. Its computational performance was assessed by application to several sizes of carbon nanotubes, $(C_{12})_n$ and water clusters, $(H_2O)_{5n}$. We used the [14s9p]/(4s3p) generally contracted basis set for C and O atoms and [8s4p]/(3s2p) for H atoms. All calculations were carried out on an Intel Xeon (2.8 GHz) processor.

To examine the performance of the EBA, we measured the central processing unit (CPU) times for computing ERIs without the integral cut-off technique. We first dealt with C_{24} by changing the *virtual* number of elements (N_E) from 1 to 24. $N_E = 1$ corresponds to the complete EBA calculation and $N_E = 24$, that is, $N_E = N_A$ to the conventional calculation. Fig. 2 shows the CPU times of the ERI computation with respect to N_E. The CPU times with $N_E = 1$ and 24 are 31 922 and 40 792 s, respectively. It means that the EBA technique reduces the CPU times of the ERI computation by about 20% in comparison with the conventional scheme.

As mentioned before, the reduction of the computational cost by the EBA is expected to be a factor of $(N_E/N_A)^4$. The timing data in Fig. 2 are well fit to $(N_E/N_A)^4$, where the number of atoms N_A is constant. Thus, the EBA would be more efficient as the target system becomes larger. In addition, the CPU times with

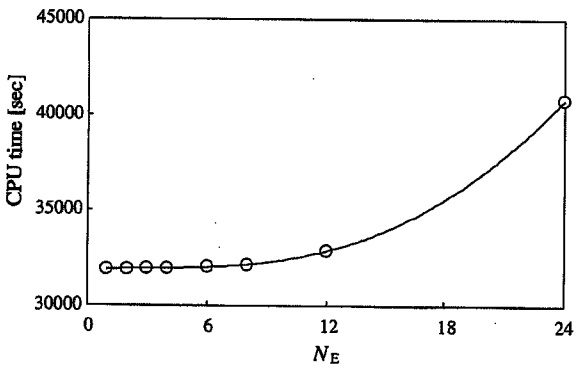

Fig. 2. CPU time of the ERI computation of C_{24} with respect to the *virtual* number of elements N_E from 1 to 24.

Table 1
CPU times for computing all ERIs in carbon nanotubes and water clusters

Molecule	# of ERIs	CPU time (s)		
		Present (t_{EBA})	GAMESS (t_{GAM})	t_{GAM}/t_{EBA}
Carbon nanotubes $(C_{12})_n$				
C_{12}	74 988 381	2040.5	5736.7	2.81
C_{24}	1 192 111 206	31922.3	95998.5	3.01
C_{36}	6 022 147 131	159232.6	486419.5	3.05
Water clusters $(H_2O)_{5n}$				
$H_{10}O_5$	73 090 095	1313.6	1788.9	1.36
$H_{20}O_{10}$	1 161 885 115	20627.0	31249.5	1.51
$H_{30}O_{15}$	5 869 373 685	104048.5	158245.5	1.52

$2 \leqslant N_E \leqslant 8$ are close to that with $N_E = 1$. The behavior is important for practical calculations. Because most of systems treated by ab initio calculations consist of less than 10 chemical elements.

Table 1 compares the CPU times of our program with those of the GAMESS package [20] for computing ERIs. It can be seen that the total CPU times of our program were always shorter than those of the GAMESS program. The ratios of the total CPU time of our program to that of the GAMESS program reveal that the advantage of our program increases with system size. This is expected to hold true even in much larger molecules.

3. Concluding remarks

We proposed a new algorithm, elementary basis algorithm (EBA), for rapid computation of ERIs over GTOs in large molecular systems. The bare bones of the EBA are the separation of the basis functions into two parts: an elementary basis part including exponents and coefficients, and an atomic basis part, i.e., atomic coordinates. Since all of these are assigned to atoms in the conventional algorithm, all computations must be done in the atomic quadruple loops. In the EBA, computations can be partly carried out in elementary loops, which are much more efficient than atomic loops. We applied the EBA to the ACE method of Ishida and developed the program. Numerical tests confirm the effectiveness of the EBA. The EBA lends itself particularly well to large-scale molecules composed of few chemical elements.

Recently, Takashima and Kitamura [21] proposed an algorithm that is based on the similar concept of dividing the information of basis sets. They focused on parallel computation and combined it with the Obara-Saika algorithm [5], as opposed to the ACE algorithm that we have employed.

In a separate research, we have developed the ACE-RR algorithm [13], which improves on the ACE-b3k3 algorithm using angular momentum reduced expressions and their recurrence relations. ACE-RR has the smallest FLOP count of one set of ERIs with large basis set. The combination of the EBA and ACE-RR algorithms will enable large-scale computations to become more rapid and accurate.

Acknowledgements

A part of this work was supported by a NAREGI Nano-Science Project of the Japanese Ministry of Education, Culture, Sports, Science and Technology (MEXT), the Joint Studies Program (2002-2004) of the Institute for Molecular Science, by a Grant-in-Aid for Young Scientists (A) 'KAKENHI 14703005' from Japanese Society for the Promotion of Science (JSPS), and by a Waseda University Grant for Special Research Projects.

References

[1] S.F. Boys, Proc. R. Soc. London Ser. A 200 (1950) 542.
[2] M. Head-Gordon, J.A. Pople, J. Chem. Phys. 89 (1988) 5777.
[3] K. Ishida, Int. J. Quantum Chem. 59 (1996) 209.
[4] T. Yanai, K. Ishida, H. Nakano, K. Hirao, Int. J. Quantum Chem. 76 (2000) 396.
[5] S. Obara, A. Saika, J. Chem. Phys. 84 (1986) 3963.
[6] H. Taketa, S. Huzinaga, K. O-ohata, J. Phys. Soc. Jpn. 21 (1966) 2313.
[7] M. Dupuis, J. Rys, H.F. King, J. Chem. Phys. 65 (1976) 111.
[8] L.E. McMurchie, E.R. Davidson, J. Comput. Phys. 26 (1978) 218.
[9] J.A. Pople, W.J. Hehre, J. Comput. Phys. 27 (1978) 161.
[10] T.P. Hamilton, H.F. Schaefer III, Chem. Phys. 150 (1991) 163.
[11] R. Lindh, U. Ryu, B. Liu, J. Chem. Phys. 95 (1991) 5889.
[12] P.M.W. Gill, B.G. Johnson, J.A. Pople, Int. J. Quantum Chem. 40 (1991) 745.
[13] M. Kobayashi, H. Nakai, unpublished.
[14] J.C. Burant, G.E. Scuseria, M.J. Frisch, J. Chem. Phys. 105 (1996) 8969.
[15] L. Greengard, The Rapid Evaluation of Potential Fields in Particle Systems, MIT Press, 1987.
[16] C.A. White, M. Head-Gordon, J. Chem. Phys. 101 (1994) 6593.
[17] M.C. Strain, G.E. Scuseria, M.J. Frisch, Science 271 (1996) 51.
[18] W. Kohn, Phys. Rev. 115 (1959) 809.
[19] E. Schwegler, M. Challacombe, J. Chem. Phys. 105 (1996) 2726.
[20] M.W. Schmidt, K.K. Baldridge, J.A. Boatz, S.T. Elbert, M.S. Gordon, J.J. Jensen, S. Koseki, N. Matsunaga, K.A. Nguyen, S. Su, T.L. Windus, M. Dupuis, J.A. Montgomery, J. Comput. Chem. 14 (1993) 1347.
[21] H. Takashima, K. Kitamura, Chem. Phys. Lett. 377 (2003) 43.

—Article—

Ab Initio Molecular Orbital Study of the Electron Emission Mechanism of $TiCl_3$ as a Reductant for an Electroless Deposition Process

Takuya SHIMADA,[a] Isao KOMATSU,[a] Takayuki HOMMA,[a]* Hiromi NAKAI,[b]* and Tetsuya OSAKA[a]

[a]Department of Applied Chemistry, School of Science and Engineering, Waseda University (Okubo, Shinjuku-ku, Tokyo 169-8555, Japan)

[b]Department of Chemistry, School of Science and Engineering, Waseda University (Okubo, Shinjuku-ku, Tokyo 169-8555, Japan)

Received November 29, 2003 ; Accepted March 5, 2004

The oxidation mechanism of $TiCl_3$ as a reductant for an electroless deposition process was studied by ab initio molecular orbital method. The reaction process of $TiCl_3$ proceeds with the substitution of Cl^- to OH^-. Net charge and spin density of the reactant, product, and intermediates were evaluated. It was suggested that the electron emission of $TiCl_3$, which is originated by the oxidation of Ti(III) to Ti(IV), took place when Cl is replaced by OH^- to form $Ti(OH)_4$. The catalytic activity of the metal surface, which is one of the most important factors for the electroless deposition process, was studied using a Pd_4 cluster as a model surface. It was suggested that the Pd_4 cluster enhanced the reaction of $TiCl_3$ to emit the electron. The effect of solvation is also taken into account in terms of the dielectric field constant. It was indicated that the heat of oxidation reaction shifted to an exothermic reaction with decreasing dielectric constant, indicating that the reaction preferentially proceeds in the vicinity of solid/liquid interface. However, it was indicated that the reaction could proceed in the bulk solution, suggesting that appropriate stabilization such as formation of complex is required for the application of the $TiCl_3$ to the electroless deposition process.

Key Words : Electroless Deposition Process, Molecular Orbital Study, $TiCl_3$, Effect of Solvation

1 Introduction

Electroless deposition processes are widely used in the various fields of micro and nano fabrication, featuring its capability to form precise deposits on to wide, non-flat surfaces.[1] In the electroless deposition process, the electron is supplied by the oxidation reaction of the reductant. Since the deposited metal surface should act as the catalyst for this oxidization reaction, combinations of the reductant and the metal species, which could be deposited, are limited.

In our previous studies, the oxidation mechanisms of various reductants were studied at the elementary reaction level using ab initio molecular orbital (MO) method.[2-4] The major advantage of this approach is its ability for quantitative evaluation of the energy and electronic structure of the reaction intermediates, which cannot be detected by the conventional analysis methods. Through this approach, we have investigated the reaction mechanism of representative reductants such as dimethylamine borane (DMAB)[2] and hypophosphite ion[3] in detail. We also carried out preliminary study for the $TiCl_3$ reductant,[4] which is known to be applied for "non-traditional" species for the electroless deposition such as In[5] and Sb.[6] Based upon this result, in this study, we investigated the reaction mechanism of $TiCl_3$ reductant in detail.

2 Computational Method

In the preliminary study, we have proposed the electron emission reaction of $TiCl_3$ as Scheme 1.[4]

The OH^- in the solution coordinates to $TiCl_3$ and the substitution reaction of Cl^- by OH^- proceeds to form $Ti(OH)_4$. It should be noted that the electron emission of $TiCl_3$ takes place by the oxidation of Ti(III) to Ti(IV),[4] while that of hypophosphite ion and DMAB, which are typical reductants for the electroless deposition, proceeds by the substitution of H by OH^-.

Based upon this reaction pathway, we compare in terms of geometry, net charge, and spin density of intermediates to analyze the mechanism of electron emission.

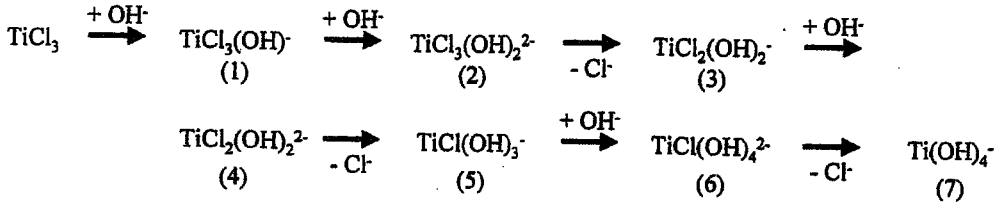

Scheme 1 Reaction pathway of $TiCl_3$ via five-coordinate intermediates (2, 4, and 6).

The geometry of each intermediate was optimized at the Hartree-Fock (HF) level. The electron correlation was taken into account for the single-point energy calculations by the Møller-Plesset 2nd perturbation (MP 2) method.

In order to investigate the catalytic activity of the metal surface for the oxidation reaction of the reductant, Pd (111) surface, expressed by a Pd_4 cluster, was used as a model surface. Following the results of our previous study on the electron transfer property and energy depend on the size of cluster for the reductant such as hypophosphite ion,[3] the adsorbate was put at the hollow site of the Pd_4 cluster. The solvation effect was taken into account by the self-consistent reaction field method with an isodensity surface polarized continuum model (SCRF-IPCM),[7] which utilized the dielectric constant value. In the IPCM calculations, the dielectric constant is changed from 1.0 (in non-polar solvent) to 78.3 (in pure water[8]).

The calculations were performed using the Gaussian 98 rev a.9.[9] The Gaussian basis sets used in the present calculations were Huzinaga's all-electron (14s10p5d)/[5s4p2d] type[10] for titanium, the AUG-cc-pVDZ[11] for oxygen and chlorine, and the cc-pVDZ[12] for hydrogen. For palladium, Kr core was replaced by an effective core potential by Hay and Wadt[13] and a valence electron was represented by a (5s5p4d)/[3s3p2d] basis set.

3 Results and Discussion

3. 1 Isolated state

Table 1 shows the HF level bond lengths of the reaction intermediates. The calculated value for the bond length of Ti-OH in $Ti(OH)_4$ is 1.829 Å, which agrees well to the experimental value of 1.80 Å,[14] indicating the validity of the calculated model. The table indicates that the bond length of Ti(III) are slightly longer than those of Ti(IV). As for the Ti-Cl bond, their lengths estimated by sum of the covalent radius and ionic bond radius are 2.31 Å and 2.61 Å, respectively.[15,16] The calculated bond lengths for the intermediate species of Ti(III) are longer than that of the covalent bond, suggesting that the Ti-Cl bond possesses the ionic bond like characters. On the other hand, the bond lengths estimated by sum of the covalent radius and ionic bond radius for Ti-OH^- are 1.98 Å and 2.20 Å, respectively,[15,16] and the calculated bond lengths for the intermediate species of Ti(III) and Ti(IV) are shorter than that estimated from the covalent bond radius. It is generally known that the covalent bond with the effect of ionic bond resonance possesses shorter length than the simple covalent bond.[17] Thus, it is expected that the Ti-OH^- bond is stabilized by this effect.

Table 1 Bond lengths of TiX_4 (X = Cl and/or OH). Ti(III) and Ti(IV) express TiX_4^- and TiX_4, respectively.

		(1) $TiCl_3(OH)$ X_{1-3} : Cl X_4 : OH /Å	(3) $TiCl_2(OH)_2$ X_{1-2} : Cl X_{3-4} : OH /Å	(5) $TiCl(OH)_3$ X_1 : Cl X_{2-4} : OH /Å	(7) $Ti(OH)_4$ X_{1-4} : OH /Å
Ti(III)	Ti-X_1	2.395	2.439	2.460	1.951
	Ti-X_2	2.395	2.439	1.936	1.951
	Ti-X_3	2.372	1.880	1.936	1.951
	Ti-X_4	1.848	1.880	1.936	1.951
Ti(IV)	Ti-X_1	2.205	2.232	2.254	1.829
	Ti-X_2	2.205	2.232	1.781	1.829
	Ti-X_3	2.205	1.761	1.781	1.829
	Ti-X_4	1.723	1.761	1.781	1.829

In our preliminary study, it was indicated that the reaction of $TiCl_3$ spontaneously proceeds and that the electron emission took place at the step (7) reaction.[4] In order to examine this point in more detail, we compare net charges and spin densities of the intermediates. The net charge and the distributions of spin densities of the intermediates before and after the electron emission are shown in Table 2, which were calculated at the MP 2 level. It is indicated that the charge of Cl and OH changes to positive when $TiCl_3(OH)$ turns from trivalent to tetravalent, whereas no significant changes are observed for the charge of Ti. Similar tendency is observed for the trivalent and tetravalent $Ti(OH)_4$ species at which the electron transfer takes place. This indicates that the charge is mainly transferred from the ligand (Cl, OH) parts. However, the spin density of these intermediates suggested that Ti becomes unstable since there are whole spin densities. These results indicate that this reaction system is strongly influenced by the ligands. It is also suggested that change in bond strength between Ti-Cl and Ti-OH^-, *i.e.*, the covalent bond character of Ti-OH^- initiates the electron emission.

3. 2 On the Pd cluster

In the previous section, the reaction of $TiCl_3$ in its 'iso-

Table 2 Net charge and local spin density of TiX_4 (X = Cl and/or OH). Ti(III) and Ti(IV) express TiX_4^- and TiX_4, respectively.

			(1) $TiCl_3(OH)$ X_{1-3} : Cl X_4 : OH	(3) $TiCl_2(OH)_2$ X_{1-2} : Cl X_{3-4} : OH	(5) $TiCl(OH)_3$ X_1 : Cl X_{2-4} : OH	(7) $Ti(OH)_4$ X_{1-4} : OH
net charge	Ti(III)	Ti	+1.731	+2.001	+2.024	+2.154
		X_1	−0.685	−0.751	−0.756	−0.788
		X_2	−0.685	−0.751	−0.754	−0.788
		X_3	−0.678	−0.750	−0.754	−0.788
		X_4	−0.682	−0.750	−0.760	−0.788
	Ti(IV)	Ti	+1.907	+2.029	+2.125	+2.129
		X_1	−0.472	−0.505	−0.537	−0.533
		X_2	−0.472	−0.505	−0.530	−0.533
		X_3	−0.472	−0.510	−0.530	−0.533
		X_4	−0.490	−0.510	−0.530	−0.533
spin density	Ti(III)	Ti	+1.008	+0.958	+1.015	+1.010
		X_1	0.000	+0.016	−0.005	−0.002
		X_2	0.000	+0.016	−0.005	−0.002
		X_3	−0.003	+0.005	−0.005	−0.002
		X_4	−0.006	+0.005	0.000	−0.002

Table 3 Change in net charge and spin density of the reaction pathway via five-coordinate intermediates (2, 4, and 6).

		(1) $TiCl_3(OH)^-$	(2) $TiCl_3(OH)_2^{2-}$	(3) $TiCl_2(OH)_2^-$	(4) $TiCl_2(OH)_3^{2-}$	(5) $TiCl(OH)_3^-$	(6) $TiCl(OH)_4^{2-}$	(7) $Ti(OH)_4^-$
reductant	net charge	−0.668	−1.050	−0.841	−1.087	−0.231	−1.720	−0.089
	spin density	+0.999	+0.033	+1.000	+0.055	+0.190	+1.001	+0.017
Pd cluster	net charge	−0.332	−0.950	−0.159	−0.913	−0.769	−0.280	−0.911
	spin density	+0.001	+0.967	0.000	+0.945	+0.810	−0.001	+0.983

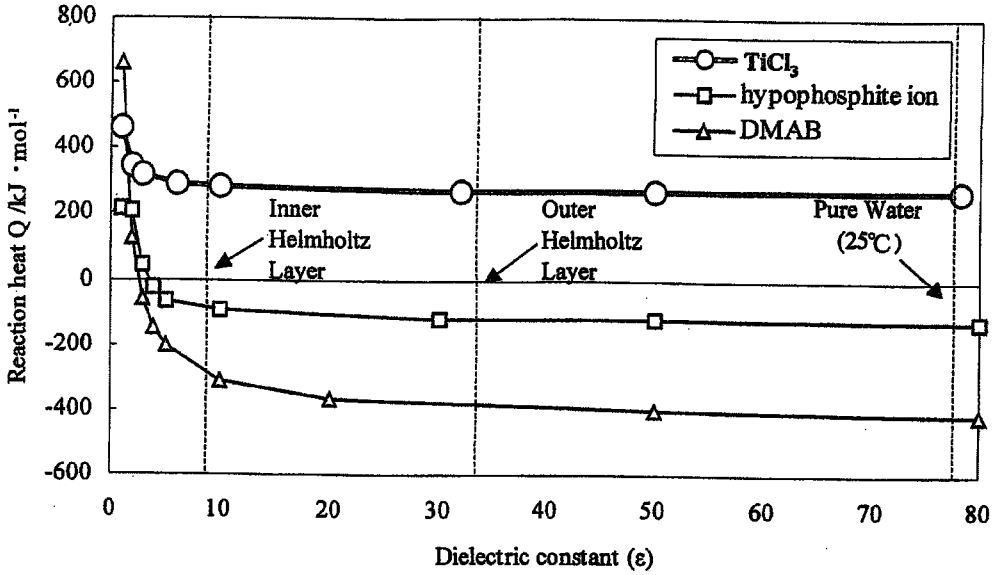

Fig. 1 Solvation effects on the substitution reaction of $TiCl_3$.

lated' state was evaluated as fundamental examination. Based upon these results, in this section, the reaction of $TiCl_3$ on the Pd surface is investigated to evaluate the effect of its catalytic activity, which plays a key role for the overall reactions.

In our previous study,[4] it was indicated that all of the intermediate species were stabilized at the surface of Pd cluster. In order to investigate this in detail, the mechanism is examined in terms of net charge and spin density.

Table 3 shows the change in net charge and spin density of intermediates via five-coordinate intermediates pathway. First, in the case of the four-coordinate intermediates, (1) and (3), charge and spin remain at the reductant part, whereas they begin to shift to the Pd metal cluster part in the case of (5), and are finally transferred to the metal cluster part for the intermediates (7). This result indicates that the electron emission takes place to form $Ti(OH)_4^-$. On the other hand, charge and spin are transferred to the metal cluster part for the five-coordinate intermediates (2) and (4). Such an electron transfer from dianion state intermediates to the metal part leads further stabilization compared with the case of the four-coordinate intermediates. However, charge and spin remain at the reductant part in the case of (6), since they are transferred to the Pd cluster part on (5). Thus, it is expected that the reductant is much reactive and driving the next reaction step, *i.e.* the electron emission. Divalent changes in charge at the reductant part which are accompanied by the reaction from (6) to (7), are due to emission of Cl^- anion plus electron transfer to the metal cluster part. Change in charge is +0.631 at the Pd cluster part. Thus, the oxidation of Ti from trivalent to tetravalent state took place to accept electron to the Pd cluster from reductant species, whereas it occurred to form $Ti(OH)_4$ on isolated state. These results indicate that the Pd surface enhances the reaction of $TiCl_3$ and electron emission.

3. 3 Solvation effects

Next, we examine the solvation effect using the SCRF-IPCM method, focusing upon the reaction heat (Q) defined by

$$TiCl_3OH^- + 3OH^- = Ti(OH)_4 + 3Cl^- + e^- + Q(kJ/mol) \quad (1)$$

which is calculated to be +436.1 kJ/mol in isolated state. The value of Q decreases exponentially as the dielectric constant (e) becomes higher ; namely, from +465.6 kJ/mol at e=1.0 to 269.1 kJ/mol at e=78.3.

Fig. 1 shows the change of Q by taking the solvation effect into account. In this figure, we show two levels corresponding to the dielectric constants of the inner and outer Helmholtz layers, which are estimated by the Bockris-Devanathan-Muller model[18] to be 6.0 and 32.0, respectively.

In Fig. 1, the results for hypophosphite ion[3] and DMAB[19] are also plotted. The results for these reduc-

tants show that only the reaction in the inner layer is exothermic. Therefore, their oxidation reaction is expected to proceed preferentially at the solid/liquid interface. Such a tendency is also expected from the calculated value of the heat of electron emission reaction for $TiCl_3$ (+559.3 kJ/mol), indicating the exothermic state. On the other hand, the heat of $TiCl_3$ is still exothermic where the dielectric constant is near the pure water, indicating that $TiCl_3$ is reactive even in pure water. This corresponds to the case with practical bath system in which $TiCl_3$ must be stabilized using complex compound such as EDTA.[5-6]

4 Summary

In the present work, we have investigated the electron emission mechanism of the $TiCl_3$ reductant for the electroless deposition by ab initio MO method.

The reaction of $TiCl_3$ proceeds with substitution reactions of Cl^- by OH^-. As the reaction proceeds, the energy of the intermediates was stabilized due to the difference in the stability between Ti-Cl and Ti-OH^- bonds and it is expected that the electron emission of $TiCl_3$ took place at the reaction of $TiCl(OH)_3$ and OH^- to produce $Ti(OH)_4$, by changing the valence of Ti from trivalent to tetravalent, while that of hypophosphite ion and DMAB, which are typical reductants, proceeds by the substitution of H by OH^-. Furthermore, it was also expected that all of the intermediate species were stabilized on the surface of the metal such as Pd, which enhances the electron emission reaction of $TiCl_3$ by accepting the emitted electron from the reductant species. From the analysis on the effect of solvation, it was indicated that the reaction was influenced significantly, and could proceed even in pure water corresponding to the case with practical system.

As a result, by means of the MO method, the electron emission mechanism of $TiCl_3$ was clarified in addition to typical reductant, and the practical characteristics, that is, metal surface enhances the reaction and $TiCl_3$ is a reactive reductant was demonstrated and elucidated. In future, it is expected that this method could analyze for reaction mechanism of various reductants and, moreover, achieve total modeling of the electroless deposition process including metal deposition and catalytic activity in combination with experimental approaches.

Acknowledgements

This work was financially supported in part by the Research Grant from the Shorai-Foundation and Grant-in-Aid for a Scientific Research Project on the Priority Area of "Highly Functionized Global Interface Integration" from the Ministry of Education, Culture, Sports, Science and Technology, and was performed at the 21st Century Center of Excellence (COE) Program "Practical Nano-Chemistry" from The Ministry of Education, Culture, Sports, Science and Technology, Japan.

References

1) C. R. Shipley, *Plat. Surf. Finish.*, **71**, 92 (1984).
2) T. Homma, H. Nakai, M. Onishi, and T. Osaka, *J. Phys. Chem. B*, **103**, 1774 (1999).
3) H. Nakai, T. Homma, I. Komatsu, and T. Osaka, *J. Phys. Chem. B*, **105**, 1701 (2001).
4) T. Homma, H. Nakai, I. Komatsu, A. Tamaki, and T. Osaka, *Electrochim. Acta*, **47**, 47 (2001).
5) A. Senda, Y. Takano, and T. Nakagawa, *J. Surf. Fin. Soc. Jpn.*, **43**, 694 (1992).
6) A. Senda, Y. Takano, and T. Nakagawa, *J. Surf. Fin. Soc. Jpn.*, **43**, 589 (1992).
7) J. B. Foresman, T. A. Keith, K. B. Wiberg, J. M. Snoonian, and J. J. Frisch, *Phys. Chem.*, **100**, 16098 (1996).
8) The Chemical Society of Japan, *Kagaku-binran-kisohenn*, Maruzen, Tokyo, p. II-501 (1984) (in Japanese).
9) M. J. Frisch, G. W. Trucks, H. B. Schlegel, G. E. Scuseria, M. A. Robb, J. R. Cheeseman, V. G. Zakrzewski, J. A. Montgomery, R. E. Stratmann, J. C. Burant, S. Dapprich, J. M. Millam, A. D. Daniels, K. N. Kudin, M. C. Strain, O. Farkas, J. Tomasi, V. Barone, M. Cossi, R. Cammi, B. Mennucci, C. Pomelli, C. Adamo, S. Clifford, J. Ochterski, G. A. Petersson, P. Y. Ayala, Q. Cui, K. Morokuma, D. K. Malick, A. D. Rabuck, K. Raghavachari, J. B. Foresman, J. Cioslowski, J. V. Ortiz, B. B. Stefanov, G. Liu, A. Liashenko, P. Piskorz, I. Komaromi, R. Gomperts, R. L. Martin, D. J. Fox, T. Keith, M. A. Al-Laham, C. Y. Peng, A. Nanayakkara, C. Gonzalez, M. Challacombe, P. M. W. Gill, B. G. Johnson, W. Chen, M. W. Wong, J. L. Andres, M. Head-Gordon, E. S. Replogle, and J. A. Pople, Gaussian 98 ; Gaussian, Inc., Pittsburgh PA (1998).
10) S. Huzinaga, Gaussian basis sets for molecular calculations (1984).
11) R. A. Kendall, T. H. Dunning Jr., and R. J. J. Harrison, *Chem. Phys.*, **96**, 6796 (1992).
12) D. E. Woon and T. H. Dunning Jr., *J. Chem. Phys.*, **98**, 1358 (1993).
13) P. J. Hay and W. R. Wadt, *J. Chem. Phys.*, **82**, 299 (1985).
14) J. A. Tossell, *J. Magn. Reson.*, **94**, 301 (1991).
15) J. D. Lee, *a new CONCISE INORGANIC CHEMISTRY*, VNR International, London p. 93 (1977).
16) W. B. Pearson, *Crystal chemistry and physics of metals and alloys*, John Wiley and Sons, New York, p. 153 (1972).
17) F. A. Cotton, G. Wilkinson, and P. L. Gaus, *Basic Inorganic Chemistry*, John Wiley and Sons, New York, p. 87 (1995).
18) J. O'M. Bockris, M. A. V. Devanathan, and K. Muller, *Proc. Roy. Soc. (London)*, **A 274**, 55 (1963).
19) T. Homma, A. Tamaki, H. Nakai, and T. Osaka, *J. Electroanal. Chem.*, **559**, 131 (2003).

New recurrence relations for the rapid evaluation of electron repulsion integrals based on the accompanying coordinate expansion formula

Masato Kobayashi and Hiromi Nakai[a)]
Department of Chemistry, School of Science and Engineering, Waseda University, Tokyo 169-8555, Japan

(Received 26 November 2003; accepted 11 June 2004)

We present an algorithm for the rapid computation of electron repulsion integrals (ERIs) over Gaussian basis functions based on the accompanying coordinate expansion (ACE) formula. The present algorithm uses equations termed *angular momentum reduced* expressions and introduces two types of recurrence relations to ACE formulas. Numerical efficiencies are assessed for $(p\ p|p\ p)$ and $(sp\ sp|sp\ sp)$ ERIs by using the floating-point operation count. The algorithm is suitable for calculating ERIs for the same exponents but different angular momentum functions, such as L shells and derivatives of ERIs. The present algorithm is also capable of calculating ERIs with highly contracted Gaussian basis functions. © *2004 American Institute of Physics.*
[DOI: 10.1063/1.1778712]

I. INTRODUCTION

In quantum chemical calculations, rapid evaluation of electron repulsion integrals (ERIs) is very important. Several effective algorithms have been proposed for this purpose.[1–20]

The PRISM algorithm presented by Gill and Pople[9] is one of the most efficient, and has been adopted in the GAUSSIAN program package.[21] This algorithm uses two types of recurrence relations (RRs) effectively: the vertical recurrence relation (VRR) by Obara and Saika,[10] which increases the orbital angular momentum quantum number, and the horizontal recurrence relation (HRR) by Head-Gordon and Pople,[11] which relates the integral values to the same angular momentum quantum numbers.

The PRISM algorithm is particularly effective for basis functions with the same exponents but different angular momentums because their ERIs can be constructed from the same $(s\ s|s\ s)^{(m)}$ functions using the VRR and HRR. For example, the N-31G basis sets[22,23] have the same exponent for s and p type functions. They are called L shells. A similar situation appears when gradients and Hessians of potential energies are computed. The first derivative of ERI, which is required for computing the gradient, can be expressed by using ERIs with Gaussian functions higher and lower than the original function by a single angular momentum.

The accompanying coordinate expansion (ACE) algorithm by Ishida[1–8] provides another efficient method. It is designed to minimize the total floating-point operation (FLOP) count. The optimal coordinate expansions are chosen for bra- and ket-pairs independently of the three formula types 1–3. The ACE-$b3k3$ formula, in which type-3 expansions are used for both bra- and ket-pairs, is effective for highly contracted Gaussian functions. For functions with an identical exponent but different angular momentums, such as L shells and derivatives, the ACE algorithm computes the ERIs individually. The overall effectiveness is low in such cases because of the absence of useful RRs, unlike in the PRISM algorithm, which has HRRs and VRRs.

In the following section, we derive two RRs for the ACE formula: a quasi-HRR and a quasi-VRR. Next, we explain how to use these RRs in computing ERIs. We schematize this algorithm and demonstrate its effectiveness. Finally, we compare the FLOP count of the present algorithm with previous ones.

II. THEORY AND ALGORITHM

In the ACE-$b3k3$ algorithm, a primitive ERI can be expressed by

$$[\varphi_\lambda^{\mathrm{A}}\varphi_\mu^{\mathrm{B}}|\varphi_\nu^{\mathrm{C}}\varphi_\xi^{\mathrm{D}}]=S_{\lambda\mu}^{\mathrm{AB}}S_{\nu\xi}^{\mathrm{CD}}\sum_{\{\mathrm{N}_3\}}C_4^{\mathrm{ABCD}}\{\mathrm{N}_3\}H_{4\ \lambda\mu\nu\xi}^{\mathrm{ABCD}}\{\mathrm{N}_3\}, \tag{1}$$

where $\varphi_\lambda^{\mathrm{A}}$ is a primitive Gaussian basis function centered at coordinate A, and has the exponent $\alpha_\lambda^{\mathrm{A}}$ and the quantum number $\mathrm{L_A}=(l_{\mathrm{A}}m_{\mathrm{A}}n_{\mathrm{A}})$, the sum of which ($L_{\mathrm{A}}=l_{\mathrm{A}}+m_{\mathrm{A}}+n_{\mathrm{A}}$) gives the orbital angular momentum quantum number. We omit the normalization factors. The contracted Gaussian basis function ϕ^{A} is given by

$$\phi^{\mathrm{A}}=\sum_{\lambda=1}^{K_{\mathrm{A}}}d_\lambda^{\mathrm{A}}\varphi_\lambda^{\mathrm{A}}, \tag{2}$$

and the contracted ERI is expressible as

$$(\phi^{\mathrm{A}}\phi^{\mathrm{B}}|\phi^{\mathrm{C}}\phi^{\mathrm{D}})=\sum_{\lambda=1}^{K_{\mathrm{A}}}\sum_{\mu=1}^{K_{\mathrm{B}}}\sum_{\nu=1}^{K_{\mathrm{C}}}\sum_{\xi=1}^{K_{\mathrm{D}}}d_\lambda^{\mathrm{A}}d_\mu^{\mathrm{B}}d_\nu^{\mathrm{C}}d_\xi^{\mathrm{D}}[\varphi_\lambda^{\mathrm{A}}\varphi_\mu^{\mathrm{B}}|\varphi_\nu^{\mathrm{C}}\varphi_\xi^{\mathrm{D}}], \tag{3}$$

where d_λ^{A} is the contraction coefficient of $\varphi_\lambda^{\mathrm{A}}$ and K_{A} is the contraction length of ϕ^{A}. The set $\{\mathrm{N}_3\}$ represents summation indices,

$$\{\mathrm{N}_3\}=\{M_{\mathrm{A}}M_{\mathrm{B}}M_{\mathrm{C}}M_{\mathrm{D}}i'j'k'h'i''j''k''h''\}. \tag{4}$$

These obey the following restrictions:

a)Electronic mail: nakai@waseda.jp

$$0\leqslant M_A\leqslant L_A,\quad 0\leqslant i'\leqslant L_A-M_A,\quad 0\leqslant i''\leqslant L_A-M_A-i',$$
$$0\leqslant M_B\leqslant L_B,\quad 0\leqslant j'\leqslant L_B-M_B,\quad 0\leqslant j''\leqslant L_B-M_B-j',$$
$$0\leqslant M_C\leqslant L_C,\quad 0\leqslant k'\leqslant L_C-M_C,\quad 0\leqslant k''\leqslant L_C-M_C-k',$$
$$0\leqslant M_D\leqslant L_D,\quad 0\leqslant h'\leqslant L_D-M_D,\quad 0\leqslant h''\leqslant L_D-M_D-h'. \tag{5}$$

$S^{AB}_{\lambda\mu}$ and $S^{CD}_{\nu\xi}$ are given by,

$$S^{AB}_{\lambda\mu}=(2\pi)^{-1/4}\left(\frac{\pi}{\gamma_1}\right)^{2/3}\exp\left(-\alpha^A_\lambda\alpha^B_\mu\frac{\overline{AB}^2}{\gamma_1}\right),$$
$$S^{CD}_{\nu\xi}=(2\pi)^{-1/4}\left(\frac{\pi}{\gamma_2}\right)^{2/3}\exp\left(-\alpha^C_\nu\alpha^D_\xi\frac{\overline{CD}^2}{\gamma_2}\right), \tag{6}$$

where

$$\gamma_1=\alpha^A_\lambda+\alpha^B_\mu,\quad \gamma_2=\alpha^C_\nu+\alpha^D_\xi. \tag{7}$$

C_4^{ABCD} in Eq. (1) is termed the accompanying coordinate part, and is given by

$$C_4^{ABCD}\{N_3\}=\sum_{\{M\}}D^{A3}_{i'i''}D^{B3}_{j'j''}D^{C3}_{k'k''}D^{D3}_{h'h''}, \tag{8}$$

where

$$D^{A3}_{i'i''}=\sum_{\{i'\}}\sum_{\{i''\}}D^{A3x}_{i'_xi''_x}D^{A3y}_{i'_yi''_y}D^{A3z}_{i'_zi''_z}, \tag{9}$$

$$D^{A3x}_{i'_xi''_x}=\binom{l_A}{M_{Ax}}\binom{l_A-M_{Ax}}{i'_x}\times\binom{i'_x}{i''_x}AB_x^{l_A-M_{Ax}-i'_x}CD_x^{i'_x-i''_x}AC_x^{i''_x}. \tag{10}$$

The sets $\{M\}$, $\{I'\}$, and $\{I''\}$ represent summation indices,

$$\{M\}=\{M_AM_BM_CM_D\},\quad M_A=(M_{Ax}M_{Ay}M_{Az}), \tag{11}$$
$$\{i'\}=\{i'_xi'_yi'_z\},\quad \{i''\}=\{i''_xi''_yi''_z\}, \tag{12}$$

which obey the following restrictions:

$$0\leqslant M_{Ax}\leqslant l_A,\quad 0\leqslant i'_x\leqslant l_A-M_{Ax},\quad 0\leqslant i''_x\leqslant i'_x,$$
$$0\leqslant M_{Ay}\leqslant m_A,\quad 0\leqslant i'_y\leqslant m_A-M_{Ay},\quad 0\leqslant i''_y\leqslant i'_y,$$
$$0\leqslant M_{Az}\leqslant n_A,\quad 0\leqslant i'_z\leqslant n_A-M_{Az},\quad 0\leqslant i''_z\leqslant i'_z,\ldots, \tag{13}$$
$$M_{Ax}+M_{Ay}+M_{Az}=M_A,$$
$$i'_x+i'_y+i'_z=i',$$
$$i''_x+i''_y+i''_z=i'',\ldots, \tag{14}$$
$$M_{Ax}+M_{Bx}+M_{Cx}+M_{Dx}=\text{even},\ldots. \tag{15}$$

The efficient computation of accompanying coordinate part C_4^{ABCD} is discussed in detail in Ref. 2.

$H^{ABCD}_{4\lambda\mu\nu\xi}$ is termed the core part, and is given by

$$H^{ABCD}_{4\lambda\mu\nu\xi}\{N_3\}=\sum_{i_1}^{[(M_A+M_B)/2]}\sum_{i_2}^{[(M_C+M_D)/2]}G_{i_1i_2}\sigma_A^{b_A+d_A}\sigma_B^{a_B+c_B}\sigma_C^{d_C+b_C}\sigma_D^{c_D+a_D}\frac{\sigma_1^{M_A+M_B-i_1}\sigma_2^{M_C+M_D-i_2}}{(\sigma_1+\sigma_2)^{M-i_1-i_2+1/2}}\times\sum_{s_1}^{a_B+b_A}\sum_{s_2}^{c_D+d_C}(-)^{s_1+s_2}\binom{a_B+b_A}{s_1}\binom{c_D+d_C}{s_2}\times\left(\frac{\sigma_1}{\sigma_1+\sigma_2}\right)^{i'+j'+s_1}\left(\frac{\sigma_2}{\sigma_1+\sigma_2}\right)^{k'+h'+s_2}F_{\zeta+s_1+s_2}(z), \tag{16}$$

where

$$\sigma_1=\frac{1}{2\gamma_1},\quad \sigma_2=\frac{1}{2\gamma_2}, \tag{17}$$
$$\sigma_A=\frac{\alpha^A_\lambda}{\gamma_1},\quad a_B=L_A-M_A-i',\quad a_D=i'-i'',$$
$$\sigma_B=\frac{\alpha^B_\mu}{\gamma_1},\quad b_A=L_B-M_B-j',\quad b_C=j'-j'',$$
$$\sigma_C=\frac{\alpha^C_\nu}{\gamma_2},\quad c_D=L_C-M_C-k',\quad c_B=k'-k'',$$
$$\sigma_D=\frac{\alpha^D_\xi}{\gamma_2},\quad d_C=L_D-M_D-h',\quad d_A=h'-h'', \tag{18}$$
$$M=(M_A+M_B+M_C+M_D)/2, \tag{19}$$
$$\zeta=i'+j'+k'+h'+M-i_1-i_2, \tag{20}$$
$$G_{i_1i_2}=(-1)^{M_A+M_B+M-(i_1+i_2)}\sum_{\{I\}}g_xg_yg_z, \tag{21}$$
$$g_x=\binom{M_{Ax}+M_{Bx}}{2i_{1x}}\binom{M_{Cx}+M_{Dx}}{2i_{2x}}(2i_{1x}-1)!!\times(2i_{2x}-1)!!(2M_x-2i_{1x}-2i_{2x}-1)!!. \tag{22}$$

The set $\{I\}$ also represents summation indices

$$\{I\}=\{i_{1x}i_{1y}i_{1z}i_{2x}i_{2y}i_{2z}\}, \tag{23}$$

which obey the restrictions

$$0\leqslant i_{1x}\leqslant[(M_{Ax}+M_{Bx})/2],\ldots,$$
$$0\leqslant i_{2x}\leqslant[(M_{Cx}+M_{Dx})/2],\ldots, \tag{24}$$
$$i_1=i_{1x}+i_{1y}+i_{1z},\quad i_2=i_{2x}+i_{2y}+i_{2z}, \tag{25}$$
$$2M_x=M_{Ax}+M_{Bx}+M_{Cx}+M_{Dx}. \tag{26}$$

$F_m(z)$ is the molecular incomplete Γ function, and is given by

$$F_m(z)=\int_0^1 t^{2m}\exp(-zt^2)dt, \tag{27}$$

where

$$z=\frac{\overline{\mathrm{PQ}}^2}{4\delta}, \tag{28}$$

$$\mathbf{P}=\sigma_A\mathbf{A}+\sigma_B\mathbf{B}, \quad \mathbf{Q}=\sigma_C\mathbf{C}+\sigma_D\mathbf{D}, \tag{29}$$

$$\delta=\frac{1}{4\gamma_1}+\frac{1}{4\gamma_2}. \tag{30}$$

In this paper, we focus on the rapid computation of the core part. An effective algorithm for computing the core part that has been described previously[2] uses the following equations:

$$\tilde{F}_m(z)=\frac{F_m(z)}{\sqrt{\sigma_1+\sigma_2}}, \tag{31}$$

$$F_{mn}=\left(\frac{\sigma_1}{\sigma_1+\sigma_2}\right)^m\left(\frac{\sigma_2}{\sigma_1+\sigma_2}\right)^n\tilde{F}_{m+n}(z), \tag{32}$$

$$G_{mn}^{pq}=\sigma_A^p\sigma_B^q\sum_{t=0}^{\mu}(-)^t\binom{\mu}{t}F_{m+t,n}, \tag{33}$$

$$g_{mM_1}^{pq}=\sigma_A^p\sigma_B^q\sigma_1^{M_1}\sum_{t=0}^{\mu}(-)^t\binom{\mu}{t}F_{m+t-M_1,0}, \tag{34}$$

$$H_{mn}^{pqrs}=\sigma_C^r\sigma_D^s\sum_{t=0}^{\nu}(-)^t\binom{\nu}{t}G_{m,n+t}^{pq}, \tag{35}$$

$$h_{mnM_2}^{pqrs}=\sigma_C^r\sigma_D^s\sum_{t=0}^{\nu}(-)^t\binom{\nu}{t}\times\begin{cases}\sigma_2^{M_2}G_{m,n+t-M_2}^{pq} & (n+t-M_2\geq 0)\\ \sigma_2^{n+t}g_{m,-n-t+M_2}^{pq} & (n+t-M_2<0),\end{cases} \tag{36}$$

where $\mu=L_A+L_B-m$, $\nu=L_C+L_D-n$. Equations (35) and (36) correspond to the core part $H_{4\lambda\mu\nu\xi}^{\mathrm{ABCD}}$.

Here, we define *angular momentum reduced* (AMR) expressions as an extension of Eqs. (33)–(36),

$$G_{mn(R_1)}^{pq}=\sigma_A^p\sigma_B^q\sum_{t=0}^{\mu-R_1}(-)^t\binom{\mu-R_1}{t}F_{m+t,n}, \tag{37}$$

$$g_{mM_1(R_1)}^{pq}=\sigma_A^p\sigma_B^q\sigma_1^{M_1}\sum_{t=0}^{\mu-R_1}(-)^t\binom{\mu-R_1}{t}F_{m+t-M_1,0}, \tag{38}$$

$$H_{mn(R_1R_2)}^{pqrs}=\sigma_C^r\sigma_D^s\sum_{t=0}^{\nu-R_2}(-)^u\binom{\nu-R_2}{t}G_{m,n+t(R_1)}^{pq}, \tag{39}$$

$$h_{mnM_2(R_1R_2)}^{pqrs}=\sigma_C^r\sigma_D^s\sum_{t=0}^{\nu-R_2}(-)^u\binom{\nu-R_2}{t}\times\begin{cases}\sigma_2^{M_2}G_{m,n+t-M_2(R_1)}^{pq} & (n+t-M_2\geq 0)\\ \sigma_2^{n+t}g_{m,-n-t+M_2(R_1)}^{pq} & (n+t-M_2<0),\end{cases} \tag{40}$$

where R_1 and R_2 denote the AMR level for the bra- and ket-pair, respectively, and are restricted by $0\leq R_1\leq\mu$ and $0\leq R_2\leq\nu$. Using $\sigma_A+\sigma_B=1$ and $\sigma_C+\sigma_D=1$, we can easily derive the following RRs for AMR expressions:

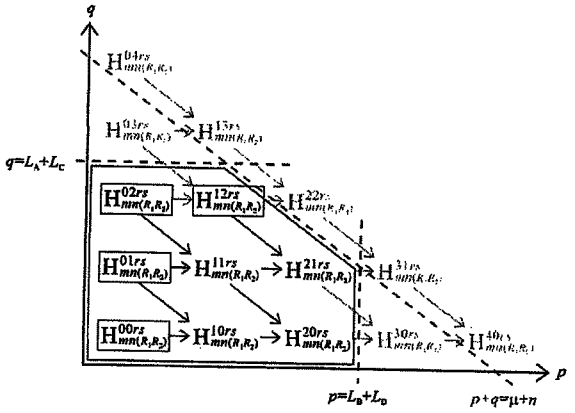

FIG. 1. Computational scheme for core part $H_{mn(R_1R_2)}^{pqrs}$ using the bra-ACE-HRR (39).

$$H_{mn(R_1R_2)}^{pqrs}=H_{mn(R_1R_2)}^{p,q-1,r,s}-H_{mn(R_1R_2)}^{p+1,q-1,r,s}, \tag{41}$$

$$h_{mnM_2(R_1R_2)}^{pqrs}=h_{mnM_2(R_1R_2)}^{p,q-1,r,s}-h_{mnM_2(R_1R_2)}^{p+1,q-1,r,s}, \tag{42}$$

$$H_{mn(R_1R_2)}^{pqrs}=H_{mn(R_1R_2)}^{p,q,r,s-1}-H_{mn(R_1R_2)}^{p,q,r+1,s-1}, \tag{43}$$

$$h_{mnM_2(R_1R_2)}^{pqrs}=h_{mnM_2(R_1R_2)}^{p,q,r,s-1}-h_{mnM_2(R_1R_2)}^{p,q,r+1,s-1}. \tag{44}$$

Since all terms in these RRs have the same level of angular momentum reduction, we call them ACE-HRRs. Equations (41) and (42) are termed bra-ACE-HRRs since they change only (p,q) related to the bra-pair. Similarly, Eqs. (43) and (44) are called the ket-ACE-HRRs. Although similar recurrence formulas are given in Ref. 2, they are based on traditional expressions (33)–(36), instead of AMR expressions (37)–(40). Thus, the computational scheme in Ref. 2 differs from the present scheme defined in terms of ACE-HRRs.

Figure 1 schematizes the computational procedure with the bra-ACE-HRR [Eq. (41)], with $L_A=L_B=L_C=L_D=1$, $m=0$, and $n=1$. This appears in the computation of the core part $H_{mn(R_1R_2)}^{pqrs}$ for the $(p\ p|p\ p)$ ERI. The necessary conditions for the parameters p and q are

$$0\leq p\leq L_B+L_D, \tag{45}$$

$$0\leq q\leq L_A+L_C, \tag{46}$$

$$\max(0,[(L_A+L_B)/2]-m)\leq p+q\leq\mu+n. \tag{47}$$

The upper boundaries are shown by the dashed lines in the figure. The region satisfying the above three conditions is the area enclosed by the solid line. Thus, we have to calculate eight $H_{mn(R_1R_2)}^{pqrs}$ terms. The arrows in Fig. 1 indicate the calculation using the bra-ACE-HRR (41). The tips of the pair of arrows correspond to the left-hand side of Eq. (41), and their roots correspond to the right-hand side. Note that the calculations using the ACE-HRRs can be executed outside the contraction loops. Consequently, the expensive computations of $H_{mn(R_1R_2)}^{pqrs}$ based on Eqs. (37) and (39) are only performed for

$$p=\min(w,L_B+L_D), \tag{48}$$

$$q=w-p, \tag{49}$$

where

$$\max(0,[(L_A+L_B)/2]-m)\leqslant w\leqslant \mu+n. \tag{50}$$

In Fig. 1, core parts satisfying Eqs. (48)–(50) are $H^{00rs}_{mn(R_1R_2)}$, $H^{01rs}_{mn(R_1R_2)}$, $H^{02rs}_{mn(R_1R_2)}$, and $H^{12rs}_{mn(R_1R_2)}$ as shown in the box.

The ket-ACE-HRR (43) works efficiently for the ket-pair (r,s) as well. There, expensive computations based on Eq. (39) are only performed for

$$r=\min(w',L_B+L_D), \tag{51}$$

$$s=w'-r, \tag{52}$$

where

$$\max(0,[(L_C+L_D)/2]-n)\leqslant w'\leqslant \nu+m. \tag{53}$$

Once the core parts corresponding to Eqs. (51)–(53) are obtained in the contraction loops, the other core parts are calculated by using Eq. (43) outside the loops. For another core part $h^{pqrs}_{mnM_2(R_1R_2)}$, the bra- and ket-ACE-HRRs (42) and (44), respectively, work to reduce the computational cost. The conditions (48), (49), (51), and (52) correspond to the expensive computations of the core parts $h^{pqrs}_{mnM_2(R_1R_2)}$, where the ranges of w and w' given by

$$\max(0,[(L_A+L_B)/2]-m-M_1)\leqslant w\leqslant \mu-M_1, \tag{54}$$

$$\max(0,[(L_C+L_D)/2]-n-M_2)\leqslant w'\leqslant \nu+m-M_2 \tag{55}$$

should be used in place of Eqs. (50) and (53), respectively.

Next, we present a different set of RRs. Applying the binomial coefficient relation,

$$\binom{n-1}{r-1}+\binom{n-1}{r}=\binom{n}{r}, \tag{56}$$

to the AMR expressions yields the following RRs:

$$H^{pqrs}_{mn(R_1R_2)}=H^{pqrs}_{mn(R_1+1,R_2)}-H^{pqrs}_{m+1,n(R_1R_2)}, \tag{57}$$

$$h^{pqrs}_{mnM_2(R_1R_2)}=h^{pqrs}_{mnM_2(R_1+1,R_2)}-h^{pqrs}_{m+1,n,M_2(R_1R_2)}, \tag{58}$$

$$H^{pqrs}_{mn(R_1R_2)}=H^{pqrs}_{mn(R_1,R_2+1)}-H^{pqrs}_{m,n+1(R_1R_2)}, \tag{59}$$

$$h^{pqrs}_{mnM_2(R_1R_2)}=h^{pqrs}_{mnM_2(R_1,R_2+1)}-h^{pqrs}_{m,n+1,M_2(R_1R_2)}. \tag{60}$$

Because the AMR levels on the left-hand side of these RRs are lower than those on the right-hand side, they are called ACE-VRRs. Equations (57) and (58) in particular are called bra-ACE-VRRs since they modify only R_1 and m, which are related to the bra-pair. Similarly, Eqs. (59) and (60) are called ket-ACE-VRRs. These RRs have not been proposed in previous ACE formulas because no RRs corresponding to Eqs. (57)–(60) had been established for the traditional expressions (33)–(36) prior to the present study.

Figure 2 schematize the computational procedure using the bra-ACE-VRR (57) with $L_A+L_B=2$. This appears in the computation for the bra-pair $(p\ p|$ or $(d\ s|$. The restrictions on R_1 and m are

$$R_1\geqslant 0, \tag{61}$$

$$m\geqslant 0, \tag{62}$$

$$0\leqslant R_1+m\leqslant L_A+L_B. \tag{63}$$

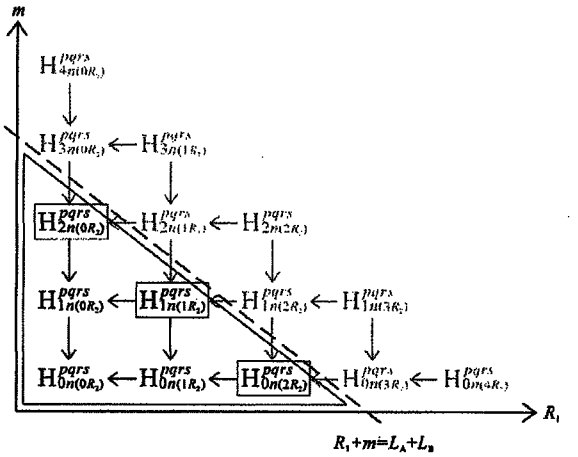

FIG. 2. Computational scheme for core part $H^{pqrs}_{mn(R_1R_2)}$ using the bra-ACE-VRR (55).

The upper boundary is shown by the dashed line in Fig. 2. The core parts, which need to be calculated, correspond to the region enclosed by the solid line, i.e., six $H^{pqrs}_{mn(R_1R_2)}$ terms. The arrows in Fig. 2 indicate the calculation with the bra-ACE-VRR (57). The tips and roots of the arrows correspond to the left- and right-hand sides of Eq. (57), respectively. As in the case of ACE-HRRs, the computation using the ACE-VRRs can be executed outside the contraction loops.

The expensive computations of $H^{pqrs}_{mn(R_1R_2)}$ based on Eq. (37) are eventually reduced to the core parts satisfying

$$R_1+m=L_A+L_B. \tag{64}$$

In Fig. 2, they correspond to $H^{pqrs}_{2n(0R_2)}$, $H^{pqrs}_{1n(1R_2)}$, and $H^{pqrs}_{0n(2R_2)}$ as shown in the box. The reduction given by Eq. (58) is also applicable to the computations of $h^{pqrs}_{mnM_2(R_1R_2)}$ using Eq. (38). Furthermore, using Eq. (64), Eqs. (37) and (38) can be simplified to

$$G^{pq}_{mn(\mu)}=\sigma^p_A\sigma^q_B F_{mn}, \tag{65}$$

$$g^{pq}_{mM_1(\mu)}=\sigma^p_A\sigma^q_B\sigma_1^{M_1}F_{m-M_1,0}. \tag{66}$$

These simple expressions, which should be computed in the quadruple contraction loops, guarantee to reduce the total FLOP count.

The usage of the ket-ACE-VRRs (59) and (60) partially places the computations of the core parts out of the double contraction loops as well. The following constraint applies to calculations involving Eqs. (39) and (40):

$$R_2+n=L_C+L_D. \tag{67}$$

This simplifies Eqs. (39) and (40) to

$$H^{pqrs}_{mn(\mu\nu)}=\sigma^r_C\sigma^s_D G^{pq}_{mn(\mu)}, \tag{68}$$

$$h^{pqrs}_{mnM_2(\mu\nu)}=\sigma^r_C\sigma^s_D\begin{cases}\sigma_2^{M_2}G^{pq}_{m,n-M_2(\mu)} & (n\geqslant M_2)\\ \sigma_2^n g^{pq}_{m,-n+M_2(\mu)} & (n<M_2).\end{cases} \tag{69}$$

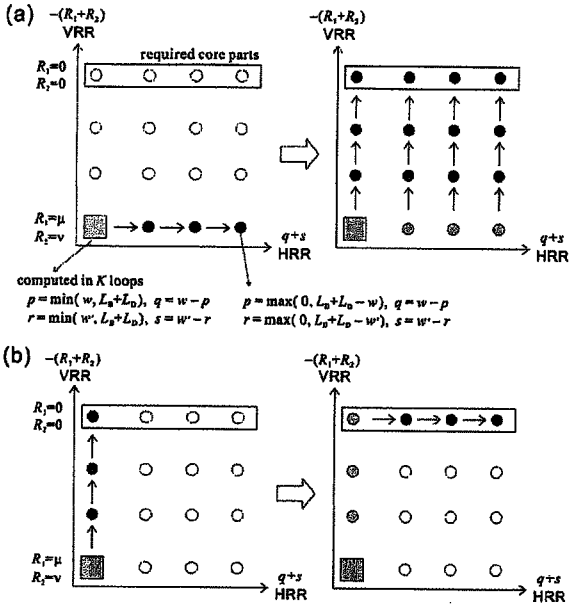

FIG. 3. Schematic of the combination of ACE-HRR and ACE-VRR.

Effective combination of the above two RRs, that is, ACE-HRRs and ACE-VRRs, is important to achieving high performance. Figure 3 shows schematics of two possible combinations. In Fig. 3(a), the first step adopts the ACE-HRRs, while the second step uses the ACE-VRRs. The situation is reversed in Fig. 3(b). The required core part is the same in both cases, and is shown in the box. The core part calculated in the contraction loops (denoted by gray squares) is also the same. The black circles in Fig. 3 correspond to the core parts to be calculated in that step, the gray circles to those which have already been obtained, and the white circles to those which have never been computed. The computational costs associated with using the ACE-HRRs is comparable in both RR combinations. However, fewer core parts are calculated with the ACE-VRRs in Fig. 3(b) than in Fig. 3(a). This indicates that the procedure drawn in Fig. 3(b) is more effective.

Figure 4 shows the computational algorithm using the present two RRs. Here,

$$K_{\mathrm{bra}}=K_{\mathrm{A}}K_{\mathrm{B}}, \tag{70}$$

$$K_{\mathrm{ket}}=K_{\mathrm{C}}K_{\mathrm{D}}. \tag{71}$$

First, computations of Eqs. (31), (32), (65), and (66) are carried out in the quadruple contraction loop. Next, calculations involving Eqs. (68) and (69) are performed in the double loop. The subsequent processes are executed outside the loops. As discussed in Fig. 3, ACE-VRRs (57)–(60) are used before applying ACE-HRRs (41)–(44). All necessary core parts $H_{4\lambda\mu\nu\xi}^{\mathrm{ABCD}}$ of Eq. (16) have now been calculated. In the final step, the accompanying coordinate parts C_4^{ABCD} of Eq. (8) are computed and multiplied by the core parts in order to obtain ERIs, according to Ref. 2.

loop over K_{ket}
  loop over K_{bra}
    calculate $\tilde{F}_m(z)$
    calculate F_{mn}
    calculate $G_{mn(\mu)}^{pq}$ (for the restricted p and q)
    calculate $g_{mM_1(\mu)}^{pq}$ (for the restricted p and q)
  end loop over K_{bra}
  calculate $H_{mn(\mu\nu)}^{pqrs}$ (for the restricted p, q, r, and s)
  calculate $h_{mnM_2(\mu\nu)}^{pqrs}$ (for the restricted p, q, r, and s)
end loop over K_{ket}
calculate $H_{mn(R_1R_2)}^{pqrs}$ using ACE-VRR (for the restricted p, q, r, and s)
calculate $h_{mnM_2(R_1R_2)}^{pqrs}$ using ACE-VRR (for the restricted p, q, r, and s)
calculate all necessary $H_{mn(R_1R_2)}^{pqrs}$ using ACE-HRR
calculate all necessary $h_{mnM_2(R_1R_2)}^{pqrs}$ using ACE-HRR
calculate accompanying coordinate part

FIG. 4. Algorithm for computing ERIs using ACE-HRR and ACE-VRR.

III. COMPUTATIONAL PERFORMANCE

We assess the computational performance of the present algorithm using the FLOP count method, which has been widely employed to compare algorithms ever since Head-Gordon and Pople[11] introduced the idea. The total FLOP count of ERI evaluation is commonly given by

$$xK_{\mathrm{bra}}K_{\mathrm{ket}}+yK_{\mathrm{ket}}+z. \tag{72}$$

For simplicity, all contraction lengths are assumed to be equal,

$$K_{\mathrm{A}}=K_{\mathrm{B}}=K_{\mathrm{C}}=K_{\mathrm{D}}\equiv K, \tag{73}$$

$$K_{\mathrm{bra}}=K_{\mathrm{ket}}=K^2. \tag{74}$$

Then, the FLOP count can be expressed in terms of K,

$$xK^4+yK^2+z. \tag{75}$$

Note that this assumption does not come from the limitation of the present algorithm. We simply use the expression to compare the present algorithm with previous ones.

Table I shows FLOP count parameters (x, y, z) for (p $p|p$ p) ERIs. Because the present algorithm performs the computations involving RRs outside the K^4 and K^2 loops, x and y decrease and z increases in comparison with those of the conventional ACE-$b3k3$ algorithm. Parameter x of the present algorithm is the lowest in Table I, and is equal to that of the PRISM algorithm. This indicates that our method and the PRISM method both become more effective as the contraction length K increases.

Tables II compares the total FLOP counts with $K=5$, 10, and 15 for (p $p|p$ p) ERIs. The FLOP count of the present algorithm is comparable to that of the PRISM algorithm, but lower than that of the others. The FLOP count ratios with respect to the present algorithm are also shown in parentheses in Table II. While the ratio of the Pople-Hehre (PH) (Ref. 12) algorithm decreases as K increases, those of the other

TABLE I. FLOP count parameters (x,y,z) for $(p\ p|p\ p)$ ERIs.[a,b]

Algorithm	x	y	z
ACE-RR (present)	70	183	2490
ACE-$b3k3$ (Ishida)[c]	75	205	2318
PRISM (Gill and Pople)[d]	70	168	2904
Pople and Hehre[e]	220	2300	4000
Gill, Head-Gordon, and Pople[f]	300	610	680
Dupuis and Marquez[g]	440	140	650
Lindh, Ryu, and Liu[h]	691	30	330
Head-Gordon and Pople[i]	750	0	243
McMurchie and Davidson[j]	1100	600	0
Dupuis, Rys, and King[k]	904	30	0

[a]Except for the calculation of $\tilde{F}_m(z)$.
[b]Total FLOP count is given by Eq. (72).
[c]Reference 2. This FLOP count is not optimized for $(p\ p|p\ p)$ type of ACE-$b3k3$ formula.
[d]Reference 9.
[e]Reference 12.
[f]Reference 13.
[g]Reference 17.
[h]Reference 14.
[i]Reference 11.
[j]Reference 15.
[k]Reference 16.

TABLE III. FLOP count parameters (x,y,z) for $(sp\ sp|sp\ sp)$ ERIs.[a,b]

Algorithm	x	y	z
ACE-RR (present)	155	774	4548
ACE-$b3k3$ (Ishida)[c]	349	572	4282
Pople and Hehre[d]	220	2300	4000
Gill, Head-Gordon, and Pople[e]	450	1300	1700
Lindh, Ryu, and Liu[f]	753	30	800
Head-Gordon and Pople[g]	1400	30	800
McMurchie and Davidson[h]	1500	1700	0
Dupuis, Rys, and King[i]	1056	30	0

[a]Except for the calculation of $\tilde{F}_m(z)$.
[b]Total FLOP count is given by Eq. (72).
[c]Reference 8. This estimated value is given by the sum of the FLOP of $(pp|pp)$, $(pp|ps)$, $(ps|ps)$, and so on, i.e., maximum value of FLOP count.
[d]Reference 12.
[e]Reference 13.
[f]Reference 14.
[g]Reference 11.
[h]Reference 15.
[i]Reference 16.

algorithms increase. Thus, with the exception of the PH algorithm, the present algorithm is more efficient for highly contracted ERIs than previous algorithms.

In the conventional ACE formula, the ERIs with L shells are evaluated individually, e.g., $(pp|pp)$, $(pp|ps)$, and $(ps|ps)$ for $(sp\ sp|sp\ sp)$ ERIs. By contrast, since the PH algorithm evaluates all corresponding ERIs simultaneously, it is more efficient for L shells than the original ACE algorithm. However, the ACE-HRRs and ACE-VRRs of the present algorithm enable us to compute those ERIs simultaneously. Table III compares FLOP count parameters (x, y, z) for $(sp\ sp|sp\ sp)$ ERIs. Note that the parameters corresponding to ACE-$b3k3$ are estimated by summing up individual FLOP parameters for $(pp|pp)$, $(pp|ps)$, $(ps|ps)$, and so on, which are taken from Ref. 8. Thus, the estimation corresponds to the maximum value. Clearly, the present algorithm is quite efficient for $(sp\ sp|sp\ sp)$ ERIs with higher contraction given that it exhibits the lowest x values.

Table IV shows total FLOP counts with comparatively small contractions $(K=1-3)$ for the $(sp\ sp|sp\ sp)$ ERIs. Except in the case of $K=1$, i.e., primitive functions, all FLOP count ratios exceed 1.00. It is worth noting that the total FLOP counts for $K=1$ are much lower than those for $K=3$. For example, when we use N-31G basis sets, both $(sp\ sp|sp\ sp)$ ERIs for $K=1$ and 3 should be computed as well as their mixtures. In this case, computing $(sp\ sp|sp\ sp)$ ERIs for $K=3$ would be more expensive than for the others. Thus, the present algorithm is expected to be the most efficient for L shells such as N-31G basis sets.

Figure 5 shows the FLOP count per primitive ERI of the $(sp\ sp|sp\ sp)$ type for $K_{\mathrm{bra}}=K_{\mathrm{ket}}=K_{\mathrm{pair}}$, that is,

$$f(K_{\mathrm{pair}};x,y,z)=x+y/K_{\mathrm{pair}}+z/K_{\mathrm{pair}}^2. \tag{76}$$

The function $f(K_{\mathrm{pair}};x,y,z)$ becomes $(x+y+z)$ at $K_{\mathrm{pair}}=1$. In the limit $K_{\mathrm{pair}}\to\infty$, $f(K_{\mathrm{pair}};x,y,z)$ approaches x.

TABLE II. FLOP counts for $(p\ p|p\ p)$ ERIs. FLOP count ratios with respect to the present algorithm are shown in parentheses.[a]

Algorithm	$K=5$	$K=10$	$K=15$
ACE-RR (present)	50 815 (1.00)	720 790 (1.00)	3 587 415 (1.00)
ACE-$b3k3$ (Ishida)[b]	54 318 (1.07)	772 818 (1.07)	3 845 318 (1.07)
PRISM (Gill and Pople)[c]	50 854 (1.00)	719 704 (1.00)	3 584 454 (1.00)
Pople and Hehre[d]	199 000 (3.92)	2 434 000 (3.38)	11 659 000 (3.25)
Gill, Head-Gordon, and Pople[e]	203 430 (4.00)	3 061 680 (4.25)	15 325 430 (4.27)
Dupuis and Marquez[f]	279 150 (5.49)	4 414 650 (6.12)	22 307 150 (6.22)
Lindh, Ryu, and Liu[g]	432 955 (8.52)	6 913 330 (9.59)	34 988 955 (9.75)
Head-Gordon and Pople[h]	468 993 (9.23)	7 500 243(10.41)	37 968 993(10.58)
McMurchie and Davidson[i]	702 500(13.82)	11 060 000(15.34)	55 822 500(15.56)
Dupuis, Rys, and King[j]	565 750(11.13)	9 043 000(12.55)	45 771 750(12.76)

[a]Except for the calculation of $\tilde{F}_m(z)$.
[b]Reference 2.
[c]Reference 9.
[d]Reference 12.
[e]Reference 13.
[f]Reference 17.
[g]Reference 14.
[h]Reference 11.
[i]Reference 15.
[j]Reference 16.

TABLE IV. FLOP counts for $(sp\ sp|sp\ sp)$ ERIs. FLOP count ratios with respect to the present algorithm are shown in parentheses.[a]

Algorithm	$K=1$	$K=2$	$K=3$
ACE-RR (present)	5477 (1.00)	10 124 (1.00)	24 069(1.00)
ACE-$b3k3$ (Ishida)[b]	5203 (0.95)	12 154 (1.20)	37 699(1.57)
Pople and Hehre[c]	6520 (1.19)	16 720 (1.65)	42 520(1.77)
Gill, Head-Gordon, and Pople[d]	3450 (0.63)	14 100 (1.39)	49 850(2.07)
Lindh, Ryu, and Liu[e]	1583 (0.29)	12 968 (1.28)	62 063(2.58)
Head-Gordon and Pople[f]	2230 (0.41)	23 320 (2.30)	114 470(4.76)
McMurchie and Davidson[g]	3200 (0.58)	30 800 (3.04)	136 800(5.68)
Dupuis, Rys, and King[h]	1086 (0.20)	17 016 (1.68)	85 806(3.57)

[a]Except for the calculation of $\bar{F}_m(z)$.
[b]Reference 2.
[c]Reference 12.
[d]Reference 13.
[e]Reference 14.
[f]Reference 11.
[g]Reference 15.
[h]Reference 16.

Since, in the Dupuis-Rys-King (DRK) (Ref. 16) algorithm, $z=0$ and y is small, $f(K_{\text{pair}};x,y,z)$ does not change much: $f(K_{\text{pair}};x,y,z)=1056$ and 1086 at $K_{\text{pair}}=1$ and ∞, respectively. By contrast, in the case of ACE-RR, ACE-$b3k3$, and PH, $f(K_{\text{pair}};x,y,z)$ decreases rapidly with K_{pair}. It is noted that, for ACE-RR, $f(K_{\text{pair}};x,y,z)$ is at its minimum in the range of $K_{\text{pair}}\geqslant 3$. While $f(K_{\text{pair}};x,y,z)$ for PH has larger values than that for ACE-$b3k3$ at $K_{\text{pair}}\leqslant 13$, the opposite is true at $K_{\text{pair}}\geqslant 14$. This is because the FLOP parameter y of PH is larger than that of ACE-$b3k3$, whereas x of PH is smaller than that of ACE-$b3k3$: $(x,y)=(220, 2300)$ and (349, 572) for PH and ACE-$b3k3$, respectively. In the case of the present ACE-RR algorithm, *both* x and y are smaller than those of PH. Thus, there is no crossing between the PH and ACE-RR curves in Fig. 5.

The present algorithm is expandable in certain directions. It can be easily combined with the ACE general contraction (GC) scheme developed by Yanai *et al.*[8] It is applicable to the solid harmonic (SH) Gaussian basis function and ACE-SH algorithm.[3–7] In addition, it is expected to be efficient in computing the first and second derivatives of ERIs,

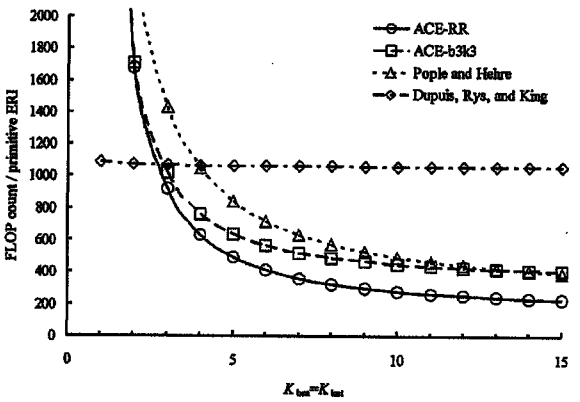

FIG. 5. FLOP count per primitive ERI of the $(sp\ sp|sp\ sp)$ class for $K_{\text{bra}}=K_{\text{ket}}$.

which are required in geometry optimization and frequency calculations, respectively.

Furthermore, it is available for the two-particle integrals peculiar to the nuclear orbital plus molecular orbital (NOMO) method.[24–27] The NOMO method determines nuclear and electronic wave functions simultaneously by using the orbital approach. In the NOMO method, nucleus-nucleus repulsion integrals and electron-nucleus attraction integrals are evaluated like ERIs. The primitive Gaussian functions are usually adopted as nuclear basis functions (NBFs). As noted in Ref. 26, it is reasonable that the exponents of NBFs are the same for s, p, and higher angular momentum functions. We would, for example, have to compute a $(spd\ spd|spd\ spd)$ type integral. Thus, the present algorithm is effective for two-particle integrals involving nuclear orbitals.

IV. CONCLUDING REMARKS

In the present study, we have developed an efficient algorithm, based on the ACE formulas, for the computation of ERI. We first derived two RRs for the ACE formulas, namely, ACE-HRRs and ACE-VRRs. We compared the efficiency of the present algorithm with those of previous algorithms by comparing FLOP counts. We showed that the present algorithm is more efficient, especially for ERIs with L shells and highly contracted basis functions. The applicability of our algorithm can be expanded to the GC scheme,[8] the SH Gaussian basis function,[3–7] the derivatives of ERI, and the two-particle integrals used in the NOMO method.[24–27]

The present ACE-RR method is an improvement on the ACE-$b3k3$ formula, which is especially designed for the evaluation of highly contracted ERIs. Note that the present method is not necessarily robust for all sorts of ERIs. We need to select the optimum algorithm, as the case may be, as well as PRISM[9] and conventional ACE algorithms.[1] For example, in the case of primitive ERIs ($K=1$), efficient RRs of the ACE-$b1k1$ formula would enable the most rapid evaluation. In our next study, RRs of other types of ACE formulas will be derived, and new selection diagrams will be presented.

The present study focused on a rapid computation of individual ERIs. However, we have also been developing a method, termed elementary basis algorithm (EBA),[20] to improve the total performance of ERI computation by separating the information on Gaussian functions into its atomic and elementary components. We expect that the combination of the present ACE-RR formulas and the EBA technique will allow rapid computation of ERIs in large molecular systems.

ACKNOWLEDGMENTS

We gratefully acknowledge Professor S. Nagase and Professor M. Schmidt for their helpful suggestions at the beginning of this study. This study was supported in part by a 21st century Center Of Excellence (COE) "Practical Nano-Chemistry" from the Japanese Ministry of Education, Culture, Sports, Science, and Technology (MEXT), a NAREGI Nano-Science Project of the MEXT, a Nanotechnology Re-

searchers Network Project from the MEXT, a Grant-in-Aid for Young Scientists (A), Grant No. "KAKENHI 14703005" from Japanese Society for the Promotion of Science (JSPS), and a Waseda University Grant for Special Research Projects.

APPENDIX: ESTIMATION OF FLOP COUNT PARAMETERS *x* AND *y* OF (*sp sp*|*sp sp*) CLASS ERI

We shall derive the FLOP count parameters for the case of $(sp\ sp|sp\ sp)$ ERIs as an example.

The L shell contains s and p type Gaussian basis functions that can be defined as follows:

$$\phi_s=\sum_{\lambda=1}^{K} d_{s,\lambda}\exp(-\alpha_\lambda r^2), \tag{A1}$$

$$\phi_{p_t}=\sum_{\lambda=1}^{K} d_{p,\lambda} r_t \exp(-\alpha_\lambda r^2), \tag{A2}$$

where $t=x, y, z$. In the computation of $(sp\ sp|sp\ sp)$ ERIs, the coefficients of the p type function are absorbed in the incomplete Γ function,

$$\tilde{F}_m(z)=d^{\mathrm{A}}_{p,\lambda}d^{\mathrm{B}}_{p,\mu}d^{\mathrm{C}}_{p,\nu}d^{\mathrm{D}}_{p,\xi}\frac{F_m(z)}{\sqrt{\sigma_1+\sigma_2}}. \tag{A3}$$

In the K^4 loop, first, the F_{mn} terms are computed as follows:

$$F_{00}=\tilde{F}_0(z) \quad (0\ \text{FLOP}), \tag{A4}$$

$$F_{10}=\left(\frac{\sigma_1}{\sigma_1+\sigma_2}\right)\tilde{F}_1(z), \quad F_{01}=\left(\frac{\sigma_2}{\sigma_1}\right)F_{10} \quad (2\ \text{FLOPs}), \tag{A5}$$

$$F_{20}=\left(\frac{\sigma_1}{\sigma_1+\sigma_2}\right)^2\tilde{F}_2(z), \quad F_{11}=\left(\frac{\sigma_2}{\sigma_1}\right)F_{20},$$

$$F_{02}=\left(\frac{\sigma_2}{\sigma_1}\right)F_{11} \quad (3\ \text{FLOPs}), \tag{A6}$$

$$F_{21}=\left\{\left(\frac{\sigma_1}{\sigma_1+\sigma_2}\right)^2\left(\frac{\sigma_2}{\sigma_1+\sigma_2}\right)\right\}\tilde{F}_3(z),$$

$$F_{12}=\left(\frac{\sigma_2}{\sigma_1}\right)F_{21} \quad (2\ \text{FLOPs}), \tag{A7}$$

$$F_{22}=\left\{\left(\frac{\sigma_1}{\sigma_1+\sigma_2}\right)^2\left(\frac{\sigma_2}{\sigma_1+\sigma_2}\right)^2\right\}\tilde{F}_4(z) \quad (1\ \text{FLOP}). \tag{A8}$$

Then, a summation has to be performed over $G^{pq}_{mn(\mu)}$ and $g^{pq}_{m\lambda_1(\mu)}$ in the K^4 loop. But first, the following ${}^{\mathrm{preadd}}G^{pq}_{mn(\mu)}$ need to be calculated:

$${}^{\mathrm{preadd}}G^{00}_{mn(\mu)}=F_{mn} \quad (0\ \text{FLOP}), \tag{A9}$$

$${}^{\mathrm{preadd}}G^{p0}_{mn(\mu)}={}^{\mathrm{preadd}}G^{p-1,0}_{mn(\mu)}\sigma_{\mathrm{A}} \quad (1\ \text{FLOP}), \tag{A10}$$

$${}^{\mathrm{preadd}}G^{pq}_{mn(\mu)}={}^{\mathrm{preadd}}G^{p,q-1}_{mn(\mu)}\sigma_{\mathrm{B}} \quad (1\ \text{FLOP}). \tag{A11}$$

The ${}^{\mathrm{preadd}}G^{pq}_{mn(\mu)}$ are subject to the constraint $0\leqslant w'(=p+q)\leqslant 2+n$. The total FLOP of Eqs. (A9)–(A11) rises to 27. For $(p\ p|$ bra type, $G^{pq}_{mn(\mu)}$ are summed as follows:

$$(pp|G^{pq}_{mn(\mu)}+={}^{\mathrm{preadd}}G^{pq}_{mn(\mu)} \quad (1\ \text{FLOP}), \tag{A12}$$

where "$A+=B$" denotes "adding B to A." The required $(pp|G^{pq}_{mn(\mu)}$ are constrained by Eq. (50). Total FLOP of Eq. (A12) then rises to 34. For $(p\ s|$ bra type, these are computed as follows:

$$(ps|G^{pq}_{mn(\mu)}+={}^{\mathrm{preadd}}G^{pq}_{mn(\mu)}\left(\frac{d^{\mathrm{A}}_{p,\lambda}d^{\mathrm{B}}_{s,\mu}}{d^{\mathrm{A}}_{p,\lambda}d^{\mathrm{B}}_{p,\mu}}\right) \quad (2\ \text{FLOPs}). \tag{A13}$$

The $(sp|$ and $(ss|$ types are calculated in similar fashion to the $(ps|$ type. Given the restriction of Eq. (50), the FLOP count to compute $(ps|$, $(sp|$, and $(ss|$ type $G^{pq}_{mn(\mu)}$ rises to 84. According to Eq. (54), the only $g^{pq}_{m\lambda_1(\mu)}$ required is

$$(pp|g^{00}_{11(1)}+=\sigma_1 F_{10} \quad (2\ \text{FLOPs}). \tag{A14}$$

Thus, the total FLOP count in the K^4 loop, i.e., FLOP parameter x, rises to 155.

In the K^2 loop, $H^{pqrs}_{mn(\mu\nu)}$ and $h^{pqrs}_{mnM_2(\mu\nu)}$ need to be summed. But first, the following ${}^{(**|}H^{pqrs}_{mn(\mu\nu)}$ and ${}^{(**|}h^{pqrs}_{mnM_2(\mu\nu)}$ need to be calculated:

$${}^{(**|}H^{pq00}_{mn(\mu\nu)}={}^{(**|}G^{pq}_{mn(\mu)} \quad (0\ \text{FLOP}), \tag{A15}$$

$${}^{(**|}H^{pqr0}_{mn(\mu\nu)}={}^{(**|}H^{p,q,r-1,0}_{mn(\mu\nu)}\sigma_{\mathrm{C}} \quad (1\ \text{FLOP}), \tag{A16}$$

$${}^{(**|}H^{pqrs}_{mn(\mu\nu)}={}^{(**|}H^{p,q,r,s-1}_{mn(\mu\nu)}\sigma_{\mathrm{D}} \quad (1\ \text{FLOP}), \tag{A17}$$

$${}^{(**|}h^{pq00}_{m0M_2(\mu\nu)}={}^{(**|}g^{pq}_{mM_2(\mu)} \quad (0\ \text{FLOP}), \tag{A18}$$

$${}^{(**|}h^{pq00}_{mnM_2(\mu\nu)}=\begin{cases}{}^{(**|}G^{pq}_{m,n-M_2(\mu)}\sigma_2^{M_2} & (n\geqslant M_2)\\ {}^{(**|}g^{pq}_{m,-n+M_2(\mu)}\sigma_2^{n} & (n<M_2)\end{cases} \quad (1\ \text{FLOP}), \tag{A19}$$

$${}^{(**|}h^{pqr0}_{mnM_2(\mu\nu)}={}^{(**|}h^{p,q,r-1,0}_{mnM_2(\mu)}\sigma_{\mathrm{C}} \quad (1\ \text{FLOP}), \tag{A20}$$

$${}^{(**|}h^{pqrs}_{mnM_2(\mu\nu)}={}^{(**|}h^{p,q,r,s-1}_{mnM_2(\mu)}\sigma_{\mathrm{D}} \quad (1\ \text{FLOP}), \tag{A21}$$

where "$(**|$" is either "$(pp|$," "$(ps|$," "$(sp|$," or "$(ss|$." The required ${}^{(**|}H^{pqrs}_{mn(\mu\nu)}$ are subject to the constraint $0\leqslant w'(=r+s)\leqslant 2+m$. $h^{pqrs}_{101(\mu\nu)}$, $h^{pqrs}_{111(\mu\nu)}$, $h^{pqrs}_{211(\mu\nu)}$, $h^{pqrs}_{121(\mu\nu)}$, and $h^{pqrs}_{221(\mu\nu)}$ are constrained by $0\leqslant w'\leqslant 2$, and $h^{pqrs}_{011(\mu\nu)}$, $h^{pqrs}_{112(\mu\nu)}$, and $h^{pqrs}_{222(\mu\nu)}$ by $w'=0$. Total FLOP of Eqs. (A15)–(A17) rises to 63 and that of Eqs. (A18)–(A21) to 17. For the $|p\ p)$ ket type, $H^{pqrs}_{mn(\mu\nu)}$ and $h^{pqrs}_{mnM_2(\mu\nu)}$ are summed as follows:

$${}^{(**|pp)}H^{pqrs}_{mn(\mu\nu)}+={}^{(**|}H^{pqrs}_{mn(\mu\nu)} \quad (1\ \text{FLOP}), \tag{A22}$$

$${}^{(**|pp)}h^{pqrs}_{mnM_2(\mu\nu)}+={}^{(**|}h^{pqrs}_{mnM_2(\mu\nu)} \quad (1\ \text{FLOP}). \tag{A23}$$

The required ${}^{(**|pp)}H^{pqrs}_{mn(\mu\nu)}$ and ${}^{(**|pp)}h^{pqrs}_{mnM_2(\mu\nu)}$ are constrained by Eqs. (53) and (55), respectively. Total FLOP of Eqs. (A22) and (A23) rise to 197 and 47, respectively. For the $|p\ s)$ ket type, these are computed as follows:

$$^{(**|ps)}H^{pqrs}_{mn(\mu\nu)} += {}^{(**|}H^{pqrs}_{mn(\mu\nu)} \times \left(\frac{d^{C}_{p,\nu} d^{D}_{s,\xi}}{d^{C}_{p,\nu} d^{D}_{p,\xi}} \right) \quad (2 \text{ FLOPs}), \tag{A24}$$

$$^{(**|ps)}h^{pqrs}_{mnM_2(\mu\nu)} += {}^{(**|}h^{pqrs}_{mnM_2(\mu\nu)} \times \left(\frac{d^{C}_{p,\nu} d^{D}_{s,\xi}}{d^{C}_{p,\nu} d^{D}_{p,\xi}} \right) \quad (2 \text{ FLOPs}). \tag{A25}$$

The $|sp)$ and $|ss)$ types are calculated in similar fashion to the $|ps)$ type. Taking into account the constraint imposed by Eq. (53), the FLOP count to compute $|ps)$, $|sp)$, and $|ss)$ type $H^{pqrs}_{mn(\mu\nu)}$ and $h^{pqrs}_{mnM_2(\mu\nu)}$ rise to 408 and 42, respectively. Total FLOP count in the K^2 loop, i.e., FLOP parameter y, rises 774.

Thus, the FLOP count parameters x and y for $(sp\ sp|sp\ sp)$ ERIs are evaluated to be $x=155$ and $y=774$. Since the estimation of FLOP parameter z is tedious and has less importance, we omit it in this appendix.

[1] K. Ishida, Int. J. Quantum Chem. **59**, 209 (1996).
[2] K. Ishida, J. Comput. Chem. **19**, 923 (1998).
[3] K. Ishida, J. Chem. Phys. **109**, 881 (1998).
[4] K. Ishida, J. Chem. Phys. **111**, 4913 (1999).
[5] K. Ishida, J. Chem. Phys. **113**, 7818 (2000).
[6] K. Ishida, in *Recent Research Developments in Quantum Chemistry*, edited by S. G. Pandalai (Transworld Research Network, India, 2001), Vol. 2, pp. 147–223.
[7] K. Ishida, J. Comput. Chem. **23**, 378 (2002).
[8] T. Yanai, K. Ishida, H. Nakano, and K. Hirao, Int. J. Quantum Chem. **76**, 396 (2000).
[9] P. M. W. Gill and J. A. Pople, Int. J. Quantum Chem. **40**, 753 (1991).
[10] S. Obara and A. Saika, J. Chem. Phys. **84**, 3963 (1986).
[11] M. Head-Gordon and J. A. Pople, J. Chem. Phys. **89**, 5777 (1988).
[12] J. A. Pople and W. J. Hehre, J. Comput. Phys. **27**, 161 (1978).
[13] P. M. W. Gill, M. Head-Gordon, and J. A. Pople, J. Phys. Chem. **94**, 5564 (1990).
[14] R. Lindh, U. Ryu, and B. Liu, J. Chem. Phys. **95**, 5889 (1991).
[15] L. E. McMurchie and E. R. Davidson, J. Comput. Phys. **26**, 218 (1978).
[16] M. Dupuis, J. Rys, and H. F. King, J. Chem. Phys. **65**, 111 (1976).
[17] M. Dupuis and A. Marquez, J. Chem. Phys. **114**, 2067 (2001).
[18] T. P. Hamilton and H. F. Schaefer, III, Chem. Phys. **150**, 163 (1991).
[19] S. Ten-no, Chem. Phys. Lett. **211**, 259 (1993).
[20] H. Nakai and M. Kobayashi, Chem. Phys. Lett. **388**, 50 (2004).
[21] M. J. Frisch, G. W. Trucks, H. B. Schlegel *et al.*, GAUSSIAN 03, Revision B.02, Gaussian, Inc., Pittsburgh, PA, 2003.
[22] R. Ditchfield, W. J. Hehre, and J. A. Pople, J. Chem. Phys. **54**, 724 (1971).
[23] W. J. Hehre, R. Ditchfield, and J. A. Pople, J. Chem. Phys. **56**, 2257 (1972).
[24] M. Tachikawa, H. Mori, H. Nakai, and K. Iguchi, Chem. Phys. Lett. **290**, 437 (1998).
[25] H. Nakai, K. Sodeyama, and M. Hoshino, Chem. Phys. Lett. **345**, 118 (2001).
[26] H. Nakai, Int. J. Quantum Chem. **86**, 511 (2002).
[27] H. Nakai and K. Sodeyama, J. Chem. Phys. **118**, 1119 (2003).

Energy density analysis of cluster size dependence of surface-molecule interactions: H_2, C_2H_2, C_2H_4, and CO adsorption onto Si(100)-(2×1) surface

Hiromi Nakai,[a] Michio Katouda,[b] and Yoshiumi Kawamura
Department of Chemistry, School of Science and Engineering, Waseda University, Tokyo 169-8555, Japan

(Received 26 March 2004; accepted 17 June 2004)

Adsorption of H_2, C_2H_2, C_2H_4, and CO onto a Si(100)-(2×1) surface has been treated theoretically using $Si_{12n-3}H_{8n+4}$ ($n=1-4$) clusters. The energy density analysis (EDA) proposed by Nakai has been adopted to examine surface-molecule interactions for different cluster sizes. EDA results for the largest model cluster $Si_{45}H_{36}$ have shown that the adsorption-induced energy density variation in Si atoms decays with distance from the adsorption site. Analysis of this decay, which can be carried out using the EDA technique, is important because it enables verification of the reliability of the model cluster used. In the cases of H_2, C_2H_2, C_2H_4, and CO adsorption onto the Si(100)-(2×1) surface, it is found that at least a $Si_{21}H_{20}$ cluster is necessary to treat the surface-molecule interaction with chemical accuracy. © *2004 American Institute of Physics.*
[DOI: 10.1063/1.1781121]

I. INTRODUCTION

The interaction between molecules and solid surfaces is a topic of great interest for experimental as well as theoretical studies. Its understanding is a prerequisite to elucidating the mechanisms of molecular adsorption, corrosion, and heterogeneous catalytic reaction. To treat the surface-molecule interaction theoretically, we often use a cluster model based on the assumption that the interaction is local or that at least its influence is confined to within the model cluster. However, there were no techniques to verify the validity of this assumption using existing model clusters.

Thus, we have determined the appropriate model cluster size as follows: One way is to check the reproducibility of experimental adsorption energies, geometries, and/or vibrational frequencies of adsorbates. If there are no experimental data, this empirical method cannot be used. The other is to adopt as large cluster size as the computational resources, such as memory and time, allow. Clearly, this method is not a satisfactory scientific approach. What would be a suitable nonempirical and scientific way of determining the appropriate cluster size? To find out, we should estimate how deep the effect of the surface-molecule interaction penetrates into the solid.

We recently proposed a simple analysis technique called energy density analysis (EDA),[1] which partitions the total energy of molecules, computed using Hartree-Fock (HF) or Kohn–Sham type density functional theory (DFT),[2,3] into atomic energy densities with no extra computing cost. We have reported the applicability and reproducibility of the EDA technique in *cis*, *trans*-enol isomerization,[4] proton transfer reactions,[5] and internal methyl rotations.[6]

In the present study, EDA is applied to the analysis of surface-molecule interactions and the determination of the appropriate cluster size. Numerical assessments are carried out for H_2, C_2H_2, C_2H_4, and CO adsorption onto Si(100)-(2×1) surface. Section II explains the methods of the electronic-structure calculation, the geometry optimization, and the EDA. Results and discussion are presented in Sec. III and summary is given in Sec. IV.

II. COMPUTATIONAL METHODS

This study focuses on the adsorption of H_2, C_2H_2, C_2H_4, and CO molecules onto a Si(100)-(2×1) surface. Four different silicon clusters, Si_9H_{12}, $Si_{21}H_{20}$, $Si_{33}H_{28}$, and $Si_{45}H_{36}$, whose artificial dangling bonds are capped by hydrogen atoms, are adopted as a theoretical model. Figure 1 shows the model clusters and the labeling of atoms. Si dimers in the first layer represent the (2×1) reconstruction. In Figs. 1(a)–1(d), the numbers 1–5 denote the layer number. The letters $A-D$ correspond to the unit: unit A is the central cluster; B is the nearest neighbor, etc.

The electronic structures of the adsorbed and separated systems were obtained by DFT calculations using the B3LYP hybrid functional,[7] which consists of the HF (exact) exchange, the Slater exchange,[8] the Becke (B88) exchange,[9] the Vosco–Wilk–Nusair correlation,[10] and the Lee–Yang–Parr correlation[11] functionals. Correlation-consistent polarization plus valence double zeta (cc-pVDZ) basis sets of Dunning[12] were adopted for H, C, O, and Si atoms.

Geometry optimizations were performed at the B3LYP/cc-pVDZ level, in which all the atoms of the adsorbates and the Si dimer in the first layer are relaxed. With the exception of Si dimers, all Si–Si bond distances were fixed at the experimental value for the bulk solid (2.352 Å).[13] The capping Si–H bond distances were fixed at 1.480 Å, which is the experimental value in SiH_4.[14] In the optimization, the sym-

[a]Author to whom correspondence should be addressed. Fax: +81-3-3205-2504. Electronic mail: nakai@waseda.jp
[b]Present address: Department of Theoretical Studies, Institute for Molecular Science, Okazaki 444-8585, Japan.

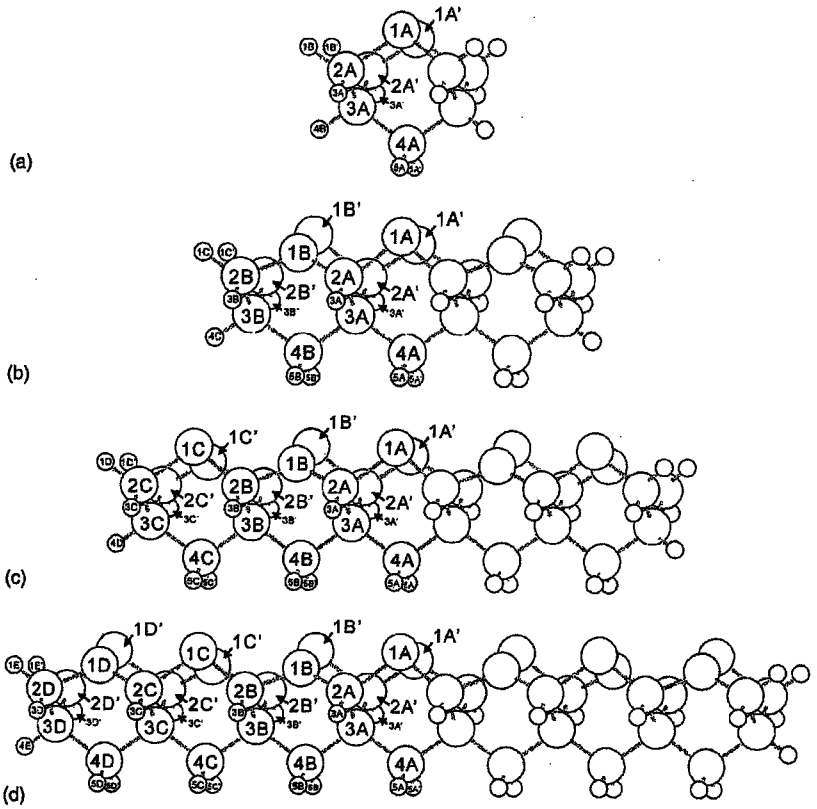

FIG. 1. Cluster models of Si(100)-(2×1) surface. (a) Si_9H_{12}, (b) $Si_{21}H_{20}$, (c) $Si_{33}H_{28}$, and (d) $Si_{45}H_{36}$.

metries of the system are constrained to C_{2v} for the ideal and unbuckled surface and C_s for the buckled surface, respectively. The electronic-state calculations were performed using the GAMESS program package.[15]

The EDA technique resolves the total energy obtained by the DFT calculations into atomic contributions as follows:

$$E^A = E^A_{NN} + T^A_S + E^A_{Ne} + E^A_{CLB} + E^A_{XC}, \tag{1}$$

where E^A_{NN} is nuclear repulsion energy density, T^A_S kinetic energy density, E^A_{Ne} nuclear attraction energy density, E^A_{CLB} Coulomb energy density, and E^A_{XC} exchange-correlation energy density, respectively. The sum of these atomic energy densities is equal to the total energy of the system. The atomic energy density for the exchange-correlation term E^A_{XC} is evaluated by the partial sum for the numerical quadrature technique,

$$E^A_{XC} = \sum_g^{grid} \omega_g p_A(\mathbf{r}_g) F_{XC}(\mathbf{r}_g), \tag{2}$$

where $\omega_g(\mathbf{r})$ is the weight, $p_A(\mathbf{r})$ is the partition function, and $F_{XC}(\mathbf{r})$ is the exchange-correlation functional. Energy densities for the other terms, calculated by the analytical integration of the Kohn–Sham orbitals, are evaluated using a method analogous to the Mulliken population analysis.[16] For example, the Coulomb energy density for atom A, E^A_{CLB}, is evaluated via

$$E^A_{CLB} = \tfrac{1}{2} \sum_{\mu \in A} (\mathbf{PJ})_{\mu\mu}, \tag{3}$$

where $\mathbf{P}$ is the atomic orbital basis density matrix and $\mathbf{J}$ is given by

$$\mathbf{J}_{\mu\nu} = \sum_\lambda \sum_\sigma P_{\lambda\sigma} (\chi_\mu \chi_\nu | \chi_\lambda \chi_\sigma). \tag{4}$$

Details of the partitioning scheme are explained elsewhere.[1] The EDA results depend on the used basis set such as the Mulliken population analysis. The usage of diffuse functions sometimes gives unreliable results in the Mulliken population analysis. By contrast, the EDA results are not sensitive to the diffuse function. In our experience, the EDA gives an unreasonable result when poor basis sets such as STO-3G are used.[1]

The EDA calculations were carried out for the adsorbed and separated systems by linking the original EDA code[17] with GAMESS.[15] By comparing atomic energy densities of the adsorbed and separated systems, we estimated the effect of the surface-molecule interaction in the Si clusters.

III. RESULTS AND DISCUSSION

A. Clean surface

We first examine the clean Si(100)-(2×1) surface. Three types of surface geometries are investigated: (i) ideal surfaces, where the bulk geometry is retained even in the first layer and no surface reconstruction occurs, and (ii) unbuckled and (iii) buckled surfaces, where surface Si dimers form by surface reconstruction. The difference between the latter two is the geometry of the Si dimers. Unbuckled dimers are parallel to the surface, while buckled ones are not. Figure 2

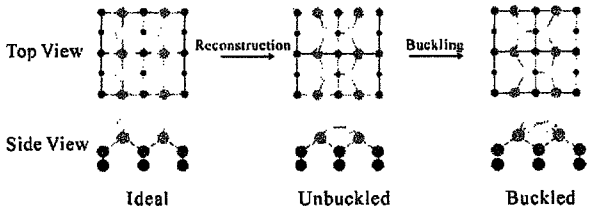

FIG. 2. Scheme for reconstruction and buckling of Si dimer on Si(100) surface.

schematizes the three types of surface geometries. The model clusters (Fig. 1) exhibit a C_{2v} type symmetry in the case of the unbuckled surface as well as the ideal surface and a C_s type symmetry in the case of the buckled surface.

Table I shows the atomic energy densities in the $Si_{45}H_{36}$ model cluster for the three types of Si surfaces, as evaluated by the EDA technique. The first column corresponds to the ideal surface, the second to the unbuckled surface, and the third to the buckled surface. Because certain Si atoms are equivalent to each other due to symmetry, we only tabulate the values for representative atoms.

The summation of atomic energy densities corresponding to the total energy is listed in the bottom row. The total energy changed from −13 046.647 77 to −13 046.969 43, and subsequently to −13 047.035 85 hartree as a result of formation and buckling of Si dimers. The energy difference in the first step is −201.8 kcal/mol. This large value indicates the importance of surface reconstruction in this system. In the $Si_{45}H_{36}$ model cluster, there are seven Si dimers. The averaged stabilization energy is estimated to be about 30 kcal/mol per Si dimer.

Using the EDA results, we can evaluate the stabilization energy of the Si dimer itself by the surface reconstruction. In the ideal surface, the atomic energy densities of the Si atoms in the first layer, denoted by $Si_{1\alpha}$ and $Si_{1\alpha'}$ ($\alpha=A-D$), are about −289.42 hartree. The corresponding value is about −289.45 hartree in the unbuckled reconstruction surface. The stabilization energies are estimated to be −34.2, −35.4, −35.8, and −38.4 kcal/mol for the $Si_{1\alpha}$-$Si_{1\alpha'}$ ($\alpha=A-D$) dimers, respectively.

The Si atoms in the second, third, and fourth layers, denoted by $Si_{2\alpha}$, $Si_{3\alpha}$, and $Si_{4\alpha}$ ($\alpha=A-D$), respectively, have atomic energy densities in the range of −289.47 to −289.48 hartree. During the reconstruction process, their energy density changes are comparatively small, indicating that these Si atoms behave like a bulk atom. It should be noted that, even in the reconstruction surface, the atomic energy densities of Si dimers are higher than those of bulk Si atoms. This is because surface Si atoms have dangling bonds, whereas bulk Si atoms do not. These results are related to the high activity of Si atoms and dimers on the surface.

The total energy of the system changes by −41.7 kcal/mol in the second step as a result of buckling of the Si dimers. The average stabilization energy of a single Si dimer is about 6 kcal/mol, a small value, and yet significant enough to indicate that a buckled surface is more stable than an unbuckled one. While various experimental and theoretical studies have investigated whether it is buckled or unbuckled surfaces that are more stable in the ground state, the topic remains controversial.[18–26] Head-Gordon *et al.* have shown that DFT calculations support the stability of buckled surfaces, whereas multireference perturbation theory calculations yield opposite results.[26] The present DFT results are consistent with existing DFT data. The buckling stabilizes the upper Si atoms in the dimer, while destabilizing the lower ones. For example, the atomic energy densities of Si_{1A} and $Si_{1A'}$ are −289.4876 and −289.4292 hartree, respectively. They are, respectively, lower and higher than the atomic energy density of the unbuckled case which is −289.4516 hartree.

B. Adsorbed system

Next, we examine the mechanism of adsorption onto Si clusters. Table II shows the calculated adsorption energies of H_2, C_2H_2, C_2H_4, and CO onto $Si_{12n-3}H_{8n+4}$ clusters ($n=1-4$), in which adsorptions occur on the single Si dimer. Buckled surfaces are used as an isolated system to calculate the adsorption energies, which exhibit a dependence on cluster size. For example, the adsorption energy of H_2 onto Si_9H_{12}, $Si_{21}H_{20}$, $Si_{33}H_{28}$, and $Si_{45}H_{36}$ is 60.0, 54.4, 52.9, and 53.0 kcal/mol, respectively. This cluster size dependence of the adsorption energy weakens with increasing cluster size. Similar trends are observed for C_2H_2, C_2H_4, and CO adsorptions.

Table II also shows the adsorption energies reported by previous theoretical and experimental studies.[27–62] In the case of H_2 adsorption, the calculated and experimental values differ by less than 4.5 kcal/mol. The adsorption energy of H_2 calculated in the present study using a $Si_{45}H_{36}$ cluster is close to the B3LYP result Steckel obtained using the giant cluster $Si_{89}H_{60}$,[31] the difference being less than 2 kcal/mol. However, the difference from results obtained using a plane wave basis is about 10 kcal/mol.[29,31,34,35] For C_2H_2 adsorption, the present and previous results calculated using cluster models[39–42] are in the range of 60–72 kcal/mol. Previous results calculated using the plane wave basis are in the range of 52–80 kcal/mol. Most calculated adsorption energies are overestimated compared with experimental values by more than 10 kcal/mol, except for the results of Refs. 44 and 53. Recent scanning tunneling microscopic studies have reported that C_2H_2 adsorbs on a Si(100) surface in three different configurations at room temperature.[41,49] The low adsorption energy obtained in the experimental study[55] may correspond to less stable configurations or may be due to large repulsion between adsorbates. For C_2H_4 adsorption, the adsorption energy obtained in the present study using the $Si_{45}H_{36}$ cluster agrees with those calculated in previous studies.[39,42,44,54,56–58] Its discrepancy with the experimental value is about 7 kcal/mol. In the case of CO adsorption, the adsorption energy calculated with the $Si_{45}H_{36}$ cluster agrees well with the experimental value: 12.75 and 11.6 kcal/mol for calculated and experimental[59] values, respectively.

Table III shows the variation in atomic energy densities induced by H_2 adsorption onto $Si_{12n-3}H_{8n+4}$ clusters ($n=1-4$). In H_2 adsorption, the main changes are seen in the H_2 adsorbate and the Si_{1A} and $Si_{1A'}$ atoms, which correspond to the Si dimer of the central unit. The energy changes

TABLE I. Atomic energy densities of ideal, unbuckled, and buckled Si surfaces in hartree and energy density changes by reconstruction and buckling of Si dimers in kcal/mol.

	Ideal surface (hartree)	Unbuckled surface (hartree)	Buckled surface (hartree)	Reconstruction (kcal/mol)	Buckling (kcal/mol)
Si 1*A*	−289.4243	−289.4516	−289.4876	−17.1	−22.6
Si 1*A'*	−289.4243	−289.4516	−289.4292	−17.1	14.0
Si 2*A*	−289.4665	−289.4632	−289.4620	2.1	0.7
Si 2*A'*	−289.4665	−289.4632	−289.4621	2.1	0.7
Si 3*A*	−289.4773	−289.4661	−289.4670	7.0	−0.6
Si 4*A*	−289.4745	−289.4873	−289.4822	−8.0	3.2
Si 1*B*	−289.4243	−289.4525	−289.4290	−17.7	14.7
Si 1*B'*	−289.4243	−289.4525	−289.4875	−17.7	−22.0
Si 2*B*	−289.4665	−289.4591	−289.4620	4.6	−1.8
Si 2*B'*	−289.4665	−289.4591	−289.4618	4.6	−1.7
Si 3*B*	−289.4773	−289.4665	−289.4671	6.7	−0.4
Si 4*B*	−289.4745	−289.4842	−289.4822	−6.1	1.3
Si 1*C*	−289.4243	−289.4528	−289.4881	−17.9	−22.2
Si 1*C'*	−289.4243	−289.4528	−289.4275	−17.9	15.8
Si 2*C*	−289.4664	−289.4581	−289.4604	5.2	−1.5
Si 2*C'*	−289.4664	−289.4581	−289.4613	5.2	−2.0
Si 3*C*	−289.4758	−289.4664	−289.4672	5.9	−0.5
Si 4*C*	−289.4744	−289.4886	−289.4833	−8.9	3.3
Si 1*D*	−289.4219	−289.4525	−289.4294	−19.2	14.5
Si 1*D'*	−289.4219	−289.4525	−289.4853	−19.2	−20.6
Si 2*D*	−289.4738	−289.4651	−289.4634	5.5	1.1
Si 2*D'*	−289.4738	−289.4651	−289.4687	5.5	−2.3
Si 3*D*	−289.4826	−289.4828	−289.4824	−0.1	0.3
Si 4*D*	−289.4740	−289.4826	−289.4779	−5.4	2.9
H 3*A*	−0.5845	−0.5833	−0.5833	0.7	0.0
H 3*A'*	−0.5845	−0.5833	−0.5833	0.7	0.0
H 5*A*	−0.5856	−0.5871	−0.5876	−1.0	−0.3
H 5*A'*	−0.5856	−0.5871	−0.5863	−1.0	0.5
H 3*B*	−0.5845	−0.5823	−0.5834	1.4	−0.7
H 3*B'*	−0.5845	−0.5823	−0.5833	1.4	−0.7
H 5*B*	−0.5856	−0.5871	−0.5862	−1.0	0.6
H 5*B'*	−0.5856	−0.5871	−0.5876	−1.0	−0.3
H 3*C*	−0.5845	−0.5822	−0.5833	1.5	−0.7
H 3*C'*	−0.5845	−0.5822	−0.5828	1.5	−0.3
H 5*C*	−0.5855	−0.5880	−0.5878	−1.5	0.1
H 5*C'*	−0.5855	−0.5880	−0.5866	−1.5	0.9
H 3*D*	−0.5856	−0.5850	−0.5847	0.4	0.2
H 3*D'*	−0.5856	−0.5850	−0.5859	0.4	−0.5
H 5*D*	−0.5864	−0.5877	−0.5868	−0.9	0.6
H 5*D'*	−0.5864	−0.5877	−0.5875	−0.9	0.1
H 1*E*	−0.5875	−0.5877	−0.5863	−0.1	0.9
H 1*E'*	−0.5875	−0.5877	−0.5879	−0.1	−0.1
H 4*E*	−0.5851	−0.5921	−0.5891	−4.4	1.9
Total	−13 046.6478	−13 046.9694	−13 047.0358	−201.8	−41.7

in the second, third, and fourth layer of the central unit in the $H_2/Si_{45}H_{36}$ system, namely, (Si_{2A},$Si_{2A'}$), Si_{3A}, and Si_{4A}, are (−2.46, −3.98), −2.20, and −0.85 kcal/mol, respectively. Thus, EDA reproduces the decay in H_2 adsorption effects with layer depth. A similar decay is observed with increasing distance along the surface. For example, the energy changes in the first layer in the $H_2/Si_{45}H_{36}$ system, namely, Si_{1A}, Si_{1B}, Si_{1C}, and Si_{1D} are 8.53, −0.22, −0.14, and 0.05 kcal/mol, respectively. The decay parallel and normal to the surface is seen in all cluster models.

Figure 3 shows the energy changes in Si atoms in the $Si_{45}H_{36}$ cluster due to H_2, C_2H_2, C_2H_4, and CO adsorption. The horizontal axis corresponds to the cluster units *A*–*D*. The four curves correspond to the sum of the energy change of Si atoms in the first to fourth layers. Figure 3(a) shows the energy change in Si atoms of the $Si_{45}H_{36}$ cluster induced by H_2 adsorption. As mentioned above, a rapid decay is observed both parallel and normal to the surface. In the nearest neighbor unit *B*, the maximum change is less than 2.0 kcal/mol. In the second nearest neighbor and the farthest units, *C* and *D*, the maximum changes are less than 0.5 kcal/mol. These results mean that the effect of H_2 adsorption is so local that it can be represented within the $Si_{45}H_{36}$ cluster.

Figures 3(b)–3(d) shows the energy variation in Si atoms of the $Si_{45}H_{36}$ cluster as a result of C_2H_2, C_2H_4, and CO adsorption. As in the case of H_2 adsorption, the energy density change is observed to decay in the depth direction. The energy density variation at the adsorption unit *A* decays

TABLE II. Adsorption energies of H_2. C_2H_2, C_2H_4, and CO molecules in kcal/mol.

Adsorbate	Method	Basis set	Model	Adsorption energy	Reference
H_2	B3LYP	cc-pVDZ	Si_9H_{12}	60.60	Present study
	B3LYP	cc-pVDZ	$Si_{21}H_{20}$	54.38	Present study
	B3LYP	cc-pVDZ	$Si_{33}H_{28}$	52.89	Present study
	B3LYP	cc-pVDZ	$Si_{45}H_{36}$	53.00	Present study
	CASSCF(4,4)	ECP/DZP qualitiy	Si_9H_{12}	56.7	27
	CI	TZP/DZP qualitiy	Si_9H_{12}	55.3	27
	BLYP	DNP	Si_9H_{12}	45.2	28
	PW91	Plane wave	$Si_{21}H_{20}$	44.7	29
	BLYP	Plane wave	$Si_{21}H_{20}$	44.3	29
	B3LYP	6-311G**	$Si_{21}H_{20}$	52.78	30
	CCSD(T)	6-311G(d,p)/6-31G(d)/3-21G	Si_9H_{12}	65.2	31
	MP2	6-311G(2d,2p)/6-31G(d)/3-21G	Si_9H_{12}	61.9	31
	PW91	6-311G(d,p)/6-31G(d)/3-21G	$Si_{89}H_{60}$	44.8	31
	B3LYP	6-311G(d,p)/6-31G(d)/3-21G	$Si_{89}H_{60}$	51.6	31
	QMC	...	$Si_{27}H_{24}$	58.57±3.00	32
	B3LYP	6-311G(d,p)/6-31G(d)	$Si_{48}H_{36}$	51.19	33
	BLYP	Plane wave	12 dimers slab	42.9	29
	GGA	Plane wave	slab	43.4	34
	PW91	Plane wave	4 dimers slab	44.97	35
	PW91	Plane wave	8 dimers slab	43.0	31
	Expt.			57.2±2	36
	Expt.			57.2±2	37
	Expt.			55.3±5	38
C_2H_2	B3LYP	cc-pVDZ	Si_9H_{12}	70.39	Present study
	B3LYP	cc-pVDZ	$Si_{21}H_{20}$	65.08	Present study
	B3LYP	cc-pVDZ	$Si_{33}H_{28}$	63.54	Present study
	B3LYP	cc-pVDZ	$Si_{45}H_{36}$	63.73	Present study
	B3LYP	6-311G**	Si_9H_{12}	60.2	39
	B3LYP	6-31G(d)	$Si_{15}H_{16}$	66.7	40
	B3LYP	6-31G*	$Si_{15}H_{16}$	71.5	41
	B3LYP	6-31G*	Si_9H_{12}	66.0	42
	PW91	Plane wave	1 dimer slab	64.8	43
	LDA	Plane wave	4 dimers slab	54.9	44
	PW91	Plane wave	8 dimers slab	63.2	45
	PW91	Plane wave	2 dimers slab	68.5	46
	PBE	Plane wave	2 dimers slab	60.7	47
	PBE	Plane wave	2 dimers slab	62.7	48
	LDA	Plane wave	12 dimers slab	73.8	49
	PBE	Plane wave	2 dimers slab	79.6	50
	PW91	Plane wave	2 dimers slab	63.4	51
	BLYP	Plane wave	2 dimers slab	65.7	52
	BLYP	Plane wave	2 dimers slab	52.1	53
	PBE	Plane wave	2 dimers slab	63.2	54
	Expt.			46.1±2.0	55
C_2H_4	B3LYP	cc-pVDZ	Si_9H_{12}	51.13	Present study
	B3LYP	cc-pVDZ	$Si_{21}H_{20}$	46.17	Present study
	B3LYP	cc-pVDZ	$Si_{33}H_{28}$	44.38	Present study
	B3LYP	cc-pVDZ	$Si_{45}H_{36}$	44.55	Present study
	B3LYP	6-311G**	Si_9H_{12}	43.2	39
	B3LYP	6-31G*	Si_9H_{12}	45.9	42
	LDA	Plane wave	4 dimers slab	36.2	44
	PW91	Plane wave	1 dimer slab	41.7	56
	PBE	Plane wave	2 dimers slab	48.4	57
	PBE	Plane wave	2 dimers slab	44.7	54
	Expt.			38.0±1.5	58
CO	B3LYP	cc-pVDZ	Si_9H_{12}	12.30	Present study
	B3LYP	cc-pVDZ	$Si_{21}H_{20}$	14.99	Present study
	B3LYP	cc-pVDZ	$Si_{33}H_{28}$	13.76	Present study
	B3LYP	cc-pVDZ	$Si_{45}H_{36}$	12.75	Present study
	BPL	6-31G(d,p)	Si_9H_{12}	14.5	59
	MP2	6-31G(d)	Si_9H_{12}	4.20	60
	B3LYP	LANL2DZ	Si_9H_{12}	12.88	60
	B3P86	6-31G(d,p)	Si_9H_{12}	14.2	61
	PW91	Plane wave	1 dimer slab	19.0	62
	Expt.			11.6	59

TABLE III. Variation in energy density (kcal/mol) induced by H_2 adsorption onto Si_9H_{12}, $Si_{21}H_{20}$, $Si_{33}H_{28}$, and $Si_{45}H_{36}$ clusters. Differences in energy density with respect to the $Si_{45}H_{36}$ cluster are shown in parentheses.

		Si_9H_{12}		$Si_{21}H_{20}$		$Si_{33}H_{28}$		$Si_{45}H_{36}$	
Adsorbate	H	−3.11	(−0.47)	−2.68	(+0.04)	−2.62	(−0.02)	−2.64	(0.00)
	H′	−3.11	(−0.90)	−2.25	(+0.04)	−2.21	(+0.00)	−2.21	(0.00)
Cluster	Si 1*A*	−4.29	(−12.82)	8.63	(−0.10)	8.19	(+0.34)	8.53	(0.00)
	Si 1*A*′	−23.82	(+5.67)	−31.70	(+2.21)	−29.66	(+0.17)	−29.49	(0.00)
	Si 2*A*	−3.79	(−1.33)	−2.56	(+0.10)	−2.42	(−0.05)	−2.46	(0.00)
	Si 2*A*′	−6.04	(−2.06)	−3.97	(−0.00)	−3.94	(−0.04)	−3.98	(0.00)
	Si 3*A*	−2.23	(−0.02)	−2.34	(+0.14)	−2.20	(−0.00)	−2.20	(0.00)
	Si 4*A*	−0.96	(−0.10)	−1.37	(+0.51)	−0.85	(−0.00)	−0.85	(0.00)
	Si 1*B*			2.06	(−2.28)	−0.14	(−0.08)	−0.22	(0.00)
	Si 1*B*′			−1.72	(+0.33)	−1.31	(−0.07)	−1.38	(0.00)
	Si 2*B*			0.02	(+0.11)	0.12	(+0.00)	0.12	(0.00)
	Si 2*B*′			−0.16	(+0.04)	−0.09	(−0.11)	−0.11	(0.00)
	Si 3*B*			−0.48	(+0.06)	−0.41	(−0.01)	−0.42	(0.00)
	Si 4*B*			−2.18	(+0.47)	−1.79	(+0.09)	−1.70	(0.00)
	Si 1*C*					−0.50	(+0.36)	−0.14	(0.00)
	Si 1*C*′					0.62	(−0.22)	0.39	(0.00)
	Si 2*C*					−0.07	(+0.04)	−0.03	(0.00)
	Si 2*C*′					0.04	(−0.00)	0.04	(0.00)
	Si 3*C*					−0.11	(+0.08)	−0.03	(0.00)
	Si 4*C*					−0.29	(+0.02)	−0.27	(0.00)
	Si 1*D*							0.05	(0.00)
	Si 1*D*′							−0.11	(0.00)
	Si 2*D*							−0.01	(0.00)
	Si 2*D*′							−0.12	(0.00)
	Si 3*D*							−0.06	(0.00)
	Si 4*D*							−0.01	(0.00)
	H 3*A*	−0.49	(−0.95)	0.47	(−0.01)	0.50	(−0.03)	0.47	(0.00)
	H 3*A*′	−0.88	(−0.10)	−0.79	(+0.01)	−0.79	(+0.01)	−0.78	(0.00)
	H 5*A*	0.26	(+0.26)	0.31	(−0.32)	0.00	(+0.00)	0.00	(0.00)
	H 5*A*′	0.12	(+0.14)	−0.41	(+0.39)	−0.01	(−0.01)	−0.02	(0.00)
	H 3*B*			0.03	(−0.02)	0.01	(−0.00)	0.01	(0.00)
	H 3*B*′			0.16	(−0.04)	0.12	(−0.00)	0.12	(0.00)
	H 5*B*			−0.29	(−0.05)	−0.31	(−0.02)	−0.33	(0.00)
	H 5*B*′			0.06	(+0.03)	0.09	(−0.00)	0.08	(0.00)
	H 3*C*					−0.02	(+0.00)	−0.02	(0.00)
	H 3*C*′					0.00	(−0.02)	−0.01	(0.00)
	H 5*C*					−0.04	(−0.00)	−0.04	(0.00)
	H 5*C*′					−0.03	(−0.00)	−0.04	(0.00)
	H 3*D*							−0.01	(0.00)
	H 3*D*′							−0.01	(0.00)
	H 5*D*							0.01	(0.00)
	H 5*D*′							0.01	(0.00)
	H 1*B*	0.16							(0.00)
	H 1*B*′	−0.47							(0.00)
	H 4*B*	0.89							(0.00)
	H 1*C*			−0.15					(0.00)
	H 1*C*′			−0.08					(0.00)
	H 4*C*			−0.53					(0.00)
	H 1*D*					0.01			(0.00)
	H 1*D*′					0.01			(0.00)
	H 4*D*					0.08			(0.00)
	H 1*E*							0.01	(0.00)
	H 1*E*′							−0.01	(0.00)
	H 4*E*							0.03	(0.00)
Total		−60.60	(−7.60)	−54.38	(+1.38)	−52.89	(−0.11)	−53.00	(0.00)

with depth for C_2H_2, C_2H_4, and CO adsorption. Decay in energy density variation along the surface is also seen in the case of H_2 adsorption. The maximum energy density changes at the second nearest unit *B* are less than 4 kcal/mol in C_2H_2, C_2H_4, and CO adsorption. The decay in energy density variation along the horizontal direction is a little bit slower in the case of CO adsorption compared with the other adsorption species. EDA reveals the difference in the decay behavior of the interaction between the surface and the various adsorbates.

Table III shows, in parentheses, the difference of the energy density changes with respect to the $H_2/Si_{45}H_{36}$ case.

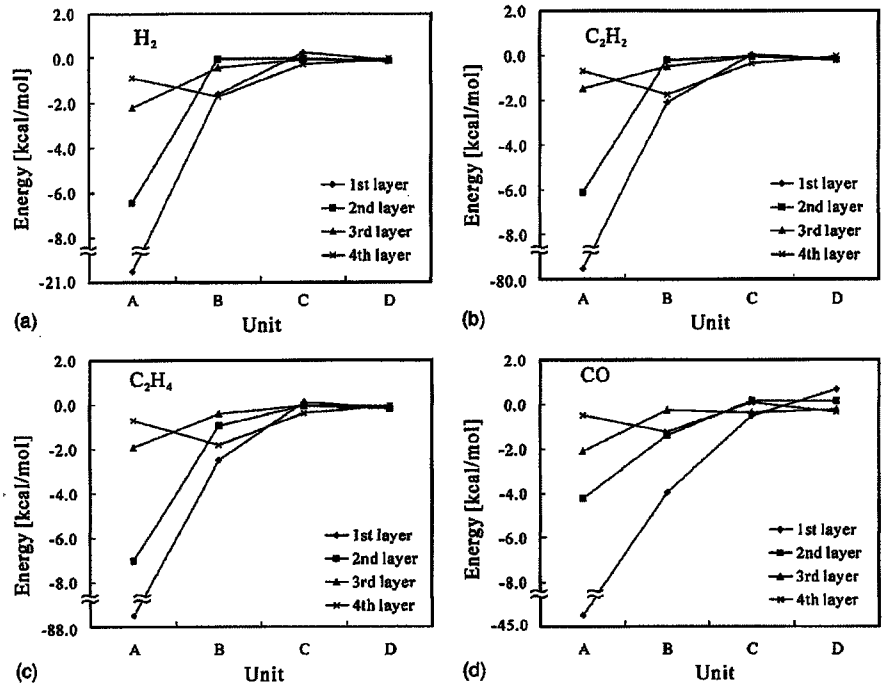

FIG. 3. Unit dependence of energy density variation in Si atoms of the $Si_{45}H_{36}$ cluster as a result of (a) H_2, (b) C_2H_2, (c) C_2H_4, and (d) CO adsorption.

These values indicate the cluster size dependence of the atomic energy change due to H_2 adsorption. The averaged difference in each layer is plotted in Fig. 4(a). In the Si_9H_{12} cluster, which includes only adsorption site A, the maximum discrepancy is about 12.8 kcal/mol. By contrast, the maximum discrepancy in the $Si_{21}H_{20}$ cluster corresponding to the $A+B$ site is less than 2.5 kcal/mol. Similarly, the maximum discrepancy in the $Si_{33}H_{28}$ for the $A+B+C$ site is less than 0.5 kcal/mol. Thus, we conclude that the usage of a model cluster larger than $Si_{33}H_{28}$ is necessary to reproduce H_2 adsorption process with chemical accuracy. Figure 4(b)–4(d) shows the averaged differences of energy densities with respect to the C_2H_2, C_2H_4, and CO/$Si_{45}H_{36}$ cases, respectively. For C_2H_2, C_2H_4, and CO adsorption, the maximum discrepancies of the energy density variation for $Si_{21}H_{20}$ and $Si_{33}H_{28}$ clusters are less than 2 and 0.5 kcal/mol, respec-

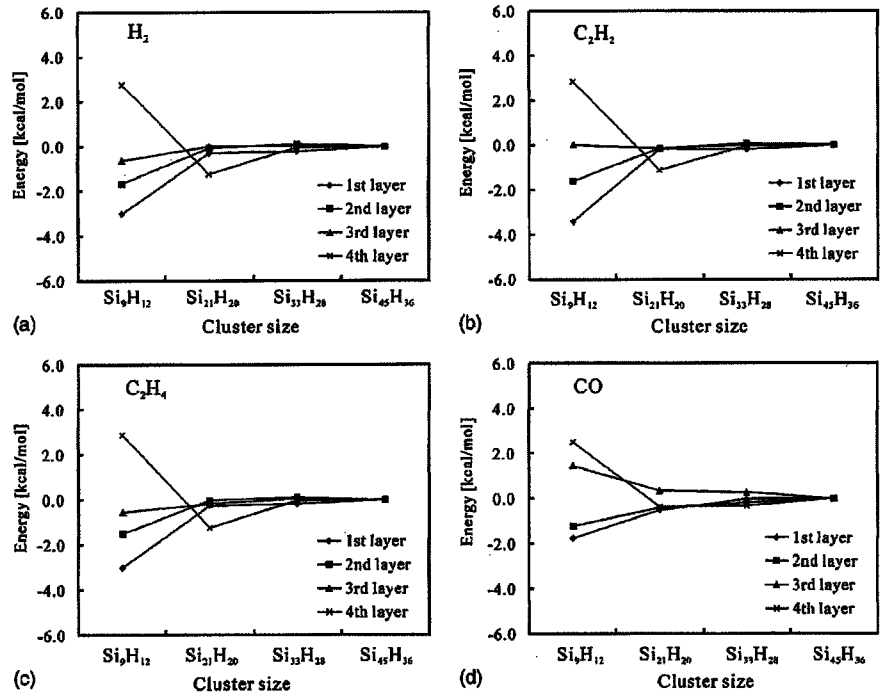

FIG. 4. Cluster size dependence of energy density change in the first to fourth layer during (a) H_2, (b) C_2H_2, (c) C_2H_4, and (d) CO adsorption. Averaged differences with respect to the case of the $Si_{45}H_{36}$ cluster are plotted.

tively. Thus, the usage of the model cluster larger than $Si_{21}H_{20}$ or $Si_{33}H_{28}$ gives the adsorption energy with chemical accuracy (kcal/mol order).

IV. SUMMARY

The EDA technique was applied to the adsorption of H_2, C_2H_2, C_2H_4, and CO molecules onto a Si(100)-(2×1) surface. EDA results for a clean surface revealed the local stabilization of the surface by reconstruction and buckling of surface Si dimers. EDA could evaluate the energetic changes in the model clusters induced by the adsorptions. We found that the adsorption effects in the model clusters decay with distance from the adsorption site. The cluster size dependence of adsorption-induced energy density changes, which can be estimated by EDA, provides important data as to how large a cluster is needed to describe the surface-molecule interaction with the desired accuracy.

ACKNOWLEDGMENTS

Part of the calculations was performed at the Research Center for Computational Science (RCCS) of the Okazaki National Research Institutes and the Media Network Center (MNC) of Waseda University. This study was partially supported by a Grant-in-Aid for Young Scientists (A) "KAKENHI 14703005" from the Japanese Society for the Promotion of Science (JSPS); by a NAREGI Nano-Science Project of the Japanese Ministry of Education, Culture, Sports, Science, and Technology (MEXT); by a Nanotechnology Researchers Network Project from the MEXT; and by the 21st century Center Of Excellence (21COE) "Practical Nano-Chemistry" from MEXT, Japan.

[1] H. Nakai, Chem. Phys. Lett. **363**, 73 (2002).
[2] W. Kohn and L. J. Sham, Phys. Rev. **140**, A1133 (1965).
[3] P. Hohenberg and W. Kohn, Phys. Rev. **136**, B864 (1964).
[4] H. Nakai and K. Sodeyama, Chem. Phys. Lett. **365**, 203 (2002).
[5] H. Nakai and K. Sodeyama, J. Mol. Struct.: THEOCHEM **637**, 27 (2003).
[6] Y. Kawamura and H. Nakai, Chem. Phys. Lett. **368**, 673 (2003).
[7] P. J. Stephens, F. J. Devlin, C. F. Chabalowski, and M. J. Frisch, J. Phys. Chem. **98**, 11623 (1994).
[8] J. C. Slater, Phys. Rev. **81**, 385 (1951).
[9] A. D. Becke, Phys. Rev. A **38**, 3098 (1988).
[10] S. H. Vosco, L. Wilk, and M. Nusair, Can. J. Phys. **58**, 1200 (1980).
[11] C. Lee, W. Yang, and R. G. Parr, Phys. Rev. B **37**, 785 (1988).
[12] T. H. Dunning, Jr., J. Chem. Phys. **90**, 1007 (1989).
[13] *CRC Handbook of Chemistry and Physics*, edited by D. R. Lide, 76th ed. (CRC, Boca Raton, 1995).
[14] R. D. Levine and R. B. Bernstein, *Molecular Reaction Dynamics and Chemical Reactivity* (Oxford University Press, New York, 1987).
[15] M. W. Schmidt, K. K. Baldridge, J. A. Boatz *et al.*, J. Comput. Chem. **14**, 1347 (1993).
[16] R. S. Mulliken, J. Chem. Phys. **23**, 1833 (1955).
[17] H. Nakai, EDA 2002, Waseda University, Tokyo, 2002.
[18] H. N. Waltenburg and J. T. Yates, Jr., Chem. Rev. (Washington, D.C.) **95**, 1589 (1995).
[19] R. J. Hamers and Y. Wang, Chem. Rev. (Washington, D.C.) **96**, 1261 (1996).
[20] Y. Kondo, T. Amakusa, M. Iwatsuki, and H. Tokumoto, Surf. Sci. **453**, L318 (2000).
[21] T. Yokoyama and K. Takayanagi, Phys. Rev. B **61**, R5078 (2000).
[22] T. Mitsui and K. Takayanagi, Phys. Rev. B **62**, R16251 (2000).
[23] G. Le Lay, A. Cricenti, C. Ottaviani, P. Perfetti, T. Tanikawa, I. Matsuda, and S. Hasegawa, Phys. Rev. B **66**, 153317 (2002).
[24] K. Hata, S. Yoshida, and H. Shigekawa, Phys. Rev. Lett. **89**, 286104 (2002).
[25] M. Matsumoto, K. Fukutani, and T. Okano, Phys. Rev. Lett. **90**, 106103 (2003).
[26] Y. Jung, Y. Shao, M. S. Gordon, D. J. Doren, and M. Head-Gordon, J. Chem. Phys. **119**, 10917 (2003).
[27] Z. Jing and J. L. Whitten, J. Chem. Phys. **102**, 3867 (1995).
[28] S. Pai and D. Doren, J. Chem. Phys. **103**, 1232 (1995).
[29] E. Penev, P. Kratzer, and M. Scheffler, J. Chem. Phys. **110**, 3986 (1999).
[30] E. S. Tok and H. Chuan Kang, J. Chem. Phys. **115**, 6550 (2001).
[31] J. A. Steckel, T. Phung, K. D. Jordan, and P. Nachtigall, J. Phys. Chem. B **105**, 4031 (2001).
[32] C. Filippi, S. B. Healy, P. Kratzer, E. Pehlke, and M. Scheffler, Phys. Rev. Lett. **89**, 166102 (2002).
[33] Y. Okamoto, J. Phys. Chem. B **106**, 570 (2002).
[34] F. M. Zimmermann and X. Pan, Phys. Rev. Lett. **85**, 618 (2000).
[35] E. Pehlke, Phys. Rev. B **62**, 12932 (2000).
[36] M. L. Wise, B. G. Koehler, P. Gupta, P. A. Coon, and S. M. George, Surf. Sci. **258**, 166 (1991).
[37] U. Höfer, L. Li, and T. F. Heinz, Phys. Rev. B **45**, 9485 (1992).
[38] M. C. Flowers, N. B. H. Jonathan, Y. Liu, and A. Morris, J. Chem. Phys. **99**, 7038 (1993).
[39] R. Konečný and D. J. Doren, Surf. Sci. **417**, 169 (1998).
[40] X. Lu and M. C. Lin, Phys. Chem. Chem. Phys. **2**, 4213 (2000).
[41] S. Mezhenny, I. Lyubinetsky, W. J. Choyke, R. A. Wolkow, and J. T. Yates, Jr., Chem. Phys. Lett. **344**, 7 (2001).
[42] M. A. Phillips, N. A. Besley, P. M. W. Gill, and P. Moriarty, Phys. Rev. B **67**, 035309 (2003).
[43] Y. Imamura, Y. Morikawa, T. Yamasaki, and H. Nakatsuji, Surf. Sci. Lett. **341**, L1091 (1995).
[44] A. J. Fisher, P. E. Blöchl, and G. A. D. Briggs, Surf. Sci. **374**, 298 (1997).
[45] D. C. Sorescu and K. D. Jordan, J. Phys. Chem. B **104**, 8259 (2000).
[46] W. A. Hofer, A. J. Fisher, and R. A. Wolkow, Surf. Sci. **475**, 83 (2001).
[47] Y. Morikawa, Phys. Rev. B **63**, 033405 (2001).
[48] J. Cho, L. Kleinman, C. T. Chan, and K. S. Kim, Phys. Rev. B **63**, 073306 (2001).
[49] W. Kim, H. Kim, G. Lee, Y. Hong, K. Lee, C. Hwang, D. Kim, and J. Koo, Phys. Rev. B **64**, 193313 (2001).
[50] R. Miotto, A. C. Ferraz, and G. P. Srivastava, Phys. Rev. B **65**, 075401 (2002).
[51] O. Pulci, P. L. Silvestrelli, M. Palummo, F. Ancilotto, and R. Del Sole, Phys. Status Solidi C **0**, 2997 (2003).
[52] R. Di Felice, C. A. Pigedoli, C. M. Bertoni *et al.*, Surf. Sci. **532**, 982 (2003).
[53] P. L. Silvestrelli, O. Pulci, M. Palummo, R. Del Sole, and F. Ancilotto, Phys. Rev. B **68**, 235306 (2003).
[54] J. Cho and L. Kleinman, Phys. Rev. B **69**, 075303 (2004).
[55] P. A. Taylor, R. M. Wallace, C. C. Cheng, W. H. Weinberg, M. J. Dresser, W. J. Choyke, and J. T. Yates, Jr., J. Am. Chem. Soc. **114**, 6754 (1992).
[56] W. Pan, T. Zhu, and W. Yang, J. Chem. Phys. **107**, 3981 (1997).
[57] R. Miotto, A. C. Ferraz, and G. P. Srivastava, Surf. Sci. **507**, 12 (2002).
[58] L. Clemen, R. M. Wallace, P. A. Taylor, M. J. Dresser, W. J. Choyke, W. H. Weinberg, and J. T. Yates, Jr., Surf. Sci. **268**, 205 (1992).
[59] D. Hu, W. Ho, X. Chen, S. Wang, and W. A. Goddard III, Phys. Rev. Lett. **78**, 1178 (1997).
[60] F. T. Bacalzo, D. G. Musaev, and M. C. Lin, J. Phys. Chem. B **102**, 2221 (1998).
[61] F. Bacalzo-Gradden and M. C. Lin, J. Phys. Chem. B **103**, 7270 (1999).
[62] Y. Imamura, N. Matsui, Y. Morikawa, M. Hada, T. Kubo, M. Nishijima, and H. Nakatsuji, Chem. Phys. Lett. **287**, 131 (1998).

A Hybrid Approach Combining Energy Density Analysis with the Interaction Energy Decomposition Method

YOSHIUMI KAWAMURA, HIROMI NAKAI
Department of Chemistry, School of Science and Engineering, Waseda University, Tokyo 169-8555, Japan

Received 11 June 2004; Accepted 26 July 2004
DOI 10.1002/jcc.20117
Published online 17 September 2004 in Wiley InterScience (www.interscience.wiley.com).

Abstract: We propose a new analysis technique for characterizing molecular interactions that combines an energy decomposition scheme, such as the Kitaura–Morokuma decomposition method, with energy density analysis, which partitions the total energy of the system into atomic contributions. The combined scheme, termed Interaction-EDA, enables us to estimate the *local* contribution of interaction energy components, such as electrostatic, exchange, polarization, and charge transfer. The evaluation of the local interaction energy is rather important in large systems. For a numerical assessment, the Interaction-EDA method is applied to the process of CO adsorption on Si(100) − (2 × 1) surface.

 J Comput Chem 25: 1882–1887, 2004

Key words: interaction-EDA; Si(100) surface; CO adsorption; energy decomposition; RVS-SCF method

Introduction

The interaction between molecules is fundamental and essential to understanding chemical phenomena. There have been several attempts to analyze the interaction energy from *ab initio* quantum chemistry calculations. Kitaura and Morokuma (KM) have proposed an analysis that decomposes the interaction energy into electrostatic (ES), exchange (EX), polarization (PL), and charge transfer (CT) components in a Hartree–Fock (HF) level of theory.[1,2] Individual components are calculated by the self-consistent field (SCF) procedure with the Fock and overlap matrix whose off-diagonal blocks are partially eliminated. The wave function used in the KM scheme is not antisymmetrized. Bagus et al.[3] and Stevens et al.[4] have independently improved on the KM scheme, with their constrained space orbital variation (CSOV) method and the reduced variational space (RVS) SCF method, respectively. In these methods, the energy components are calculated by the SCF procedure with the constrained molecular orbital (MO) spaces. In contrast to the KM scheme, the wave function of each energy component satisfies the Pauli exclusion principle. Several other schemes and a modified version of the existing scheme to decompose the interaction energy have been proposed.[5–12] All of these have focused on how to divide the interaction energy. In characterizing the interaction between large molecules such as biomolecules and surface-adsorbate interactions, it is important to determine which atom or substituent contributes most to the interaction. However, no attempt has been made to estimate the locality of the interaction energy components.

Nakai has recently proposed an analysis technique termed energy density analysis (EDA),[13] which partitions the total energy of molecules, computed using a HF or Kohn–Sham type density functional theory (DFT),[14,15] into atomic energy densities at no extra computing cost. Nakai and coworkers have reported the applicability and reproducibility of the EDA technique in *cis, trans*-enol isomerization and proton transfer reactions in malonaldehyde, tropolone, and 9-hydroxyphenalenone,[16,17] internal methyl rotations in halogenated toluenes,[18] and adsorption on Si(100) surface.[19]

In the present study, we combine the existing energy decomposition scheme with EDA. This combination, which we have termed Interaction-EDA, enables us to divide the interaction energy components such as ES, EX, PL, and CT into *local* contributions. As in standard EDA calculations, Interaction-EDA does not require much more computational cost than the energy decomposition scheme itself. We apply the Interaction-EDA technique to CO adsorption on Si(100) − (2 × 1) surface as a test case. The

Correspondence to: H. Nakai; e-mail: nakai@waseda.jp

Contract/grant sponsor: Grant-in-Aid for Young Scientists (A); [from the Japanese Society for the Promotion of Science (JSPS)]; Contract/grant number: KAKENHI 14703005

Contract/grant sponsors: Nanotechnology Support Project (a project of MEXT); the 21st Century Center of Excellence (21COE) "Practical Nano-Chemistry" from MEXT; Research Fellowships for the JSPS for young scientists.

present results demonstrate that the surface Si dimer plays an important role in the surface–adsorbate interaction. For the first time, a detailed and/or quantitative discussion is possible based on the local interaction energy estimated using the Interaction-EDA method.

Theoretical Aspects

EDA can be combined with one of several versions of the interaction energy decomposition method. The combination procedure is almost the same regardless of which version of the decomposition method is used. In the present study, we focus on the combination with the RVS-SCF method proposed by Stevens et al.[4]

First, we outline the EDA technique. EDA resolves the total energy obtained by the HF calculation into atomic contributions as follows:

$$E^{A} = E^{A}_{NN} + T^{A} + E^{A}_{Ne} + E^{A}_{CLB} + E^{A}_{EX}, \tag{1}$$

where E^{A}_{NN} is nuclear repulsion energy density, T^{A} kinetic energy density, E^{A}_{Ne} nuclear attraction energy density, E^{A}_{CLB} Coulomb energy density, and E^{A}_{EX} is exchange energy density. The superscript A denotes atom A. The total nuclear repulsion energy is expressed by

$$E_{NN} = \frac{1}{2}\sum_{A}\sum_{B\neq A}\frac{Z_A Z_B}{|\mathbf{R}_A - \mathbf{R}_B|}, \tag{2}$$

where Z_α and $\mathbf{R}_\alpha$ (α = A, B, ...) are nuclear charge and coordinate of atom α, respectively. The atomic contribution of the nuclear repulsion energy is evaluated from

$$E^{A}_{NN} = \frac{1}{2}\sum_{B\neq A}\frac{Z_A Z_B}{|\mathbf{R}_A - \mathbf{R}_B|}. \tag{3}$$

Energy densities for the other terms, calculated by the analytical integration of the HF orbitals $\{\chi_\mu\}$, are evaluated using a method analogous to Mulliken population analysis.[20] The kinetic energy density for atom A is evaluated from

$$T^{A} = \sum_{\mu\in A}\sum_{\nu} P_{\mu\nu}\left\langle \chi_\nu\left| -\frac{1}{2}\nabla^2 \right|\chi_\mu\right\rangle \equiv \sum_{\mu\in A}\sum_{\nu} P_{\mu\nu}T_{\nu\mu} = \sum_{\mu\in A}(\mathbf{PT})_{\mu\mu}, \tag{4}$$

where $\mathbf{P}$ is the atomic orbital (AO) basis density matrix. Similarly, Coulomb and exchange energy densities are evaluated as follows.

$$E^{A}_{CLB} = \frac{1}{2}\sum_{\mu\in A}\sum_{\nu}\sum_{\lambda}\sum_{\sigma} P_{\mu\nu}\langle\chi_\nu(1)\chi_\sigma(2)|\chi_\mu(1)\chi_\lambda(2)\rangle P_{\lambda\sigma} \equiv \sum_{\mu\in A}\sum_{\nu} P_{\mu\nu}J_{\nu\mu} = \sum_{\mu\in A}(\mathbf{PJ})_{\mu\mu}, \tag{5}$$

$$E^{A}_{EX} = \frac{1}{4}\sum_{\mu\in A}\sum_{\nu}\sum_{\lambda}\sum_{\sigma} P_{\mu\nu}\langle\chi_\nu(1)\chi_\sigma(2)|\chi_\lambda(1)\chi_\mu(2)\rangle P_{\lambda\sigma} \equiv \sum_{\mu\in A}\sum_{\nu} P_{\mu\nu}K_{\nu\mu} = \sum_{\mu\in A}(\mathbf{PK})_{\mu\mu}. \tag{6}$$

Some modification is needed for the nuclear attraction term. Half of the nuclear attraction energy is divided into electrons through AO, whereas the other half is divided into nuclei. Consequently, the nuclear attraction energy density is evaluated from

$$E^{A}_{Ne} = \frac{1}{2}\sum_{\mu\in A}\sum_{\nu} P_{\mu\nu}\left\langle \chi_\nu\left| -\sum_{B}\frac{Z_B}{|\mathbf{R}_B - \mathbf{r}|}\right|\chi_\mu\right\rangle + \frac{1}{2}\sum_{\mu}\sum_{\nu} P_{\mu\nu}\left\langle \chi_\nu\left| -\frac{Z_A}{|\mathbf{R}_A - \mathbf{r}|}\right|\chi_\mu\right\rangle \equiv \frac{1}{2}\sum_{\mu\in A}\sum_{\nu}\sum_{B} P_{\mu\nu}V_{B,\nu\mu} + \frac{1}{2}\sum_{\mu}\sum_{\nu} P_{\mu\nu}V_{A,\nu\mu} = \frac{1}{2}\sum_{\mu\in A}\sum_{B}(\mathbf{PV}_B)_{\mu\mu} + \frac{1}{2}\sum_{\mu}(\mathbf{PV}_A)_{\mu\mu}, \tag{7}$$

where $\mathbf{r}$ is the electronic coordinate. The EDA partitioning has been proposed not only for the HF method but also the DFT or HF/DFT hybrid method. Details of the partitioning scheme are explained elsewhere.[13]

The RVS-SCF method partitions the interaction energy into three components: (ES + EX), PL, and CT. For simplicity, we consider the interaction between two fragments, namely fragments I and II. Figure 1 schematizes the reduced spaces of the Fock matrix for the combined system I + II. The basis of the Fock matrix is both occupied and virtual MOs in the individual fragments I and II, which are solved separately and orthogonalized in the combined system. Because of the orthogonalization, even the partial matrix within each fragment is not diagonal. The original Fock matrix for the combined system has nonzero partial matrices as shown in Figure 1a. Some of the partial matrices are set to zero in the RVS-SCF calculation. Here, gray squares show the partial matrices with the original matrix elements and 0s represent those set to zero. That is, the mixed spaces are reduced by using the Fock matrices in Figure 1.

In the first step of the RVS-SCF method, the Fock matrix in Figure 1b is adopted. Diagonalization of this Fock matrix gives the total energy E_1 excluding the relaxation of occupied MOs in either fragment. The sum of the total energies in the separated system is defined by E_0. The difference between E_0 and E_1 corresponds to the ES + EX interaction energy:

$$E_{ES+EX} = E_1 - E_0. \tag{8}$$

Here, we apply the EDA technique to E_0 and E_1. The total energy is partitioned into atomic contributions as follows:

$$E_0 = \sum_{A} E^{A}_0, \tag{9}$$

$$E_1 = \sum_{A} E^{A}_1. \tag{10}$$

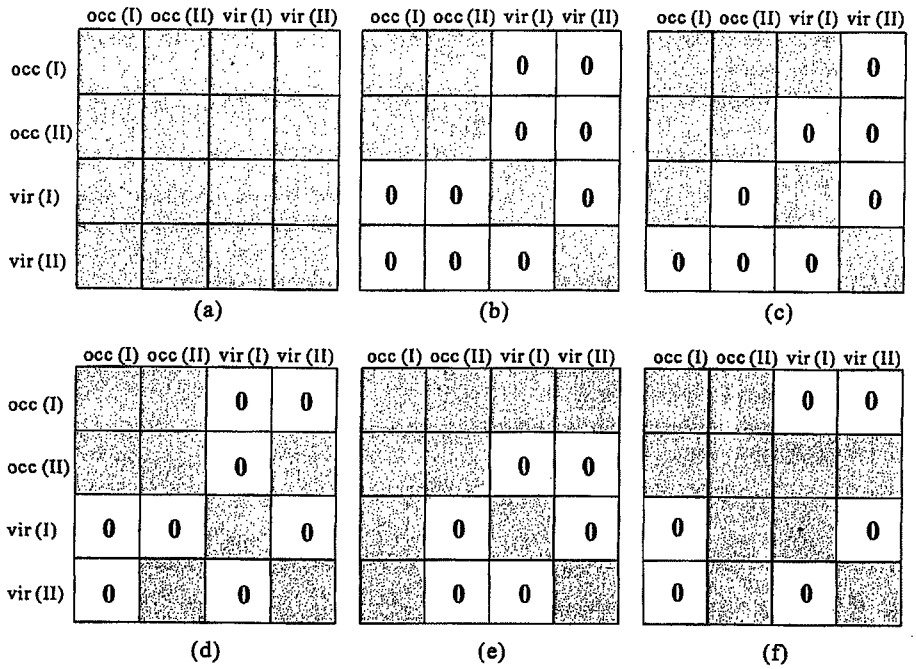

Figure 1. Reduced spaces of the Fock matrix for the combined system. Basis of the Fock matrices are occupied and virtual MOs of fragments I and II, as denoted by occ (I), occ (II), vir (I), and vir (II), respectively. Gray subspaces have nonzero elements. Elements of **0** (zero) subspaces are set to zero. Reduced Fock matrices of (a), (b), (c), (d), (e), and (f) are used for calculating E_{I+II}, E_1, $E_{2(I)}$, $E_{2(II)}$, $E_{3(I\rightarrow II)}$, and $E_{3(II\rightarrow I)}$, respectively.

Substituting eqs. (9) and (10) into eq. (8) gives

$$E_{ES+EX} = \sum_A E_1^A - \sum_A E_0^A = \sum_A (E_1^A - E_0^A). \quad (11)$$

Once we define the atomic contribution of the ES + EX interaction E_{ES+EX}^A as

$$E_{ES+EX}^A \equiv E_1^A - E_0^A. \quad (12)$$

Equation (12) can be rewritten as

$$E_{ES+EX} = \sum_A E_{ES+EX}^A. \quad (13)$$

The SCF calculation using the Fock matrix of Figure 1c, which gives the total energy $E_{2(I)}$, leads to mixing of the occupied and virtual MOs within fragment I. By using the EDA technique, the total energy $E_{2(I)}$ is partitioned into atomic contributions:

$$E_{2(I)} = \sum_A E_{2(I)}^A. \quad (14)$$

The PL energy of fragment I is estimated by

$$E_{PL(I)} = E_{2(I)} - E_1. \quad (15)$$

Thus, the atomic contributions of $E_{PL(I)}$ is obtained by subtracting E_1^A from $E_{2(I)}^A$:

$$E_{PL(I)}^A = E_{2(I)}^A - E_1^A. \quad (16)$$

The total and atomic contributions of the PL energy of fragment II, $E_{PL(II)}$ and $E_{PL(II)}^A$, respectively, are obtained by solving the Fock matrix of Figure 1d and subtracting as in eqs. (15) and (16).

The SCF calculation with the Fock matrix of Figure 1e, which gives the total energy $E_{3(I\rightarrow II)}$, leads to delocalization from the occupied MOs of fragment I to the virtual MOs of fragment II. The energy difference between $E_{2(I)}$ and $E_{3(I\rightarrow II)}$ corresponds to the CT energy from fragment I to II. Because EDA gives the atomic contribution of $E_{3(I\rightarrow II)}$, the atomic contributions of the CT interaction from fragment I to II is estimated by

$$E_{CT(I\rightarrow II)}^A = E_{3(I\rightarrow II)}^A - E_{2(I)}^A. \quad (17)$$

Similarly, the total and atomic contributions of the CT interaction energy from fragment II to I are evaluated by using the Fock matrix in Figure 1f.

The total interaction energy E_{INT} is obtained by subtracting E_0 from E_{I+II}, the latter being calculated by the standard SCF procedure with the full Fock matrix of the combined system as shown in Figure 1a.

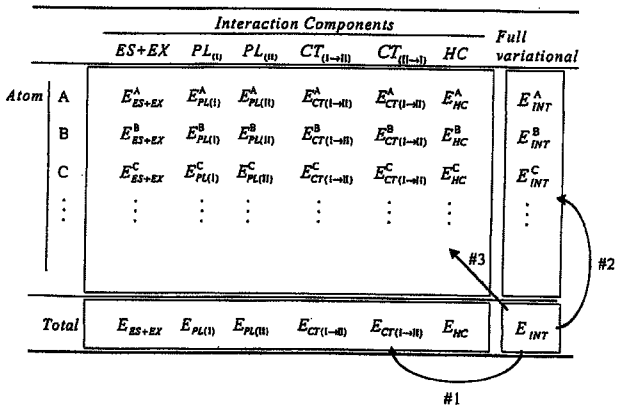

Figure 2. Schematic relationship between the RVS-SCF, EDA, and Interaction-EDA methods, indicated by arrows #1, #2, and #3, respectively.

$$E_{INT} = E_{(I+II)} - E_0. \tag{18}$$

The sum of the ES + EX, PL, and CT interaction energy components differs from E_{INT} by E_{HC}, which corresponds to higher coupling terms. Finally, the interaction energy is represented by

$$E_{INT} = E_{ES+EX} + E_{PL(I)} + E_{PL(II)} + E_{CT(I\to II)} + E_{CT(II\to I)} + E_{HC}. \tag{19}$$

$E_{(I+II)}$, and hence E_{INT} and E_{HC}, can be partitioned into atomic contributions by the EDA technique. In a manner similar to eq. (19), the atomic contribution of the total interaction energy is expressed by

$$E^A_{INT} = E^A_{ES+EX} + E^A_{PL(I)} + E^A_{PL(II)} + E^A_{CT(I\to II)} + E^A_{CT(II\to I)} + E^A_{HC}. \tag{20}$$

Figure 2 schematically compares the RVS-SCF energy decomposition, EDA, and Interaction-EDA methods. The interaction energy is partitioned into its components by the energy decomposition method. This step is represented by arrow #1 in Figure 2. The EDA technique resolves the interaction energy into atomic contributions, which is shown by arrow #2 in Figure 2. The combination of the energy decomposition method and EDA, that is, Interaction-EDA, gives matrix elements, which represent the atomic contributions of the interaction energy components. This partitioning corresponds to arrow #3 in Figure 2.

Numerical Assessment

Numerical assessment of the Interaction-EDA scheme was performed for the asymmetric adsorption process of CO adsorption onto a Si(100) − (2 × 1) surface. A $Si_{33}H_{28}$ cluster was used as a model for the Si(100) − (2 × 1) surface. The artificial dangling bonds of Si atoms were capped by hydrogen atoms. Figure 3 shows the model cluster and labeling of atoms. The numbers 1–5 denote the layer number. The letters A–D correspond to the unit: unit A is the central cluster; B is the nearest neighbor, etc. The CO molecule asymmetrically adsorbs onto the Si_{1A} atom of the surface Si dimer.

The electronic structures of the adsorbed and isolated systems were obtained by HF calculations. The correlation-consistent polarization plus valence double zeta (cc-pVDZ) basis sets of Dunning[21] were adopted for H, C, O, and Si atoms. Geometry optimizations for the adsorbed system were performed at the HF/cc-pVDZ level, in which all the atoms of the adsorbates and the Si dimer in the first layer are relaxed. With the exception of Si dimers, all Si–Si bond distances were fixed at the experimental value for the bulk solid (2.352 Å).[22] The capping Si—H bond distances were fixed at 1.480 Å, which is the experimental value in SiH_4.[23] The electronic structure calculations were performed using the GAMESS program package.[24] The EDA calculations were carried out by linking the original EDA code[25] with GAMESS.[24]

Table 1 shows the Interaction-EDA results for CO adsorption on the $Si_{33}H_{28}$ model cluster. The geometry of the adsorption system is close to that obtained by the previous DFT study.[19] The calculated adsorption energy is −8.05 kcal/mol, which is slightly lower than the experimental value of −11.6 kcal/mol.[26] The difference is mainly due to the absence of the electron-correlation effect. The bottom row of Table 1 corresponds to the RVS-SCF results. The largest contribution to destabilization is seen in the ES + EX component—65.13 kcal/mol. The PL and CT components contribute to stabilization. The largest contribution is the adsorbate-to-surface CT component, which corresponds to the σ-donation effect. The difference between the sum of ES + EX, PL, and CT components and the full variational value is shown in the HC component. The small value of the HC component (−1.05 kcal/mol) does not mean that the HC is small in the case of CO adsorption onto the Si(100) − (2 × 1) surface. As mentioned later, it is the result of cancellation among its atomic contributions.

The right column of Table 1 shows the full variational values corresponding to standard EDA results. These values reflect the change in atomic energy density due to the adsorption. The largest changes are seen in the C atom of the adsorbate and the Si_{1A} atom, which corresponds to the Si dimer of central unit A. The energy density changes of the Si atoms in the cluster decay with increasing distance from the adsorbate. Similar results have been obtained in our previous DFT study.[19]

Next, we examine the interaction energy density components. All components of capped H atoms are below 1 kcal/mol. The ES + EX interaction is a repulsive interaction between

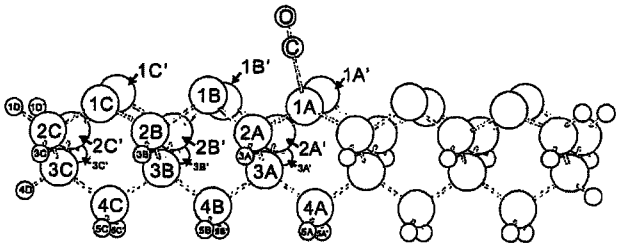

Figure 3. $Si_{33}H_{28}$ model cluster of the Si(100) − (2 × 1) surface.

Table 1. Interaction Energy Density Components for CO Adsorption on a $Si_{33}H_{28}$ Cluster (in kcal/mol).

			PL		CT			
		ES + EX	Surface	Adsorbate	Surface to adsorbate	Adsorbate to surface	HC	Full variational
O		−1.21	−0.05	6.12	0.96	2.01	−0.44	7.40
C		34.49	−23.69	−14.57	−19.04	29.23	7.53	13.94
Si	1A	42.00	−0.07	−8.89	−0.54	−48.81	3.28	−13.03
	1A′	−2.25	3.49	−0.71	1.08	−1.55	−1.24	−1.17
	2A	−1.67	3.28	0.05	0.99	−2.54	−2.95	−2.84
	2A′	−0.46	−0.03	−0.06	−0.19	−0.02	−0.12	−0.89
	3A	−0.26	1.45	0.65	0.11	0.18	0.46	2.60
	4A	−0.89	0.35	−0.84	−0.02	−0.57	0.75	−1.22
	1B	−0.47	−0.93	−0.38	0.86	−0.46	−0.76	−2.15
	1B′	−0.15	0.01	−0.20	0.16	−0.16	−0.19	−0.53
	2B	−0.02	−0.37	−0.03	0.20	−0.02	−0.15	−0.39
	2B′	−0.07	0.00	−0.09	0.07	−0.06	0.07	−0.08
	3B	0.19	−0.23	0.28	−0.08	0.21	−0.35	0.04
	4B	−0.70	−0.59	−0.50	0.32	−0.45	0.61	−1.30
	1C	0.00	0.03	−0.02	0.01	−0.01	−0.09	−0.09
	1C′	−0.02	0.04	0.01	0.02	0.00	−0.09	−0.06
	2C	0.00	−0.02	−0.04	0.04	−0.02	−0.04	−0.07
	2C′	−0.02	0.01	−0.05	0.03	−0.03	−0.01	−0.07
	3C	0.00	0.02	0.01	−0.01	0.01	0.01	0.03
	4C	−0.07	0.04	−0.12	0.07	−0.09	0.07	−0.10
H	3A	−0.06	−0.11	0.10	0.12	0.03	−0.55	−0.47
	3A′	−0.01	−0.07	0.04	0.12	0.01	−0.24	−0.15
	5A	0.13	−0.16	0.13	0.02	0.10	−0.27	−0.05
	5A′	0.10	−0.09	0.12	0.00	0.10	−0.20	0.02
	3B	−0.01	0.07	0.01	0.04	0.00	−0.10	0.02
	3B′	0.00	0.04	0.01	0.02	0.01	−0.05	0.03
	5B	0.08	−0.20	0.08	0.03	0.07	−0.22	−0.16
	5B′	0.04	−0.31	0.07	0.07	0.05	−0.18	−0.26
	3C	0.00	0.01	0.01	0.02	0.00	−0.06	−0.02
	3C′	0.01	0.00	0.02	0.00	0.01	−0.03	0.00
	5C	0.02	−0.01	0.03	0.00	0.02	−0.06	0.00
	5C′	0.02	0.01	0.03	−0.01	0.02	−0.03	0.04
	1D	0.00	0.02	0.01	0.03	0.00	−0.08	−0.03
	1D′	0.00	−0.01	0.01	0.02	0.01	−0.06	−0.03
	4D	0.01	−0.02	0.02	0.01	0.01	−0.05	−0.02
Total		65.13	−16.00	−18.81	−11.40	−25.94	−1.05	−8.05

Si_{1A} and carbon atoms, and is equal to 42.00 and 34.49 kcal/mol, respectively. The ES + EX energy density components of neighboring atoms, O, $Si_{1A'}$, and Si_{2A}, contribute to stabilization slightly: −1.21, −2.25, and −1.67 kcal/mol, respectively. The ES + EX components of the other atoms are less than 1 kcal/mol.

The PL interaction of the surface mainly stabilizes C atom of the adsorbate. The surface $Si_{1A'}$ and Si_{2A} atoms are destabilized by 3.49 and 3.28 kcal/mol, respectively. Even in the third layer, Si_{3A} atoms are destabilized by 1.45 kcal/mol. The PL interaction of the adsorbate stabilizes both C and Si_{1A} atoms, by 14.57 and 8.89 kcal/mol, respectively. The O atom is destabilized by 6.12 kcal/mol. The PL energy density components of the other atoms are less than 1 kcal/mol.

The surface-to-adsorbate CT interaction stabilized the C atom by a considerable 19.04 kcal/mol. This corresponds to the well-known π-back donation effect. The O atom of the adsorbate destabilized slightly (0.96 kcal/mol) because π electrons are supplied from the surface to π antibonding MOs of CO. The $Si_{1A'}$ and Si_{2A} atoms are destabilized by about 1 kcal/mol with decreasing electron density. The adsorbate-to-surface CT interaction is the σ donation, and is larger than the π-back donation in this case. Both C and O atoms are destabilized while surface Si_{1A} atoms are greatly stabilized by the σ-donation.

While the total HC interaction component is as small as 1 kcal/mol, its atomic contributions are larger for C, Si_{1A}, $Si_{1A'}$, and Si_{2A} atoms: 7.53, 3.28, −1.24, and −2.95 kcal/mol, respectively. This result indicates that the HC interaction is important

not only in the adsorption site (C and Si_{1A}) but also in the neighbor region ($Si_{1A'}$ and Si_{2A}). The small value (−1.05 kcal/mol) of the total HC component comes from the cancellation among its atomic contributions.

The present results using Interaction-EDA demonstrate that the surface Si dimer plays an essential role in the CO adsorption process. Si atoms in the neighbor region of the adsorption site also contribute the surface–adsorbate interaction. The contribution depends on the interaction component; for example, Si atoms even in the third layer are destabilized by 1.45 kcal/mol by the surface PL interaction. H atoms capping the dangling bond of edge Si atoms scarcely contribute the surface–adsorbate interaction. This indicates that the present Si cluster model is reliable because of less edge effect. Thus, Interaction-EDA is found to be a useful technique for charactering surface–adsorbate interactions, or more generally, chemical interactions.

Conclusion

We have proposed a new technique termed Interaction-EDA for the analysis of molecular interactions. The technique combines EDA and any one of several energy decomposition methods, such as KM, CSOV, and RVS-SCF. Interaction-EDA partitions the interaction energy components obtained from the energy decomposition method into site-dependent local energy densities. The application of Interaction-EDA to the CO/Si(100) − (2 × 1) system revealed that the individual interaction energy components have a local character but exhibit varying dependence on distance from the adsorption site. Using Interaction-EDA, we can estimate how far the interaction energy components penetrate into the model silicon cluster.

References

1. Morokuma, K. J Chem Phys 1971, 55, 1236.
2. Kitaura, K.; Morokuma, K. Int J Quantum Chem 1976, 10, 325.
3. Bagus, P. S.; Hermann, K.; Bauschlicher, C. W., Jr. J Chem Phys 1984, 80, 4378.
4. Stevens, W. J.; Fink, W. H. Chem Phys Lett 1987, 139, 15.
5. Nagase, S.; Fueno, T.; Yamabe, S.; Kitaura, K. Theor Chim Acta 1978, 49, 309.
6. Reed, A. E.; Weinhold, F. J Chem Phys 1983, 78, 4066.
7. Chalasinski, G.; Szczesniak, M. M. Mol Phys 1988, 62, 205.
8. Frey, R. F.; Davidson, E. R. J Chem Phys 1989, 90, 5555.
9. Chen, W.; Gordon, M. S. J Phys Chem 1996, 100, 14316.
10. Roeggen, I. Chem Phys 1992, 162, 271.
11. Glendening, E. D.; Streitwieser, A. J Phys Chem 1994, 100, 2900.
12. Korchowiec, J.; Uchimaru, T. J Chem Phys 2000, 112, 1623.
13. Nakai, H. Chem Phys Lett 2002, 363, 73.
14. Hohenberg, P.; Kohn, W. Phys Rev B 1964, 136, 864.
15. Kohn, W.; Sham, L. J. Phys Rev A 1965, 140, 1133.
16. Nakai, H.; Sodeyama, K. Chem Phys Lett 2002, 365, 203.
17. Nakai, H.; Sodeyama, K. J Mol Struct (Theochem) 2003, 637, 27.
18. Kawamura, Y.; Nakai, H. Chem Phys Lett 2003, 268, 673.
19. Nakai, H.; Katouda, M.; Kawamura, Y. J Chem Phys 2004, 121, 4893.
20. Mulliken, R. S. J Chem Phys 1955, 23, 1833.
21. Dunning, T. H., Jr. J Chem Phys 1989, 90, 1007.
22. Lide, D. R. CRC Handbook of Chemistry, Physics; CRC Press: Boca Raton, FL, 1995, 76th ed.
23. Levine, R. D.; Bernstein, R. B. Molecular Reaction Dynamics, Chemical Reactivity; Oxford University Press: New York, 1987.
24. Schmidt, M. W.; Baldridge, K. K.; Boatz, J. A.; Elbert, S. T.; Gordon, M. S.; Jensen, J. J.; Koseki, S.; Matsunaga, N.; Nguyen, K. A.; Su, S.; Windus, T. L.; Dupuis, M.; Montgomery, J. A. J Comput Chem 1993, 14, 1347.
25. Nakai, H. "EDA 2002," Waseda University, Tokyo, 2002.
26. Hu, D.; Ho, W.; Chen, X.; Wang, S.; Goddard, W. A., III. Phys Rev Lett 1997, 78, 1178.

Short-time Fourier transform analysis of *ab initio* molecular dynamics simulation: Collision reaction between $NH_4^+(NH_3)_2$ and NH_3

Yusuke Yamauchi and Hiromi Nakai[a)]
Department of Chemistry, School of Science and Engineering, Waseda University, Tokyo 169-8555, Japan

Yoshiki Okada
Nanomaterial Processing Laboratory, RIKEN (The Institute of Physical and Chemical Research), 2-1 Hirosawa, Wako-shi, Saitama 351-0198, Japan

(Received 21 July 2004; accepted 21 September 2004)

An analyzing technique of the *ab initio* molecular dynamics simulation is proposed with the use of short-time Fourier transform (ST-FT). The ST-FT analysis demonstrates the dynamical change of the vibrational states in the simulated system. Numerical assessments are preformed for the collision reaction of the ammonia cluster ion $NH_4^+(NH_3)_2$ with the ammonia monomer NH_3. Spectrogram obtained by the ST-FT method, which corresponds to the time evolution of vibrational power spectra, clarifies the relationship between the vibrational states and the reaction channels such as nonreactive collision, substitution, and incorporation. © *2004 American Institute of Physics.*
[DOI: 10.1063/1.1814978]

I. INTRODUCTION

Atomic motion in a chemical reaction is of great interest in fundamental chemistry.[1] The *ab initio* molecular dynamics (AIMD) technique can reproduce the dynamical process of a chemical reaction following bond formation and/or cleavage since the quantum chemical calculations are performed "on the fly" to obtain the potential energy and atomic force. Owing to this advantage, AIMD simulations have become popular in recent years. Geometrical changes in the chemical reaction are frequently analyzed, by using a snapshot, for example. Discussions on dynamical changes of vibrational states have been very limited[2] because the technique for analyzing AIMD simulations is not sufficiently developed.

We propose an analyzing technique of the AIMD results with the use of short-time Fourier transform (ST-FT), which is one of the familiar techniques in the field of information technology as time-frequency analysis. So far, there have been many works[3–5] to perform Fourier transform (FT) of the velocity autocorrelation function (VACF), which gives a power spectrum corresponding to density of the vibrational states. However, the conventional FT technique diminishes and/or averages the dynamical information. By contrast, Kobayashi, Saito, and Ohtani[6] recently reported analyzing ultrafast spectroscopy results using the ST-FT technique. They have clearly demonstrated the vibrational frequency shifts on the geometrical relaxation of retinal. Since the AIMD simulation as well as the ultrafast spectroscopy can also describe the dynamical change of chemical bonds intrinsically, the ST-FT analysis should clearly demonstrate the changes of vibrational states time by time.

Numerical tests of the present ST-FT analysis of the AIMD simulation were performed for the collision reaction between $NH_4^+(NH_3)_2$ and NH_3. This reaction is the initial step of the ion-induced nucleation process of ammonia. We have previously studied the collision reaction of the ammonia cluster ion with the ammonia monomer by experimental[7] and theoretical[8–10] approaches.

This paper has an organization as follows: The following section describes the ST-FT technique to apply the AIMD simulation. In Sec. III, we present the results of numerical tests for the ST-FT analysis of the collision reactions. Power spectra of ammonia monomer and cluster ions under equilibrium conditions are shown as reference data in this section. In what follows, the spectrograms obtained by the ST-FT for the nonreactive collision, substitution, and incorporation processes are presented in order to examine the dynamical change of the vibrational states. Finally, we provide a summary of the present study.

II. ST-FT ANALYSIS OF AIMD SIMULATION

In this study, we attempt to apply the ST-FT technique to the results of the AIMD simulations. The ST-FT is performed on VACF given by

$$\langle \mathbf{v}(t)\cdot\mathbf{v}(t+t')\rangle = \frac{1}{N}\sum_{i}^{N} \mathbf{v}_i(t)\cdot\mathbf{v}_i(t+t'), \tag{1}$$

where N is the number of atoms and $\mathbf{v}_i$ is the velocity vector of the ith atom. Since the VACF does not depend on the time origin, t, under equilibrium, we can set $t=0$ as follows:

$$\langle \mathbf{v}(t)\cdot\mathbf{v}(t+t')\rangle = \langle \mathbf{v}(0)\cdot\mathbf{v}(t')\rangle. \tag{2}$$

Thus, the power spectrum is given by the conventional FT as

$$S(\omega) = \frac{1}{2\pi}\int_{-\infty}^{\infty} \langle \mathbf{v}(0)\cdot\mathbf{v}(t')\rangle \exp(-i\omega t')dt', \tag{3}$$

where S and ω correspond to the intensity and the frequency of the vibrational states, respectively. Under nonequilibrium

a)Author to whom correspondence should be addressed. Electronic mail: nakai@waseda.jp

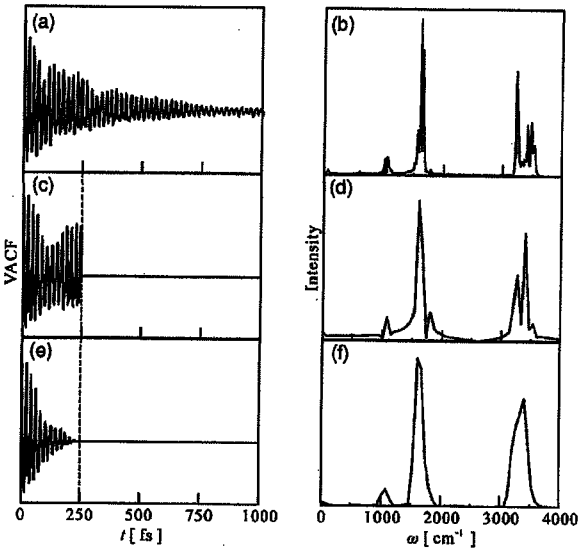

FIG. 1. The VACFs and their power spectrum obtained by FT [(a) and (b)], ST-FT with rectangular window [(c) and (d)], and ST-FT with Hanning window [(e) and (f)]. The window length T of 250 fs is used.

conditions, VACF is not only a function of t' but also t. The ST-FT technique adopts a window function $h(t'-t)$ having a window length of T, which works to extract the necessary information. The ST-FT of VACF is expressed by

$$S(t,\omega)=\frac{1}{2\pi}\int_{-\infty}^{\infty}\langle \mathbf{v}(t)\cdot\mathbf{v}(t+t')\rangle h(t'-t) \times \exp(-i\omega t')dt'. \tag{4}$$

Consequently, the power spectrum involves t as well as ω as a variable.

The performance of the ST-FT is influenced by the window function, namely, its shape and length. Figures 1(a) and 1(b) show the VACF of NH_3 under equilibrium conditions and the corresponding power spectrum, respectively. Figure 1(c) shows the VACF by using the rectangular window function[11] given by

$$h(t'-t)=\begin{cases}\dfrac{1}{2T}(=\text{const}), & -T\leq t'-t\leq T\\ 0, & \text{otherwise.}\end{cases} \tag{5}$$

Since the window length T is set to 250 femtoseconds (fs) in Fig. 1(c), there is a discontinuity in the VACF at $t'=250$ fs. The ST-FT of Eq. (4) to the partial VACF in Fig. 1(c) yields the power spectrum shown in Fig. 1(d). Figures 1(e) and 1(f) show the partial VACF and the corresponding power spectrum, respectively, by using the Hanning window function:[11]

$$h(t'-t)=\begin{cases}\dfrac{1}{2}-\dfrac{1}{2}\cos\left\{\dfrac{\pi(t'-t+T)}{T}\right\}, & -T\leq t'-t\leq T\\ 0, & \text{otherwise.}\end{cases} \tag{6}$$

In Fig. 1(e), the discontinuity in the VACF at $t'=250$ fs disappears. The difference indiscontinuity causes a larger degree of noise in Fig. 1(d) than in 1(f). For the analysis hereafter, therefore, we adopt the Hanning window function.

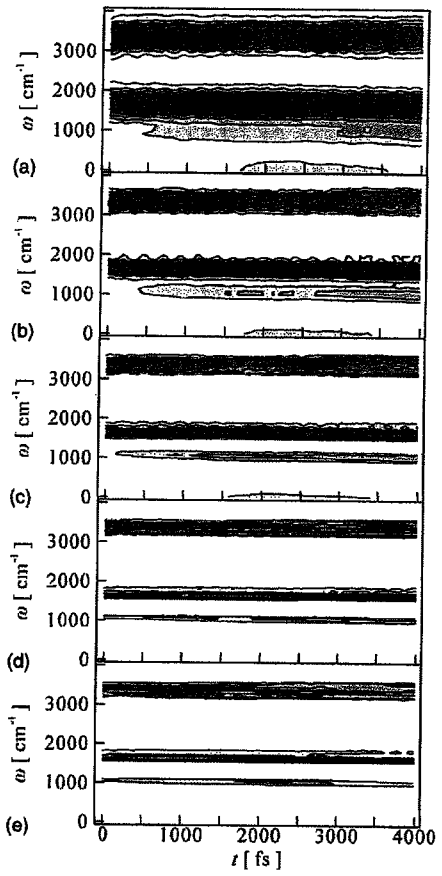

FIG. 2. Window length dependence of spectrogram. The window lengths are (a) 75, (b) 150, (c) 250, (d) 750, and (e) 1500 fs.

A spectrogram is a two-dimensional contour map of the power spectrum, in which the horizontal and the vertical axes correspond to t and ω, respectively, and contour lines or the shades of gray express the intensity. Figure 2 shows the spectrogram for the VACF of NH_3 under equilibrium conditions. The window length of T is varied: (a) 75, (b) 150, (c) 250, (d) 750, and (e) 1500 fs. The window length T is related to the resolution of frequency $\Delta\omega$ since the uncertainty of the time-frequency analysis defines the relationship between T and $\Delta\omega$:

$$\Delta\omega=\frac{1}{2cT}, \tag{7}$$

where c is the velocity of light. For example, the resolution $\Delta\omega$ is 222, 111, 67, 22, and 11 cm^{-1} for $T=75$, 150, 250, 750, and 1500 fs, respectively. The resolution is improved for a long window length, whereas the dynamical information is diminished and/or averaged. In the present study, we adopt $T=250$ fs corresponding to Fig. 2(c), which resolves the power spectrum into three vibrational states: $\omega=1000-1100$, 1500–2000, and 3100–3600 cm^{-1}. The first and second states correspond to the symmetric and degener-

ate H–N–H bending modes, respectively. In the third state, there are two N–H stretching modes: symmetric and degenerate.

III. NUMERICAL TESTS OF ST-FT ANALYSIS

A. AIMD simulations of collision reaction

Collision reaction between $NH_4^+(NH_3)_2$ and NH_3 was examined by AIMD simulation by combining an original molecular dynamics (MD) program with the quantum chemistry calculation package GAMESS.[12] Density functional theory[13,14] with B3LYP functional,[15] which consists of the Hartree–Fock or exact exchange, the Slater exchange,[16] the Becke (B88) exchange,[17] the Vosco–Wilk–Nusair correlation,[18] and the Lee–Yang–Parr correlation[19] functionals, and 6-31G(d,p) (Refs. 20 and 21) basis sets was used to compute potential energy and atomic force. Velocity Verlet method[2,22] with a time step of 0.25 fs was adopted for the numerical integration of the equation of motion. As reference data, AIMD simulations of NH_3 and $NH_4^+(NH_3)_{n-1}$ ($n=1-4$) under the equilibrium condition were also carried out using the same computational level.

The procedure of AIMD simulation of the collision reaction is as follows: First, 1000 steps of AIMD simulations are carried out separately for NH_3 and $NH_4^+(NH_3)_2$, in order to achieve equilibrium. The individual internal energies of NH_3 and $NH_4^+(NH_3)_2$ given in the equilibrated simulation are 1.2 times as large as their zero-point energies, which are estimated by summing the harmonic vibrational frequencies computed at the B3LYP/6-31G(d,p) level. Next, the translation energy of 0.1 eV is added to the internal energy of the cluster ion. The AIMD simulations of the collision are started at the separation of ~20 Å using several orientations.

We found that the AIMD trajectories fall into three categories: nonreactive collision, substitution, and incorporation. These three processes can be expressed with labeling the nitrogen atoms as follows:

Nonreactive collision:

$$({}^1NH_4^+)({}^2NH_3)({}^3NH_3)+{}^4NH_3 \rightarrow ({}^1NH_4^+)({}^2NH_3)({}^3NH_3)+{}^4NH_3. \quad (8)$$

Substitution:

$$({}^1NH_4^+)({}^2NH_3)({}^3NH_3)+{}^4NH_3 \rightarrow ({}^1NH_4^+)({}^3NH_3)({}^4NH_3)+{}^2NH_3. \quad (9)$$

Incorporation:

$$({}^1NH_4^+)({}^2NH_3)({}^3NH_3)+{}^4NH_3 \rightarrow ({}^1NH_4^+)({}^2NH_3)({}^3NH_3)({}^4NH_3). \quad (10)$$

In the present study, we analyzed in detail three typical trajectories corresponding to the three processes, i.e., nonreactive collision, substitution, and incorporation.

Time changes of the N–N distances, namely, $R({}^1N-{}^2N)$, $R({}^1N-{}^3N)$, and $R({}^1N-{}^4N)$ are described in Fig. 3 by broken, dotted, and solid lines, respectively. In Fig. 3(a), the solid line gradually declines, attaining a minimum at $t=1450$ fs. The vertical broken line indicates the time.

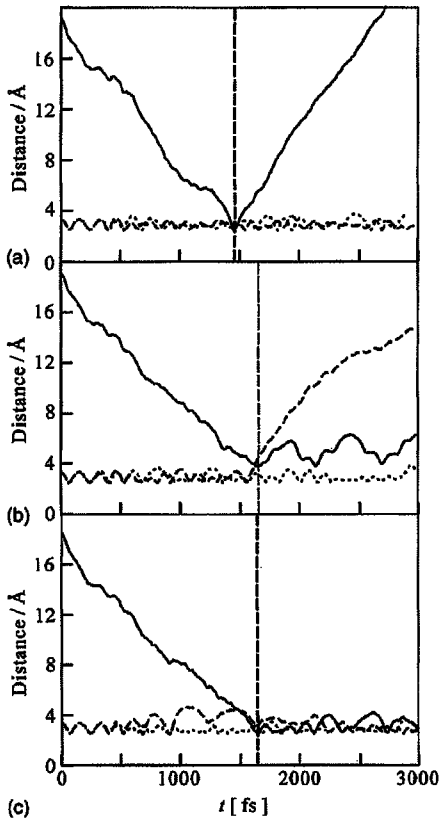

FIG. 3. Time evolution of N–N distances in (a) nonreactive collision, (b) substitution, and (c) incorporation. Solid, broken, and dotted lines correspond to $R({}^1N-{}^4N)$, $R({}^1N-{}^2N)$, and $R({}^1N-{}^3N)$, respectively.

After collision, the solid line climbs monotonically. The broken and dotted lines oscillate around 3.0 Å with a maximum amplitude of 0.6 Å. The amplitude increases slightly after the collision. In Fig. 3(b), the solid line decreases until $t=1650$ fs and then oscillates with a large amplitude. This means that the ammonia monomer incorporates into the cluster ion. By contrast, the broken line rises in the range $t \geq 1550$ fs, which indicates that the ammonia monomer $^2NH_3$ is dissociating from the cluster ion. There is no significant change in the oscillation of the dotted line. The substitution reaction in Eq. (9) is therefore accomplished. In Fig. 3(c), $R({}^1N-{}^4N)$ reaches a minimum at $t=1650$ fs and then oscillates around 3.2 Å with a comparatively small amplitude. The broken and dotted lines oscillate throughout the simulation. These results indicate that the incorporation reaction in Eq. (10) occurs. Note that a comparatively large-amplitude vibration is included in $R({}^1N-{}^2N)$ in the range $t=700-1600$ fs, which corresponds to the initial step of the collision between the cluster ion and the monomer.

B. Power spectra in the equilibrium state

Power spectra of (a) NH_3, (b) NH_4^+, (c) $NH_4^+(NH_3)$, (d) $NH_4^+(NH_3)_2$, and (e) $NH_4^+(NH_3)_3$ under equilibrium conditions are offered in Fig. 4. These are obtained by the ST-FT of VACFs using the Hanning window function of T

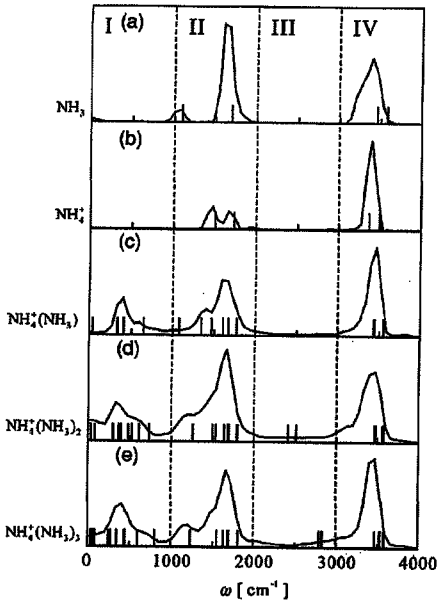

FIG. 4. Power spectra of (a) NH_3, (b) NH_4^+, (c) $NH_4^+(NH_3)$, (d) $NH_4^+(NH_3)_2$, and (e) $NH_4^+(NH_3)_3$ in an equilibrium condition. Vibrational frequencies in the harmonic approximation are represented by short lines on the horizontal axes.

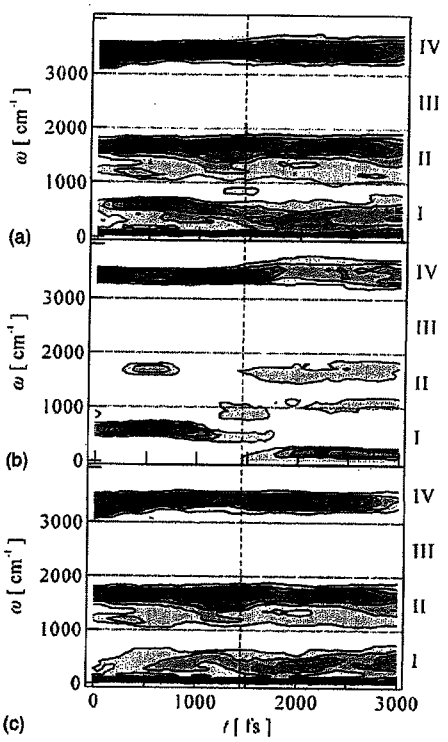

FIG. 5. Spectrograms obtained by ST-FT of VACFs for (a) the total system, (b) the monomer $^4NH_3$, and (c) the cluster ion $^1NH_4^+(^2NH_3)(^3NH_3)$ in the nonreactive collision process. The darker the shade of gray, the stronger the intensity.

=250 fs. Since the VACF depends on the time origin t even for the AIMD simulation under the quasiequilibrium condition, averaging the VACF over t is performed before the ST-FT. The vibrational frequencies in the harmonic approximation, which are estimated using Hessian matrices calculated by the B3LYP/6-31G(d,p) method, are also described by the short lines on the horizontal axes in Fig. 4.

We have divided the power spectra in Fig. 4 into four regions: regions I, II, III, and IV corresponding to the frequencies of 0–1000, 1000–2000, 2000–3000, and 3000–4000 cm^{-1}, respectively. In Fig. 4(a), there are no peaks in regions I and III. Two peaks in region II correspond to H–N–H bending modes. The lower one is symmetric bending and the upper one is degenerate bending. A broad peak in region IV involves symmetric and degenerate N–H stretching modes. Similarly, regions II and IV in Fig. 4(b) involve the H–N–H bending and N–H stretching modes, respectively. Region I in Figs. 4(c)–4(e) involves bending modes of the N–H···N hydrogen bonds, which include wagging and twist. Region II shows stretching modes of the hydrogen bonds, which occur at around 1700 cm^{-1}, in addition to the H–N–H bending modes. While there exist two vibrational states in region III [Figs. 4(d) and 4(e)] that are obtained in the harmonic approximation, no clear peaks appear in the power spectra. Region IV is similar in character to those in Figs. 4(a) and 4(b): it exhibits N–H stretching modes.

C. Spectrogram for the nonreactive collision process

Spectrogram, which is a time evolution of power spectrogram, presents the dynamical changes of the vibrational states. Figure 5 shows the spectrogram for the nonreactive collision, which corresponds to Fig. 3(a). In order to clarify the peak origin, we decompose the spectrogram for the total system (a), into those of the monomer NH_3 (b), and the cluster ion $NH_4^+(NH_3)_2$ (c). The vertical broken line shows the timing of the collision, at which a minimum appears in the solid line of $R(^1N-^4N)$ in Fig. 3(a). There are no peaks in region III, which is consistent with the power spectra under equilibrium condition shown in Fig. 4.

The peaks in regions II and IV in Fig. 5(b) correspond to those in Fig. 4(a). Figure 5(b) also involves several peaks in region I, which do not appear in Fig. 4(a). The band around 600 cm^{-1} seen at $t=0-1000$ fs is due to the interaction between the monomer and the cluster ion. Note that the distance between the monomer and the cluster ion is very large: that is, $R(^1N-^4N)\geqslant 6.8$ Å in $t=0-1000$ fs. This long-range interaction is thought to be the attraction between the positive charge of the cluster ion and the dipole moment of the monomer. The attraction locks the free rotation of the monomer. Thus, the peak around 600 cm^{-1} is assigned to the locking mode, which has been discussed in classical treatments such as average dipole orientation theory.[23]

The intensity of the peak around 3400 cm^{-1} corresponding to the N–H stretching frequency is enhanced in the range $t=1000-1500$ fs. It occurs immediately after the appearance of the locking mode and before or at the same time as the monomer collides with the cluster ion. After the collision, its intensity rapidly decreases. This enhancement is specific to the nonreactive collision. By contrast, it is the N–H···N

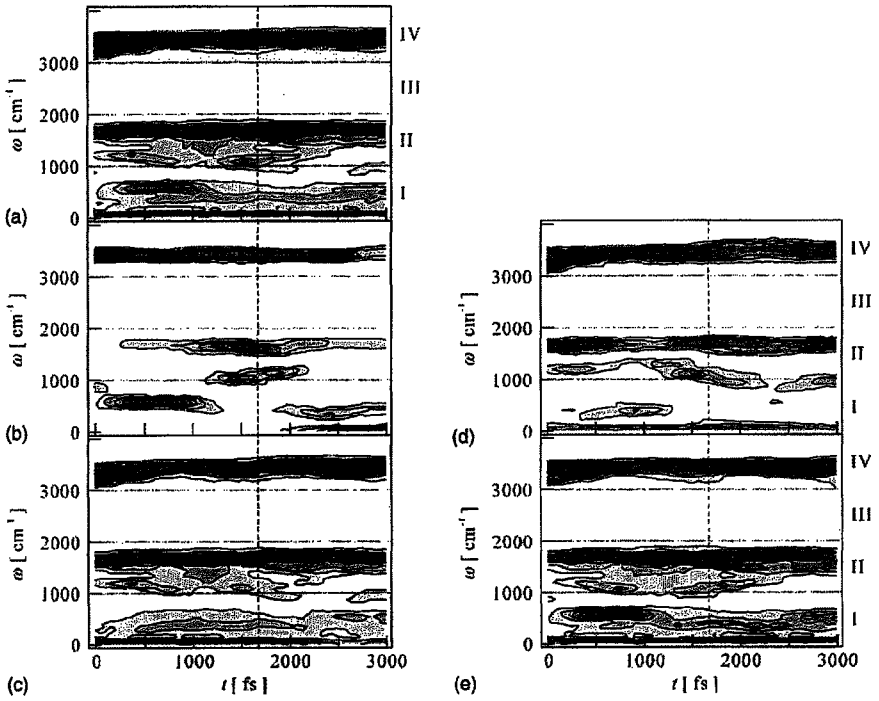

FIG. 6. Spectrograms obtained by ST-FT of VACFs for (a) the total system, (b) the monomer $^4NH_3$, (c) the cluster ion $^1NH_4^+(^2NH_3)(^3NH_3)$, (d) the monomer $^2NH_3$, and (e) the cluster ion $^1NH_4^+(^3NH_3)(^4NH_3)$ in the substitution process. The darker the shade of gray, the stronger the intensity.

stretching mode that is enhanced in the case of the substitution and incorporation processes, as discussed later. The difference is presumably related to the geometry of the collision. In the nonreactive collision, hydrogen atoms in the monomer collide with the cluster ion, while in the substitution and incorporation processes, it is the nitrogen atoms in the monomer that enter the collision.

D. Spectrogram for the substitution process

The spectrogram for the substitution is shown in Fig. 6, which corresponds to Fig. 3(b). As in the case of Fig. 5, the spectrogram for the total system is decomposed into those of the monomer and the cluster ion. Since the composition of the monomer and the cluster ion is different for the reactants and the products of the substitution reaction, as described in Eq. (9), Figs. 6(b) and 6(c) correspond to the composition of the reactants and Figs. 6(d) and 6(e) to that of the products.

The character of the spectrogram for the total system in Fig. 6(a) exhibits a similar trend to that in Fig. 5(a): strong peaks are found in regions II and IV throughout the reaction, and a peak around 600 cm^{-1} appears at the beginning of the collision. This is because the product in the substitution is the same as that in the nonreactive collision in molecular formula.

The peak around 600 cm^{-1} at $t=700$ fs in Fig. 6(b) is due to the motion of the monomer, which is assigned to the locking modes. Region II in Fig. 6(b) is characteristic for the substitution process. A comparatively strong intensity appears around 1600 cm^{-1} at $t=1500$ fs, which is close to the timing of the collision. It is assigned to the stretching mode of the intermolecular N–H···N hydrogen bond. At the same time or slightly later, a frequency shift is seen in other place: 1100→1200 cm^{-1}. In the power spectrum of NH_3 described in Fig. 4(a), the peak at 1089 cm^{-1} is assigned to the symmetric H–N–H bending mode. The H–N–H bending modes are located at 1259 and 1231 cm^{-1} in the power spectra of (d) $NH_4^+(NH_3)_2$ and (e) $NH_4^+(NH_3)_3$ in Fig. 4, respectively. The frequency shift suggests that the monomer is incorporated into the cluster ion. The enhancement of the intensity around 3400 cm^{-1}, which is seen in the nonreactive collision, is not observed in Fig. 6(b).

In Fig. 6(d), the H–N–H bending and/or N–H···N stretching motion at around 1600 cm^{-1}, was observed from the beginning of the simulation. As for the peak in the range 900–1300 cm^{-1}, a redshift was observed within $t=1000$–2000 fs. By contrast, a blueshift was observed in Fig. 6(b). Since the blueshift signals the incorporation of the monomer into the cluster ion, the redshift indicates dissociation of the monomer is dissociated from the cluster ion.

E. Spectrogram for the incorporation process

The spectrogram for the incorporation is shown in Fig. 7 whose geometrical change is described in Fig. 3(c). As in the case of Figs. 5 and 6, the ST-FT of VACFs for the total system, the monomer, and the cluster ion was carried out to obtain the spectrograms in Figs. 7(a), 7(b), and 7(c), respectively. The spectrogram in Fig. 7(a) has several features that differ from those in Figs. 5(a) and 6(a). The most characteristic change appears in region I: an intense peak at around 300 cm^{-1} after $t=1500$ fs. Another feature is that the intensity in region IV decreases after $t=1000$ fs. No such features are observed in region II of Fig. 7(a).

Figure 7(b) reveals that the locking mode in region I and the stretching mode of the hydrogen bond in region II are induced within $t=700$–1400 fs. Again the intensity of the

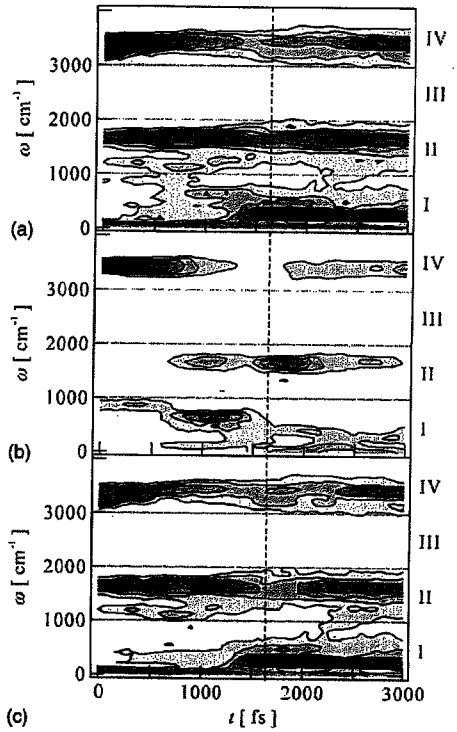

FIG. 7. Spectrograms obtained by ST-FT of VACFs for (a) the total system, (b) the monomer $^4NH_3$, and (c) the cluster ion $^1NH_4^+(^2NH_3)(^3NH_3)$ in the incorporation process. The darker the shade of gray, the stronger the intensity.

N–H···N stretching mode is enhanced as a result of the collision. The substitution reaction shows a similar trend [Fig. 6(b)]. However, the timing is slightly different: in Fig. 6(b), the enhancement occurs before, rather than after, the collision. The occurrence or enhancement of the N–H···N stretching peak is related to the incorporation process.

The low frequency mode around 300 cm^{-1} in region I in Fig. 7(c), which is generated after $t=1500$ fs, is originated from the motion of the cluster ion. The generation of the low frequency mode appears to be synchronized with the enhancement of the N–H···N stretching mode, and hence, the formation of the hydrogen bond between the monomer and the cluster ion. The strong intensity of the low frequency mode suggests that the excess internal energy, especially from the formation of the hydrogen bond, is distributed to the cluster ion. This low frequency mode is not observed in the case of substitution. In substitution, dissociation of another hydrogen bond is promoted by the excess internal energy. Therefore, we conclude that the low frequency mode determines the reaction channel, i.e., whether it will be an incorporation or substitution process.

IV. CONCLUSION

The present study has proposed an analyzing technique for the AIMD simulation with the use of ST-FT. While the conventional FT technique diminishes the dynamical information, the ST-FT technique combined with the AIMD method presents the time evolution of the vibrational states in the system. We examined the dependence of the ST-FT analysis on the window function. It was classified that the ST-FT analysis is applicable for the dynamics of molecular vibrations except for ultrafast processes as core-excitation dynamics, which occurs within 100 fs.

Numerical assessments of the ST-FT analysis were performed for the three processes in the collision reaction between $NH_4^+(NH_3)_2$ and NH_3, i.e., nonreactive collision, substitution, and incorporation. Spectrograms obtained by the ST-FT technique, which indicate the time evolution of vibrational power spectra, are found to be effective in interpreting the relation between the vibrational states and the reaction channels. Furthermore, the decomposition of the total-system spectrogram into the fragment ones is helpful for a detailed account.

ACKNOWLEDGMENTS

Part of the calculations was performed at the Research Center for Computational Science (RCCS) of National Institutes of Natural Sciences and the Media Network Center (MNC) of Waseda University. This study was partially supported by a Grant-in-Aid for Young Scientists (A) Grant No. "KAKENHI 14703005" from the Japanese Society for the Promotion of Science (JSPS), by a NAREGI Nano-Science Project of the Japanese Ministry of Education, Culture, Sports, Science and Technology (MEXT), by the 21st Century Center of Excellence (21COE) "Practical Nano-Chemistry" from MEXT, and by a grant from the Association for the Progress of New Chemistry, Japan.

[1] R. D. Levine and R. B. Bernstein, *Molecular Reaction Dynamics* (Oxford University Press, New York, 1974).
[2] S. Hayashi, E. Tajkhorshid, and K. Schulten, Biophys. J. **85**, 1440 (2003).
[3] M. P. Allen and D. J. Tildesley, *Computer Simulation of Liquids* (Clarendon, Oxford, 1987).
[4] D. E. Sagnella and M. E. Tuckerman, J. Chem. Phys. **108**, 2073 (1998).
[5] M. E. Tuckerman and M. L. Klein, Chem. Phys. Lett. **283**, 147 (1998).
[6] T. Kobayashi, T. Saito, and H. Ohtani, Nature (London) **414**, 531 (2001).
[7] T. Orii, Y. Okada, and K. Takeuchi, J. Chem. Phys. **113**, 8026 (2000).
[8] H. Nakai, T. Goto, Y. Okada, T. Orii, K. Takeuchi, M. Ichihashi, and T. Kondow, J. Chem. Phys. **112**, 7409 (2000).
[9] H. Nakai, T. Goto, T. Ichikawa, Y. Okada, T. Orii, and K. Takeuchi, Chem. Phys. **26**, 201 (2000).
[10] H. Nakai, Y. Yamauchi, A. Matsuda, Y. Okada, and K. Takeuchi, J. Mol. Struct.: THEOCHEM **592**, 61 (2002).
[11] D. B. Percival and A. T. Walden, *Spectral Analysis for Physical Applications: Multitaper and Conventional Univariate Techniques* (Cambridge University Press, Cambridge, 1993).
[12] M. W. Schmidt, K. K. Baldrige, J. A. Boatz *et al.*, J. Comput. Chem. **14**, 1347 (1993).
[13] P. Hohenberg and W. Kohn, Phys. Rev. **136**, B864 (1964).
[14] W. Kohn and L. J. Sham, Phys. Rev. **140**, A1133 (1965).
[15] A. D. Becke, J. Chem. Phys. **98**, 5648 (1993).
[16] J. C. Slater, Phys. Rev. **81**, 385 (1951).
[17] A. D. Becke, Phys. Rev. A **38**, 3098 (1988).
[18] S. H. Vosco, L. Wilk, and M. Nusair, Can. J. Phys. **58**, 1200 (1980).
[19] C. Lee, W. Yang, and R. G. Parr, Phys. Rev. B **37**, 785 (1988).
[20] P. C. Hariharan and J. A. Pople, Theor. Chim. Acta **28**, 213 (1973).
[21] M. M. Francl, W. J. Petro, W. J. Hehre, J. S. Binkley, M. S. Gordon, D. J. DeFrees, and J. A. Pople, J. Chem. Phys. **77**, 3654 (1982).
[22] W. C. Swope, H. C. Andersen, P. H. Berens, and K. R. Wilson, J. Chem. Phys. **76**, 637 (1982).
[23] T. Su and M. T. Bowers, Int. J. Mass Spectrom. Ion Phys. **12**, 347 (1973).

Available online at www.sciencedirect.com
SCIENCE DIRECT
Journal of Molecular Structure 735–736 (2005) 211–216
Journal of MOLECULAR STRUCTURE
www.elsevier.com/locate/molstruc

Theoretical study on excitation dynamics of 5-dibenzosuberene and its derivatives

Hiromi Nakai*, Takeshi Baba

Department of Chemistry, School of Science and Engineering, Waseda University, 3-4-1 Okubo, Shinjuku-ku, Tokyo 169-8555, Japan

Received 16 September 2004; revised 25 September 2004; accepted 27 September 2004
Available online 13 December 2004

Abstract

The present study theoretically investigated structures and dynamics of 5-dibenzosuberene (DBCH), 5-dibenzosuberenol (DBCH-5-ol), and 5-dibenzosuberenone (DBCH-5-one) in the excited states, in order to clarify specific behavior of transient species of DBCH-5-one in picosecond time region. The theoretical results confirm that the transient species observed in picosecond time-resolved absorption spectra of DBCH and DBCH-5-ol correspond to the S_1 state and those in nanosecond ones to the T_1 state. On the other hand, both picosecond and nanosecond transient species of DBCH-5-one are shown to be the T_1 state, which means that the lifetime of S_1 transient species is shorter than the picosecond order. Furthermore, the short lifetime of the S_1 transition species is found to be due to large transition probability of $S_1 \rightarrow T_1$ intersystem crossing. Since the S_1 state has n–π^* character and the T_1 state π–π^* one, the spin–orbit coupling and, therefore, the transition probability between the S_1 and T_1 states are large, which corresponds to El-Sayed rule.

Keywords: Dibenzocycloheptene; Excitation dynamics; Ab initio study; Time-resolved absorption spectroscopy; Spin–orbit coupling

1. Introduction

In order to interpret the mechanism of photochemical reactions, it is of great importance to clarify the structures and dynamics of photolytically generated transient molecular species, including singlet and triplet excited states such as S_1 and T_1, and ionic radicals, which play key roles in the physical and chemical processes involved. Time-resolved absorption spectroscopy is useful for specifying the transient species and estimating their lifetimes. Time-resolved Raman spectroscopy is a powerful tool for obtaining structural information on the transient species.

Takahashi and co-workers have applied time-resolved techniques to various compounds [1]. They reported excitation dynamics of 5-dibenzosuberene (5H-dibenzo[a,d]cycloheptene; DBCH) and its derivatives, i.e. 5-dibenzosuberenol (5H-dibenzo[a,d]cycloheptene-5-ol; DBCH-5-ol), and 5-dibenzosuberenone (5H-dibenzo[a,d]-cycloheptene-5-one; DBCH-5-one), in the picosecond–nanosecond time domain [2]. Similar spectral features were shown in picosecond time-resolved absorption spectra of DBCH and DBCH-5-ol, which were assigned to $S_1 \rightarrow S_n$ excitation. The intensities of the absorption bands at 600 nm of DBCH and at 608 nm of DBCH-5-ol involve two decay components, i.e. (13.6 ps, 1.7 ns) and (13.4 ps, 1.3 ns), respectively. By contrast, the wavelength of the absorption band and its time evolution of DBCH-5-one were drastically different from those of DBCH and DBCH-5-ol. Immediately after the pumping, a broad band without structure was observed at around 420 nm. At about a 10 ps delay time, two peaks at 413 and 430 nm were seen to emerge from the broad 420 nm band, becoming increasingly distinct with time. The absorption spectra of T_1 transient species of these three compounds, which were found by laser flash photolysis in the nanosecond time region, were shown to be very similar. Furthermore, the spectrum of T_1 transient species of DBCH-5-one is essentially the same as the spectrum obtained by picosecond time-resolved absorption spectroscopy. Thus, it was clarified that only S_1 transient species of DBCH-5-one has a complicated behavior. Although Takahashi et al. speculated that the existence of

* Corresponding author. Tel.: +81 3 5286 3452; fax: +81 3 3205 2504.
E-mail address: nakai@waseda.jp (H. Nakai).

0022-2860/$ - see front matter © 2004 Elsevier B.V. All rights reserved.
doi:10.1016/j.molstruc.2004.11.009

a carbonyl group might be related with the complicated behavior of the S_1 transient species of DBCH-5-one, they could not discuss about the dynamics of the transient species.

The aim of the present study is to clarify the origin for the specific behavior of the picosecond time-resolved absorption spectrum of DBCH-5-one by comparing among the S_1 and T_1 transient species of DBCH, DBCH-5-ol, and DBCH-5-one theoretically. In Secction 2, we mention the computational methods involving the geometry optimization for S_0 and T_1 states, the electronic-structure calculation for low-lying singlet and triplet states, and estimation of the transition probability of $S_1 \rightarrow T_1$ intersystem crossing. In Section 3, results and discussion are shown separately in five subsections: i.e. structures in the S_0 and T_1 states, $S_0 \rightarrow S_n$ excitation, $S_1 \rightarrow S_n$ excitation, $T_1 \rightarrow T_n$ excitation, $S_1 \rightarrow T_1$ intersystem crossing. Finally, we summarize the present results in Section 4.

2. Computational methods

The present study theoretically dealt with ground and low-lying singlet and triplet excited states of DBCH, DBCH-5-ol, and DBCH-5-one, which are shown in Fig. 1. To our knowledge, structures of these compounds are not known even in the ground state, while structures of closely related compounds, 5H-dibenz[b,f]azepine and 5H-dibenz[b,f]oxepin, in which the $-CH_2-$ bridge of DBCH in replaced by –NH– and –O– bridges, respectively, were determined by X-ray diffraction [3,4]. Thus, geometry optimizations of the three compounds in the S_0 and T_1 states were carried out by the density functional theory (DFT) method. The B3LYP hybrid functional [5,6], which comprises the Hartree–Fock (exact) exchange, the Slater exchange [7], the Becke exchange [8], the Vosco–Wilk–Nusair correlation [9] and the Lee–Yang–Parr correlation [10] functionals, was adopted in the DFT calculations. In the optimization, the basis sets used for H, C, and O were the correlation-consistent polarization plus valence double zeta (cc-pVDZ) sets of Dunning [11]. The symmetries of the compounds are constrained to *Cs* point group. The geometry optimizations were performed with the use of GAUSSIAN 03 program [12].

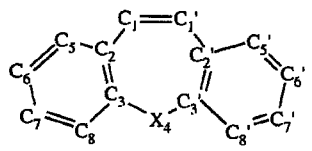

(a) DBCH:X=CH2
(b) DBCH-5-ol:X=CH(OH)
(c) DBCH-5-one:X=CO

Fig. 1. Molecular formula of DBCH derivatives.

Next, low-lying singlet and triplet excited states of the three DBCH derivatives at the S_0 and T_1 optimized geometries were carried out by the multi-configuration quasi-degenerate perturbation theory (MCQDPT) method [13] using the valence double zeta basis sets of Dunning (D95V) [14]. In the MCQDPT method, the state-averaged complete-active-space self-consistent-field (SA-CASSCF) [15–17] wave function is adopted as a zeroth-order function and dynamical electron correlation is take into account by the second-order perturbation theory. The active space in DBCH includes four bonding π and four antibonding π^* orbitals. In DBCH-5-ol and DBCH-5-one, one *n*-type orbital corresponding to 5-position substituent of central cycloheptatriene ring was added to the above eight active orbitals. Thus, the active space in DBCH is (10e, 10o) and those in DBCH-5-ol and DBCH-5-one (12e, 11o), where (*ne*, *mo*) means *n*-electrons in *m*-orbitals.

Finally, we estimated transition probability between low-lying singlet and triplet states. The transition probability for the intersystem crossing is proportional to square of the expectation value of the spin–orbit coupling (SOC). The Breit–Pauli SOC Hamiltonian is given by

$$H_{SO} = \frac{\alpha^2}{2}\left\{\sum_{i,N}\frac{Z_N}{r_{iN}^3}(\mathbf{r}_{iN}\times\mathbf{p}_i)\cdot\mathbf{s}_i - \sum_{i,j}\frac{1}{r_{ij}^3}(\mathbf{r}_{ij}\times\mathbf{p}_i)\cdot(\mathbf{s}_i+2\mathbf{s}_j)\right\} \quad (1)$$

where α is the fine structure constant, Z the nuclear charge, and $\mathbf{r}$, $\mathbf{p}$, and $\mathbf{s}$ the coordinate, momentum, and spin operators, respectively. Labels i and j run over electrons and N over nuclei. The first term is the one-electron SOC operator and the second term the two-electron one. The SOC constants between the low-lying singlet and triplet states $\langle\psi_S|H_{so}|\psi_T\rangle$ are evaluated with the use of MCQDPT wave functions [18]. The MCQDPT and spin–orbit MCQDPT calculations were performed using a GAMESS program [19].

3. Results and discussion

3.1. Structures in the S_0 and T_1 states

Geometry optimizations of DBCH, DBCH-5-ol, and DBCH-5-one were carried out for the singlet ground state (S_0) and the first triplet excited state (T_1) at the B3LYP/cc-pVDZ level. Optimized geometrical parameters of these compounds are shown in Table 1. DBCH derivatives have 'butterfly like' structures with the central seven-membered ring in a boat conformation and its 'wings', namely, two phenyl rings, bent backwards. The dihedral angles ϕ between the two planes of the phenyl rings are calculated

Table 1
Bond distances (in Å) and dihedral angle ϕ (in degree) with two-phenyl group in DBCH, DBCH-5-ol, and DBCH-5-one for the S_0 and T_1 states optimized at the B3LYP/cc-pVDZ level. Values in parenthesis are different from the S_0 values

	S_0	T_1	
(a) DBCH			
C_1–C_1'	1.356	1.468	(0.112)
C_1–C_2 C_1'–C_2'	1.465	1.396	(−0.069)
C_2–C_3 C_2'–C_3'	1.416	1.450	(0.034)
C_3–C_4 C_3'–C_4'	1.513	1.512	(−0.000)
C_2–C_5 C_2'–C_5'	1.410	1.445	(0.035)
C_5–C_6 C_5'–C_6'	1.392	1.378	(−0.015)
C_6–C_7 C_6'–C_7'	1.398	1.411	(0.013)
C_7–C_8 C_7'–C_8'	1.396	1.405	(0.009)
C_8–C_3 C_8'–C_3'	1.400	1.391	(−0.009)
ϕ	128.3	151.7	(23.4)
(b) DBCH-5-ol			
C_1–C_1'	1.357	1.469	(0.112)
C_1–C_2 C_1'–C_2'	1.465	1.396	(−0.070)
C_2–C_3 C_2'–C_3'	1.415	1.450	(0.035)
C_3–C_4 C_3'–C_4'	1.523	1.528	(0.005)
C_2–C_5 C_2'–C_5'	1.411	1.445	(0.034)
C_5–C_6 C_5'–C_6'	1.392	1.378	(−0.014)
C_6–C_7 C_6'–C_7'	1.399	1.410	(0.011)
C_7–C_8 C_7'–C_8'	1.396	1.407	(0.011)
C_8–C_3 C_8'–C_3'	1.399	1.387	(−0.012)
C_4–O	1.427	1.429	(0.002)
ϕ	126.6	146.6	(20.0)
(c) DBCH-5-one			
C_1–C_1'	1.353	1.460	(0.107)
C_1–C_2 C_1'–C_2'	1.452	1.389	(−0.064)
C_2–C_3 C_2'–C_3'	1.421	1.454	(0.033)
C_3–C_4 C_3'–C_4'	1.504	1.511	(0.007)
C_2–C_5 C_2'–C_5'	1.417	1.449	(0.032)
C_5–C_6 C_5'–C_6'	1.387	1.374	(−0.013)
C_6–C_7 C_6'–C_7'	1.401	1.411	(0.010)
C_7–C_8 C_7'–C_8'	1.388	1.398	(0.010)
C_8–C_3 C_8'–C_3'	1.411	1.399	(−0.012)
C_4=O	1.229	1.230	(0.002)
ϕ	161.9	180.0	(18.1)

to be 128.3, 126.6, and 161.9° in DBCH, DBCH-5-ol, and DBCH-5-one, respectively, in the S_0 state. It means that DBCH-5-one is more nearly planar than DBCH and DBCH-5-ol. The difference comes from the bonding character of 5-position carbon atom: that is, sp^2 bonding for DBCH-5-one and sp^3 ones for DBCH and DBCH-5-ol. In the T_1 state, the dihedral angles ϕ become 151.7, 146.4, and 180.0° for DBCH, DBCH-5-ol, and DBCH-5-one, respectively. Thus, these compounds increase the planarity by the $S_0 \rightarrow T_1$ excitation.

Another big change in structure by the $S_0 \rightarrow T_1$ transition is seen in C_1–C_1' bond. Since the C_1–C_1' distances are calculated to be 1.356, 1.357, and 1.353 Å for DBCH, DBCH-5-ol, and DBCH-5-one, respectively, in the S_0 state, C_1–C_1' bonds correspond to double bond. On the other hand, in the T_1 state, the C_1–C_1' distances are elongated, i.e. 1.468, 1.469, and 1.460 Å, respectively. These distances correspond to C–C single bond. The change of bonding character at C_1–C_1' by the $S_0 \rightarrow T_1$ excitation affects the adjacent bonds, C_1–C_2 and C_1'–C_2' which are shorten by about 0.07 Å.

3.2. $S_0 \rightarrow S_n$ excitation

The singlet ground and low-lying excited states of three DBCH compounds were calculated by the MCQDPT method. Table 2 shows the excitation character, excitation energy, and oscillator strength. Since the geometries of these compounds are fixed at the S_0 optimized structure as discussed in Section 3.1, the excitation energies shown in Table 2 correspond to the vertical excitation. Ultraviolet absorption spectra of these compounds were observed by Takahashi's group [20]. The calculated excited states having strong intensities can be assigned to the observed absorption peaks.

All excitation characters of DBCH shown in Table 2 are π–π^* excitation. The low-lying singlet excited states of DBCH-5-ol and DBCH-5-one involve n–π^* excitation character in addition to π–π^* one, since they have n-type orbitals at OH and C=O groups in central cycloheptatriene ring, respectively. Positions of n–π^* states in DBCH-5-ol and DBCH-5-one are different. The n–π^* state of DBCH-5-one is low, whereas that of DBCH-5-ol is relatively high. Consequently, the S_1 state of DBCH-5-one has the n–π^* character, whereas that of DBCH-5-ol as well as DBCH the π–π^* character.

3.3. $S_1 \rightarrow S_n$ excitation

Picosecond time-resolve absorption spectra of DBCH and DBCH-5-ol [1,2] were reported to have the absorption bands at 600 nm (2.07 eV) and 608 nm (2.04 eV), respectively. These bands were experimentally assigned to the excitation from the S_1 transient species, of which geometries were relaxed. Generally, the stable geometry in the S_1 state is close to that in the corresponding T_1 state. We adopted the T_1 optimized geometry as the structure of the S_1 transient species. Table 3 shows the $S_1 \rightarrow S_n$ excitation energies and their oscillator strengths.

The $S_1 \rightarrow S_2$ excitation energies of DBCH and DBCH-5-ol are calculated to be 2.13 and 1.48 eV, respectively, which reasonably correspond to the transient absorption bands: i.e. 2.07 and 2.04 eV, respectively. These theoretical results confirm the experimental assignment of the picosecond time-resolved absorption spectra. By contrast, the $S_1 \rightarrow S_2$ and $S_1 \rightarrow S_3$ excitation energies of DBCH-5-one are calculated to be 0.26 and 1.30 eV, respectively. Since the S_1 state has the n–π^* character, the oscillator strength of the excitation to the S_2 state having the π–π^* character is weak and that to the S_3 state having the n–π^* one is comparatively strong. Both excitation energies, however, are much smaller

Table 2
Low-lying singlet excited states calculated by the MCQDPT method using S_0 optimized geometry

	Excitation character	Excitation energy (eV)	Oscillator strength	Band peak (eV) [20]
(a) DBCH				
S_1 ($1^1A''$)	π–π^*	4.48	0.000	
S_2 ($2^1A''$)	π–π^*	4.98	0.697	4.38
S_3 ($2^1A'$)	π–π^*	5.37	0.003	
S_4 ($3^1A''$)	π–π^*	5.51	0.041	5.56
S_5 ($3^1A'$)	π–π^*	5.80	0.004	
(b) DBCH-5-ol				
S_1 ($1^1A''$)	π–π^*	4.71	0.003	
S_2 ($2^1A''$)	π–π^*	4.92	0.018	4.41
S_3 ($2^1A'$)	π–π^*	5.27	0.006	
S_4 ($3^1A''$)	π–π^*	5.27	0.742	5.58
S_5 ($3^1A'$)	π–π^*	6.36	0.030	
S_6 ($4^1A''$)	n–π^*	6.43	0.082	
(c) DBCH-5-one				
S_1 ($1^1A''$)	n–π^*	1.93	0.001	
S_2 ($2^1A'$)	π–π^*	2.45	0.053	3.58
S_3 ($2^1A''$)	π–π^*	3.06	0.040	4.03
S_4 ($3^1A'$)	π–π^*	4.25	0.001	
S_5 ($3^1A''$)	π–π^*	5.57	0.377	4.92
S_6 ($4^1A'$)	n–π^*	6.10	0.026	

than the picosecond time-resolved absorption bands at 2.85 and 2.99 eV.

3.4. $T_1 \rightarrow T_n$ excitation

Absorption spectra of DBCH, DBCH-5-ol, and DBCH-5-one were measured by laser flash photolysis in the nanosecond time region [1,2]. Since the absorption bands observed around 415–435 nm were quenched by oxygen, these bands were experimentally assigned to the T_1 transient species. Table 4 shows the $T_1 \rightarrow T_n$ excitation energies and their oscillator strengths, calculated at the T_1 optimized geometry. While the S_1 state of DBCH-5-one has the n–π^* character, the T_1 state the π–π^* character. For DBCH and DBCH-5-ol, both S_1 and T_1 states correspond to the π–π^* state.

Table 3
Low-lying singlet excited states calculated by the MCQDPT method using T_1 optimized geometry. The excitation energies are estimated from the S_1 level

	Excitation character	Excitation energy from S_1 (eV)	Oscillator strength ($S_1 \rightarrow S_n$)
(a) DBCH			
S_1 ($1^1A''$)	π–π^*	0.00	
S_2 ($2^1A'$)	π–π^*	2.13	0.002
S_3 ($3^1A'$)	π–π^*	2.84	0.002
S_4 ($2^1A''$)	π–π^*	3.08	0.000
(b) DBCH-5-ol			
S_1 ($1^1A''$)	π–π^*	0.00	
S_2 ($2^1A'$)	π–π^*	0.73	0.000
S_3 ($3^1A'$)	π–π^*	1.48	0.002
S_4 ($2^1A''$)	π–π^*	1.81	0.000
S_5 ($3^1A'$)	π–π^*	2.77	0.000
S_6 ($3^1A''$)	n–π^*	2.84	0.000
(c) DBCH-5-one			
S_1 ($1^1A''$)	n–π^*	0.00	
S_2 ($2^1A'$)	π–π^*	0.26	0.002
S_3 ($3^1A'$)	n–π^*	1.30	0.022
S_4 ($2^1A''$)	π–π^*	1.72	0.001

Table 4
Low-lying triplet excited states calculated by the MCQDPT method using T_1 optimized geometry. The excitation energies are estimated from the T_1 level

	Excitation character	Excitation energy from T_1 (eV)	Oscillator strength ($T_1 \rightarrow T_n$)
(a) DBCH			
T_1 ($1^3A''$)	π–π^*	0.00	
T_2 ($1^3A'$)	π–π^*	1.61	0.000
T_3 ($2^3A''$)	π–π^*	2.41	0.003
T_4 ($2^3A'$)	π–π^*	2.61	0.000
(b) DBCH-5-ol			
T_1 ($1^3A''$)	π–π^*	0.00	
T_2 ($1^3A'$)	π–π^*	1.59	0.001
T_3 ($2^3A''$)	π–π^*	2.56	0.000
T_4 ($2^3A'$)	π–π^*	2.74	0.002
T_5 ($3^3A''$)	n–π^*	3.17	0.000
(c) DBCH-5-one			
T_1 ($1^3A''$)	π–π^*	0.00	
T_2 ($2^3A''$)	n–π^*	0.42	0.000
T_3 ($1^3A'$)	π–π^*	0.55	0.002
T_4 ($2^3A'$)	n–π^*	1.33	0.002
T_5 ($3^3A'$)	π–π^*	1.40	0.000
T_6 ($3^3A''$)	π–π^*	1.46	0.008
T_7 ($4^3A''$)	n–π^*	2.97	0.001
T_8 ($4^3A'$)	π–π^*	3.29	0.001

Table 5
Spin–orbit coupling constants between low-lying singlet and triplet excited states of DBCH, DBCH-5-ol, and DBCH-5-one calculated by the spin–orbit MCQDPT method

	SOC constant (cm^{-1})
(a) DBCH	
S_1 (π–π^*) ↔ T_1 (π–π^*)	0.00
(b) DBCH-5-ol	
S_1 (π–π^*) ↔ T_1 (π–π^*)	0.00
(c) DBCH-5-one	
S_1 (n–π^*) ↔ T_1 (π–π^*)	63.36
S_1 (n–π^*) ↔ T_2 (n–π^*)	0.18
S_2 (π–π^*) ↔ T_1 (π–π^*)	0.02
S_2 (π–π^*) ↔ T_2 (n–π^*)	8.75

The absorption bands at 415 nm (2.99 eV) for DBCH and at 423 nm (2.93 eV) for DBCH-5-ol are assigned to respective $T_1 \rightarrow T_3$ excitation. For DBCH-5-one, these exist several low-lying states in the visible region. From the energetic point of view, we assign two bands of DBCH-5-one at 434 nm (2.86 eV) and 415 nm (2.99 eV) to $T_1 \rightarrow T_7$ and $T_1 \rightarrow T_8$ excitations, respectively. These excitations also correspond to the absorption bands observed in the picosecond time-resolved absorption spectra of DBCH-5-one. Therefore, it is expected that the lifetime of the S_1 transient species of DBCH-5-one is shorter than the picosecond order.

3.5. $S_1 \rightarrow T_1$ transition

In order to clarify the difference in lifetime of the S_1 transient species among DBCH, DBCH-5-ol, and DBCH-5-one, we estimated the transition probability between S_1 and T_1 states. Table 5 shows the SOC constants, of which squares are proportional to transition probability for the intersystem crossing. The SOC constants between the S_1 and T_1 states of DBCH and DBCH-5-ol are nearly equal to zero. The SOC Hamiltonian given in Eq. (1) requires a change in orbital angular momentum as well as spin angular momentum. Since the S_1 and T_1 states of DBCH and DBCH-5-ol have the same π–π^* configuration, the SOC constants become small. On the other hand, the SOC constant between S_1 and T_1 states of DBCH-5-one is calculated to be large, because they have different characters: namely, n–π^* and π–π^* configurations, respectively. In reverse, the S_2 and T_2 states of DBCH-5-one have π–π^* and n–π^* configurations, respectively. Thus, the SOC constants of the $S_1 \rightarrow T_2$ and $S_2 \rightarrow T_1$ transitions are calculated to be small, whereas that of the $S_2 \rightarrow T_2$ one large. As a consequence, the discussion about the S_1 transient species of DBCH-5-one is suitable for El-Sayed selection rule [21,22], which states that organic molecules with lowest excited states of n–π^* configuration often exhibit very fast intersystem crossing.

4. Summary

In the present study, we treated the low-lying singlet and triplet states of DBCH, DBCH-5-ol, and DBCH-5-one theoretically. The excitation energies at the S_0 optimized structures reasonably agree with the experimental ultraviolet absorption bands. By examining the $S_1 \rightarrow S_n$ and $T_1 \rightarrow T_n$ excitations at the T_1 optimized structures, we attempted to assign both picosecond and nanosecond time-resolved absorption spectra of the three compounds. It is confirmed that the transient species of DBCH and DBCH-5-ol observed in picosecond time domain correspond to the S_1 state and those in nanosecond ones to the T_1 state. On the other hand, both picosecond and nanosecond transient species of DBCH-5-one are shown to be the T_1 state. The $S_1 \rightarrow T_1$ transition probability of DBCH-5-one was calculated to be much larger than those of DBCH and DBCH-5-ol, which means that the lifetime of the S_1 transition species is much shorter than the others. This short lifetime of the S_1 transient species is the origin for the specific behavior of the picosecond time-resolved absorption spectrum of DBCH-5-one. This conclusion is consistent with El-Sayed rule.

Acknowledgements

The authors are grateful to Prof. Hiroaki Takahashi for valuable discussion and comments. Part of the calculations was performed at the Research Center for Computational Science (RCCS) of the Okazaki National Research Institutes and the Media Network Center (MNC) of Waseda University. This study was partially supported by a Grant-in-Aid for Young Scientists (A) 'KAKENHI 14703005' from the Japanese Society for the Promotion of Science (JSPS), the Joint Studies Program (2002–2004) of the Institute for Molecular Science, a NAREGI Nano-Science Project of the Japanese Ministry of Education, Culture, Sports, Science and Technology (MEXT), and the 21st century Center Of Excellence (21COE) 'Practical Nano-Chemistry' from MEXT.

References

[1] H. Takahashi, in: J. Laane, H. Takahashi, A. Bandrauk (Eds.), Structure and Dynamics of Electronic Excited States, Springer, Berlin, 1999, p. 36.
[2] M. Sakai, M. Mizuno, H. Takahashi, J. Raman Spectrosc. 29 (1998) 919.
[3] J.P. Reboul, B. Cristau, J.C. Soyfer, Acta Crystallogr. B36 (1980) 2683.
[4] J.A.G. Drake, D.W. Jones, Acta Crystallogr. B38 (1982) 200.
[5] A.D. Becke, J. Chem. Phys. 98 (1993) 5648.
[6] P.J. Stevens, J.F. Devlin, C.F. Chabalowski, M.J. Frish, J. Chem. Phys. 98 (1998) 11623.
[7] J.C. Slater, Phys. Rev. 81 (1951) 385.
[8] A.D. Becke, Phys. Rev. A 38 (1988) 3098.

[9] S.H. Vosco, L. Wilk, M. Nusair, Can. J. Phys. 58 (1980) 1200.
[10] C. Lee, W. Yang, R.G. Parr, Phys. Rev. B 37 (1988) 785.
[11] T.H. Dunning Jr., J. Chem. Phys. 90 (1989) 1007.
[12] M.J. Frisch, G.W. Trucks, H.B. Schlegel, G.E. Scuseria, M.A. Robb, J.R. Cheeseman, J.A. Montgomery Jr., T. Vreven, K.N. Kudin, J.C. Burant, J.M. Millam, S.S. Iyengar, J. Tomasi, V. Barone, B. Mennucci, M. Cossi, G. Scalmani, N. Rega, G.A. Petersson, H. Nakatsuji, M. Hada, M. Ehara, K. Toyota, R. Fukuda, J. Hasegawa, M. Ishida, T. Nakajima, Y. Honda, O. Kitao, H. Nakai, M. Klene, X. Li, J.E. Knox, H.P. Hratchian, J.B. Cross, C. Adamo, J. Jaramillo, R. Gomperts, R.E. Stratmann, O. Yazyev, A.J. Austin, R. Cammi, C. Pomelli, J.W. Ochterski, P.Y. Ayala, K. Morokuma, G.A. Voth, P. Salvador, J.J. Dannenberg, V.G. Zakrzewski, S. Dapprich, A.D. Daniels, M.C. Strain, O. Farkas, D.K. Malick, A.D. Rabuck, K. Raghavachari, J.B. Foresman, J.V. Ortiz, Q. Cui, A.G. Baboul, S. Clifford, J. Cioslowski, B.B. Stefanov, G. Liu, A. Liashenko, P. Piskorz, I. Komaromi, R.L. Martin, D.J. Fox, T. Keith, M.A. Al-Laham, C.Y. Peng, A. Nanayakkara, M. Challacombe, P.M.W. Gill, B. Johnson, W. Chen, M.W. Wong, C. Gonzalez, J.A. Pople, GAUSSIAN 03, Revision C.02, Gaussian, Inc., Pittsburgh PA, 2003.
[13] H. Nakano, J. Chem. Phys. 99 (1993) 7983.
[14] T.H. Dunning Jr., P.J. Hay, in: H.F. Schaefer III. (Ed.), Modern Theoretical Chemistry vol. 3, Plenum, New York, 1976, pp. 1–28.
[15] B.O. Roos, P.R. Taylor, P.E.M. Siegbahn, Chem. Phys. 48 (1980) 157.
[16] H.-J. Werner, P.J. Knowles, J. Chem. Phys. 82 (1985) 5053.
[17] P.J. Knowles, H.-J. Werner, Chem. Phys. Lett. 115 (1985) 259.
[18] D.G. Fedorov, J.P. Finley, Phys. Rev. A 64 (2001) 042502.
[19] M.W. Schmidt, K.K. Baldridge, J.A. Boatz, S.T. Elbert, M.S. Gordon, J.H. Jensen, S. Koseki, N. Matsunaga, K.A. Nguyen, S.J. Su, T.L. Windus, M. Dupuis, J.A. Montgomery, J. Comput. Chem. 14 (1993) 1347.
[20] H. Takahashi, private communication.
[21] M.A. El-Sayed, J. Chem. Phys. 38 (1963) 2834.
[22] S.K. Lower, M.A. El-Sayed, Chem. Rev. 66 (1966) 199.

Short-Time Fourier Transform Analysis of *Ab Initio* Molecular Dynamics Simulation: Collision Reaction between CN and C_4H_6

MARI TAMAOKI, YUSUKE YAMAUCHI, HIROMI NAKAI
Department of Chemistry, School of Science and Engineering, Waseda University, 3-4-1 Okubo, Shinjuku-ku, Tokyo 169-8555, Japan

Received 17 September 2004; Accepted 30 November 2004
DOI 10.1002/jcc.20183
Published online in Wiley InterScience (www.interscience.wiley.com).

Abstract: Collision reactions between cyano radical (CN) and dimethylacetylene (C_4H_6) are thought to occur in the atmosphere of Saturn's moon Titan. However, it is difficult to reproduce reactions occurring in unique environments to study their dynamical processes. In this study, collision reactions between CN and C_4H_6 were investigated using *ab initio* molecular dynamics (AIMD) simulations. The simulation results were categorized into three kinds: nonreactive collision, incorporation, and substitution. Short-time Fourier transform analysis of velocity autocorrelation functions obtained by the AIMD simulations, which has been recently developed by our research group, was performed to examine the nonequilibrium condition of the vibrational states. Spectrograms, which correspond to the time evolution of power spectra, clarify the relationship between the three reaction channels and the dynamical changes of the vibrational states.

 J Comput Chem 26: 436–442, 2005

Key words: short-time Fourier transform; *ab initio* molecular dynamics simulation; cyano radical; dimethylacetylene; collision reaction

Introduction

The driving force of the reaction between interstellar molecules is thought to be the radiation of ultraviolet and cosmic rays, which produces the ionic species. Therefore, the major process to create the interstellar molecules was thought to be an ion–molecule reaction. This assumption, however, could not account for the abundance of molecular species in the interstellar space. In recent years, several kinds of reactions, such as neutral–neutral reactions, are proposed to complement the ion–molecule ones.[1–3] Among them, radical reactions are now thought to be advantageous to create the molecules under the unique condition of an ultracold temperature around 10 K and an ultralow density, because they have none or less of an energy barrier and are exothermic.

The reactions between cyano radical (CN) and unsaturated hydrocarbons play crucial roles in prebiotic chemistry, which evolve toward complex organic molecules. These reactions take place in the atmosphere of Saturn's moon Titan. Balucani et al.[4] studied the collision reaction between cyano radical and dimethylacetylene (C_4H_6) by crossed molecular beam experiments together with the Rice–Ramsperger–Kassel–Marcus (RRKM) theory[5] and quantum chemical calculation. Experimental kinetic parameters were reasonably reproduced by the theoretical methods.

The present study examined the dynamics of the collision reaction between CN and C_4H_6 by performing *ab initio* molecular dynamics (AIMD) simulations. The AIMD simulation can give a quantitative description of the chemical reaction including the generation and the cleavage of bonds, because the simulation is performed *"on the fly"* on the potential energy hypersurface obtained by the *ab initio* quantum calculations. However, it requires the expensive computational cost. Thus, the number of atoms involved in the system is very limited. In the interstellar space, the opportunity of collision between the molecules is very scarce, and the system can be approximated as an isolated one. Therefore, we

Correspondence to: H. Nakai; e-mail: nakai@waseda.jp

Contract/grant sponsor: Grant-in-Aid for Young Scientists (A); [from the Japanese Society for the Promotion of Science (JSPS)]; Contract/grant number: KAKENHI 14703005

Contract/grant sponsor: NAREGI Nano-Science Project of the Ministry of Education, Culture, Sports, Science, and Technology (MEXT)

Contract/grant sponsor: 21st century Center of Excellence (21COE) "Practical Nano-Chemistry" from MEXT

Contract/grant sponsor: Association for the Progress of New Chemistry, Japan

adopted CN plus C_4H_6 as a whole system and investigated their collisions with different initial conditions.

We further performed short-time Fourier transform (ST-FT) of the velocity autocorrelation functions (VACFs) obtained by the AIMD simulations. The combination of the ST-FT technique and the AIMD simulations, which has been recently proposed by our research group[6] and Hayashi et al.,[7] can reveal the dynamical information of the vibrational states. We investigated the collision dynamics of ammonia cluster ions with the use of the ST-FT technique, while Hayashi et al. examined the excitation dynamics of bacteriorhodopsin. The present application of the ST-FT technique to the AIMD simulated results gives a reasonable interpretation for the relationship between the vibrational state and the reaction channels.

This article has an organization as follows. Computational methods of the AIMD simulation and the ST-FT analysis are described in the next section. Results of the simulations of the collision reaction of CN with C_4H_6 are shown in Section III. Moreover, we analyze the results by spectrogram in the same section. Finally, we summarize the present work.

Computational Methods

AIMD Simulation

AIMD simulations of the collision reaction of CN with C_4H_6 were performed by combining an original MD program with a quantum chemical calculation package, GAUSSIAN03.[8] Unrestricted Hartree–Fock (UHF)[9] and 6-31G(d,p) basis sets[10,11] were used to compute the potential energy and atomic force. The validity of this computational level is assessed in the Appendix. The velocity Verlet method[12] with a time step of 0.25 femtoseconds (fs) was adopted for the numerical integration of the equation of motion. As reference data, AIMD simulations of CN, CH_3, C_4H_6, C_4H_3N, and C_5H_6N under the equilibrium condition were also carried out at the same computational level.

The procedure of AIMD simulations of the collision reaction is as follows. First, 10,000 steps of AIMD simulations are carried out separately for CN and C_4H_6 to achieve an equilibrium condition. The individual internal energies of CN and C_4H_6 given in the equilibrated simulations are 1.6 and 1.2 times as large as their zero-point energies, which are estimated by summing the harmonic vibrational frequencies computed at the UHF/6-31G(d,p) level. Next, the translation energy of 0.32 eV, which corresponds to the experimental collision energy,[4] is added to the internal energy of the CN. The AIMD simulations of the collision are started at the separation of ~15 Å using 50 different initial orientations.

ST-FT Analysis

In this study, we attempt to apply the ST-FT technique to the results of the AIMD simulations. The ST-FT performed for VACFs is given by

$$\langle \mathbf{v}(t) \cdot \mathbf{v}(t+t') \rangle = \frac{1}{N} \sum_{i}^{N} \mathbf{v}_i(t) \cdot \mathbf{v}_i(t+t'), \tag{1}$$

where N is the number of atoms and $\mathbf{v}_i$ is the velocity of the i-th ion. Because the VACF does not depend on the time origin t under equilibrium, we can set $t = 0$ as follows,

$$\langle \mathbf{v}(t) \cdot \mathbf{v}(t+t') \rangle = \langle \mathbf{v}(0) \cdot \mathbf{v}(t') \rangle. \tag{2}$$

Thus, the power spectrum is given by the conventional Fourier transform (FT) as

$$S(\omega) = \frac{1}{2\pi} \int_{-\infty}^{\infty} \langle \mathbf{v}(0) \cdot \mathbf{v}(t') \rangle \exp(-i\omega t') dt' \tag{3}$$

where S and ω correspond to the intensity and the frequency of the vibrational state in the equilibrium condition, respectively. Under the nonequilibrium condition, VACF is not only a function of t' but also t. The ST-FT technique adopts a window function $h(t' - t)$ with a window length of T, which works to extract necessary information from a sequential data. The ST-FT of the VACF is expressed by

$$S(t, \omega) = \int_{-\infty}^{\infty} \langle \mathbf{v}(t) \cdot \mathbf{v}(t+t') \rangle h(t'-t) \exp(-i\omega t') dt'. \tag{4}$$

Consequently, the power spectrum involves t as well as ω as a variable. For the analysis hereafter, we adopt the Hanning window function:[13]

$$h(t'-t) = \begin{cases} \frac{1}{2} - \frac{1}{2}\cos\left\{\frac{\pi(t'-t+T)}{T}\right\} & -T \le t'-t \le T \\ 0 & \text{otherwise} \end{cases} \tag{5}$$

The two-dimensional contour map of the power spectrum is called a spectrogram, in which the horizontal and the vertical axes correspond to t and ω, respectively, and contour lines or the shades express the intensity. The window length of T is related to the resolution of frequency $\Delta\omega$, because the uncertainty principle of the time-frequency analysis defines the relationship between T and $\Delta\omega$:

$$\Delta\omega = \frac{1}{2cT}. \tag{6}$$

The resolution is improved for a long window length, whereas the dynamical information is diminished and/or averaged. In the present study, $T = 0.5$ picoseconds (ps) is adopted.

Results and Discussion

AIMD Simulation of Collision Reaction

The collision between CN and C_4H_6 was simulated by the AIMD method using 50 different initial orientations. To distinguish car-

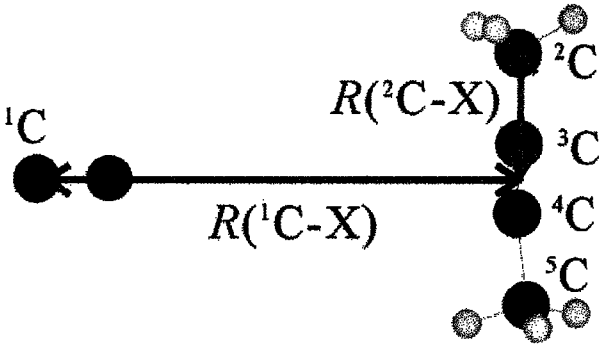

Figure 1. Labeling of carbon atoms and definition of C—X distances in the collision reaction between CN and C_4H_6. X is the center of ^{3}C and ^{4}C. Large dark balls correspond to carbon atoms, the large light balls to nitrogen atoms, and the small balls to hydrogen atoms. [Color figure can be viewed in the online issue, which is available at www.interscience.wiley.com.]

bon atoms, we use the labeling illustrated in Figure 1; ^{1}C belongs to CN, ^{2}C, ^{3}C, ^{4}C, and ^{5}C to C_4H_6. ^{2}C and ^{5}C are CH_3 binding to ^{3}C≡^{4}C. In Figure 1, distances between carbon atoms are also defined: $R(^1$C—X) and $R(^2$C—X) (X is the center of ^{3}C≡^{4}C bond).

The geometrical distribution of the products after 1.25-ps simulation is plotted in Figure 2, whose vertical axis is $R(^2$C—X) and horizontal axis $R(^1$C—X). The broken vertical and horizontal lines correspond to 2.5 Å. From the products shown in Figure 2, the AIMD simulations fall into three categories. First one locates in the range of $R(^1$C—X) ≥ 2.5 Å and $R(^2$C—X) ≤ 2.5 Å, where CN collides with C_4H_6 without changing chemical species; nonreactive collision occurs. Second one locates in the range of $R(^1$C—X) ≤ 2.5 Å and $R(^2$C—X) ≤ 2.5 Å, where the CN is incorporated into C_4H_6. The last one locates in the range of $R(^1$C—X) ≤ 2.5 Å and $R(^2$C—X) ≥ 2.5 Å, where methyl radical (CH_3) is dissociated from C_4H_6 while CN is incorporated; substitution occurred.

The three processes are expressed as follows.

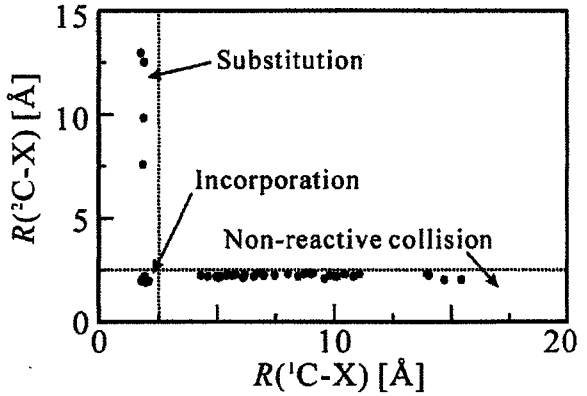

Figure 2. The geometrical distribution of the products for the 50 trajectories after 1.25-ps simulation.

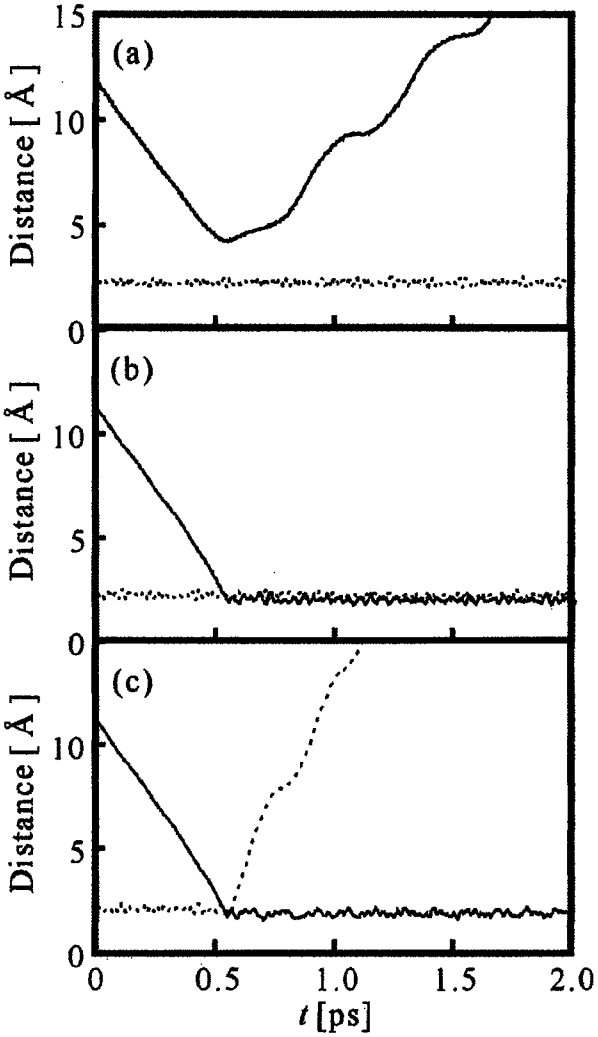

Figure 3. Time evolution of C—X distances in (a) nonreactive collision, (b) incorporation, and (c) substitution. The solid and the dotted lines correspond to $R(^1$C—X) and $R(^2$C—X), respectively.

Nonreactive collision:

$$CN + CH_3C{\equiv}CCH_3 \rightarrow CN + CH_3C{\equiv}CCH_3 \quad (7)$$

Incorporation:

$$CN + CH_3C{\equiv}CCH_3 \rightarrow CNCH_3C{=}CCH_3 \quad (8)$$

Substitution:

$$CN + CH_3C{\equiv}CCH_3 \rightarrow CNC{\equiv}CCH_3 + CH_3 \quad (9)$$

In the present study, we analyzed in detail three typical simulation results corresponding to the above reaction channels. Figure 3

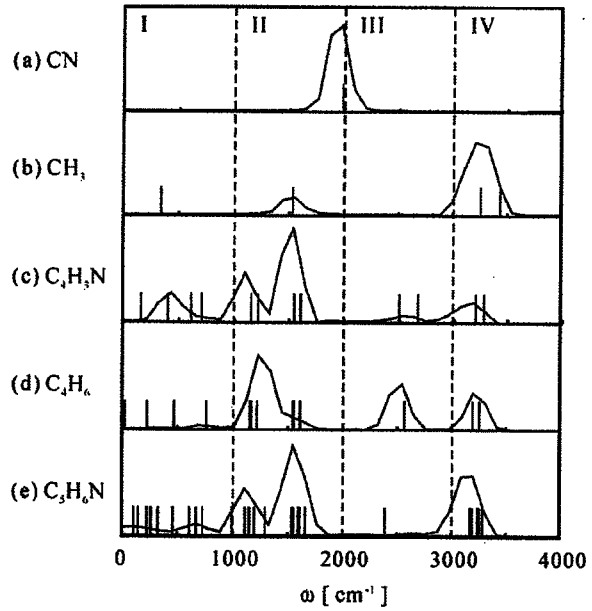

Figure 4. Power spectra of (a) CN, (b) CH_3, (c) C_4H_3N, (d) C_4H_6, and (e) C_5H_6N in an equilibrium condition. Vibrational frequencies in the harmonic approximation are described by the short lines on the horizontal axes.

shows the time change of the C—X distances in the simulations corresponding to (a) nonreactive collision, (b) incorporation, and (c) substitution. Time development of $R(^1C—X)$ and $R(^2C—X)$ are described by the solid and dotted lines, respectively. In Figure 3a, the solid line, $R(^1C—X)$ gradually declines, attaining a minimum around $t = 0.55$ ps, which means that the collision occurs then. After the collision, the solid line climbs monotonically. The dotted line, $R(^2C—X)$ oscillates around 2.0 Å throughout the simulation. In Figure 3b, the solid line gradually decreases until 0.55 ps, and then oscillates around 1.9 Å. The dotted line oscillates around 2.0 Å throughout the simulation. This means that the collision occurs at 0.55 ps, followed by the incorporation of CN into C_4H_6. In Figure 3c, the solid line declines until $t = 0.55$ ps and then oscillates around 2.0 Å. This means that after the collision at $t = 0.55$ ps, CN is incorporated into the C_4H_6. By contrast, the dotted line rises after the collision, which indicates that CH_3 dissociates from C_4H_6. Consequently, the substitution reaction eq. (9) is accomplished.

Power Spectra of the Equilibrium State

Power spectra of (a) CN, (b) CH_3, (c) C_4H_3N, (d) C_4H_6, and (e) C_5H_6N under equilibrium condition are presented in Figure 4. These are obtained by the ST-FT of VACFs using the Hanning window function of $T = 0.5$ ps. Because the VACF depends on the time origin t even for the AIMD simulation under the quasi-equilibrium condition, averaging the VACF over t is performed before the ST-FT. Vibrational frequencies in the harmonic approximation, which are estimated using Hessian matrices calculated at the UHF/6-31G(d,p) level, are also described by short lines on the horizontal axes in Figure 4.

We have divided the power spectra in Figure 4 into four regions: I, II, III, and IV corresponding to the frequency of 0–1000, 1000–2000, 2000–3000, and 3000–4000 cm^{-1}, respectively. In Figure 4a, there are no peaks in regions I, III, and IV. The C≡N stretching mode is observed in region II. Two peaks observed in regions II and IV in Figure 4b correspond to H—C—H bending and C—H stretching modes, respectively. Although there exists a vibrational state for the umbrella mode in region I obtained by the harmonic approximation, no clear peaks appear in the power spectra. In Figure 4c, region I involves C—C≡N bending mode and region II C—C stretching and H—C—H bending modes. In region III, the lower peak corresponds to C≡N stretching mode and the higher one to C≡C stretching mode. Region IV involves the C—H stretching mode. The power spectra of Figure 4d are alike Figure 4e. In region III, only one peak is observed; that is, the C≡C stretching mode. In Figure 4e, the intensities of peaks in regions II and IV, which involve C—C stretching, H—C—H bending, and C—H stretching modes, are very high.

Spectrogram for the Nonreactive Collision Process

The spectrogram for the nonreactive collision in Figure 3a is shown in Figure 5. Figure 5a is obtained by the ST-FT of VACFs averaging all atoms in the system, (b) and (c) within CN and C_4H_6, respectively. Thus, Figure 5b and c reveals the origin of Figure 5a.

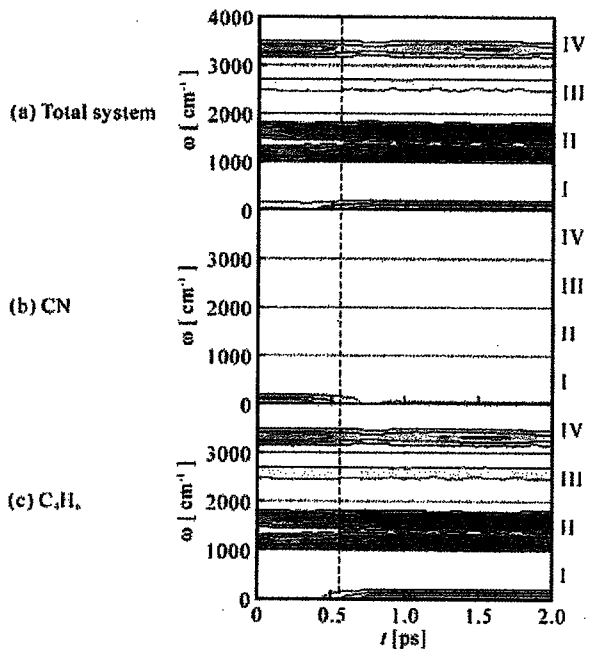

Figure 5. Spectrograms obtained by ST-FT of VACFs for (a) total system, (b) CN, and (c) C_4H_6 in the nonreactive collision process. The intensity is expressed by the shades: darker means stronger intensity. [Color figure can be viewed in the online issue, which is available at www.interscience.wiley.com.]

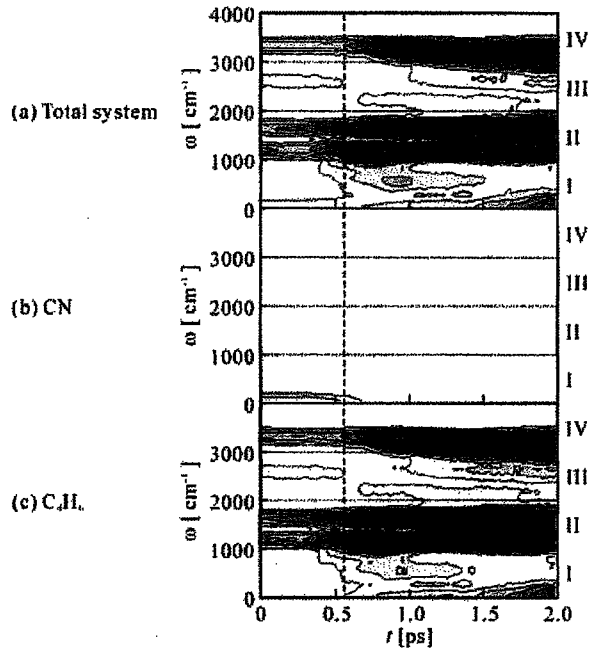

Figure 6. Spectrograms obtained by ST-FT of VACFs for (a) total system, (b) CN, and (c) C_4H_6 in the incorporation process. The intensity is expressed by the shades: darker means stronger intensity. [Color figure can be viewed in the online issue, which is available at www.interscience.wiley.com.]

A vertical broken line shows the timing of the collision, at which a minimum appears in the solid line of $R(^1C—X)$ in Figure 3a. In Figure 5a, the frequencies of the peaks are conserved throughout the collision process. In Figure 5b, the C≡N stretching mode at about 2000 cm^{-1} in Figure 4a is not observed, because its intensity is very weak compared to other peaks. According to Figure 4a, this is the only vibrational state of CN. However, in low frequencies in region I, a peak is observed. This peak is translation and rotation of CN coupled with its frequency, because its intensity decreases after the collision at 0.55 ps occurs. In Figure 5c, peaks around 1200, 1500, 2500, and 3200 cm^{-1} are assigned to C—C stretching, H—C—H bending, C≡C stretching, and C—H stretching modes, respectively. Near 0 cm^{-1}, a peak appears after the collision. This is assigned to the translation and rotation of C_4H_6 caused by the collision with CN at 0.55 ps.

Spectrogram for the Incorporation Process

The spectrogram for the incorporation, of which the geometrical change described in Figure 3b, is shown in Figure 6. As in the case for Figure 5, the ST-FT analysis of VACFs for the total system, CN, and C_4H_6 is carried out to obtain the spectrograms in Figure 6a, b, and c, respectively. In Figure 6, the most characteristic change appears in regions II and IV after the collision; intensities of peaks are very strong with the disappearance of the C≡N stretching mode. In Figure 6b, the peaks near 0 cm^{-1} disappears at the timing of the collision. This means that the translation and rotation of CN are reduced by the collision. In Figure 6c, a peak around 2500 cm^{-1} of C≡C stretching mode disappears as the collision occurs. Strong peaks appearing at 1200, 1500, and 3200 cm^{-1} are assigned to C—C stretching, H—C—H bending, and C—H stretching modes, respectively. These figures indicate that the energy of newly formed C—C≡N bond energy is distributed over several vibrational modes.

Spectrogram for the Substitution Process

The spectrograms for the substitution, which correspond to Figure 3c, are shown in Figure 7. As in the cases for Figures 5 and 6, Figure 7a, b, and c is obtained by the ST-FT of VACFs for the total system and each reactant, CN, and C_4H_6, respectively. Because the reactants and the products are different in the substitution reaction, as described in eq. (9), ST-FT of VACFs for each product, CH_3 and C_4H_3N are performed to obtain Figure 7d and e. In Figure 7a, the peak in region III disappears and those in regions II and IV become wider after the collision occurs. A strong peak is observed in region I after the collision. Figure 7b indicates that a peak near 0 cm^{-1} in region I is assigned to translation and rotation. This peak becomes wide by the collision with C_4H_6. In Figure 7c, the peak around 2500 cm^{-1}, which is assigned to the C≡C stretching mode, disappears at around 0.55 ps, when the collision occurs. These changes in Figure 7b and c indicate that as a result of collision between CN and C_4H_6, molecules with different chemical compositions are produced. In Figure 7d, peaks with strong intensity appear after the collision in region I. The lower peak around 0 cm^{-1} is enhanced by the collision with CN. A higher peak around 350 cm^{-1} is assigned to the CH_3 umbrella mode, which is characteristic for creating the CH_3 radical. This vibrational state seems to be the red shift of the peaks in region II before the collision. In region II, two peaks change to one peak around 1500 cm^{-1} after the collision, because CH_3 is a part of C_4H_6 before the collision and therefore, C—C stretching and H—C—H bending modes exist. By dissociation of CH_3, C—C stretching mode disappears. Also, in region IV, a narrow peak at 3200 cm^{-1} changes to a broad peak. Figure 4b accounts for this change. After the collision occurs, 3200 cm^{-1} of asymmetric C—H stretching and 3400 cm^{-1} of symmetric C—H stretching modes appear. In Figure 7e, a broad band appearing around 160 cm^{-1} after the collision is assigned to the C—C≡N bending mode. In region II, two strong peaks appear around 1200 and 1600 cm^{-1}. These peaks correspond to C—C stretching and H—C—H bending modes. In region IV, around 3200 cm^{-1}, C—H stretching mode is observed. These features of Figure 7d and e are involved or hidden in Figure 7b and c, because the CH_3 and C_4H_3N are part of the CN and C_4H_6.

The most crucial difference between the incorporation in Figure 6 and the substitution in Figure 7 lies in the regions I, II, and IV. In Figure 6, strong peaks appear in the regions II and IV. By contrast, a strong peak appears only in region I at lower frequency in Figure 7. From this comparison, it is found that the newly formed bond energy is distributed to a wide range in the incorporation, while the energy is concentrated on the C—C≡N bending mode in the substitution reaction.

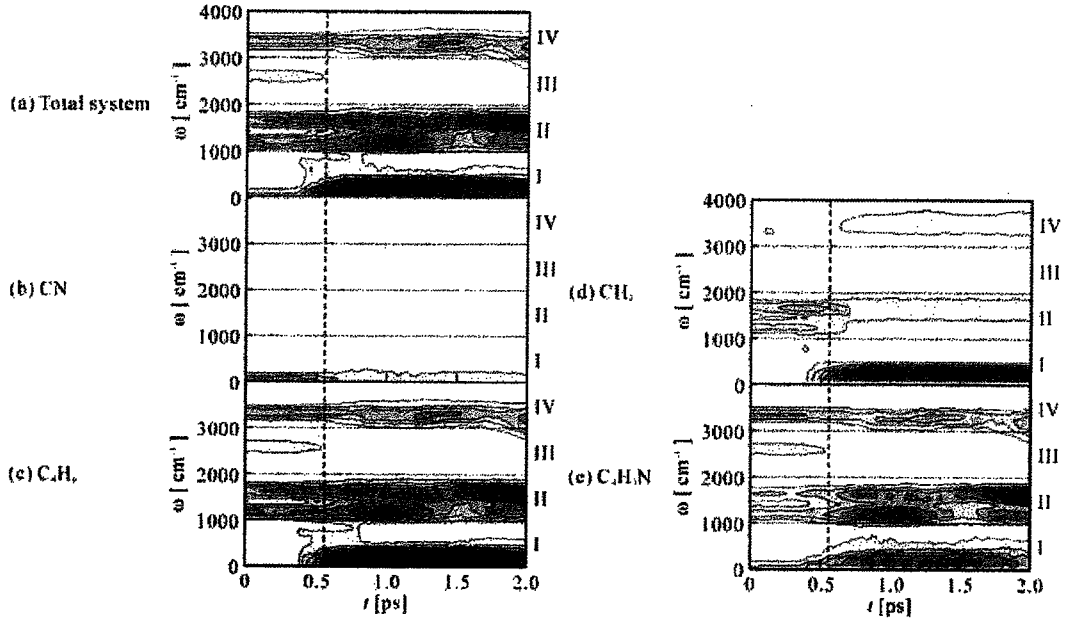

Figure 7. Spectrograms obtained by ST-FT of VACFs for (a) total system, (b) CN, (c) C_4H_6, (d) CH_3, and (e) C_4H_3N in the substitution process. The intensity is expressed by the shades: darker means stronger intensity. [Color figure can be viewed in the online issue, which is available at www.interscience.wiley.com.]

Conclusion

We have performed the AIMD simulation of the collision reaction between cyano radical (CN) and dimethyl acetylene (C_4H_6). Three reaction channels, that is, nonreactive collision, incorporation, and substitution, have reproduced by the AIMD simulation. The ST-FT technique has been applied for analyzing the dynamical process of the collision reaction. In the nonreactive collision, peaks do not change much throughout the simulation. In the incorporation and substitution reactions, C≡C stretching mode disappears at the timing of the collision; instead, H—C—H bending, C—C stretching, and C—H stretching modes are enhanced. The big difference between the incorporation and the substitution channels is the existence of the low frequency modes that are assigned to the C—C≡N bending mode of C_4H_3N and the umbrella mode of CH_3. Thus, the power spectra and its time evolution, spectrogram, obtained by the ST-FT of VACFs are found to be useful to interpret the relation between the vibrational states and the reaction channels. Not only the ST-FT of VACFs of the total system, but also that of the partial system give a detailed account.

Acknowledgment

Part of the calculations was performed at the Research Center for Computational Science (RCCS) of the National Institutes of Natural Sciences and the Media Network Center (MNC) of Waseda University.

Appendix

The AIMD simulations in the present study adopted the UHF method with the use of 6-31G(d,p) basis sets. Validity of this computational level was assessed by comparing the density functional theory (DFT) calculations with the B3LYP hybrid functional,[14] which consists of the HF or exact exchange, the Slater exchange,[15] the Becke (B88) exchange,[16] the Vosco–Wilk–Nusair correlation,[17] and the Lee–Yang–Parr correlation functionals.[18] Figure 8 shows the energy diagrams including reactant, intermediate, product, and transition state (TS) for the collision reaction between CN and C_4H_6, of which optimized geometries and energies were calculated at the UHF/6-31G(d,p) level (a) and the B3LYP/6-31G(d,p) level (b). Two energy levels for the intermediates correspond to *trans*- and *cis*- forms of $CNCH_3C{=}CCH_3$, which are the products of the incorporation process in eq. (8). There are two TSs, among the two intermediates and the product, $CNC{\equiv}CCH_3 + CH_3$. The energy levels of the intermediates, TSs, and product are calculated to be (−61.1, −60.0, −59.7, −17.7, −28.4) and (−63.2, −62.0, −57.7, −24.8, −32.4) in kcal/mol at the UHF and the B3LYP levels, respectively. The energy differences lie in the range of 2–7 kcal/mol. Thus, the energy profile at the UHF level, which is thought to be essential for the AIMD simulations, qualitatively or semiquantitatively agrees with that at the B3LYP level as well as the previous study,[4] which adopted the B3LYP/6-311+G(d,p) level.

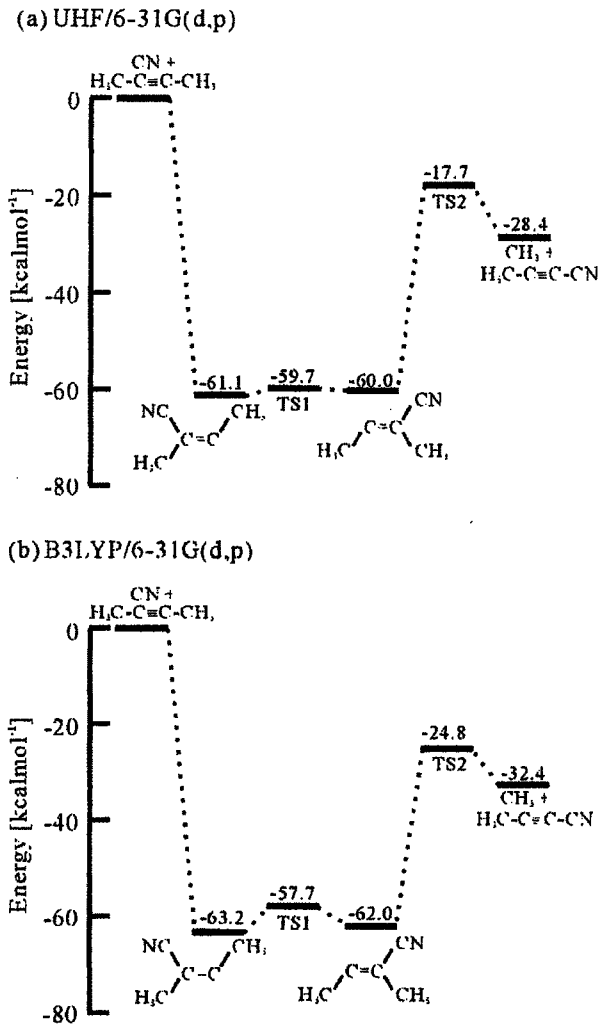

Figure 8. Energy diagrams of the collision reaction between CN and C_4H_6, calculated by (a) UHF and (b) B3LYP with the 6-31G(d,p) basis sets. The vertical line is the relative energy to the reactants.

References

1. Bettens, R. P. A.; Lee, H. H.; Herbst, E. Astrophys J 1995, 443, 664.
2. Turner, B. E.; Terzieva, R.; Herbst, E. Astrophys J 1999, 518, 699.
3. Smith, I. W. M.; Herbst, E.; Chang, Q. Mon Not R Astron Soc 2004, 350, 323.
4. Balucani, N.; Asvany, O.; Chang, A. H. H.; Lin, S. H.; Lee, Y. T.; Kaiser, R. I.; Bettinger, H. F.; Schleyer, P. v. R.; Schaefer, H. F., III. J Chem Phys 1999, 111, 7472.
5. Eyring, H.; Lin, S. H.; Lin, S. M. Basis Chemical Kinetics; Wiley: New York, 1980.
6. Yamauchi, Y.; Nakai, H.; Okada, Y. J Chem Phys 2004, 121, 11098.
7. Hayashi, S.; Tajkhorshid, E.; Schulten, K. Biophys J 2003, 85, 1440.
8. Frisch, M. J.; Trucks, G. W.; Schlegel, H. B.; Scuseria, G. E.; Robb, M. A.; Cheeseman, J. R.; Montgomery, J. A., Jr.; Vreven, T.; Kudin, K. N.; Burant, J. C.; Millam, J. M.; Iyengar, S. S.; Tomasi, J.; Barone, V.; Mennucci, B.; Cossi, M.; Scalmani, G.; Rega, N.; Petersson, G. A.; Nakatsuji, H.; Hada, M.; Ehara, M.; Toyota, K.; Fukuda, R.; Hasegawa, J.; Ishida, M.; Nakajima, T.; Honda, Y.; Kitao, O.; Nakai, H.; Klene, M.; Li, X.; Knox, J. E.; Hratchian, H. P.; Cross, J. B.; Adamo, C.; Jaramillo, J.; Gomperts, R.; Stratmann, R. E.; Yazyev, O.; Austin, A. J.; Cammi, R.; Pomelli, C.; Ochterski, J. W.; Ayala, P. Y.; Morokuma, K.; Voth, G. A.; Salvador, P.; Dannenberg, J. J.; Zakrzewski, V. G.; Dapprich, S.; Daniels, A. D.; Strain, M. C.; Farkas, O.; Malick, D. K.; Rabuck, A. D.; Raghavachari, K.; Foresman, J. B.; Ortiz, J. V.; Cui, Q.; Baboul, A. G.; Clifford, S.; Cioslowski, J.; Stefanov, B. B.; Liu, G.; Liashenko, A.; Piskorz, P.; Komaromi, I.; Martin, R. L.; Fox, D. J.; Keith, T.; Al-Laham, M. A.; Peng, C. Y.; Nanayakkara, A.; Challacombe, M.; Gill, P. M. W.; Johnson, B.; Chen, W.; Wong, M. W.; Gonzalez, C.; Pople, J. A. Gaussian 03, Revision A.1; Gaussian, Inc.: Pittsburgh, PA, 2003.
9. Roothan, C. C. J. Rev Mod Phys 1951, 23, 69.
10. Ditchfield, R.; Hehre, W. J.; Pople, J. A. J Chem Phys 1971, 54, 724.
11. Hehre, W. J.; Ditchfield, R.; Pople, J. A. J Chem Phys 1972, 56, 2257.
12. Swope, W. C.; Andersen, H. C.; Berens, P. H.; Wilson, K. R. J Chem Phys 1982, 76, 637.
13. Percival, D. B.; Walden, A. T. Spectral Analysis for Physical Applications: Multitaper and Conventional Univariate Techniques; Cambridge University Press: Cambridge, MA, 1993.
14. Becke, A. D. J Chem Phys 1993, 98, 5648.
15. Slater, J. C. Phys Rev 1951, 81, 385.
16. Becke, A. D. Phys Rev A 1988, 38, 3098.
17. Vosco, S. H.; Wilk, L.; Nusair, M. Can J Phys 1980, 58, 1200.
18. Lee, C.; Yang, W.; Parr, R. G. Phys Rev B 1988, 37, 785.

学 会 要 旨

The 6th Japan-China Symposium on Theoretical Chemistry (CSTC)
Institute for Fundamental Chemistry, (Kyoto), April 2002

O-08

Ab Initio Molecular Dynamics Simulation of Collision Reaction and Excitation Dynamics

Hiromi Nakai and Yusuke Yamauchi
Department of Chemistry, School of Science and Engineering, Waseda University, Tokyo 169-8555, Japan

I. Introduction

In the last few decades, molecular dynamics (MD) simulation based on the use of effective empirical potentials has proven to be an instrument of invaluable help in the understanding of the behavior of complex systems. More recently, *ab initio* MD simulation, which is the combination of standard MD, that is, numerical integration of the classical equations of motion of a system, and accurate electronic structure calculations to obtain the internuclear forces, has added a new dimension to this approach. Due to the explicit treatment of the electronic structure and the resulting forces acting on the atoms, forming and breaking of bonds can be studied in contrast to the conventional MD calculations done in the past. The electronic structure calculations are performed as the MD simulation proceeds. Since the combination with the electronic structure calculations is also computationally expensive, applications of the *ab initio* MD simulations are limited now; for example, less than 1000 atoms and shorter than a hundred picoseconds. In the present study, we have applied the *ab initio* MD technique to collision reaction between ammonia cluster ions and ammonia monomer and, also, to excitation dynamics of psoralens.

II. *Ab initio* MD simulation of collision reaction

Dynamics of ion-induced nucleation process has been important in many scientific and technological fields. Some groups suggested that an initial step of the ionic nucleation involves a metastable state. Okada *et al.* measured reaction cross sections between ammonia cluster ions $NH_4^+(NH_3)_{n-1}$ (n = 3-9) and deuterated ammonia monomer ND_3. They reported that collision reaction between them includes fusion and evaporation processes:

Fusion : $$NH_4^+(NH_3)_{n-1} + ND_3 \rightarrow NH_4^+(NH_3)_{n-m}ND_3 + (m\text{-}1)NH_3 \quad (1)$$

Evaporation : $$NH_4^+(NH_3)_{n-1} + ND_3 \rightarrow NH_4^+(NH_3)_{n-m-1} + ND_3 + mNH_3 \quad (2)$$

In the present study, we applied *ab initio* MD simulation to the collision reaction. Our original MD program, which is based on the Gear's predictor- corrector algorithm, is combined with Gaussian 98 program to calculate *ab initio* or semi-empirical molecular orbital (MO) calculations. Many of samplings with different initial geometries are performed to evaluate reaction cross sections by the *ab initio* MD simulations, in which the semi-empirical PM3 method is used. Figure 1 shows the relationship between the initial geometry and the resulting collision reaction. Collision energy (E_c) and cluster size (n) dependences of the fusion and evaporation cross sections are directly seen in Fig. 1. For n = 3 and E_c = 0.1 eV, the fusion region is largest because of strong

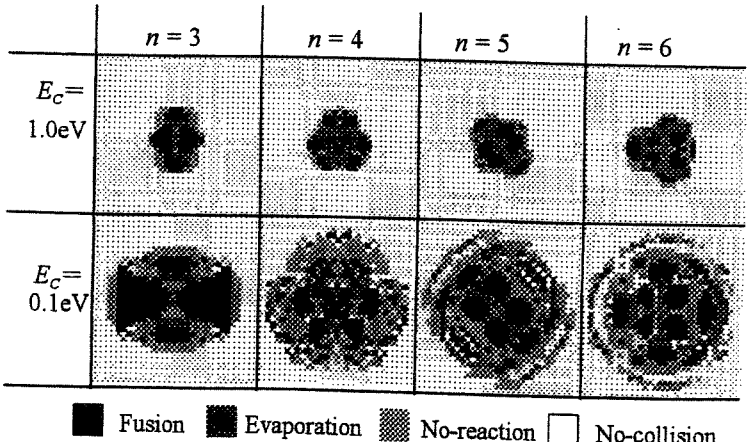

Fig. 1. Relationship between initial geometry and collision reaction.

force field of the center ion.

Table I shows the fusion and evaporation cross sections evaluated from Fig. 1. The calculated values are in reasonable agreement with the experimental ones.

Table I. Calculated and experimental cross sections for fusion and evaporation (in Å²).

E_C (eV)	Cluster size n	Fusion Calc.	Fusion Exptl.	Evaporation Calc.	Evaporation Exptl.
0.1	3	56.6	80.3	8.6	1.4
	4	44.9	57.0	11.3	10.3
	5	45.1	53.4	19.9	11.2
	6	43.5	72.2	25.2	40.2
1.0	3	13.7	14.1	30.1	38.5
	4	17.4	13.1	57.3	38.4
					53.2
					98.7

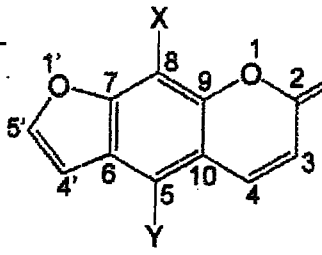

X=H, Y=H

X=H, Y=OCH_3

X= OCH_3, Y= H

III. *Ab initio* MD simulation of excitation dynamics

Photochemical reactivity of psoralens toward DNA has long been used in the treatment of skin disorders. However, consecutive addition at the two sites, which results in the cross-linking DNA, is also considered responsible for some undesired side effects such as skin cancer. 8-Methoxypsoralen (8-MOP) is more effective than the other psoralen derivatives such as 5-methoxypsoralen (5-MOP). Investigation of the excitation dynamics of psoralen compounds is crucial to clarify the effectiveness of 8-MOP. In the present study, we applied *ab initio* MD simulation to the excitation dynamics.

We have developed another MD program based on the Verlet algorithm. The electronic structure calculations are performed at the B3LYP/cc-pVDZ level in every MD steps. Figure 2 shows the plots of the O1-C2 distance in psoralen and 8-MOP in the T_1 state dynamics. The stable geometry in the S_0 ground state is used as an initial one. The initial velocity is set to be zero. Whereas the O1-C2 distance in psoralen is vibrating around 1.45 Å, that in 8-MOP is elongated to 2.2 Å. This ring-opening structure is due to the three-center bond O(methoxy)-O1-C2.

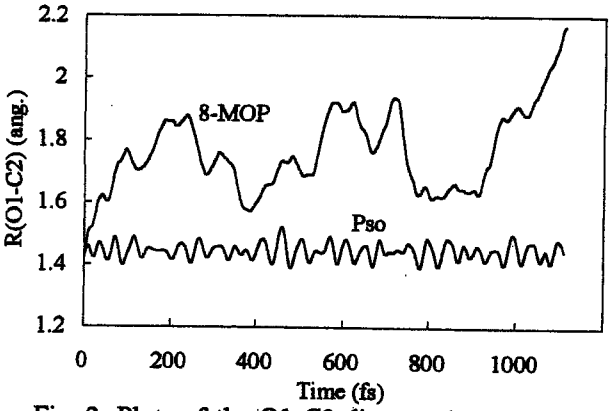

Fig. 2. Plots of the O1-C2 distance in psoralen and 8-MOP in the T_1 state dynamics.

Figure 3 shows the spin density in psoralen and 8-MOP in the T_1 state dynamics. The spin density of psoralen does not change much. On the contrary, the spin density at C3 moves to O1 in 8-MOP as the O1-C2 distance changes. The double bond between C3 and C4 is one of the active sites in the photoaddition to DNA. The ab initio MD simulation results indicate that 8-MOP has only one active site C4'=C5' whereas psoralen has two active sites. Therefore, 8-MOP does not lead to undesirable cross-linking DNA.

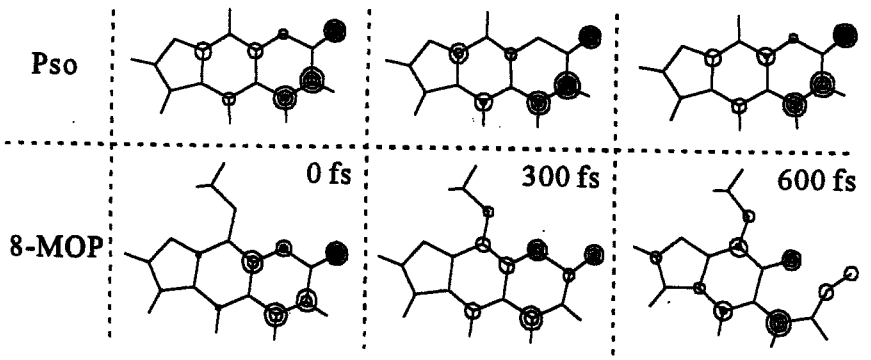

Fig. 3. Snapshots of spin density of psoralen and 8-MOP in the T_1 state at t = 0, 300, and 600 fs.

Excited State Processes in Electronic and Bio Nano-Materials, August 11-16, 2003 Los Alamos, New Mexico, USA

Title: "Theoretical study of the band structure of rutile and anatase titanium dioxide"

Authors: Hiromi Nakai,[1,2] Jochen Heyd,[1] and Gustavo E. Scuseria[1]

Affiliation: (1) Rice University, Department of Chemistry

(2) Waseda University, Department of Chemistry

Abstract:

Electronic state calculations for rutile and anatase titanium dioxide TiO_2 have bee carried out by using the periodic boundary condition (PBC) code of the Gaussian development version (GDV) program. In addition to the pure DFT method such as LDA and PBE, we have adopted the HF/DFT hybrid method referring to HSE03, which has been recently developed by our laboratory. Serious underestimation of the band gap obtained by the pure DFT method has been improved by the HSE03 hybrid functional. Some excited state properties of TiO_2 are also calculated by using the HSE03 functional.

226th ACS National Meeting,
New York, September 2003.

37.

DEVELOPMENT OF NONADIABATIC MOLECULAR THEORY FOR SIMULTANEOUS DETERMINATION OF NUCLEAR AND ELECTRONIC WAVE FUNCTIONS: AB INITIO NOMO THEORY. ***Hiromi Nakai***, *Department of Chemistry, Rice University, 6100 South Main,MS-60, Houston, TX 77005-1892, nakai@waseda.jp*

We have developed a simultaneous determination method of nuclear and electronic wave functions without the Born-Oppenheimer (BO) approximation, which is termed as ab initio NOMO theory. The Hartree-Fock (HF) equations have been derived for the nuclear orbital (NO), which is one-nucleus wave function, and the electronic molecular orbital (MO). Many-body effects have been examined and found that the electron-nucleus correlations are very important in our treatment. The separation of vibrational motion from the translational and rotational ones is also important in case adopting the Gaussian basis functions for the NOs. To represent the vibrational and electronic excited states, we applied the configuration interaction (CI) method to the NOMO theory.

226.

DEVELOPMENT OF ENERGY DENSITY ANALYSIS AND ITS APPLICATIONS.

***Takeshi Baba*[1], *Yoshiumi Kawamura*[1], and *Hiromi Nakai*[2]**. *(1) Department of Chemistry, Waseda University, 3-4-1 Okubo, Shinjuku-ku, Tokyo 169-8555, Japan, Fax: +81-3-3205-2504, baba.takeshi@aoni.waseda.jp, kawamura@toki.waseda.jp, (2) Department of Chemistry, Rice University, 6100 South Main,MS-60, Houston, TX 77005-1892, nakai@waseda.jp*

We have proposed a new technique for analyzing the results of the ab initio calculations such as HF, DFT, and hybrid methods. Our technique termed as Energy Density Analysis (EDA) partitions the total energy of the molecular system into atomic energy densities without extra computation cost. In the EDA technique, all the terms of kinetic, nuclear attraction, Coulomb, HF (exact) exchange, and exchange-correlation energies are divided into their atomic contributions. Furthermore, it is applicable to systems involving external field. For example, the EDA can give individual energies of solute and solvent in the solvation system. Numerical tests of the EDA technique have been performed, modifying GAMESS program developed by Prof. Mark Gordon's group.

226th ACS National Meeting,
New York, September 2003.

PHYS 243 [644847]: Numerical assessment of the ab initio NOMO theory

Keitaro Sodeyama, Department of Chemistry, Waseda University, 3-4-1 Okubo, Shinjuku-ku, Tokyo 169-8555, Japan, Fax: +81-3-3205-2504, sodeyama@suou.waseda.jp, and Hiromi Nakai, Department of Chemistry, Rice University, 6100 South Main,MS-60, Houston, TX 77005-1892, nakai@waseda.jp

The ab initio NOMO theory has been developed for treating the nuclear motion quantum mechanically and determining nuclear and electronic wave functions simultaneously. This method introduces the nuclear orbital (NO), as a one-nucleus wave function, and then expresses the total nuclear wave function by the antisymmetric (or symmetric) product of NOs. The HF, CI, CC, and MBPT models are applicable to the NOMO method. We here assess the reliability of these methods by numerical tests. We numerically examine the effect of the contaminations of the translation and rotation motions.

226th ACS National Meeting,
New York, September 2003.

PHYS **357 [644793]: Surface system modeling by the energy density analysis**

Yoshiumi Kawamura. Department of Chemistry, Waseda University, 3-4-1 Okubo, Shinjuku-ku, Tokyo 169-8555, Japan. kawamura@toki.waseda.jp. and **Hiromi Nakai**. Department of Chemistry, Rice University, 6100 South Main.MS-60, Houston, TX 77005-1892, nakai@waseda.jp

In the electronic structure calculation, solid surface is modeled by using the periodic boundary condition or finite cluster. Results of the calculation depend on the size of unit cell or cluster. Recently, our group has developed the Energy Density Analysis (EDA), which divides the total energy of molecular systems into atomic energy density. In this study, the convergence of the energy densities in the surface model is examined with respect to the cluster size and external field.

226th ACS National Meeting,
New York, September 2003.

New algorithm for the rapid computation of molecular integrals: Elementary Basis Algorithm

Masato Kobayashi and Hiromi Nakai

ABSTRACT

Computation of molecular integrals, especially electron repulsion integrals (ERIs) is still one of the time-consuming steps in the ab initio calculations. Many of efficient algorithms to compute ERIs have been proposed so far, which have commonly examined the FLOP counts for a set of ERIs. Several cutoff techniques have been also presented in order to reduce the number of ERIs computed explicitly. Some of them would bring the linear dependence of the computation cost on system size. Decreasing the prefactor should be essential in the linear scaling techniques. We focus not only on the individual computation cost for a set of ERIs but also on the total cost for the ERIs computed explicitly. This study develops a new algorithm, termed as "Elementary Basis Algorithm" for reducing the total cost of computing ERIs. We here employ the accompanying coordinate expansion method developed by Ishida. Numerical efficiency will be discussed.

1st Asian Pacific Conference on Theoretical & Computational Chemistry,
Okazaki, May 2004.

Nuclear Dynamics Analysis of Core-excited BF_3 by Wavelet Transform Technique

Takao Otsuka and Hiromi Nakai

Department of Chemistry, School of Science and Engineering, Waseda University
3-4-1 Okubo, Shinjuku-ku, Tokyo 169-8555, Japan

The complex decay dynamics of core-excited molecules has become interesting with the recent development of tunable synchrotron radiation in soft X-ray region. By various experimental techniques such as X-ray photoelectron and emission, Auger electron and the combined coincidence spectroscopy, the nuclear motion induced by the core-excitation has been reported in spite of its very short lifetime. It is very difficult to understand the significant vibration modes involving the core-excitation dynamics. In this study, we focus on the nuclear motion of the core-excited molecule within the time scale of 100 fs. We apply the wavelet transform technique to analyze the short time dynamics of the core-excited molecule for the first time.

An *ab initio* molecular dynamics simulation is carried out for the core-excitation dynamics of BF_3 molecule at the configuration interaction with singles (CIS) level. Figure 1 shows the time development of potential energy of BF_3 molecule. At t = 0, BF_3 molecule is excited to the core-excited state. The structural deformation from planar to umbrella is found in the simulation. Figure 2 shows the results of the time-frequency analysis obtained by wavelet transform of the velocity auto-correlation function. The horizontal axis is the time steps and the vertical axis is the frequency corresponding to the molecular vibration. Frequency for the umbrella mode is shifted from around 700 cm^{-1} in the ground state to around 600 cm^{-1} in the core-excited state. This shift, which is caused by the structural deformation, occurs within 100 fs after the core-excitation. Thus, the wavelet approach demonstrates that it is possible to explain the core-excitation dynamics before Auger decay. Further details would be presented.

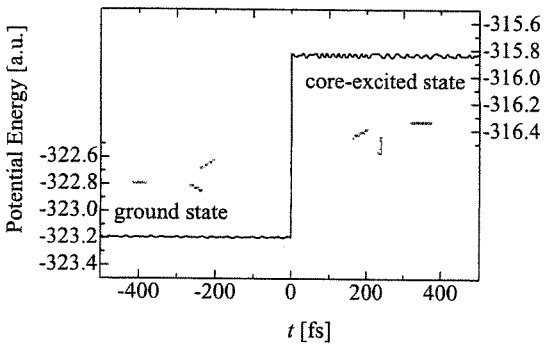

Fig 1. Time development of potential energy.

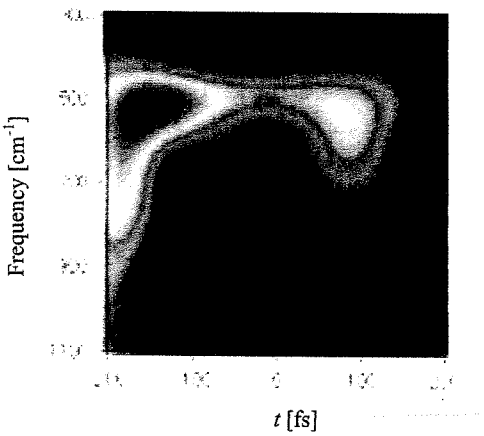

Fig 2. Time-frequency analysis by wavelet transform.

1st Asian Pacific Conference on Theoretical & Computational Chemistry,
Okazaki, May 2004.

Combination of Energy Density Analysis and Energy Decomposition Method

Yoshiumi Kawamura and Hiromi Nakai

Department of Chemistry, School of Science and Engineering, Waseda University, Shinjuku, Tokyo 169-8555, Japan

We have recently developed the energy density analysis (EDA) [1], which partitions the total energy of molecular system into the atomic contributions by using the analogy of Mulliken population analysis. In this study, we have combined the EDA and the conventional energy decomposition methods, such as Morokuma decomposition [2] in order to investigate the molecular interactions. Combination of the EDA and the energy decomposition methods, which is termed Interaction-EDA, enables us to partition the interaction energy components (electrostatic + exchange (ES+EX), polarization (PL), charge transfer (CT)) into local atomic contributions (Fig. 1). Table 1 shows the Interaction-EDA results for CO adsorption on Si(100) surface by using $Si_{33}H_{28}$ model cluster (Fig. 2). The repulsive interaction is mainly due to the ES+EX components of the C atom of adsorbate and Si atoms in the first layer. The CT from adsorbate to surface, which corresponds to well-known σ-donation, leads to about 50 and 6 kcal/mol stabilization of Si atoms in the first and second layers, respectively. Destabilization of C and O atoms by the CT from adsorbate to surface are about 29 and 2 kcal/mol.

Table 1. Interaction-EDA results for CO adsorption on $Si_{33}H_{28}$ clsuter in kcal/mol.

		ES+EX	PL		CT		Total	Full variational
			S	A	S→A	A→S		
Adsorbate	O	-1.2	0.0	6.1	1.0	2.0	7.8	7.4
	C	34.5	-23.7	-14.6	-19.0	29.2	6.4	13.9
A	1L	39.8	3.4	-9.6	0.5	-50.4	-16.2	-14.2
	2L	-4.3	6.5	0.0	1.6	-5.1	-1.3	-7.5
	3L	-0.5	2.9	1.3	0.2	0.4	4.3	5.2
	4L	-0.9	0.4	-0.8	0.0	-0.6	-2.0	-1.2
B	1L	-0.6	-0.9	-0.6	1.0	-0.6	-1.7	-2.7
	2L	-0.1	-0.4	-0.1	0.3	-0.1	-0.4	-0.5
	3L	0.2	-0.2	0.3	-0.1	0.2	0.4	0.0
	4L	-0.7	-0.6	-0.5	0.3	-0.4	-1.9	-1.3
C	1L	0.0	0.1	0.0	0.0	0.0	0.0	-0.1
	2L	0.0	0.0	-0.1	0.1	-0.1	-0.1	-0.1
	3L	0.0	0.0	0.0	0.0	0.0	0.0	0.0
	4L	-0.1	0.0	-0.1	0.1	-0.1	-0.2	-0.1
Total		65.1	-16.0	-18.8	-11.4	-25.9	-7.0	-8.1

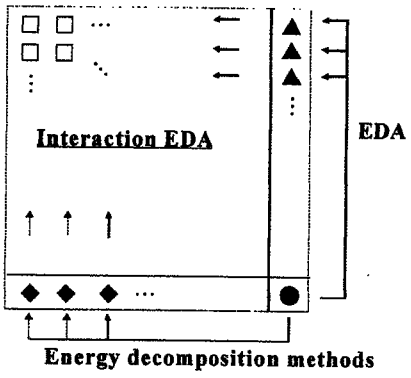

Figure 1. Schematic illustration of Interaction-EDA.

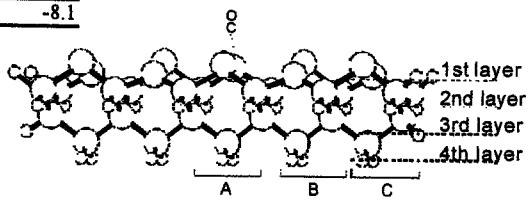

Figure 2. $Si_{33}H_{28}$ model cluster.

[1] H. Nakai, Chem. Phys. Lett. 363, 73-79 (2002).
[2] K. Morokuma, J. Chem. Phys. 55, 1236 (1971).
[3] W. J. Stevens, W. H. Fink, Chem. Phys. Lett. 139, 15 (1987).

1st Asian Pacific Conference on Theoretical & Computational Chemistry,
Okazaki, May 2004.

Many-body effects in nonadiabatic molecular theory for simultaneous determination of nuclear and electronic wave functions

Keitaro Sodeyama, Hiroyoshi Kiryu, Kaito Miyamoto, and Hiromi Nakai

Department of Chemistry, School of Science and Engineering, Waseda University, Okubo, Shinjuku-ku, Tokyo 169-8555, Japan

We have developed a simultaneous determination method of nuclear and electronic wave functions without Born-Oppenheimer (BO) approximation in order to treat the nuclear motion.[1-3] The Hartree-Fock (HF) equations have been derived for the nuclear orbital (NO), which is one-nucleus wave function, and the electronic molecular orbital (MO). This method is termed the *ab initio* NOMO/HF theory.

Many-body effects such as nucleus–nucleus and electron–nucleus correlations have also examined in the non-BO theory. The many-body perturbation theory (MBPT), the coupled cluster double (CCD), and the Brueckner double (BD) methods have been applied.[4] From the numerical results, the electron–nucleus correlation is greater than the nucleus–nucleus one. The electron–nucleus correlations of N_2 and F_2 molecules become larger than those of H_2, D_2, and T_2 molecules. It is because the attraction force is expected to be stronger as the nuclear charge becomes larger. Furthermore, "core electron"–nucleus correlation is greater than "valence electron"–nucleus one. It follows from these results that the short-range interaction between electron and nucleus is very important in our treatment.

To treat the short-range interaction, we apply the transcorrelated method[5] to *ab initio* NOMO theory. A fixed geminal, which is a function of distances between electron and nucleus, is adopted for correlation function in the transcorrelated Hamiltonian. A frozen Gaussian geminal (FROGG)[6] is used for the fixed geminal, which involves the effect of the nuclear charge. To assess the many-body effects estimated by their methodology, *ab initio* NOMO/full-configuration interaction (CI) method using the determinant CI algorithm[7] is developed.

---

[1] M. Tachikawa, K. Mori, H. Nakai, K. Iguchi, *Chem. Phys. Lett.*, **290**, 437 (1998).
[2] H. Nakai, *Int. J. Quantum Chem.* **86**, 511 (2002).
[3] H. Nakai, K. Sodeyama, M. Hoshino, *Chem. Phys. Lett.*, **345**, 118 (2001).
[4] H. Nakai, K. Sodeyama, *J. Chem. Phys.*, **118**, 1119 (2003).
[5] S. F. Boys, N. C. Handy, *Proc. Roy. Soc. A.* **310**, 43 (1969).
[6] S. Ten-no, O. Hino, *Int. J. Mol. Sci.*, **3**, 459 (2002).
[7] P. J. Knowles, N. C. Handy, *Chem. Phys. Lett.*, **109**, 417 (1984).

1st Asian Pacific Conference on Theoretical & Computational Chemistry,
Okazaki, May 2004.

Spectrogram analysis of collision reaction using *ab initio* molecular dynamics simulation

Yusuke Yamauchi [a], Yoshiki Okada [b], Hiromi Nakai [a]

[a] *Department of Chemistry, School of Science and Engineering, Waseda University, Shinjuku, Tokyo 169-8555, Japan*

[b] *RIKEN (The Institute of Physical and Chemical Research), Wako, Saitama 351-0198, Japan*

The collision reaction of $NH_4^+(NH_3)_2$ with NH_3 was simulated using *ab initio* molecular dynamics (AIMD) method. AIMD simulation is a combination of *ab initio* quantum chemistry calculation and classical molecular dynamics simulation. The *ab initio* calculation was performed at the DFT (B3LYP)/ 6-31G(d, p) level. The velocity Verlet algorithm was used for numerical integration for solving equation-of-motion. Then the results of the simulation were analyzed by spectrogram, which was obtained by the short-time Fourier transformation of time correlation function.

The AIMD simulations for the collision reaction are categorized into three processes; namely adsorption, substitution and non-reactive collision. Figure 1 shows time development of inter-monomer distances for the adsorption process. The spectrogram for this trajectory is shown in Figure 2. When the monomer is incorporated into the cluster ion, the intensity of low frequency modes (300–400 cm^{-1}) is remarkably increased. This strong peak corresponds to the stretching mode between NH_4^+ and NH_3. This change is not seen in the spectrogram for the substitution and non-reactive collision.

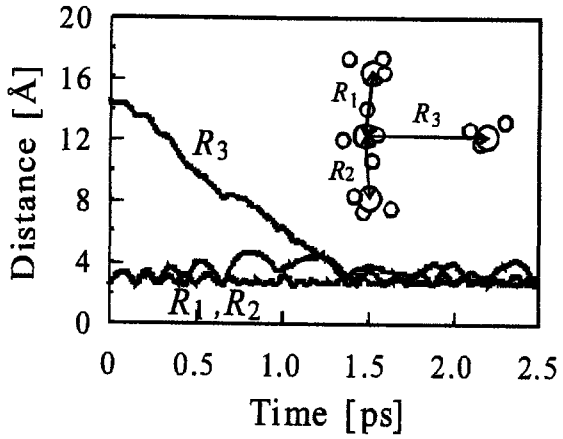

Fig. 1. Time development of inter-monomer distances for the adsorption process.

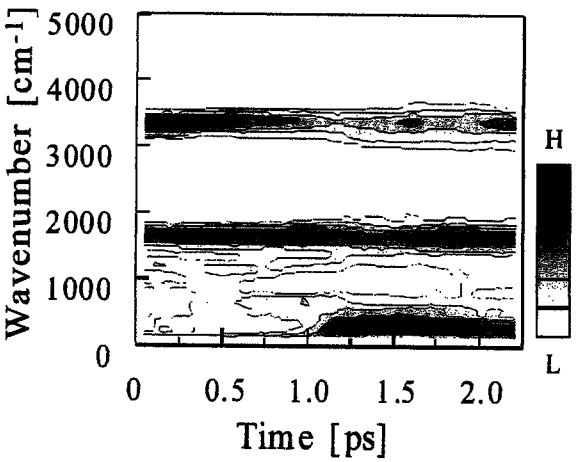

Fig. 2. Vibration spectrogram for the adsorption process.

1st Asian Pacific Conference on Theoretical & Computational Chemistry,
Okazaki, May 2004.

New algorithm for the rapid evaluation of electron repulsion integrals

Masato Kobayashi,[a] Hiromi Nakai,[a] Michio Katouda,[b] and Shigeru Nagase [b]

[a] *Department of Chemistry, School of Science and Engineering, Waseda University*
Okubo, Shinjuku-ku, Tokyo 169-8555, Japan
[b] *Department of Theoretical Study, Institute for Molecular Science*
Myodaiji, Okazaki 444-8585, Japan

The computation of molecular integrals over Gaussian basis functions, especially electron repulsion integrals (ERIs), is still one of the most time-consuming steps in *ab initio* calculations. Many of efficient algorithms have been proposed up to now. In this presentation, we will show two newly developed approaches to calculate molecular integrals.

First, we have developed *elementary basis algorithm* (EBA),[1] which focuses on the total computational cost for all ERIs computed explicitly. In modern *ab initio* calculations, we can treat large-size systems such as nano-clusters and bio-molecules. Most of systems, which we usually deal with, are made up of a maximum of 10 chemical elements. For example, deoxyribonucleic acid (DNA) containing over 1,000 atoms consists of 6 chemical elements; namely, C, H, O, N, P, and S. In the conventional programs, all computations were carried out in the atomic loops. In the EBA, parts of computations are carried out in the elementary loops, which are much more efficient than the atomic ones. We have implemented the EBA code combined with the accompanying coordinate expansion (ACE) algorithm of Ishida,[2] which is the most efficient algorithm in the floating-point operation (FLOP) count. Numerical efficiency is investigated by measuring the timing data for the ERI computations.

Next, we have developed ACE-RR method,[3] which reduces the individual computational cost for a set of ERIs. This method is based on the ACE formula. For the basis functions with the same exponent but different angular momentums, such as L shells, gradients, and Hessians, the conventional ACE algorithm computes all corresponding ERIs individually. We have developed a new algorithm, which can efficiently deal with these ERIs, by using two types of recurrence relation (RR), ACE-HRR and ACE-VRR. The efficiency has been confirmed by comparing the FLOP count of the ACE-RR algorithm with those of the previous algorithms.

---

[1] H. Nakai and M. Kobayashi, Chem. Phys. Lett., *in press*.

[2] K. Ishida, Int. J. Quantum Chem. **59**, 209 (1996).

[3] M. Kobayashi and H. Nakai, J. Chem. Phys., *submitted.*

1st Asian Pacific Conference on Theoretical & Computational Chemistry,
Okazaki, May 2004.

Energy Density Analysis for Chemical Bonds in Molecules

Yasuaki Kikuchi, Motoki Ishii, Takeshi Baba and Hiromi Nakai

Department of Chemistry, School of Science and Engineering, Waseda University, Shinjuku, Tokyo 169-8555, Japan

Chemical bonds in molecules have been of great interest in fundamental chemistry and physics. However, the chemical bond is not directly measurable. The understanding and evaluation of the chemical bonds are essential to lead to basic concepts in many chemical and physical phenomena. Nakai[1] has recently proposed a new scheme, termed energy density analysis (EDA), to partition the total energy of the quantum chemical calculation into atomic contributions. Numerical applications[2-4] of the EDA have supported its reliability and usefulness, especially for the intramolecular energy transfer. However, the EDA could not describe the chemical bonds because it could not partition the energy into the bonding region. In the present study, we improve the EDA to describe the chemical bonds termed as Bond-EDA, and apply it to some fundamntal but interesting chemical bondings.

The Bond-EDA technique gives bond energy densities for all atomic pairs involving the calculated systems. For example, the Bond-EDA of ethane evaluates the bond energy densities not only for C-H and C-C bonds, but also for H-H bonds. In this case, the bond energy densities of C-C and C-H bonds are negative values, namely, −118.26 and −80.15 kcal/mol, corresponding to the covalent bond, and those between H atoms of two methyl groups are positive value (2.22 kcal/mol) corresponding to the steric repulsion.

Table 1 shows the Bond-EDA results for the Diels-Alder reaction between 1-phenyl-1,3-butadiene and styrene producing *ortho*- and *meta*-isomers. While the bond energy for the two bonds are close to each other in the product, there exists a great difference between them in the transition state. This trend of the bond energy agrees with that of the bond distance.

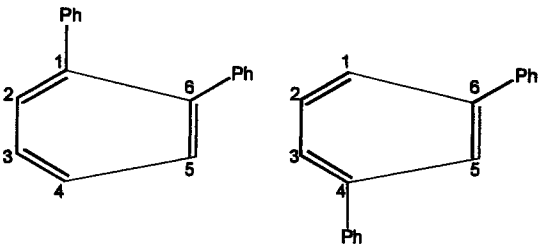

ortho-isomer *meta*-isomer

Figure 1. Labelling for the Diels-Alder reaction between 1-phenyl-1,3-butadiene and styrene.

Table 1. Bond energy (kcal/mol) and bond distance (Å) for the Diels-Alder reaction between 1-phenyl-1,3-butadiene and styrene.

		Transition state		Product	
		Bond distance	Bond energy	Bond distance	Bond energy
ortho-isomer	C_1-C_6	2.50	-28.2	1.57	-108.2
	C_4-C_5	1.98	-71.1	1.53	-118.8
meta-isomer	C_1-C_6	2.15	-55.1	1.54	-120.4
	C_4-C_5	2.24	-45.2	1.54	-114.5

[1] H. Nakai, Chem. Phys. Lett., 363, 73-79 (2002).
[2] H. Nakai, and K. Sodeyama, Chem. Phys. Lett., 365, 203-210 (2002).
[3] Y. Kawamura, and H. Nakai, Chem. Phys. Lett., 368, 673-679 (2003).
[4] H. Nakai, and K. Sodeyama, J. Mol. Structure (THEOCHEM), 637, 27-35 (2003).

EMT2004 the 5th International Symposium on ELECTROCHEMICAL
MICRO & NANO SYSTEM TECHNOLOGIES,
Tokyo, September 2004.

DENSITY FUNCTIONAL THEORY STUDY OF THE OXIDATION MECHANISMS OF REDUCTANTS AT THE METAL SURFACE FOR ELECTROLESS DEPOSITION PROCESSES

Takuya Shimada[1], Kaoruho Sakata[1], Syuuichi Odagiri[1],
Hiromi Nakai[2], Takayuki Homma[1], Tetsuya Osaka[1]

[1]Department of Applied Chemistry and [2]Department of Chemistry, Waseda University
3-4-1 Okubo, Shinjuku-ku, Tokyo 169-8555, Japan

Electroless deposition processes are widely applied for the fabrication of advanced functional devices such as micro electronic devices and systems. In these processes, an electron for reductive deposition of metal ion is supplied by 'the oxidation reaction of reductant' at 'the metal surface', which acts as a catalyst for the reaction. Although these two characteristics are significant issues of the electroless deposition process, they have not been well understood yet. In the present work, we employed Density Functional Theory (DFT) calculations to elucidate the oxidation mechanism of the representative reductants for the electroless deposition processes, such as dimethylamine borane (DMAB), hypophosphite ion, and formaldehyde, at various metal surfaces in terms of the reaction intermediates and the transition states, which cannot be achieved by the experimental approaches.

A general pathway for the oxidation reaction of the reductants has been proposed by van den Meerakker, in which the reaction is initiated by dehydrogenation and proceeds via three-coordinate intermediate species [1]. On the other hand, we have proposed an alternative pathway via five-coordinate intermediate ones, which is initiated by addition of OH^- [2]. In addition, we also proposed total reaction pathway via all intermediates. The results of the calculations indicated that the oxidation reactions of the three reductants in an isolated system took place via the pathway, which didn't form the dianion intermediate species. On the other hand, it was also indicated that the reactions at the metal surface proceeds via five-coordinate pathway, which does include the formation of the dianion species. It is suggested that the stabilization effect of dianion species by the adsorption dominates the other intermediates (Fig. 1, step2). In other words, it is indicated that the metal surface acts as a catalyst for the oxidation reaction of the reductants, mainly by this stabilization effect.

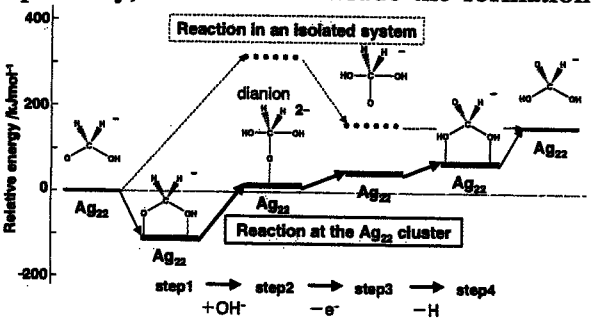

Fig. 1 The energy profile for the oxidation process of formaldehyde via five-coordinate pathway in an isolated system and at the silver surface.

As described, the DFT calculations were confirmed to be an effective tool to analyze the oxidation mechanism of the reductants, such as the catalytic activity of the metal surfaces.

This work was performed at the 21st Century Center of Excellence (COE) Program "Practical Nano-Chemistry", MEXT, Japan, and was financially supported in part by the Grant-in-Aid for Scientific Research (C), MEXT, Japan

[1] J.E.A.M. van den Meerakker, *J. Appl. Electrochem.*, **11**, 395 (1981). [2] T. Homma, H. Nakai, I. Komatsu, A. Tamaki, T. Osaka, *Electrochimica Acta*, **47**, 47 (2001).

EMT2004 the 5th International Symposium on ELECTROCHEMICAL
MICRO & NANO SYSTEM TECHNOLOGIES,
Tokyo, September 2004.

CHARACTERIZATION OF STRAINED SILICON WAFER SURFACE BY DENSITY FUNCTIONAL THEORY ANALYSIS

Kaoruho Sakata[1], Nobuhiro Kubo[1], Hiromi Nakai[2],
Takayuki Homma[1], Tetsuya Osaka[1]

[1] Department of Applied Chemistry and [2] Department of Chemistry,
Waseda University, Okubo, Shinjuku, Tokyo 169-8555, Japan

Strained Si technology is expected to be a promising alternative for the replacement of conventional (bulk) Si wafers for the ULSI device manufacturing and attracts much attention since the strain-induced enhancement of carrier transport enables to increase the devise speed and decrease the power consumption considerably[1]. In order to fabricate the "strained" layer, a thin layer of Si is pseudomorphically grown on a thick, relaxed SiGe layer whose lattice constant is expanded in accordance with the Ge contents. Such a strain in the Si-Si bonds, on the other hand, is expected to change not only the electronic properties but also the chemical properties, such as the reactivity, of the Si layer surface. Especially, it is significant to characterize its reactivity with trace metal species in order to prepare the ultra clean surface, which is required for the ULSI device processes. However, such a property of the strained Si surface has not been understood yet. In the present work, we attempt to investigate the reactivity of the strained Si surface in detail, especially focusing on that with Cu species, by using Molecular Orbital (MO) and Density functional theory (DFT) calculations.

The strain in the Si layer is expressed as the change in the Si-Si bond length and the changing behavior of the electron state was evaluated. Then the reactivity with Cu species was estimated by calculating the adsorption energy of Cu to the "strained" Si surfaces. As for a model to investigate the Si surface, Si_{18} (100) cluster, shown in Fig.1, was applied. All of the edge parts (dangling bonds) of the Si cluster was terminated with H except for the adsorption site for the Cu atom, which was set as the "on top" site. The Si–Si distance was varied from 2.35Å (bulk Si) to 2.46Å (bulk Ge). The Gaussian basis sets applied for the calculation were 6-31G** for Si, H and Cu. All of the DFT calculations were performed using the B3LYP method as implemented in the GAUSSIAN 03 package.

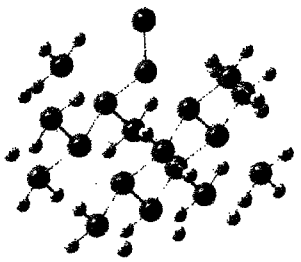

Fig.1 Si_{18} (100) cluster model

The results of the calculation revealed that the adsorption energy at the strained Si was larger than that for the bulk (non-strained) Si, suggesting that the strain in the Si-Si bonds induced the reaction with metal species. In order to investigate the origin of such a difference in the adsorption energy, the HOMO and LUMO of the clusters were investigated. It was clarified that the HOMO showed slight change due to the strain, whereas the LUMO for the strained case was more stabilized than that for the non-strained case. It was suggested that such a change in the stability of LUMO could be an origin of the change in reactivity, which was induced by the strain in the Si-Si bonds.

This work was performed at the 21st Century Center of Excellence (COE) Program "Practical Nano-Chemistry", MEXT, Japan, and was financially supported in part by the Grant-in-Aid for Scientific Research (C), MEXT, Japan

Reference: [1] K. Rim, *et al.*, Solid-State Electronics, 47, 1133-1139 (2003)

2004 Joint International Meeting (206th Meeting of The Electrochemical Society (ECS) and 2004 Fall Meeting of The Electrochemical Society of Japan (ECSJ)), Hawaii, October 2004.

Density Functional Theory Study on the Reaction Mechanism of Reductants for Electroless Silver Deposition Processes

T. Shimada[1], H. Nakai[2], T. Homma[1], T. Osaka[1]

[1]Department of Applied Chemistry and [2]Department of Chemistry, Waseda University
3-4-1 Okubo, Shinjuku-ku, Tokyo 169-8555, Japan

Electroless deposition processes are widely used in the various fields of microfabrication. In these processes, the electron is supplied by the oxidation reaction of the reductant. However, the reaction process is so complex that the mechanism has not been clarified yet. In this study, we employed Density Functional Theory (DFT) calculation to investigate the oxidation mechanism of representative reductants such as dimethylamine borane (DMAB), hypophosphite ion, and formaldehyde at the silver surface. This method has capability to provide quantitative evaluation of the oxidation mechanism at the elementary level, which cannot be achieved by the experimental approaches. Since the deposited metal surface should act as the catalyst for the oxidation reaction of reductants, we investigated the local interaction between silver surface and reductants by Energy Density Analysis (EDA) [1], which has capability to estimate the local energies of each atom composing the molecule.

All of the DFT calculations were performed using the B3LYP method as implemented in the GAUSSIAN 98 package. As for a model surface, we use $Ag_{22}(111)$ cluster (Fig. 1). Ag–Ag distance is fixed at its bulk lattice value of 2.889 Å. The Gaussian basis sets were 6-31G** for boron, phosphorous, carbon and hydrogen, 6-31+G** for oxygen in which diffuse functions, and Hay & Wadt for silver are argumented.

We investigated the oxidation reaction pathway of the three reductants at the silver surface. A general reaction pathway has been proposed by van den Meerakker, in which the reaction proceeds via three-coordinate intermediate species, initiated by dehydrogenation [2]. On the other hand, we have proposed an alternative pathway via five-coordinate species, initiated by addition of OH^- (Scheme 1) [3]. The results of the calculations suggested that the oxidation reaction of the three reductants at the silver surface took place via five-coordinate pathway rather than via three-coordinate one. It was also indicated that the rate-determining step of the five-coordinate pathway is the coordination of OH^- to the reductants adsorbed on the silver surface.

Then, the catalytic activity of the silver surface for the oxidation reaction of the reductants was investigated by the EDA. It was indicated that the energy level of the reductant part was high, that is, unstable, whereas that of the silver cluster part was low due to the adsorption. The total energy level calculated from the sum of both values also indicated the stable condition, as is seen in Fig. 2. It is expected that the exposed silver surface, which is under unstable condition, tends to be stabilized by the adsorption. It was also suggested that the adsorbed reductant was destabilized to obtain driving force to proceed to the next reaction step.

The rate-determining step, i. e., the coordination of OH^- was also analyzed in terms of adsorption geometry by the EDA. In the case of formaldehyde where the silver surface acts as a catalyst for the reaction, the OH^- and the reductant were destabilized at the silver cluster. On the other hand, smaller destabilization was observed from both OH^- and the reductant in the case of hypophosphite ion, where the silver surface does not act as a catalyst. It was considered that such a difference could be due to the difference of the adsorption geometry.

As described, we applied theoretical calculations to investigate the reaction mechanism of the electroless silver deposition processes and demonstrated that the favorable pathways of various reductants at the silver surface can be predicted in terms of the intermediates, and the factors of catalytic activity of metal surface can be also evaluated by the energy changes of each molecule.

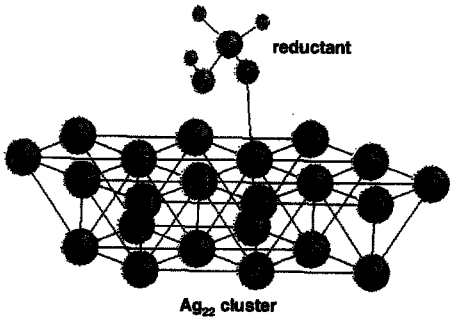

Fig. 1 Calculation model for reductant (intermediate of formaldehyde) adsorbed on the $Ag_{22}(111)$ cluster.

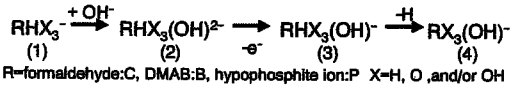

Scheme 1 Reaction pathway of reductants via five-coordinate intermediate.

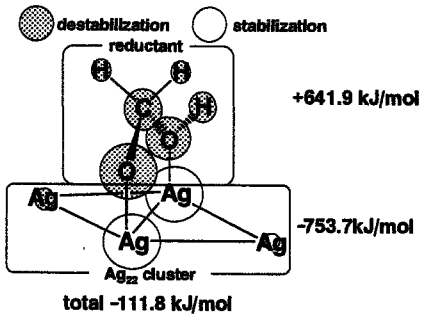

Fig. 2 Energy Density Analysis of formaldehyde (Scheme 1 (1)) adsorbed on the $Ag_{22}(111)$ cluster.

References
1. H. Nakai, *Chem. Phys. Lett.*, 363, 73 (2002).
2. J.E.A.M. van den Meerakker, *J. Appl. Electrochem.*, **11**, 395 (1981).
3. T. Homma, H. Nakai, I. Komatsu, A. Tamaki, T. Osaka, *Electrochimica Acta*, **47**, 47 (2001).

Acknowledgements
This work was financially supported in part by the Research Grant from the Shorai-Foundation and Grant-in-Aid for a Scientific Research (C) from the Ministry of Education, Culture, Sports, Science and Technology, and was performed at the 21st Century Center of Excellence (COE) Program "Practical Nano-Chemistry" from The Ministry of Education, Culture, Sports, Science and Technology, Japan.

2004 Joint International Meeting (206th Meeting of The Electrochemical Society (ECS) and 2004 Fall Meeting of The Electrochemical Society of Japan (ECSJ)), Hawaii, October 2004.

Density Functional Theory Study on the Oxidation Mechanisms of Aldehydes as Reductants for Electroless Deposition Process

K. Sakata[1], T. Shimada[1], H. Nakai[2], T. Homma[1], T. Osaka[1]
1 Department of Applied Chemistry,
2 Department of Chemistry,
Waseda University
3-4-1 Okubo, Shinjuku-ku, Tokyo 169-8555, Japan

Electroless deposition process is a powerful technique to form various functional surfaces for electronic devices and systems. In order to elucidate its mechanism to achieve further precise control of the properties, numbers of studies have been carried out mainly by experimental approaches. However, the reaction mechanism is so complex that a reasonable model has not been established yet. Therefore, we have been studying the electroless deposition process by Molecular Orbital (MO) and Density functional theory (DFT) calculations, which can investigate oxidation reaction process of reductants (including their intermediate species) and catalytic activity of metal surface at an element level[1)-3)].

In this study, we focus upon aldehydes as the reducing agent, which are mainly used for electroless copper deposition. We investigate the oxidation mechanisms of aldehydes, *i.e.*, formaldehyde (***H***CHO), acetaldehyde (***CH₃***CHO), and glyoxylic acid (***COOH***CHO) to study the functional group effect for the reaction processes.

All DFT calculations were performed using the B3LYP method as implemented in the GAUSSIAN 98 package. As for a model surface, $Cu_{22}(111)$ cluster was used. Cu–Cu distance was fixed at its bulk lattice value of 2.556Å. The Gaussian basis sets were 6-31G** for carbon and hydrogen, 6-31+G** for oxygen in which diffuse functions, and Hay & Wadt for Cu were used.

First, we investigated three kinds of the aldehydes to clarify their oxidation mechanisms in isolated state. Van den Meerakker proposed a general reaction pathway, in which the reaction proceeds via three-coordinate intermediate species, initiated by dehydrogenation[4)]. On the other hand, we have proposed the reaction pathway via five-coordinate species, initiated by addition of OH^-[1)-3)]. By comparing the energy diagram of the reaction pathways via three-coordinate and five-coordinate by relative energy on the basis of reactants, it was indicated that the oxidation reactions of the three aldehydes on the Cu surface took place via five-coordinate pathway, rather than via-three coordinate one.

Next, in order to investigate the reaction mechanism more in detail, the effect of solvation was investigated, which was taken into account by the self-consistent reaction field method with an isodensity polarized continuum model (SCRF-IPCM). It was indicated that the reactions of the three aldehydes are endothermic in the balk solution, whereas the reactions are exothermic in the vicinity of the metal/liquid interface, suggesting that the oxidation reaction of aldehydes proceeds preferentially at the metal surface region.

Furthermore, their oxidation mechanisms at the metal surface were also studied since the catalytic activity of the metal surface is one of the most important issues for the electroless deposition reaction. For this, adsorption energy and desorption energy of three aldehydes were estimated, and from the results, it was suggested that glyoxylic acid, whose functional group is electron-withdrawing, tend to adsorb weakly onto the Cu surface.

Then, in order to explain the origin of the smaller adsorption and desorption energy of glyoxylic acid than other aldehydes, we investigated the local interaction between Cu surface and three aldehydes by Energy Density Analysis (EDA)[5)], which is able to estimate the energies of each atom of molecule.

The results of EDA analysis indicated that small interaction between glyoxylic acid and Cu surface results in the smaller adsorption and desorption energy of glyoxylic acid, suggesting the effect of substitution of the functional group on the oxidation mechanism.

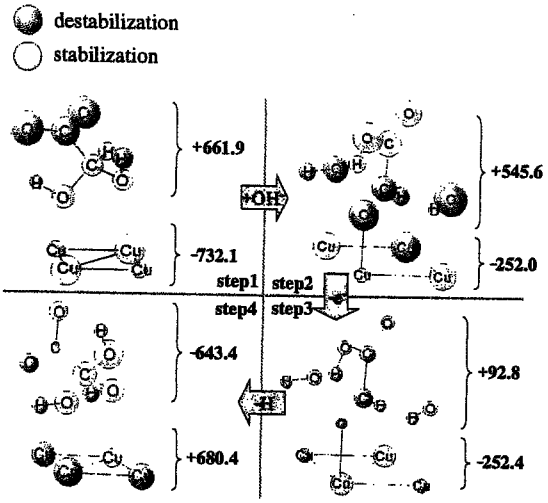

Figure 1 Energy difference [kJ/mol] among each step of oxidation. The energy is divided into glyoxylic acid and metal by using Energy Density Analysis. (via five-coordinate pathway)

References

1) T. Homma, H. Nakai, M. Onishi, T. Osaka, *J. Phys. Chem. B*, 103, 1774-1778 (1999).
2) T. Homma, I. Komatsu, A. Tamaki, H. Nakai, T. Osaka, *Electrochimica Acta*, 47, 47-53 (2001).
3) H. Nakai, T. Homma, I. Komatsu, T. Osaka, *J. Phys. Chem. B*, 105, 1701-1704 (2001).
4) J.E.A.M. van den Meerakker, *J. Appl. Electrochem.*, 11 395 (1981).
5) H. Nakai, *Chem.Phys.Lett.*, 363, 73-79 (2002).

Acknowledgements

This work was financially supported in part by the Research Grant from the Shorai-Foundation and Grant-in-Aid for a Scientific Research (C) from the Ministry of Education, Culture, Sports, Science and Technology, and was performed at the 21st Century Center of Excellence (COE) Program "Practical Nano-Chemistry" from The Ministry of Education, Culture, Sports, Science and Technology, Japan.

The World Association of Theoretically Oriented Chemists,
Cape Town, January 2005.

ES-P35 **Development of energy density analysis.**

Hiromi Nakai, *Department of Chemistry, School of Science and Engineering, Waseda University, 3-4-1 Okubo, Shinjuku-ku, Tokyo 169-8555, JAPAN*

We have proposed a novel analysis technique, energy density analysis (EDA),[1] to understand the energetic change inside the system. The EDA technique partitions the total energy of molecules computed using *ab initio* molecular orbital (MO) theory or density functional theory (DFT) into atomic energy densities without extra computing costs. The information given by the EDA is useful to interpret the mechanism of chemical reaction,[2-4] to verify the theoretical modeling,[5] and so on. We have also developed the EDA technique such as combination with Kitaura-Morokuma type energy decomposition method (Interaction-EDA)[6] and partitioning the energy density into bonding region (Bond-EDA).[7] The combination of the short-time Fourier transform technique with the EDA leads to a new two-dimension image, energy transfer spectrogram (ETS),[8] which specifies molecular vibrational modes related with intramolecular and/or intermolecular energy transfer in ab initio molecular dynamics simulation of chemical reaction. Details are discussed in the presentation.

*E-mail: nakai@waseda.jp

[1] H. Nakai, Chem. Phys. Lett., 363 (1-2), 73 (2002).
[2] H. Nakai, K. Sodeyama, Chem. Phys. Lett., 365 (3-4), 203 (2002).
[3] H. Nakai, K. Sodeyama, J. Mol. Struct. (THEOCHEM), 637 (1-3), 27 (2003).
[4] Y. Kawamura, H. Nakai, Chem. Phys. Lett., 368 (5-6), 673 (2003).
[5] H. Nakai, M. Katouda, Y. Kawamura, J. Chem. Phys., 121 (10), 4893 (2004)
[6] Y. Kawamura, H. Nakai, J. Comp. Chem., 25 (15), 1882 (2004).
[7] H. Nakai, Y. Kikuchi, J. Theor. Comp. Chem., in press (2004).
[8] Y. Yamauchi, H. Nakai, J. Chem. Phys., submitted (2004).

第 6 回理論化学討論会,
大阪大学（大阪），2002 年 5 月.

Energy Density Analysis (EDA)

（早大理工）　中井　浩巳

§1. 緒言

昨今の量子化学計算の進歩は、いかに大きな系の物理量を、いかに高精度に求めるか、ということに集中してきた。量子化学計算を用いた応用研究においては、実験値を精度良く再現したにもかかわらず、「なぜか」がなかなか見い出せないことがある。これは計算結果から、物理・化学現象の理解を導くための解析(analysis)手法が欠けているためである。本研究では、分子系のエネルギーを構成原子に分割するための新しい手法、Energy Density Analysis (EDA)を提案する。また、いくつかの応用例により、その信頼性および有用性を検討する。

§2. 理論[1]

Kohn-Sham(KS)法に対する EDA には、二つの分割法が含まれる。一方は、分点を用いた求積法により計算される交換相関エネルギーの分割である。原子 A の交換相関エネルギー密度を、

$$E_{XC}^{A} = \sum_{g}^{grid} \omega_g p_A(\mathbf{r}_g) F_{XC}(\mathbf{r}_g) \tag{1}$$

のように定義する。ここで、$\omega_g(\mathbf{r})$は分点の重み、$p_A(\mathbf{r})$は分割関数である。他方は、KS 軌道を用いた解析積分により計算されるその他のエネルギーの分割である。例えば、（相互作用のない）運動エネルギーT_Sは、

$$T_S[\rho] = \sum_{\mu}\sum_{\nu} P_{\mu\nu}\langle\chi_\nu|\hat{t}|\chi_\mu\rangle = \sum_{\mu}\sum_{\nu} P_{\mu\nu}T_{\nu\mu} = \sum_{\mu}(\mathbf{PT})_{\mu\mu} \tag{2}$$

のように書け、Mulliken の電子密度解析の類推から、$(\mathbf{PT})_{\mu\mu}$を原子軌道χ_μに対する運動エネルギー密度と定義することができる。これらにより、全エネルギーの分割が達成される。

§3. 結果と考察

本研究では、まず、水分子に対して EDA を適用した。図 1 は、平衡構造(実験値)から両方の O-H 距離を伸ばした場合(a)と、片方の O-H 距離を伸ばした場合(b)の結果である。計算レベルは、B3LYP/cc-pVDZ である。(a)では、結合距離の増加とともに O, H_a, H_b 原子いずれも不安定化している。(b)では、結合距離が増加している O と H_b 原子は不安定化しているが、H_a 原子のエネルギー密度はほとんど変化していないことがわかる。このように、EDA により得られる各原子のエネルギー密度は、我々の直感とうまく対応していることがわかる。現在、種々の興味ある現象に EDA を適用している。[2]

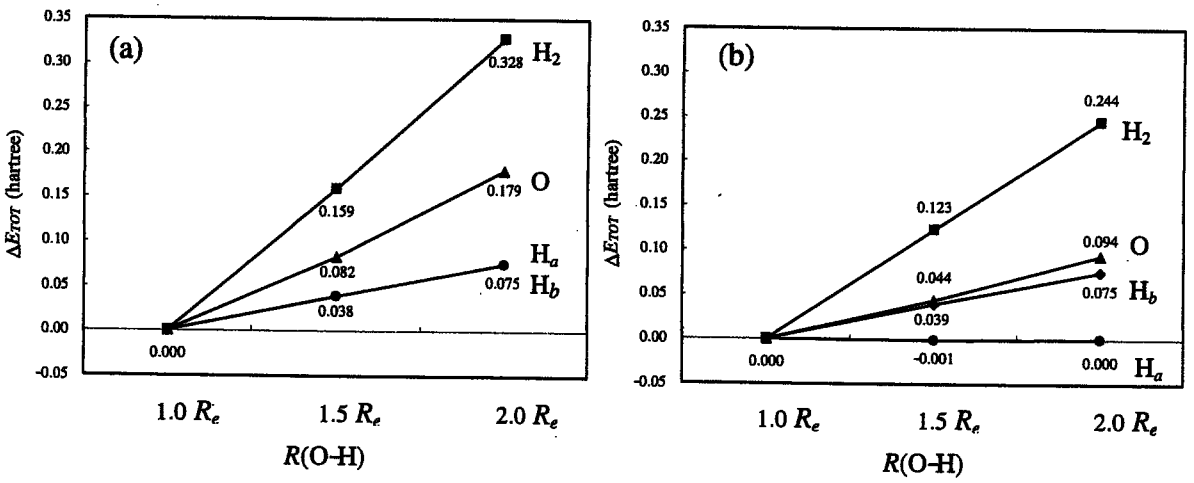

Figure 1. Total energy density changes (ΔE_{TOT}) of H_a, H_b, and O in H_2O in the homogeneous (a) and heterogeneous (b) bond-breaking processes, with respect to the values in the stable H_2O molecule..

[1] H. Nakai, J. Chem. Phys., submitted.
[2] 馬場、中井、P1；河村、中井、P2；菊池、河村、中井、P3；袖山、星野、中井、P4、第 6 回理論化学討論会，大阪大学（吹田），2002 年 5 月.

第 6 回理論化学討論会,
大阪大学（大阪），2002 年 5 月.

Energy Density Analysis (EDA) による 3 中心結合の解析

（早大理工）○馬場 健, 中井 浩巳

【緒言】 3 中心 4 電子結合に代表される超原子価結合は，分子軌道を用いてはじめて説明される現象である。しかしながら，実際の系において対応する分子軌道を見出すのはしばしば困難であり，電荷密度解析などの手法では知見を得ることが難しかった。最近当研究室で分子系のエネルギーを構成原子に分割するための新しい手法である Energy Density Analysis(EDA) [1, 2]が提案された。そこで本研究では，いくつか興味ある 3 中心結合をもつ化合物（超原子価化合物）に対して EDA を適用し，本手法の適用範囲を探るとともにこれまで得られなかった 3 中心結合に関する情報を得ることを目的とする。

【結果と考察】 まず，3 中心 4 電子結合をもつ典型的な分子のひとつである I_3^- に対して EDA を適用した（計算レベル：B3LYP/DZP）。I^-+I_2 が I_3^- になると 35kcal/mol 安定化する。これを EDA により構成原子ごとに分割すると，I^- から電子を I_2 に移動したことにより，I_a は 27kcal/mol 不安定化し，I_b, I_c はそれぞれ 34, 28kcal/mol 安定化する。EDA により得られる描像は，3 中心結合の特徴をよく表している。

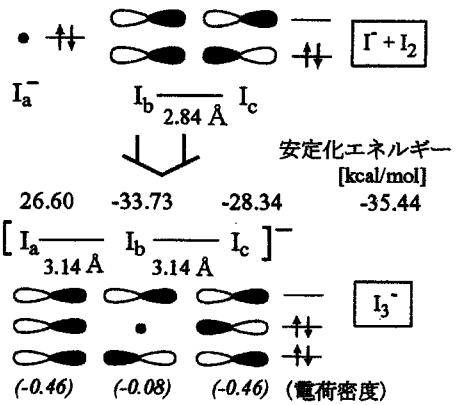

Fig.1. I^-+I_2 系と I_3^- の比較

ハロゲン化メチルとアンモニアによる反応（Menshutkin 反応）のような S_N2 反応の遷移状態(TS)は求核攻撃を受ける部位を中心とした超原子価化合物である(Fig.2)。そこで，臭化メチルとアンモニアやメチルアミン類の反応の遷移状態に対して EDA を適用し，S_N2 反応における置換基効果と 3 中心結合の関係を調べた（計算レベル：B3LYP/cc-pVDZ）。$I^-+I_2 \rightarrow I_3^-$ と同様に 3 中心 4 電子結合ができる TS では，いずれもアミンは不安定化，CH_3 と Br は安定化している。また，Menshutkin 反応の活性化エネルギーは，メチル基が多く置換したアミンほど下がることが実験的に知られている[3]。計算結果はこの傾向を再現している。EDA によると，これはメチル置換体になるほどアミンの不安定化が小さくなるためであり，TS の構造が反応物側にシフトすることとも対応している。

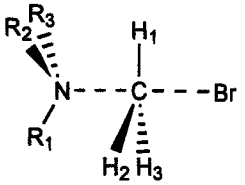

Fig.2. Menshutkin 反応の遷移状態 (10-C-5)

Table 2. CH_3Br とメチルアミン類の反応における遷移状態の活性化エネルギーと構造

		NH_3	$MeNH_2$	Me_2NH
活性化エネルギー [kcal/mol]				
TOTAL		27.87	23.87	22.59
amine		75.25	59.33	50.65
	N	*17.01*	*15.19*	*14.55*
	R_1	*19.41*	*15.28*	*11.98*
	R_2	*19.41*	*14.43*	*11.98*
	R_3	*19.41*	*14.43*	*12.14*
CH_3		−41.76	−30.90	−23.90
	C	*−46.27*	*−36.63*	*−31.24*
	H_1	*1.50*	*2.22*	*1.94*
	H_2	*1.50*	*1.75*	*2.70*
	H_3	*1.50*	*1.75*	*2.70*
Br		−5.62	−4.56	−4.17
TSの構造				
R(N−C) [Å]		1.705	1.804	1.838
R(Br−C) [Å]		2.764	2.667	2.636
A(H_1−C−N) [°]		103.8	100.8	99.1

[1] H. Nakai, *J. Chem. Phys.*, submitted. [2] 中井，第 6 回理論化学討論会（大阪），1O12A, (2002)
[3] K. Okamoto, S. Fukui and H. Shingu, *Bull. Chem. Soc. Jpn.*, **40**, 1920 (1967).

第 6 回理論化学討論会,
大阪大学（大阪），2002 年 5 月.

Energy Density Analysis (EDA) によるプロトン移動過程の解析

（早大理工）○袖山慶太郎，星野稔，中井浩巳

【序】当研究室では最近、分子系のエネルギーを構成原子に分割するための新しい手法である Energy Density Analysis (EDA) を提案した。[1,2] 本研究では EDA をプロトン移動過程に適用し、新しい視点からこの現象のメカニズムを検討する。

【プロトン・トンネリング】Malonaldehyde (MA)の分子内プロトン・トンネリングによる２つの配置と、結合交代による各原子のエネルギー密度変化を図１に示す。計算方法は B3LYP、基底関数は cc-pVDZ を用いた。トンネリングにより水素原子(H1)との結合が共有結合から水素結合に変化した酸素原子(O2)は不安定化し、反対側の酸素原子(O3)が安定化している様子が数値的にわかる。さらに O2 に対して C4, H7 また O3 に対して C6, H9 とエネルギー密度変化の影響が減衰振動しながら伝わっていることも興味深い。

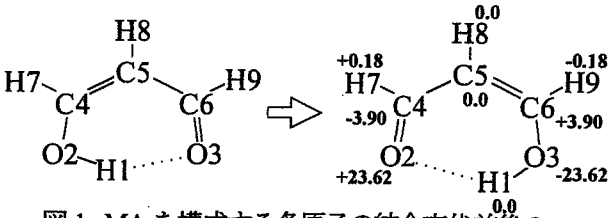

図 1. MA を構成する各原子の結合交代前後のエネルギー密度変化 [kcal/mol]

【cis-trans 異性化】MA の cis-trans 異性化は、面外経由の遷移状態(TS1)の方が面内経由(TS2)よりも有利であることが知られている。これを表 1 の EDA による結果から検討すると ΔE_{TS1}, ΔE_{TS2}, ΔE_{trans} はどれも水素結合の安定化を失うことによる H1 と O3 の大きな不安定化が生じている。また、H1 と共有結合している O2 は ΔE_{TS1}, ΔE_{trans} において安定化している。これは水素結合が無くなり H1-O2 結合がより強固になったためと考えられる。これに対して、ΔE_{TS2} のみ O2 の大きな不安定化が見られ、このことが TS2 が不利な原因となっている。これは TS2 では∠H1-O2-C4 がほぼ直線となり、O2 の sp^3 性が弱められたためである。

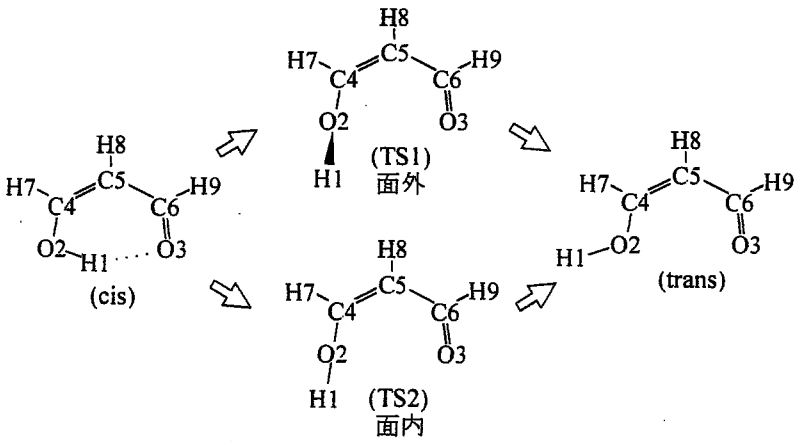

図 2. MA の cis-trans 異性化の反応経路

表 1. MA を構成する原子の cis 体からのエネルギー密度変化 [kcal/mol]

	ΔE_{TS1}	ΔE_{TS2}	ΔE_{trans}
H1	8.53	13.64	11.32
O2	-4.55	14.89	-4.99
O3	9.15	7.86	8.97
C4	1.52	4.87	-0.82
C5	10.30	10.65	7.36
C6	-5.50	-10.48	-9.51
H7	-0.37	0.01	1.11
H8	0.63	-0.42	0.30
H9	1.04	0.87	1.08
TOTAL	20.75	41.89	14.82

[1] H. Nakai, J. Chem. Phys., submitted. [2] 中井、1O12A；第 6 回理論化学討論会、大阪大学（吹田）、2002 年 5 月

第 6 回理論化学討論会,
大阪大学（大阪），2002 年 5 月.

Energy Density Analysis (EDA) による メチル基内部回転運動の解析

（早大理工） ○河村芳海、中井浩巳

【緒言】

メチル基内部回転運動は、非共有結合に関する基礎的な問題として興味深い。置換トルエン類のメチル基内部回転障壁は、励起によって大きく変化することが知られており、当研究室では、励起状態における新しい超共役相互作用の発見により、そのメカニズム解明に成功した[1-5]。しかし、エタンの基底状態における大きな回転障壁（4.67 mHartree）に対して、そのメカニズムは完全に解明されていない。本研究では、基底状態の内部回転運動について、当研究室で最近提案された Energy Density Analysis (EDA) [6,7]を用いて解析を行う。

【結果と考察】

エタン及び置換トルエン類である *o*-Fluorotoluene (*o*-FT)について EDA を適用し、メチル基回転に伴うエネルギー変化を構成原子に分割した。計算レベルは B3LYP、基底関数は cc-pVDZ である。エタンは、メチル基回転に伴う構造緩和の有無による障壁の変化は小さい （有 4.71; 無 4.92 mHartree)。構造緩和の無い場合に対して、メチル基回転に伴う原子のエネルギー密度変化を Table 1 に示す。メチル基回転に対して、相関エネルギー密度や交換エネルギー密度の変化は小さい。Staggered 構造が不安定になるのは水素同士の立体反発と予想される。しかし、EDA の結果は静電的相互作用($\Delta E_{n\text{-}e}+\Delta E_{Coul}+\Delta E_{nuc}$)によってはむしろ-6.63 mHartree 安定化した。一方で kinetic エネルギーは 13.60 mHartree と不安定化しており、水素だけでなく炭素も 4.51mHartree と大きく不安定化している。Figure 1 に *o*-FT のメチル基回転に伴うエネルギー密度変化を示す。ここでも、メチル基の面内水素とフッ素の立体反発よりも、むしろメチル基近傍の炭素のエネルギー密度変化が著しい。

Table 1. エタンのメチル基回転に伴う C, H の各エネルギー密度成分の変化 [mHartree]。それぞれ kinetic エネルギー(E_{kine})、核-電子引力エネルギー($E_{n\text{-}e}$)、クーロンエネルギー(E_{Coul})、交換エネルギー(E_{exc})、相関エネルギー(E_{corr})、核間反発エネルギー(E_{nuc})、全エネルギー(E_{total})。

atom	ΔE_{elec}					ΔE_{nuc}	ΔE_{total}
	ΔE_{kine}	$\Delta E_{n\text{-}e}$	ΔE_{Coul}	ΔE_{exc}	ΔE_{corr}		
C	4.51	-8.62	5.86	-0.55	-0.04	0.00	1.16
H	0.76	-2.43	1.20	-0.17	-0.02	1.05	0.43
Total	13.60	-31.85	18.89	-2.14	-0.22	6.32	4.92

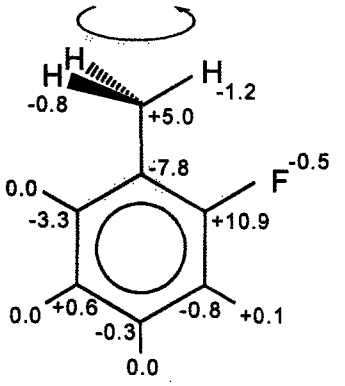

Figure 1. *o*-FT のメチル基回転に伴う各原子のエネルギー密度変化 [mHartree]

[1] H. Nakai, M. Kawai, Chem. Phys. Lett., 307 (1999) 272. [2]H. Nakai, M. Kawai, J. Chem. Phys., 113 (2000) 2168. [3]H. Nakai, Y. Kawamura, Chem. Phys. Lett., 318 (1999) 298. [4]Y. Kawamura, T. Nagasawa, H. Nakai, J. Chem. Phys., 114 (2001) 8357. [5]M. Kawai, H. Nakai, Chem. Phys., 273 (2001) 191. [6] H. Nakai, J. Chem. Phys., submitted. [7] 中井(1O12A)、第6回理論化学討論会、大阪大学、2002年5月.

第 6 回理論化学討論会,
大阪大学（大阪），2002 年 5 月.

Ab initio MD シミュレーションによる励起状態ダイナミクスの研究

（早大理工）○山内佑介、中井浩巳

ソラレン化合物は皮膚病の光化学治療に用いられ、その励起ダイナミクスについてさまざまな研究がなされてきた。図 1 は 3 種類のソラレン化合物の過渡吸収スペクトルである。ここで 8-MOP に関して三重項励起状態(T_1)に帰属されている 450nm 付近のピーク強度が他の 2 つより弱いという特徴が見られる。我々は Ab initio MD シミュレーションを用いてこれら 3 種類の化合物の励起緩和を比較検討した。図 2 は基底状態(S_0)から T_1 へ垂直励起させた後の構造緩和と、その構造における S_0 と T_1 のポテンシャルエネルギーを示している。励起にともない 8-MOP では O1-C2 結合が開裂し、S_0 と T_1 のエネルギー差が小さくなっている。

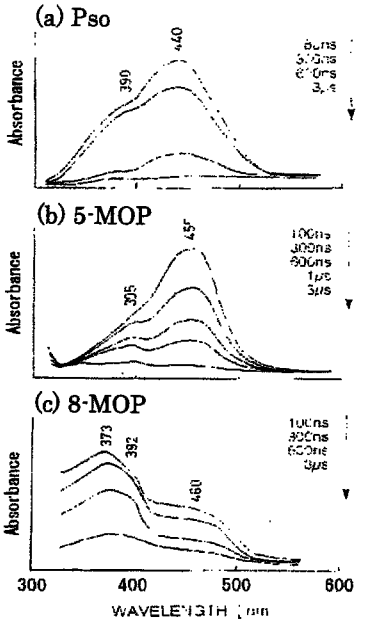

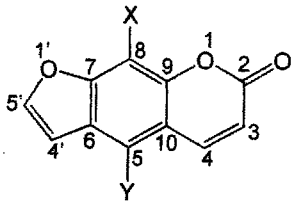

X=H, Y=H : Psoralen
X=H, Y=OCH3 : 5-MOP
X=OCH3, Y=H : 8-MOP

図 1 ソラレン化合物の過渡吸収スペクトル

*) Y.Uesugi, H.Takahashi, Symposium on "Structure, Dynamics and Control of Excited States",1995, Hawaii.

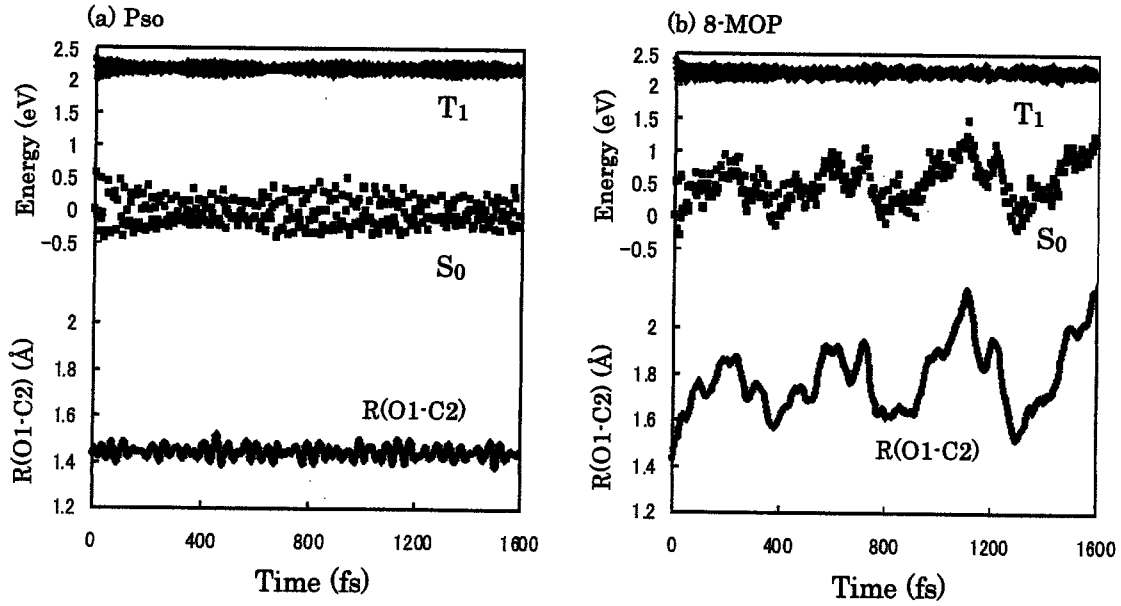

図 2　Psoralen (a)と 8-MOP (b)についての T_1 状態のポテンシャルエネルギーと O1-C2 結合距離の変化および T_1 構造に対する S_0 ポテンシャルエネルギー

第 6 回理論化学討論会,
大阪大学（大阪），2002 年 5 月.

TDDFT 計算の効率化とその応用

（早大理工）○千葉真人、中井浩巳

【序】現在、高精度な励起状態理論としてクラスター展開に基づく方法（SAC-CI, CCLR）と摂動論に基づく方法（MRMP, MRQDPT, CASPT2）が広く受け入れられている。これらの方法は 0.1eV オーダーの誤差で励起エネルギーを計算できるという特長を持つ。しかし、これらの理論は分子のサイズ（N）の増加に対して、計算時間の増加率が非常に大きいという欠点を持つ。一方、最近急速に発展してきた DFT 法を励起状態計算に拡張した TDDFT 法が注目を集めている。これは用いる行列の次元数が CIS レベルであり、N^5 で計算量が増加する。本研究では TDDFT 計算プログラムを作成して、その信頼性を確かめ、その更なる効率化について検討する。

【理論とプログラミング】本研究では、TDDFT 法の Tamm-Dancoff 近似である TDDFT/TDA 理論[1]に基づいてプログラムを作成した。TDDFT/TDA では励起エネルギー（ω）の決定式は次のように書ける。

$$AX = \omega X \tag{1}$$

ここで行列 A の要素は次のように書ける。

$$A_{ai\sigma,bj\tau} = \delta_{ij}\delta_{ab}\delta_{\sigma\tau}(\varepsilon_{a\sigma} - \varepsilon_{i\tau}) + (a_\sigma i_\sigma \mid b_\tau j_\tau) + (a_\sigma i_\sigma \mid w \mid b_\tau j_\tau) \tag{2}$$

(2)式の第三項は TDDFT 法に固有な項で、交換相関積分項である。

$$(a_\sigma i_\sigma \mid w \mid b_\tau j_\tau) = \int \phi^*_{a\sigma}(r)\phi_{i\sigma}(r)\frac{\delta^2 E_{XC}}{\delta\rho_\sigma(r)\delta\rho_\tau(r')}\phi^*_{b\tau}(r')\phi_{j\tau}(r')drdr' \tag{3}$$

この項により TDDFT 法は CIS 法と類似の手続きであるにもかかわらず、電子相関を含んだ励起エネルギーの計算ができる。今回作成したプログラムでは KS 方程式に見られる交換相関項と同様、(3)式の計算は分点を用いた数値積分により計算することにした。更に、B3LYP などの Hybrid な汎関数にも対応するように(ab|ij)型の積分も計算できるようにした。

尚、本プログラムは DFT 部分については HONDO98 を使用している。

【結果と考察】TDDFT/TDA 法の信頼性を確認するために、ベンゼンについて一重項及び三重項励起状態を計算した。用いた交換相関汎関数は SVWN である。構造は SVWN で最適化した構造、基底関数は 6-31G である。その計算値と実験値の比較を表 1 に示す。このように 6-31G レベルでも 0.3eV 程度の誤差で実験結果を再現している。

表 1. ベンゼンの励起エネルギー計算結果[eV]

State	TDDFT/TDA SVWN	Exptl. [2]
1^1B_{2u+}	5.33	4.90
1^1B_{1u-}	6.24	6.20
1^1E_{1u-}	7.20	6.95
1^3B_{1u+}	3.59	3.94
1^3E_{1u+}	4.53	4.75
1^3B_{2u-}	5.15	5.60

【References】[1] S. Hirata, M.Head-Gordon, Chem.Phys.Lett.314(1999)291, [2]B. O. Roos, K. Andersson, and M..P. Fuischer, Chem.Phys.Lett.192(1992)5

第 6 回理論化学討論会，
大阪大学（大阪），2002 年 5 月．

Energy Density Analysis (EDA) による固体表面モデルの検討

（早大理工）○菊池那明・河村芳海・中井浩巳

§ 1．緒言

固体表面の吸着や触媒反応を理論的に取り扱う場合，表面の一部を切り出すクラスターモデルがよく用いられる。しかし，クラスターモデルを用いた計算では結果がクラスターのサイズや形状に大きく依存するという問題がしばしば生じる。本研究では，当研究室で最近開発された新しい解析手法である Energy Density Analysis (EDA)[1,2] を用いてクラスターモデルの妥当性を検討する。

§ 2．方法

サイズや形状の異なる Pt クラスターモデルと，それらへの CO 吸着状態に対して DFT(B3LYP) 計算を行い，その結果を EDA によって解析した。基底関数は，Pt には Hay-Wadt の 10e-RECP に valence basis として (3s,3p,3d)/[3s,2p,2d] を，C に対して cc-pVDZ を，O に対して aug-cc-pVDZ を，それぞれ用いた。

§ 3．結果と考察

図1 は，EDAによって見積もられた各 Pt 原子のエネルギー密度を，孤立原子との差で表示したものである。これらの結果を，最近接原子数 n を横軸にとりまとめると図2 のようになり，n の増加とともにエネルギー密度が増加するという傾向が見られた。クラスターを切り出したことによる人為的な端が不安定になっているのも n との関係から理解できる。また，Pt_7 の中心原子 (n=6) が極端に安定になっていることもわかる。

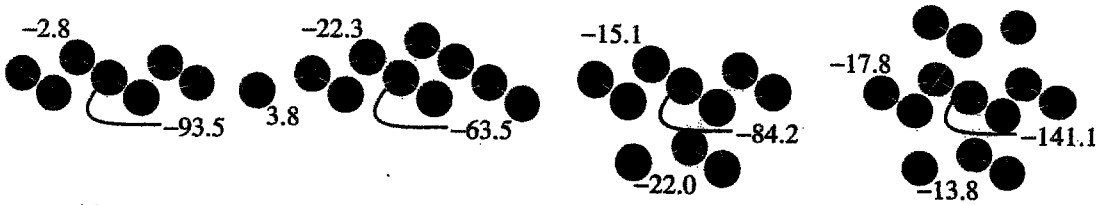

図1: Pt_n クラスターにおける Pt 原子のエネルギー密度変化 [kcal/mol]

次に CO 吸着状態に対するエネルギー密度変化を比較した（図3）。一層のみのモデルである (a) と (b) では，C, O, および中心の Pt 原子のエネルギー密度は，比較的近い値である。しかし，第 2 層も考慮した (c) では，(a), (b) と大きく異なることがわかる。このように，クラスターのサイズや形状によって，吸着点近傍の原子でさえエネルギー密度変化が大きく異なることが示された。

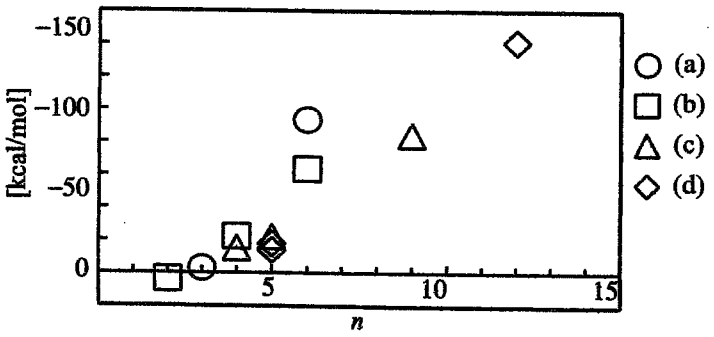

図2: エネルギー密度の隣接原子数依存性

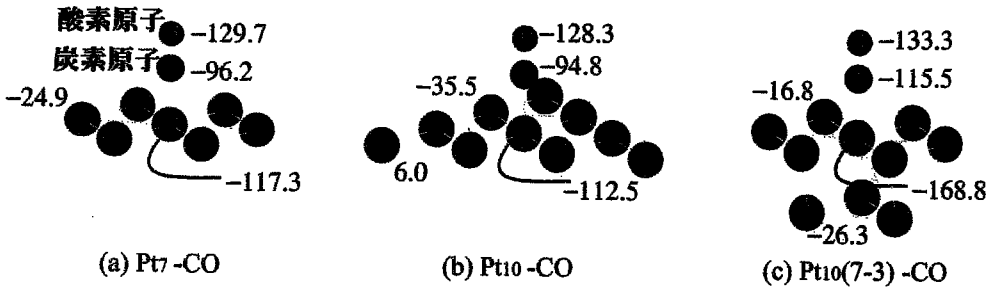

図3: Pt_n - CO 吸着状態における各原子のエネルギー密度変化

[1] H. Nakai, J. Chem. Phys., submitted.
[2] 中井, 1O12A, 第6回理論化学討論会, 大阪大学（吹田）, 2002年5月.

日本コンピュータ化学会 2002 春季年会,
北とぴあ（東京），2002 年 7 月.

1O08

エネルギー密度解析の提案とその応用

中井　浩巳
早稲田大学理工学部化学科（〒169-8555　東京都新宿区大久保 3-4-1）

【緒言】分子軌道(MO)法や密度汎関数理論(DFT)などの量子化学計算を用いた応用研究のボトルネックは、観測量を如何に高精度で再現するかというステップから、「なぜか」を導き出すステップに移行しつつある。これは、計算結果から物理・化学現象の理解を導くための解析法が欠けているためである。たとえば、固体表面や生体分子における反応やエネルギー移動を検討する場合、全系のエネルギー変化だけでは不十分で、活性部位のエネルギー変化を見積もる必要がある。そこで本研究では、全系のエネルギーを構成原子に分割するための新しい解析法(EDA; Energy Density Analysis)[1]を提案する。また、いくつかの興味ある現象に応用する。

【理論】EDA では、二つの分割スキームを提案している。

(i) 交換相関エネルギーE_{XC}の分割：原子 A の交換相関エネルギー密度を次式で計算される。

$$E_{XC}^{A} = \sum_{g}^{grid} \omega_g p_A(\mathbf{r}_g) F_{XC}(\mathbf{r}_g) \qquad (1)$$

ここで、ω_g(r)は分点の重み、p_A(r)は分割関数である。

(ii) 運動エネルギーT_S, 核引力エネルギーE_{NA}, クーロンエネルギーE_{CLB}の分割：Mulliken の電子密度解析の類推を用いる。例えば、原子 A のクーロンエネルギー密度は次式で計算される。

$$E_{CLB}^{A} = \frac{1}{2}\sum_{\mu\in A}(\mathbf{PG})_{\mu\mu} \qquad (2)$$

【結果と考察】Si(100)表面のモデルとして Si_9H_{12}, $Si_{17}H_{20}$, $Si_{21}H_{20}$ クラスターを用いて、CO 吸着過程を検討した。計算レベルは、B3LYP/cc-pVDZ である。吸着による各原子のエネルギー変化を調べるために、分離系および吸着系に EDA を適用した。図 1 は、Si_9H_{12} クラスターに対する結果で、安定化・不安定化の度合いを球の大きさで示している。これを見ると、吸着により CO が不安定化し、吸着サイトの Si 原子が安定化していることがわかる。CO の不安定化は、C□O 結合が緩んだことによる。つまり、EDA を用いると、吸着活性化の様子がエネルギー変化で解析できるわけである。表 I は、3 つのクラスターモデルに対する結果の比較で、それぞれよく似た傾向を示している。一方、表 II に Pt_n (n = 1, 7, 10)クラスターへの CO 吸着過程に対する EDA の結果を示す。ここでも CO が活性化、表面が安定化している様子が見られるが、そのエネルギー変化はクラスターサイズによって大きく異なっている。表 I,II の比較から、共有結合性結晶ではクラスターサイズに対する収束性が速いのに対して、金属結晶では収束性が遅いことがわかる。このように、EDA は結果の解析だけでなくモデリングに対しても重要な知見を与えてくれる。

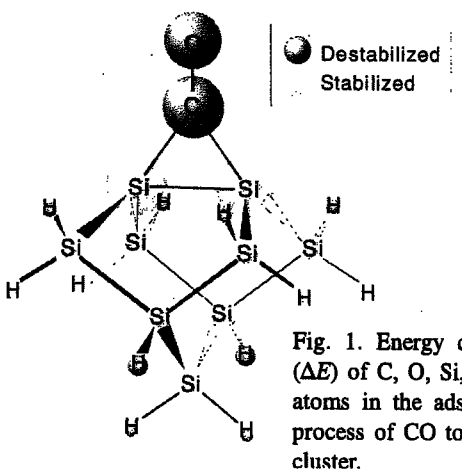

Fig. 1. Energy changes (ΔE) of C, O, Si, and H atoms in the adsorption process of CO to Si_9H_{12} cluster.

Table I. Energy changes (ΔE) of C, O, Si, and H atoms in the adsorption process of CO to Si_9H_{12}, $Si_{17}H_{20}$, and $Si_{21}H_{20}$ clusters.

Atom		Si_9H_{12}-CO		$Si_{17}H_{20}$-CO		$Si_{21}H_{20}$-CO	
		n	ΔE	n	ΔE	n	ΔE
C			35.5		35.6		37.0
O			28.3		29.3		28.0
Si	1a	2	-33.0	2	-34.7	2	-33.1
	1b	0		0		4	-0.7
	2a	4	-1.4	4	-0.6	4	-1.7
	2b	0		0		4	-0.6
	3a	2	-0.9	2	-0.8	2	-0.9
	3b	0		4	-0.4	0	
	3c	0		0		2	0.1
	4a	1	-0.3	1	0.0	1	-0.2
	4b	0		2	0.0	0	
	4c	0		0		2	0.6
	5a	0		2	0.2	0	
H	1b	4	0.3	4	0.2	0	
	1c	0		0		2	0.0
	2b	0		4	0.0	0	
	3b	4	0.0	0		4	-0.3
	3d	0		0		4	0.0
	4c	2	1.1	2	1.1	0	
	4d	0		4	-0.1	0	
	4e	0		0		2	0.0
	5a	2	0.2	0		2	0.0
	5b	0		2	0.0	0	
	5c	0		0		4	0.2
	6a	0		4	0.0	0	
Total			-6.2		-7.3		-13.6

[a] (1,2,3,...) and (a,b,c,...) indicate the layer and the site, respectively. For example, 1a indicate the nearest site from the C2 axis in the first layer.
[b] n indicates the number of equivalent atoms.

Table II. Energy changes (ΔE) of C, O, and Pt atoms in the adsorption process of CO to Pt_n (n = 1, 7, 10) clusters.

Atom		Pt-CO		Pt_7-CO		Pt_{10}-CO	
		n	ΔE	n	ΔE	n	ΔE
C			+55.3		+98.0		+48.9
O			+21.0		+33.8		+30.0
Pt	1a	1	-102.4	1	-23.8	1	-73.5
	1b	0		6	-22.1	6	-1.3
	2a	0		0		3	-1.8
Total			-26.1		-24.6		-7.8

[1] H. Nakai, Chem. Phys. Lett., submitted.

日本コンピュータ化学会2002春季年会,
北とぴあ（東京），2002年7月.

1O11 ソラレン化合物のDNA光付加反応の電子的メカニズムに関する理論的研究

○中田彩子、馬場健、高橋博彰、中井浩巳

早稲田大学理工学部化学科（〒169-8555 東京都新宿区大久保3-4-1）

【緒言】 ソラレン化合物(Fig. 1)はDNA中のチミン残基と2段階光付加反応(Fig. 2)を起こしてDNAの異常増殖を抑制する働きを持ち、乾癬や白斑などの皮膚病の治療薬として幅広く用いられている。この光付加反応の1段階目では、UV-A光(300-400nm)の照射によってソラレン化合物のフラン環、ピロン環の二つの光活性部位のどちらか一方がチミン残基と付加してモノ付加体が作られる(Step-I)。それらが更にUV-A光を吸収すると、もう一方の環が別のチミン残基と2段階目の付加反応を起こしてジ付加体を作りDNA間を架橋する(Step-II)。しかし、ジ付加体は副作用の原因となるため、2段階目の付加反応を起こさないソラレン化合物の開発が重要である。フランモノ付加体**2a**は2段階目の付加反応を起こすが、ピロンモノ付加体**2b**は起こさないことが実験によって知られている。本研究では、ソラレン化合物の単体、フランモノ付加体、ピロンモノ付加体の励起状態を比較検討し、ピロンモノ付加体が2段階目の付加反応を起こさない原因を解明する。また、特に治療に効果的とされる8-メトキシソラレン(8-MOP)と他のソラレン化合物とを比較し、8-MOPが治療に効果的な要因を探る。

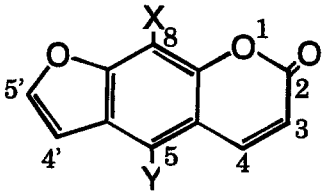

psoralen : X=H, Y=H
5-MOP : X=H, Y=OCH_3
8-MOP : X=OCH_3, Y=H

Fig. 1. ソラレン化合物

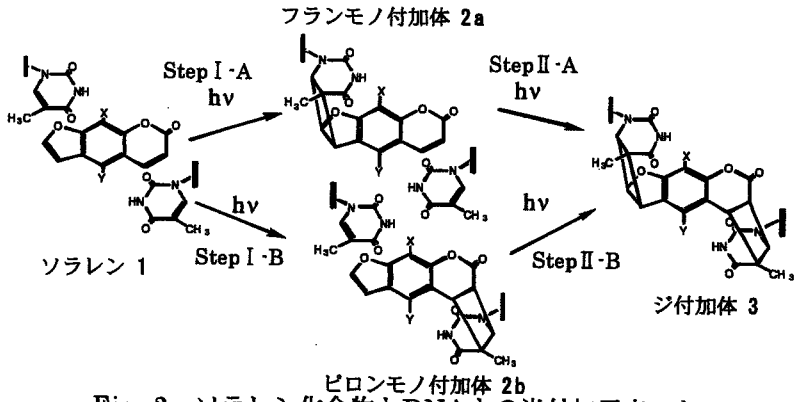

Fig. 2. ソラレン化合物とDNAとの光付加反応スキーム

【結果と考察】 各化合物の安定構造をDFT計算により求め、その構造における励起状態をTDDFT法で求めた。計算レベルはB3LYP/cc-pVDZである。TDDFT計算によって、ソラレン化合物単体でのUVスペクトルをかなり良い精度で再現し、各励起状態を帰属することができた。$S_0 \rightarrow S_1$ 励起エネルギーはソラレン化合物の単体、フランモノ付加体、ピロンモノ付加体の順で大きくブルーシフトしている(Fig. 3)。特に、ピロンモノ付加体はUV-A光の範囲では励起されないため、ピロンモノ付加体を経由してジ付加体が生成されることはないことが示された。また、T_1状態ではS_0状態の安定構造に近い閉環構造と、O_1-C_2結合が開裂した開環構造(Fig. 4)が得られ、ソラレン・5-MOPでは閉環構造が、8-MOPでは開環構造がより安定であった。フランモノ付加体においても8-MOPはT_1状態において開環安定構造をとる。これらの開環構造では2段階目の反応部位が結合交替のため単結合化しているため、2段階目の付加反応は起こらない。このことが8-MOP治療効果と密接な関係があると考えられる。

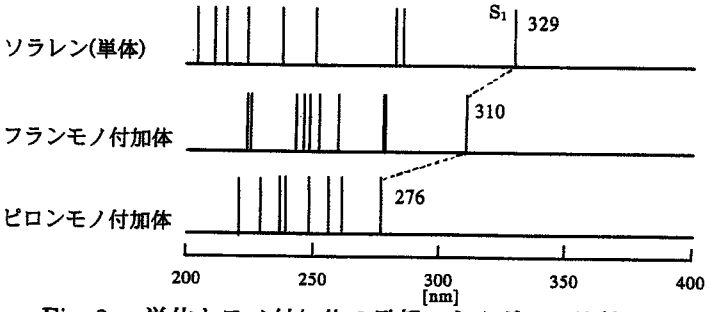

Fig. 3. 単体とモノ付加体の励起エネルギーの比較

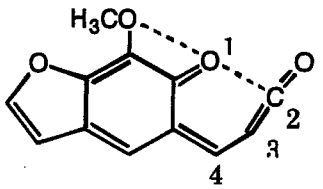

Fig. 4. 8MOPのT_1開環構造

第 29 回生体分子科学討論会,
岡崎共同研究機構・
コンファレンスセンター（愛知），2002 年 7 月.

ソラレン化合物の DNA への光付加反応における励起状態ダイナミクスの理論的研究

○中田彩子、馬場健、高橋博彰、中井浩巳（早大理工）
ayakota@asagi.waseda.jp

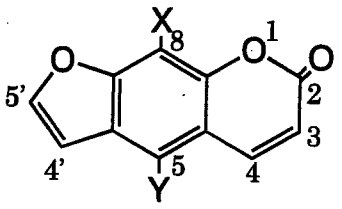

psoralen：X=H, Y=H
5-MOP：X=H, Y=OCH_3
8-MOP：X=OCH_3, Y=H

Fig. 1. ソラレン化合物

【研究背景と目的】ソラレン化合物は乾癬や白斑などの皮膚病の治療薬であり、DNA 中のチミン残基と光付加反応を起こして、DNA の異常増殖を抑制する作用を持つ。ソラレンと DNA との光付加反応は 2 段階付加反応である。1 段階目では、UV-A(300-400nm)光を照射することによって、ソラレンのフラン環、ピロン環の 2 つの光活性部位のうちどちらか一方がチミン残基に付加してモノ付加体をつくる(Step-I)。それらが更に UV-A 光を吸収すると、もう一方の環が別のチミン残基と 2 段階目の付加反応を起こしてジ付加体を作り DNA 間を架橋する(Step-II)。しかし、ジ付加体は副作用の原因となるため、2 段階目の付加反応を起こさないソラレン化合物の開発が重要である。このような背景からソラレン化合物の励起状態に対して過渡吸収スペクトルなど様々な実験的研究が行われている。その結果、特に治療に効果的である 8-メトキシソラレン(8-MOP)だけが三重項(T_1)状態での挙動が異なることが確認されている。また、フランモノ付加体 **2a** は 2 段階目の付加反応を起こすが、ピロンモノ付加体 **2b** は起こさないことも確認されている。しかし、これらの原因は明らかでなかった。本研究では、量子化学的手法を用いてソラレン化合物の励起状態を求め、8-MOP の T_1 状態における特異性の原因を探り、治療における効果との関連を調べる。また、フランモノ付加体、ピロンモノ付加体に対しても励起状態を考察し、ピロンモノ付加体が 2 段階目の付加反応を起こさない原因を解明する。

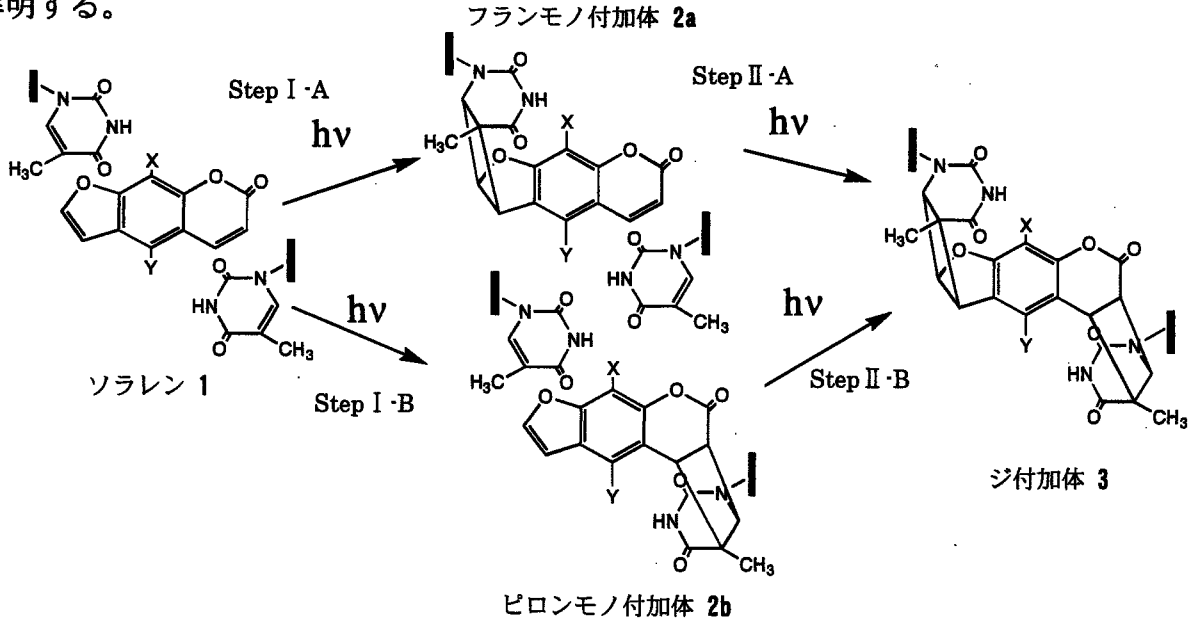

Fig. 2. ソラレン化合物と DNA との光付加反応スキーム

【計算方法】ソラレン、5-MOP、8-MOP の S_0 および T_1 安定構造を DFT 計算により求め、さらにそれらのモノ付加体、ジ付加体の安定構造を求めた。また、各化合物の単体、モノ付加体およびピロンモノ付加体の安定構造における励起状態を TDDFT 法で求め、それらの相違を検討した。すべての DFT 計算の交換相関汎関数には B3LYP、基底関数には cc-pVDZ を用いた。

【結果と考察】ソラレン、5-MOP では T_1 状態で、S_0 状態の安定構造 1 に近い閉環構造 2 と、O_1-C_2 結合が開裂した開環構造 4 が得られた(Fig. 3)。8-MOP は T_1 状態で他の化合物より開環構造(Fig. 4)が安定化しており、閉環安定構造は得られなかった。8-MOP は T_1 閉環安定構造をとらないことが Ab initio MD シミュレーションでも確認された。フランモノ付加体においても 8-MOP は T_1 状態において開環安定構造をとる。これらの開環構造では 2 段階目の反応部位が結合交替のため単結合化しているため、2 段階目の付加反応は起こらない。そのため 8-MOP からは副作用の原因となるジ付加体が生成されず、治療に効果的であることがわかった。

一重項励起状態に関して、ソラレン化合物単体での UV スペクトルをかなり良い精度で再現し、各励起状態を帰属することができた。実験では観測されていない 5-MOP の S_1 状態も求めることができた。モノ付加体では、4',5'位か 3,4 位の活性部位がなくなるため、励起配置や励起エネルギーが二つのモノ付加体で大きく異なる。単体と付加体の励起エネルギーを比較すると、$S_0 \rightarrow S_1$ 励起エネルギーはソラレン化合物の単体、フランモノ付加体、ピロンモノ付加体の順で大きくブルーシフトしている(Fig. 5)。特に、ピロンモノ付加体は UV-A 光の範囲では励起されないため、ピロンモノ付加体を経由してジ付加体が生成されることはないことが示された。

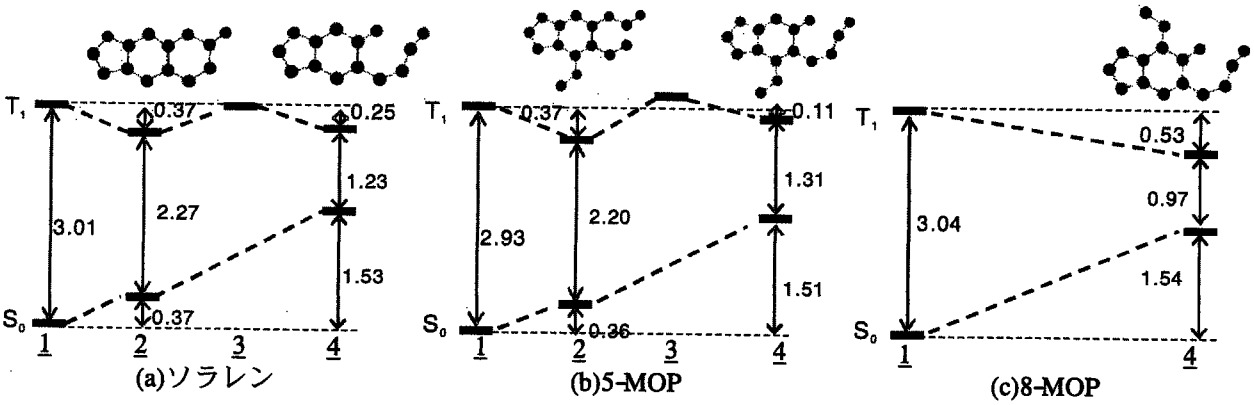

Fig. 3. 構造緩和に対するエネルギー変化[eV]

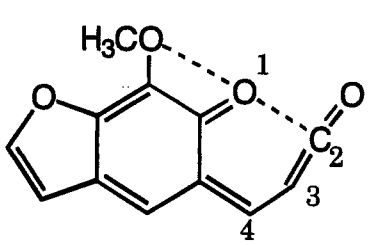

Fig. 4. 8-MOP の T_1 開環構造

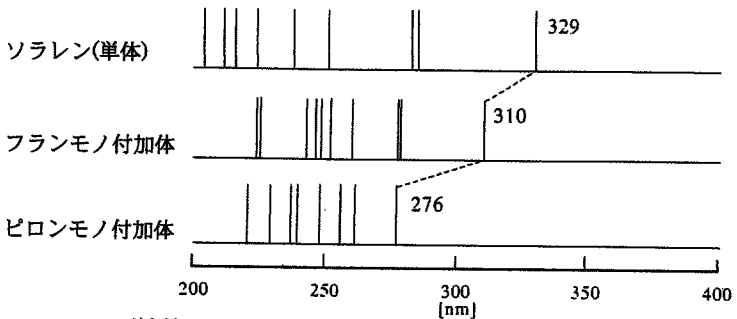

Fig. 5. 単体とモノ付加体の励起エネルギーの比較

東京工芸大学（厚木），2002年9月.

無電解析出反応における析出金属の触媒活性に関する理論計算とエネルギー密度解析(EDA)

（早大理工）○島田拓哉，阪田薫穂，中井浩巳，本間敬之，逢坂哲彌

Theoretical study and Energy Density Analysis (EDA) of metal catalytic activity for electroless deposition processes

T. Shimada, K. Sakata, H. Nakai, T. Homma, T. Osaka (Waseda Univ.)

1.目的

無電解析出プロセスはエレクトロニクス分野等において広く用いられているが，その反応機構は金属イオンの還元析出と還元剤の酸化反応が同時に進行し，更に析出した金属表面が還元剤の酸化反応に対して触媒活性を持つという複雑な反応である．今後より精密な析出挙動の制御が求められており，反応機構の詳細な解析が必要になると考えられる．そこで我々は理論計算を用いて，無電解析出反応の解析を試みている．この方法は反応中間体の分子の最適構造，電荷そしてエネルギーを算出することができ，従来の解析方法にはない利点を多く有している．またエネルギー密度解析(EDA)[1]という解析法は系全体のエネルギーを原子ごとに分割する事で，原子単位での解析が可能である．そこで本検討においてはこれらの方法を用いて無電解析出の反応機構を分子・原子レベルから検討を行った．

2. 方法

本検討では代表的還元剤であるジメチルアミンボラン(DMAB)[2]，次亜リン酸[3]，ホルムアルデヒドの酸化反応に着目し，孤立系並びに金属(Cu，Pd)表面上におけるこれら還元剤の反応機構を検討した．

計算にはGaussian98を用い，EDAにはオリジナルのプログラムを組み込んで改良したHONDO99を用いた．分子の構造最適化並びにエネルギー計算には密度汎関数法(DFT)を用いた．パラメータにはB3LYPを用いた．金属表面はCu, Pdの(1 1 1)面，構成原子を4つとする金属クラスターモデルを用いた．基底関数としてB,C,P,Hには6-31G**, N,Oには分散関数を組み込んだ6-31+G**，金属にはHay & Wadt ECPを用いた．

3. 結果

還元剤の各状態における最適構造・エネルギーを計算し，ダイアグラムを作成した．図1にCu上におけるホルムアルデヒドの分子構造とダイアグラムを示す．横軸は反応座標1：$CH_2O(OH)^-$，2：$CH_2O(OH)_2^{2-}$，3：$CH_2O(OH)_2^-$，4：$CHO(OH)_2^-$，縦軸は孤立系のエネルギーを0とした相対エネルギーである．その結果どの金属上においても全ての還元剤は系全体(—■—)の方が孤立系(—◆—)よりもエネルギーが安定し，還元剤は金属に吸着した状態で反応が進行することが示唆された．

更にEDAを用いて図1の反応座標1における原子ごとの安定化エネルギーを計算した結果を図2に示す．●が大きい程安定化，○が大きい程不安定化を表している．図2より金属表面が大きく安定化し，逆に吸着分子は孤立系よりも大きく不安定化していることがわかった．

更に図2より吸着サイトの原子(O, Cu)の安定化・不安定化が最も大きく，また電荷移動も大きいことから，これら吸着サイトの原子間での相互作用が系全体の安定化並びに反応機構に大きな影響を及ぼす事が示唆された．

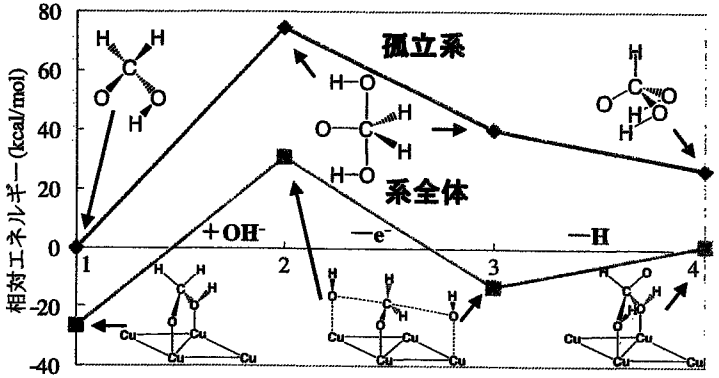

図1　Cu上でのホルムアルデヒドの酸化反応エネルギーダイアグラム

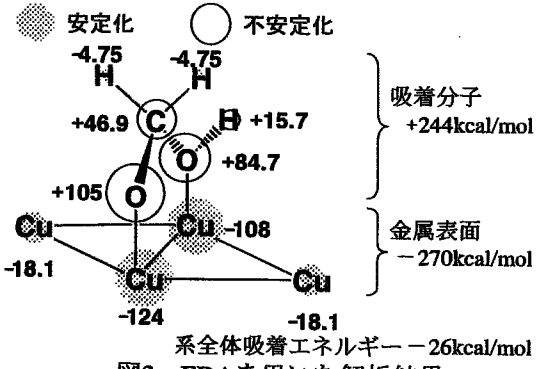

図2　EDAを用いた解析結果

参考文献

[1] H. Nakai, *Chem. Phys. Lett.*, *in press* (2002)
[2] T. Homma, H. Nakai, M. Onishi, T. Osaka, *J. Phys. Chem.*, B **103**, 1774 (1999)
[3] H. Nakai, T. Homma, I. Komatsu, T. Osaka, *J. Phys. Chem.*, B **105**, 1701 (2001)

分子構造総合討論会 2002,
神戸国際会議場（兵庫），2002 年 10 月.

4P011

アンチモン(V)ポルフィリン錯体の励起状態と光化学反応に関する理論的研究

（早大理工）○馬場 健，副田 隆介，中井 浩巳

【緒言】ポルフィリン環にP, BiやSbなど15族典型元素が導入された錯体は軸配位子と3中心結合を作り，超原子価化合物となる。図1に示すようなメチル基とメトキシ基が配位したアンチモン(V)ポルフィリン錯体では，光照射によりSb-O結合が特異的に解離を起こすことが報告されている[1]。本研究ではこのアンチモン(V)ポルフィリン錯体の基底状態および励起状態における電子構造を量子化学計算により求め，光化学反応のメカニズムを理論的に検討した。

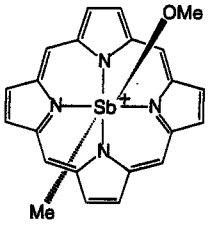

図1 $[Sb(FBP)(Me,OMe)]^+$

【結果と考察】 まず $[Sb(FBP)(Me,OMe)]^+$ (FBP: Free Base Porphin)について構造最適化をB3LYPレベルで行った。つぎにこの構造をもとにTDDFT(B3LYP)計算により一重項励起状態への励起エネルギーを計算した。基底関数は全ての計算で，SbにはLanL2DZdpを，H,C,N,OにはCC-pVDZを用いた。最適化された構造(図2)はポルフィリン環がほぼ平面を維持し，Sbもポルフィリン環からほとんどずれない。この錯体の(π-π*)励起($1^1A'$, $1^1A''$, $3^1A'$, $3^1A''$)は，ポルフィリン(FBP)のQ,Bバンドとよく一致する(表1)。さらに$[Sb(FBP)(Me,OMe)]^+$では，FBPとは異なる励起状態が存在する。それはメトキシ基のn軌道からポルフィリン環のπ*軌道への励起($2^1A'$, $2^1A''$)と，σ軌道(Sbのs軌道とメトキシ基Oのp軌道)とπ軌道(ポルフィリン環)が混ざった軌道からポルフィリン環のπ*軌道への励起($4^1A'$, $4^1A''$)である。これらの励起状態はほとんど強度を持たず，ポルフィリンのBバンドに対応する励起($3^1A'$, $3^1A''$)が大きい強度をもつ。

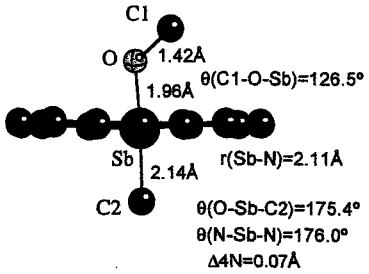

図2 $[Sb(FBP)(Me,OMe)]^+$ の最適化構造

表1 FBPおよび$[Sb(FBP)(Me,OMe)]^+$の励起状態

FBP				[Sb(V)FBP(Me,OMe)]$^+$			
	Exc. En.	Osc. Str.			Exc. En.	Osc. Str.	Main configuration
$1\,^1B_{3u}$	2.264	0.0000	π–π*(Q)	$1\,^1A'$	2.336	0.0001	Por(π)–Por(π*)(Q)
$1\,^1B_{2u}$	2.420	0.0000	π–π*(Q)	$1\,^1A''$	2.337	0.0000	Por(π)–Por(π*)(Q)
$2\,^1B_{3u}$	3.306	0.4275	π–π*(B)	$2\,^1A''$	3.107	0.0042	OMe(n)–Por(π*)
$2\,^1B_{2u}$	3.477	0.6362	π–π*(B)	$2\,^1A'$	3.158	0.0041	OMe(n)–Por(π*)
$3\,^1B_{2u}$	3.736	0.5077	π–π*	$3\,^1A'$	3.335	0.5467	Por(π)–Por(π*)(B)
$3\,^1B_{3u}$	3.836	0.7750	π–π*	$3\,^1A''$	3.337	0.5539	Por(π)–Por(π*)(B)
				$4\,^1A''$	3.643	0.0029	Sb-O(σ),Por(π)-Por(π*)
				$4\,^1A'$	3.654	0.0049	Sb-O(σ),Por(π)-Por(π*)
				$5\,^1A''$	3.776	0.0873	Por(π)–Por(π*)
				$5\,^1A'$	3.786	0.1453	Por(π)–Por(π*)

Exc. En.: Excitation energy [eV]. Osc. Str.: Oscillator strength

さらに，メチル基およびメトキシ基をそれぞれ最適化構造から軸方向へ離していったときの励起状態の変化を図3に示す。メチル基，メトキシ基を離していくにつれ，Q,Bバンドにあたる(π-π*)励起は高エネルギー側へシフトする。メトキシ基を離していくと，$4^1A'$, $4^1A''$(σ(Sb-O)-π*)励起状態がすぐに$3^1A'$, $3^1A''$(π-π*;Bバンド)励起状態と交差する。一方，メチル基の解離ではこれら励起状態は交差しない。この置換基の距離に依存した励起状態の挙動は，実験におけるメトキシ基の特異な光解離に対応する。

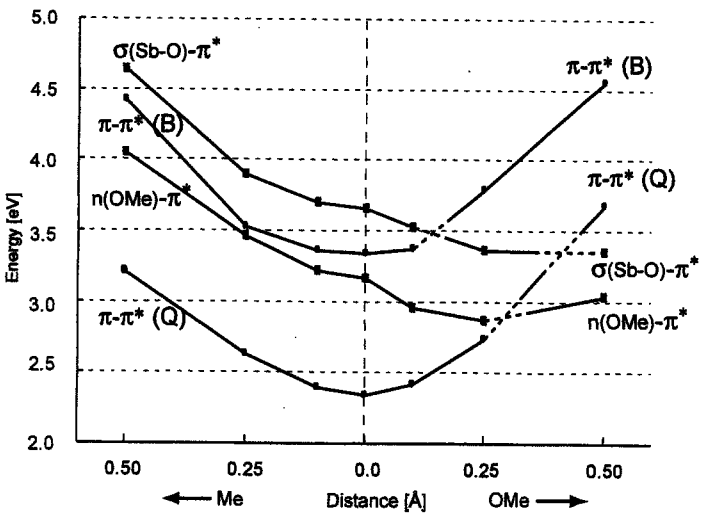

図3 置換基の解離距離による一重項励起状態の変化

[1] K.-y. Akiba, G. Mori, private communication.

1C14 Energy Density Analysis (EDA)の QM/MM 法への拡張とその応用

(早大理工) ○河村芳海、中井浩巳

【序】近年、量子化学計算はその理論の発展と共に物理・化学現象の解釈やそのメカニズム解明に広く用いられるようになった。金属酸化物結晶や生体分子などナノサイズの系に対しては、計算機資源の制約から、すべて量子論で取り扱うのではなく活性点のみ量子力学的(QM)に取り扱い、周りの場は分子力学的(MM)に取り扱う QM/MM 法が多く用いられている。しかし QM/MM 法を用いる際には、QM と MM の境界をどこに設けるか、そして MM の場の強さをどのように設定するか、という問題があり、この決定の多くは経験に基づいて行われている。当研究室では最近、量子化学計算から得られる全エネルギーを構成原子に分割する Energy Density Analysis (EDA)という新しい解析方法を提案し[1]、種々の系に対して適用することでその有用性を示してきた[2,3]。本研究では、EDA を QM/MM 法に対して拡張し、QM/MM 法による取り扱いの妥当性を検討した。特に、金属酸化物結晶に対する QM/MM 法である Madelung Potential (MP) model に対して EDA を適用し、その評価を行った。

【結果と考察】MP model を用いた MgO 結晶の計算に対して EDA を適用し、QM 部分、MM 部分のサイズに対する凝集エネルギーの収束性を調べた。QM 部分の計算方法は B3LYP、基底関数は cc-pVDZ を用いた。Table 1 に、MM 場のサイズを変えた場合の全エネルギーの変化を示す。QM 部分は Mg_4O_4 cluster、MP の強さは$|q|$=2.0 とした。MM 場のサイズを大きくするにしたがって、全系のエネルギーは大きく減少する。一方、EDA を用いると、QM 部分だけのエネルギーを定義することができ、これによって MM 場のサイズに対する収束性を評価することができる。Table 1 から、MP を回りに 12 層置くことによって QM 部分のエネルギーが 0.1 mHartree のオーダーで収束していることがわかる。次に、MP の電荷を変化させ、MM 場の強さに対する QM 部分の収束性を検討した。QM 部分の表現の妥当性は、結晶状態から原子に分解するのに要するエネルギーである凝集エネルギーの実験値と比較することにより評価した。Fig. 1 に MP の電荷を変化させたときの凝集エネルギーの変化を示す。$|q|$=1.4 の時、凝集エネルギーは実験値と一致し、この QM サイズに対して適切な MM 場の強さと考えられる。しかし、QM 部分を $Mg_{16}O_{16}$ cluster に大きくすると、QM 部分内のサイトに依存して凝集エネルギーが変化する (Fig. 2)。これらの凝集エネルギーはサイトによらず一定になるのが妥当なモデルと考えられるが、これは QM 部分を大きくしても一致せず、MP model による取り扱いの限界を示している。

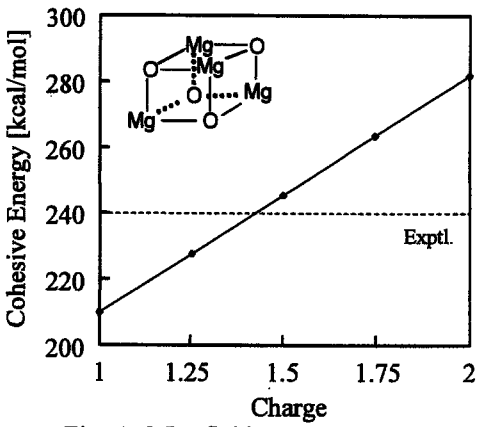

Fig. 1. MM field strength dependence for cohesive energy in Mg_4O_4 cluster.

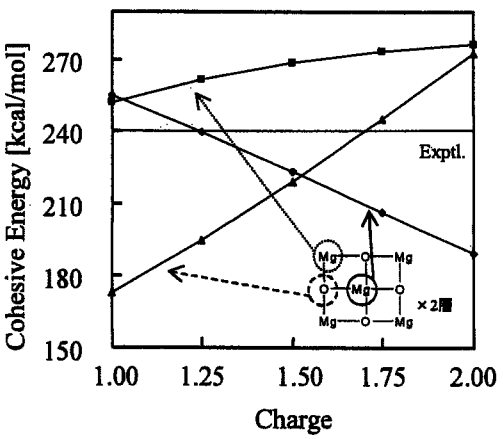

Fig. 2. MM field strength dependence for cohesive energy in Mg_9O_9 cluster.

[1] H. Nakai, Chem. Phys. Lett., *in press*. (2002).

[2] H. Nakai, K. Sodeyama., J. Mol. Struct.: THEOCHEM, *submitted*; Chem. Phys. Lett., *submitted*.

[3] 馬場・中井(P1), 河村・中井(P2), 菊池・河東田・河村・中井(P3), 袖山・星野・中井(P4), 中井(1O12A), 第 6 回理論化学討論会(大阪), 2002.

Table 1. Total energies of QM/MM system and QM part. [in Hartree]

Model	Number of MP	QM/MM system	QM part
#0	0 (no MP)	-1101.596657	-1101.596657
#1	56 (4×4×4)	-1148.033554	-1102.488647
#2	208 (6×6×6)	-1277.331583	-1102.473272
#3	504 (8×8×8)	-1531.559887	-1102.475605
#4	992 (10×10×10)	-1952.865636	-1102.474847
#5	1720 (12×12×12)	-2583.412492	-1102.475174
#6	2736 (14×14×14)	-3436.310418	-1102.475136
#7	4088 (16×16×16)	-4640.878186	-1102.475101

2P114　Energy Density Analysis (EDA)による固体表面反応の解析

（早大理工）　○河東田 道夫，中井 浩巳

【序】 固体表面反応を理論的に取り扱う際には、固体表面と吸着分子間の相互作用が局所的であるとの予想に基づき、クラスターモデルがよく用いられる。また、固体表面の周期性に着目し、電子状態に周期境界条件を課した周期モデルを用いる場合もある。いずれのモデルでも得られる結果は用いるクラスターサイズあるいはユニットセルサイズに依存する。しかしながら、多くの応用研究では、これらのサイズはモデルの妥当性という観点からではなく、計算資源の制約から決定されることがほとんどである。最近、当研究室では量子化学計算により得られた系全体のエネルギーを構成原子に分割する新しい解析手法、Energy Density Analysis (EDA)を提案した[1]。本研究ではEDAを固体表面反応に適用して、クラスターモデルおよび周期モデルによる取扱いの妥当性を検討した。

【クラスターモデルに対するEDA】

本研究では、Si (100)表面へのアセチレン、エチレン、CO 分子の吸着過程を取扱った。用いたクラスターモデルは Si_9H_{12} クラスター、計算レベルはB3LYP/cc-pVDZ である。Fig. 1 にアセチレンの吸着過程におけるエネルギー密度曲線を示す。アセチレンの吸着過程に対するエネルギー変化は、吸着に直接関与する表面 Si 原子の安定化とアセチレンの炭素原子の不安定化 (活性化)によって支配されている。また、炭素原子のエネルギー密度の上昇とH-C-C結合角の変化に良い相関があることも示された。エチレンやCO 分子の吸着においても、吸着サイトの表面Si原子の安定化および吸着子の不安定化という類似の挙動が得られた。特にCO 分子の吸着では先に炭素原子の不安定化が起こり、後から酸素原子の不安定化が起こるという興味深い結果も得られた。

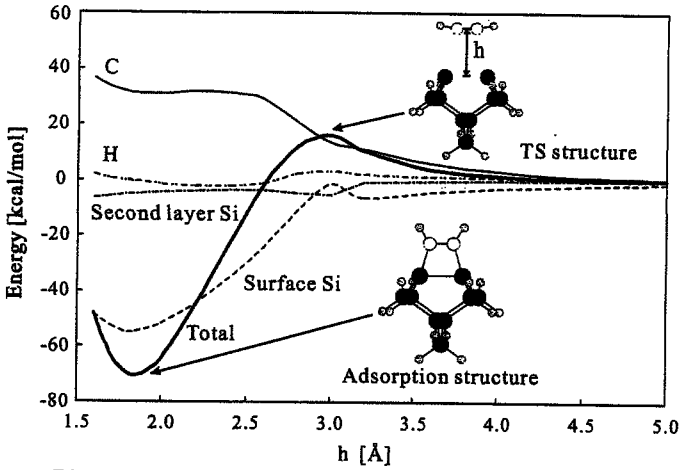

Figure 1. Energy density curves of C, H, surface Si and second layer Si in acetylene adsorption process.

【周期モデルに対するEDA】

先に提案されたEDA は孤立系に対する定式化であるので、本研究ではまずEDA の周期系への拡張を試みた。周期系でのKohn-Sham (KS) 軌道を基底関数展開すると、密度行列はユニットセルの並進ベクトル $\mathbf{g}$ の index を持ち、さらに波数ベクトル $\mathbf{k}$ に対する積分で表される次式の形となる。

$$P_{\mu\nu}(\mathbf{g}) = \int_{\mathrm{BZ}} d\mathbf{k} \exp(i\mathbf{kg}) \sum_{i}^{\mathrm{Norbital}} C^{*}_{\mu i}(\mathbf{k}) C_{\nu i}(\mathbf{k}) \theta[\varepsilon_F - \varepsilon_i(\mathbf{k})] \qquad (1)$$

ここでε_F はFermi level、θはKS 軌道の占有・非占有を区別するためのステップ関数である。この密度行列の表式より、KS 軌道を用いた解析積分により計算されるエネルギーは孤立系の場合と同様に分割できる。例えば、運動エネルギーT_sの分割は単位セルの並進ベクトル $\mathbf{g}$ の和を取り、

$$T_s^A = \sum_{\mathbf{g}} \sum_{\mu \in A} \sum_{\nu} P_{\mu\nu}(\mathbf{g}) \langle \chi_\mu(\mathbf{r}) | \hat{t} | \chi_\nu(\mathbf{r}-\mathbf{g}) \rangle = \sum_{\mathbf{g}} \sum_{\mu \in A} \sum_{\nu} P_{\mu\nu}(\mathbf{g}) T_{\mu\nu}(\mathbf{g}) \quad (2)$$

と表される。単位セルの並進ベクトル $\mathbf{g}$ の和を取らなければ、各ユニットセル間の運動エネルギーにも分割される。また、電子密度も(1) 式の密度行列を用いると、次式で表される。

$$\rho(\mathbf{r}) = \sum_{\mathbf{g}} \sum_{\mu\nu} P_{\mu\nu}(\mathbf{g}) \chi^{*}_{\mu}(\mathbf{r}) \chi_\nu(\mathbf{r}-\mathbf{g}) \qquad (3)$$

いったん電子密度が求まると、交換-相関エネルギーは分点を用いた求積法で計算されるので、各原子への分割は孤立系の場合と同様に分割される。以上により、周期系における全エネルギーの分割が達成される。

[1] H. Nakai, Chem. Phys. Lett., *in press* (2002).

分子構造総合討論会 2002,
神戸国際会議場（兵庫），2002 年 10 月.

4P130　FEM(有限要素法)基底による原子核波動関数の数値的解法の開発

（早大理工[a]，豊田中研[b]）　○星野　稔[a]，兵頭　志明[b]，中井　浩巳[a]

【序】

有限要素法(FEM)は、偏微分方程式の数値解法の一つで、主に構造力学や流体力学などマクロな系に対して適用されてきたが、ミクロな現象、つまり Schrödinger 方程式に対する応用は限定されたものであった[1-3]。我々はこれまで Gauss 基底を用いた原子核波動関数の取り扱いを提案してきた[4-6]。振動に対する基底としては Gauss 基底は良い振る舞いをするが、回転に対しては良くないことが示された。そこで本研究では、FEM 基底を用いて原子核波動関数を数値的に求めることを試みた。回転のみを扱う場合と回転と振動を同時に扱う場合について検討した。

【回転運動に対する波動関数】

まず分子を剛体であると仮定し、回転運動のみを取り扱った。剛体回転子に対する Schrödinger 方程式は厳密解が存在するので、FEM による取り扱いに対して信頼性を検討した。本研究では、回転角θとϕを変数分離し、与えられた量子数 m に対する波動関数$\Theta(\theta)$を求めた。FEM では各要素内のみで非零となる関数を基底として用いる。ここでは 1～4 次 Lagrange 補間関数を用いて検討した。FEM で扱う行列の次元数 N_{dim} は補間関数の次数 N_{order} と要素数 $N_{element}$ の積、$N_{dim} \approx N_{order} \times N_{element}$ である。また基底関数の直交性が良いため、行列の非零率は低く $N_{nonzero} \approx N_{dim} \times (2N_{order} + 1)$で見積もられる。Table 1 に次元数($N_{dim}$)を変化させて得られたエネルギー固有値を示す。1 次 Lagrange 補間関数に対しては $l = 0$～10 の結果を、2～4 次の補間関数に対しては $l = 10$ の結果のみを示す。量子数 $l \leq 1$ では、正確な波動関数が変数($t = \cos\theta$)の 1 次関数となるので N_{dim} に依存せず、常に厳密解と一致していることがわかる。$l \geq 2$ に対して l の増加とともに厳密解とのずれが大きくなること、次元数(N_{dim})の増加とともにそのずれが改善されることなどがわかる。更に、補間関数の次数(N_{order})を上げることで急激に厳密解に近づくことも示された。

Table 1. Energy eigen values of the rotational motion calculated by the FEM

			E_l (FEM)					
N_{order}	l	E_l (exact)	$N_{dim} = 5$	10	50	100	500	1000
	0	0	0.000000	0.000000	0.000000	0.000000	0.000000	0.000000
	1	2	2.000000	2.000000	2.000000	2.000000	2.000000	2.000000
	2	6	6.583592	6.120689	6.004159	6.001020	6.000040	6.000010
	3	12	15.714286	12.805333	12.028969	12.007128	12.000281	12.000070
	4	20	33.416408	22.886039	20.110569	20.027400	20.001084	20.000271
1st	5	30	-	37.574143	30.309720	30.077658	30.003090	30.000771
	6	42	-	58.670776	42.713003	42.181773	42.007299	42.001823
	7	56	-	89.144882	57.430030	56.372314	56.015145	56.003785
	8	72	-	133.734260	74.588176	72.690409	72.028567	72.007146
	9	90	-	198.905831	94.327286	91.184874	90.050075	90.012544
	10	110	-	-	116.796401	111.910824	110.082810	110.020781
2nd	10	110	-	-	111.024913	110.091202	110.000179	110.000011
3rd	10	110	-	-	110.122959	110.003283	110.000000	110.000000
4th	10	110	-	-	110.008584	110.000063	110.000000	110.000000

【回転および振動に対する波動関数】

次に回転と振動のカップルする例として、バネで結ばれた 2 原子分子の運動を取り扱う。この場合、変数は原子間距離 r と回転角θ, ϕの 3 変数となる。波動関数$\Psi(r, \theta, \phi)$は、(1)式の汎関数に変分法を適用することで得られる。

$$J[\Psi] = \iiint \left\{ -\frac{\hbar^2}{2\mu}\left[\frac{1}{2}r^2\left(\frac{\partial\Psi}{\partial r}\right)^2 + \frac{1}{2}\left(1-\cos^2\theta\left(\frac{\partial\Psi}{\partial\cos\theta}\right)^2 + \frac{1}{2}\cdot\frac{1}{1-\cos^2\theta}\left(\frac{\partial\Psi}{\partial\phi}\right)^2\right] + \frac{1}{2}r^2\left(E - \frac{1}{2}\kappa(r-r_0)^2\right)\Psi^2\right\} dr d\cos\theta d\phi \qquad (1)$$

ここで、μは換算質量、κは力の定数、r_0は平衡核間距離、E はエネルギー固有値である。FEM 基底として Lagrange 補間関数を用いる。今後、μ, κ, r_0 を変化させて回転・振動そして両者のカップリングに与える影響を数値的に検討する。

[1] L. R. Ram-Mohan, D. Dossa, J. Shertzer, Comput. Phys., (1990) 50. [2] N. Sato, S. Iwata, J. Chem. Phys., 89 (1988) 2932.

[3] S. R. White, J. W. Wilkins, Phys. Rev., B39 (1989) 5819. [4] M, Tachikawa, K. Mori, H. Nakai, K. Iguchi, Chem. Phys. Lett., 290 (1998) 437. [5] H. Nakai, Int. J. Quantum Chem., 86 (2002) 511. [6] H. Nakai, K Sodeyama, M Hoshino, Chem. Phys. Lett., 345 (2001) 118.

分子構造総合討論会 2002,
神戸国際会議場（兵庫），2002 年 10 月.

4P048　Ab initio MDシミュレーションによる銅クラスターイオンの衝突反応の研究

（早大理工）　○渥美 照夫，河村 芳海，山内 佑介，中井 浩巳

【序】銅はメタノールの合成触媒として工業的に広く用いられており、その触媒メカニズムについても表面科学や理論化学の手法により数多く研究されてきた。最近、豊田工大の近藤教授のグループでは、サイズ選別された銅クラスターイオンとメタノールの衝突実験を行い、サイズにより特異的な反応が起こることを報告している。

$Cu_n^+ + CH_3OH \rightarrow Cu_n^+(CH_3OH)$　(1)　化学吸着
$Cu_n^+ + CH_3OH \rightarrow Cu_{n-1}^+(H_2O) + CuCH_2$　(2)　$CuCH_2$ 生成と水の吸着
$Cu_n^+ + CH_3OH \rightarrow Cu_{n-1}^+(CH_3OH) + Cu$　(3)　銅原子の脱離とメタノールの吸着

(1)は $n \geq 4$ で観測され、サイズの増加とともに反応断面積が減少する。(2)は $n = 4, 5$ でのみ観測される。(3)は $n = 2$ で観測される。$n = 3$ ではいずれの反応断面積も非常に小さい。本研究では、DFT 法および ab initio MD (AIMD)シミュレーションによりこの衝突反応を取り扱い、反応のメカニズムとダイナミクスを明らかにすることを目指した。

【DFT 計算による反応メカニズムの検討】
本研究では、まず DFT (B3LYP)計算により、Cu_n^+($n = 2$ - 4)とメタノールの衝突反応(1)-(3)に対する反応物、生成物、そして中間体の構造、エネルギー、電子状態を調べた。用いた基底関数は、Cu が Huzinaga [5s4p2d]、H, C, O が cc-pVDZ である。Fig. 1 に、この衝突反応のエネルギーダイアグラムと対応する構造を示す。吸着エネルギーは $n = 2, 4$ においてそれぞれ 82, 71 kcal/mol であるのに対して、$n = 3$ では 37 kcal/mol と小さく、反応が起こりにくいという実験結果を支持している。また $n = 3$ では、(2)及び(3)の反応が吸熱的であることも実験結果に対応している。いずれのクラスターについても、(2)の反応に比べて(3)の方がエネルギー的に有利であることもわかる。ただ、$n = 3$ 及び 4 では、(2)の生成物の中間体と考えられるメタノールが解離吸着する構造 (Fig. 1(e), (f))が得られた。特に、$n = 4$ ではこの中間体における Cu_4^+ クラスターの構造は平面ではなく四面体であることは興味深い。

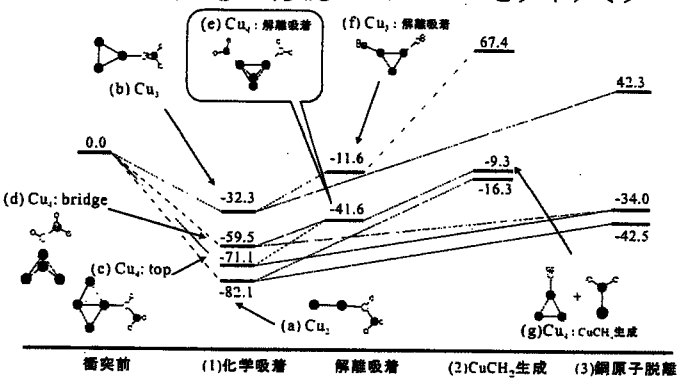

Figure 1. 銅クラスターイオンとメタノール衝突反応のエネルギーダイアグラム[kcal/mol]

【AIMD シミュレーションによる反応ダイナミクスの検討】
衝突反応のダイナミクスを調べるために AIMD シミュレーションを行った。ここでは、熱力学的には不利な(2)の反応が観測されている $n = 4$ について調べた。衝突前に、Cu_4^+ クラスターとメタノールのそれぞれに、零点エネルギーの 1.5 倍のエネルギーを与えて平衡化させたのち、Cu_4^+ クラスターに衝突エネルギー E_c = 0.2, 1.0 eV を与えて衝突させた時のトラジェクトリを Fig. 2 に示す。C - O 間距離は、どちらの場合でも振幅が 0.5 Å 程度の振動をしておりメタノールの解離は見られなかった。Cu_4^+ クラスターとメタノールの衝突は、100 fs に一回程度の割合で起こっている。一方、非常にゆっくりした周期(≥ 500 fs)で Cu_4^+ クラスターは平面構造と四面体構造の間を変化している。平面構造は(Fig. 1(c))の吸着構造に、四面体構造は(Fig. 1(d))の吸着構造に近いことが確かめられ、メタノールの配向による Cu_4^+ クラスターの構造変化が確認された。

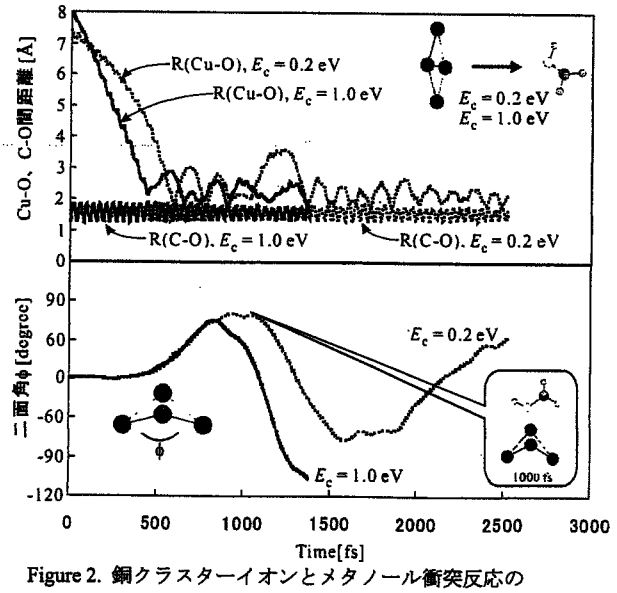

Figure 2. 銅クラスターイオンとメタノール衝突反応の AIMD シミュレーションのトラジェクトリ (E_c=0.2, 1.0 eV)

（社）表面技術協会第 107 回講演大会，
工学院大学（東京），2003 年 3 月．

無電解銅めっきにおける還元剤としてのアルデヒド類の反応機構に関する理論計算解析

（早大理工）○阪田薫穂，島田拓哉，中井浩巳，本間敬之，逢坂哲彌

キーワード｛無電解めっき，還元剤，アセトアルデヒド，グリオキシル酸，DFT｝

1. 緒言　無電解めっき反応は種々の電荷移動が伴い非常に複雑であり，そのメカニズムの詳細は未だに不明点が多い．このため，これまでに反応機構について電気化学的手法を用いた研究が数多くなされてきたが，更なる詳細な解明のために我々は理論・計算化学を用いた解析を進めている [1]．本検討では，回路実装分野などに広く用いられている無電解銅めっきプロセスに着目し，その代表的な還元剤であるホルムアルデヒド，および官能基をメチル基にかえたアセトアルデヒド，またカルボキシル基にかえたグリオキシル酸に焦点をあてた．これらの還元剤について孤立系並びに銅上における酸化反応機構を比較することで，アルデヒドの官能基の差異が反応機構に与える影響を検討した．

2. 検討方法　アセトアルデヒド及びグリオキシル酸の酸化反応機構における最安定の経路を求めるため，孤立系および銅上でのエネルギーダイアグラムを作成し，各還元剤でエネルギー・電荷等の比較検討を行った．全ての計算は代表的なパッケージである Gaussian98 を用い，計算方法は密度汎関数法（DFT 法）を用いた．汎関数は B3LYP を用いた．金属表面は Cu(111)面を表したサイズ 4 のクラスターを用い，吸着構造の構造最適化を行った後，サイズ 22 で一点計算を行った．基底関数は C,H には cc-pVDZ，O には分散関数を組み込んだ aug-cc-pVDZ，Cu には Hay&Wadt ECP を用いた．

3. 結果及び考察　これまでの検討でホルムアルデヒドは銅上で水酸基の配位の後，5 配位状態を経由し水素の脱離が起こるという 5 配位経路を取ることが示唆されている．本検討ではアセトアルデヒドおよびグリオキシル酸に関して孤立系及び金属上での酸化反応のエネルギーダイアグラムを作成し，ホルムアルデヒドの場合と比較検討した．その結果，アセトアルデヒドの場合は孤立系，金属上共にホルムアルデヒドと非常によく似たエネルギーダイアグラムが得られ，金属上において 5 配位経由を取ることが示唆された．また，グリオキシル酸に関しては，銅上ではエネルギーダイアグラムの形状はホルムアルデヒドは異なるものの，基本的には 5 配位経由を取ることが示唆された．また，これら還元剤の吸着エネルギー及び脱離エネルギーを比較するとグリオキシル酸は銅上で吸着しにくく脱離しやすいことがわかった（図 1）．これは，官能基が電子吸引性のグリオキシル酸は銅との相互作用が小さいからであると考えられ，官能基の置換基効果が反応機構に影響を与えることが示唆された．

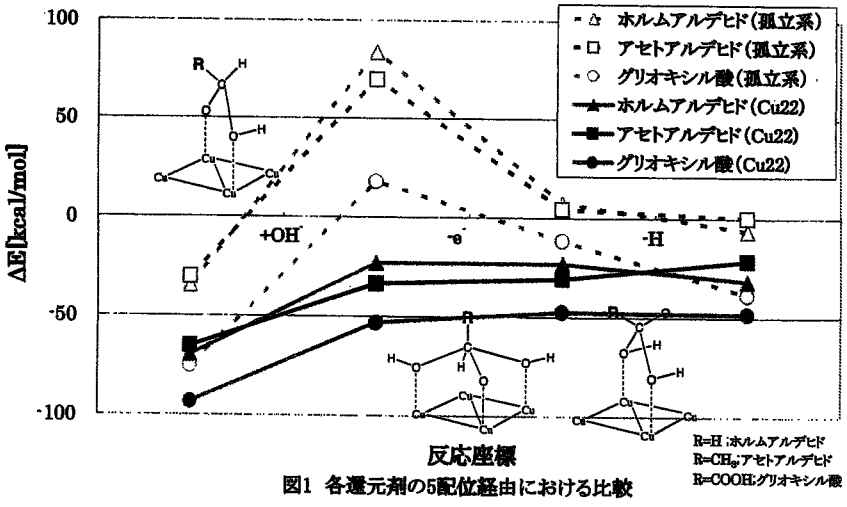

図1 各還元剤の5配位経由における比較

本研究は NEDO 産業技術研究助成事業，および文部科学省 21 世紀 COE プログラム「実践的ナノ化学教育研究拠点」の助成により実施したものである．

1) T. Homma, I. Komatsu, A. Tamaki, H. Nakai, T. Osaka, *Electrochimica Acta*,47,47-53(2001)

○Kaoruho SAKATA, Takuya SHIMADA, Hiromi NAKAI, Takayuki HOMMA, Tetsuya OSAKA

日本化学会第 83 回春季年会,
早稲田大学（東京), 2003 年 3 月.

アンチモン(V)ポルフィリン錯体の光解離に関する理論的研究

（早大理工）○副田隆介・馬場健・中井浩巳

Theoretical study on photochemical dissociation of antimony porphyrin complex

(Waseda Univ.) SOEDA Ryusuke; BABA Takeshi; NAKAI Hiromi

緒言　ポルフィリン環の中心にアンチモンを挿入したアンチモン(V)ポルフィリン錯体は軸配位子を持ち、超原子価状態をとることができる。その中で、$[Sb(FBP)(CH_3,OCH_3)]^+$ (FBP: Free base porphin) や $[Sb(FBP)(CH_3,OH)]^+$ (Fig.1)はUV光照射によりSb-O結合が特異的に切れることが報告されている。本研究ではこれらの錯体の基底状態と励起状態を量子化学計算で求め、光解離反応を理論的に検討した。

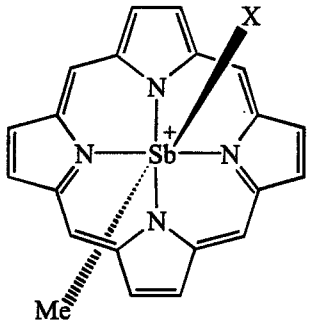

Fig.1. $[Sb(FBP)(CH_3,X)]^+$
X=OCH_3, CH_3

結果・考察　$[Sb(FBP)(CH_3,OCH_3)]^+$についてB3LYPレベルで構造最適化し、その構造を基にTDDFT(B3LYP)で一重項励起状態の計算を行ったところ、ポルフィリン環のπ-π*励起(Bバンド、UV光付近の強い吸収帯に対応)だけが強い遷移確率を持った。また、最適化構造を基にメチル基、メトキシ基をそれぞれ軸方向に離したときの励起状態の変化を検討した（Fig.2)。メトキシ基を離して行くとπ-π*(B)励起状態はnonbonding-π*励起状態(軸方向の3中心非結合性軌道からπ*軌道への励起)と交差し、nonbonding-π*励起状態はn(OCH_3)-antibonding励起状態(OCH_3のn軌道から、軸方向3中心反結合性軌道への励起)と交差している。しかし、メチル基を離しても安定構造近傍では状態間の交差はないことが分かった。同様な結果は$[Sb(FBP)(CH_3,OH)]^+$においても見られた。この置換基の解離距離に依存した励起状態の挙動は、アンチモン(V)ポルフィリン錯体の特異的な光解離反応に対応すると考えられる。

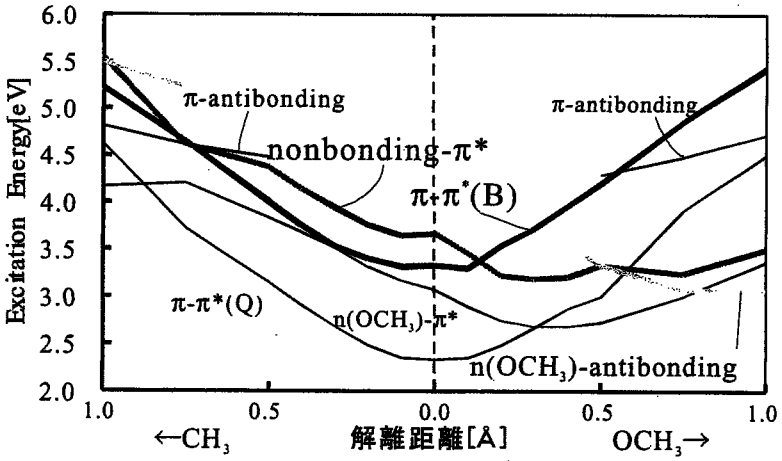

Fig.2. $[Sb(FBP)(CH_3,OCH_3)]^+$の励起状態

日本化学会第 83 回春季年会,
早稲田大学（東京），2003 年 3 月.

無電解析出における還元剤酸化反応に対する金属触媒活性の理論的及び実験的検討

（早大理工）○島田拓哉，阪田薫穂，中井浩巳，本間敬之，逢坂哲彌

Theoretical and experimental study of metal catalytic activity on anodic oxidation of reductants for electroless deposition process

(School of Sci. & Eng., WASEDA Univ.) Takuya SHIMADA, Kaoruho SAKATA, Hiromi NAKAI, Takayuki HOMMA, Tetsuya OSAKA

1. 背景　無電解析出プロセスは機能性薄膜形成の分野等において広く用いられているが，その反応機構には未だ不明な点が多い．この反応は金属イオンの還元析出と還元剤の酸化反応が同時に進行し，更には析出した金属表面が還元剤の反応に対して触媒活性を持つという複雑な反応である．今後より精密な析出挙動の制御を行うことが求められており，反応機構の詳細な解析が必要になる．

そこで我々は理論計算を用いて還元剤の酸化反応の解析を試みている．本検討では電気化学的実験手法との比較を行い，理論実験両面からの反応機構の解析を行った．

2. 方法　本検討では代表的還元剤であるホルムアルデヒドとグリオキシル酸の酸化反応を解析した．本検討では銅上における還元剤の反応機構について解析をした．

理論計算は Gaussian98 によって行った．分子の構造最適化・エネルギー計算に DFT 法を用いた．金属表面は(1 1 1)面，構成原子を 4 及び 22 とするクラスターモデルを用いた．

実験は還元剤のアノード分極測定を行った．浴組成は還元剤 0.1mol/l ，クエン酸 0.1mol/l を基本組成として，銅電極を用いて pH12.5，室温の範囲で測定を行った．

3. 結果考察　計算結果よりホルムアルデヒド・グリオキシル酸共に銅上において下図のような反応機構であることが示唆された．更には，グリオキシル酸の銅への吸着力がホルムアルデヒドの約半分であり不安定化のエネルギーもやや小さいことが確認された．一方アノード分極測定の結果からグリオキシル酸の酸化還元ピークがホルムアルデヒドのピークよりも低く，卑な方向にシフトしていることが確認された．以上よりグリオキシル酸の吸着力・不安定化エネルギーがそれぞれピークの低減・卑へのシフトに影響すると考えられ，理論実験両面からの検討が無電解析出の反応機構の解析において有効であることが示唆された．

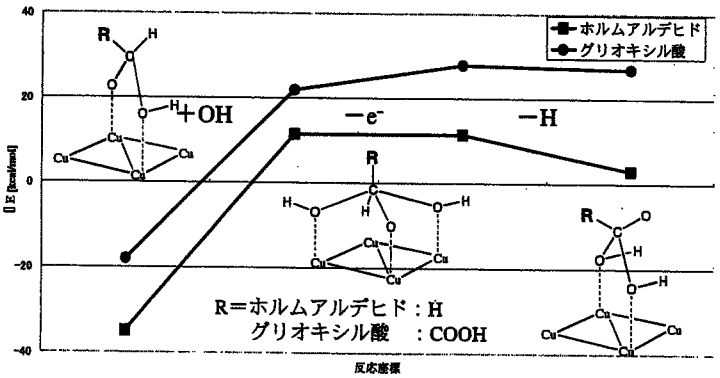

図　各還元剤の酸化反応エネルギーダイアグラム

第 7 回理論化学討論会,
岡崎コンファレンスセンター（愛知),
2003 年 5 月.

2P08 ガウス基底周期境界条件計算による酸化チタン光触媒活性の理論的解析

○中井 浩巳[1,2]、Gustavo E. Scuseria[2]
[1]早稲田大学理工学部化学科 [2]Rice University, Dept. Chemistry

【緒言】Honda-Fujishima 効果[1]が発見されて以来、二酸化チタンは光触媒および光電気化学の中心的役割を果たしてきた。その後も多くの工学的研究がなされ、二酸化チタンを用いた様々な製品が我々の身の回りに普及している。現在重点的に研究されている問題には、可視光応答性と電荷分離の高効率化がある。前者に対しては、2001 年に Asahi ら[2]が窒素ドープすることにより成功している。しかし、上記の問題の解決には、光触媒反応および光電気化学反応に対する分子論的・電子論的理解が不可欠である。本研究では、ガウス基底周期境界条件(PBC)計算により、anatase 型二酸化チタンの電子状態を計算し、光触媒活性のメカニズムを理論的に解析することを目指す。

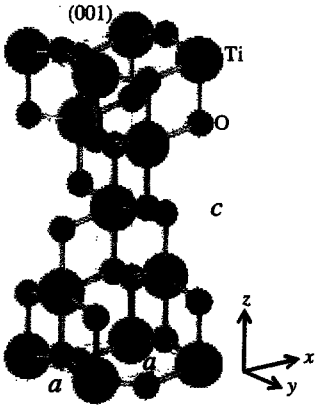

Fig. 1. Unit cell of anatase TiO_2.

【計算方法】PBC 計算に用いた Unit Cell は、バルク(3D)が$(TiO_2)_4$、(001)表面(2D)の$(TiO_2)_5$ である(図 1)。予備計算としてバルクに対する Unit Cell Size 依存性を調べたが、TiO_2 あたりの全エネルギーは 10^{-5} hartree の精度で一致した。Auxiliary Function による電子密度の展開および Fast Multipole Method (FMM)を用いることにより、クーロン積分計算の効率化を図った。Auxiliary Function を用いない場合に比べて、10 倍程度の計算時間が短縮された。すべての計算は、Gaussian Development Version (GDV)を用いて行った。

Table I. Cohesive energy and minimum band gap of anatase TiO_2 bulk and (001) surface.

System	Geometry	Basis Set	Functional	Cohesive Energy (eV)	Min Gap (eV)
Bulk	SP	STO-3G	LDA	29.61	4.07
		STO-3G	PBE	26.16	4.19
		6-31G	LDA	20.82	2.08
		6-31G	PBE	17.42	2.17
	OPT	6-31G	PBE	17.49	2.20
Surface	SP	STO-3G	LDA	28.57	3.58
		STO-3G	PBE	25.26	3.67
		6-31G	LDA	20.36	1.86
		6-31G	PBE	17.11	1.91
		6-311G	LDA	20.18	1.83
		6-311G	PBE	16.93	1.90
	OPT	6-31G	PBE	17.20	2.30
Expt.				20	3.2

【結果と考察】バルクおよび(001)表面に対して凝集エネルギーおよびバンドギャップを表 1 に示す。凝集エネルギーは Double-ζクラスでまずまず実験値を再現しているが、バンドギャップは実験値より大きく過小評価している。バルクに対する構造最適化の効果は小さいが、表面のバンドギャップには 0.4eV 程度の blue-shift をもたらしている。図 2 は、表面第 1 層または第 4 層の O 原子を N 原子と置換した場合の Density-of-States である。N-dope によりバンドギャップが red-shift しており、Asahi らの実験結果とも対応している。現在、HF/DFT hybrid 法を用いた計算を行っているが、exact exchange 項の計算がネックとなっている。そこで、誤差関数を用いた分割により交換積分の打ち切るωPBEh 法[3]を PBC 計算に適用する予定である。

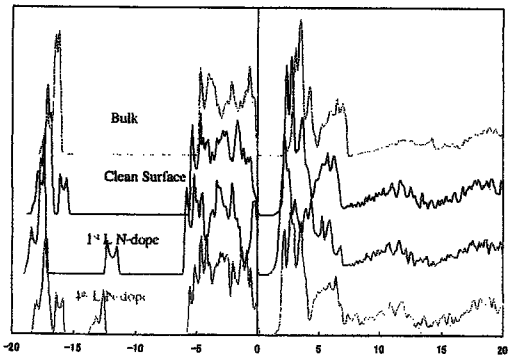

Fig. 2. DOS of anatase TiO_2 bulk, (001) surface, and N-doped (001) surface.

[1]A.Fujishima, K. Honda, *Nature (London)*, **238**, 37 (1972).
[2]R.Asahi, T. Morikawa, T. Ohwaki, K. Aoki, Y. Taga, *Science*, **293**, 269 (2001).
[3]J.Heyd, G. E. Scuseria, *J. Chem. Phys*, in press (2003).

第 7 回理論化学討論会,
岡崎コンファレンスセンター（愛知),
2003 年 5 月.

2P09

Energy Density Analysis による酸化チタン光触媒活性の理論的解析

○河村芳海・中井浩巳

<序>

光照射による酸化チタン(TiO_2)の電荷分離及び再結合過程は、その酸化還元反応の鍵となる重要なステップであり、その触媒反応の高効率化のために作用機構の解明が望まれている。電子状態理論でこのような過程を取り扱うには、周期境界条件を用いるか、有限個のクラスターを切り出すといったモデル化を行う必要がある。クラスターモデルの場合は特に、バルクとして Madelung Potential (MP)などを置く QM/MM 法が用いられるが、この MM 場の強さや大きさ、用いるクラスターのサイズに結果が依存するという問題がある。当研究室で最近提案した Energy Density Analysis (EDA) [1]は、電子状態計算で得られる全エネルギーを構成原子に分割する方法である。EDA を用いると、クラスター部分のみのエネルギーが定義できるため、得られる Energy Density を用いて適切な MP の数や強さ、クラスターサイズを決定することができる[2]。本研究では、光触媒としてよく用いられる二酸化チタンの anatase 構造について、そのクラスターサイズと MM 場に対する Energy Density の収束性を検討した。

<結果と考察>

まず、MM 場の大きさに対する凝集エネルギーの収束性を検討した。クラスターサイズは Ti_2O_4、周りに置く MP の強さは(q_{Ti}, q_O)=(+2.0, -1.0)とした。Table 1 に周りに置く MP の数に対する凝集エネルギーの依存性を示す。周りに 5 層以上の MP を置くことにより、凝集エネルギーが収束していることがわかる。次に、用いるクラスターのサイズ・形に対する凝集エネルギーの依存性を検討した(Fig. 1)。ここでは、MP を置かない Bare Cluster 及び、クラスターの端の酸素原子を ECP でキャップする Total Ion Potential (TIP)モデルに対しても評価を行った。どのモデルにおいても、クラスターのサイズ・形に依存して凝集エネルギーが大きく変化するが、Ti_8O_{16} 程度で収束している。Ti_9O_{18} クラスターにおける周りの MM 場の強さに対する Energy Density の依存性を Fig. 2 に示す。各原子の Energy Density は(q_{Ti}, q_O)=(+3.0, -1.5)付近のとき最もばらつきが小さく、均一なバルクの表現に近い。しかしこの場合においても、キャップされている酸素原子に対して、キャップされていないチタン原子のばらつきは大きく、特にクラスターの端に位置するチタン原子は、最も安定な Ti 原子に比べて大きく不安定化しており、モデルの記述の不十分さを示している。

[1] H. Nakai, Chem. Phys. Lett., 363, 73-79 (2002).
[2] 河村芳海、中井浩巳、分子構造総合討論会（神戸）1C14、2002.

Table 1. 凝集エネルギーの MP の数に対する依存性(SVWN/STO-3G).

Model	MP layer	Number of MPs	Cohesive energy [eV]
#0	0*0*0	0	20.58
#1	3*3*3	156	23.38
#2	5*5*5	744	23.39
#3	7*7*7	2052	23.39
#4	9*9*9	4368	23.39

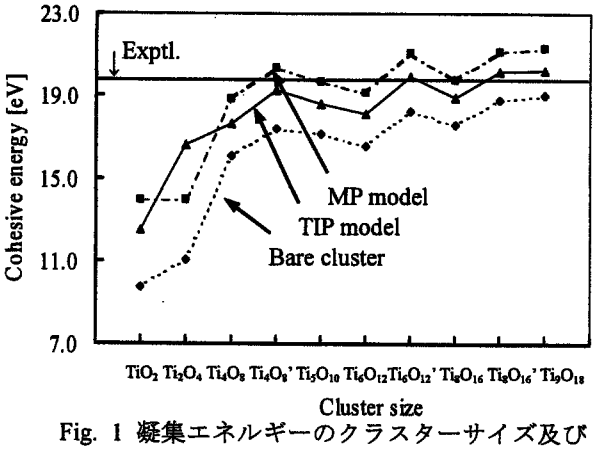

Fig. 1 凝集エネルギーのクラスターサイズ及び形に対する依存性(BLYP/STO-3G).

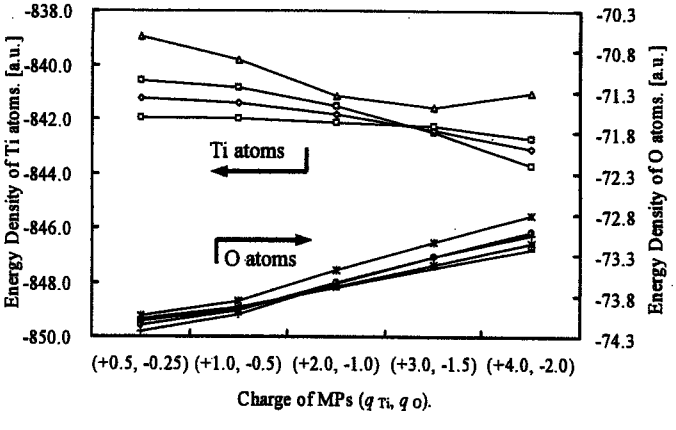

Fig. 2. Ti_9O_{18} クラスターにおける各原子の Energy Density の電荷依存性(BLYP/STO-3G).

第7回理論化学討論会,
岡崎コンファレンスセンター（愛知),
2003年5月.

1O08B

分子積分計算の高速化：Element Basis 法の開発

（早大理工）　○小林　正人、中井　浩巳

1．序

これまでに様々な研究者によって、分子積分、特に電子反撥積分(ERI)を高速に計算する手法が開発されてきた。近年の電子状態計算では、階層構造を用いてクーロン積分を評価する FMM 法や数値的な打ち切り手法などの開発、発展に伴って、大規模系の電子状態計算の linear scaling（Order-*N*）が可能となってきている。しかし、計算の精度を保つためには数十 Å 離れた基底関数に対しても ERI を計算することが重要である。この場合、高速化のためには order よりもむしろ prefactor の向上が必要である。今までに提案された積分計算アルゴリズムの評価には、1組の ERI の計算に対する浮動小数点演算数（FLOP 計数）がしばしば用いられ、議論されてきた。われわれは prefactor の向上を目指すべく、これまでに十分に議論されてきた1組の ERI の計算ではなく、計算すべき ERI すべてを視野に入れて高速化する計算アルゴリズムの開発を行った。

2．Element Basis 法の概念

化学が扱う元素は 100 を超えるが、実際に我々が対象とする系は、DNA のような生体高分子でも C, H, O, N, P, S の6種類であり、10種を超えることは少ない。近年注目を集めているフラーレンやカーボンナノチューブにいたっては、単一の元素からできていることは言うまでもない。Boys がガウス型基底関数を提唱して以来、「同一の元素には同一の基底関数系を用いる」というのが一般的である。しかし、従来の積分計算アルゴリズムではこの情報は全く使われていない。

そこで、今回われわれが提案する Element Basis 法では、基底関数の情報を2つの部分に分割する。Cartesian ガウス型基底関数は、

$$\phi(\mathbf{r}) = \sum_{k}^{K_A} d_k (r_x - R_x)^l (r_y - R_y)^m (r_z - R_z)^n \qquad -\alpha_k r^2 \tag{1}$$

と表され、中心座標 **R** 及び指数α、係数 d から成っている。従来のアルゴリズムでは、これらをすべて原子に割り当てていたが、Element Basis 法では **R** は原子に、αと d は元素に割り当てて使用する。

この基底関数の関係を E-R 図にあらわしたものが Fig.1 である。E-R 図は各要素の従属関係を表した図であり、——は1対1の対応関係を、⟶は1対多の対応関係を表す。参考のため従来からの general contraction のスキームも併記した。従来のアルゴリズムでは、独立に取り扱うべき指数および係数の組はそれぞれ A*L*K, A*L*J であった。今回の手法では、E*L*K, E*L*J となり、効率化が図れることとなる。

3．Element Basis 法の ACE への適用

Element Basis 法を適用するには、ERI の表式として初めから座標部分と指数部分に分かれているものを用いるほうが有利である。そのような表式として、今回われわれは東京理科大の石田氏が提案した ACE-b3k3 表式[1,2]を用いた。これを用いると ERI は

$$\mathrm{ERI} = \sum_{\{\mathbf{N}_3\}} C_4\{\mathbf{N}_3\} H_4\{\mathbf{N}_3\} \tag{2}$$

と表される。ここで、C_4 はガウス関数の中心座標 **R** に依存する随伴座標部で、H_4 は主にガウス関数の指数αの情報で計算する核部である。われわれは Element Basis + ACE-b3k3 プログラムを開発した[3]。プログラムの効率化・最適化は現在行っている段階であるが、現時点での timing data は Table 1 に示すとおりである。本手法は、大規模系の計算ほど有利である。

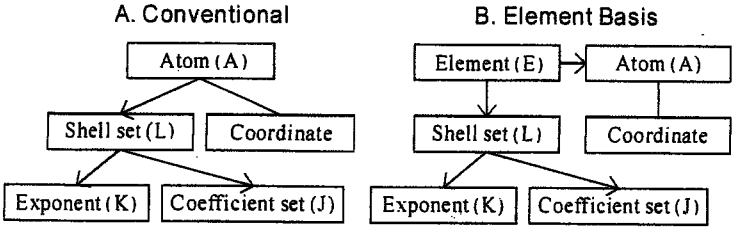

Fig. 1. Entity-Relationship (E-R) diagrams of basis functions on some concepts for computing molecular integrals. In the bracket is number of entities.

Table 1. CPU times for computing all ERIs (in seconds)

Molecule	Dimension	CPU time[a]		
		Present	Gaussian[b]	GAMESS[c]
H_2O	31	2.5	6.5	6.5
C_6H_6	132	679.0	2203.5	2289.3
$C_{11}H_6O_3$	236	8279.2	---	25475.5

[a]Calculation environment : Xeon 2.8GHz / 4096MB Memory
[b]Use PRISM algorithm.
[c]Use PH algorithm.
[d]Basis set : H:8s4p/3s2p, C & O:14s9p/4s3p

[1] K. Ishida, Int. J. Quantum Chem., **59**, 209 (1996).
[2] T. Yanai, K. Ishida, H. Nakano, and K. Hirao, Int. J. Quantum Chem., **76**, 396 (2000).
[3] H. Nakai and M. Kobayashi, *to be published.*

2P10

Energy Density Analysis (EDA) を用いた主成分分析による機能性材料の設計

（早大理工）　○竹内真理、中田彩子、中井浩巳

1. 序　ドラッグデザインなどで代表される機能性材料の設計には分子論的な理解が重要となる。ドラッグデザインにおいて有効と考えられる分子の候補は多数存在し、それらを全て合成した上で医学・薬学的なテストを行い新薬の候補を探し出すにはかなりの労力を要する。そこで電子状態計算を用いればその時間や費用は大幅に軽減できる。しかしながら、生体分子はその大きさがあまりにも大きく、また反応する部位もわからないものが多いため従来の電子状態計算で全ての分子を理論的に取り扱うのは非常に困難である。本研究では、候補となる分子だけの電子状態計算から得られたパラメータを用いて、主成分分析による統計解析によって候補を絞る方法を検討した。今回採用したパラメータは、先に我々が提案したエネルギー密度解析(EDA)[1-4]により得られる各原子のエネルギー密度(変化)である。検討した系は、比較的簡単な系として(1)芳香族における配向性、もう少し複雑な系として(2)*Calophyllum* クマリン類の抗 HIV-1 活性である。

2. 結果と考察

2.1 置換芳香環について　13 種の置換芳香環に対して電子状態計算（B3LYP/6-31G(d)）を行った。用いた置換基は X=NH_2(1), OH(2), OCH_3(3), $NHCOCH_3$(4), CH_3 (5), F (6), Cl (7), Br (8), COH(9), $COOCH_3$ (10), COOH (11), $COCH_3$ (12), CN (13)である。1～5 がオルトーパラ配向性活性化基、6～8 がオルトーパラ配向性不活性化基、そして 9～13 がメタ配向性不活性化基である。Fig. 1 にベンゼンとそれぞれ X=NH_2, Cl, COOH の置換体とのエネルギー密度変化を示す。これより環上のエネルギー分布に特徴が出ていることがわかる。そこで、ベンゼンとそれぞれの化合物とのエネルギー密度変化を変量として主成分分析を行った。その結果を Fig. 2 に示す。比較的置換基の性質に対応するように分かれた。縦軸の第 1 主成分は置換基が結合している炭素原子の安定性に対応していた。横軸の第 2 主成分はオルト、メタおよびパラ位の炭素と水素原子の総合的な安定性に対応し、特にオルト位の炭素と水素原子の成分が大きい。分子全体の電子状態を考慮した結果、新しい 3 つのグループに分けられた。

2.2 *Calophyllum* クマリンについて　近年、抗 HIV-1 活性を示す化合物として、*Calophyllum* クマリンが注目されている。その中には非常に強い抗 HIV-1 活性を示すもの（(+)-calanolide A）もあるが、非常に似た構造をしたクマリンは弱い活性であったり、不活性であったりする。25 種の *Calophyllum* クマリン化合物に対して電子状態計算（B3LYP/6-31G(d)）を行い、エネルギー密度を変量として共通する骨格に対する主成分分析を行った。その結果を Fig. 3 に示す。第 1 主成分は分子骨格の違いを、第 2 主成分は置換基の違いを示している。第 2 主成分において正の値を持つ分子は置換基がフェニル基であり、負の値を持つ分子は置換基がメチル基あるいはプロピル基である。従って、EDA を用いた主成分分析では、構造の情報だけでなく電子状態も反映していることがわかる。今回の解析では、5 つのグループに分類された。下側に位置するグループ A, B, C はいずれも不活性または活性が不明なものが集まった。逆に上側に位置するグループ D, E は、不活性な分子は 2 つだけでほとんどが活性な分子であった。

[1] H. Nakai, Chem. Phys. Lett., 363, 73-79 (2002).
[2] H. Nakai, K. Sodeyama, Chem. Phys. Lett., 365, 203-210 (2002).
[3] Y. Kawamura, H. Nakai, Chem. Phys. Lett., 368, 673-679 (2003).
[4] H. Nakai, K. Sodeyama, J. Mol. Structure (THEOCHEM), in press.

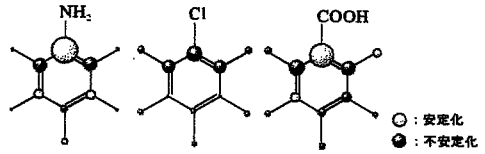

Fig. 1 エネルギー密度変化

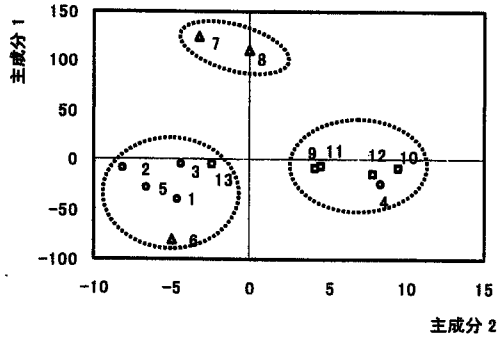

Fig. 2　置換芳香環に対する主成分分析

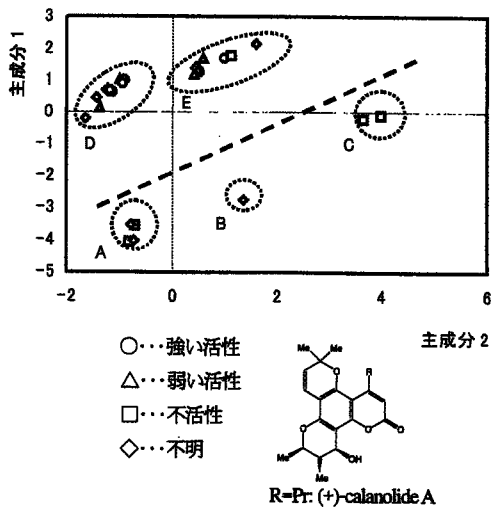

Fig. 3　*Calophyllum* クマリンに対する主成分分析

日本コンピュータ化学会 2003 春季年会,
北とぴあ（東京），2003 年 5 月.

1P12　酸化チタンバルクおよび表面に対するガウス基底周期境界条件計算

○中井　浩巳[1,2]、Gustavo E. Scuseria[2]

[1] 早稲田大学理工学部化学科（〒169-8555 東京都新宿区大久保 3-4-1）

[2] Rice University, Dept. Chemistry (6100 South Main, Houston, TX 77005, USA)

【緒言】1972 年に Fujishima - Honda[1]により半導体電極を用いた水の光分解が報告されて以来、二酸化チタンは光触媒および光電気化学の中心的役割を果たしてきた。その後も、Kawai - Sakata[2]による有機廃棄物分解への応用、Grätzel ら[3]による光増感太陽電池の開発などさまざまな工学的研究がなされてきた。2001 年には Asahi ら[4]が窒素ドープすることにより可視応答光触媒を開発した。これらの現象に対してその学理は必ずしも十分には理解されていない。本研究では、anatase 型二酸化チタンのバルクおよび表面に対してガウス基底周期境界条件(PBC)計算を行い、光触媒のメカニズムの解明を目指す。

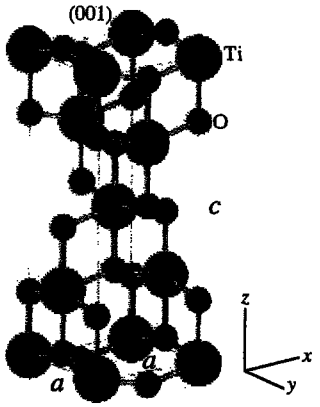

Fig. 1. Unit cell of anatase TiO_2.

【計算方法】図 1 に示す Unit Cell を用いてバルク(3D)および(001)表面(2D)の PBC 計算を行った。予備計算としてバルクに対する Unit Cell Size 依存性を調べたが、TiO_2 あたりの全エネルギーは 10^{-5} hartree の精度で一致した。Auxiliary Function による電子密度の展開および Fast Multipole Method を用いることにより、クーロン積分計算の効率化を図った。すべての電子状態計算は、Gaussian Development Version (GDV)を用いて行った。

Table I. Cohesive energy and minimum band gap of anatase TiO_2 bulk and (001) surface.

System	Geometry	Basis Set	Functional	Cohesive Energy (eV)	Min Gap (eV)
Bulk	SP	STO-3G	LDA	29.61	4.07
		STO-3G	PBE	26.16	4.19
		6-31G	LDA	20.82	2.08
		6-31G	PBE	17.42	2.17
	OPT	6-31G	PBE	17.49	2.20
Surface	SP	STO-3G	LDA	28.57	3.58
		STO-3G	PBE	25.26	3.67
		6-31G	LDA	20.36	1.86
		6-31G	PBE	17.11	1.91
		6-311G	LDA	20.18	1.83
		6-311G	PBE	16.93	1.90
	OPT	6-31G	PBE	17.20	2.30
Exptl.				20	3.2

【結果と考察】表 1 にバルクおよび(001)表面に対して凝集エネルギーおよびバンドギャップを示す。凝集エネルギーは Double-ζクラスでまずまず実験値を再現している。しかし、よく知られているように、バンドギャップは実験値より大きく過小評価している。バルクに対する構造最適化の効果は小さいが、表面のバンドギャップには 0.4eV 程度の blue-shift をもたらしている。図 2 は、表面第 1 層または第 4 層の O 原子を N 原子と置換した場合のバンド構造である。計算レベルは PBE/6-31G なのでバンドギャップは過小評価しているが、N-dope によりバンドギャップが red-shift していることが分かる。これは Asahi らの実験結果とも対応している。

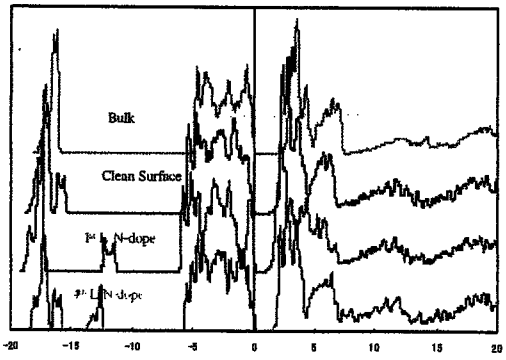

Fig. 2. DOS of anatase TiO_2 bulk, (001) surface, and N-doped (001) surface.

[1]A.Fujishima, K. Honda, *Nature (London)*, **238**, 37 (1972).

[2]T. Kawai, T.Sakata, *Nature (London)*, **282**, 283 (1979); **286**, 474 (1980).

[3]B. O'Regan, M.Gratzel, *Nature (London)*, **353**, 737 (1991).

[4]R.Asahi, T. Morikawa, T. Ohwaki, K. Aoki, Y. Taga, *Science*, **293**, 269 (2001).

日本コンピュータ化学会 2003 春季年会,
北とぴあ（東京），2003 年 5 月.

1P13

Energy Density Analysis の酸化チタン系への適用

○河村芳海・中井浩巳
早稲田大学理工学部化学科（〒169-8555 東京都新宿区大久保 3-4-1）

【緒言】二酸化チタンを用いた光触媒反応は、太陽電池などへの応用の期待から、その可視応答化、高効率化のための研究が多くなされてきた。しかし電荷分離や再結合、酸化還元反応の素過程のメカニズムは詳細に理解されていない。電子状態計算はこれら反応素過程を取り扱うのに有用なツールであるが、表面上での反応を取り扱うには、通常 Embedded Cluster モデルもしくは Periodic モデル[1]といった何らかのモデル化が必要となる。バルクとして Madelung Potential (MP)などを置く MP model では、MP を置く数や強さ、用いるクラスターのサイズの選択に任意性があり、問題となる。当研究室で最近提案した Energy Density Analysis (EDA) [2]は、電子状態計算で得られる全エネルギーを構成原子に分割する方法である。EDA を用いると、クラスター部分のみのエネルギーが定義できるため、得られる Energy Density を用いて適切な MP の数や強さ、クラスターサイズを決定することができる[3]。本研究では、光触媒としてよく用いられる二酸化チタンの anatase 構造について、クラスターモデルでの取り扱いの妥当性について検討を行った。

【結果と考察】まず、MP の数に対する収束性を検討した。クラスターサイズは Ti_2O_4、周りに置く MP の強さは(q_{Ti}, q_O)=(+2.0, -1.0)とした。Table 1 に周りに置く MP の数に対する凝集エネルギーの依存性を示す。周りに 5 層以上の MP を置くことにより、凝集エネルギーが収束していることがわかる。次に、クラスターのサイズ・形に対する凝集エネルギーの依存性を検討した(Fig. 1)。ここでは、MP を置かない Bare Cluster 及び、クラスターの端の酸素原子を ECP でキャップする Total Ion Potential (TIP)モデルに対しても評価を行った。どのモデルにおいても、クラスターのサイズ・形に依存して凝集エネルギーが大きく変化するが、Ti_8O_{16} 程度で収束している。Ti_9O_{18} クラスターにおける周りの MP の強さに対する Energy Density の依存性を Fig. 2 に示す。各原子の Energy Density は(q_{Ti}, q_O)=(+2.0, -1.0)~(+3.0, -1.5)のとき最もばらつきが小さく、均一なバルクの表現に近い。しかしこの場合においても、キャップされていないクラスターの端に位置する Ti 原子は、最も安定な Ti 原子に比べて+26.9 eV と大きく不安定化しており(Fig. 3)、モデルの記述の不十分さを示している。

Table 1. 凝集エネルギーの MP の数に対する依存性(SVWN/STO-3G).

Model	MP layer	Number of MPs	Cohesive energy [eV]
#0	0*0*0	0	20.58
#1	3*3*3	156	23.38
#2	5*5*5	744	23.39
#3	7*7*7	2052	23.39
#4	9*9*9	4368	23.39

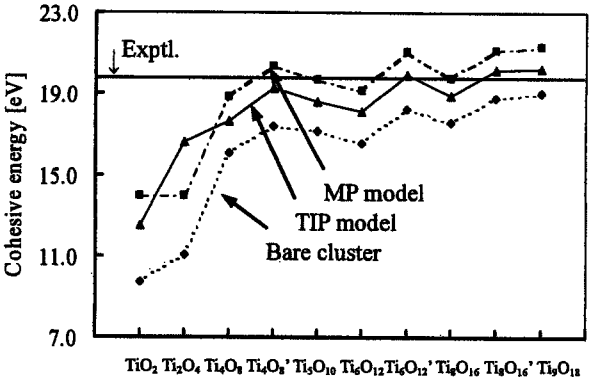

Fig. 1 凝集エネルギーのクラスターサイズ及び形に対する依存性(BLYP/STO-3G).

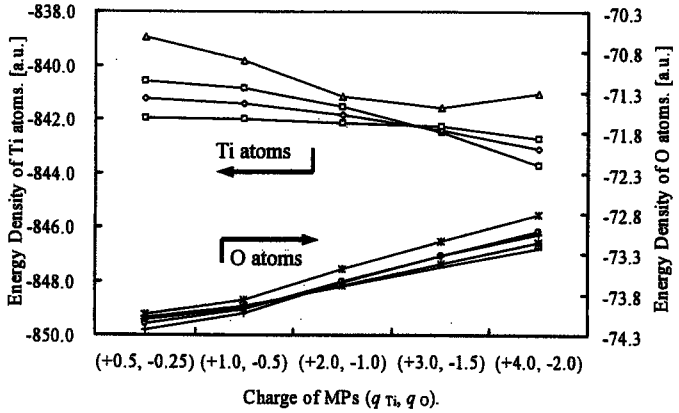

Fig. 2. Ti_9O_{18} クラスターにおける各原子の Energy Density の電荷依存性(BLYP/STO-3G).

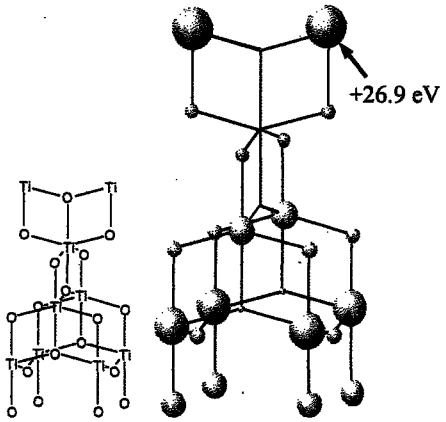

Fig. 3. Ti_9O_{18} クラスター, (q_{Ti}, q_O)=(+2.0, -1.0), TIP モデルにおける構成原子の Energy Density. 球の大きさは最安定な原子からの不安定化を示す.

[1] 中井浩巳、G. E. Scuseria、日本コンピュータ化学会春季年会(東京) 1P12、2003.
[2] H. Nakai, Chem. Phys. Lett., 363, 73-79 (2002).
[3] 河村芳海、中井浩巳、分子構造総合討論会 (神戸) 1C14、2002.

日本コンピュータ化学会 2003 春季年会,
北とぴあ（東京），2003 年 5 月.

1O08　Element Basis 法を用いた分子積分計算の高速化 : 大規模系計算に向けて

○小林　正人、中井　浩巳
早稲田大学理工学部化学科（〒169-8555　東京都新宿区大久保 3-4-1）

【緒言】 分子積分、特に電子反撥積分(ERI)の計算は、*ab initio* 計算におけるボトルネックの一つであり、これまでに様々な高速計算アルゴリズムが提案されてきた。これらのアルゴリズムの評価には、1 組の ERI の計算に対する浮動小数点演算数（FLOP 計数）がしばしば用いられ、議論されてきた。最近の傾向としては、数値的な打ち切りを行う screening の手法や、階層構造を用いてクーロン積分を評価する FMM 法などが検討されている。これらの方法は、いずれも系が十分大きくなれば Order-*N* になることが保証されている。しかし、精度を保つためには、数十 Å 離れた基底関数に対しても ERI を計算する必要がある。その場合、order よりもむしろ prefactor の向上が不可欠となる。われわれは、この prefactor の向上を目指すために、これまでに十分検討されてきた 1 組の ERI の計算に着目するのではなく、計算すべき ERI すべてを視野に入れた高速計算アルゴリズムを検討した。

【Element Basis 法の概念】 通常われわれが対象とする分子は、高々10 種類程度の元素から成り立っている。例えば、1000 原子以上からなる DNA であっても、C, H, O, N, P, S の 6 種類の元素から成り立っている。フラーレンやカーボンナノチューブの場合、単一の元素からできていることは言うまでもない。Boys がガウス型基底関数を提唱して以来、「同一の元素には同一の基底関数系を用いる」というのが一般的である。しかし、従来の積分計算アルゴリズムではこの情報は全く使われていない。

そこで、今回われわれが提案する Element Basis 法では、基底関数の情報を 2 つの部分に分割する。Cartesian ガウス型基底関数は、

$$\phi(\mathbf{r}) = \sum_{k}^{K_A} d_k (r_x - R_x)^l (r_y - R_y)^m (r_z - R_z)^n \exp(-\alpha_k r^2) \qquad (1)$$

と表され、中心座標 **R** 及び指数α、係数 d から成っている。従来のアルゴリズムでは、これらをすべて原子に割り当てていたが、Element Basis 法では **R** は原子に、αと dは元素に割り当てて使用する。

この基底関数の関係を E-R 図にあらわしたものが Fig.1 である。E-R 図は各要素の従属関係を表した図であり、── は 1 対 1 の対応関係を、⟶は 1 対多の対応関係を表す。参考のため従来からの segmented contraction のスキームも併記した。

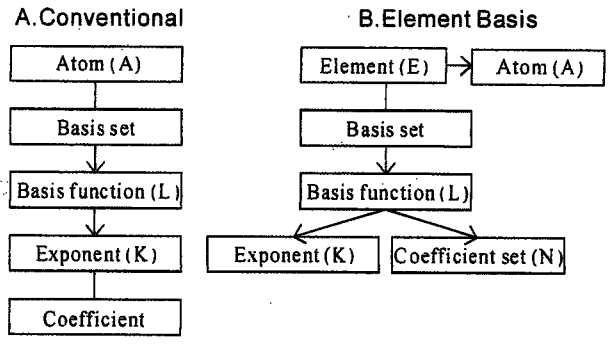

Fig. 1. Entity-Relationship (E-R) diagrams of basis functions on some concepts for computing molecular integrals. In the bracket is number of entities.

【Element Basis 法の ACE への適用】 Element Basis 法を適用するには、ERI の表式として初めから座標部分と指数部分に分かれているものを用いるほうが有利である。そのような表式として、今回われわれは東京理科大の石田氏が提案した ACE-b3k3 表式[1,2]を用いた。これを用いると ERI は

$$\mathrm{ERI} = \sum_{\{\mathbf{N}_3\}} C_4\{\mathbf{N}_3\} H_4\{\mathbf{N}_3\} \qquad (2)$$

と表される。ここで、C_4はガウス関数の中心座標 **R** に依存する随伴座標部で、H_4は主にガウス関数の指数αの情報で計算する核部である。われわれは Element Basis + ACE-b3k3 プログラムを開発した[3]。プログラムの効率化・最適化は現在行っている段階であるが、現時点での timing data は Table 1 に示すとおりである。本手法は、大規模系の計算ほど有利である。

Table 1. CPU times for computing all ERIs (in seconds).

Molecule	Dimension	CPU time[a]		
		Present	Gaussian[b]	GAMESS[c]
H_2O	31	2.5	6.5	6.5
C_6H_6	132	679.0	2203.5	2289.3
$C_{11}H_6O_3$	236	8279.2	---	25475.5

[a]Calculation environment : Xeon 2.8GHz / 4096MB Memory
[b]Use PRISM algorithm.
[c]Use PH algorithm.
[d]Basis set : H:8s4p/3s2p, C & O:14s9p/4s3p

[1] K. Ishida, Int. J. Quantum Chem., **59**, 209 (1996).
[2] T. Yanai, K. Ishida, H. Nakano, and K. Hirao, Int. J. Quantum Chem., **76**, 396 (2000).
[3] H. Nakai and M. Kobayashi, *to be published.*

日本コンピュータ化学会 2003 春季年会,
北とぴあ（東京），2003 年 5 月.

1005

Energy Density Analysis (EDA)を用いた主成分分析
－機能性材料の設計に向けて－

○竹内真理、中田彩子、中井浩巳
早稲田大学理工学部化学科（〒169-8555 東京都新宿区大久保 3-4-1）

【緒言】 機能性材料の設計には分子論的な理解が重要となる。例えばドラッグデザインでは、有効と思われる分子の候補は多数存在する。それらを全て合成し、医学・薬学的なテストを行い新薬の候補を見出すにはかなりの労力を要する。電子状態計算を用いればその時間や費用を大幅に軽減できる。しかし、生体分子はその大きさがあまりにも大きく、また反応する部位もわからないものが多いため、従来の電子状態計算で全ての分子を理論的に取り扱うのは非常に困難である。本研究では、候補となる分子だけの電子状態計算から得られたパラメータを用いて、主成分分析による統計解析によって候補を絞る方法を検討した。今回採用したパラメータは先に我々が提案したエネルギー密度解析(EDA)[1-4]により得られる各原子のエネルギー密度(変化)である。検討した系は、比較的簡単な系として(I)芳香族における配向性、もう少し複雑な系として(II)*Calophyllum* クマリン類の抗 HIV-1 活性である。

【結果と考察】

(I)置換芳香環について

X=NH_2(1), OH(2), OCH_3(3), $NHCOCH_3$(4), CH_3 (5), F (6), Cl (7), Br (8), COH (9), $COOCH_3$ (10), COOH (11), $COCH_3$ (12), CN (13)の置換芳香環の基底状態での安定構造を DFT 計算（B3LYP/6-31G(d)）により求めた。それぞれの置換基は 1～5 がオルト－パラ配向性活性化基、6～8 がオルト－パラ配向性不活性化基、そして 9～13 がメタ配向性不活性化基である。Fig. 1 にベンゼンとそれぞれ X=NH_2, Cl, COOH の置換体とのエネルギー密度変化を示す。これより環上のエネルギー分布に特徴が出ていることがわかる。そこで、ベンゼンとそれぞれの化合物とのエネルギー密度変化を変量として主成分分析を行った。その結果を Fig. 2 に示す。比較的置換基の性質に対応するように分かれた。縦軸の第 1 主成分の固有ベクトルを見ると、置換基が結合している炭素原子の安定性に対応していた。横軸の第 2 主成分はオルト、メタおよびパラ位の炭素と水素原子の総合的な安定性に対応し、特にオルト位の炭素と水素原子の成分が大きい。分子全体の電子状態を考慮した見方をした結果、新しい 3 つのグループに分けられた。

(II) *Calophyllum* クマリン類について

Calophyllum クマリンのうち、いくつかの化合物は抗 HIV-1 活性を示す。特に(+)-calanolide A が最も強い抗 HIV-1 活性を示すが、非常に似た構造をしたクマリンは弱い活性であったり、不活性であったりする。25 種の *Calophyllum* クマリン化合物の基底状態での安定構造を DFT 計算（B3LYP/D95V）により求めた。エネルギー密度を変量として、共通する骨格に対する主成分分析を行った。第 1 主成分は分子骨格の違いを、第 2 主成分は置換基の違いを示している。第 2 主成分に対して正の値を持つ分子は置換基がフェニル基であり、負の値を持つ分子は置換基がメチル基あるいはプロピル基である。従って、EDA を用いた主成分分析は、構造の情報だけでなく、電子状態も反映していることがわかる。このような主成分分析では 5 つのグループに分類された。下側に位置するグループ A, B, C はいずれも不活性または活性が不明なものが集まった。逆に上側に位置するグループ D, E は、不活性な分子は 2 つだけでほとんどが活性な分子であった。

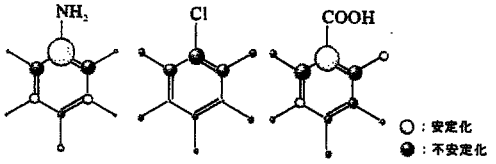

Fig. 1 エネルギー密度変化

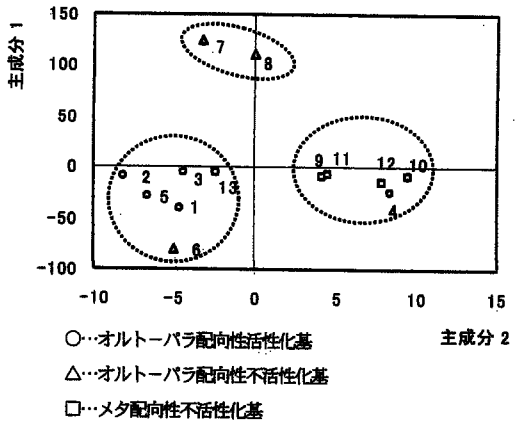

Fig. 2 置換芳香環に対する主成分得点

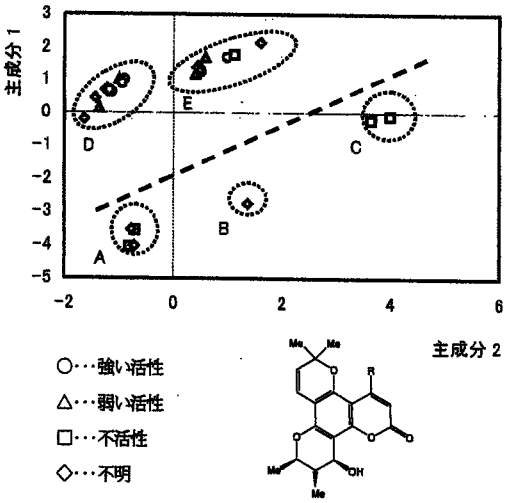

Fig. 3 *Calophyllum* クマリンに対する主成分得点

[1] H. Nakai, Chem. Phys. Lett., 363, 73-79 (2002).
[2] H. Nakai, K. Sodeyama, Chem. Phys. Lett., 365, 203-210 (2002).
[3] Y. Kawamura, H. Nakai, Chem. Phys. Lett., 368, 673-679 (2003).
[4] H. Nakai, K. Sodeyama, J. Mol. Structure (THEOCHEM), in press

分子構造総合討論会 2003,
京都テルサ（京都），2003 年 9 月.

AIMD/EDA によるエネルギー移動過程の理論的研究

（早大理工）○山内佑介・中井浩巳

【緒言】

化学反応は全系のポテンシャルエネルギー超曲面上の安定な経路に沿って進行するが、それにともなう局所的なエネルギー変化が問題になることも多い。たとえば金属表面における活性点の移動や、タンパク質の特定部位の不安定化により進行する反応などがそれである。しかしながら局所的なエネルギー変化を見積もるための理論的な方法はそれほど多くない。Ab initio 計算の結果に対する新しい解析手法として、最近当研究室によって energy density analysis（EDA）が提案された [1]。この手法は Kohn-Sham の密度汎関数理論（KS-DFT）に基づいて分子の全エネルギーを各原子に分割することで、全系におけるエネルギー的に安定あるいは不安定な部位が記述できる。これまでに異性化反応や表面系の吸着反応に対して EDA を用いた研究が行われ、その有効性が確認されている [2, 3]。

一方、化学反応における原子核の運動を時々刻々と追跡するためのツールとして ab initio molecular dynamics（AIMD）シミュレーションが存在する。この方法では ab initio 計算によって得られた力場を用いて古典運動方程式を解くことで、従来の方法では困難であった結合の生成や開裂を伴う化学反応のダイナミクスを取り扱うことができる。例えば我々は AIMD シミュレーションを用いてクラスターイオン衝突反応のメカニズムについて研究を行った [4]。

本研究では特に化学反応中のエネルギー移動過程に対する理論的アプローチとして、EDA と AIMD シミュレーションを組み合わせた AIMD/EDA を提案する。これにより分子内あるいは分子間における局所的なエネルギーの移り変わりを直接観察することが可能となる。

【計算方法】

EDA によって分割された各原子のエネルギーは以下の式となる。

$$E^{\mathrm{A}} = T_{\mathrm{S}}^{\mathrm{A}} + E_{\mathrm{NE}}^{\mathrm{A}} + E_{\mathrm{CLB}}^{\mathrm{A}} + E_{\mathrm{XC}}^{\mathrm{A}} + E_{\mathrm{NN}}^{\mathrm{A}} \tag{1}$$

右辺の各項はそれぞれ運動、核電子引力、古典的クーロン、KS 交換相関、核間反発のエネルギーを示している。ここで KS 交換相関エネルギーを除く各エネルギーは、Mulliken の電子密度解析の手続きと同様にして、KS 軌道について和をとることで各原子に分割される。たとえば

$$E_{\mathrm{CLB}}^{\mathrm{A}} = \frac{1}{2}\sum_{\mu\in\mathrm{A}}(\mathbf{PG})_{\mu\mu}, \text{ where } \quad G_{\nu\mu} = \sum_{\rho}\sum_{\sigma} P_{\rho\sigma}(\chi_\nu\chi_\mu \mid \chi_\sigma\chi_\rho) \tag{2}$$

である。また KS 交換相関エネルギーは、

$$E_{\mathrm{XC}}^{\mathrm{A}} = \sum_{g}^{\mathrm{GRID}} \omega_g p_{\mathrm{A}}(\mathbf{r}_g) F_{\mathrm{XC}}(\mathbf{r}_g) \tag{3}$$

として定義されている。ここで ω_g はグリッドの重み、p_A は分割パラメータである。

AIMD における MD 部分には以下に示す速度 Verlet アルゴリズムを利用している。

$$\mathbf{r}^{n+1} = \mathbf{r}^n + \Delta t\,\mathbf{v}^n + \frac{(\Delta t)^2}{2m}\mathbf{f}^n \tag{4}$$

$$\mathbf{v}^{n+1} = \mathbf{v}^n + \frac{\Delta t}{2m}(\mathbf{f}^{n+1} + \mathbf{f}^n) \tag{5}$$

ここで Δt は MD における時間ステップである。AIMD/EDA のために、本研究室で独自に開発された EDA および MD プログラムを電子状態計算プログラムである GAMESS とリンクして実行した。

【結果と考察】

AIMD/EDA の信頼性を確認するために、300K における水クラスターイオンダイマー $H^+(H_2O)_2$ とアンモニアクラスターイオンダイマー $H^+(NH_3)_2$ に対して計算を行った。AIMD シミュレーションによる 1ps の時間の軌道が得られた。これらのクラスターイオンは 1 つのプロトンを中心として各モノマーが左右に配置した構造をもつ。中心のプロトンから、2 つのモノマーまでの距離をそれぞれ R1、R2 とする。平衡構造は $H^+(H_2O)_2$ と $H^+(NH_3)_2$ の前者が R1−R2 = 0、後者が R1−R2 ≠ 0 である。Fig.. 1 は構造の時間変化を示している。R1+R2 と R1−R2 はそれぞれモノマー間の距離と中心プロトンの運動に対応している。$H^+(H_2O)_2$ のプロトン移動と比べて、$H^+(NH_3)_2$ の方が振動の周期や振幅が大きい。Fig.. 2 は EDA によって中心プロトンと各モノマーに分割されたエネルギーの時間変化を示している。分割されたエネルギーの変化について、まず中心プロトンのエネルギーの振舞は R1+R2 というモノマー間の振動に対応している。すなわちフレーム分子の振動に対して中心プロトンが安定化または不安定化する様子を記述している。またモノマーのエネルギーは $H^+(NH_3)_2$ では周期的であるが $H^+(H_2O)_2$ では乱雑である。これらの結果から $H^+(H_2O)_2$ は平衡位置まわりで微小振動しており、対する $H^+(NH_3)_2$ は対称な 2 つの平衡構造の間を大振幅振動しているという描像を得ることができた。

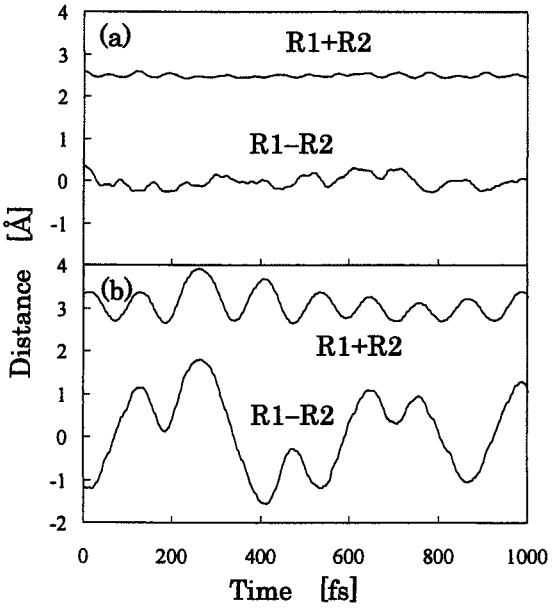

Fig.1. Reaction coordinates by AIMD simulation of (a) $H^+(H_2O)_2$ and (b) $H^+(NH_3)_2$. R1 and R2 means the distances between center hydrogen to monomers.

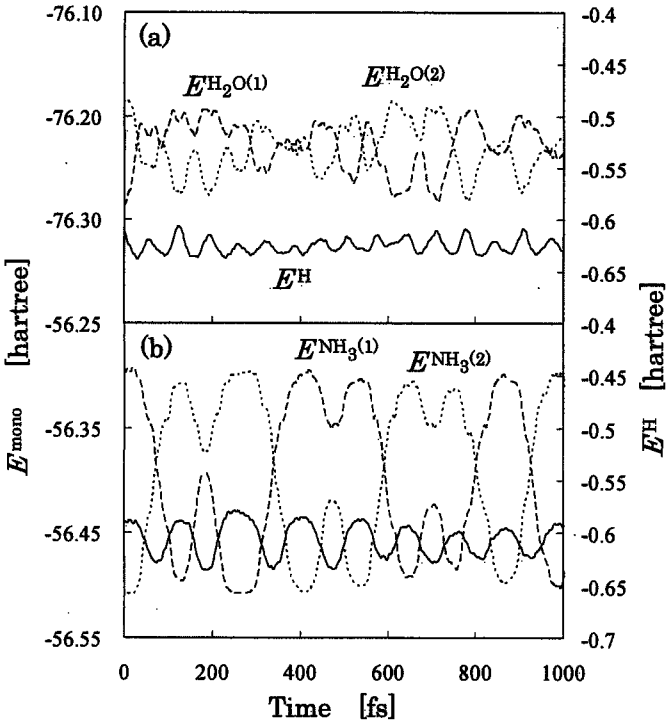

Fig.2. Energy components by AIMD/EDA of (a) $H^+(H_2O)_2$ and (b) $H^+(NH_3)_2$. E^{mono} and E^H indicates energy of monomer and center proton, respectively.

[1] H. Nakai, Chem. Phys. Lett., 363, 73-79 (2002).

[2] H. Nakai, K. Sodeyama, Chem. Phys. Lett., 365, 203-210 (2002).

[3] Y. Kawamura, H. Nakai, Chem. Phys. Lett., 368, 673-679 (2003).

[4] H. Nakai, Y. Yamauchi, A. Matsuda, Y. Okada, K. Takeuchi, J. Mol. Structure (THEOCHEM), 592, 61-67 (2002).

分子構造総合討論会 2003,
京都テルサ（京都），2003 年 9 月.

Ab initio MD 計算による分子の内殻励起ダイナミクスに関する理論的研究

（早大理工）　○大塚教雄・山内佑介・中井浩巳

【序】

近年の放射光分光の技術向上は、分子の内殻励起直後の原子運動とその緩和過程に新しい概念をもたらした。波長可変の放射光を用いて分子内の特定原子の内殻電子を共鳴励起させる事で、内殻正孔状態での超高速な分子構造変化や内殻励起による選択的な化学結合解離などの新しい現象が多数報告され、その可能性と応用性に大変興味が持たれている。このような分子の内殻励起や内殻イオン化の電子状態変化は、それに伴う分子内原子の運動と密接に関連し、脱励起過程に大きな影響を及ぼしていることが予想される。そのため、内殻励起から電子緩和前までの数 10fs の時間スケールに対する分子運動の変化は、電子緩和後の機構を理解する上で重要であると考えられる。これまで、内殻励起から電子緩和までの理論的な取り扱いは、内殻電子のイオン化または励起した正孔状態からの定式化から行われており、分子の運動を無視してきた。本研究では、基底状態から内殻励起状態への電子状態変化が分子運動にどのような影響を与えるのか、ab initio MD 計算から分子の内殻励起ダイナミクスの検討を行う。

【計算方法】

MD 計算部分は速度 verlet 法に基づいたアルゴリズムを用い、time step を 0.1fs とした。ab initio MD 計算は、本研究室で独自に開発された MD プログラムを電子状態計算プログラム Gaussian98 とリンクすることで行った。

【計算結果】

1. 内殻励起エネルギーと基底関数依存性

まず、内殻励起エネルギーと基底関数の依存性について考察する。表 1 に、BF_3 分子の内殻励起エネルギーと主な配置を示した（CIS/cc-pVDZ 基底と更に augment、Rydberg 関数の組み合わせ）。ここで、BF_3 分子は D3h 対称性を持つ平面分子であり、B-F 結合距離を 1.313Å、角 FBF を 120°とした。cc-pVDZ 基底関数を用いた CIS 計算では、BF_3 分子の B1s→$2a_2''$ に対応する内殻励起状態 $^1A_2''$ への内殻励起エネルギーの計算値は 200.5eV となり、約 5eV の誤差があった。また、B1s→$3a_1'$ に対

表 1. CIS 計算による内殻励起エネルギーの基底依存性

Basis set	Exc.energy	State	Main Configurations ($\|C_{ia}\| > 0.3$)
cc-pVDZ	200.53	$^1A_2''$	0.54245($B1s^{-1}2a_2''$) + 0.45335($B1s^{-1}3a_2''$)
	207.03	$^1A_1'$	0.65960($B1s^{-1}3a_1'$)
cc-pVDZ+Ryd	200.54	$^1A_2''$	0.61662($B1s^{-1}5a_2''$)
	206.71	$^1A_1'$	0.34442($B1s^{-1}3a_1'$) - 0.41659($B1s^{-1}7a_1'$) + 0.40158($B1s^{-1}9a_1'$)
aug-cc-pVDZ	200.54	$^1A_2''$	0.61126($B1s^{-1}3a_2''$)
	206.58	$^1A_1'$	0.47721($B1s^{-1}3a_1'$) - 0.37917($B1s^{-1}4a_1'$)
aug-cc-pVDZ+Ryd	200.53	$^1A_2''$	0.62007($B1s^{-1}6a_2''$)
	206.56	$^1A_1'$	0.30433($B1s^{-1}3a_1'$) - 0.38779($B1s^{-1}7a_1'$) + 0.35336($B1s^{-1}10a_1'$)
Exp.			
	195.5	B1s → $2a_2''$	
	198.2	B1s → $3a_1'$	

応する内殻励起状態 $^1A_1'$ との相対的なエネルギーについてもその差が見られた。これは、augment、Rydberg 関数を加えても内殻励起エネルギーの大きな改善は見られなかった。

2. CIS 計算による内殻励起 BF_3 分子のポテンシャルエネルギー曲面

内殻励起状態と分子構造に関する考察を行う。図 1 に、BF_3 分子の B-F 結合距離と B-F3 平面距離（3 つの F 原子が作る平面と B 原子間との距離）に関する内殻励起状態 $^1A_2''$ のポテンシャル曲面を示す（CIS/cc-pVDZ 基底）。BF_3 分子は基底状態では、D3h 対称性の平面構造である。cc-pVDZ 基底関数を用いた CIS 計算では、内殻励起状態 $^1A_2''$ での BF_3 分子の構造は、B-F3 平面距離が約 0.4Å の C3v 対称性が安定構造であることが分かる。内殻励起による電子状態変化は、分子の構造と運動に大きく影響することが示唆される。

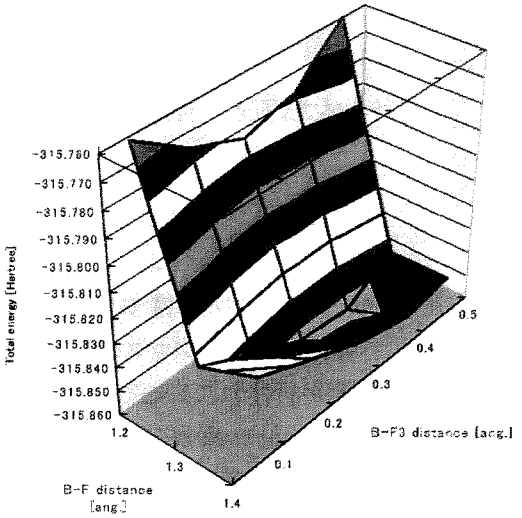

図 1. CIS/cc-pVDZ 計算による内殻励起状態 $^1A_1''$ のポテンシャルエネルギー曲面

3. Ab initio MD 計算による内殻励起 BF_3 分子のダイナミクス

Ab initio MD 計算による BF_3 分子の計算の結果を示す。図 2(a)に全エネルギーの変化を示す。t=300fs の時に基底状態から内殻励起状態 $^1A_2''$ に移る。図 2(b)には、各時間における B-F3 平面間距離の変化を示した。基底状態では、B 原子は F3 平面を中心とした面外振幅振動をしている。内殻励起状態（t=300fs 以降）になると、B 原子は F3 平面から離れて、新しい運動を示す。図 2(c)に内殻励起（t=300fs）前後の 50fs 間の軌跡を示す。内殻励起後約 20fs の間に B 原子は F3 平面から約 0.5Å の距離まで移動していることが分かる。このように、内殻励起による電子状態変化と数 10fs 内の高速な分子構造変化の関連性が示された。

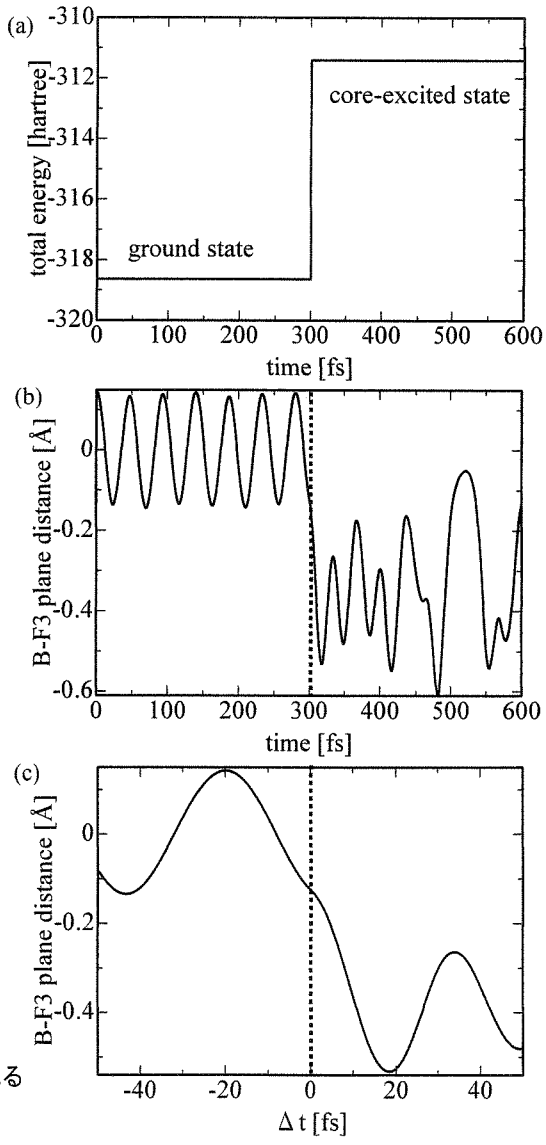

図 2. ab initio MD（CIS/STO-3G）計算による内殻励起 BF_3 分子のダイナミクス

分子構造総合討論会 2003,
京都テルサ（京都），2003 年 9 月.

ab initio 法による水クラスターイオン[$H^+(H_2O)_n$ (n=2-6)]の核生成過程に関する理論的研究

（早大理工[a]・理研[b]）○小澤志保[a]、山内佑介[a]、河井葉子[b]、山口悟[b]、
岡田芳樹[b]、中井浩巳[a]

【序】

結晶成長初期過程における核生成現象は典型的な非平衡過程である。酸性雨発生機構などの自然現象のみならず、半導体生成プロセスや生体反応などに関連していることから重要視され、理論と実験の両面から様々な研究が行われている。しかしながら、核生成進行の挙動についての理解はいまだ不十分である。そこで我々は、*ab initio* 法に基づき衝突断面積に注目したアプローチと、脱励起過程に注目したアプローチによって、核生成ダイナミクスの解明を目指した。

均一核生成に対して、イオン核生成のプロセスはマイクロクラスターに準安定状態を持ち、反応速度が著しく増大することが知られている。理研の岡田らはサイズ選別した水クラスターイオンを様々な分子に衝突させる実験を行った。

水クラスターイオン＋水: $H^+(H_2O)_n + D_2O$ (1)

水クラスターイオン＋アセトン: $H^+(H_2O)_n + CH_3COCH_3$ (2)

水クラスターイオン＋DMSO: $H^+(H_2O)_n + CH_3SOCH_3$ (3)

その結果、イオンにモノマーが取り込まれる吸着、クラスターが分解する解離、という 2 つの反応過程が存在することが明らかになり、その反応断面積の値は衝突エネルギーやクラスターサイズの変化に対して、それぞれ特徴的な変化を示すことがわかった。しかしその違いについての原因は明らかでない。本研究では各反応における引力的ポテンシャルに基づく衝突断面積を、*ab initio* 法を用いて理論的に求める。この結果から各反応の特徴やマイクロクラスターについて議論する。

また、我々は衝突反応（吸着）とその後に続く脱励起過程を *ab initio* molecular dynamics (AIMD) シミュレーションにより再現し、より高い振動励起状態にあると考えられるクラスターが、安定して結晶成長するための効率の良い過程を検討する。

【水クラスターイオン[$H^+(H_2O)_n$ (n=2-6)]核生成過程の解析的衝突断面積】

距離 R、並進エネルギー E_{col} および衝突パラメータ b が与えられているとき、衝突に対する障壁として遠心障壁を加味した有効ポテンシャル $V_{eff} = V(R) + E_{col}\, b^2/R^2$ を考える。この時 V_{eff} は遠心斥力と $V(R)$ の遠距離性引力部分の組み合わせの結果として生じ、$R = R_{max}$ で局所的な最大値をもつ。衝突断面積を求めるためには以下の式を陰関数的に解き、R_{max} および b_{max} を求めればよい。

$$\frac{1}{2}\mu(\dot{R}^2)_{R\max} = \left[E_{col} - V(R) - E_{col}\frac{b^2}{R^2}\right]_{R\max} \geq 0, \tag{4}$$

$$\left[E_{col} - V(R_{\max}) - E_{col}\frac{b^2}{R_{\max}^2}\right]_{b\max} = 0. \tag{5}$$

これより、衝突断面積 σ は $\sigma = \pi b_{max}^2$ として得ることができる。

図 1 および図 2 に結果を示す。まず水クラスターイオン[$H^+(H_2O)_n$]の H_3O^+ を中心とする構造に対して衝突断面積を求めた。n=4 までは中心の H_3O^+ が H_2O により遮蔽されるが、衝突断面積は緩やかに増加し

ている。結果として H_3O^+を中心とする構造での衝突断面積はnの増加に伴って単調増加を示し、衝突実験の反応断面積をある程度再現している。続いて、水クラスターイオンの $H_5O_2^+$を中心とする構造の衝突断面積を求めた。この構造は *ab initio* 計算ではn=2,4,6 に安定構造の存在が予想できた。実験の振動スペクトル解析ではn=2,6 に $H_5O_2^+$を中心とする安定構造の存在が予測されている。ここで $H_5O_2^+$を中心とする構造の衝突断面積は、H_3O^+を中心とする構造と比べ n=6 で減少しており、実験の挙動と一致している。結果としてn=6では $H_5O_2^+$を中心とする構造をとることが断面積という物性から予測できた。

水クラスターイオンにアセトンまたはDMSOを衝突させる衝突断面積は、水モノマーを衝突させた場合と似た挙動を示している。その反応確率は水、アセトン、DMSO の順に大きくなっており、その傾向はプロトン親和性に比例していることが分かった。

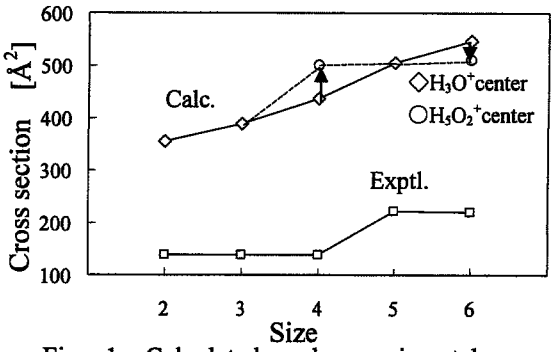

Fig. 1. Calculated and experimental cross section of $H^+(H_2O)_n + H_2O$ (n=2-6).

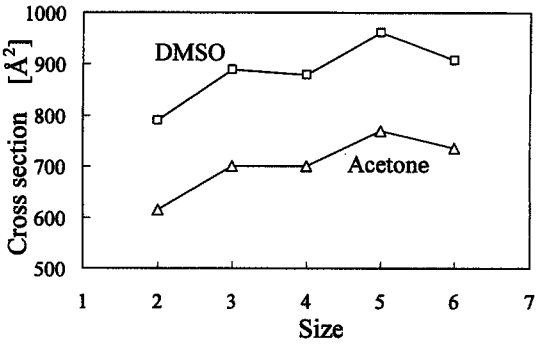

Fig. 2. Calculated collision cross section of $H^+(H_2O)_n$ + X (n=2-6), where X indicates Acetone or DMSO.

【水クラスターイオン$[H^+(H_2O)_n$ (n=2)]振動緩和のAIMD シミュレーション】

高い振動励起状態にある水クラスターイオンが、不反応分子の衝突により脱励起される過程を考察する。そのために以下の反応をAIMD シミュレーションによって扱った。

$$\begin{cases} H^+(H_2O)_1 + H_2O \rightarrow H^+(H_2O)_2^* & (6) \\ H^+(H_2O)_2^* + N_2 \rightarrow H^+(H_2O)_2 + N_2^* & (7) \end{cases}$$

ここで＊は振動励起状態にある分子を表す。(6)の反応によって振動励起された $H^+(H_2O)_2^*$が生成するが、これは分子振動緩和(IVR)および分子間振動エネルギー移動の 2 種類の過程によって緩和される。そこで衝突後の $H^+(H_2O)_2$のトラジェクトリーからIVR の進行が異なる4つの状態を取り出し、(7)の反応における $H^+(H_2O)_2^*$の初期条件とした。その4 つの状態に対し、N_2 を様々な配向から衝突させた。シミュレーションから $H^+(H_2O)_2$とN_2の間でのエネルギー移動の様子を観察した。図3は1つのトラジェクトリーにおける $H^+(H_2O)_2$と N_2 の全エネルギーの時間変化を示している。衝突に伴い $H^+(H_2O)_2$ の全エネルギーがN_2へ移動している様子が見られる。

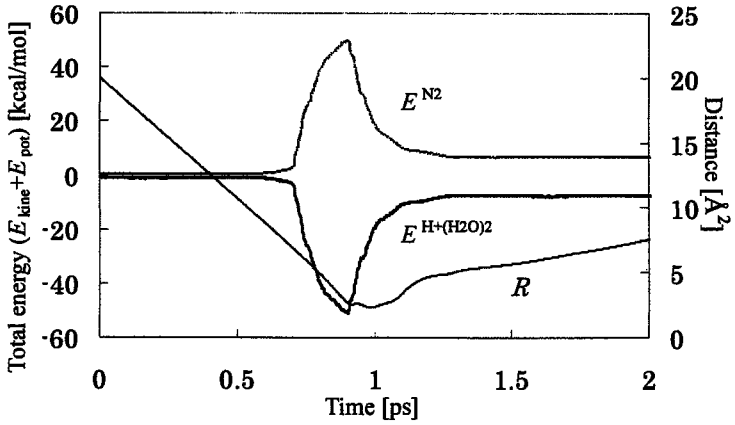

Fig. 3. Time evolution of total energy for $H^+(H_2O)_2$ and N_2 ($E^{H+(H2O)2}$, E^{N2}), and distance between $H^+(H_2O)_2$ and N_2 (R).

分子構造総合討論会 2003,
京都テルサ（京都），2003 年 9 月.

Energy Density Analysis (EDA)の GAMESS への組み込みといくつかの応用

(早大理工) ○河村芳海、馬場健、中井浩巳

1. 緒言

近年の電子状態理論の発展により、量子化学計算は生体分子など巨大分子に対しても高精度に物理量を求められるようになった。しかし、通常これらの計算から得られるエネルギーは、単一のスカラー量であり、エネルギー移動過程など分子内部でのエネルギー変化をみることは困難である。当研究室で提案した Energy Density Analysis (EDA)は、量子化学計算で得られる全エネルギーを構成原子に分割する解析方法であり、これまでさまざまな系に適用することにより、種々の現象、反応メカニズムの解明に有用であることを示してきた[1-4]。当発表では、EDA を量子化学計算パッケージ GAMESS.US に組み込み、さまざまな系への適用例を示すと共に、エネルギー分割法などと組み合わせた結果について述べる。

2. 理論

EDA では、次の手順で各エネルギー成分を構成原子に分割する。Kintic energy 項 T_s は、原子軌道(AO)に基づいた分割を行い、atomic energy density T_S^A を得る。

$$T_S = \sum_{\mu}\sum_{\nu} P_{\mu\nu}\left\langle \chi_\nu \middle| \hat{t} \middle| \chi_\mu \right\rangle = \sum_{\mu}\sum_{\nu} P_{\mu\nu}T_{\nu\mu} = \sum_{\mu}(\mathbf{PT})_{\mu\mu},$$

$$T_S^A = \sum_{\mu\in A}(\mathbf{PT})_{\mu\mu}$$

Nucleus-electron attraction 項、Coulomb interaction 項、Exact exchange 項も同様に分割される。これにより Hartree-Fock エネルギーに対する分割が達成される。この分割は Mulliken population analysis (MPA)の類推に基づいているが、同様に Löwdin population analysis (LPA)に基づいて直交化基底を用いた分割を行うこともできる。すなわち、

$$T_S^A(\text{Löwdin}) = \sum_{\mu\in A}(\mathbf{P'T'})_{\mu\mu} = \sum_{\mu\in A}\left\{\left(\mathbf{S}^{1/2}\mathbf{PS}^{1/2}\right)\left(\mathbf{S}^{-1/2}\mathbf{TS}^{-1/2}\right)\right\}_{\mu\mu}$$

Kohn-Sham 法においては、exchange-correlation 項を分点の重みω_g、partition function p_A を用いて次のように分割する。

$$E_{XC}^A = \sum_{g}^{grid}\omega_g p_A(\mathbf{r}_g)F_{XC}(\mathbf{r}_g)$$

3. 応用

3.1 表面吸着過程に対する EDA

固体表面に対する分子吸着過程は触媒反応や電極反応の素過程として興味深い。本研究では Si(100)表面に対する CO 分子吸着過程を EDA を用いて解析した。表面のモデルとしては、クラスターの端を水素原子でキャップする Capped bond model を用い、Si_9H_{12} クラスター(Fig. 1)を用いた。基底関数は 6-31G(*d*,*p*)、DFT 法の汎関数は B3LYP である。

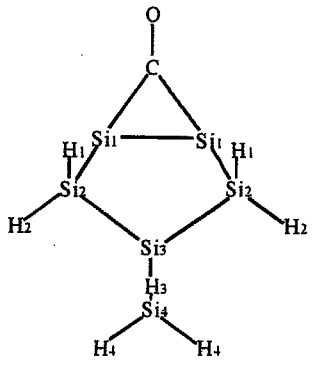

Fig. 1. Si_9H_{12} クラスター.

また、HF 法については MPA 及び LPA に基づく分割をそれぞれ計算した。吸着による各原子のエネルギー密度変化を EDA を用いて計算した結果を table 1 に示す。この系に対しては、HF 法について、MPA に基づく分割と LPA に基づく分割で定性的挙動が異なっている。Löwdin に基づく分割は、表面第 1 層の Si dimer が大きく安定化し、吸着子が不安定化するという挙動を与えている。DFT 法における分割では HF 法における Löwdin と定性的に似た挙動を示している。

Table 1. Si_9H_{12} cluster への CO 分子吸着に伴うエネルギー密度変化 (kcal/mol).

	HF		DFT
	Mulliken	Löwdin	Mulliken
Si1	1.9	-25.2	-32.4
Si2	-0.9	1.3	0.8
Si3	-0.4	-1.9	-2.7
Si4	-2.5	0.6	-0.6
H1	0.5	0.1	0.2
H2	0.1	0.3	0.2
H3	0.2	0.6	-0.1
H4	0.3	0.1	0.2
C	-19.2	11.7	40.0
O	16.3	31.8	15.6
Total	-2.2	-2.2	-10.3

3.2 相互作用エネルギーの局所的な値への分割

水素結合など弱い結合により形成される分子系の相互作用は重要な研究分野であり、実験、理論両面から長年研究がなされている。量子化学計算において相互作用エネルギーは、孤立系と相互作用系のエネルギーの差分をとることで計算される。その相互作用の詳細な解析のために、相互作用エネルギーを物理的意味のあるコンポーネントに分割する手法が Morokuma により提案されて以来[5]、いくつかの分割手法が提案されてきた。Reduced Variational Space SCF method (RVS) は変分空間を適当に制限して SCF を行うことにより、相互作用エネルギーを静電及び交換(ESX)、分極(POL)、電荷移動(CT)相互作用コンポーネントに分割する手法である[6]。EDA と RVS を組み合わせることにより、相互作用エネルギーを物理的意味づけされた局所的な値に分割することが可能となり、分子間の相互作用の有用な解析手段のひとつとなることが期待される。Table 2 に、水二量体の相互作用に EDA/RVS を適用した結果を示す。計算レベルは HF/6-311++G(2*d*,2*p*)、単量体の構造は実験値に固定し、二量体間の距離を最適化した。相互作用エネルギーのうち重要な静電及び交換相互作用は水素結合している水素と酸素に由来するものであることがわかる。

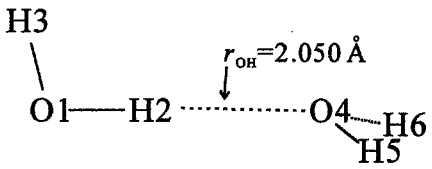

Fig. 2. 水二量体.

Table 2. 水二量体に対する EDA/RVS の結果 (kcal/mol). HF/6-311++G(2*d*,2*p*)

	ESX	POL	CT	Total	Full variational
O1	1.94	-5.74	-4.32	-8.12	-8.51
H2	-1.75	6.52	4.22	8.98	9.52
H3	-1.37	-0.90	-0.40	-2.67	-2.78
O4	-3.56	-0.74	-0.62	-4.92	-5.26
H5	1.08	0.07	0.21	1.35	1.48
H6	1.08	0.08	0.20	1.36	1.48
Total	-2.60	-0.70	-0.72	-4.02	-4.07

[1] H. Nakai, Chem. Phys. Lett., 363, 73-79 (2002).
[2] H. Nakai, K. Sodeyama, Chem. Phys. Lett., 365, 203-210 (2002).
[3] Y. Kawamura, H. Nakai, Chem. Phys. Lett., 368, 673-679 (2003).
[4] H. Nakai, K. Sodeyama, J. Mol. Structure (THEOCHEM), in press.
[5] K. Morokuma, J. Chem. Phys., 55, 1236 (1971).
[6] W. J. Stevens, W. H. Fink, Chem. Phys. Lett., 139, 15-22 (1987).

分子構造総合討論会 2003,
京都テルサ（京都），2003 年 9 月.

4Pa109

無電解析出における還元剤酸化反応の置換基効果に関する DFT 計算による検討

（早大理工）○阪田薫穂，島田拓哉，中井浩巳，本間敬之，逢坂哲彌

1．緒言

めっき技術は工業的に重要な技術の１つとなっているが，その中でも外部電源を必要としない成膜プロセスである無電解めっきは，微細加工技術などに多用されている．しかし，その反応機構は種々の電子移動を伴うために非常に複雑であり，未解明点も多い．また，析出した金属表面が還元剤の酸化反応に対して触媒活性を持たなければ電子の供給が行われず，析出が連続的に起こらないが，このような還元剤の反応に対する金属表面の触媒活性の起源についても不明点が多い．このように定量的な解釈が困難であることから，これまでの無電解めっきの特性向上の研究は試行錯誤的に行われることが多かった．しかし，無電解めっきプロセスをナノレベルの微細構造形成に広く応用可能とするためには，反応プロセスの精密な制御が必要であり，そのためには反応メカニズムの詳細を明らかにする必要がある．無電解めっき反応についてはこれまでも様々な電気化学的手法を用いた検討がなされてきたが，更なる詳細な解明のために，我々は従来の実験的手法に加え，理論・計算化学を用いた解析を進めている[1),2),3)]．本検討では，回路実装分野などに広く用いられている無電解銅めっきプロセスに着目し，その代表的な還元剤であるホルムアルデヒド，および官能基をメチル基にかえたアセトアルデヒド，カルボキシル基にかえたグリオキシル酸，アルデヒド基にかえたグリオキサールに着目した．そして，これらの還元剤の銅上における酸化反応機構を比較することで，アルデヒドの官能基の差異が反応機構に与える影響を検討した．

2．検討方法

アセトアルデヒド，グリオキシル酸，及びグリオキサールの酸化反応機構における最安定の経路を求めるため，孤立系および銅表面上でのエネルギーダイアグラムを作成し，各還元剤でエネルギー・電荷等の比較検討を行った．全ての計算は代表的なパッケージである Gaussian98 を用い，計算方法には密度汎関数法（DFT 法）を用いた．汎関数は B3LYP を用いた．金属表面は Cu(111)面を表したサイズ 4 のクラスターを用い，吸着構造の構造最適化を行った後，サイズ 22 で一点計算を行った．基底関数は C,H には cc-pVDZ，O には分散関数を組み込んだ aug-cc-pVDZ，Cu には Hay&Wadt ECP を用いた．また，更なる詳細な検討のため Energy Density Analysis (EDA)[4)]を用いて個々の構成原子ごとのエネルギーの解析を行った．

3．結果及び考察

これまでの検討でホルムアルデヒドは銅上で水酸基の配位の後，5 配位状態を経由し水素の脱離が起こるという 5 配位経路を取ることが示唆されている[1)]．本検討ではアセトアルデヒド，グリオキシル酸，グリオキサールに関して孤立

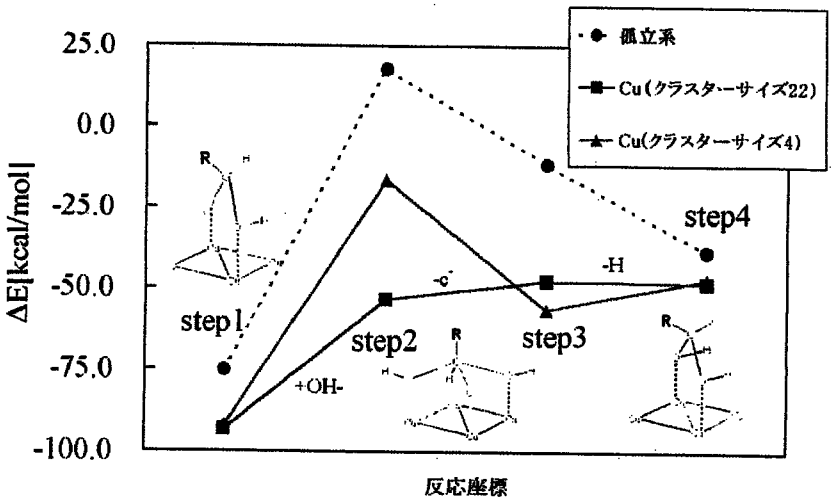

図1．グリオキシル酸 5配位経由エネルギーダイアグラム(Rは官能基)

系及び金属上での酸化反応のエネルギーダイアグラムを作成し，ホルムアルデヒドの場合と比較検討した．その結果，アセトアルデヒド，グリオキサール，グリオキシル酸は共に銅上において5配位経由を取ることが示唆された．また，これら還元剤の吸着エネルギー及び脱離エネルギーを比較すると，官能基が電子吸引性であるグリオキシル酸やグリオキサールは銅に吸着しにくく脱離しやすいことが示唆された．更にEDAを用いて原子ごとのエネルギーの偏りを調べたところ，グリオキシル酸やグリオキサールが吸着・脱離エネルギーが小さいのは，還元剤の吸着部位と銅との相互作用が小さいからであると考えられ，官能基の置換基効果が反応機構に影響を与えることが示唆された．またEDAによる解析では，5配位経由において前のステップから，原子ごとのエネルギーがどのように変化しているかを解析した．その結果，水酸基の配位および電子放出過程では金属側は安定化し還元剤側は不安定化しているのに対し，水素脱離の過程では金属側は不安定化し還元剤側は安定化していることが示唆された．

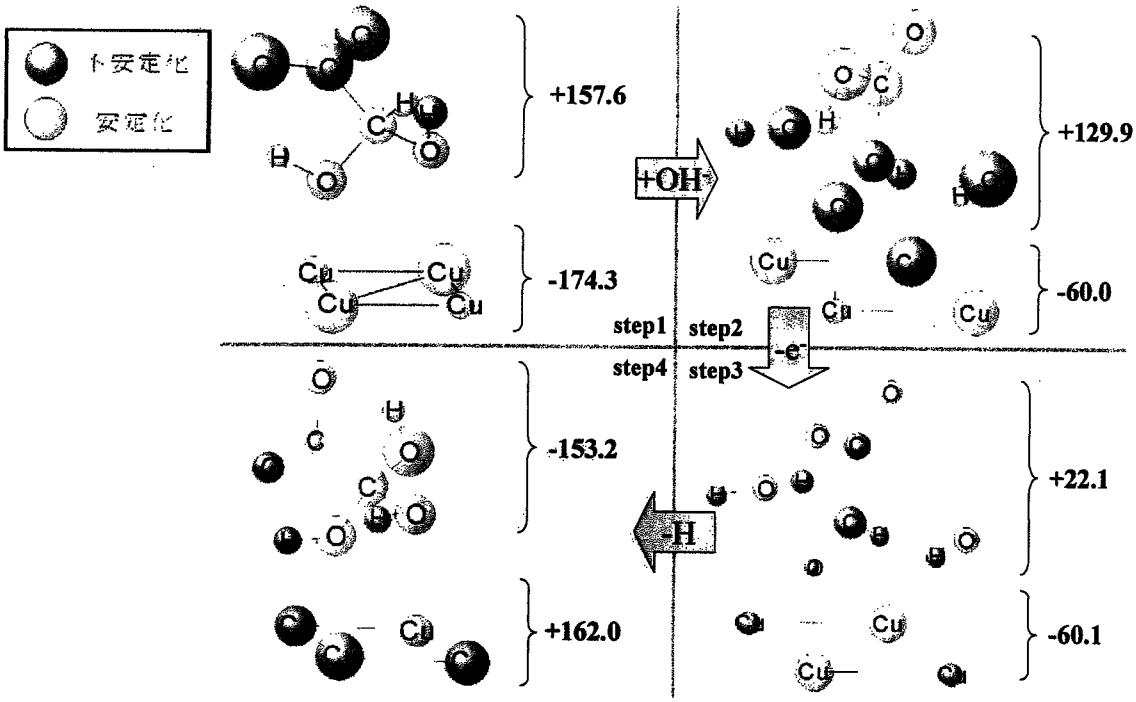

図2. グリオキシル酸，5配位経由のEDAによる解析

図中の値は，前のステップからのエネルギーの差分を還元剤と金属に分割したものである．[kcal/mol]

本研究はNEDO産業技術研究助成事業(00A33010a)，文部科学省特定領域研究(14040220)，および文部科学省21世紀COEプログラム「実践的ナノ化学教育研究拠点」の助成により実施したものである．

4．文献

1) T. Homma, I. Komatsu, A. Tamaki, H. Nakai, T. Osaka, *Electrochimica Acta*, 47, 47-53 (2001)

2) T. Homma, H. Nakai, M. Onishi, T. Osaka, *J. Phys. Chem. B*, 103, 1774-1778 (1999)

3) H. Nakai, T. Homma, I. Komatsu, T. Osaka, *J. Phys. Chem. B*, 105, 1701-1704 (2001)

4) H. Nakai, *Chem.Phys.Lett.*, 363, 73-79 (2002)

21COE International Symposium on 'Practical Nano-Chemistry',
早稲田大学（東京），2003 年 12 月.

原子核と電子の運動を量子的に取り扱う ab initio NOMO法の開発

袖山慶太郎，中井浩巳

早稲田大学理工学部化学科　東京都新宿区大久保3-4-1
sodeyama@suou.waseda.jp

従来の多くの化学計算は、原子核は動かないものとするBorn-Oppenheimer (BO)近似を採用しており、そこから得られる電子の波動関数のみを用いて様々な化学現象を取り扱ってきた。それに対して、原子核と電子の運動の両方を同時に量子的に扱うことのできるab initio NOMO (Nuclear Orbital and Molecular Orbital)法[1]では、電子と同時に原子核の波動関数も求めることが可能である。原子核を量子的に扱えるという特性を活かして、これまでに我々はプロトン・トンネリングといった原子核の量子論的効果が重要な系や、分子の振動といった原子核が運動している状態に対してab initio NOMO法を適用し、一定の成果を収めてきた[2]。Figure 1にマロンアルデヒド(MA)分子におけるプロトン・トンネリング波動関数を示す。広がった核の波動関数が重なって、トンネリングパスができていることがわかる。また、Figure 2にHeH^+およびLiH分子における、振動励起状態と振動基底状態の間の差核密度図を示す。より白くなっている部分が、振動励起したことにより核密度の増えた部分を表しており、異核二原子分子が振動している様子が表現されていることがわかる。

Figure 1. Proton density map in MA.

更なるab initio NOMO法の発展のために定量性の向上は重要な課題である。これまでに、電子と原子核の相関を多体効果により考慮する、NOMO/MBPT, CCD法を開発してきた[3]。この方法でも、原子の核電荷が大きくなるにつれて、計算精度が悪くなっていくことがわかっている。したがって、より重い元素に対しても定量的な理論を開発するため、電子-電子間の近距離相互作用を考慮できるTranscorrelated Hamiltonian[4]を用いる方法をab initio NOMO法に適用する。近距離相互作用を表す関数には、frozen Gaussian geminal (FROGG)[5]を用いる。

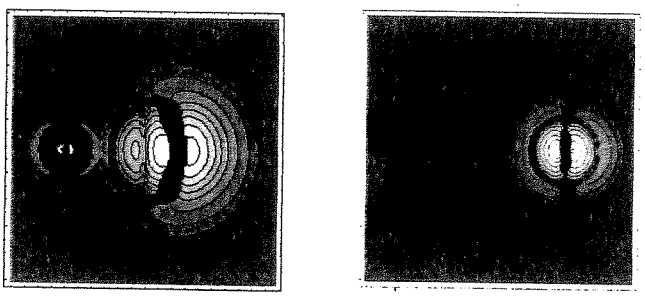

HeH^+　　LiH

Figure 2. Nuclear density difference maps for the vibrational excitations ($v = 0 \rightarrow 1$) of HeH^+ and LiH.

[1] H. Nakai, *Int. J. Quantum Chem.*, **86**, 511 (2002).
[2] H. Nakai, K. Sodeyama, M. Hoshino, *Chem. Phys. Lett.*, **345**, 118 (2001).
[3] H. Nakai, K. Sodeyama, *J. Chem. Phys.*, **118**, 1119 (2003).
[4] S. F. Boys, N. C. Handy, *Proc. Roy. Soc. A*, **310**, 43 (1969).
[5] S. Ten-no, *Chem. Phys. Lett.*, **330**, 169 (2000).

Development of ab initio NOMO theory : quantum mechanical treatment for nuclear and electronic motions

Keitaro Sodeyama and Hiromi Nakai
Department of Chemistry, Waseda University, Ohkubo, Shinjuku-ku, Tokyo 169-8555, Japan.
E-mail: sodeyama@suou.waseda.jp

21COE International Symposium on 'Practical Nano-Chemistry',
早稲田大学（東京），2003 年 12 月.

P34

AIMDとEDAを使ったエネルギー移動過程の解析

山内佑介，中井浩巳

早稲田大学理工学部化学科　東京都新宿区大久保3-4-1
yamauchi@ruri.waseda.jp

化学反応における原子核の運動を時々刻々と追跡するためのツールとしてab initio molecular dynamics(AIMD)シミュレーションが広く用いられるようになってきた。この手法はab initio計算によって得られた力場を用いて古典運動方程式を解くことで、従来の分子シミュレーションで困難とされた結合の生成や開裂を伴う化学反応のダイナミクスを取り扱うことができる。我々は以前AIMDシミュレーションを用いてソラレンの励起状態ダイナミクスやクラスターイオン衝突反応メカニズムを明らかにした[1, 2]。AIMDの手続きに見られるように化学反応は全系のポテンシャルエネルギー超曲面上の安定な経路に沿って進行するとされるが、それにともなう局所的なエネルギー変化が問題になることも多い。この問題に対する解析手法として、当研究室でenergy density analysis(EDA)が提案された[3]。EDAはKohn-Shamの密度汎関数理論(KS-DFT)に基づいて分子の全エネルギーを各原子に分割することで、局所的なエネルギーの安定化あるいは不安定化を記述できる。本研究ではAIMDとEDAを用いて化学反応におけるエネルギー移動を研究した。

EDAによって原子ごとに分割されたエネルギーは以下の式となる。

$$E^A = T_S^A + E_{NE}^A + E_{CLB}^A + E_{XC}^A + E_{NN}^A \qquad (1)$$

右辺の各項はそれぞれ運動、核電子引力、古典的クーロン、KS交換相関、核間反発のエネルギーを示している。ここでエネルギーは、Mullikenの電子密度解析と同様に、KS軌道について和をとることで各原子に分割される。たとえば

$$E_{CLB}^A = \frac{1}{2}\sum_{\mu\in A}(\mathbf{PG})_{\mu\mu}, \text{ where } \quad G_{\nu\mu} = \sum_{\rho}\sum_{\sigma} P_{\rho\sigma}(\chi_\nu\chi_\mu \mid \chi_\sigma\chi_\rho) \qquad (2)$$

である。KS交換相関エネルギーについては、グリッドの重み関数と分割関数を使って分割した。

AIMDにおけるMD部分には以下に示す速度Verletアルゴリズムを利用している。

$$\mathbf{r}^{n+1} = \mathbf{r}^n + \Delta t\,\mathbf{v}^n + \frac{(\Delta t)^2}{2m}\mathbf{f}^n, \quad \mathbf{v}^{n+1} = \mathbf{v}^n + \frac{\Delta t}{2m}(\mathbf{f}^{n+1} + \mathbf{f}^n) \qquad (3)$$

ここでΔtはMDにおける時間ステップである。今回は本研究室で開発したMDおよびEDAプログラムを電子状態計算プログラムであるGAMESS-USとリンクして実行した。

右図に$NH_4^+(NH_3)_2 + NH_3$衝突過程のシミュレーション結果を示す。全系のエネルギーをモノマーごとに分割している。NH_3(3)がクラスターに衝突し、クラスターからNH_3(1)が分解した。時間t=0 [fs]におけるNH_3(3)のエネルギーは-56.486 [a.u.]、t=2500におけるNH_3(1)のエネルギーは-56.481であり、-0.005のエネルギーが移動している。

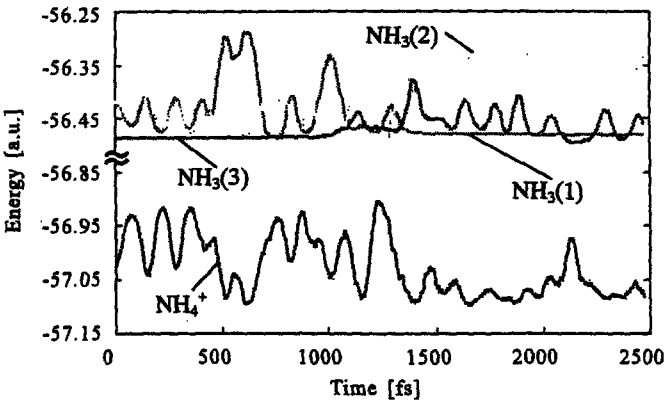

[1] H. Nakai, Y. Yamauchi, A. Matsuda, Y. Okada, and K. Takeuchi, *J. Mol. Structure (Theochem)* **592**, 61 (2002).
[2] H. Nakai, Y. Yamauchi, A. Nakata, T. Baba, and H.Takahashi, *J. Chem. Phys.* **119**, 4223 (2003).
[3] H. Nakai, *Chem. Phys. Lett.* **363**, 73 (2002).

ANALYSIS FOR ENERGY TRANSFER USING AIMD AND EDA.

Yusuke Yamauchi and Hiromi Nakai
Department of Chemistry, Waseda University, Ohkubo, Shinjuku-ku, Tokyo 169-8555, Japan.
E-mail: yamauchi@ruri.waseda.jp

21COE International Symposium on 'Practical Nano-Chemistry',
早稲田大学（東京），2003 年 12 月.

TDDFT法によるソラレン化合物のDNA光付加反応に関する理論的研究

中田彩子，中井浩巳

早稲田大学理工学部化学科　東京都新宿区大久保3-4-1
ayakota@asagi.waseda.jp

【緒言】ソラレン化合物は乾癬などの皮膚病の治療薬であり、DNA中のチミン残基と2段階光付加反応を起こして、DNAの異常増殖を抑制する。1段階目では、UV-A(300-400nm)光を照射することによって、ソラレンのフラン環、ピロン環の2つの光活性部位のうち一方がチミン残基に付加してモノ付加体を生成する(Step-I)。それらが更にUV-A光を吸収すると、もう一方の環が別のチミン残基と2段階目の付加反応を起こしてジ付加体を作りDNA間を架橋する(Step-II)。しかしジ付加体は副作用の原因となるため、２段階目の付加反応を起こさないソラレン化合物の開発が重要である。このような背景からソラレン化合物の励起状態に対して様々な実験的研究が行われている。その結果、特に治療に効果的である8-メトキシソラレン(8-MOP)だけが三重項(T_1)状態での挙動が異なることや、フランモノ付加体は2段階目の付加反応を起こすが、ピロンモノ付加体は起こさないことが確認されている。しかし、これらの原因は明らかでなかった。本研究では、量子化学的手法を用いてソラレン化合物の励起状態を求め、8-MOPのT_1状態における特異性の原因を探り、治療における効果との関連を調べる。また、フランモノ付加体、ピロンモノ付加体に対しても励起状態を考察し、ピロンモノ付加体が2段階目の付加反応を起こさない原因を解明する。
【結果】各化合物の安定構造をDFT計算によって求め、その構造における励起状態をTDDFT法で求めた。ソラレン・5-MOPではT_1状態で、S_0状態の安定構造に近い閉環構造と、O1-C2結合が開裂した開環構造が得られた。8-MOPはT_1状態で他の化合物より開環構造が安定化しており、閉環安定構造は得られなかった[1]。フランモノ付加体においても8-MOPはT_1状態では開環安定構造をとる。これらの開環構造では2段階目の反応部位が結合交替のため単結合化しているため、2段階目の付加反応は起こらない。そのため8-MOPからは副作用の原因となるジ付加体が生成されないことが分かった。一重項励起状態に関して、ソラレン化合物単体でのUVスペクトルをかなり良い精度で再現し、各励起状態を帰属することができた。モノ付加体では、4',5'位か3,4位の活性部位がなくなるため、励起配置や励起エネルギーが二つのモノ付加体で大きく異なる。$S_0 \rightarrow S_1$励起エネルギーはソラレン化合物の単体、フランモノ付加体、ピロンモノ付加体の順で大きくブルーシフトしている。特に、ピロンモノ付加体はUV-A光の範囲では励起されないため、ピロンモノ付加体を経由してジ付加体が生成されることはないことが示された[2]。

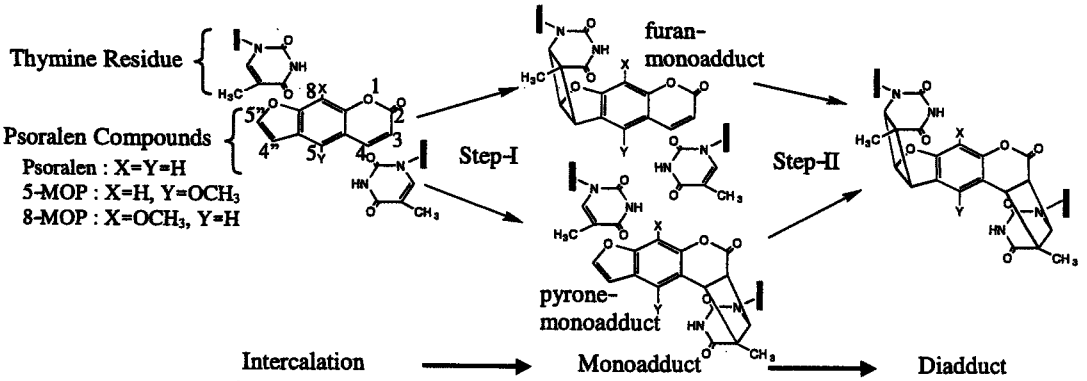

Fig. 1. Photoaddition scheme of psoralen compound to DNA.

[1] H. Nakai, Y. Yamauchi, A. Nakata, T. Baba, H. Takahashi, *J. Chem. Phys.*, **119**, 4223 (2003).
[2] A. Nakata, T. Baba, H. Takahashi, H. Nakai, *J. Comput. Chem., in press.*

THEORETICAL STUDY OF THE PSORALEN-DNA PHOTOADDITION REACTION BY TIME DEPENDENT DENSITY FUNCTIONAL THEORY

Ayako Nakata and Hiromi Nakai
Department of Chemistry, Waseda University, Ohkubo, Shinjuku-ku, Tokyo 169-8555, Japan.
E-mail: ayakota@asagi.waseda.jp

21COE International Symposium on 'Practical Nano-Chemistry',
早稲田大学（東京），2003 年 12 月.

無電解析出における還元剤酸化反応機構の理論的解析

島田拓哉[1]、本間敬之[1]、中井浩巳[2]、逢坂哲彌[1]

[1]早稲田大学理工学研究科応用化学専攻　東京都新宿区大久保3-4-1
[2]早稲田大学理工学研究科化学専攻　東京都新宿区大久保3-4-1
takuya@fuji.waseda.jp

無電解めっきは外部電源を使用しない薄膜形成プロセスであり，エレクトロニクスなどの様々な分野において広く用いられ，工業的に重要な技術の１つとなっている．しかしこの反応は固液界面での金属イオンのカソード析出反応と還元剤のアノード酸化反応が並列して進行するため，種々の電荷移動を伴う．更に析出した金属が還元剤の酸化反応に対して触媒活性を持たなければ析出が連続的に起こらない為，この析出機構は複雑で不明な点も多い．今後ナノレベルでのより精密な析出挙動の制御を行うことが求められており，反応機構の詳細な解析が必要になっている．

本検討ではこの析出機構の中でも最も重要な還元剤の酸化反応に注目し，反応中間体のエネルギーや電荷を原子・分子レベルから解析可能な理論計算を用いて詳細な解析を行った．代表的還元剤であるジメチルアミンボラン(DMAB)，次亜リン酸，及びホルムアルデヒドの酸化反応に着目し，孤立系並びに金属(Cu，Ag，Pd)表面上におけるこれら還元剤の反応機構を検討した．更にはEnergy Density Analysis(EDA)[1]を用いて触媒活性に影響を与える因子の究明を行った．

計算にはGaussian98を用い，EDAにはオリジナルのプログラムを組み込んで改良したHONDO99を用いた．分子の構造最適化並びにエネルギー計算には密度汎関数法(DFT)を用いた．パラメータにはB3LYPを用いた．金属表面はCu，Ag，Pdの(1 1 1)面，構成原子を４及び22とする金属クラスターモデルを用いた．基底関数としてB,C,P,Hには6-31G**，N,Oには分散関数を組み込んだ6-31+G**，金属にはHay & Wadt ECPを用いた．

Fig.1に代表的還元剤の酸化反応を示す．Meerakkerによって提案された3配位中間体を経由する4ステップの経路に対して，従来の我々の検討より先に水酸基の配位が起こる5配位中間体を経由する経路を提案している[2]．金属表面(Cu，Ag，Pdクラスター)上での還元剤の最適構造並びに系全体のエネルギー計算を各ステップで行いダイアグラムを作成し，比較検討を行った．

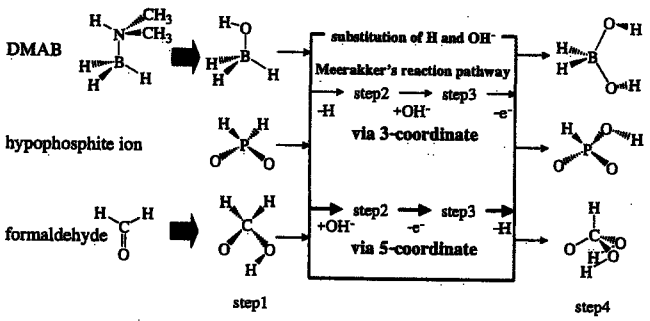

Fig.1 reaction pathways of typical reductants

その結果，DMAB，次亜リン酸では孤立系においては５配位中間体経由，ホルムアルデヒドでは変則的な5配位経由が有利であることが示唆され，金属上では全て５配位経由が有利な経路であることが示唆された．

更にEDAを用いて原子ごとの吸着前後のエネルギー差を計算した結果をFig.2に示す．Fig.2より吸着によって金属クラスターが安定化し，逆に還元剤分子は不安定化している．つまり，この不安定化が次のステップへの駆動力になると考えられ，この金属表面の還元剤に対する不安定化が触媒活性の要因の一つであると示唆された．

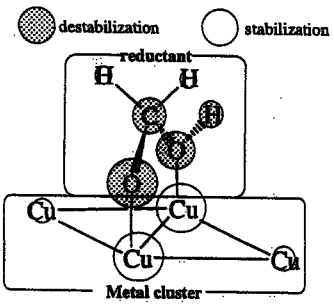

Fig.2 EDA of formaldehyde(step1) on Cu

[1] H. Nakai, Chem. Phys. Lett. **363** 73 (2002)
[2] T. Homma, H. Nakai, I. Komatsu, A. Tamaki, and T. Osaka, Electrochimica Acta, **47**, 47 (2001)

THEORETICAL STUDY OF OXIDATION MECHANISM OF REDUCTANTS FOR ELECTROLESS DEPOSITION PROCESS

Takuya Shimada[1], Takayuki Homma[1], Hiromi Nakai[2], Tetsuya Osaka[1]
[1]Major in Applied Chemistry, [2]Chemistry, Graduate School of Science and Engineering, Waseda University, Okubo, Shinjuku-ku, Tokyo 169-8555, Japan.　E-mail: takuya@fuji.waseda.jp

表面技術協会第 109 回講演大会,
東京都立大学（東京），2004 年 3 月.

無電解銀めっきにおける還元剤酸化反応機構の理論計算解析

（早大理工）○島田拓哉，中井浩巳，本間敬之，逢坂哲彌

キーワード｛無電解銀めっき，還元剤，触媒活性，理論計算解析｝

1. 緒言　無電解銀めっきプロセスはエレクトロニクス分野をはじめとした先端領域で検討が進められているが，その反応は一般の無電解めっきと同様に複雑であることが知られており，現在もその詳細な解明は殆ど行われていないのが現状である．これまでに我々は理論計算を用いて Cu 表面での還元剤酸化反応の分子レベルからの解析を行っている [1]．本検討では代表的還元剤であるホルムアルデヒド，ジメチルアミンボラン(DMAB)，次亜リン酸の Ag 表面での反応機構の解析を行い，さらに Ag 表面の還元剤に対する触媒活性発現の起源についてエネルギー密度解析(EDA)を用いた検討を行った．

2. 検討方法　計算には Gaussian98 を用い，EDA にはオリジナルのプログラムを組み込んで改良した GAMESS を用いた．分子の構造最適化並びにエネルギー計算には密度汎関数法(DFT)を用いた．パラメータには B3LYP を用いた．金属表面は Ag，Cu，Pd の(1 1 1)面，構成原子を 4 及び 22 とするクラスターモデルを用いた．基底関数として B,C,P,H には 6-31G**, O には分散関数を組み込んだ 6-31+G**, 金属には Hay & Wadt ECP を用いた．

3. 結果及び考察　本検討で用いた 3 種類の還元剤はすべて Cu 表面と同様に，Ag 表面でも Scheme1 に示すような 5 配位中間体を経由する経路であることが示唆された．

更に Ag 表面の還元剤に対する触媒活性を検討するために，EDA を用いて各反応座標における全エネルギーを原子ごとに分割し，Ag_4 クラスター上での還元剤及び Ag_4 クラスター自身にエネルギーを割り振ってまとめた表を Table 1 に示す．その結果，Ag 表面が触媒活性を示さない次亜リン酸の反応の場合のみ Ag_4 クラスターのエネルギー変化が小さく，特に電子放出過程が不安定化する(Table 1 下線部)．つまり Ag 表面の次亜リン酸酸化反応に対する影響が小さく，電子が放出されにくい傾向が見られた．他の金属表面を用いた場合と比較検討を行った結果，触媒活性を示さない組み合わせの場合のみ特に電子放出過程の金属クラスターの安定化に差異が見られたことから，この電子放出過程が金属表面の還元剤酸化反応に対する金属触媒活性を司る要素の一つであることが示唆された．

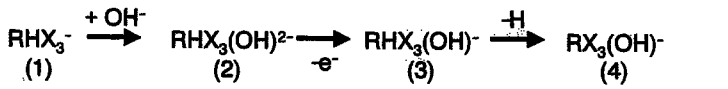

R=formaldehyde:C, DMAB:B, hypophosphite ion:P　X=H and/or OH

Scheme 1 Reaction pathway of reductants via five-coordinate intermediate

Table 1 Energy shift of reductants and clusters by EDA (kJ/mol)

reaction steps	(1)	(2)	(3)	(4)
formaldehyde	0.00	358.15	257.81	146.79
Ag_4	0.00	-121.63	-171.33	1.40
total	0.00	236.52	86.48	148.20
DMAB	0.00	656.69	582.05	326.59
Ag_4	0.00	-306.71	-417.69	-215.39
total	0.00	349.99	164.36	111.20
hypophosphite ion	0.00	232.97	110.65	117.87
Ag_4	0.00	-6.55	3.59	-8.59
total	0.00	226.42	114.24	109.28

4. 参考文献

1) T. Homma, A. Tamaki, H. Nakai, and T. Osaka, *Journal of Electroanalytical Chemistry*, **559**, 131 (2003).

○Takuya SHIMADA, Hiromi NAKAI, Takayuki HOMMA, Tetsuya OSAKA

日本化学会第 84 回春季年会,
関西学院大学（西宮），2004 年 3 月.

結合領域へのエネルギー密度の分割法

（早大理工）○菊池那明・中井浩巳

Partitioning of Energy Density for Chemical Bond Region (Waseda Univ.)
KIKUCHI, Yasuaki; NAKAI, Hiromi

緒言　分子内の化学結合を理解することは、昔から化学的・物理学的に非常に重要である。当研究室では最近、量子化学計算により得られた全エネルギーを構成原子ごとに分割する解析手法、Energy Density Analysis (EDA)[1]を開発し、その有用性を確かめてきた。本研究ではこれを結合領域へと拡張し、化学結合や分子間相互作用をより詳細に解析する方法、Bond EDA (BEDA)を提案する。また、種々の化学的現象に応用する。

理論　EDA は主に、Mulliken の電子密度解析の類推を用いた分割スキームを採用している。Mulliken の電子密度解析では、その非対角項を用いて結合次数を見積もることができる。BEDA ではそれと同様、EDA の非対角項を用いて結合エネルギーを見積もる。

結果と考察　エタンとエチレン両分子の化学結合を、BEDA を用いて検討した。計算レベルは HF/cc-pVDZ である。図 1 はエタンに対して BEDA を適用した結果である。結合が存在する炭素—炭素間、炭素—水素間のエネルギー密度は絶対値の大きな負の値を持ち、結合による安定化を示している。結合していない水素—水素間、炭素—水素間では絶対値の小さい正の値を持ち、これは立体効果に対応するものと考えられる。また、水素—水素間のエネルギー密度はその距離に依存して小さくなっている。図 2(a),(b),(c)はそれぞれエチレンの基底状態、平面および bisect 構造をした三重項状態に対して BEDA を適用した結果である。炭素—炭素結合における結合エネルギー密度は結合次数の減少とともに不安定化しており、図 2(c)の炭素—炭素結合は一重結合であるエタン（図 1）のそれとほぼ等しい。

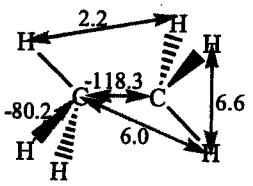

図 1. エタン分子のエネルギー密度

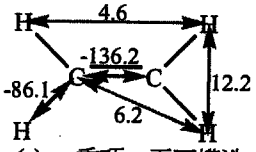

(a) 一重項・平面構造

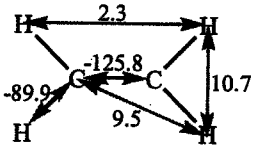

(b) 三重項・平面構造

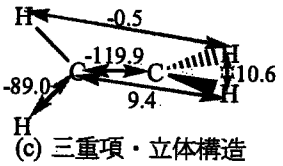

(c) 三重項・立体構造

図 2. エチレン分子のエネルギー密度

[1] H. Nakai, *Chem. Phys. Lett.*, 363, 73-79 (2002).

日本化学会第 84 回春季年会，
関西学院大学（西宮），2004 年 3 月．

Ab initio NOMO 法における並進・回転運動の分離に関する一考察

（早大理工）　○宮本開任・袖山慶太郎・中井浩巳

Removal of translational and rotational motions from nuclear wave function: *ab initio* NOMO theory (School of Science and Engineering, Waseda University) MIYAMOTO, Kaito; SODEYAMA, Keitaro; NAKAI, Hiromi

【緒言】当研究室では、電子と核を同時に量子的に扱うことのできる Nuclear Orbital + Molecular Orbital (NOMO)法[1-4]の開発を行ってきた。現在、同様の方法を研究するグループが世界的に増えてきているが、大きく分けて二つの流れがある。一つは、Adamowiczらによる geminal で電子と核の軌道を表現する方法[5]であり、定量性には優れているが、計算コストが莫大になるため 3 原子分子ですら計算できないといった問題点がある。もう一つは当研究室が行っている Gauss 関数で電子と核の軌道を表現する方法である。これは計算コストが前者に比べ短縮でき、また、巨大系の注目している部分に関して選択的に核を量子的に扱うことが可能である。Gauss 関数では、振動・並進・回転という核の運動のうち、振動状態の記述は得意である反面、並進・回転を正確に記述できず、定量性に問題が生じる。今回は、この並進および回転運動を分離する方法を提案する。

【並進運動の分離】NOMO 法の波動関数を厳密な並進運動の波動関数((1)式)に射影することによって NOMO 法の核の波動関数の並進運動成分を求める。この波動関数の並進運動成分を(2)式で表す。ここで Ψ_{3N}^{n} は、NOMO 法の核の波動関数を表す。このとき、NOMO 法におけるエネルギーの並進運動成分は(3)式で表される。ここで **k** は厳密な並進運動の波動関数の波数ベクトルを表している。

$$\psi_T = \exp(i\mathbf{k}\cdot\mathbf{r}_G) \qquad (1)$$

$$|\Psi_{Trans}\rangle = \int_{-\infty}^{\infty} d\mathbf{k} |\psi_T\rangle\langle\psi_T|\Psi_{3N}^{n}\rangle \qquad (2)$$

$$E_{Trans} = \int_{-\infty}^{\infty} d\mathbf{k} \langle\Psi_{3N}^{n}|\psi_T\rangle\langle\psi_T|-\sum_{M}^{N}\frac{1}{2m_M}\nabla_M^2|\psi_T\rangle\langle\psi_T|\Psi_{3N}^{n}\rangle \qquad (3)$$

H_2 分子への適応例を以下に示す。(2)式の下線で示してある部分は H_2 分子の核の波動関数と並進運動の波動関数の重なりを示している。(3)式の点線部はある波数 **k** における H_2 分子のエネルギーのうち NOMO 波動関数に混入している並進運動エネルギーを表している。そのエネルギーの分布を図 1 に示す。高い準位の並進運動が NOMO 法の核の波動関数に混入しているため NOMO 法のエネルギーが大きくなっていることが分かる。

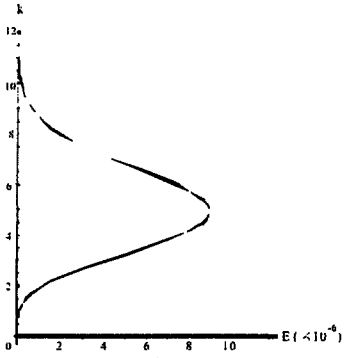

図 1. NOMO 波動関数に混入している並進運動エネルギーの分布 [hartree]

【回転運動の分離】NOMO 法の波動関数を回転運動の波動関数((4)式)に射影することによって NOMO 法の核の波動関数に含まれる回転運動成分を求める。本来、振動と回転はカップルしているが今回は近似的に回転運動の波動関数を剛体回転子の波動関数とみなしている。このとき、NOMO 法におけるエネルギーの回転運動成分は(5)式で表される。

$$|\Psi_{Rot}\rangle = \sum_{l}|\psi_R^{l}\rangle\langle\psi_R^{l}|\Psi_{3N}^{n}\rangle \qquad (4)$$

$$E_{Rot} = \sum_{l}\langle\Psi_{3N}^{n}|\psi_R^{l}\rangle\langle\psi_R^{l}|-\sum_{M}^{N}\frac{1}{2m_M}\nabla_M^2|\psi_R^{l}\rangle\langle\psi_R^{l}|\Psi_{3N}^{n}\rangle \qquad (5)$$

[1] M. Tachikawa, K. Mori, H. Nakai, K. Iguchi, Chem. Phys. Lett., 290 (1998) 437.
[2] H. Nakai, Int. J. Quantum Chem., 86 (2002) 511.
[3] H. Nakai, K. Sodeyama, M. Hoshino, Chem. Phys. Lett., 345 (2001) 118.
[4] H. Nakai, K. Sodeyama, J. Chem. Phys., 118 (2003) 1119.
[5] M. Cafiero, S. Bubin, L. Adamowicz, Phys. Chem. Chem. Phys., 5 (2003) 1491.

ナノ学会第2回大会,
学士会館（東京），2004年5月.

量子化学計算における新しい解析法の開発と応用：Energy Density Analysis

Development of new analyzing technique for electronic-structure calculation: Energy Density Analysis

河村芳海，菊池那明，馬場健，河東田道夫，石井基樹，中井浩巳
（早大理工）

Abstract: We have recently proposed a new analyzing technique for the electronic-structure calculation termed energy density analysis (EDA), which partitions the total energy of molecular system into the atomic contributions. In this study, we have extended the EDA technique to repartition the energy into the atoms and bond region (Bond-EDA) (i), to QM/MM methods (ii), to combine with the energy decomposition methods (Interaciton-EDA) (iii).

近年の電子状態理論の発展と計算機の進歩により、ナノサイズの分子に対しても高精度な量子化学計算を行うことが可能になりつつある。電子状態計算で得られるエネルギーは単一の量であり、特に系内のエネルギー移動などをみることは困難である。当研究室で提案した Energy Density Analysis [1] は、HF および DFT 計算で得られる全エネルギーを構成原子に分割する簡便な解析方法で、これまで様々な系に適用してその有用性を確認してきた [2-4]。本研究では、EDA の有用性をさらに広げるためにいくつかの方法論的な拡張を行った。

(i) 結合領域へのエネルギーの分割：これまで原子のみに分割していたエネルギーを、結合領域にも分割するように再定式化した(Bond-EDA)。これにより励起や化学反応に伴う系内の結合エネルギーの変化を見積もることができる。

(ii) QM/MM 法との組み合わせ：QM/MM 法に対して EDA 法を拡張することにより、MM 場存在下における QM 部のエネルギーを見積もることを可能にした。これにより、イオン結晶における Madelung ポテンシャル存在下のクラスターや、溶媒効果を考慮した場合の溶質のエネルギーを見積もることにより、MM ポテンシャルの妥当性の評価を行った。

(iii) エネルギー分割法との組み合わせ：分子間相互作用の詳細な解析のために、Kitaura-Morokuma 法など、相互作用エネルギーを物理的に意味のあるいくつかのコンポーネントに分割する方法が古くから提案されている。そのひとつである Reduced Variational Space (RVS) SCF 法と EDA を組み合わせることにより、相互作用エネルギーコンポーネントを局所領域に分割する手法を開発した (Interaction-EDA)。Si(100)表面に対する CO 分子吸着対する Interaction-EDA の結果を Table 1 に示す。反発的相互作用である静電-交換相互作用のほとんどは、C 原子と吸着サイトの Si 原子(A-1L)のみに由来することがわかる。また、吸着子から表面への電子移動相互作用は、σ-donation により C 原子が不安定化、A-1L, 2L の Si 原子を安定化させていることがわかる。

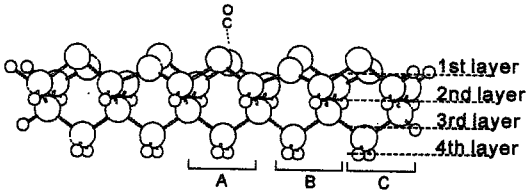

Figure 1. CO adsorption onto $Si_{33}H_{28}$ cluster.

Table 1. Interaction-EDA results for CO adsorption on $Si_{33}H_{28}$ cluster in kcal/mol.

		ES+EX	PL		CT		Total	Full variational
			S	A	S→A	A→S		
Adsorbate	O	-1.2	0.0	6.1	1.0	2.0	7.8	7.4
	C	34.5	-23.7	-14.6	-19.0	29.2	6.4	13.9
A	1L	39.8	3.4	-9.6	0.5	-50.4	-16.2	-14.2
	2L	-4.3	6.5	0.0	1.6	-5.1	-1.3	-7.5
	3L	-0.5	2.9	1.3	0.2	0.4	4.3	5.2
	4L	-0.9	0.4	-0.8	0.0	-0.6	-2.0	-1.2
B	1L	-0.6	-0.9	-0.6	1.0	-0.6	-1.7	-2.7
	2L	-0.1	-0.4	-0.1	0.3	-0.1	-0.4	-0.5
	3L	0.2	-0.2	0.3	-0.1	0.2	0.4	0.0
	4L	-0.7	-0.6	-0.5	0.3	-0.4	-1.9	-1.3
C	1L	0.0	0.1	0.0	0.0	0.0	0.0	-0.1
	2L	0.0	0.0	-0.1	0.1	-0.1	-0.1	-0.1
	3L	0.0	0.0	0.0	0.0	0.0	0.0	0.0
	4L	-0.1	0.0	-0.1	0.1	-0.1	-0.2	-0.1
Total		65.1	-16.0	-18.8	-11.4	-25.9	-7.0	-8.1

[1] H. Nakai, Chem. Phys. Lett., 363 (2003) 73.
[2] H. Nakai, K. Sodeyama, Chem. Phys. Lett., 365 (2002) 203.
[3] Y. Kawamura, H. Nakai, Chem. Phys. Lett., 368 (2003) 673.
[4] H. Nakai, K. Sodeyama, J. Mol. Structure (THEOCHEM), 637 (2003) 27.

* Yoshiumi Kawamura, Yasuaki Kikuchi, Takeshi Baba, Michio Katouda, Motoki Ishii, Hiromi Nakai: Dept. of Chemistry, Waseda Univ., Tokyo 169-8555

ナノ学会第 2 回大会,
学士会館（東京），2004 年 5 月.

AIMD シミュレーションを用いたクラスターの反応ダイナミクスに関する理論的研究

Theoretical study on the reaction dynamics of cluster using AIMD simulation

渥美照夫、小澤志保、山内佑介、中井浩巳
（早大理工）

Abstract: Reaction dynamics of collision reactions between small clusters and typical molecules were investigated using *ab initio* molecular dynamics (AIMD) simulation. Collision reactions of (i) copper cluster ion with methanol, (ii) protonated water cluster with nitrogen and (iii) ammonium cluster ion with ammonia monomer were dealt with. Short-time Fourier spectrum analysis was used for understanding the time development of vibrational modes in the non- equilibrium dynamics.

ナノクラスターの反応制御は理論的また工業的に重要な課題である。中でも小さなサイズのクラスターの衝突反応についての研究は結晶成長初期過程のモデルとして広く行われてきた。結晶成長の初期過程は核生成とよばれ、マジックナンバーの存在など小さなサイズ特有の挙動を示すことが知られている。本研究では *ab initio* molecular dynamics (AIMD) シミュレーションを用いて、(i)銅クラスターイオンとメタノール、(ii)水クラスターイオンと窒素分子、(iii)アンモニアクラスターイオンとアンモニアモノマーの衝突反応を取り扱った。

例として(iii)のアンモニアクラスターイオンとモノマーの衝突反応の結果を示す。AIMD シミュレーションでは、以下の 3 つの反応過程が見られた。

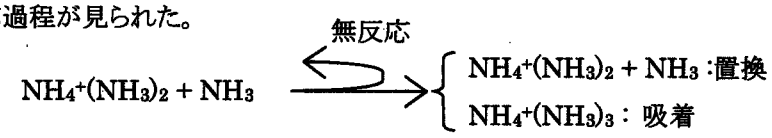

Fig. 1 は短時間フーリエ変換によって得られた衝突過程における無反応衝突と吸着反応に対して得られたスペクトログラムである。スペクトログラムとは、反応過程における各原子の速度相関関数を短時間フーリエ変換したもので、分子振動の時間発展を表している。無反応衝突に比べて、吸着反応では低波数の振動が誘起されていることがわかる。

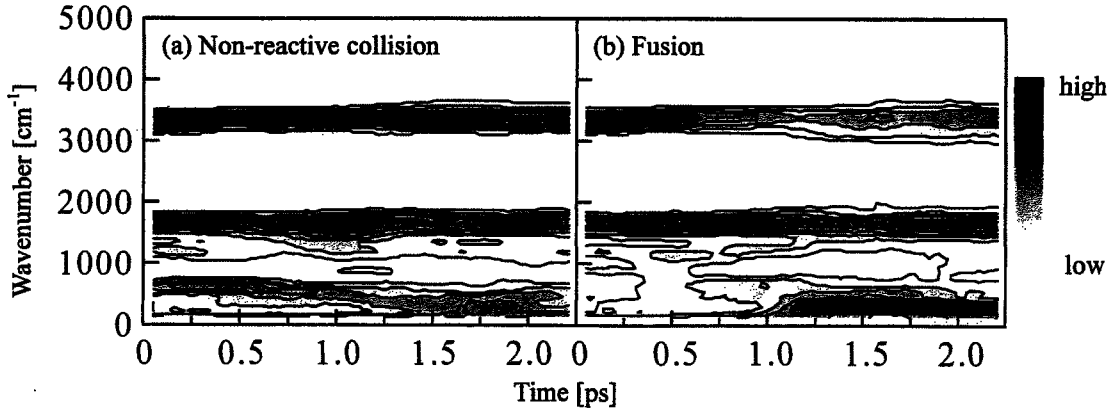

Fig. 1. Spectrogram for (a)non-reactive collision and (b)fusion process of collision reaction between $NH_4^+(NH_3)_2$ and NH_3.

Teruo Atsumi, Shiho Ozawa, Yusuke Yamauchi, Hiromi Nakai: Dept. of Chem., Sch. of Sci. & Eng., Waseda Univ., Tokyo 169-8555

日本コンピュータ化学会 2004 春季年会,
東京工業大学（東京），2004 年 5 月.

2002

内殻励起ダイナミクスに対する Wavelet 変換を用いた解析

○大塚 教雄、中井 浩巳
早稲田大学理工学部化学科（〒169-8555 東京都新宿区大久保 3-4-1）

【緒言】1986 年、仏国の Morin と Nenner らによる HBr のオージェ崩壊前の内殻励起状態での原子移動という新しい概念の実験報告以降、内殻励起状態の緩和過程を解明する研究が盛んに行われてきた。近年では、光電子またはオージェ電子と生成物の同時計測技術が確立し、固体表面吸着物や有機高分子表面からの解離生成物と共鳴内殻励起依存性が詳細に研究され、内殻励起状態での分子運動との密接な関係が示唆されている。内殻励起・内殻イオン化状態の寿命内で起こる大きな分子構造の変化は、脱励起後の分子の断片化・イオン化反応の理解に重要となってくる。内殻励起から電子緩和までの時間スケールは、一般に数 10 フェムト秒オーダーの超高速緩和であるため、そのダイナミクスを理解することは難しい。本研究では、約 100 フェムト秒内の内殻励起状態にある分子運動に焦点をしぼり、ab initio 分子動力学法（ab initio MD）による計算とウェーブレット変換を用いた解析から内殻励起分子のダイナミクスに関する知見を報告する。

【方法】ウェーブレット変換は、マザーウェーブレットと呼ばれる基底関数によって、時系列を切り出した時の信号の大きさを示すものである。解析対象となる時系列 $x(t)$とマザーウェーブレット $\psi(t)$によって、

$$W(t',s)=\frac{1}{\sqrt{s}}\int_{-\infty}^{\infty}x(t)\overline{\psi}\left(\frac{t-t'}{s}\right)dt$$

と定義される。s と t'によってマザーウェーブレットの伸縮比、シフト量を決定することにより、基底状態－内殻励起状態の時間－周波数解析を行うことができ、ある周波数成分のエネルギーが特定の時間にどれだけ存在していたかを見ることができる。

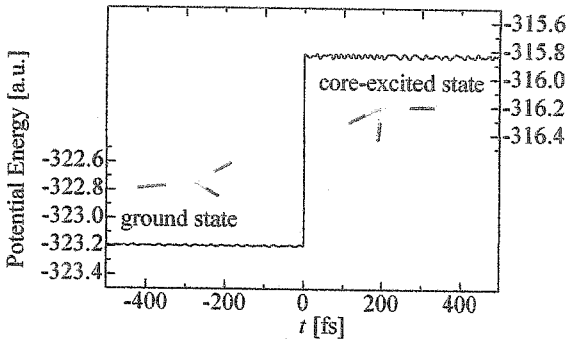

Fig 1. Time development of potential energy.

【結果】BF_3 分子の内殻励起ダイナミクスの結果を示す。ab initio MD 計算は、速度 Verlet 法に基づいたアルゴリズムを用い、内殻励起状態は CI-singles レベルで計算を行った。図 1 は、ポテンシャルエネルギーの時間発展を示している。$t=0$ で基底状態から内殻励起状態へ励起される。内殻励起に伴い BF_3 分子は平面構造からピラミッド構造への構造変化を示した。図 2 に速度自己相関関数のウェーブレット変換の結果を示す。横軸は時間軸、縦軸は振動数である。内殻励起状態におけるウェーブレット解析からは、100 fs 以内に 500 cm^{-1} から 700 cm^{-1} の振動数幅を見ることが出来る。特に 50 fs 付近で 600 cm^{-1} 付近の振動ピークが見られ、これは A_1 対称性の変角振動に対応し、内殻励起寿命内の大きな分子構造変化を支持する。また振動エネルギーの分布は、基底状態の E'対称性振動から内殻励起状態の E 対称性、そして A_1 対称性振動へと移動していることが見られた。発表当日は更に詳細な報告を行う。

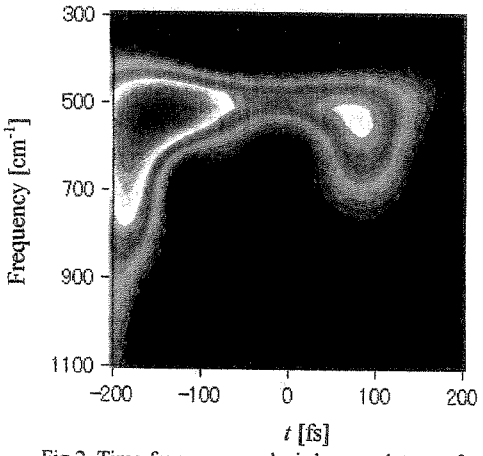

Fig 2. Time-frequency analysis by wavelet transform.

日本コンピュータ化学会 2004 春季年会,
東京工業大学（東京），2004 年 5 月.

2O01

結合エネルギー密度解析(Bond-EDA)の開発とその応用

○菊池 那明、中井 浩巳
早稲田大学理工学部化学科（〒169-8555 新宿区大久保 3-4-1）

【緒言】

分子内の化学結合を理解することは、昔から化学的・物理学的に非常に重要である。当研究室では最近、量子化学計算により得られた全エネルギーを構成原子ごとに分割する解析手法、Energy Density Analysis (EDA)[1]を開発し、その有用性を確かめてきた[2-4]。本研究ではこれを結合領域へと拡張し、化学結合や分子間相互作用をより詳細に解析する方法、Bond-EDA を提案する。また、種々の化学的現象に応用する。

【理論】

EDA は主に、Mulliken の電子密度解析の類推を用いた分割スキームを採用している。Mulliken の電子密度解析では、その非対角項を用いて結合次数を見積ることができる。Bond-EDA ではそれと同様、EDA の非対角項を用いて結合エネルギーを見積る。例えば、原子 A-B 間の kinetic energy は、

$$T^{AB}=2\sum_{\mu\in A}\sum_{\nu\in B}P_{\mu\nu}T_{\nu\mu} \qquad (1)$$

と、見積られる。

【結果と考察】

エタン分子の化学結合とその C-C 間結合の解離過程(Fig. 1)を、Bond-EDA を用いて検討した。計算レベルは HF/cc-pVDZ である。Table 1 にその結果を示す。結合が存在する C-C 間、C-H 間の結合エネルギー密度は絶対値の大きな負の値を持ち、結合による安定化を示している。結合していない H-H 間、C-H 間では絶対値の小さい正の値を持ち、これは立体効果に対応するものと考えられる。また、H-H 間の結合エネルギー密度はその距離に依存して小さくなっている。原子に割り当てられるエネルギーは、単原子分子状態の HF エネルギー(炭素原子：-23648.75 kcal/mol、水素原子：-313.30 kcal/mol)と同程度であり、その大部分が内殻電子からの寄与であると考えられる。エタン分子が解離して 2 つのメチルラジカルになる反応では、全体として約 67 kcal/mol の反応熱が必要となる。その大部分は C-C 間の結合エネルギー密度の寄与であるが、その他 C-H 間の反発の消滅や C-H 間結合の安定化などの寄与も少なくないことがわかる。このように Bond-EDA を用いると、化学反応による結合の開裂・生成に伴うエネルギー変化を詳細に解析することが可能である。また、この Bond-EDA を Diels-Alder 反応の解析[5]や、カーボンナノチューブの特性の解析[6]に応用した成果は、本学会にてポスター発表する。

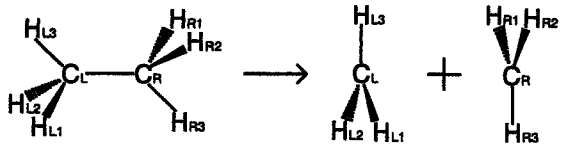

Fig. 1. Dissociation Process of Ethane.

Table 1. Results of the Bond-EDA for Dissociation Process [kcal/mol]. The values in brackets are the difference between C_2H_6 and CH_3+CH_3.

		C_2H_6	CH_3+CH_3	
Atomic energy density, E^{AA}				
C_L		-23666.61	-23661.30	(+5.32)
H_{Li}	(×3)	-311.37	-306.41	(+4.96)
C_R		-23666.61	-23661.30	(+5.32)
H_{Ri}	(×3)	-311.37	-306.41	(+4.96)
Bond energy density, E^{AB}				
C_L-H_{Li}	(×3)	-80.15	-91.43	(-11.28)
H_{Li}-H_{Lj}	(×3)	6.62	9.36	(+2.74)
C_R-H_{Ri}	(×3)	-80.15	-91.43	(-11.28)
H_{Ri}-H_{Rj}	(×3)	6.62	9.36	(+2.74)
C_L-H_{Ri}	(×3)	5.99	0.00	(-5.99)
C_R-H_{Li}	(×3)	5.99	0.00	(-5.99)
C_L-C_R		-118.26	0.00	(+118.26)
H_{Li}-H_{Ri}	(×3)	-3.06	0.00	(+3.06)
H_{Li}-H_{Rj}	(×6)	2.22	0.00	(-2.22)
Total		-49720.80	-49653.43	(+67.36)
Heat of Reaction (Exptl.)				87.60

[1] H. Nakai, Chem. Phys. Lett., 363, 73-79 (2002).
[2] H. Nakai, and K. Sodeyama, Chem. Phys. Lett., 365, 203-210 (2002).
[3] Y. Kawamura, and H. Nakai, Chem. Phys. Lett., 368, 673-679 (2003).
[4] H. Nakai, and K. Sodeyama, J. Mol. Structure (THEOCHEM), 637, 27-35 (2003).
[5] 石井基樹, 菊池那明, 馬場健, 中井浩巳, 日本コンピュータ化学会 2004 春季年会, 2P13.
[6] 倉林佑二, 菊池那明, 中井浩巳, 日本コンピュータ化学会 2004 春季年会, 2P20.

日本コンピュータ化学会 2004 春季年会,
東京工業大学（東京），2004 年 5 月.

2O03

新しい漸化式を用いた電子反撥積分の高速計算アルゴリズムの開発：ACE-RR 法

○小林　正人、中井　浩巳
早稲田大学理工学部化学科（〒169-8555　東京都新宿区大久保 3-4-1）

【緒言】

次式で表される電子反撥積分(ERI)の計算は、量子化学計算の大きなボトルネックであり、これまでにさまざまな計算方法が提案されてきた。

$$\mathrm{ERI} = \int \phi_\lambda^{\mathrm{A}}(\mathbf{r}_1)\phi_\mu^{\mathrm{B}}(\mathbf{r}_1)\frac{1}{|\mathbf{r}_2-\mathbf{r}_1|}\phi_\nu^{\mathrm{C}}(\mathbf{r}_2)\phi_\xi^{\mathrm{D}}(\mathbf{r}_2)\,d\mathbf{r}_1 d\mathbf{r}_2 \qquad (1)$$

この ERI を厳密に計算すると、$O(N^4)$の計算コストがかかるが、近年は高速多重極展開(FMM)によるクーロン相互作用の見積もりや、Fragment MO 法などの分割計算手法の開発により、十分大きい系においては $O(N)$が実現されつつある。この場合高速化のためには、prefactor の向上が不可欠となる。当研究室においても、これまでに elementary basis algorithm (EBA)[1]を提案し、大規模系における ERI 計算の prefactor 向上に成功した。

本研究では、随伴座標展開(ACE)表式[2]で表された ERI に対して、新しい 2 種類の漸化関係式(RR)を導出し、それを用いて計算の効率化を図る ACE-RR 法[3]を提案する。この方法はガウス型軌道の軌道角運動量を変化させて計算する必要のある *sp* 型の基底関数や、ERI の gradient 計算に特に有効である。

【ACE-RR アルゴリズム】

(1)で示した ERI は、ACE-b3k3 表式[2]を用いると、(2)式のように表すことができる。

$$\mathrm{ERI} = S_{\lambda\mu}^{\mathrm{AB}} S_{\nu\xi}^{\mathrm{AB}} \sum_{\mathbf{N}_3} C_4^{\mathrm{ABCD}}\{\mathbf{N}_3\} H_{4\lambda\mu\nu\xi}^{\mathrm{ABCD}}\{\mathbf{N}_3\} \qquad (2)$$

$H_{4\lambda\mu\nu\xi}^{\mathrm{ABCD}}$ の計算を行うための新しい表式として、新しく角運動量減少表式(AMR formula)を開発した。

$$F_{mn} = \left(\frac{\sigma_1}{\sigma_1+\sigma_2}\right)^m \left(\frac{\sigma_1}{\sigma_1+\sigma_2}\right)^n \frac{F_{m+n}(z)}{\sqrt{\sigma_1+\sigma_2}} \qquad (3)$$

$$G_{mn(R_1)}^{pq} = \sigma_{\mathrm{A}}{}^p \sigma_{\mathrm{B}}{}^q \sum_{t=0}^{\mu-R_1} (-)^t \binom{\mu-R_1}{t} F_{m+t,n} \qquad (4)$$

$$H_{mn(R_1R_2)}^{pqrs} = \sigma_{\mathrm{C}}{}^r \sigma_{\mathrm{D}}{}^s \sum_{t=0}^{\nu-R_2} (-)^t \binom{\nu-R_2}{t} G_{m,n+t(R_1)}^{pq} \qquad (5)$$

ここで R_1 及び R_2 はそれぞれ bra 及び ket 側の角運動量減少次数(AMR level)である。表式通りに計算した場合は、(3)及び(4)式は、基底関数の縮約の 4 乗に、(5)式は 2 乗に比例した計算コストを要する。さらに我々は、これらの表式が満足する以下のような RR を見出した。

$$H_{mn(R_1R_2)}^{pqrs} = H_{mn(R_1R_2)}^{pq-1rs} - H_{mn(R_1R_2)}^{p+1q-1rs} \qquad (6)$$

$$H_{mn(R_1R_2)}^{pqrs} = H_{mn(R_1+1R_2)}^{pqrs} - H_{m+1n(R_1R_2)}^{pqrs} \qquad (7)$$

(6)式は AMR level の等しいものの間の関係式なので、ACE 水平漸化関係式(ACE-HRR)、(7)式は AMR level の異なるものの間の関係式なので、ACE 垂直漸化関係式(ACE-VRR)と呼ぶ。ACE-HRR と ACE-VRR の計算スキームをそれぞれ Fig. 1 と Fig. 2 に模式的に示す。これらの関係式を使用した計算は、基底関数の縮約の大きさには依存しない。したがって、特に原子自然軌道(ANO)のような大きな基底関数を用いた計算の高速化に効果がある。また、ACE-VRR を使用することにより角運動量量子数の変化をリーズナブルに行うことができるので、*s* 関数と *p* 関数で同じ指数を用いる *sp* 殻の計算も、高速に行うことが可能となる。

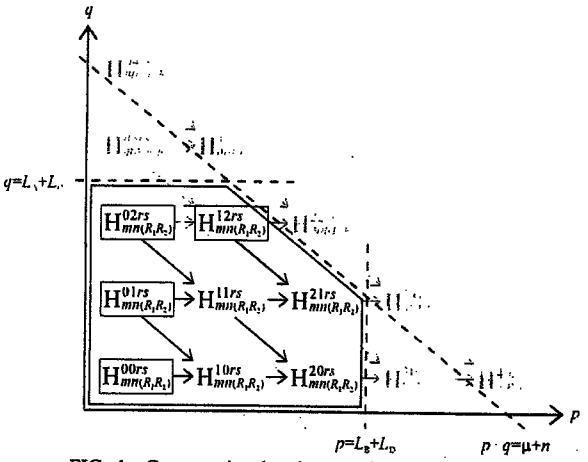

FIG 1. Computational scheme of core part $H_{mn(R_1R_2)}^{pqrs}$ using the bra-ACE-HRR.

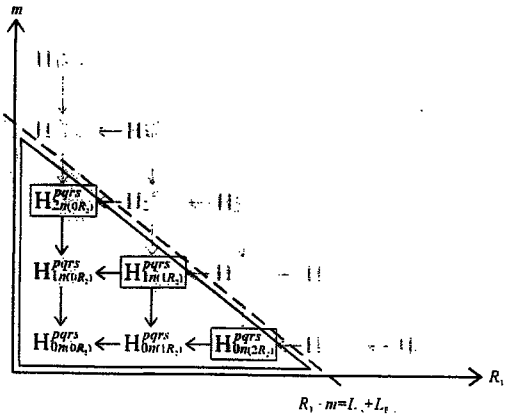

FIG 2. Computational scheme of core part $H_{mn(R_1R_2)}^{pqrs}$ using the bra-ACE-VRR.

[1] H. Nakai and M. Kobayashi, Chem. Phys. Lett. **388**, 50 (2004).
[2] K. Ishida, Int. J. Quantum Chem., **59**, 209 (1996).
[3] M. Kobayashi and H. Nakai, J. Chem. Phys., *submitted*.

日本コンピュータ化学会 2004 春季年会,
東京工業大学（東京），2004 年 5 月.

2P10

二酸化チタンの光触媒反応に関する理論的研究

○石川佳奈、河村芳海、中井浩巳
早稲田大学理工学部化学科（〒169-8555　東京都新宿区大久保 3-4-1）

≪緒言≫　二酸化チタンを用いた光触媒反応は、その水や有機物に対する酸化分解能力から、抗菌・防汚・脱臭作用としての応用が期待され、その高効率化のための研究が多くなされてきた。その反応スキームは、光励起により価電子帯に生じた正孔および伝導帯に生じた電子が、それぞれ酸化及び還元反応を引き起こすことによるものとされている。その反応活性点及び素過程の理解は、光触媒反応の高効率化のために重要である。本研究では、光活性の点から最も効果的とされているアナターゼ型二酸化チタン表面に対する水吸着過程及び光励起状態を、電子状態計算により検討した。

≪方法≫　二酸化チタンのアナターゼ構造(101)および(001)表面に対する水 1 分子吸着について、クラスターモデルを用いて検討した(Fig. 1)。また、二酸化チタンはイオン性結晶であるため、バルクの原子を点電荷(q_{Ti}=+2, q_O= −1)でモデル化した。構造最適化は HF、基底関数は 6-21G で行った。励起状態の計算については CIS 法を用いた。

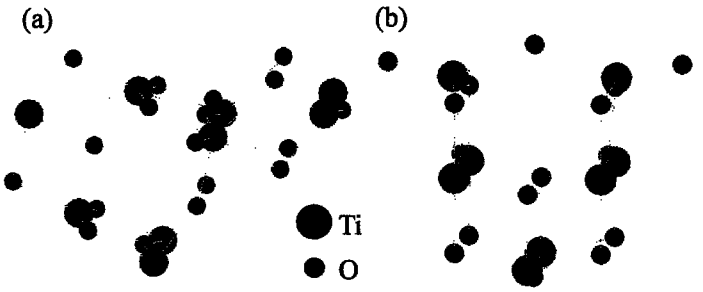

Fig. 1. Ti_9O_{18} (101) cluster (a)と Ti_8O_{16} (001) cluster (b)の図.

≪結果と考察≫　基底状態の水 1 分子吸着構造について、(101)面では解離吸着の吸着エネルギー 0.31eV に対して、水分子が表面の Ti 原子に垂直に吸着した分子状吸着の方が 1.92eV と大きく安定化している(Fig. 2)。一方、(001)面では表面の Ti 原子と架橋 O 原子の間の結合が開裂することによって Ti 原子それぞれにヒドロキシル基が吸着した解離吸着構造の吸着エネルギーが 3.40eV となり、分子状吸着の 0.48eV よりも安定化していることがわかる(Fig. 3)。(001)表面の励起状態における電子密度に注目すると、O1 が減少、Ti2 が増加していることがわかり、電荷分離によってそれぞれ正孔と電子が生じた状態であると考えることができる(Fig. 4)。水分子解離吸着状態における励起エネルギーは 5.31eV であり、この安定な解離吸着構造の励起状態を経由することによって、活性酸素種であるヒドロキシラジカルが生成すると考えられる。

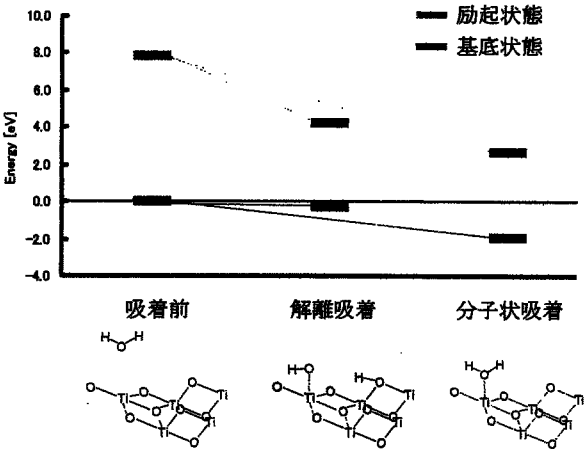

Fig. 2. Ti_9O_{18} クラスターにおける水分子吸着スキーム.

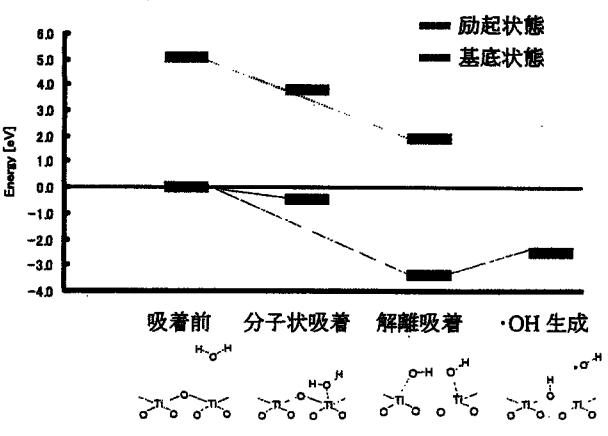

Fig. 3. Ti_8O_{16} クラスターにおける水分子吸着スキーム.

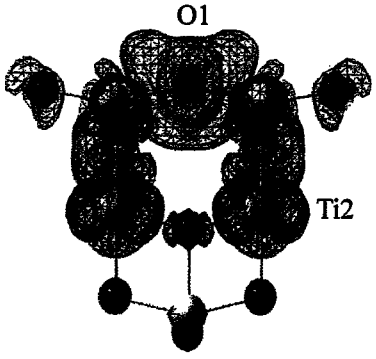

Fig. 4. Ti_8O_{16} cluster における差電子密度図.

日本コンピュータ化学会 2004 春季年会,
東京工業大学（東京），2004 年 5 月.

2P13

結合エネルギー密度解析(Bond EDA)を用いた化学反応メカニズムの検討

○石井基樹、菊池那明、馬場健、中井浩巳
早稲田大学理工学部化学科（〒169-8555 東京都新宿区大久保 3-4-1）

【緒言】

古くから化学反応のメカニズムを解明するために、理論的手法が用いられてきた。例えば、Diels-Alder 反応はフロンティア電子論によって定性的な説明がなされてきた。しかし、高活性・高選択性の反応設計が期待される現代では、このような定性的な理解だけでは不十分で、より定量的な検討が不可欠である。最近当研究室で提案されたエネルギー密度解析(EDA)[1]は、量子化学計算の定量性を下げることなく解析できる手法で、様々な応用[2-5]が期待されている。特に、結合エネルギーを見積ることのできる Bond-EDA[6]は、化学反応中に起こる結合の生成・開裂を検討するのに有用な手法として期待される。本研究では、Bond-EDA を用いて Diels-Alder 反応のメカニズムがどのように説明されるかを検討する。

【結果と考察】

<u>配向選択性</u> 1-メトキシブタジエンとアクロレインの Diels-Alder 反応には、生成物がオルト異性体しか得られないという配向選択性がある。反応障壁は、HF/cc-pVDZ レベルでオルト異性体(42.9kcal/mol)の方がメタ異性体(44.9kcal/mol)より小さく計算された。Table 1 に反応物から遷移状態、生成物に変化する際の結合長と結合エネルギーを示す。これらは Bond-EDA により初めて見積られた値である。どちらの異性体も環化付加で生成する結合のうち C_4-C_5 の方が C_1-C_6 よりも安定化が大きかった。この大小関係は結合長に対応し、フロンティア電子論で予想された軌道の重なり方にも対応する。遷移状態でのこのような違いは生成物ではほとんど見られない。

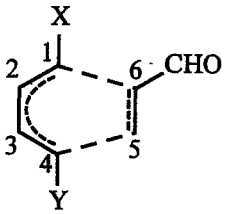

ortho: X=OMe, Y=H
meta: X=H, Y=OMe

Fig.1. Diels-Alder reaction between 1-methoxybutadiene and acrolein

Table 1. Bond lengths (Å) and bond energy (kcal/mol) in the Diels-Alder reaction.

		TS		Product	
		Bond length	Bond energy	Bond length	Bond energy
ortho	C1-C6	2.49	-39.7	1.53	-122.9
	C4-C5	1.99	-71.9	1.53	-120.2
meta	C1-C6	2.22	-47.4	1.53	-129.2
	C4-C5	2.12	-64.4	1.53	-128.3

<u>反応性</u> ブタジエン(1)とエチレン(2)、無水マレイン酸(3)、無水マレイン酸にルイス酸を加えた場合(4)の Diels-Alder 反応は、1+2、1+3、1+4 の順番で反応速度が大きくなることが知られている。反応障壁はその順で小さくなり、HF/cc-pVDZ レベルでは 1+2 で 44.5、1+3 で 38.6、1+4 で 37.1kcal/mol である。ここで、Bond-EDA を適用したところ、反応物と遷移状態の結合エネルギーの変化は Table 2 のようになった。結合の生成する C_1-C_6, C_4-C_5 では約 46kcal/mol 程度の安定化が得られており、全ての反応であまり違いが見られない。一方、1+3 と 1+4 では、C_5-C_6 が二重結合から一重結合になるにもかかわらず安定化することがわかった。また、その大きさは 1+4 で 14.6kcal/mol と一番大きく、反応速度の順番にも対応した。この反応は C_5-C_6 部分の安定化が反応速度に重要であることが Bond-EDA により明らかになった。

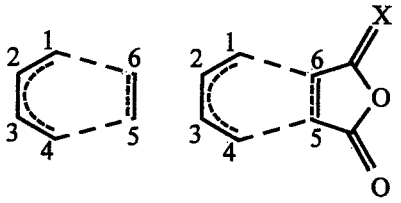

(a)1+2 (b) X=O : 1+3
X=OBF$_3$: 1+4

Fig.2. Diels-Alder reaction of (a)1+2, (b)1+3, 1+4

Table 2. Bond energy changes in the Diels-Alder reaction between butadiene and ethylene or maleic anhydride.

	C1-C2	C2-C3	C3-C4	C4-C5	C5-C6	C1-C6
1+2	8.1	-4.7	8.1	-46.6	1.5	-46.6
1+3	10.8	0.4	10.8	-47.4	-13.3	-47.4
1+4	10.9	0.8	11.5	-48.8	-14.6	-46.1

[1] H. Nakai, Chem. Phys. Lett., **363**, 73-79 (2002). [2] H. Nakai, K. Sodeyama, Chem. Phys. Lett., **365**, 203-210 (2002). [3] Y. Kawamura, H. Nakai, Chem. Phys. Lett., **368**, 673-679 (2003). [4] H. Nakai, K. Sodeyama, J. Mol. Structure (THEOCHEM), **637**, 27-35 (2003). [5] 倉林佑二, 菊池那明, 中井浩巳, SCCJ2004 春季年会, 2P20. [6] H. Nakai, Y. Kikuchi, J. Chem. Phys., *to be submitted*; 菊池那明, 中井浩巳, SCCJ2004 春季年会, 2O01.

日本コンピュータ化学会 2004 春季年会,
東京工業大学（東京），2004 年 5 月.

2P18

短時間フーリエ変換を用いたAIMDシミュレーションの解析

○玉置麻理、山内佑介、渥美照夫、中井浩巳
早稲田大学理工学部化学科（〒169-8555 東京都新宿区大久保 3-4-1）

【緒言】 化学反応に伴う個々の原子の運動を時々刻々と追跡することは、化学における大きな目標の 1 つである。この目標に対するアプローチの 1 つとして、理論面では分子シミュレーションのテクニックが発展した。*ab initio* 分子動力学(AIMD)シミュレーションは、量子化学計算によって得られたポテンシャル超曲面(PES)上で古典運動方程式を解くことで、核座標の時間変化を計算する強力な手法である。しかしながらこれまでのところ、この AIMD シミュレーションの結果に対する解析手法は、従来の分子シミュレーションに適用されていたものが主であった。本研究では星間分子のラジカル反応のシミュレーション結果に対して短時間フーリエ変換を適用することにより、この新しい解析手法の有用性およびその拡張性について検討する。

【理論】 AIMD シミュレーションは、上述のとおり、従来の分子シミュレーションで扱うことが困難であった結合の生成や開裂を含む化学反応を、化学的～分光学的な精度で記述できる。本研究では特に振動モードの時間変化に注目し、非平衡ダイナミクスを表現するために短時間フーリエ変換による解析を AIMD シミュレーションに初めて利用した。短時間フーリエ変換は、本来定常信号に対する解析手法であるフーリエ変換を、window function と呼ばれる関数を使って非定常の信号に対しても使えるようにする理論である。速度の相関関数とスペクトルの関係を示す以下の式

$$S(\omega,t)=\frac{1}{2\pi}\int_T^t \langle v(t+\tau)\cdot v(\tau)\rangle e^{-i\omega\tau}d\tau$$

を用い、得られたスペクトルの時間変化をスペクトログラムと呼ばれるグラフを用いて表すことにより、化学反応における振動モードの移り変わりを視覚的、数値的に解析することが可能となる。

【結果と考察】 上記の解析手法の適用対象として、星間物質として知られるシアノラジカル(CN·)とジメチルアセチレン(C_4H_6)の衝突反応を扱った。この反応は、土星の衛星 Titan のシアノ化学や、生物以前の原始地球における窒素化学などを知る上で非常に興味深い。初期条件として CN·に衝突エネルギー0.32eV を与えて C_4H_6 に衝突させる AIMD シミュレーションを行った。初期配向の異なる 53 本のトラジェクトリを計算した。シミュレーションの AI 部分(量子化学計算)には非制限 Hartree-Fock 法、基底関数に 6-31G(d,p)を用いた。また、MD 部分(運動方程式の数値積分)には速度 Verlet アルゴリズムを使い、時間刻み 0.25fs とした。

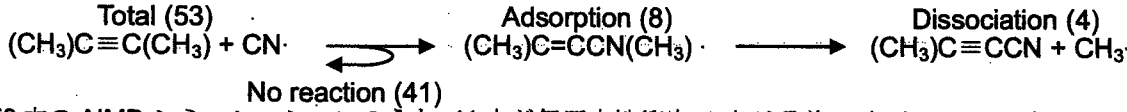

53 本の AIMD シミュレーションのうち、41 本が無反応性衝突、8 本が吸着、4 本がメチルラジカル(CH_3·)解離であった。これら三種類の反応について、それぞれ代表的なスペクトログラムを下に示す。(a)無反応の図では衝突過程を通じて振動モードにほとんど変化が見られない。(b)吸着の図では CH_3 横揺れ(～1150cm^{-1})や CH_3 変角(～1550cm^{-1})、CH 伸縮(～3200cm^{-1})といったモードが誘起されており、新たに生成した C－CN 間の結合エネルギーが、C_5H_6N·の内部振動エネルギーに分配している様子が見られる。(c)ラジカル解離の図では、CCN 変角 (～350cm^{-1})が誘起しており、結合エネルギーを分子内の運動エネルギーで分配できないためにポテンシャルエネルギーによる緩和、すなわち CH_3·解離へと反応が進行することが確認できた。このように AIMD シミュレーションと ST-FT による解析方法は非平衡ダイナミクスを詳細に記述することが可能である。また、本研究で扱った反応は、明らかなラジカル反応である。そこで、スピン密度変化に対しても短時間フーリエ変換を適用することにより、どのような情報が引き出されるかを検討した。

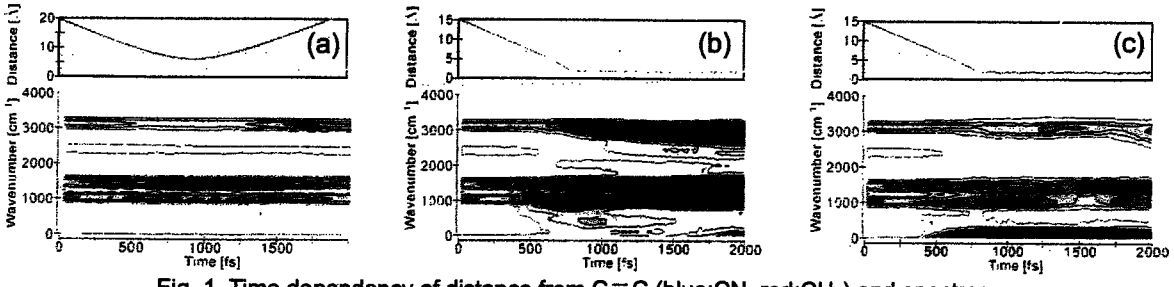

Fig. 1. Time dependency of distance from C≡C (blue:CN, red:CH_3) and spectrogram;
(a)no reaction, (b)adsorption, and (c)CH_3 dissociation.

日本コンピュータ化学会 2004 春季年会,
東京工業大学（東京），2004 年 5 月.

2P20

カーボンナノチューブのサイズ依存性に関する理論的研究

○倉林佑二、菊池那明、中井浩巳
早稲田大学理工学部化学科 （〒169-8555 東京都新宿区大久保 3-4-1）

【緒言】

カーボンナノチューブ(CNT)は強靭な機械的強度や電導性などが注目されており、実験・理論の両面から広く研究されている。電気特性については、CNT の構造を規定するカイラルベクトル(*n*,*m*)により、*n*−*m* が 3 の倍数の場合、金属的、その他が半導体的であるといわれているが、これは 1 次元無限鎖を仮定した拡張 Hückel 法から導かれた結論である[1]。ところで、実際の CNT は有限の長さを有しており、サイズの違いによって、無限鎖とは異なる物性を持つ可能性が予想される。本研究では、CNT のサイズ依存性を *ab initio* 計算により理論的に検討する。

【計算方法】

本研究では、金属・半導体的な代表として(*n*,*n*)および(*n*,0) CNT を主に取り扱う。(*n*,*n*)および(*n*,0) CNT は C_{4n} をユニットセルにもっている。ここでは、$(C_{4n})_N$ (N=1, 3, 5, 7, 9) に対する *ab initio* 計算を行った。いずれの CNT も末端の C 原子は H 原子でキャップを行った。また、1 次元周期境界条件(PBC)を課した計算も行った。PBC 計算では全ての C 原子は等価なので、1 原子あたりのエネルギーは全エネルギーをユニットセルサイズで割ることにより求められる。一方、クラスター計算ではすべての C 原子が等価にならない。そこで、当研究室で開発されたエネルギー密度解析(EDA)[2]を用いることにより、各 C 原子のエネルギーを見積った。

【結果と考察】

Fig. 1 に、クラスターサイズを変化させたときの各 CNT の凝集エネルギーを示す。これより、カイラルベクトルが等しい場合は、クラスターサイズが大きくなるにつれて、PBC 計算によって見積られた凝集エネルギーに収束する傾向が見られた。

Fig. 2 に(5,5) CNT、Fig. 3 に(5,0) CNT のサイズがそれぞれ$(C_{20})_N$(N=1, 3, 5, 7, 9)であるクラスターの各サイトごとの C 原子のエネルギーの違いを示す。(5,5) CNT では、どのサイズの場合でも末端を除けば各 C 原子の持つエネルギーに大きな差は見られない。一方、(5,0) CNT では、C_{20}、C_{60}、C_{180} では Fig. 2 と類似した挙動を示すが、C_{100} と C_{140} で特異な振動が見られた。この振動は末端と中心に節を持つように見える。このような CNT の特異なサイズ依存性は実験的に報告されてはいない。今後、他の CNT についてもこのような特異なサイズ効果を示すものがあるかを調べるとともに、その物理的意味を考えていきたい。

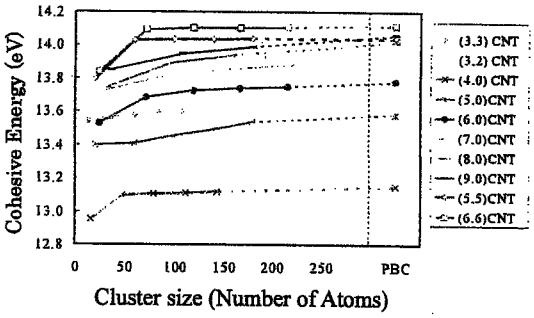

Fig. 1. Number of Atoms vs CNT Cohesive Energy

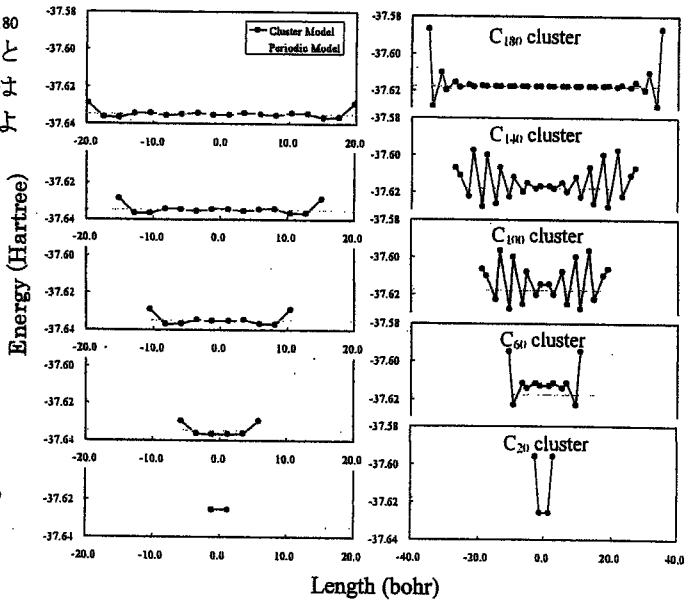

Fig. 2. (5,5) CNT site Energy　　Fig. 3. (5,0) CNT site Energy

[1] R. Saito, M. Fujita, G. Dresselhaus, and M. S. Dresselhaus, *Appl. Phys. Lett.*, **60**, 2204 (1992).
[2] H. Nakai, *Chem. Phys. Lett.*, **363**, 73 (2002).

第 8 回理論化学討論会,
広島大学（広島），2004 年 6 月.

2B2b 電子反撥積分の高速計算法: 随伴座標展開 (ACE)表式に対する漸化関係式の導出

（早大理工）
○小林正人・中井浩巳

近年の Gauss 型基底関数展開による電子状態計算では、高速多重極展開(FMM)法や Fragment MO 法などの手法の発達により、計算時間の $O(N)$が実現されつつある。この状況下においても、電子反撥積分(ERI)の求積は計算時間の prefactor の大きな要素となっている。

$$\mathrm{ERI} = \int \phi_\lambda^{\mathrm{A}}(\mathbf{r}_1)\phi_\mu^{\mathrm{B}}(\mathbf{r}_1)\frac{1}{|\mathbf{r}_2-\mathbf{r}_1|}\phi_\nu^{\mathrm{C}}(\mathbf{r}_2)\phi_\xi^{\mathrm{D}}(\mathbf{r}_2)\,d\mathbf{r}_1 d\mathbf{r}_2 \qquad (1)$$

当研究室ではこれまでに elementary basis algorithm (EBA)を提案し、大規模系計算の prefactor 改善に成功した[1]。

個々の ERI の高速計算法は、これまでに様々な研究者によって提案されている。これらは大別すると 2 つの異なるアプローチを取っている。一方は、高い軌道角運動量量子数をもった ERI を基本積分$[0]^{(m)}$から漸化的に求める方法である。もう一方は、これを低い角運動量量子数の ERI を経ずに直接求めるものである。現在、個々の ERI を最も高速に求めるアルゴリズムは随伴座標展開(ACE)法[2]であり、これは後者の分類に当たる。しかし、ACE 法は角運動量量子数を柔軟に変化させることができないため、Pople 型基底関数系に登場する *sp* 型の基底関数や ERI の gradient、Hessian といった微分の計算には適していなかった。

本研究では、ACE-b3k3 表式で表された ERI に対して、ACE-HRR と ACE-VRR という 2 種類の新しい漸化関係式(RR)を導出した[3]。これらは、新しく導入した角運動量減少(AMR)表式を用いて、以下のように与えられる。

$$\text{ACE-HRR:}\quad H^{pqrs}_{mn(R_1R_2)} = H^{pq-1rs}_{mn(R_1R_2)} - H^{p+1q-1rs}_{mn(R_1R_2)} \qquad (2)$$

$$\text{ACE-VRR:}\quad H^{pqrs}_{mn(R_1R_2)} = H^{pqrs}_{mn(R_1+1R_2)} - H^{pqrs}_{m+1n(R_1R_2)} \qquad (3)$$

また、ACE 法にこれらの RR を用いた ERI の計算アルゴリズム、ACE-RR 法を開発した[3]。これを用いることによって、ACE 法の弱点であった *sp* 型の基底関数や、ERI の gradient 計算も効率的に行うことができる。

ACE-RR 法とこれまでの方法における (*sp sp* | *sp sp*)型 ERI 計算の浮動小数点演算(FLOP)計数の比較を Table 1 に示す。ACE-RR 法はxのパラメータが最小となっており、縮約の大きい ERI の計算に特に有効である。また ACE-RR 法は、角運動量量子数を変化させない ERI に対しても有効であり、縮約の大きさに関して(*sp sp* | *sp sp*)型の ERI と同じような傾向が確認された。

Table 1. Comparison of the estimated FLOP count parameters for (*sp sp* | *sp sp*) ERIs.

Algorithm	x	y	z
present (Kobayashi and Nakai)	163	736	4 548
ACE-b3k3 (Ishida)	349	572	4 282
Pople and Hehre	220	2 300	4 000
Gill, Head-Gordon, and Pople	450	1 300	1 700
Lindh, Ryu, and Liu	753	30	800
Head-Gordon and Pople	1 400	30	800
McMurchie and Davidson	1 500	1 700	0
Dupuis, Rys, and King	1 056	30	0

[a]Except for the calculation of $F_m(z)$.
[b]Total FLOP count is given by $xK^4 + yK^2 + z$.

[1] H. Nakai and M. Kobayashi, Chem. Phys. Lett. **388**, 50 (2004).
[2] K. Ishida, Int. J. Quantum Chem. **59**, 209 (1996).
[3] M. Kobayashi and H. Nakai, J. Chem. Phys., *submitted*.

第 8 回理論化学討論会,
広島大学（広島），2004 年 6 月.

2A2b　エネルギー移動スペクトログラムの提案

（早大理工）
○山内佑介・中井浩巳

緒言 反応ダイナミクスを理解する上で、エネルギー移動と振動モードとの関係は重要であり、古くから研究が行われてきた。例えば Bixon-Jortner によって無輻射遷移に伴う電子-振動状態間のエネルギー移動を、直感的に"promoting modes"と"accepting modes"に分けて考えるという概念が報告されている。本研究では、*ab initio* molecular dynamics (AIMD)シミュレーションにより反応ダイナミクスを追跡し、その結果からエネルギー移動に関与しているモードを定量的に取り出す方法を検討した。

理論 ミクロカノニカルアンサンブルを扱う MD シミュレーションで保存される全エネルギーE は、ポテンシャル V と運動エネルギーT に分けることができる。これまで運動エネルギーを部分系 T_m に分割することは可能であったが、ポテンシャルエネルギーの分割は不可能であった。しかしながら Energy Density Analysis (EDA)[1]によって部分系のポテンシャルエネルギーV_m が求まり、したがって部分系の全エネルギーE_m が計算可能になった。E_m の変化によって、系内のエネルギー移動量が見積もられる。

$$E = \sum_{m\in\text{system}} E_m = \sum_m (T_m + V_m) \rightarrow \text{conserv.} \qquad (1)$$

さらにシミュレーションから得られた非平衡状態の時系列データを解析するために、短時間フーリエ変換(ST-FT)の手法を用いた。ST-FT では無限時間のデータ $f(\tau)$の一部を窓関数 $h(t - \tau)$によって切り出し、フーリエ変換を行う。ST-FT の結果得られる $S(t,\omega)$の像をスペクトログラムと呼ぶ。

$$S(t,\omega) = \int f(\tau)h(\tau - t)\exp(-i\omega\tau)d\tau \qquad (2)$$

速度の自己相関関数のフーリエ変換はパワースペクトルとしてよく知られている。今回は式(1)で示されたエネルギーE_m の時間変化に対して自己相関関数を求め、そのフーリエ変換をエネルギー移動スペクトルと名付けた。

$$f(\tau) \equiv \left\langle \dot{E}_m(\tau)\cdot\dot{E}_m(\tau-\tau_0)\right\rangle_m \qquad (3)$$

結果 二つの CO_2 の衝突反応について B3LYP/6-31G(d)レベルの密度汎関数法による AIMD シミュレーションを行った。その結果に対する振動スペクトログラムおよびエネルギー移動スペクトログラムを図 1 に示す。2 つの分子の衝突は約 2.5ps で起こっている。CO_2 は大気主成分の中で数少ない三原子分子であり、2 つの伸縮モード（対称(100); 逆対称(001)）に加えて変角モード(010)を有する。通常のパワースペクトログラム(A)では約 670cm^{-1}、1360cm^{-1}、2400cm^{-1} のピークが見られ、それぞれ(010)、(100)と(020)、(001)に帰属できる。一方エネルギー移動スペクトログラム(B)では、衝突の瞬間のみピークが観察され、その振動数は約 680cm^{-1}、1200cm^{-1}、1860cm^{-1} であった。これらのモードはそれぞれ(010)、(020)、(030)と予想される。特に大きなピークを持つ(020)だけ低波数側に大きくシフトしている。これは衝突時の相互作用によるモードのシフトであると考えられる。

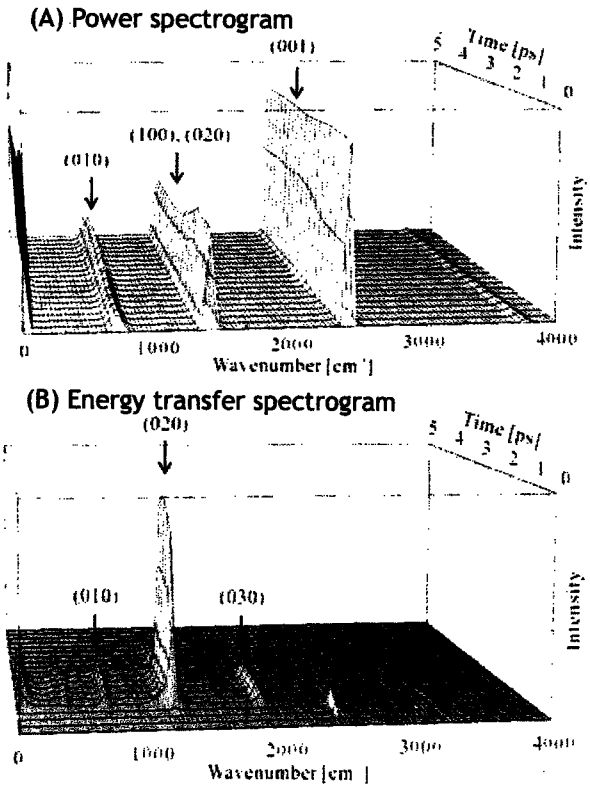

Figure 1. (A) Vibration spectrogram and (B) energy transfer spectrogram.

[1] H. Nakai, Chem. Phys. Lett., 363, 73-79 (2002).

第 8 回理論化学討論会,
広島大学（広島），2004 年 6 月.

1C1b AIMD シミュレーションにおける SCF 収束性の向上

（早大理工）
○渥美照夫・中井浩巳

1. 緒言 *ab initio* molecular dynamics (AIMD)シミュレーションとは、*ab initio* MO/DFT 計算から求められる力場を用いて MD シミュレーションを行う方法であり、結合の生成・開裂を伴う化学反応ダイナミクスを追跡できるという特長を持つ。しかし、各時間ステップごとに *ab initio* MO/DFT 計算を行うために、計算コストが非常に大きいという欠点がある。そこで本研究では、連続した核座標変化を伴うという AIMD シミュレーションの性質を利用して、ボトルネックである SCF 計算の収束性の向上を検討した。本手法は、AIMD シミュレーションだけでなく、構造最適化における SCF 収束性の向上にも利用できると考えている。

2. 理論 従来の AIMD シミュレーションでは、構造最適化の場合と同様、1 ステップ前の収束値(MO あるいは Density)を初期値として用いて、SCF 収束性の向上が計られてきた。本研究では、これまで全く用いられなかった 2 ステップ以前の情報も使用して、より良い初期値を予測することを検討した。その方法として、種々の補間法や DIIS が考えられるが、ここではまず最もシンプルな Lagrange 補間(2~8 次)を採用した。予測値としては、MO 係数を採用した。

3. 結果と考察 Lagrange 補間による予測の有効性を 2 種類の AIMD シミュレーションにより検討した。

(A)メタノールの(111)軸に対する回転 ($\Delta\theta$=0.1°)
(B)メタノールの分子振動 (Δt=0.1fs)

ab initio MO/DFT 計算は、B3LYP/D95V レベルで Gaussian98 パッケージを用いて行った。MD 計算は、velocity Verlet 法に基づく独自のプログラムを用いた。図 1 は、(i)毎回新しく初期値を作成する(0th)、(ii)1 ステップ前の収束値を初期値とする(1st)、(iii)4 次の Lagrange 補間による初期値を予測する(4th)場合に対して 1~30 ステップにおける SCF 回数をプロットしたものである。(A)、(B)両シミュレーションにおいて、今回の(iii)の SCF 収束性が最も良いことが分かる。特に(A)の回転系では常に 4 回以下で収束している。図 2 は、図 1 の場合について初期値と収束値に対するエネルギー差を対数表示したものである。Lagrange 補間を用いると(A)では 10^{-11}a.u. 程度、(B)では、10^{-6}~10^{-10}a.u.まで予測できていることが分かる。表 1 は、1~30 ステップまでの SCF 回数の総和をまとめたもので、図 1 のデータに加えて、Lagrange 補間の次数を変化させた場合の結果も示している。(A)では 3 次で、(B)では 6 次で収束性が最も良いことが分かる。

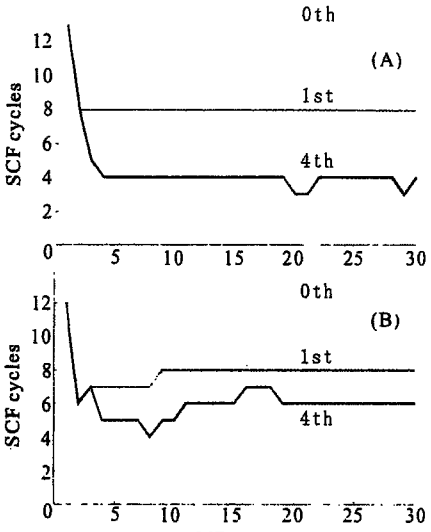

図 1. 各ステップの SCF 回数

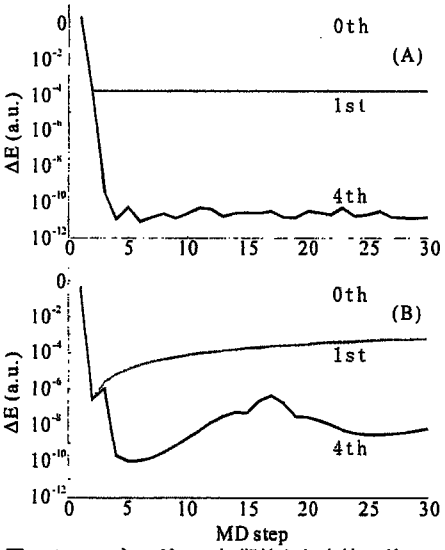

図 2. SCF エネルギーの初期値と収束値の差ΔE

表 1. 30 ステップに必要な全 SCF 回数

initial guess	(A)rotation	(B)vibration
0th	390	360
1st	245	236
2nd	161	214
3rd	124	197
4th	131	182
5th	142	169
6th	155	166
7th	159	170
8th	171	175

第 8 回理論化学討論会,
広島大学（広島），2004 年 6 月.

1P08　水クラスターイオンの冷却過程に関する *ab initio* MD シミュレーション

（早大理工[a]・理研[b]）
○小澤志保[a]・山内佑介[a]・岡田芳樹[b]・中井浩巳[a]

【序】 結晶成長は、酸性雨の生成やオゾン層の破壊のメカニズムと関連していることや、半導体・たんぱく質工学等に多用されている現象で、多くの分野において注目されている。しかし、その成長メカニズムは未だ明らかでない部分が多いため、制御には至っていない。結晶が成長するためには、衝突によってクラスターに分子が取り込まれた後、振動励起状態にあるクラスターが冷却される必要がある。このメカニズムを解明するため、本研究では*ab initio* molecular dynamics (AIMD) シミュレーションを用いて、水クラスターダイマーイオン[$H^+(H_2O)_2$]の生成過程およびN_2との衝突による冷却過程を検討した。

【方法】 以下の 2 段階の反応を AIMD シミュレーション(B3LYP/D95V レベル)で扱った。

$$\begin{cases} H^+(H_2O) + H_2O \rightarrow H^+(H_2O)_2 & (1) \\ H^+(H_2O)_2 + N_2 \rightarrow H^+(H_2O)_2 + N_2 & (2) \end{cases}$$

(1)では、それぞれ 300K で平衡化した後、衝突させた。(2)では、(1)によって生成した$H^+(H_2O)_2$に対してN_2を衝突させた。その際、冷却過程に対するN_2の衝突エネルギー(E_{col})依存性を調べた。$H^+(H_2O)_2$-N_2間のエネルギー移動量はEDA[1)]を用いて求めた。

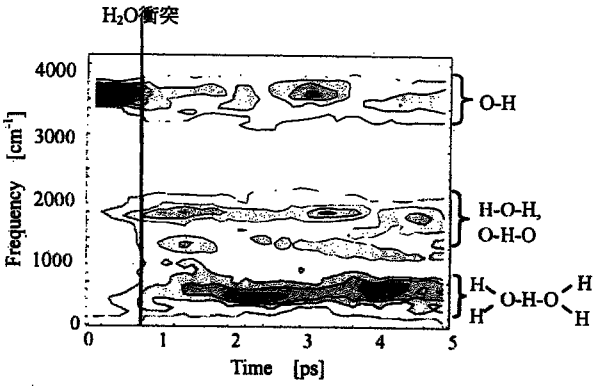

図 1. 過程(1)に対するスペクトログラム

【結果・考察】 図 1 は速度相関関数を短時間フーリエ変換して得た過程(1)のスペクトログラムである。スペクトログラムは分子振動の時間変化を表し、強度の変化(色の濃淡)により各振動状態の存在確率を表す。

3850cm^{-1}付近のO-H伸縮振動は、衝突前には大きい強度を持つが、衝突後ダイマー全体に分配されている。3ps付近で再びピークが見られるが、衝突前と比べると強度は小さい。1300～1800 cm^{-1}付近の振動は中心プロトンや∠HOH変角に由来するもので、第 1 のピークが衝突直後に見られる。これも次第に分配され、第 2、第 3 のピークは強度が小さくなっている。200～600 cm^{-1}付近の振動は、2 つのH_2Oのワギングやロッキングに対応するもので衝突後しばらくして 2.5ps に第 1 のピークが現れる。4ps の第 2 のピークの強度はさらに大きくなっている。これより衝突直後は局所的な振動が強く、次第にダイマー全体に分配されていくことがわかる。図 2 は過程(2)におけるエネルギー移動のE_{col}依存性を示している。N_2の衝突エネルギーが高い場合はクラスターが温まり、低くなると$H^+(H_2O)_2$からN_2へのエネルギー移動が起こり、$H^+(H_2O)_2$が冷却されていることがわかる。

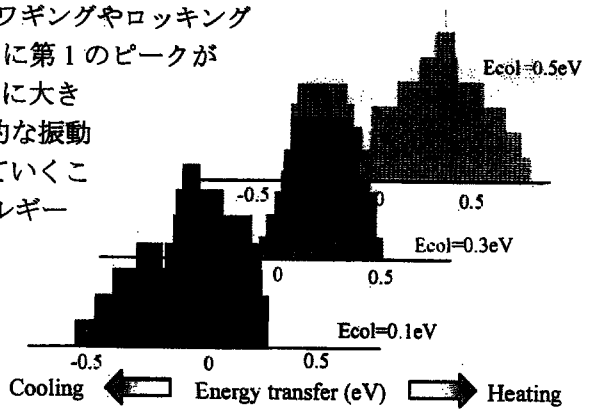

図 2. 衝突後の$H^+(H_2O)_2$のエネルギー移動量

1)H.Nakai, Chem.Phys.Lett.,363,73-79(2002)

星間物質ワークショップ2004,
野辺山宇宙電波観測所（長野），2004年8月.

Analysis of AIMD simulation for the collision reaction between cyano radical and 2-butyne

○玉置麻理、山内佑介、中井浩巳
早大理工（〒169-8555 東京都新宿区大久保 3-4-1）

【緒言】 シアノラジカルと不飽和炭化水素の反応は、燃焼化学や大気化学、そして星間化学などの分野から重要である。特に、星間化学としての反応は、土星の衛星 Titan の大気が原始地球に似ていることから、生命誕生の鍵を握っているとされ、今夏、土星に到着したCassiniによる探査も始まり、非常に注目を集めている。N. Balucaniらは、シアノラジカル(CN)と2-ブチン(C_4H_6)の衝突反応を、交差ビーム法により追跡した[1]。しかしながら Balucani らの研究では、反応のエネルギーダイアグラムを求めるにとどまり、反応ダイナミクスに関する詳細な議論がなされていなかった。本研究では、同反応の *ab initio* molecular dynamics (AIMD)シミュレーションを行い、特に振動モードの時間変化に注目して、非平衡ダイナミクスを表現するために、短時間フーリエ変換をシミュレーション結果に適用した。

【理論】 AIMD シミュレーションは、量子化学計算によって得られたポテンシャル超曲面(PES)上で古典運動方程式を解くことで、核座標の時間変化を計算する強力な手法である。本研究では、初期条件として CN ラジカルを C_4H_6 から 15Å 離し、CN ラジカルに衝突エネルギー0.32 eV を与えて C_4H_6 に衝突させる AIMD シミュレーションを行った。初期配向の異なる 50 本のトラジェクトリを計算した。シミュレーションの *ab initio* 部分には非制限 Hartree-Fock 法、基底関数に 6-31G(d,p)を用いた。また、MD 部分(運動方程式の数値積分)には速度 Verlet アルゴリズムを使い、時間刻み 0.25 fs とした。

短時間フーリエ変換は、本来定常信号に対する解析手法であるフーリエ変換を、窓関数と呼ばれる関数を使って非定常の信号に対しても使えるようにする手法である。速度の自己相関関数とパワースペクトルの間には、次式が成り立つ。

$$S(\omega,t)=\frac{1}{2\pi}\int_{-T}^{T}\langle v(t+\tau)\cdot v(\tau)\rangle e^{-i\omega\tau}d\tau$$

パワースペクトルの時間変化はスペクトログラムと呼ばれる。本研究では、AIMD シミュレーションの結果に対するスペクトログラムを求めることにより、化学反応における振動モードの移り変わりを追跡した。

【結果と考察】 AIMD シミュレーションによって再現されたトラジェクトリは、以下の三種類の反応に分類することができた。

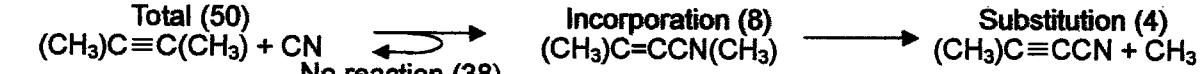

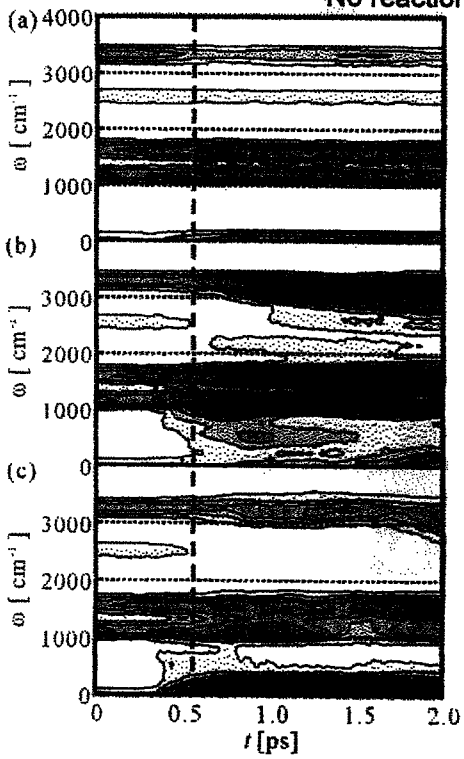

Fig. 1. Spectrogram; (a)no reaction, (b)incorporation, and (c)substitution. The broken line is the timing of the collision.

50 本の AIMD シミュレーションのうち、38 本が無反応性衝突、8 本が吸着、4 本が置換(CH_3ラジカル解離)であった。これら三種類の反応について、それぞれ代表的なスペクトログラムを左に示す。(a)無反応の図では衝突過程を通じて振動モードにほとんど変化が見られない。(b)吸着の図では CH_3 横揺れ+CC 伸縮(~1150cm^{-1})や CH_3 変角(~1550cm^{-1})、CH 伸縮(~3260cm^{-1})といったモードが誘起されており、新たに生成した C-CN 間の結合エネルギーが、C_5H_6N の内部振動エネルギーに分配している様子が見られる。(c)置換の図では、CCN 変角 (~160cm^{-1})や CH_3 のアンブレラモード(~340cm^{-1})が誘起しており、新たに生成した C-CN 間の結合エネルギーを分子内の振動エネルギーで分配できないために、ポテンシャルエネルギーによる緩和、すなわち CH_3 ラジカル解離へと反応が進行することが分かった。炭化水素の豊富な惑星や、その衛星の大気の不飽和ニトリルの生成において、同反応は置換反応が重要な役割を占めていると考えられる。

このように AIMD シミュレーションと短時間フーリエ変換による解析方法によって、この衝突反応における振動モードと反応経路の関係を導き出すことができた。また、スピン密度変化に対しても短時間フーリエ変換を適用することにより、この反応のラジカル移動のダイナミクスについても検討した。

[1] N. Balucani et. al., J. Chem. Phys., 111, (1999) , 7472.

分子構造総合討論会 2004,
広島国際会議場（広島），2004 年 9 月.

3C05 時間依存密度汎関数法（TDDFT）を用いた内殻励起に関する理論的研究

(早大理工) ○今村 穣，大塚 教雄，中井 浩巳

【序】時間依存密度汎関数法(TDDFT)は莫大な計算コストを必要とせず定量的な結果を与えることから、近年、価電子励起状態の計算に盛んに用いられている。一方、内殻励起状態に関しては、これまで体系的な研究は行われていない。本研究では、一般的な汎関数（BLYP, B3LYP など）を用いた内殻励起状態の TDDFT 計算より、その問題点を明らかにした。さらにその問題を解決するためにモデル汎関数、モデルポテンシャルを検討した。

【計算方法】本研究では、C, N, O, Ne など第 2 周期原子を含む分子（原子）の内殻励起状態を TDDFT 計算により検討した。用いた汎関数は、LDA, BLYP, B3LYP, BHandHLYP である。比較として、TDHF 計算も行った。更に、以下のモデルポテンシャル、モデル汎関数に関しても、Gaussian03 に組み込み、検討した。

LB94: LDA ポテンシャルの漸近的な振舞いを改良するモデルポテンシャルが、Leeuwen と Baerends（LB94）らにより提案されている。

$$\upsilon_{xc,\sigma}^{LB94}(r) = -\beta\rho_\sigma^{1/3}(r)\frac{\chi_\sigma^2}{1+3\beta\chi_\sigma \sinh^{-1}(\chi_\sigma)} \qquad \chi_\sigma = \frac{|\nabla\rho_\sigma|}{\rho_\sigma^{4/3}}, \beta = 0.05$$

SCF 計算においてのみ、このポテンシャルは、LDA ポテンシャルと共に考慮される。このポテンシャルの形は、漸近的な振舞いの向上だけでなく、内殻へのポテンシャルの寄与も大きいことがわかっており、内殻励起エネルギーの精度の向上が期待される。

B88m: Becke により提案されたユニタリー不変な関数 D は、以下のように表される。

$$D_\sigma = \frac{(\nabla\rho_\sigma)^2}{4\tau_\sigma\rho_\sigma}, \quad \tau_\sigma = \sum_i |\nabla\phi_{i,\sigma}|^2$$

この D は、一つの軌道のみで電子状態が表される領域で 1 の値を与える関数である。D の振舞いを調べるために、D の関数を用いてネオン原子の電子密度の分割を行った（図 1）。ひとつの軌道が支配的な

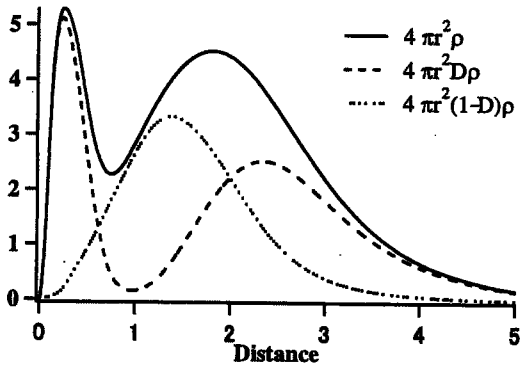

図 1　ネオンの分割された電子分布

的な内殻領域および漸近的領域では、Dρにより電子が抽出されている。一方、結合領域では複数の軌道が関わっており D が小さい値となるため、(1 −D)ρ により電子が抽出されている。この D の関数を用いて、Becke88 交換項を内殻電子の寄与が支配的な部分とその他の部分に分割する。

$$E_x = \sum_\sigma [c_1 \int d\mathbf{r}(1-D_\sigma)\rho_\sigma(\mathbf{r})e_x^{B88} + c_2 \int d\mathbf{r} D_\sigma \rho_\sigma(\mathbf{r})e_x^{B88}]$$

パラメーターc_1, c_2は、内殻励起エネルギーの結果を再現するようにそれぞれ 1.45, 1.55 に決定した。相関項として、LYP 汎関数を用いた。

計算に用いた分子構造は、すべて B3LYP レベルで最適化を行った。基底関数は、cc-pVTZ、Rydberg 励起の場合は、更に Dunning-Hay Double Rydberg(s,p)基底を加えたものを用いた。

【結果と考察】表１にさまざまな汎関数による 1s 軌道からπ*軌道への内殻励起エネルギーを示す。括弧内の数字は、実験値からの誤差を表し、表中の太字原子はその原子の 1s 軌道から電子が励起することを表す。TDHF は、すべての分子において励起エネルギーを 7-16 eV 程度過大評価する。一方、Pure DFT 法である LDA, BLYP は 15 eV 以上過少に評価することが明らかになった。Hybrid 法は、Pure DFT 法と Hybrid 法の中間の結果を再現することがわかった。これは、Exact な交換項により Pure DFT による過少評価が補正されたためと考えられる。今回新たに組み込んだ LB94, B88m の誤差は、1.58, 0.54 eV といずれの方法よりもはるかに良い値を与えている。LB94 の場合は、実験値よりも過少評価する傾向があるが、B88m でははっきりした傾向が見られなかった。TDDFT では記述の精度が低いと報告されている Rydberg 励起に関しても検討を行った。表２は、1s 軌道から 3p 軌道への内殻励起エネルギーを示す。Rydberg 励起においても、LB94, B88m は、ネオン原子の場合を除き精度の高い結果を再現した。ネオン原子の誤差が他の分子に比べ大きい理由は、ネオンの深い内殻 1s 軌道の記述が十分でないためと考えられる。また、LB94, B88m は、窒素や一酸化炭素の価電子励起に関しても BLYP に近い精度で励起エネルギーを再現することを確認した。

表１ 1s→π* type core excitation energies in eV at TDDFT/cc-pVTZ.

	TDHF	LDA	BLYP	B3LYP	BHHLYP	LB94	B88m	Expt.
CO	294.42 (7.0)	267.84 (-19.6)	271.35 (-16.1)	276.18 (-11.2)	283.57 (-3.8)	284.88 (-2.5)	287.78 (0.4)	287.4
CH_2O	294.40 (8.4)	266.48 (-19.6)	270.25 (-15.8)	275.27 (-10.8)	282.98 (-3.0)	284.70 (-1.3)	286.39 (0.4)	286.03
$\boldsymbol{C_2}H_2$	296.06 (10.3)	266.38 (-19.4)	269.98 (-15.8)	275.35 (-10.4)	283.63 (-2.2)	284.65 (-1.1)	286.01 (0.2)	285.8
$\boldsymbol{C_2}H_4$	294.84 (10.1)	265.37 (-19.3)	269.07 (-15.6)	274.37 (-10.3)	282.56 (-2.1)	283.80 (-0.9)	284.96 (0.3)	284.7
$\boldsymbol{N_2}$	412.26 (11.3)	378.38 (-22.6)	382.53 (-18.5)	388.57 (-12.4)	397.98 (-3.0)	399.39 (-1.6)	400.9 (-0.1)	401.0
OC	550.13 (15.9)	507.67 (-26.5)	512.41 (-21.8)	519.89 (-14.3)	531.70 (-2.5)	535.14 (0.9)	532.81 (-1.4)	534.2
OH_2C	545.96 (15.2)	504.68 (-26.1)	509.51 (-21,3)	516.75 (-14.1)	528.18 (-2.6)	528.15 (-2.7)	529.71 (-1.1)	530.8
MAE	11.16	21.88	17.83	11.94	2.76	1.58	0.54	

表２ 1s→3p core excitation energies in eV at TDDFT/cc-pVTZ + Double Rydberg(s,p).

	LDA	BLYP	BHHLYP	LB94	B88m	Expt.
CH_4	265.81(-22.2)	269.23(-18.8)	285.93(-2.1)	286.87(-1.1)	288.35(0.4)	287.98
NH_3	376.66(-25.8)	380.64(-21.9)	400.13(-2.4)	400.37(-2.1)	402.16(-0.3)	402.5
OH_2	506.42(-29.5)	511.04(-24.9)	533.03(-2.9)	532.64(-3.3)	534.93(-1.0)	535.9
Ne	824.72(-42.4)	830.61(-36.5)	860.43(-6.7)	859.76(-7.3)	862.07(-5.0)	867.1
MAE	29.97	25.50	3.49	3.46	1.67	

分子構造総合討論会 2004,
広島国際会議場（広島），2004 年 9 月.

1C02　電子状態理論における重心運動の取り扱いに関する一考察

(早大理工) ○袖山慶太郎，宮本開任，星野稔，中井浩巳

【緒言】当研究室では、電子と原子核の波動関数を同時に決定することのできる ab initio NOMO 法の開発を行ってきた[1-4]。Ab initio NOMO 法では、電子と原子核の軌道を Gauss 関数で表現している。Gauss 関数は、振動・並進・回転という原子核の運動のうち、振動状態の記述に有利であるが、並進・回転運動を正確に記述することが困難であり、従来の NOMO 法では定量的な結果を得ることが出来ない。これまで我々は、重心の位置を原子核のみから近似的に求めることで並進運動の分離を行ってきたが、今回の発表では、より厳密に重心の位置を電子および原子核を含む全粒子から求めた場合についても検討する。これらの方法をそれぞれ *ntf*-NOMO 法および *tf*-NOMO 法と呼ぶ。さらに Born-Oppenheimer (BO)近似に基づく従来の MO 法における重心運動の取り扱いに関しても考察する。本研究では、現在最も高精度に測定されている観測量の一つである Rydberg 定数に対して上記３つの方法を適用し、それぞれの物理的意味について考察する。

【方法】並進運動を分離する前の電子および原子核の運動エネルギー項をそれぞれ T_e, T_n とすると、並進運動を分離する操作をした後の運動エネルギー項 T_e', T_n' は以下のようになる。

NOMO 法:　$\hat{T}_e' = \hat{T}_e \ , \ \hat{T}_n' = \hat{T}_n$　(1)

tf-NOMO 法:　$\hat{T}_e' = (1-\frac{m_e}{M_T})\hat{T}_e \ , \ \hat{T}_n' = (1-\frac{M_Z}{M_T})\hat{T}_n$　(2)

ntf-NOMO 法:　$\hat{T}_e' = \hat{T}_e \ , \ \hat{T}_n' = (1-\frac{M_Z}{M_{nT}})\hat{T}_n$　(3)

MO 法:　$\hat{T}_e' = \hat{T}_e \ , \ \hat{T}_n' = 0$　(4)

ここで m_e, M_Z はそれぞれ電子および原子番号 Z である原子核の質量、M_T, M_{nT} は全粒子および全原子核の質量の和である。式(3)で原子の計算をする場合、M_Z と M_{nT} は等しくなるため $T_n'=0$ となる。H から Ne^{9+} までの一電子系原子に対して *ntf*-NOMO/HF 法及び *tf*-NOMO/HF 法を適用した。基底関数は、電子に cc-pVQZ の指数に対応した原始関数を用い、原子核に(17s) (1.0×10^3 - 1.0×10^{11} cm^{-1})[2]を用いた。

【結果と考察】並進運動を分離しない NOMO/HF 法、*ntf*-NOMO/HF 法および *tf*-NOMO/HF 法の、MO/HF 法からの全エネルギー差を Table 1 に示す。NOMO/HF 法では、原子番号の増加につれて MO/HF 法との差が大きくなり、Ne^{9+} において 0.84 hartree になっている。これは原子核の大きな並進運動が混入することによる誤差である。また式(3)より、*ntf*-NOMO/HF

Table 1. NOMO/HF、*ntf*-NOMO/HF および *tf*-NOMO/HF 法による、一電子系原子の全エネルギー [hartree]　(括弧内は MO/HF 法との差を示す。)

	NOMO/HF		*ntf*-NOMO/HF		*tf*-NOMO/HF		MO/HF
H	-0.466206	(0.033741)	-0.499947	(0.000000)	-0.499307	(0.000640)	-0.499947
He^+	-1.928417	(0.071466)	-1.999884	(0.000000)	-1.999233	(0.000651)	-1.999884
Li^{2+}	-4.375068	(0.124911)	-4.499979	(0.000000)	-4.499118	(0.000861)	-4.499979
Be^{3+}	-7.804116	(0.195857)	-7.999972	(0.000000)	-7.998785	(0.001187)	-7.999972
B^{4+}	-12.22145	(0.278513)	-12.499959	(0.000000)	-12.498424	(0.001535)	-12.499959
C^{5+}	-17.61222	(0.387720)	-17.999943	(0.000000)	-17.997942	(0.002001)	-17.999943
N^{6+}	-24.01038	(0.489548)	-24.499925	(0.000000)	-24.497584	(0.002341)	-24.499925
O^{7+}	-31.402790	(0.597113)	-31.999904	(0.000000)	-31.997197	(0.002707)	-31.999904
F^{8+}	-39.80534	(0.694539)	-40.499877	(0.000000)	-40.496995	(0.002883)	-40.499878
Ne^{9+}	-49.16188	(0.837979)	-49.999854	(0.000001)	-49.996499	(0.003355)	-49.999854

法は MO/HF 法によるエネルギーと理論的に一致するはずだが、実際に Ne^{9+} における *ntf*-NOMO/HF 法と MO/HF 法とのエネルギー差は 1.0×10^{-6} hartree となり、両方法の一致が数値的に確かめられた。これに対して *tf*-NOMO/HF 法では、H で 6.4×10^{-4} hartree、Ne^{9+} で 3.4×10^{-3} hartree、MO/HF 法の結果よりも高い全エネルギーが得られた。これは non-BO 効果によるものと考えられるが、その大きさが妥当であるか確かめるために *tf*-NOMO/HF 法、*ntf*-NOMO 法および MO 法によって Rydberg 定数を求めた(Fig. 1, Table 2)。原子核の質量を∞としている MO/HF 法では、式(4)より原子核の運動エネルギーはゼロであり、R_∞ が得られる。一方、原子の場合、*ntf*-NOMO/HF 法では式(3)より原子核の運動エネルギーがゼロとなり、結果的に MO 法と同様に R_∞ が得られる。Table 2 から厳密な R_∞ の値と計算値を比較したところ 1-10 cm^{-1} の誤差の範囲で R_∞ の値が求められた。さらに R_∞ は本来全ての元素に対して一定値であるが、*ntf*-NOMO/HF 法および MO/HF 法から求めた R_∞ のうち、最大値と最小値の差は 11 cm^{-1} となった。*tf*-NOMO/HF 法では式(2)より、電子と原子核両方の運動エネルギーを扱っているため、R_Z が求められる。MO/HF 法との全エネルギーの差が最大である Ne^{9+} において R_Z の厳密解との差は 3 cm^{-1} であり、*tf*-NOMO/HF 法と MO/HF 法から得られる全エネルギーの差は non-BO 効果によることが明らかになった。

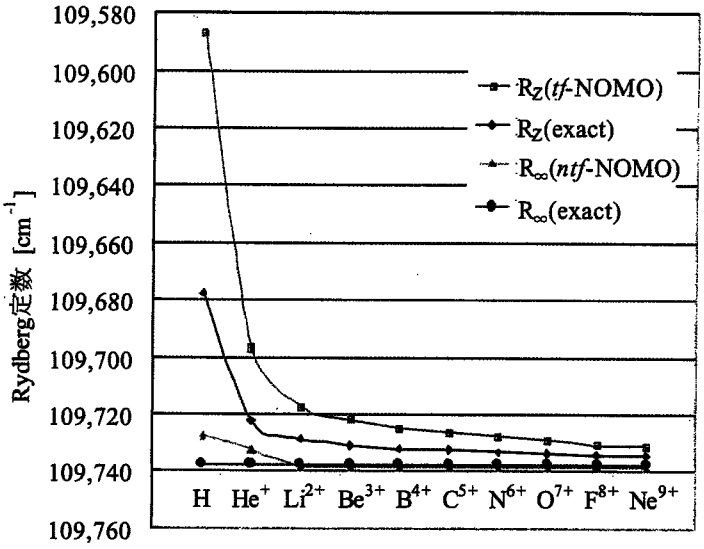

Fig. 1. *tf*-NOMO/HF 法および *ntf*-NOMO 法による一電子系原子の Rydberg 定数

Table 2. *tf*-NOMO/HF 法、*ntf*-NOMO 法および MO 法による一電子系原子の Rydberg 定数 [cm^{-1}]

	R_∞			R_Z	
	ntf-NOMO	MO	exact	*tf*-NOMO	exact
H	109,727.16	109,727.16	109,737.31	109,586.60	109,677.58
He^+	109,732.39	109,732.39	109,737.31	109,696.70	109,722.27
Li^{2+}	109,738.26	109,738.26	109,737.31	109,717.27	109,728.73
Be^{3+}	109,738.39	109,738.39	109,737.31	109,722.10	109,730.63
B^{4+}	109,738.41	109,738.41	109,737.31	109,724.94	109,731.84
C^{5+}	109,738.42	109,738.42	109,737.31	109,726.22	109,732.29
N^{6+}	109,738.43	109,738.43	109,737.31	109,727.95	109,733.01
O^{7+}	109,738.43	109,738.43	109,737.31	109,729.16	109,733.55
F^{8+}	109,738.43	109,738.44	109,737.31	109,730.63	109,734.14
Ne^{9+}	109,738.44	109,738.45	109,737.31	109,731.09	109,734.30

[1] M. Tachikawa, K. Mori, H. Nakai, K. Iguchi, *Chem. Phys. Lett.*, **290** (1998) 437.
[2] H. Nakai, *Int. J. Quantum Chem.*, **86** (2002) 511.
[3] H. Nakai, K. Sodeyama, M. Hoshino, *Chem. Phys. Lett.*, **345** (2001) 118.
[4] H. Nakai, K. Sodeyama, *J. Chem. Phys.*, **118** (2003) 1119.

分子構造総合討論会 2004,
広島国際会議場（広島），2004 年 9 月.

1C03 DFT 計算に対する結合エネルギー密度解析(Bond-EDA)

(早大理工) ○菊池那明，中井浩巳

【序】分子内の化学結合を理解することは、昔から化学的・物理学的に非常に重要である。Energy Density Analysis (EDA)[1]は電子状態理論計算により得られた全エネルギーを構成原子に分割する、当研究室で最近開発された新しい解析手法である。これまでの EDA は全エネルギーを構成原子に分割するのみであったが、化学結合や分子間相互作用をより詳細に解析するには、EDA を拡張して結合領域にもエネルギー密度を分割する必要がある。そこで本研究者はこれまでに、Hartree-Fock (HF)計算より得られた全エネルギーを構成原子や結合領域にエネルギー密度として分割する Bond-EDA[2]を提案した。しかし電子相関を考慮しない HF 計算では表現不可能な現象も多く限界があるため、本研究では Bond-EDA を Density Functional Theory (DFT)に対して拡張し、種々の化学的現象に応用した。

固体表面の吸着や触媒反応を理論的に取り扱う場合、表面の一部を切り出すクラスターモデルがよく用いられるが、結果がクラスターのサイズや形状に大きく依存するという問題がしばしば生じる。このような系に対して Bond-EDA を適用することにより、クラスターの形状やサイズ依存性、クラスターモデルの妥当性に対する検討を行う。

【理論】EDA は主に、Mulliken の電子密度解析の類推を用いた分割スキームを採用している。Mulliken の電子密度解析では、非対角項を用いて結合次数を見積ることができる。Bond-EDA はこれを利用し、当研究室で開発した EDA の拡張として、その非対角項を用いて結合エネルギーを見積もる。例えば、原子 A-B 間の Kinetic Energy は、

$$T^{AB} = \sum_{\mu \in A} \sum_{\nu \in B} P_{\mu\nu} T_{\nu\mu}$$

と見積もられる。この類推を、Grid を用いた計算を行っている DFT の Exchange-Correlation 部分にも適用した。

【結果と考察】Bond-EDA を用いると、エタン分子の化学結合を次のように検討することが出来る。計算レベルは B3LYP/cc-pVDZ である。Table 1 に示す結果より、結合が存在する C-C 間、C-H 間の結合エネルギー密度は絶対値の大きな負の値を持ち、結合による安定化を示している。結合していない H-H 間、C-H 間では絶対値の小さい正の値を持ち、これは立体効果に対応するものと考えられる。また、H-H 間の結合エネルギー密度はその距離に依存して小さくなっている。原子に割り当てられるエネルギーの、単原子分子状態のエネルギーからの差は、その大部分が内殻電子からの寄与であると考えられる。

Table 1. Bond-EDA for Ethane

Atomic energy density, E^{AA}		
C	(×2)	-23735.45
H	(×6)	-313.74
Bond energy density, E^{AB}		
C-C		-148.37
C-H	(×6)	-108.44
H-H geminal	(×6)	8.62
C-H vicinal	(×6)	7.43
H-H vicinal	(×3)	-2.85
H-H vicinal	(×6)	1.86
Total		-50053.43

水素、窒素、酸素、フッ素の各分子における結合解離エネルギーを Bond-EDA を用いて解析した。計算レベルはそれぞれ HF/cc-pVDZ、B3LYP/cc-pVDZ である。Table 2 にその結果を示す。ここで“atom”は分子の生成によって原子部分がどれ

だけ安定化したかを、"bond"は結合領域がどれだけ安定化したかを、それぞれ示す。また、"total"は、結合の生成による分子全体の安定化を示している。"Exptl."は結合エネルギーの実験値であり、結合の生成によるエンタルピー変化である。Table 2 より、これらの分子では HF 計算は B3LYP 計算に比べて結合解離エネルギーの表現が悪い事がわかる。結合解離の正しく表現できる B3LYP 計算に対して拡張された Bond-EDA の結果は妥当である。また、HF 計算に対する分割に注目すると、Bond-EDA による結合領域の表現は全体的に結合解離エネルギーの実験値より大きな値となっている。一方、原子の表現はすべて負の値であり、結合状態における原子の表現が悪い事を示している。HF 計算において結合解離エネルギーの表現が悪いのは、特に原子部分のエネルギーの表現が悪くなっているためであると考察できる。

Table 2. Bond-EDA for Diatomic Molecules

		HF	B3LYP	Exptl.
H_2	atom	-12.07	2.80	
	bond	105.83	101.79	
	total	81.69	107.38	103.27
N_2	atom	-77.96	24.03	
	bond	264.74	173.52	
	total	108.82	221.58	225.05
O_2	atom	-81.14	14.28	
	bond	193.33	95.04	
	total	31.05	123.60	117.97
F_2	atom	-65.83	-4.49	
	bond	93.67	46.51	
	total	-37.98	37.52	37.00

銅表面への formate 吸着に対するクラスターモデルを用いたモデル化について、Bond-EDA を用いた検討を行う。基底関数として酸素、炭素原子には Huzinaga-Dunning の(9s,5p,1d)/[4s,2p,1d]を、水素原子には Huzinaga-Dunning の(4s,1p)/[2s,1p]を、銅原子には Christiansen の small core ECP に原子価殻の表現として(7s,6p,6d)/[3s,3p,2d]としたものを用いた B3LYP 計算を行った。銅(111)クラスターの表面に formate を吸着させた場合の吸着エネルギーと、これを Bond-EDA を用いて分割したもののクラスターサイズ(Figure 1)による変化を Figure 2 に、Cu_{40} を基準として示す。全吸着エネルギーの変化について検討すると、Cu_{18} 以上ではその吸着エネルギーが 5 kcal/mol 以内に収束することがわかる。これを Bond-EDA の分割を用いて、formate の吸着によるエネルギー変化、銅クラスターのエネルギー変化、吸着による formate-銅クラスター間の相互作用という 3 種類の要素に分割して解析すると、Cu_{28} 以上で各要素とも 10 kcal/mol 以内に収束することがわかった。

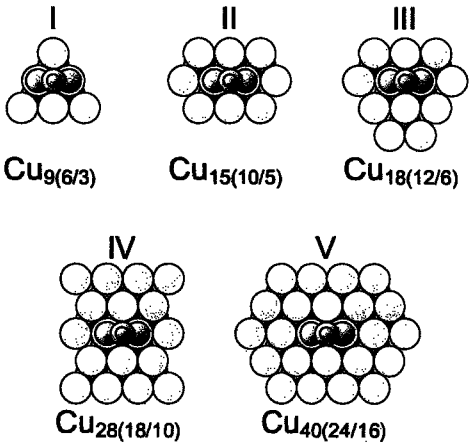

Figure 1. Calculated Cu(111) cluster model

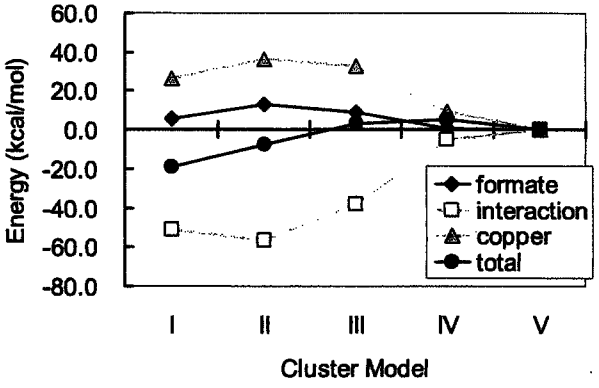

Figure 2. Cluster-size dependence of formate adsorption energy and bond energy density change at Cu(111) cluster

[1] H. Nakai, Chem. Phys. Lett., **363**, 73-79 (2002).
[2] H. Nakai and Y. Kikuchi, J. Chem. Phys., *submitted*.
[3] Z. Hu and R.J. Boyd, J. Chem. Phys., **112**, 9562-9568 (2000).

2P018　エネルギー移動スペクトログラム(ETS)による化学反応の解析

(早大理工) ○山内佑介，中井浩巳

【序】反応ダイナミクスを理解する上で、エネルギー移動と振動モードとの関係は重要であり、古くから研究が行われてきた。本研究では、*ab initio* molecular dynamics (AIMD)シミュレーションにより反応ダイナミクスを追跡し、その結果からエネルギー移動に関与しているモードを定量的に取り出す方法を検討した。

【理論】ミクロカノニカルアンサンブルを扱うMDシミュレーションで保存される全エネルギーEは、ポテンシャルVと運動エネルギーTに分けることができる。これまでTを部分系T_mに分割することは可能であったが、Vの分割は不可能であった。Energy Density Analysis (EDA)の開発によって部分系のポテンシャルエネルギーV_mが求まり、結果として部分系の全エネルギーE_mが計算可能になった。E_mの変化によって、系内のエネルギー移動量が見積もられる。

$$E = \sum_{m\in\text{system}} E_m = \sum_m (T_m + V_m) \rightarrow \text{conserv.} \quad (1)$$

さらにシミュレーションから得られた非平衡状態の時系列データを解析するために、短時間フーリエ変換(ST-FT)の手法を用いた。ST-FT では無限時間のデータ $f(t,t')$の一部を窓関数 $h(t-t')$によって切り出し、フーリエ変換を行う。ST-FT の結果得られる$S(t,\omega)$の像をスペクトログラムと呼ぶ。

$$S(t,\omega) = \int f(t,t')h(t'-t)\exp(-i\omega t')dt' \quad (2)$$

速度の自己相関関数のフーリエ変換はパワースペクトルとしてよく知られている。今回は上で示されたエネルギーE_mの時間変化に対して自己相関関数を求め、そのフーリエ変換をエネルギー移動スペクトログラム(ETS)と名付けた。

$$f(t,t') \equiv \left\langle \dot{E}_m(t)\cdot\dot{E}_m(t-t') \right\rangle_m \quad (3)$$

【結果と考察】はじめに、熱振動をしているアンモニアクラスターイオン$NH_4^+(NH_3)_2$のAIMDシミュレーションを行い、エネルギー移動スペクトロ

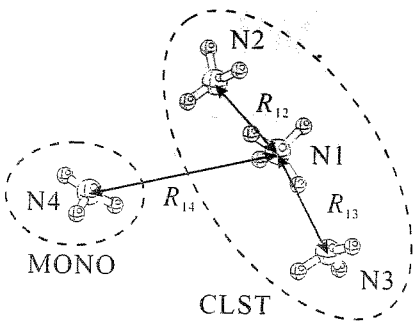

Fig. 1. Labeling of nitrogen atoms and definition of monomer, cluster and N-N distances in the system.

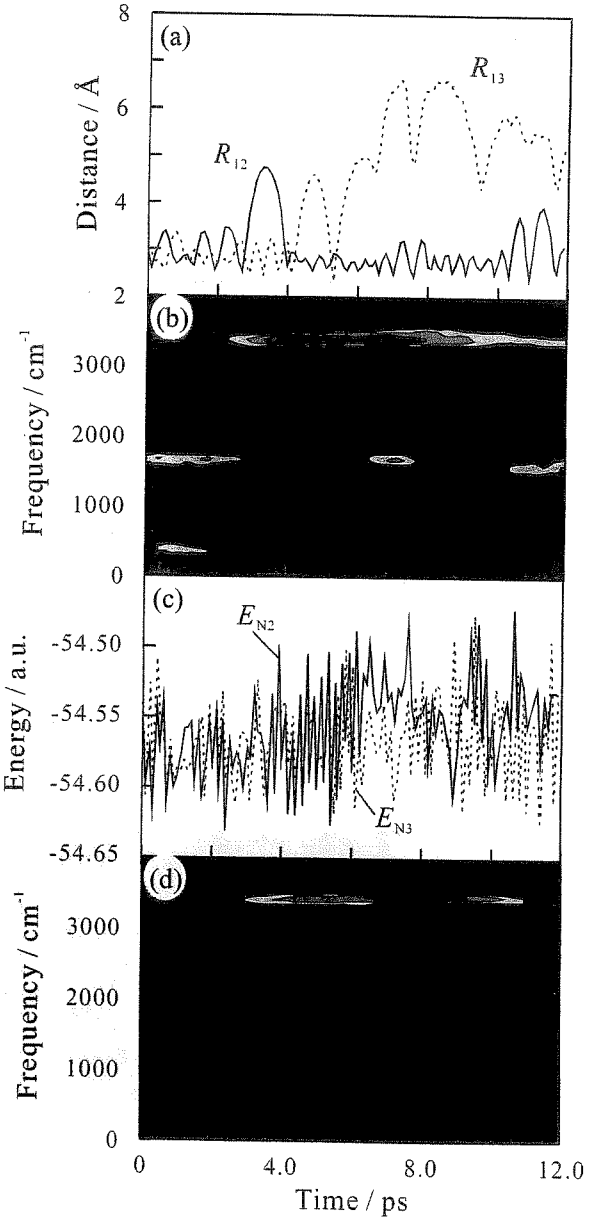

Fig. 2. (a) Time evolution of the N-N distances defined in Fig. 1, (b) power spectrogram, (c) time evolution of the local energies in nitrogen atoms, and (d) energy transfer spectrogram (ETS) in thermal motion of $NH_4^+(NH_3)_2$.

グラムの振舞いを検討した。熱運動によって中心イオンの組換えが起こっており、図 2(a)における 4.0 ps以降のR_{13}の増加はこれを示している。図 2(b)は、速度自己相関関数から得られたスペクトログラムである。約 3500 cm^{-1}のN-H伸縮、1200 – 1800 cm^{-1}のH-N-H変角、0 – 600 cm^{-1}のNH_3横揺やひねり振動が、時間変化する様子が現れている。4.0 psあたりで変角や低波数のピークが弱くなる一方、N-H伸縮のピークが強くなり、分子間結合の開裂のためにひとつのモードに運動エネルギーが集中している。図 2(c)は、EDAによって分割されたE_{N1}、E_{N2}の時間変化を示している。これらのE_mを用いて描かれたETSが図 2(d)に示されている。全時間を通して約 3500 cm^{-1}の位置にのみピークが見られる。これは、熱振動しているアンモニアクラスターイオンにおけるエネルギーのゆらぎが、主にN-H伸縮振動に対応することを意味している。続いて、$NH_4^+(NH_3)_2$とアンモニアモノマーNH_3の衝突過程のシミュレーションを多数行い、ETSによる解析を行った。図 3 は無反応衝突と吸着過程についてそれぞれN-N距離の時間変化、モノマーのエネルギーの時間変化、そしてモノマーとクラスター間のETSを示している。無反応衝突(図 3(b))では衝突の瞬間にのみモノマーのエネルギー変化が見られる。さらにETS(図 3(c))では約 2800 cm^{-1}にピークが見られ、これは中心イオンのN-H伸縮振動に対応している。一方、図 3(e)には吸着によるエネルギー変化が徐々に緩和している様子が示されている。またそのETS(図 3(f))では広い振動数領域にピークが存在する。1100 cm^{-1}のピークはN-H···N伸縮振動であり、これらの振動がエネルギー移動に関与していると考えられる。このようにETSによって、反応中のエネルギー移動と振動モードの関係を明らかにすることができた。

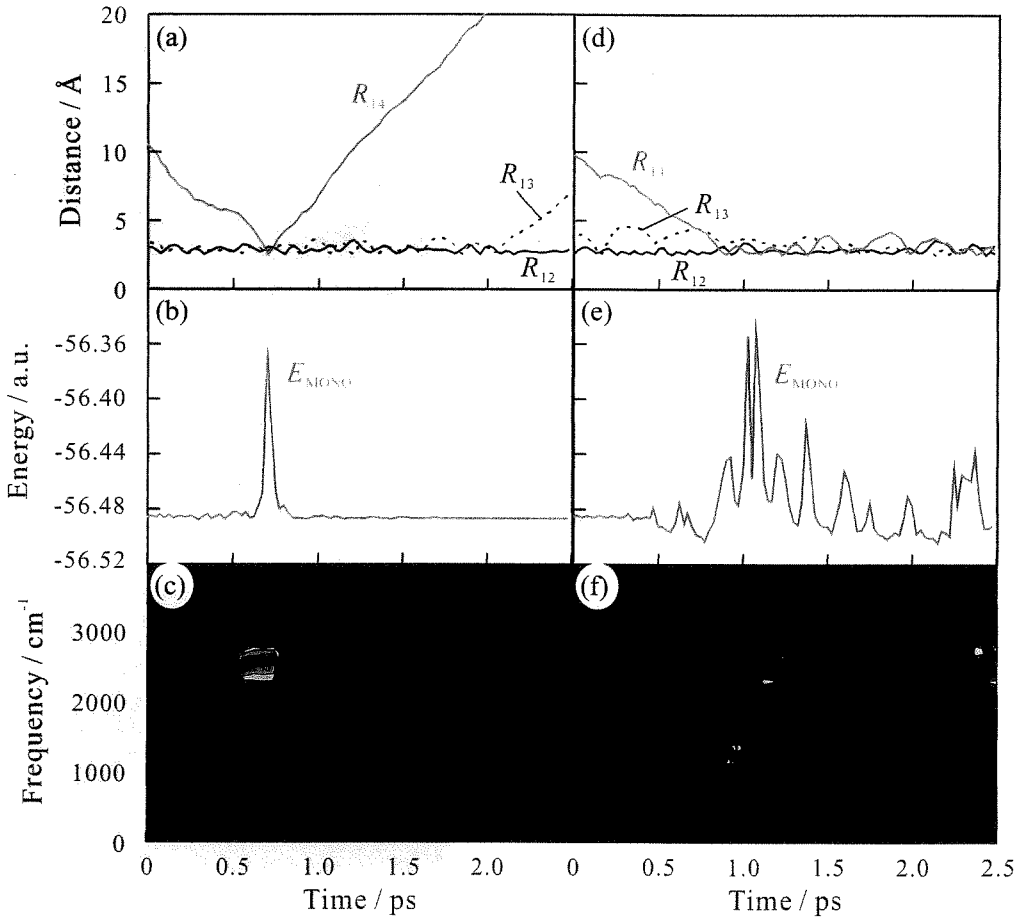

Fig. 3. Time evolution of the N-N distances defined in Fig. 1 [(a) and (d)], the local energy in the monomer [(b) and (e)], and the ETS [(c) and (f)] in non-reactive collision and incorporation, respectively.

[1] H. Nakai, Chem. Phys. Lett. **363** (2002) 73.
[2] Y. Yamauchi, H. Nakai, and Y. Okada, J. Chem. Phys., *submitted*.

分子構造総合討論会 2004,
広島国際会議場（広島），2004 年 9 月.

1P120 *Ab initio* NOMO 法における回転運動の取り扱い

(早大理工) ○星野　稔，宮本開任，中井浩巳

【序】 我々はこれまで、Born-Oppenheimer (BO)近似に基づかず、電子および原子核の波動関数を同時に求めることのできる *ab initio* NOMO 法[1-4]の開発を行ってきた。NOMO 法は原子核も量子論的に扱っているため、原子核の運動エネルギー項が存在する。原子核の運動には並進、回転、振動が含まれている。Gauss 基底は局所的な関数であるため並進および回転の空間を張るのは困難である。したがって、並進および回転運動を分離することによって、Gauss 基底を用いて原子核の運動を精度良く記述することができる。これまでの研究で並進運動を分離した NOMO (*tf*-NOMO) 法の開発を行った[2]。原子に対する *tf*-NOMO 法の計算では従来の BO 近似に基づく分子軌道法による計算結果との一致が得られた。しかし、多原子分子になると回転運動が含まれるため、並進運動の分離のみでは不十分であった。そこで本研究では、NOMO 法における回転運動の取り扱いについて考察し、並進および回転運動を分離する方法を開発した。この方法を用いて得られた結果から、その妥当性について検証する。

【理論】 Cartesian 座標系で表した角運動量演算子は式(1)のようになる。Cartesian 座標系における x, y, z 軸を対象分子の慣性主軸になるように座標変換すると、分子の回転演算子は式(2)のように表される。$\hat{L}_\alpha(\mathbf{x}), I_\alpha\ (\alpha = x, y, z)$ は、それぞれ角運動量演算子 $\hat{\mathbf{L}}(\mathbf{x})$ の慣性主軸成分、主軸慣性モーメントを表している。回転演算子および重心の並進演算子(式(3), M_Tは全質量)を non-BO Hamiltonian から引くことによって、並進および回転を分離した non-BO Hamiltonian を導出した。これより、一体近似のもとで電子および原子核の波動関数を求める translation and rotation free NOMO/HF (*trf*-NOMO/HF) 法の導出を行った。電子および原子核に対する Fock 演算子 $\hat{f}_e, \hat{f}_n$ は以下のようになる。

$$\hat{\mathbf{L}}(\mathbf{x}) = \frac{1}{i}\sum_i^N \mathbf{x}_i \times \nabla_i \tag{1}$$

$$\hat{T}_{rotation}(\mathbf{x}) = \frac{\hat{L}_x(\mathbf{x})^2}{2I_x} + \frac{\hat{L}_y(\mathbf{x})^2}{2I_y} + \frac{\hat{L}_z(\mathbf{x})^2}{2I_z} \tag{2}$$

$$\hat{T}_G(\mathbf{x}) = -\frac{1}{2M_T}\sum_i^N \nabla_i^2 - \frac{1}{M_T}\sum_{i<j}^N \nabla_i \cdot \nabla_j \tag{3}$$

$$\hat{f}_e = -\sum_e \frac{1}{2}\left(\frac{1}{m_e} - \frac{1}{M_T}\right)\nabla_e^2(\mathbf{x}_e) - \left(\frac{\hat{L}_x(\mathbf{x}_e)^2}{2I_x} + \frac{\hat{L}_y(\mathbf{x}_e)^2}{2I_y} + \frac{\hat{L}_z(\mathbf{x}_e)^2}{2I_z}\right) + \sum_i^{elec}\left(\hat{J}_i - \hat{K}_i\right) + \sum_I^{nuc}\hat{J}_I \tag{4}$$

$$\hat{f}_n = -\sum_n \frac{1}{2}\left(\frac{1}{m_n} - \frac{1}{M_T}\right)\nabla_n^2(\mathbf{x}_n) - \left(\frac{\hat{L}_x(\mathbf{x}_n)^2}{2I_x} + \frac{\hat{L}_y(\mathbf{x}_n)^2}{2I_y} + \frac{\hat{L}_z(\mathbf{x}_n)^2}{2I_z}\right) + \sum_I^{nuc}\left(\hat{J}_I \mp \hat{K}_I\right) + \sum_i^{elec}\hat{J}_i \tag{5}$$

$\hat{J}, \hat{K}$ はそれぞれ、クーロン、交換項を表している。ここで Gauss 関数の基底関数中心 $\mathbf{x}_i^0 = (x_i^0, y_i^0, z_i^0)$ を導入し、それからの変位を $\Delta\mathbf{x}_i = (\Delta x_i, \Delta y_i, \Delta z_i)$ とすると、i 番目の粒子の座標は式(6)ようになる。また、慣性モーメントを式(7)のように表し、式(8)のように Taylor 展開を行う。ただし、$I_\alpha^0, \Delta I_\alpha\ (\alpha = x, y, z)$ は、それぞれ基底関数中心から見積もった慣性モーメント、I_α^0 からの変位である。式(6), (8)における第 1 項目までの近似が剛体回転子近似に対応する。この近似における回転が純回転である。本研究では第 1 項および第 2 項までで近似した場合の計算を行い、その妥当性の検証を行った。

また、*trf*-NOMO/HF 法で得られた波動関数を参照関数として多体摂動論 (MBPT)を適用することにより、並進および回転を分離した *trf*-NOMO/MBPT*n* 法の開発を行った。

$$\mathbf{x}_i = \mathbf{x}_i^0 + \Delta\mathbf{x}_i \tag{6}$$

$$I_\alpha = I_\alpha^0 + \Delta I_\alpha \quad (\alpha = x, y, z) \tag{7}$$

$$\frac{1}{I_\alpha} = \frac{1}{I_\alpha^0}\cdot\left(1 - \frac{\Delta I_\alpha}{I_\alpha^0} + \left(\frac{\Delta I_\alpha}{I_\alpha^0}\right)^2 + \cdots + (-1)^n\cdot\left(\frac{\Delta I_\alpha}{I_\alpha^0}\right)^n + \cdots\right) \quad (\alpha = x, y, z) \tag{8}$$

【計算結果】 まず、式(6), (8)を第 1 項で近似し、原子核に対してのみ並進・回転を分離した場合の計算を行った。

● *trf*-NOMO/HF による計算結果

H_2分子に対して *trf*-NOMO/HF 法により、全エネルギーに対する原子核の基底関数依存を調べた(Fig. 1)。電子の基底関数には cc-pVTZ の primitive 関数(5s2p1d)を用いた。Fig. 1 に示すように d 型の基底関数を用いることによって、基底状態の全エネルギーが大きく改善されることが分かった。また、原子核の基底関数は 5s5p5d で 10^{-5} hartree のオーダーで収束している。Table 1 に NOMO/HF と *trf*-NOMO/HF による基底状態の全エネルギーおよび NOMO/HF の全エネルギーからのエネルギー差を示す。対象分子は H_2, D_2, T_2 である。並進・純回転を分離することによって、各分子に対してそれぞれ 0.051719, 0.037951, 0.031594 hartree の改善が全エネルギーに対して得られた。これは NOMO/HF の全エネルギーの 3～5%となり、並進と回転を分離することの重要性を示している。

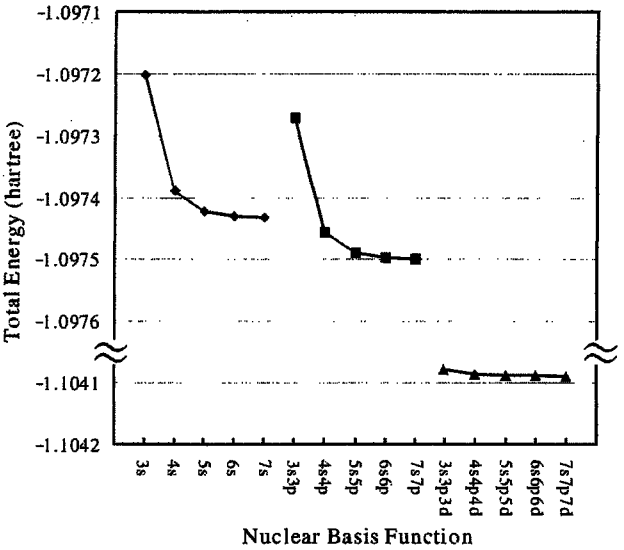

Fig. 1. Nuclear basis set dependencies for H_2 molecule.

Table 1. Total energies calculated by NOMO/HF and *trf*-NOMO/HF methods. (Differences from the total energy of NOMO/HF are shown in brackets.)

	H_2	D_2	T_2
NOMO/HF	-1.052371 (0.000000)	-1.074233 (0.000000)	-1.084308 (0.000000)
trf-NOMO/HF	-1.104090 (-0.051719)	-1.112184 (-0.037951)	-1.115902 (-0.031594)

● MBPT2 による計算結果

Fig. 2 は電子 - 核相関を取り込んだ NOMO/MBPT2、*tf*-NOMO/MBPT2、*trf*-NOMO/MBPT2 の全エネルギーを示す。対象分子は H_2, D_2, T_2 である。全エネルギーは、並進、並進・純回転を分離することで次第に下がっている。これは H_2, D_2, T_2 全ての分子に対して同じ傾向である。一方、相関エネルギーは Table 2 に示すように、Hamiltonian から並進、純回転を分離することによって電子 - 核相関が小さくなっている。つまり、NOMO/MBPT2 法における電子 - 核相関は、従来の BO 近似における電子相関のような、いわゆる粒子同士の衝突で表現される動的相関の補正だけでなく、Gauss 関数の直積では表現できない並進、回転の空間を補正する寄与が含まれている。

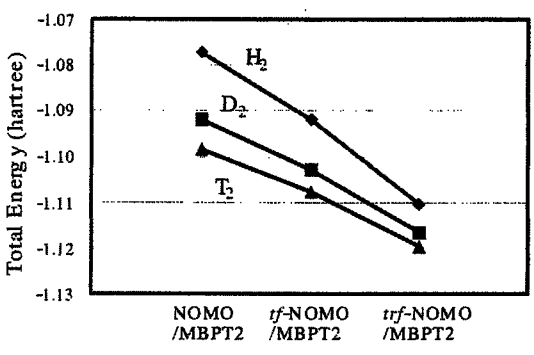

Fig. 2. Total energies calculated by MBPT2 methods.

Table 2. Electron-nucleus correlation energies for H_2, D_2 and T_2 calculated by NOMO/MBPT2, *tf*-NOMO/MBPT2 and *trf*-NOMO/MBPT2 methods.

	H_2	D_2	T_2
NOMO/MBPT2	-0.024996	-0.017552	-0.014293
tf-NOMO/MBPT2	-0.017733	-0.012373	-0.009980
trf-NOMO/MBPT2	-0.006451	-0.004583	-0.003809

[1] M. Tachikawa, K. Mori, H. Nakai, and K. Iguchi, Chem. Phys. Lett., 290 (1998) 437. [2] H. Nakai, Int. J. Quantum Chem., 86 (2002) 511. [3] H. Nakai, K. Sodeyama and M. Hoshino, Chem. Phys. Lett., 345 (2001) 118. [4] H. Nakai and K. Sodeyama, J. Chem. Phys., 118 (2003) 1119.

分子構造総合討論会 2004,
広島国際会議場（広島），2004 年 9 月.

1P119 AIMD シミュレーションにおける SCF 収束性の向上(2)

(早大理工) ○渥美 照夫、中井 浩巳

【緒言】*ab initio* molecular dynamics (AIMD)シミュレーションとは、原子核にかかる力を求める*ab initio* MO/DFT計算と、微小時間後の原子核の位置を予測する運動方程式を繰り返し解き、分子の運動を求める方法である。高精度な*ab initio* MO/DFT 計算を用いているために、結合の生成・開裂を伴う化学反応ダイナミクスを表すことが可能な一方、計算コストが高く大規模系や長時間のシミュレーションの実行が困難である。我々は、先の第8回理論化学討論会[1]でAIMDシミュレーションのボトルネックであるSCF計算を高速化する手法を提案した。本発表では、この方法を種々の系に応用することによりそのパフォーマンスの検証を行う。

【理論】これまで *ab initio* MO/DFT 計算において SCF 計算を高速に行う手法として、積分計算の高速化等により SCF 計算 1 回あたりの計算を高速に実行する方法や、DIIS のように収束性を向上させることで SCF 計算の回数を減らす方法が提案されている。しかし、これらの手法は一般的な *ab initio* MO/DFT 計算のために開発された方法である。そこで我々は、AIMD の特徴を用いる事で効率の良い SCF 計算の初期値を与え、収束性の向上を計った。

従来の AIMD シミュレーションでは SCF 計算の初期値として、経験的な Huckel 法で得られた MO(Guess=Huckel)や、直前のステップの MO(Guess=Read)が用いられてきた。これに対し、これまで用いられていなかった過去の(*n*-1)~(*n*-*m*)ステップの MO{$\mathbf{C}^{(n-1)},\cdots,\mathbf{C}^{(n-m)}$}を用い、Lagrange 補間法(1)より *n* ステップ目の MO{$\mathbf{C}^{(n)*}$}を予測し、SCF 計算の初期値とした(Guess=LI-MO)。

$$\mathbf{C}^{(n)*} = L[\mathbf{C}^{(n-1)},\mathbf{C}^{(n-2)},\mathbf{C}^{(n-3)},\cdots,\mathbf{C}^{(n-m)}] \quad (1)$$

さらに、SCF 計算による MO 間の Mixing の効果を表現するユニタリー行列(2)を求め、Lagrange 補間法(3)に反映させ *n* ステップ目の MO{$\mathbf{C}^{(n)*}$}を予測する方法(Guess=LI-MMO)を考えた。

$$\mathbf{C}^{(n-1)*}\mathbf{U}^{(n-1)} = \mathbf{C}^{(n-1)} \quad (2)$$

$$\mathbf{C}^{(n)*} = L[\mathbf{C}^{(n-1)},\mathbf{C}^{(n-2)}\mathbf{U}^{(n-1)},\cdots,\mathbf{C}^{(n-m)}\mathbf{U}^{(n-m+1)}\mathbf{U}^{(n-m+2)}\cdots\mathbf{U}^{(n-1)}] \quad (3)$$

【結果・考察】CH_3OH分子と$C_6H_6N_6O_6$分子のAIMDシミュレーションに 4 つの方法を適用しその効果を検討した。AIMD シミュレーションの条件として、*ab initio* 計算には B3LYP/D95V(Gaussian98)を、MD計算にはvelocity Verlet法を用い、時間刻みを 0.1fsとして実行した。AIMDシミュレーションの結果として、初期MOと収束MOで得られるエネルギー差ΔE_{scf} (hartree)と収束するまでにかかったSCF計算の回数N_{SCF}の時間変化をFig. 1 に、それぞれの平均値をTable 1 に示す。Fig. 1 よりCH_3OHのΔE_{scf}の平均値がLI-MOでは 2.3×10^{-5}、LI-MMOでは 1.7×10^{-11}であり、従来よく用いられているReadの 3.7×10^{-4}と比べて、より収束値に近い初期値を与えられている。その結果、LI-MMOではN_{SCF}がReadの半分の 4 回でSCF計算が収束し高速な計算が可能になっている。また、Fig. 1 からLI-MOとLI-MMOの結果を比較すると、

LI-MOでは高速化していない領域があるが、LI-MMOでは常に高速化されておりMO間のMixingの考慮が重要であることがわかる。次に$C_6H_6N_6O_6$分子のAIMDシミュレーションの結果を見ると、LI-MOでは 3.2×10^{-9}でありReadの 4.4×10^{-2}と同程度で高速化されていない。これは、$C_6H_6N_6O_6$分子のMO数が、CH_3OH分子のMO数より多いためにMixingがより多く起きているためと考えられる。しかし、LI-MMOはΔE_{scf}が 1.6×10^{-2}と小さく、N_{SCF}を比較すると従来の 2.5 倍の高速化ができている。Table 2 に、$C_6H_6N_6O_6$分子のAIMDシミュレーションの各計算部分の計算時間を示す。AIMDシミュレーションの計算のうち 8 割を占めているSCF計算をLI-MMOによって高速化することで、全体として半分の計算時間でAIMDシミュレーションが実行された。

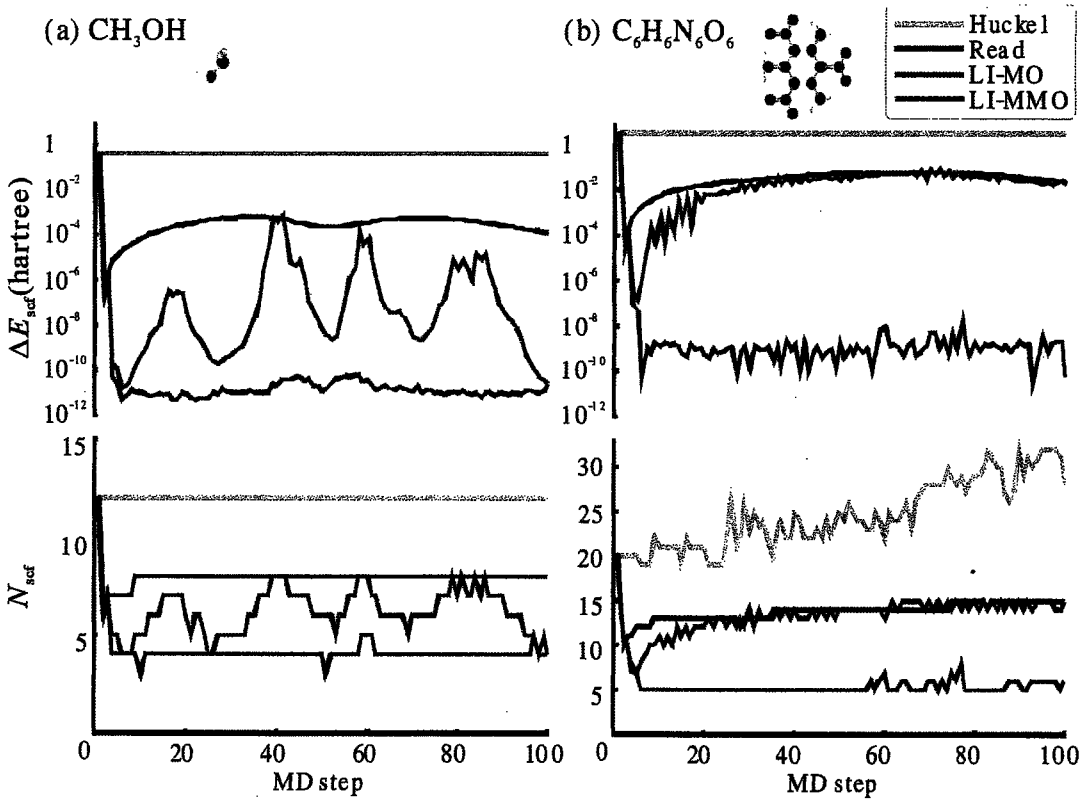

Fig. 1. ΔE_{scf} and N_{scf} in AIMD simulation of (a)CH_3OH and (b)$C_6H_6N_6O_6$.

Table 1. Average value of ΔE_{scf} and N_{scf}.

	CH_3OH		$C_6H_6N_6O_6$	
Guess	ΔE_{SCF}(hartree)	N_{SCF}	ΔE_{SCF}(hartree)	N_{SCF}
Huckel	4.2×10^{-1}	12.0	3.6×10^{0}	24.9
Read	3.7×10^{-4}	8.0	4.4×10^{-2}	13.9
LI-MO	2.3×10^{-5}	6.2	3.2×10^{-2}	13.5
LI-MMO	1.7×10^{-11}	4.0	1.6×10^{-9}	5.3

Table 2. CPU time per AIMD step in AIMD simulation of $C_6H_6N_6O_6$(sec).

	Read	LI-MMO
SCF	721	250
Force	165	165
MD	1	1
LI-MMO	-	12
Total	887	430

[CPU:Pentium4/2.0GH]

[1]渥美照夫、中井浩巳、第 8 回理論化学討論会(広島) 1C1b.

アナターゼ型酸化チタン表面での水吸着及び光励起過程に関する理論的研究

Theoretical study on water adsorption and photo-excitation process of anatase TiO_2 surface

○石川佳奈、河村芳海、中井浩巳

早稲田大学理工学部化学科

【緒言】 近年、地球規模で環境問題が深刻化している中で、酸化チタンを用いた光触媒反応は、太陽光に含まれる近紫外線をエネルギー源として利用したクリーンで理想的な触媒反応として様々な応用が期待されており、その高効率化のために多くの研究がなされてきた。酸化チタンの大きな特徴は、伝導帯に励起された電子の持つ還元力よりも正孔のもつ酸化分解力が強力な点であり、活性酸素種であると言われるヒドロキシラジカルを生じる反応が高い酸化分解力を引き出す。このヒドロキシラジカルの発生プロセスの理解は光触媒の高効率化に非常に重要であると考えられているものの、実験的に捕らえることは困難であり、未だにその発生プロセスは詳細に解明されていない。本研究では、電子状態計算を行うことにより、理論的観点から光触媒反応機構を解明することを目的とした。解明への手がかりとして、高い酸化分解能力を引き出すとされている、価電子帯の正孔によって起こる水の酸化機構及び活性酸素種であるヒドロキシラジカルの生成プロセスに注目し、酸化チタン表面への水分子の吸着過程ならびに光励起状態について検討した。

【周期モデルによる検討】 本研究では、光活性の点から最も効果的とされているアナターゼ型酸化チタン(001)表面に対する水吸着過程及び光励起状態を、電子状態計算により検討した。これまで、酸化チタンについて様々な理論的研究が行われてきたが、光触媒反応の場となる固体表面を表現するモデルには、主に周期モデルと有限クラスターモデルの 2 つがある。Ti_4O_8をユニットセルとした場合の周期境界条件(PBC)計算では、図 1 のようなDOSが得られた。凝集エネルギーは 20.6eVと求まり、実験値の 19.6eVを良く再現した。しかし、バンドギャップはDFT法を用いているために、実験値の 3.2eVに比べて 1.24eVと大きく過小評価している。別の研究で、この過小評価はHF/DFT hybrid法を用いることにより改善されることを確認している。

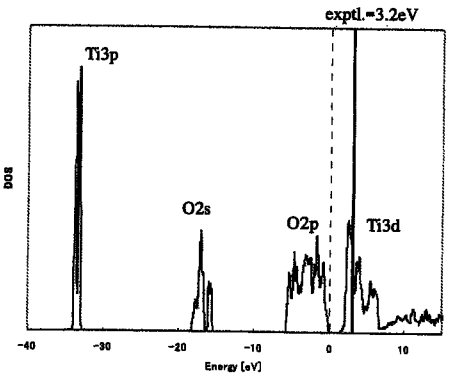

図 1. PBC計算(PBEPBE/6-21G, unit cell=Ti_4O_8)により得られたDOS

【クラスターモデルによる検討】 PBC計算では励起状態の取り扱いは困難であることから、光励起によるヒドロキシラジカルの生成過程については、結晶の一部分を切り出す有限クラスターモデルを用いて検討した。クラスターモデルを用いるに当たっては、イオン結晶を計算する際に有効であるとされている、クラスターの周りに点電荷(Madelung Potential; MP)をおいたMPモデルを適用した。クラスターはTi_8O_{16}, $Ti_{14}O_{28}$, $Ti_{18}O_{36}$の 3 つのサイズについて計算した。周囲の点電荷数は 9309 個に統一し、Tiに相当する電荷を+2, Oに相当する電荷を-1 とした。また、クラスター端のO原子を有効内殻ポテンシャル(ECP)でキャップすることで人為的な分極を防ぐTotal Ion Potential(TIP)モデルについても検討した。構造最適化はHF法とDFT法で行い、後者については汎関数にB3LYPを用いた。励起状態計算にはCIS法を適用した。これらすべての計算の基底関数は 6-21Gとした。

図 2. 用いたクラスターモデル

まず、清浄表面のクラスターについて検討した。一般にクラスターモデルは用いるサイズに結果が依存するという欠点をもつ。本研究では、クラスターサイズ依存性を評価するために凝集エネルギーを求めた(表 1)。MP モデル、TIP モデルともクラスターサイズに対してそれぞれ十分に収束していることがわかる。また、アナターゼ型酸化チタンの凝集エネルギー実験値は 19.6eV であり、これを見ると HF では過大評価、B3LYP では過小評価していることがわかる。

表 1. 凝集エネルギー計算結果 [eV]

	MP		TIP	
	HF	B3LYP	HF	B3LYP
Ti_8O_{16}	23.44	18.73	20.93	16.50
$Ti_{14}O_{28}$	23.41	18.74	21.01	16.58
$Ti_{18}O_{36}$	22.94	--	20.76	16.42

表 2. 水 1 分子吸着エネルギー計算結果(HF/6-21G) [eV]

		MP	TIP
分子状吸着	Ti_8O_{16}	0.39	0.31
	$Ti_{14}O_{28}$	0.28	0.30
解離吸着	Ti_8O_{16}	3.39	3.42
	$Ti_{14}O_{28}$	3.47	3.32

それぞれのクラスターモデルにおいて水 1 分子が吸着したときの吸着エネルギーは表 2 のようになった。MP, TIP モデルともクラスターサイズに対して 0.1eV のオーダーで収束している。また、分子状吸着の吸着エネルギー約 0.3eV に対し、解離吸着では約 3eV となり、解離吸着が有利であることがわかった。図 3 に吸着前、分子状吸着、解離吸着でのそれぞれの最適化構造を示す。解離吸着構造では、Ti-O 間の結合が開裂して 2 つのヒドロキシル基が吸着した構造(図 3(c))をとっている。

これら水 1 分子吸着の計算結果については B3LYP を用いた場合にも同様の傾向が見られた。

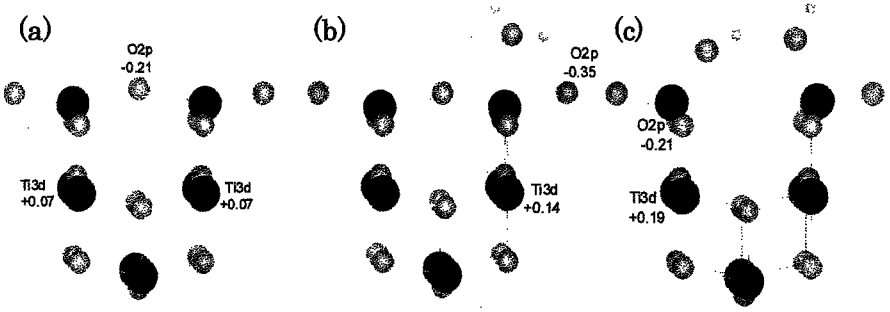

図 3. Ti_8O_{16}クラスター最適化構造((a)吸着前, (b)分子状吸着, (c)解離吸着)と励起による電子密度変化

次にTi_8O_{16}クラスターに励起状態計算を適用した結果について検討する。ここではMP モデルを用いている。励起によって電子密度が大きく変化した箇所は図 3 のとおりである。電子は表面の酸素原子から内部のチタン原子へ移動している。また、酸素の 2p軌道からチタンの 3d軌道へ電子が移動しており、励起によって電荷分離が生じていることがわかる。図 4 にTi_8O_{16}クラスターに対する水分子吸着過程のエネルギーダイアグラムを示す。ヒドロキシラジカル生成時について、基底状態では解離吸着状態から不安定化するのに対し、励起状態では安定化することがわかった。

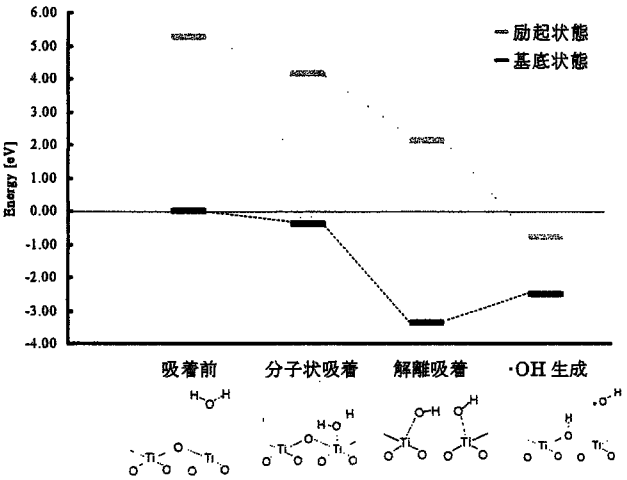

図 4. Ti_8O_{16}クラスターにおける水分子吸着スキーム

【連絡先】 石川佳奈 早稲田大学理工学部化学科中井研究室
〒169-8555 東京都新宿区大久保 3-4-1 (55 号館 S 棟 9 階 4 号室)
Phone: 03-5286-3140 Fax: 03-3205-2504 E-mail: ishikawa-kana@akane.waseda.jp

第 18 回分子シミュレーション討論会,
京都大学(京都), 2004 年 12 月.

106P シアノラジカルと不飽和炭化水素の衝突反応に対する AIMD シミュレーション

(早大理工) ○佐倉大輔、玉置麻理、山内佑介、中井浩巳

1. 緒言 シアノラジカル(CN)と不飽和炭化水素(C_nH_m)の反応は、星間化学・燃焼化学・大気化学などの分野において重要である。特に星間化学では、探査機カッシーニによる観測によって注目を集めている土星の衛星タイタンで起こる反応であり、タイタンと原始地球の環境の類似点から、生命誕生の鍵を握るとも考えられている。本研究では、アセチレン(C_2H_2)、エチレン(C_2H_4)等をはじめとする様々な不飽和炭化水素と CN の衝突反応

$$CN + C_2H_2 \longrightarrow HCCCN + H \quad (1)$$

$$CN + C_2H_4 \longrightarrow C_2H_3CN + H \quad (2)$$

$$CN + CH_3CCH \longrightarrow \begin{cases} CH_3CCCN + H \\ H_2CCCH(CN) + H \\ HCCCN + CH_3 \end{cases} \quad (3)$$

$$CN + H_2CCCH_2 \longrightarrow \begin{cases} H_2CCCH(CN) + H \\ HCCCH_2CN + H \end{cases} \quad (4)$$

$$CN + CH_3CCCH_3 \longrightarrow \begin{cases} H_2CCC(CN)(CH_3) + H \\ CH_3CCCN + CH_3 \end{cases} \quad (5)$$

$$CN + C_6H_6 \longrightarrow C_6H_5CN + H \quad (6)$$

を対象として、*ab initio* 分子動力学(AIMD)シミュレーションを行った。さらに、非平衡ダイナミクスに注目して、振動状態の時間変化を検討するため短時間フーリエ変換(ST-FT)を用いてシミュレーション結果を解析し、反応メカニズムの解明を目指した。なお、我々は既に、ST-FT をいくつかの衝突反応シミュレーションに対して適用し、その有効性を確認している[1,2]。

2. 計算方法 AIMD シミュレーションは、*ab initio* 計算によってポテンシャルを求め、それに従い原子核の運動を求める手法であり、結合の生成や開裂を含む化学反応のダイナミクスを追跡することが可能である。本研究では初期条件として、CN を不飽和炭化水素から重心間距離 20Å 離し、0.56eV の衝突エネルギーを与えて衝突させる AIMD シミュレーションを行った。初期配向はシミュレーションごとにランダムに設定した。*Ab initio* 部分は B3LYP/6-31G**レベルで、MD 部分は時間刻みを 0.25fs とした速度ベルレ法で実行した。

ST-FT は、本来定常信号に対する解析手法であるフーリエ変換を窓関数と呼ばれる関数を用いて、非定常の信号の取り扱いを可能にする手法である。速度の自己相関関数 $\langle v(t)\cdot v(t+\tau)\rangle$ とパワースペクトル S の間には次式が成り立ち、パワースペクトルの時間変化を図に表したものはスペクトログラムと呼ばれる。

$$S(\omega,t) = \frac{1}{2\pi}\int_{-\infty}^{\infty}\langle v(t)\cdot v(t+\tau)\rangle h(t,\tau)e^{-i\omega\tau}d\tau \quad (7)$$

ここで $h(t,\tau)$ は窓関数である。今回は Hanning 窓関数を用いて ST-FT を行っている。

3. 結果と考察 本研究では上式の反応について多数の AIMD シミュレーションを行った。さらにその結果に対してスペクトログラムを描き、それぞれの反応について特定の傾向・類似点がみられるか比較、検討を行った。以下には式(1)の CN と C_2H_2 反応に対する AIMD シミュレーション結果を示す。

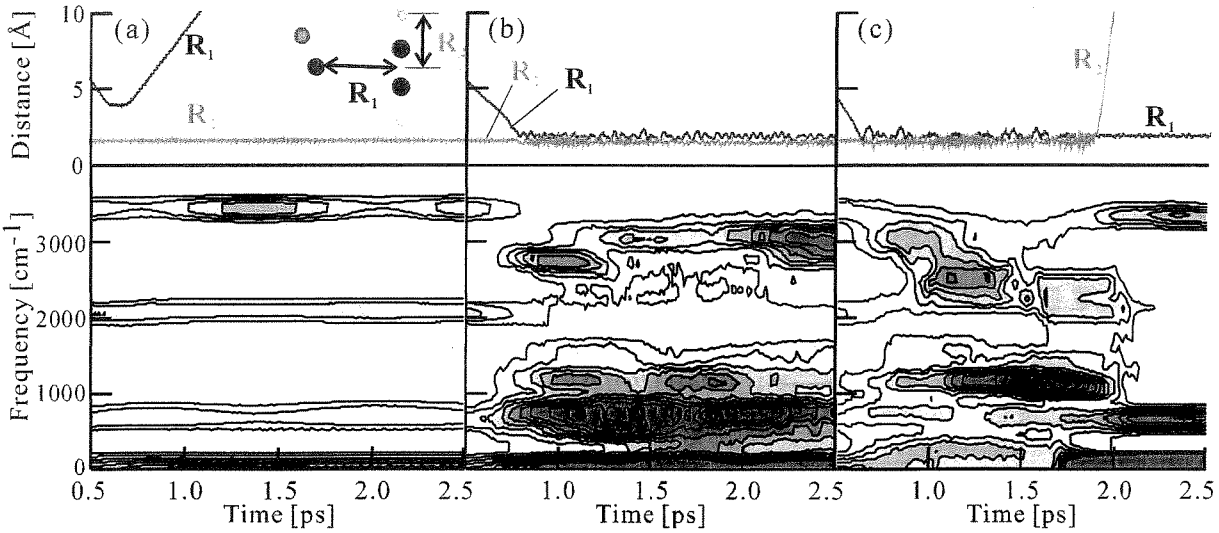

図 1. CN と C_2H_2 の衝突反応のスペクトログラム((a)無反応性衝突、(b)吸着反応、(c)H 解離反応)

図 1 の(a)、(b)、(c)はそれぞれ無反応性衝突、吸着反応、H 解離反応に対する典型的な結果である。上図は C≡C 結合の中心と CN の C との距離 R_1 および C_2H_2 の H との距離 R_2 の時間変化を表している。下図はスペクトログラムで、色の濃淡により振動モードの強弱を表している。(a)無反応性衝突のスペクトログラムでは衝突前後で振動モードに大きな変化はないが、(b)吸着反応、(c)H 解離反応では衝突によって新たな振動モードが現れている。衝突前に 3500 cm^{-1} 付近にあった CH 伸縮は、吸着により 3100 cm^{-1} 付近の sp^2 型の CH 伸縮に red shift している。また、2000 cm^{-1} の消滅は C≡C 結合が衝突とともに消滅していることを示している。CN 吸着により新たに誘起された 1300 cm^{-1} 以下の強いピークの存在は、CN の吸着エネルギーが振動エネルギーとして分子内に分配された結果と考えられる。特に(c)H 解離反応では約 1300 cm^{-1} 付近の CCH 面内変角振動が、H が解離する約 1ps 前から強く現れており、それに同期するように距離 R_2 が激しく動いている。また解離後には約 600 cm^{-1} の CCC 変角が強く現れている。一方、(b)吸着反応では約 1300 cm^{-1} の振動モードは強くは現れておらず、吸着後に約 700 cm^{-1} 付近の CCH 面外変角振動を中心とした振動が誘起されている。

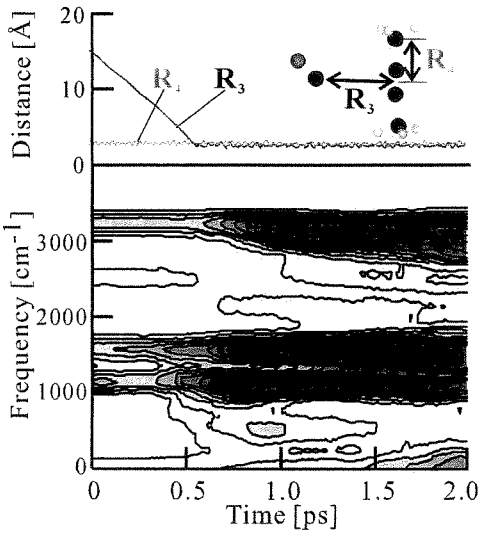

図2. CN と C_4H_6 の吸着反応のスペクトログラム[2]

図 2 は、式(5)の反応に対する結合距離 R_3、R_4 の時間変化とスペクトログラムを示している。吸着反応において、C_2H_2 の場合と同様に衝突直後から特定の振動モードが誘起しているのがわかった。しかしながら、エネルギー分配の傾向が異なっている。すなわち、C_2H_2 では主に 700 cm^{-1} のピークが誘起しているのに対し、C_4H_6 の場合は 3100 cm^{-1} (CH 伸縮)、1600 cm^{-1} (CH_3 縮重変角)、1000 cm^{-1} (CH_3 横揺れ)のすべてが強くなっている。これらの振動エネルギーの分配の違いが式(1)-(6)に示された反応選択性を決定していると考えられる。

[1] Y. Yamauchi, H. Nakai, and Y. Okada, *J. Chem. Phys.*, **121** (2004), *in press.*
[2] M. Tamaoki, Y. Yamauchi, and H. Nakai, *J. Comput. Chem., submitted.*

第 18 回分子シミュレーション討論会,
京都大学（京都），2004 年 12 月.

128P

結合エネルギー密度解析を用いた S_N2 反応の反応性に関する理論的研究

（早大理工）○鈴木潤、菊池那明、石井基樹、中井浩巳

1. 緒言

S_N2 反応は基本的な化学反応の一つであり、官能基の導入や変換、立体化学の反転など、合成化学において非常に利用価値の高い反応である。本反応は溶媒和の影響を受けやすく、気相中、CH_3OH 中、DMSO 中で反応性（求核能）が異なることが知られているが、活性化エネルギーが低く実験的な測定が困難である。そのため、理論計算による解析が数多く行われ、求核試薬の塩基性度や HSAB 理論などによって反応過程が定性的に説明されている。求核能と脱離能は互いに関連し、反応性の原因が求核基、脱離基のどちらにあるのか決定する議論は難しい。それゆえ、従来の全エネルギーのみによる解析では反応性の研究は困難である。

当研究室で開発されたエネルギー密度解析(EDA)[1]は、電子状態理論計算によって得られた全エネルギーを定量性を損なうことなく構成原子に分割できる解析法である。さらに EDA を結合領域にもエネルギーを分割できるように拡張した結合エネルギー密度解析(Bond-EDA)[2]は、局所的な分子間相互作用や反応による結合の生成・開裂をそれぞれエネルギーとして評価することが可能である。本研究では Bond-EDA を S_N2 反応に適用し、その反応性の相違についての検討を行った。反応を決定する部分を特定し、それに基づいて求核エネルギー・脱離エネルギーという新しい概念を提案する。

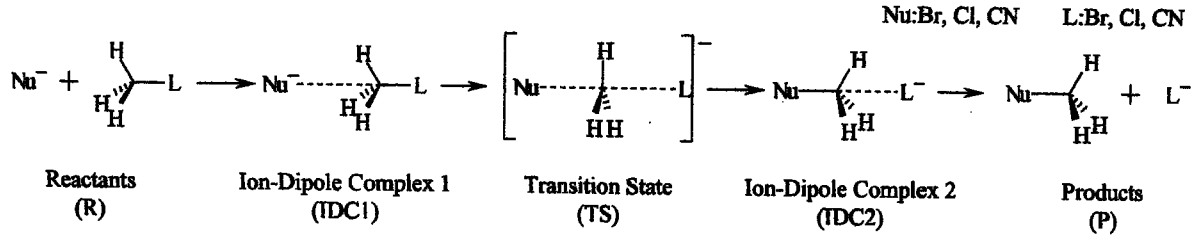

Scheme 1. S_N2 反応のモデル

2. 計算方法

本研究で解析した S_N2 反応の過程を Scheme 1 に示す。求核基(Nu)、脱離基(L)としては Br, Cl, CN を用いた。構造最適化を行い、全エネルギーの変化を比較した。その最適化された構造に対して Bond-EDA を適用し、各原子・各結合に割り当てられたエネルギーの変化を求めた。それにより、活性化エネルギーの基因を検討した。計算レベルは B3LYP 汎関数、cc-pVDZ 基底を用いた密度汎関数理論(DFT)である。

3. 結果と考察

Table 1 に Ion-Dipole Complex 1 (IDC1)を基準とした場合の活性化エネルギーと生成熱を示す。すなわち活性化エネルギーは遷移状態(TS)と IDC1 の全エネルギーの差、生成熱は Ion-Dipole Complex 2 (IDC2)と IDC1 の全エネルギーの差である。求核基(Nu)が Br, Cl, CN と変化するのに伴い、活性化エネルギーや生成熱が減少している。また、脱離基(L)が Br, Cl, CN と変化すると、活性化エネルギーと生成熱が増加している。これより、活性化エネルギーと生成熱、つまり反応性を検討するためには、Nu と L の影響を同時に評価する必要がある。

Table 1. S_N2 反応の活性化エネルギーと生成熱(kcal/mol)

Nu	L	活性化エネルギー	生成熱
Br	Br	4.49	0.0
Cl	Br	2.82	−6.0
CN	Br	0.54	−47.4
Br	Cl	8.81	6.0
Cl	Cl	6.56	0.0
CN	Cl	3.02	−41.4
Br	CN	47.93	47.4
Cl	CN	44.42	41.4
CN	CN	36.22	0.0

次に IDC1 および IDC2 の Nu と L の相互作用について Bond-EDA を用いて検討した。比較として、結合が片方にのみ存在する反応物(R)および生成物(P)における Bond-EDA の結果を調べた。Table 2 に、P および IDC2 における求核基と炭素(Nu-C)間の結合エネルギー、R および IDC1 における炭素と脱離基(C-L)間の解離エネルギーの計算値を示す。実験的に観測可能な量は P の結合エネルギーと R の解離エネルギーである。C-Br, C-Cl, C-CN の結合解離エネルギーの実験値はそれぞれ 69.5, 82.5, 122.6

kcal/molであり、Bond-EDAによる見積もりとまずまず一致している。一方、IDC2における$E^{Nu\text{-}C}$(IDC2)はLの影響を含んだ求核性の結合エネルギーである。したがって次の差を評価することによりLの影響を定量的に評価できる。

$$\Delta E^{Nu\text{-}C} = E^{Nu\text{-}C}(IDC2) - E^{Nu\text{-}C}(P)$$

同様にLの解離エネルギーに対するNuの影響は

$$\Delta E^{C\text{-}L} = E^{C\text{-}L}(IDC1) - E^{C\text{-}L}(R)$$

より評価できる。Table 2にはこれらの差分も示されており、Br, Cl, CNによる影響はそれぞれ14–19, 16–19, 22–28 kcal/molである。

Table 2. S_N2反応における生成熱に対してのBond-EDAによる解析(kcal/mol)

Nu	L	$E^{Nu\text{-}C}$(P)	$E^{Nu\text{-}C}$(IDC2)	$\Delta E^{Nu\text{-}C}$	$E^{C\text{-}L}$(R)	$E^{C\text{-}L}$(IDC1)	$\Delta E^{C\text{-}L}$
Br	Br	−78.2	−62.7	15.6	78.2	62.7	−15.6
Cl	Br	−85.5	−71.5	14.0	78.2	60.4	−17.8
CN	Br	−129.3	−110.7	18.6	78.2	51.8	−26.4
Br	Cl	−78.2	−60.4	17.8	85.5	71.5	−14.0
Cl	Cl	−85.5	−69.8	15.7	85.5	69.8	−15.7
CN	Cl	−129.3	−110.1	19.2	85.5	63.2	−22.4
Br	CN	−78.2	−51.8	26.4	129.3	110.7	−18.6
Cl	CN	−85.5	−63.2	22.4	129.3	110.1	−19.2
CN	CN	−129.3	−101.2	28.1	129.3	101.2	−28.1

活性化エネルギーは更に複雑で、TSにおけるNu-Cの部分的な結合生成、C-Lの部分的な解離、さらにそれぞれに対するL、Nuの影響が全て含まれている。Table 2と同様にBond-EDAを用いることで、Lの影響を含めたNuの部分的結合エネルギー$E^{Nu\text{-}C}$(TS)を評価できる。本研究ではこれを求核エネルギーと定義する。同様に脱離エネルギーを$E^{C\text{-}L}$(TS)で定義する。Table 3に求核エネルギー、脱離エネルギーを示す。$E^{Nu\text{-}C}$(TS)はNuの種類によってだけではなくLの種類によっても変化し、Br, Cl, CNの順に安定化することがわかる。同様に$E^{C\text{-}L}$(TS)は、Nuの種類によってBr, Cl, CNの順に減少することがわかる。この両方のエネルギーを足し合わせたエネルギー

Table 3. S_N2反応における活性化エネルギーに対してのBond-EDAによる解析(kcal/mol)

Nu	L	$E^{Nu\text{-}C}$(TS)	$E^{C\text{-}L}$(TS)	$E^{Nu\text{-}C\text{-}L}$(TS)
Br	Br	−27.0	35.7	8.8
Cl	Br	−25.0	28.1	3.1
CN	Br	−15.7	15.7	0.0
Br	Cl	−32.3	46.5	14.2
Cl	Cl	−31.6	38.3	6.7
CN	Cl	−25.5	26.5	1.0
Br	CN	−36.2	95.0	58.9
Cl	CN	−36.7	84.6	47.9
CN	CN	−36.5	64.7	28.1

$$E^{Nu\text{-}C\text{-}L}(TS) \equiv E^{Nu\text{-}C}(TS) + E^{C\text{-}L}(TS)$$

は活性化エネルギーをほぼ再現しており、活性化エネルギーの主な寄与がこの求核エネルギーと脱離エネルギーであることがわかる。

Fig. 1はS_N2反応におけるエネルギーダイアグラムである。ここに、上記の寄与をすべて図示した。本研究で求めることのできる様々な寄与は、エネルギーダイアグラム中でこのように表現することができる。

以上のように、Bond-EDAにより求められる求核エネルギー、脱離エネルギーはS_N2反応の反応性を定量的に評価できる新しい概念であることがわかった。

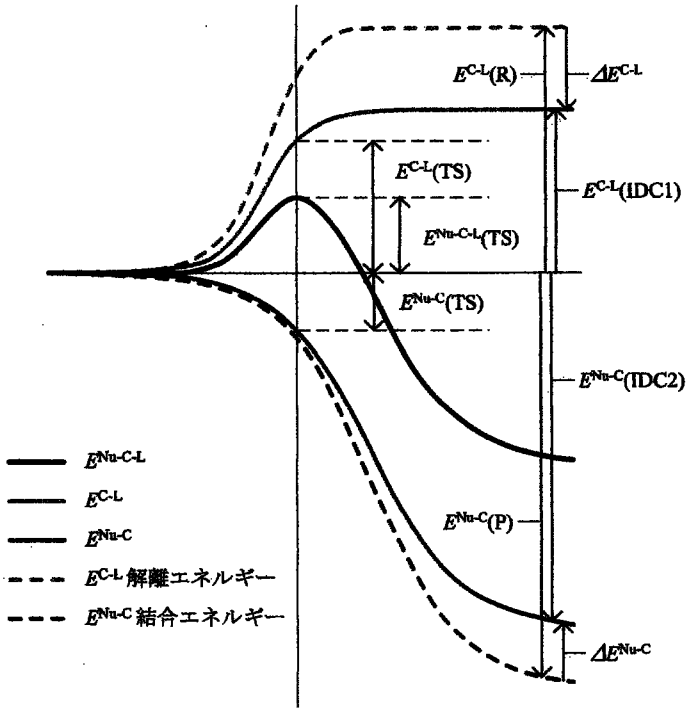

Fig. 1. S_N2反応におけるエネルギーダイアグラムのBond-EDAによる解析。図の実線部はS_N2反応モデルにおける結合領域のエネルギーを示す。また破線部は、それぞれNu、Lが存在しないときのメチル炭素とL、Nuの結合領域のエネルギーを示す。

[1] H. Nakai, Chem. Phys. Lett., **363**, 73-79 (2002).

[2] H. Nakai and Y. Kikuchi, J. Theor. Comp. Chem., *in press*.

The 2nd 21COE International Symposium on 'Practical Nano-Chemistry',
早稲田大学（東京），2004 年 12 月.

水クラスターイオン衝突過程の理論的研究: エネルギー移動スペクトログラム

山内佑介，中井浩巳

早稲田大学大学院理工学研究科化学専攻　〒169-8555 東京都新宿区大久保 3-4-1
yamauchi@ruri.waseda.jp

水クラスターイオンの結晶成長は、環境化学や工業化学など多くの分野に関わる重要な現象である。衝突によって分子を取り込んだ直後のクラスターは振動励起状態にあり、分子内エネルギー再分配または分子間エネルギー移動によって冷却されることで安定化する。このエネルギー移動のメカニズムを解明するために、我々はまずエネルギー移動スペクトログラム(ETS)を提案し、それを用いて水クラスターイオン $H^+(H_2O)_2$ と窒素分子の衝突反応を検討した。ETS は *ab initio* 分子動力学シミュレーションに対する新しい解析手法であり、化学反応におけるエネルギー移動と分子振動の関係を明らかにできる。この方法はエネルギー密度解析と短時間フーリエ変換を組み合わせて実行される。図 1 は水クラスターイオン衝突過程の ETS である。衝突による内部エネルギーの変化の違いがよく現れており、またそれぞれのエネルギー移動過程が異なる振動モードに支配されていることが分かる。

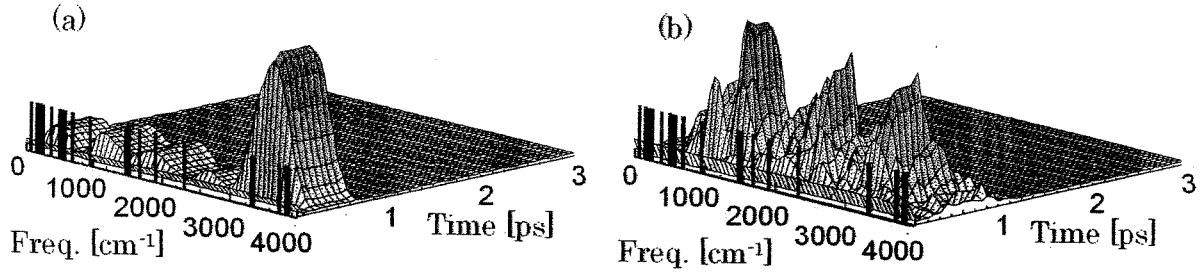

図 1 水クラスターイオン衝突過程の ETS．クラスターの内部エネルギーが(a)増加および(b)減少したトラジェクトリーに対する結果．振動数軸上の太線は調和振動数を示す．

[1] Y. Yamauchi, H. Nakai, and Y. Okada, J. Chem. Phys. **121**, (2004), *in press.*

[2] M. Tamaoki, Y. Yamauchi, and H. Nakai, J. Comput. Chem., *submitted.*

[3] Y. Yamauchi and H. Nakai, J. Chem. Phys., *submitted.*

Theoretical Study on the Collision Reaction of Protonated Water Cluster: Energy Transfer Spectrogram

Yusuke Yamauchi and Hiromi Nakai

Department of Chemistry, Waseda University, Ohkubo, Shinjuku-ku, Tokyo 169-8555, Japan

E-mail: yamauchi@ruri.waseda.jp

The 2nd 21COE International Symposium on 'Practical Nano-Chemistry',
早稲田大学（東京），2004 年 12 月.

高速な電子状態計算手法の開発

小林正人，中井浩巳

早稲田大学大学院理工学研究科化学専攻　〒169-8555 東京都新宿区大久保 3-4-1
kobayashi@suou.waseda.jp

現在、電子状態計算は分子の特徴を知るための分光機器と並ぶ有力なツールとして、理論化学の専門家でない化学者にも広く浸透するものとなっている。しかしながら、電子状態計算にかかる時間は系のサイズ N に大きく依存し、最も簡単な Hartree-Fock 法でもおよそ N の 4 乗に比例して大きくなる。このため、現在注目されているナノ材料や生体分子といった系は、電子状態計算で扱うには非常に大きなものであり、この計算コストを減らすことは重要な課題となっている。

その中でも特に計算時間のかかる電子反発積分(ERI)の高速化は、約 50 年にわたり広く研究が行われてきた。ERI は以下の式で表される。

$$\mathrm{ERI} = \int \phi_\lambda^{\mathrm{A}}(\mathbf{r}_1)\phi_\mu^{\mathrm{B}}(\mathbf{r}_1)\frac{1}{|\mathbf{r}_2-\mathbf{r}_1|}\phi_\nu^{\mathrm{C}}(\mathbf{r}_2)\phi_\xi^{\mathrm{D}}(\mathbf{r}_2)\,d\mathbf{r}_1 d\mathbf{r}_2 \qquad (1)$$

当研究室でもこれまでに、ERI の高速計算法の開発を行ってきた。ERI を高速化する方法には、系全体としての計算コストを下げるものと、一つひとつの ERI にかかる計算コストを下げるものの 2 種類が存在する。前者としては既に、元素の等しい原子に対しては同じ基底関数系を用いていることを利用した、elementary basis algorithm (EBA)を発表し、中～大規模分子系の ERI 計算の高速化が可能となった[1]。後者については最近、随伴座標展開(ACE)法[2]を改良した ACE-RR 法[3,4]を開発した。ACE 法には角運動量量子数を柔軟に変化させることができないという欠点があったため、Pople 型基底関数系に現れる *sp* 型の基底関数や ERI の gradient、Hessian といった微分の計算には適していなかった。これを ACE-HRR と ACE-VRR という 2 つの漸化関係式(RR)を用いることで解消したものが、ACE-RR 法である。これによって 3 割程度の計算時間削減をすることができた。

[1] H. Nakai and M. Kobayashi, Chem. Phys. Lett. **388**, 50 (2004).
[2] K. Ishida, Int. J. Quantum Chem. **59**, 209 (1996).
[3] M. Kobayashi and H. Nakai, J. Chem. Phys. **121**, 4050 (2004).
[4] M. Katouda, M. Kobayashi, H. Nakai, and S. Nagase, J. Theor. Comput. Chem., *in press*.

Development of Fast Method in Electronic Structure Calculation

Masato Kobayashi and Hiromi Nakai
Department of Chemistry, Waseda University, Ohkubo, Shinjuku-ku, Tokyo 169-8555, Japan
E-mail: kobayashi@suou.waseda.jp

The 2nd 21COE International Symposium on 'Practical Nano-Chemistry',
早稲田大学（東京），2004 年 12 月.

エネルギー密度解析(EDA)の結合領域への拡張とその応用

菊池 那明, 中井 浩巳

早稲田大学大学院理工学研究科化学専攻　〒169-8555 東京都新宿区大久保 3-4-1
touka@ruri.waseda.jp

分子内の化学結合を理解することは、昔から化学的・物理学的に非常に重要である。化学結合は直接的には測定されない概念であり、様々な方法を用いてその解析が行われてきた。当研究室では最近、Hartree-Fock や Density Functional Theory などの量子化学計算により得られた全エネルギーを構成原子ごとに分割する解析手法、Energy Density Analysis (EDA)[1]を開発した。本研究ではこれを結合領域へと拡張し、化学結合や分子間相互作用をより詳細に解析する方法、Bond-EDA[2,3]を提案する。また、種々の化学的現象に応用する。

Bond-EDA では、例えば原子 A-B 間の運動エネルギー項を、

$$T^{AB} = \sum_{\mu \in A} \sum_{\nu \in B} P_{\mu\nu} T_{\nu\mu}$$

と見積もる。この類推より核引力、クーロン、交換、相関の各エネルギー項も分割される。

Bond-EDA を用いると、エタン分子の化学結合を次のように解析することができる。計算レベルは B3LYP/cc-pVDZ である。Table 1 に示す結果より、結合が存在する C-C 間、C-H 間の結合エネルギー密度は絶対値の大きな負の値を持ち、結合による安定化を示している。結合していない H-H 間、C-H 間の絶対値の小さな正の値は、立体効果に対応するものと考えられる。原子に割り当てられるエネルギーは、単原子分子状態のエネルギーとほぼ等しく、その差の大部分が内殻電子からの寄与であると考えられる。

Table 1. Bond-EDA for ethane (in kcal/mol)

Atomic energy density, E^{AA}		
C	(×2)	-23735.45
H	(×6)	-313.74
Bond energy density, E^{AB}		
C-C		-148.37
C-H	(×6)	-108.44
H-H geminal	(×6)	8.62
C-H vicinal	(×6)	7.43
H-H vicinal	(×3)	-2.85
H-H vicinal	(×6)	1.86
Total		-50053.43

[1] H. Nakai, Chem. Phys. Lett., **363**, 73 (2002).
[2] H. Nakai and Y. Kikuchi, J. Theor. Comp. Chem., *in press.*
[3] H. Nakai and Y. Kikuchi, *unpublished.*

Extension and Application of Energy Density Analysis for Bonding Region

Yasuaki Kikuchi and Hiromi Nakai

Department of Chemistry, Waseda University, Ohkubo, Shinjuku-ku, Tokyo 169-8555, Japan
E-mail: touka@ruri.waseda.jp

The 2nd 21COE International Symposium on 'Practical Nano-Chemistry',
早稲田大学（東京），2004 年 12 月.

日本語

電子・核波動関数同時決定法の高精度化に向けた試み：回転運動の分離

星野　稔[1]，中井浩巳[1]

[1] 早稲田大学大学院理工学研究科化学専攻　〒169-8555 東京都新宿区大久保 3-4-1
hoshino@fuji.waseda.jp

【序】我々はこれまで、Born-Oppenheimer 近似に基づかず、電子および原子核の波動関数を同時に求めることのできる *ab initio* NOMO 法の開発を行ってきた。これまでの研究で、NOMO 法における計算精度の悪さが、分子の並進・回転運動が混入することに起因していることが指摘されてきた。以前の研究では並進運動に対して完全な分離を行い、基底状態に対して translation-free (TF)-NOMO/Hartree-Fock (TF-NOMO/HF) 法の開発を行った[1,2]。本研究では、回転運動の分離の検討を行い、回転運動を分離した NOMO 法の開発を行った。

【理論】並進(式(1))および回転演算子(式(2))を Hamiltonian から引くことによって、translation and rotation-free (TRF)-Hamiltonian (式(3))を導出した。この TRF-Hamiltonian を用いて、一体近似のもとで電子および原子核の基底状態を求めることのできる translation and rotation-free (TRF)-NOMO/Hartree-Fock 法の導出を行った。

$$\hat{T}_T(\mathbf{x}) = -\frac{1}{2M_T}\sum_i^N \nabla_i^2 - \frac{1}{M_T}\sum_{i<j}^N \nabla_i \cdot \nabla_j \qquad (1)$$

$$\hat{T}_R(\mathbf{x}) = \frac{\hat{L}_x(\mathbf{x})^2}{2I_x} + \frac{\hat{L}_y(\mathbf{x})^2}{2I_y} + \frac{\hat{L}_z(\mathbf{x})^2}{2I_z} \qquad (2)$$

$$\hat{H}_{TRF} = \hat{H} - \hat{T}_T - \hat{T}_R \qquad (3)$$

【計算結果】Table 1 には NOMO/HF, TF-NOMO/HF, TRF-NOMO/HF 法によって得られた全エネルギーおよび NOMO/HF からの全エネルギーの差を示してある。H_2, D_2, T_2 分子に対して基底状態の全エネルギーが NOMO/HF 法よりそれぞれ、-0.018516, -0.015803, -0.013083 (hartree)と大幅な改善が得られた。

Table 1. The total energies calculated by NOMO/HF, TF-NOMO/HF, TRF-NOMO/HF.

	H_2	D_2	T_2
	E_{tot}	E_{tot}	E_{tot}
NOMO/HF	-1.085574 (0.000000)	-1.096381 (0.000000)	-1.102819 (0.000000)
TF-NOMO/HF	-1.091231 (-0.005657)	-1.103072 (-0.006691)	-1.108418 (-0.005600)
TRF-NOMO/HF	-1.104090 (-0.018516)	-1.112184 (-0.015803)	-1.115902 (-0.013083)

[1] H. Nakai, *Int. J. Quantum Chem.*, **86** 511 (2002)
[2] H. Nakai, K. Sodeyama, M. Hoshino, *Chem. Phys. Lett.*, **345**, 118 (2001).

Improvement of accuracy in simultaneous determination method of electronic and nuclear wave functions: Separation of rotational motion

Minoru Hoshino[1] and Hiromi Nakai[1]
[1]Department of Chemistry, Waseda University, Ohkubo, Shinjuku-ku, Tokyo 169-8555, Japan
E-mail: hoshino@fuji.waseda.jp

The 2nd 21COE International Symposium on 'Practical Nano-Chemistry'
早稲田大学（東京），2004 年 12 月

無電解銅析出における還元剤酸化反応機構の密度汎関数法による解析

島田拓哉[1]、本間敬之[1]、中井浩巳[2]、逢坂哲彌[1]

[1]早稲田大学大学院理工学研究科応用化学専攻 〒169-8555 東京都新宿区大久保 3-4-1
[2]早稲田大学大学院理工学研究科化学専攻 〒169-8555 東京都新宿区大久保 3-4-1
takuya@fuji.waseda.jp

【研究背景】無電解銅析出は外部電源を使用しない薄膜形成プロセスであり，ナノレベルでの精密な制御を行うことが可能であることからエレクトロニクスなどの様々な分野において広く用いられているが，この反応機構は複雑で不明な点が多い．本検討ではこの反応機構の中でも最も重要な還元剤の酸化反応に注目し，反応中間体のエネルギーや電荷を原子・分子レベルから解析可能な密度汎関数法(DFT)を用いて詳細な解析を行った．代表的還元剤であるジメチルアミンボラン(DMAB)，次亜リン酸，及びホルムアルデヒドの酸化反応に着目し，Cu 表面上における還元剤の反応機構と Cu 表面の還元剤に対する触媒活性について解析した．

【結果･考察】上記還元剤の酸化反応は H と OH^-の置換反応により進行するが，脱離した H と配位する OH^-は Cu 表面上で吸着している．これを考慮に入れて酸化反応経路をエネルギーダイアグラムから推察すると全ての還元剤が先に H を脱離させ 3 配位中間体状態を経由する経路であることが示唆された(Fig 参照)．

また Cu 表面の三種の還元剤に対する触媒活性の有無と水素脱離過程のエネルギー変化の正負が対応していることが示唆され，触媒活性に起因する要素の一つと考えられる．

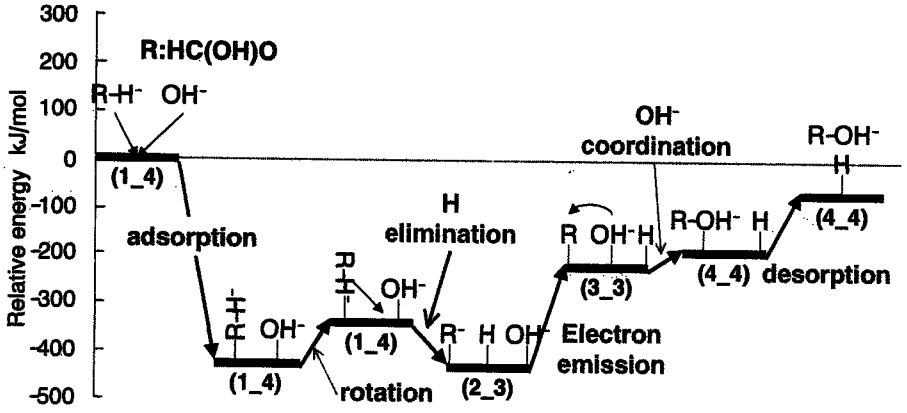

Fig. Energy diagram for oxidation reaction process of formaldehyde at the Cu_{22} cluster via three-coordinate intermediates.

DFT STUDY ON OXIDATION MECHANISM OF REDUCTANTS FOR ELECTROLESS COPPER DEPOSITION PROCESSES

Takuya Shimada[1], Takayuki Homma[1], Hiromi Nakai[2], Tetsuya Osaka[1]
[1]Major in Applied Chemistry, [2]Chemistry, Graduate School of Science and Engineering, Waseda University, Okubo, Shinjuku-ku, Tokyo 169-8555, Japan.
E-mail: takuya@fuji.waseda.jp

The 2nd 21COE International Symposium on 'Practical Nano-Chemistry',
早稲田大学（東京），2004 年 12 月.

ストレインドシリコン表面の化学的特性に対する DFT 計算による検討

RA 阪田薫穂[1]，本間敬之[1]，中井浩巳[2]，逢坂哲彌[1]

[1] 早稲田大学大学院理工学研究科応用化学専攻 〒169-8555 東京都新宿区大久保 3-4-1
[2] 早稲田大学大学院理工学研究科化学専攻 〒169-8555 東京都新宿区大久保 3-4-1
kaoruho_s@ruri.waseda.jp

ストレインドシリコンは，SiGe 上にシリコンをエピタキシャル成長させることにより作製されており，格子のひずみによりキャリア移動度およびデバイスのスピードを上げることができる．しかしこの格子のひずみは電気的な性質を変化させるだけではなく，表面のプロパティも変化させる可能性がある．特に，ウエットプロセスにおける微量金属種と表面の反応性についての知見を得ることは高度デバイス形成プロセスの確立に対して重要である．しかしストレインドシリコンウエハ表面における歪みの度合いと反応性の相関についての定量的な検討は行われていない．そこで本検討ではひずみの度合いと表面の反応性との相関を定量的に解析するために DFT 計算を用いた解析を行った．理論計算は，実験的には観測困難なシリコン表面の結合長を制御した構造やエネルギーを算出することが可能である．そこで今回の検討では，歪み度合いを変えた場合の表面のエネルギー変化や電子状態の解析，および表面に金属イオン(Cu^{2+}, Ni^{2+}, Fe^{2+})が析出したときの吸着エネルギーを算出することにより，ストレインドシリコンと通常のウエハとの表面反応性の比較を行った．また，ストレインドシリコンを表すモデルとしてクラスターモデル（サイズ 18）を用い，**Fig.1** のように結合長はバルクの値を保ったまま面内方向に伸ばすことによりひずみを表現した．その結果，ストレインドシリコンのエネルギーは通常のシリコンよりも不安定となり HOMO-LUMO ギャップも狭くなることから，表面の反応性が上がる可能性が示唆された．

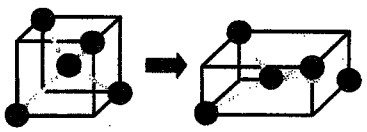

Fig. 1 ストレインドシリコンのモデルのひずませ方

Characterization of Strained Si Wafer Surface by Density Functional Theory analysis

Kaoruho Sakata[1], Takayuki Homma[1], Hiromi Nakai[2] and Tetsuya Osaka[1]

[1]Major in Applied chemistry, Graduate School of Science and Engineering, Waseda University, 3-4-1 Ohkubo, Shinjuku-ku, 169-8555, Tokyo, Japan, [2]Major in Chemistry, Graduate School of Science and Engineering, Waseda University, 3-4-1, Ohkubo, Shinjuku-ku, Tokyo 169-8555, Japan

E-mail: kaoruho_s@ruri.waseda.jp

第１５回日本 MRS 学術シンポジウム，
日本大学（東京），2004 年 12 月．

Density Functional Theory Study on the Rate Limiting Step Mechanisms of Hypophosphite Ion as a Reductant for Electroless Deposition Processes

S.Odagiri, T. Shimada, H. Nakai[1], T. Homma[2], T. Osaka[3]
Waseda University, Shinjuku-ku Tokyo, [1]nakai@waseda.jp, [2]homma@mse.waseda.ac.jp, [3]osakatet@waseda.jp

Electroless deposition processes are widely used to form functional thin films in various fields, such as advanced electronics. In these processes, electron for reductive deposition of metal ion is supplied by the oxidation reaction of reductants. Therefore, reductants play a key role in electroless deposition processes. However, the reaction processes are so complex that the mechanism has not been clarified yet. For example, the oxidation reaction of hypophosphite ion, which is a common reductant, dose not take place at the Cu surface but at the Ni surface. In this study, we employed Density Functional Theory (DFT) calculation to investigate the oxidation mechanism of hypophosphite ion. DFT calculation can estimate structures and energies of reductants. As a result, it was indicated that the rate determining step for the overall reaction was homolytic breakdown step of P-H bond in hypophosphite ion at metal surface to form the hydrogen adatom and the adsorbed phosphorus compound radical. Furthermore, energy barrier for the homolytic breakdown of the P-H bond at the Cu surface was found to be larger than that at the Ni surface. In other words, homolytic breakdown of the P-H bond hardly takes place at the Cu surface, whereas easily takes place at the Ni surface. Therefore, the difference at the rate determining step affects the oxidation reaction of hypophosphite ion at the metal surface.

第 111 回表面技術協会講演大会,
千葉工業大学（千葉），2004 年 3 月.

無電解析出における次亜リン酸 酸化反応機構の DFT による解析

（早大理工） ○小田切秀一，島田拓哉，中井浩巳，本間敬之，逢坂哲彌

キーワード[無電解析出，次亜リン酸，反応選択性，密度汎関数法（DFT）]

1. 緒言 無電解析出反応は種々の電荷移動が伴うため非常に複雑であり，そのメカニズムの詳細は未だに不明点が多い．このため，これまでに反応機構解明を目的とした電気化学的手法を用いた研究が数多くなされてきたが，更なる詳細な解明のために我々は理論・計算化学を用いた解析を進めている．本検討では，次亜リン酸は Ni 表面では酸化反応するが，Cu 表面では酸化反応しないという酸化反応選択性に焦点を当てた．われわれはこのような反応選択性が生じる理由として，Ni，Cu 各表面で次亜リン酸酸化反応経路のエネルギーダイアグラムに差異が存在するからであると仮定し，これを確かめるための検討を行った．

2.実験方法 計算には Gaussian03 プログラムを用い，分子の構造最適化並びにエネルギー計算は密度汎関数法(DFT)の一種である B3LYP を用いた．金属表面は Cu，Ni の面方位(111)，(100)，構成原子を 22 とするクラスターモデルを用いた．基底関数として P,H には 6-31G**，O には分散関数を組み込んだ 6-31+G**，金属には Hay & Wadt ECP を用いた．

3.結果及び考察 まず，次亜リン酸酸化反応は表面吸着から開始されると考え，この段階においての差異を見るために Ni 表面及び Cu 表面に対して次亜リン酸を近接させていった．計算結果は図 1 となり，Ni を用いた場合の吸着エネルギーは Cu のそれに比べ非常に大きく，次亜リン酸は Cu 表面よりも Ni 表面で安定に存在することが示された．

さらに次亜リン酸は表面吸着後にリンと水素（P-H 間）の結合を切断する段階を経由すると言われており，またこれが反応の律速段階であるとも考えられている．この段階における差異を見るために，Ni 表面上，Cu 表面上及び次亜リン酸のみの孤立系において P-H 結合長を伸長させ，エネルギーダイアグラムを作成した．計算結果は図 2 となり，Ni 表面上において P-H 結合長を伸ばした際の相対エネルギー変化が三つの系の中では最小であり，これより P-H 結合切断に必要な活性化エネルギーが最小であることが示唆された．よって，P-H 結合は Cu 表面上よりも Ni 表面上で切断されやすく，この段階の反応が比較的スムーズに進行するものと考えられる．

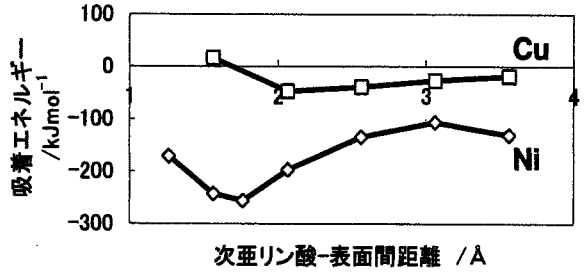

図1 次亜リン酸の表面吸着エネルギー

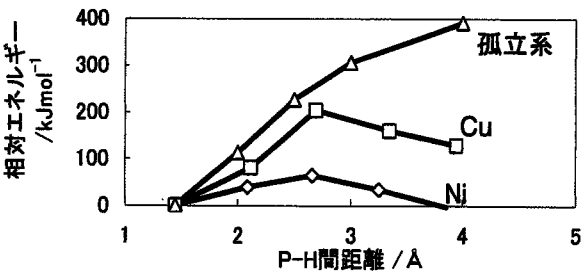

図2 次亜リン酸P-H結合切断反応のエネルギー変化

4.結言 今回の検討で次亜リン酸は Cu 表面よりも Ni 表面に吸着しやすく，続く反応段階では Cu 表面上よりも Ni 表面上で P-H 結合は切断されやすいことが示唆された．これらの差異が Ni，Cu における次亜リン酸の反応選択性に影響していると考えられる．

5.謝辞 本研究は文部科学省 21 世紀 COE プログラム「実践的ナノ化学教育研究拠点」の助成により実施したものである．

○Syuuichi ODAGIRI, Takuya SHIMADA, Hiromi NAKAI, Takayuki HOMMA, Tetsuya OSAKA

第85回日本化学会春季年会,
神奈川大学, (神奈川) 2005年3月.

エネルギー移動スペクトログラム: *ab initio* 分子動力学シミュレーションの新規な解析手法

(早大理工)○山内佑介・中井浩巳

Energy transfer spectrogram: analysis technique of *ab initio* molecular dynamics simulation (Waseda Univ.) YAMAUCHI, Yusuke; NAKAI, Hiromi

Ab initio 分子動力学(AIMD)シミュレーションは化学反応ダイナミクス研究の強力なツールである。本発表では、AIMD シミュレーションによって反応中のエネルギー移動と振動モードの関係を解明するための新しい手法[1]を報告する。通常のフーリエ変換は平衡状態の周波数解析の手法であるが、非平衡状態の時間-周波数解析を行う方法として、下式で示される短時間フーリエ変換(ST-FT)がある。

$$S(t,\omega)=\frac{1}{2\pi}\int_{-\infty}^{\infty} f(t,t')h(t'-t)\exp(-i\omega t')dt' \qquad (1)$$

ここで t, ωはそれぞれ時間と周波数を示す。さらにエネルギー移動を記述するために式(1)の f として、下式に示したエネルギー変化の時間相関関数を定義した。

$$f(t,t')\equiv\left\langle \dot{E}_i(t)\cdot\dot{E}_i(t+t')\right\rangle \quad \text{また、} \dot{E}_i(t)=\dot{T}_i(t)+\dot{V}_i(t) \qquad (2)$$

ここで T と V はそれぞれ運動エネルギーとポテンシャルエネルギーである。ポテンシャルエネルギーを部分系に分割するために、エネルギー密度解析(EDA)[2]を用いている。図1は二つの CO_2 分子の衝突反応の AIMD シミュレーション結果を示している。(a), (b)より約2.5ピコ秒で衝突が起こり、その際分子間に複雑なエネルギー移動が起きている。(c)がエネルギー移動スペクトログラムである。CO_2 は約 670、1390、2350 cm^{-1} の振動モードを持つが、この反応では主に 2350 cm^{-1} の逆対称伸縮モードを通じてエネルギーが移動していることが分かる。

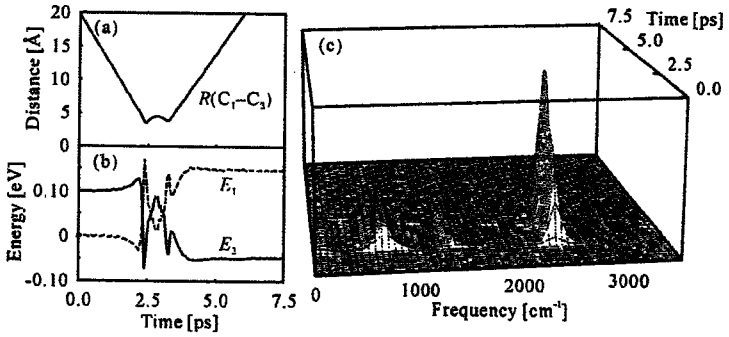

図1. 二つの CO_2 分子の衝突反応に対する AIMD シミュレーション結果. (a) C 原子間距離の時間変化, (b) 各分子に分割されたエネルギーの時間変化, (c) エネルギー移動スペクトログラム.

[1] Y. Yamauchi and H. Nakai, *J. Chem. Phys.*, *submitted*.
[2] H. Nakai, *Chem. Phys. Lett.*, 363 (2002) 73.
[3] Y. Yamauchi, H. Nakai, and Y. Okada, *J. Chem. Phys.*, 121 (2004) 11098.
[4] M. Tamaoki, Y. Yamauchi, and H. Nakai, *J. Comput. Chem.*, 26 (2005), *in press*.

第 85 回日本化学会春季年会,
神奈川大学, (神奈川) 2005 年 3 月.

直鎖アルケンのメチル基内部回転運動におけるπ*-σ*超共役効果

(早大理工) ○一色俊宏・河村芳海・中井浩巳

π*-σ* hyperconjugation mechanism on the rotational barrier of straight chain alkenes

(Waseda Univ.) ISSHIKI, Toshihiro; KAWAMURA, Yoshiumi; NAKAI, Hiromi

【緒言】メチル基の内部回転運動は、非共有結合に関する基礎的な問題として興味深い現象である。当研究室では、置換トルエンの励起に伴うメチル基回転障壁の変化について、π*-σ*超共役効果を考慮することで理論的な説明に成功した。芳香環に結合したメチル基に対しては、π*-σ*超共役はメチル基に結合した炭素とオルト炭素が反結合性のときに出現するということが経験的に分かっている。本研究では直鎖アルケンに結合したメチル基に対しても、π*-σ*超共役が存在するのか、またその発現条件は芳香環と同様であるのかを理論的に検討する。

【計算方法】扱った化合物は二位にメチル基が結合した直鎖アルケンである (Fig. 1)。計算レベルは基底状態で HF/cc-pVDZ、励起状態で CIS/cc-pVDZ とし、メチル基回転に対するポテンシャルカーブから回転障壁を計算した。

【結果・考察】まず、2-methyl-1,3,5-hexatriene (N=3)のメチル基内部回転について検討した。回転障壁は基底状態 (S_0)で 1071 cm^{-1}、励起状態 (S_1)で 436 cm^{-1}となり励起により減少した。メチル基回転に伴う励起エネルギーの変化$\Delta E_{S_0 \to S_1}$は、軌道エネルギー変化Δεと良い相関を示し (Fig. 2 (a,b))、ε_{LUMO}とε_{HOMO} (Fig. 2 (c,d))ともに回転障壁変化に寄与することが示された。Fig. 3 にHOMOとLUMOの等高線図を示す。HOMOではθ=0°、LUMOではθ=60°にπ*-σ*超共役が現れており、芳香環の場合と同様に、メチル基の置換したCとメチル基面外H近傍のCが反結合性である時に超共役が出現することが確認された。π*-σ*超共役は各配向での軌道エネルギーの安定化に寄与しており、HOMOとLUMOの超共役を考慮することで励起による回転障壁変化を説明することができた。次に、回転障壁に対する共役鎖長依存性を調べた (Table 1)。S_0での回転障壁の大きさは 1070 cm^{-1}程度で鎖長による変化は小さいが、S_1では共役鎖の伸長に伴い回転障壁は大きくなる。超共役効果に関与するメチル基の面外Hの軌道電子密度は、共役鎖の伸長に伴い減少し (Table 2)、結果として超共役効果が小さくなる。したがって、Table 1 の励起に伴う障壁変化の減少は、この超共役効果の減衰に起因することがわかった。

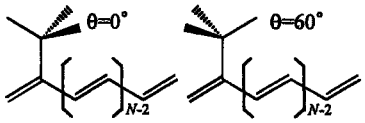

Fig.1 . メチル基置換直鎖アルケン

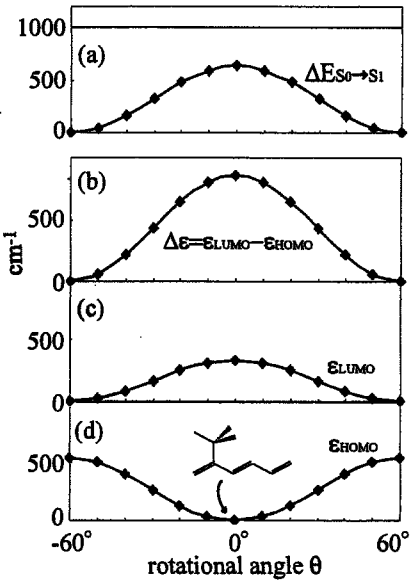

Fig. 2 . 2-methyl-1,3,5-hexatriene の
(a) 励起エネルギー変化 ($\Delta E_{S_0 \to S_1}$)
(b) 軌道エネルギー変化 (Δε)
(c) LUMOの軌道エネルギー (ε_{LUMO})
(d) HOMOの軌道エネルギー (ε_{HOMO})

Table 1 . $C_{2N}H_{2N+1}CH_3$(N=2～6)のS_0、S_1での回転障壁と励起による変化ΔE(cm^{-1})

$C_{2N}H_{2N+1}CH_3$	S_0	S_1	ΔE
N=2	1054	-157	-1211
N=3	1071	436	-635
N=4	1069	677	-391
N=5	1068	806	-263
N=6	1068	883	-185

(負の値は安定配向が逆になった事を表す)

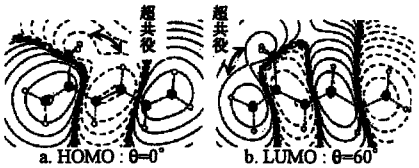

Fig. 3 . 2-methy-1,3,5-hexatriene のMO等高線図

Table 2 . 面外HのLöwdin軌道電子密度

$C_{2N}H_{2N+1}CH_3$	HOMO(θ=0°)	LUMO(θ=60°)
N=2	0.0162	0.0291
N=3	0.0069	0.0134
N=4	0.0037	0.0072
N=5	0.0022	0.0044
N=6	0.0015	0.0029

第 85 回日本化学会春季年会,
神奈川大学, (神奈川) 2005 年 3 月.

内殻励起に適した hybrid 汎関数の開発

(早大理工) ○中田彩子・今村穣・中井浩巳

Development of the hybrid functional for core excitations

(Waseda Univ.) NAKATA, Ayako; IMAMURA, Yutaka; NAKAI, Hiromi

時間依存密度汎関数法(TDDFT)は、比較的少ない計算コストで定量的な結果を与えることから、価電子励起状態の計算に盛んに用いられている。しかし、これまで内殻励起状態計算にはほとんど適用されてこなかった。本研究室ではこれまで、従来の汎関数を用いてTDDFT計算を行い、内殻励起に関する計算精度を検証してきた[1]。CO, C_2H_2, C_2H_4, H_2CO, N_2分子の 1s-π*の励起エネルギーをTDDFT, TDHF/cc-pCVTZで計算したところ、全ての分子においてTDHFは 5 eV以上過大評価、pure-TDDFTでは 15 eV以上過少評価した。それに対し、HF 交換項とDFT交換相関項の両方を含むhybrid汎関数を用いた場合は精度よい結果が得られ、特にBHHLYPは誤差 2.8 eVと最もよい結果を与えた(Table 1)。しかし、原子化エネルギーなど価電子が重要な役割を果たす物理量では、B3LYPが精度の高い結果を与える事が知られている。そこで本研究では、内殻電子および価電子の挙動がそれぞれBHHLYPおよびB3LYPに従うようなhybrid汎関数core-valence (CV)-B3LYPを提案する。具体的には、交換相関項を次式のように内殻電子、価電子の寄与に分割する。

Table 1. Mean errors of core excitation energies [eV].[1]

Method	Mean error
TDHF	+11.13
BHHLYP	-2.80
B3LYP	-11.98
BLYP	-17.89
SVWN5	-21.88

$$E_X = a_{cc}\sum_{ij}^{core} K_{ij} + 2a_{cv}\sum_{i}^{core}\sum_{m}^{valence} K_{im} + a_{vv}\sum_{mn}^{valence} K_{mn} + (1-a_{cc})E_x^S[\rho_c] + (1-a_{vv})E_x^S[\rho_v] + (1-a_{cv})\left(E_x^S[\rho] - E_x^S[\rho_c] - E_x^S[\rho_v]\right)$$
$$+ b_{cc}E_x^{B88}[\rho_c] + b_{vv}E_x^{B88}[\rho_v] + b_{cv}\left(E_x^{B88}[\rho] - E_x^{B88}[\rho_c] - E_x^{B88}[\rho_v]\right)$$

$$E_C = (1-c_{cc})E_c^{VWN}[\rho_c] + (1-c_{vv})E_c^{VWN}[\rho_v] + (1-c_{cv})\left(E_c^{VWN}[\rho] - E_c^{VWN}[\rho_c] - E_c^{VWN}[\rho_v]\right)$$
$$+ c_{cc}E_c^{LYP}[\rho_c] + c_{vv}E_c^{LYP}[\rho_v] + c_{cv}\left(E_c^{LYP}[\rho] - E_c^{LYP}[\rho_c] - E_c^{LYP}[\rho_v]\right)$$

KはHF交換項、ρ_cは内殻電子密度、ρ_vは価電子密度を表している。係数a_{cc}, b_{cc}, c_{cc}はBHHLYP、a_{vv}, b_{vv}, c_{vv}はB3LYP、a_{cv}, b_{cv}, c_{cv}は両者の平均値に一致させた。上式に対するFock演算子は、内殻軌道と価電子軌道で異なった形となるが、Roothaanの結合演算子法によりこれらを統一した。Table 2 にCV-B3LYP, B3LYP, BHHLYP/6-31GによるN_2の軌道エネルギーを示す。期待どおり、CV-B3LYPの内殻軌道エネルギーはBHHLYPに近く、価電子軌道エネルギーはB3LYPに近くなっている。軌道エネルギーはTDDFTでの励起エネルギー計算に直接影響するため、内殻励起、価電子励起エネルギーがバランスよく記述されることが期待される。今後、本手法に基づいてTDDFT法を開発し、励起エネルギーの計算精度を検証する予定である。

Table 2. Orbital energies of N_2 molecule [eV].

	B3LYP	CV-B3LYP	BHHLYP
1s	-393.234	-406.736	-406.671
1s	-393.188	-406.698	-406.605
2sσ	-32.101	-32.090	-36.031
2sσ*	-14.667	-14.629	-17.347
2pπ	-12.974	-12.988	-14.808
2pσ	-11.426	-11.502	-13.861

[1] 今村, 大塚, 中井, 分子構造総合討論会 2004, 3C05.

第85回日本化学会春季年会,
神奈川大学,（神奈川）2005年3月.

Natural Atomic Orbitalに基づくEnergy Density Analysisの改良

（早大理工）○竹内真理・馬場健・中井浩巳

Development of Energy Density Analysis based on Natural Atomic Orbital

(Waseda Univ.) TAKEUCHI, Mari; BABA, Takeshi; NAKAI, Hiromi

【緒言】　当研究室で開発されたEnergy density analysis (EDA)[1]は系全体のエネルギーを構成原子に分割する解析手法である。EDAの分割手法には電子密度解析の1つである、Mulliken population analysis (MPA)[2]の類推を用いているが、MPAには(i)負の値を与えうる、(ii)基底関数に対する依存性が大きいという欠点があることが知られている。従って、EDAの結果はMPAの影響を受ける可能性がある。電子密度解析にはMPAの欠点を補うべく、natural population analysis (NPA)[3]などが提案されている。

そこで本研究では、NPAの基底であるnatural atomic orbital (NAO)に基づくEDAを作成し、EDAの改良を試みた。そして、MPAの欠点がEDAの結果にどのような影響を及ぼすのか、また、NAOに基づくEDAではそれが改善されるかを系統的に検討した。

【理論】　AO$|\chi_\nu\rangle$に変換行列Xを作用させてNAO$|\chi'_\mu\rangle$を得る(式(1))。NAOに基づくEDAでは、例えば運動エネルギー項の分割は式(2)で表される。核電子引力エネルギー項やクーロンエネルギー項も同様に分割を行い、これらを原子ごとに部分和をとることで全エネルギーを局所的な値に分割する。

$$|\chi'_\mu\rangle = \sum_\nu X_{\nu\mu}|\chi_\nu\rangle \qquad (1)$$

$$T_S^A(NAO) = \sum_{\mu\in A}(\mathbf{P'T'})_{\mu\mu} \equiv \sum_{\mu\in A}\{(\mathbf{X^{-1}PX^{-1\dagger}})(\mathbf{X^\dagger TX})\}_{\mu\mu} \qquad (2)$$

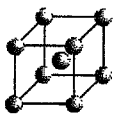

Fig. 1 Li_9^+ cluster

【結果と考察】　まず、Li_9^+ cluster (Fig. 1)に対して、MPAおよびNPAの基底関数依存性を検討した (Fig. 2(a))。MPAでは、6-31Gおよび6-31G*に対してpopulationが負の値をとり、また6-311Gおよび6-311G*で過大評価することが示された。一方、NPAでは、基底関数依存性が小さく、信頼性の高い値を与えることがわかった。Fig.2(b)は、MPA・NPAに基づくEDAの結果を示している。両者に対してそれぞれpopulationと同様の挙動が示され、NAO基底を用いることの有効性が確認できた。

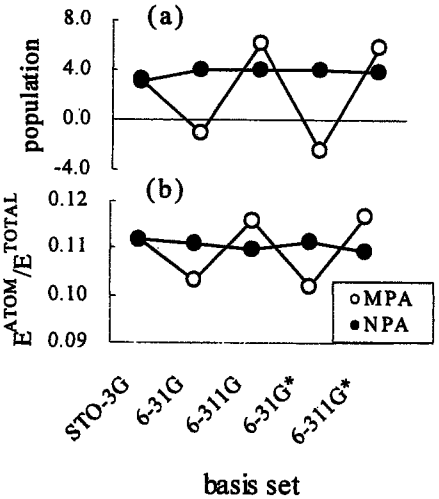

Fig. 2 (a) 中心のLiに対するpopulation (b) 中心のLiに対するEDAの結果

[1] H. Nakai, Chem. Phys. Lett., 363, 73-79 (2002).
[2] R. S. Mulliken, J. Chem. Phys. 23, 1833, 1841, 2338, 2343 (1955).
[3] A. E. Reed, R. B. Weinstock, and F. Weinhold, J. Chem. Phys. 83, 735 (1985).

第 85 回日本化学会春季年会,
神奈川大学, (神奈川) 2005 年 3 月.

Ab initio NOMO 法における回転運動の取り扱い: 振動と回転のカップリング

(早大理工) ○宮本開任・星野稔・中井浩巳

Elimination of rotational motion in *ab initio* NOMO theory:

Coupling between the rotational and vibrational motions (School of Science and Engineering, Waseda University) MIYAMOTO, Kaito; HOSHINO, Minoru; NAKAI, Hiromi

【緒言】当研究室では電子と核の波動関数を同時に求める *ab initio* NOMO 法の開発を行ってきた[1-5]。NOMO 法の電子・核の波動関数には、$3N$ 自由度(N は粒子数)の運動、つまり電子・振動・回転・並進状態が含まれている。これまで、電子および振動状態の記述には 1 粒子 Gauss 型基底関数が有効であることを実証してきたが、逆に回転および並進状態の記述には適さず、並進・回転運動を取り除くことで精度の向上を図ってきた。本研究では並進・回転運動の除去をより厳密に扱うための理論を提案し、その効果を数値的に評価した。

【理論】NOMO 法の Hamiltonian および並進・回転運動の演算子はそれぞれ式(1), (2), (3)のように表される。これらを用いると並進・回転運動を分離した TRF-NOMO 法の Hamiltonian は、式(4)のように書かれる。ここで、回転運動演算子(3)の分母の慣性モーメント $\hat{I}_\alpha^0$ は N 体演算子である。そこで、平衡座標 $\mathbf{x}_\mu^0=(x_\mu^0, y_\mu^0, z_\mu^0)$ のまわりに Taylor 展開することで、回転運動の効果を 1 体、2 体、・・・の演算子に分類する。特に 0 次項は剛体回転子に相当し、1 次項より振動-回転カップリングの効果が含まれる。式(5)を一体近似の下で変分法を適用すると、並進・回転運動を分離した TRF-NOMO/HF 方程式が導出される。

$$\hat{H}=\hat{T}+\hat{V}=\hat{T}_e+\hat{T}_n+\hat{V}_{ee}+\hat{V}_{en}+\hat{V}_{nn} \tag{1}$$

$$\hat{T}_T(\mathbf{x})=-\frac{1}{2M}\sum_\mu \nabla(\mathbf{x}_\mu)^2-\frac{1}{M}\sum_{\mu<\nu}\nabla(\mathbf{x}_\mu)\cdot\nabla(\mathbf{x}_\nu) \tag{2}$$

$$\hat{T}_R=\sum_\alpha^{x,y,z}\frac{\hat{L}_\alpha^{\,2}}{2\hat{I}_\alpha} \tag{3}$$

$$\hat{H}_{TRF}=\hat{H}-\hat{T}_T-\hat{T}_R \tag{4}$$

$$E_{TRF}=\frac{\langle\Phi_0|\hat{H}_{TRF}|\Phi_0\rangle}{\langle\Phi_0|\Phi_0\rangle} \tag{5}$$

【計算結果】Table 1 は、H_2 の基底状態に対する NOMO/HF 法、並進運動を分離した TF-NOMO/HF 法、並進運動と剛体回転子を分離した TRF0-NOMO/HF 法、さらに 1 次の振動-回転カップリングを考慮に入れた TRF1-NOMO/HF 法による全エネルギー(E_{tot})を示す。また、並進(E_{trans})・回転(E_{rot})・振動(E_{vib})・電子(E_{elec})エネルギー成分を示す。通常の NOMO/HF エネルギーにはかなりの並進・回転エネルギーが混入していることがわかる。それらを取り除くことで全エネルギーが飛躍的に改善される。また、剛体回転子の効果 (~0.030 hartree)に比べ、振動-回転カップリングの効果(~0.003 hartree)は 10%程度であることも確認された。

Table 1. Total (E_{tot}), translational (E_{trans}), rotational (E_{rot}), vibrational (E_{vib}), and electronic (E_{elec}) energies (in hartree) calculated by the TRC-, TF-, and TRF-NOMO/HF methods.

	NOMO/HF	TF-NOMO/HF	TRF0-NOMO/HF	TRF1-NOMO/HF
E_{tot}	-1.052361	-1.074307	-1.104084	-1.105728
E_{trans}	0.018339 (	0.027095)	(0.095085)	(0.099074)
E_{rot}	0.011398	0.016918	(0.080842)	(0.086430)
E_{vib}	0.006941	0.010177	0.014243	0.012644
E_{elec}	-1.089038	-1.101401	-1.118327	-1.118372

Nuclear basis sets: 7s7p7d, electronic basis sets: cc-pVTZprimitive(5s2p1d)

[1] M. Tachikawa, K. Mori, H. Nakai, K. Iguchi, *Chem. Phys. Lett.*, **290** (1998) 437.
[2] H. Nakai, *Int. J. Quantum Chem.*, **86** (2002) 511.
[3] H. Nakai, K. Sodeyama, M. Hoshino, *Chem. Phys. Lett.*, **345** (2001) 118.
[4] H. Nakai, K. Sodeyama, *J. Chem. Phys.*, **118** (2003) 1119.
[5] H. Nakai, M. Hoshino, K. Miyamoto, S. Hyodo, *J. Chem. Phys.*, *in press*.

第 85 回日本化学会春季年会,
神奈川大学, (神奈川) 2005 年 3 月.

Knowles-Handy アルゴリズムに基づく ab initio NOMO/FCI 法の開発とその応用

(早大理工) ○桐生大義・袖山慶太郎・中井浩巳

Development of ab initio NOMO/FCI method based on Knowles-Handy algorithm

(School of Science and Engineering, Waseda University) KIRYU, Hiroyoshi; SODEYAMA, Keitaro; NAKAI, Hiromi

[緒言] 我々の研究室では、電子および核の波動関数を同時に求めることのできる ab initio nuclear orbital plus molecular orbital (NOMO)法の開発を行ってきた。NOMO 法の定量性を向上させるため、これまでに核の波動関数に混入する並進および回転運動の除去や、多体効果を考慮した方法を開発してきた[1-5]。本研究では、Knowles-Handy アルゴリズム[6]に基づく NOMO/FCI 法を開発し、多体効果の記述にどのような改善が見られるか検討する。さらに NOMO/FCI 法を行うことで求められる、励起状態の波動関数、特に多粒子励起状態に関して検証する。

[基底状態] 水素分子における NOMO/FCI 法の計算結果と、NOMO/HF エネルギーを表 1 に示した。また電子-電子、電子-核及び核-核相関エネルギーも同時に示した。各相関エネルギー E_{corr} に関しては次のように見積もった。

$$E_{corr}^{tot} = E_{FCI}^{n,e} - E_{HF},$$

$$E_{corr}^{n-n} = E_{FCI}^{n} - E_{HF}, \quad E_{corr}^{e-e} = E_{FCI}^{e} - E_{HF}, \quad E_{corr}^{n-e} = E_{corr}^{tot} - E_{corr}^{n-n} - E_{corr}^{e-e}$$

ここで E_{FCI}^{e} および E_{FCI}^{n} は電子及び核それぞれ一方のみの全励起配置を考慮した場合のエネルギーである。多体効果を取り込むことにより、全エネルギーに対して 0.0714 hartree の改善が見られた。この内訳を見てみると電子-核相関の値は核-核相関に比べて非常に大きくなっており、電子-電子相関と同じオーダーであることがわかる。さらに、並進運動の効果を取り除いた TF-NOMO 波動関数を参照関数にした場合、通常の NOMO 波動関数の場合と比べて電子-核相関エネルギーは減少している。これは多体効果の一部は並進運動の記述に使われていたことを示している。

Table 1. Total and correlation energies of H_2 molecule. [hartree] (nuc:3s3p, elec:cc-pVDZ)

	E_{HF}	$E_{FCI}^{n,e}$ (E_{corr}^{tot})	E_{corr}^{n-n}	E_{corr}^{e-n}	E_{corr}^{e-e}
NOMO	-1.0495	-1.1209(-0.0714)	-0.0014	-0.0355	-0.0345
TF-NOMO	-1.0722	-1.1335(-0.0614)	-0.0008	-0.0260	-0.0346

[励起状態] 次に、今回の方法により得られた電子励起状態における振動励起状態(S_1,v=1)の波動関数を用いて、(S_0,v=0)→(S_1,v=0)および、(S_0,v=0)→(S_1,v=1)の励起に対するフランク・コンドン因子を求めた(図 1)。これは以下の式で表される核の波動関数の重なりを計算することで容易に見積もることができる。

$$\Psi_{FCI} = \left(1 + \sum_{\nu=1}^{n+N} \hat{C}_\nu\right)\Psi_{HF}$$

n および N はそれぞれ電子と核の数である。フランク・コンドン因子 v=0 を基準としたところ、実験値と良い相関を示していることがわかった。これは S_0での平衡核間距離 0.7414Å に対して S_1では 1.2928Å になることに起因する。今後はより高振動状態への適用を検討する。

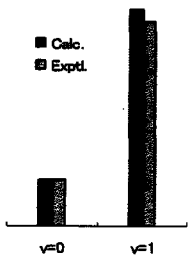

Fig.1. Franck-Condon factors of H_2 excitations from (S_0,v=0) to (S_1,v=0) and (S_1,v=1).

[1] M. Tachikawa, K. Mori, H. Nakai, K. Iguchi, Chem. Phys. Lett., 290 (1998) 437. [2] H. Nakai, Int. J. Quantum Chem., 86 (2002) 511. [3] H. Nakai, K. Sodeyama, M. Hoshino, Chem. Phys. Lett., 345 (2001) 118. [4] H. Nakai, K. Sodeyama, J. Chem. Phys., 118 (2003) 1119. [5] H. Nakai, M. Hoshino, K. Miyamoto, S. Hyodo, J. Chem. Phys., (2005) *in press*. [6] P. J. Knowles, N. C. Handy, Chem. Phys. Lett., 109 (1984) 417.

第 85 回日本化学会春季年会,
神奈川大学, (神奈川) 2005 年 3 月.

大規模電子状態計算のための divide-and-conquer 法の検証と改良

(早大理工) ○赤間知子・小林正人・中井浩巳

Assessment and improvement of divide-and-conquer method for ab initio calculation of large system

(Sch. of Sci. & Eng., Waseda Univ.) AKAMA, Tomoko; KOBAYASHI, Masato; NAKAI, Hiromi

緒言　従来の HF 及び DFT 計算のボトルネックは Fock 行列要素の計算とその対角化にあり、基底関数の数 N に対してそれぞれ $O(N^4)$、$O(N^3)$の計算コストを要する。このオーダーを落とす取り組みがこれまでに様々なされており、特に Coulomb 項に関しては高速多重極展開法などの $O(N\log N)$法が日常的に用いられている。しかし、HF 交換項や対角化の効率化の研究は行われているものの、実用段階にはいたっていない。本研究では、$O(N)$法の一つである divide-and-conquer (DC) 法[1,2]を用いた HF 計算(DC-HF)を行い、その精度や SCF 収束性などについて検証を行った。

divide-and-conquer 法の理論と Hartee-Fock 計算への適用　DC 法では全系の密度行列 ρ を部分系αの密度行列 ρ^α の和として表すことにより $O(N)$を達成している。

$$\rho_{\mu\nu} = 2\sum_{i}^{occ} C_{\mu}C_{\nu} = \sum_{\alpha} \mathbf{p}^{\alpha}_{\mu\nu}\rho_{\mu\nu} = \sum_{\alpha}\rho^{\alpha}_{\mu\nu} \quad , \quad \rho^{\alpha}_{\mu\nu} = 2\sum_{i} f_{\beta}(\varepsilon_F - \varepsilon_i^{\alpha})\sum_{\mu\nu}\mathbf{p}^{\alpha}_{\mu\nu}C^{\alpha}_{\mu}C^{\alpha}_{\nu} \qquad (1)$$

ここで、$f_\beta(x)$ は Fermi 関数である。具体的には、まず全系をいくつかの central region に分割し、その周り(buffer region)を合わせて部分系を作り、部分系の HF (または KS)方程式を解く。各部分系は共通の Fermi 準位 ε_F によってつながり、これにより全系の電子数を保存させる。全系のエネルギーは式(2)で表される。

$$E_{HF} \cong \sum_{\alpha} E^{\alpha}_{DC-HF} = \frac{1}{2}\sum_{\alpha}\sum_{\mu\nu}\rho^{\alpha}_{\mu\nu}\left(\mathbf{H}^{core}_{\mu\nu} + \mathbf{F}_{\mu\nu}\right) \qquad (2)$$

DC-HF 計算プログラムを独自に開発し、GAMESS に実装した。ポリアセチレンの計算を行ったところ、エネルギーの誤差は数 mhartree 程度で、1 iteration あたりの対角化のコストが $O(N)$となることが確かめられた(図 1)。また、図 2 に SCF 繰り返し過程における $C_{120}H_{122}$ 分子のエネルギーの収束値からの差を示した。比較として全系の HF 計算の結果も示す。全系の HF 計算ではエネルギーが単調減少して収束するのに対し、DC-HF ではエネルギーが振動し、収束値を下回ることがあることがわかった。更に収束性の悪さも見られた。この原因を探るべく、iteration ごとの自然軌道(NO)の占有数を調べた結果、2 を超えるまたは負の値をとる軌道が存在した。すなわち N-representability が満たされていないことが示された。図 3 に SCF 過程において、NO を 2 を超えて占有する電子の数の変化を示した。実際、N-representability の崩れとエネルギーが下がりすぎることは密接に関係していることがわかる。更に Fermi 準位とも相関することがわかった。したがって、Fermi 準位をうまく調整する、N-representability の崩れを改善する、などによって DC-HF 計算の収束性が向上するものと期待される。

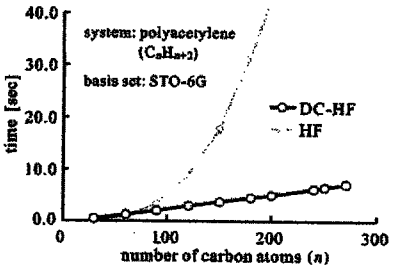

Fig. 1. Time to diagonalize Fock matrix per SCF iteration.

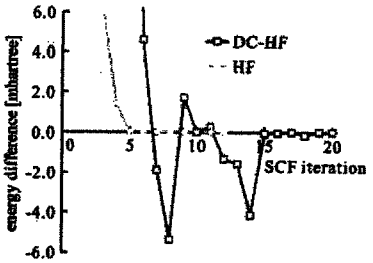

Fig. 2. Difference from converged energy in each SCF iteration.

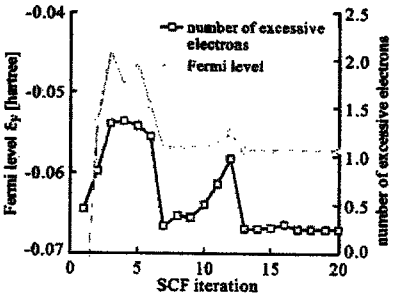

Fig. 3. Number of electrons which excessively occupy NOs and Fermi level in each iteration.

[1] W. Yang, Phys. Rev. Lett. **66**, 1438 (1991).
[2] W. Yang and T.-S. Lee, J. Chem. Phys. **103**, 5674 (1995).

第 85 回日本化学会春季年会,
神奈川大学, (神奈川) 2005 年 3 月.

Interaction-EDA を用いた Cu/Zn 触媒による Methanol 合成反応の理論的研究

(早大理工) ○飯田涼子・河村芳海・中井浩巳

A theoretical study on the methanol synthesis with Cu/Zn catalyst using Interaction-EDA

(Waseda Univ.) Iida, Ryoko ; Kawamura, Yoshiumi ; Nakai, Hiromi

【緒言】二酸化炭素からのメタノール合成反応は Cu/Zn 系の触媒を用いると効率よく行うことができる。より効果的な触媒開発に向けて、触媒作用や反応メカニズムに関する数多くの実験的、理論的研究がなされてきた。この触媒反応に対して、formate、dioxomethylene、methoxy という 3 つの中間体を経て進行すること[1]、dioxomethylene の生成過程が律速であること[2]、Zn 蒸着により活性化されること[3]が報告されている。しかし、Zn の助触媒効果については未だ明らかではない。そこで本研究では、formate から dioxomethylene が生成する過程に対して理論計算を行い、Zn の助触媒効果を検討した。

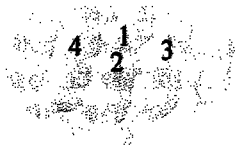

Fig. 1. $Cu_{22-N}Zn_N$ (N=0,2) クラスターモデル。
$Cu_{20}Zn_2$ #1 は 1 と 2、
$Cu_{20}Zn_2$ #2 は 3 と 4 を Zn に置換。

【計算方法】Cu(111)表面のモデルとして、Fig. 1 に示す Cu_{22} クラスターを用いた。Cu/Zn 触媒のモデルとしては Cu_{22} クラスターのうちの 2 原子を Zn 原子で置換した $Cu_{20}Zn_2$ (#1, 2) クラスターを用いた。計算レベルは Hartree-Fock 法、基底関数は C, H 原子には 6-31G**、O 原子には 6-31+G**、Cu, Zn 原子には 6-31G を用いた。

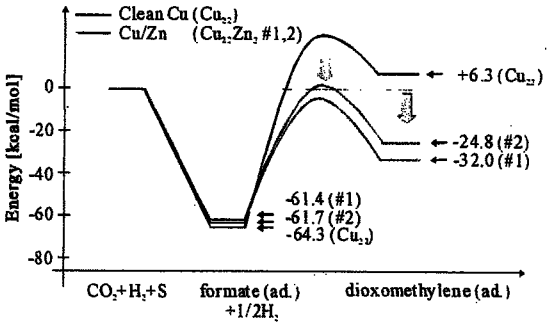

Fig. 2. Cu_{22} および $Cu_{20}Zn_2$ 上での dioxomethylene 生成のエネルギーダイアグラム

【結果と考察】Cu_{22} と $Cu_{20}Zn_2$ 上において、反応物から dioxomethylene が生成する過程のエネルギーダイアグラムを Fig. 2 に示す。 formate の生成熱は、Zn 置換による変化がほとんど見られない。一方、dioxomethylene の生成熱は、Cu_{22} のときには+6 kcal/mol と吸熱的であるのに対し、$Cu_{20}Zn_2$ では-24, -32kcal/mol と発熱的である。以上から dioxomethylene 生成過程における活性化エネルギーが Zn 置換により低下し、反応が促進されることが予想される。Table 1 に示す電子密度解析より、いずれの表面においても dioxomethylene 生成過程において表面(S)から吸着子(A)へ約 1.2 個の電子が移動することがわかる。さらに Zn 蒸着表面では Zn の位置に関わらず、Zn からより多くの電子移動が起こることもわかる。この電荷移動量の変化による影響をエネルギーの単位で見積もるため、Interaction-EDA [4]を行った (Table 2)。その結果、エネルギー的にも電荷移動相互作用に Zn が大きく関与することが示された。

Table 1. dioxomethylene生成に伴う Löwdin電子密度変化. (* はZn原子)

atom		Cu_{22}	$Cu_{20}Zn_2$ #1	$Cu_{20}Zn_2$ #2
Cu/Zn	1	-0.19	-0.25 *	-0.16
	2	-0.19	-0.25 *	-0.16
	3	-0.14	-0.17	-0.23 *
	4	-0.17	-0.17	-0.27 *
	:	:	:	:
S total		-1.21	-1.24	-1.28
A total		1.21	1.24	1.28

Table 2. Interaction-EDAによるS→A電荷移動相互作用成分 (kcal/mol). (* はZn原子)

atom		Cu_{22}	$Cu_{20}Zn_2$ #1	$Cu_{20}Zn_2$ #2
Cu/Zn	1	-100	-156 *	-45
	2	-100	-156 *	-45
	3	-125	-81	-177 *
	4	-98	-37	-130 *
	:	:	:	:
total		-235	-288	-285

[1] P.A. Taaylor, *et al.* Surf. Sci. **191**, 261 (1992).
[2] J. Nakamura, *et al.* J. Vac. Sci. Technol. A **1464**,14 (1996).
[3] T. Fujitani, J. Nakamura, Appl. Catal., **191**, 111 (2000).
[4] Y. Kawamura, H. Nakai, J. Comp. Chem., **25**, 1882 (2004).

第 85 回日本化学会春季年会,
神奈川大学, (神奈川) 2005 年 3 月.

無電解析出における還元剤酸化反応に対する銅表面触媒活性の DFT 計算による定量的解析

(早大理工) ○島田拓哉, 小田切秀一, 中井浩巳, 本間敬之, 逢坂哲彌

DFT Study on the Catalytic Activity of Copper Surface for the Oxidation Reactions of Reductants for Electroless Deposition Processes

(School of Sci. & Eng., WASEDA Univ.) ○Takuya SHIMADA, Syuuichi ODAGIRI, Hiromi NAKAI, Takayuki HOMMA, Tetsuya OSAKA

1. 背景　無電解析出は外部電源を使用しない薄膜形成プロセスであり, ナノレベルでの精密な制御を行うことが可能であることからエレクトロニクスなどの様々な分野において広く用いられているが, この反応機構は金属イオンの還元析出と還元剤の酸化反応が同時に進行し, 更に析出した金属表面が還元剤の反応に対して触媒活性を持つ複雑なものであり未だ不明点が多い. 本検討ではこの中でも最も重要な還元剤の酸化反応に注目し, 反応中間体のエネルギーや電荷を見積もり可能な密度汎関数法(DFT)を用いて定量的な解析を行った. 代表的還元剤であるジメチルアミンボラン(DMAB), 次亜リン酸, 及びホルムアルデヒドの酸化反応に着目し, 溶媒和を考慮した吸着機構, 銅表面上における還元剤の反応機構, そして銅表面の還元剤に対する触媒活性について解析した.

2. 方法　計算には Gaussian98 プログラムを用いた. 分子の構造最適化並びにエネルギー計算には密度汎関数法(DFT)の一種である B3LYP を用いた. 溶媒和計算には Cosmo Polarized Continuum model(CPCM)モデルを用いた. 銅表面は Cu(1 1 1)面, 構成原子を 4 及び 22 とするクラスターモデルを用いた. 基底関数として B,C,P,H には 6-31G**, O には分散関数を組み込んだ 6-31+G**, Cu には Hay & Wadt ECP を用いた.

3. 結果考察　上記還元剤の銅表面への吸着機構は溶液中から銅表面に近づく過程において, 障壁としての溶媒和エンタルピーを超えた後に銅表面への吸着エネルギー分だけ安定化した. 脱離機構にも同様の障壁が存在し, 還元剤によってこれらのエネルギーが異なり, 反応サイクルの観点から銅表面の触媒活性を解明する手掛かりが得られた.

一方, これらの還元剤の酸化反応は H 脱離と OH 配位の置換反応により進行するが, 還元剤と同じくこれらの分子も銅表面上で吸着していることを考慮し酸化反応のエネルギーダイアグラムを作成した(図参照). 全ての還元剤は先に H を脱離させ 3 配位中間体状態を経由する経路が最も安定であることが示唆された. また水素脱離過程のエネルギー変化の正負(図中 : H 脱離)が銅表面の還元剤に対する触媒活性の有無と対応していることが示唆され, 触媒活性の発現に寄与する要素の一つと考えられた.

4. 謝辞　本研究は文部科学省 21 世紀 COE プログラム「実践的ナノ化学教育研究拠点」の助成により実施した.

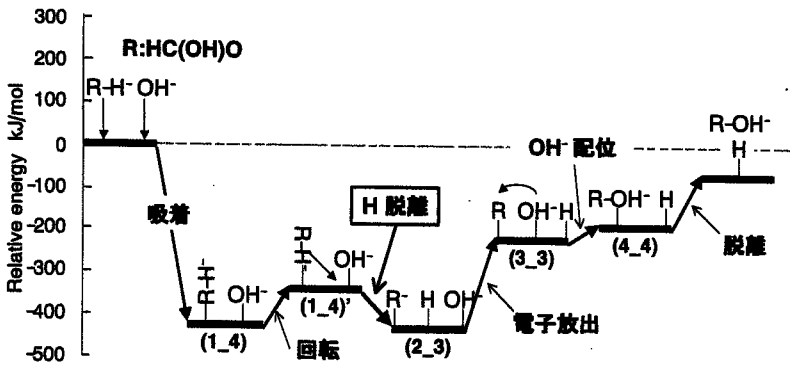

図　Cu_{22} クラスター上でのホルムアルデヒドの酸化反応エネルギーダイアグラム